

**Knud Højgaard Conference on  
Advanced Cement-Based Materials:  
Research and Teaching**

Published by BYG-DTU

Department of Civil Engineering, Brovej, Building 118, Technical University of Denmark  
2800 Kgs. Lyngby, Denmark

Tel : + 45 45 25 17 00 Fax : + 45 45 88 32 82

<http://www.byg.dtu.dk> E-mail: [jsa@byg.dtu.dk](mailto:jsa@byg.dtu.dk)

© 2006 BYG-DTU – All rights reserved.

ISBN: 87-7877-227-3

Printed by Nyt Teknisk Forlag, Ingerslevsgade 44, 1705 København V, Denmark

Credit photo 1st cover page: GPAG van Zijl and H. Stander

***Publisher's note:*** *this book has been produced from files provided by the individual contributors. The publisher makes no representation, express or implied, with regard to the accuracy of the information contained in this book and cannot accept any legal responsibility or liability for any errors or omissions that may be made.*

Knud Højgaard Conference on Advanced Cement-Based Materials: Research and Teaching  
12-15 June 2005, Technical University of Denmark, Lyngby, Denmark

**Knud Højgaard Conference on  
Advanced Cement-Based Materials:  
Research and Teaching**

Lyngby, Denmark

12-15 June 2005

**Edited by**  
**Ole Mejlhede Jensen, Mette Geiker and Henrik Stang**  
Technical University of Denmark

**Organized by:**



**Technical University of Denmark**

**Department of Civil Engineering**

**Financial Sponsor:**

**Knud Højgaards Foundation**

**Conference Organizers:**

- Ole Mejlhede Jensen (Technical University of Denmark)
- Mette Geiker (Technical University of Denmark)
- Henrik Stang (Technical University of Denmark)

**Scientific Committee:**

- Ole Mejlhede Jensen (Technical University of Denmark)
- Mette Geiker (Technical University of Denmark)
- Henrik Stang (Technical University of Denmark)
- Surendra P. Shah (Northwestern University, USA)
- David A. Lange (University of Illinois, USA)
- Dale Bentz (National Institute of Standards and Technology, USA)
- R.D. Hooton (University of Toronto, Canada)
- Victor C. Li (University of Michigan, USA)
- Jason Weiss (Purdue University, USA)



## Contents

*Pg.*

### **Foreword**

IX

Ole Mejlhede Jensen, Henrik Stang and Mette Geiker

### ***Invited Presentations***

- |    |   |    |
|----|---|----|
| 1. | <b>Engineering Skills and Future Needs</b><br>Peter Kofoed                                | 1  |
| 2. | <b>The dual nature of technical knowledge</b><br>Peter Kroes                              | 3  |
| 3. | <b>University teaching standards and evaluating teaching and pedagogy</b><br>Paul Ramsden | 17 |

### ***Research***

- |     |   |     |
|-----|---|-----|
| 4.  | <b>Investigations of the Properties of SCC:<br/>a method for measuring thixotropy and viscosity</b><br>Raissa P. Douglas, Amedeo Gregori, Zhihui Sun and Surendra P. Shah | 19  |
| 5.  | <b>A Blocking Criterion for Self-compacting Concrete</b><br>Lars N. Thrane, Henrik Stang and Mette Geiker   | 31  |
| 6.  | <b>Plastic Shrinkage of Self-compacting Concrete</b><br>Bertil Persson  | 43  |
| 7.  | <b>Measurements of Radon Exhalation Rate for Monitoring Cement Hydration</b><br>Konstantin Kovler   | 59  |
| 8.  | <b>Volume Change Mechanisms in Concrete: new Directions for Modelling</b><br>Zachary C. Grasley, David A. Lange and Yi-Shi Liu  | 77  |
| 9.  | <b>The Effect of Admixtures on the Fresh and Consolidated Behaviour of ECC</b><br>GPAG van Zijl and H. Stander  | 89  |
| 10. | <b>Investigation of early age deformation in self-compacting concrete</b><br>Oskar Esping and Ingemar Löfgren   | 103 |
| 11. | <b>Measuring techniques for autogenous strain of cement paste</b><br>Pietro Lura and Ole Mejlhede Jensen  | 119 |
| 12. | <b>Cement Hydration: Building Bridges and Dams at the Microstructure Level</b><br>Dale P. Bentz   | 135 |
| 13. | <b>Strength Development and Microstructure of Fly Ash-cement Mixes at Early Age</b><br>Kiyofumi Kurumisawa and Toyoharu Nawa  | 147 |

14.	<b>The Patch Microstructure in Concrete: Evidence that it is not an Artifact</b>	155
	Sidney Diamond and Niels Thaulow	
15.	<b>Progress towards Quantitative Understanding of Cementitious Microstructures</b>	169
	Karen Scrivener	
16.	<b>Recent Developments of Standard Test Methods for Measuring the Fluid Penetration – Resistance of Concrete and use in Performance Standards</b>	171
	R.D. Hooton	
17.	<b>Moisture Transport in Cementitious Materials – Theory and some Experimental Results</b>	187
	Lars-Olof Nilsson	
18.	<b>The Effect of PP fiber on the Compressive Strength and Water Permeability of Self-Compacting Concrete and High Performance Concrete</b>	205
	G. Ye, G. De Schutter, L. Taerwe and K. van Breugel	
19.	<b>Prediction of Chloride Ingress and Binding in Concrete</b>	215
	Mette Geiker and Erik Pram Nielsen	
20.	<b>Integrated Structures and Materials Design</b>	233
	Victor C. Li	
21.	<b>Calculation of Thermal Stresses in Concrete Pavements at Early Age</b>	247
	Jun Zhang and Zhi Hua Li	
22.	<b>On the Application of Cohesive Crack Modelling in Cementitious Materials</b>	265
	Henrik Stang, John Forbes Olesen, Peter Noe Poulsen and Lars Dick-Nielsen	
23.	<b>Micro-mechanical Analysis of Fiber Reinforced Cementitious Composites using Cohesive Crack Modelling</b>	277
	Lars Dick-Nielsen, Henrik Stang and Peter Noe Poulsen	
24.	<b>A Preliminary Numerical Investigation on the Influence of Material Variability in the Early-age Cracking Behavior of Restrained Concrete</b>	293
	Aleksandra Radlinska, Brad Pease and Jason Weiss	
25.	<b>Experimental Study of Crack Healing of Early Age Cracks</b>	311
	Nynke ter Heide, Erik Schlangen and Klaas van Breugel	
26.	<b>Cracking, Damage and Fracture in four Dimensions</b>	323
	E.N. Landis, T. Zhang, E.N. Nagy, G. Nagy and W.R. Franklin	
27.	<b>Crack Sampling, Treatment and Analysis</b>	335
	Peter Laugesen	
28.	<b>The Modeling of Micostructure to Predict Service Life of Concrete Structures</b>	347
	Kiyofumi Kurumisawa and Toyoharu Nawa	
29.	<b>Dense and Porous Areas in Concrete: An Artifact?</b>	349
	Sidney Diamond	

### ***Teaching***

30.	<b>A system of concepts to enhance the information content of online documents in concrete technology</b>	351
	Jens Borrmann and Joachim Schwarte	
31.	<b>Computer aided teaching in civil engineering materials science at the University of Stuttgart</b>	363
	Joachim Schwarte, Jens Borrmann and Hans-Wolf Reinhardt	
32.	<b>The Virtual Classroom</b>	375
	Per Møller and Mette Geiker	
33.	<b>Graduate Education in a Global Market</b>	383
	M.R. de Rooij	
34.	<b>From slump test to Gibbs' free energy: The Science of Construction Materials</b>	387
	Ole Mejlhede Jensen and Sidney Diamond	
35.	<b>Teaching Building Materials at the Technion – Israel Institute of Technology</b>	389
	Konstantin Kovler	
36.	<b>The Challenge of teaching cement chemistry to civil engineering</b>	391
	Karen Scrivener	
37.	<b>Experiences with Interactive Classroom Technologies for the Implementation of Problem-Based, Peer-Interaction Learning Environment</b>	393
	Jason Weiss, Sebastian Fait, Tom Schmit and Farshad Rajabipour	
38.	<b>Concrete as an Introduction to Civil Engineering</b>	395
	Eric N. Landis	
	<b>Author Index</b>	397



## Foreword

The Knud Højgaard conference “Advanced Cement-Based Materials – Research and Teaching” was hosted by the Department of Civil Engineering at the Technical University of Denmark (BYG•DTU). The event was financially sponsored by the Knud Højgaard Foundation.

BYG•DTU has exceptional laboratory facilities for studying structures, materials and building components. It actively cooperates with foreign research institutions, attracting many visiting foreign researchers. BYG•DTU employs 84 scientific staff members and 33 PhD students; it offers 80 courses and ~400 student projects are run each year.

The Knud Højgaard Foundation was established in 1944 by a donation from the founder of the Danish contractor MT Højgaard A/S. With the aim of promoting research and teaching in concrete technology, the Knud Højgaard Foundation has since 1999 financially sponsored a series of doctoral courses and conferences at DTU within “Advances in Cement-Based Materials”.

The conference dealt with both research and teaching with the aim of promoting international collaboration and exchanging new results from concrete research as well as ideas and views on concrete research and construction materials teaching.



*Selected, courageous conference participants enjoying Danish folk dancing during a social activity of the conference.*

The research themes of the conference were: Fresh state, Early age properties, Microstructure, Transport and Fixation of matter, Mechanics, and Cracking of cement-based materials. The teaching part concerned construction materials in general and focused in particular on concrete technology. Issues dealt with include: Teaching goals, Progression of subjects and Pedagogical form.

In addition to the above mentioned topics, three invited speakers contributed keynote talks at the conference. Peter Kofoed, from MT Højgaard, contributed with a contractors view on 'Engineering skills and future needs'. Peter Kroes, from Delft Technical University, gave philosophical insight into the 'The dual nature of technical knowledge'. Finally, Paul Ramsden, from the Higher University Academy, UK, informed about the state-of-the-art within 'University teaching standards and evaluating teaching and pedagogy'.



*Members of the conference scientific committee posing together with invited speakers.*

About 40 internationally acknowledged researchers and teachers from 13 different countries participated in the event. The untraditional focusing on both research and teaching, separate time slots for discussion together with several social activities created a positive workshop atmosphere with a lively and open debate. Attendees left with inspiration for renewing their construction materials teaching and an updated knowledge on the international research concerning advanced cement-based materials.

**Ole Mejlhede Jensen**

**Mette Geiker**

**Henrik Stang**

*December 2006, Lyngby, Denmark*

## Engineering Skills and Future Needs

Peter Kofoed, Executive Vice President  
MT Højgaard

### Abstract

In a world, where everyday life becomes increasingly depending on Information Technology, Global Positioning Systems build into wrist watches, and genetic manipulation and the continued development of these and similar hi-tech issues, research related to something as “simple” as concrete can be quite difficult to “sell” as interesting. May be this matter of fact answers why the building and construction industry still, in its daily work, has unanswered questions in relation to mix design batching, transportation, placing and curing of the most used building material in the world – our beloved concrete.

Building and construction works have been going on as long as the human race has been on earth, and it believes that it will stay as long as any civilization exists. It also believes that it will continue developing its processes and materials. And the industry is fully aware of its obligation to participate in this development, whether it is the development of techniques on the building sites, or it is in-put to the universities for advanced research.

Since 1918-1919, when the two companies Højgaard & Schultz and Monberg & Thorsen were formed, the founders and the companies have been active in both areas. Today under the new name, MT Højgaard. Not only are we behind the majority of infrastructure in Denmark – spanning from the old Lillebælt Bridge over the Great Belt Link to the Øresund Bridge, but we are also contributing to the research at various universities among the most resent, the support from Knud Højgaard’s Foundation to DTU reflected in the name of today’s conference. The Foundation supports widely culture, education, science and research, and as such, obviously, the research and development of concrete technology.

MT Højgaard, as a company, has also shown its commitments in resent years in its participation in various practical research projects and its participation in the Danish Concrete Institute and the Danish Concrete Council. We consider it as a natural obligation following our role as the leading Danish civil works contractor. Green concrete and self-compacting concrete are just subjects for two of the most resent development projects that we have joined.

Looking ahead we trust that the “Concrete Vision 2025” published by the Danish Concrete Council represents a guideline also for our efforts in the continued development of the use of concrete in a variety of structures. Like most research and development the research and development of concrete raises the need for funding, but we believe that our support, either by direct financial support or by our participation with skilled people in the research projects is a valuable investment in the future that both we, as a company, and the rest of the society will benefit from in the long term. We consider that a lot of research, that are carried out in relation to concrete, is in harmony with our wishes of increased productivity, economical optimization and improvement of the working environment at the building site. We are also confident that results from research in areas, where we can not see directly neither the process nor the application of the results in tomorrow’s production like eg. nano-technology research, in time will show us further improvements.



## The Dual Nature of Technical Knowledge

Peter Kroes  
Delft University of Technology, Delft, The Netherlands

### Abstract

Engineers make use of various kinds of knowledge in designing and developing technical artifacts. In his book *What engineers know and how they know it: Analytical studies from aeronautical history* Walter Vincenti has presented a valuable overview of these various types of knowledge. In his anatomy of engineering knowledge, however, the distinction between knowledge of functions and of structures of technical artifacts is missing. Knowledge of functions of things is knowledge about what things are for. It is different in nature from knowledge about the structure of things, about how things are, that is, what physical/chemical properties they have. We will argue that engineering knowledge has a dual nature in the sense that it consists not only of knowledge of structures, but also of knowledge of functions. This is related to the fact that technical artifacts themselves have a dual nature: the function of a technical artifact is on the one hand grounded in its physical/chemical structure, on the other in intentional human behavior. This paper analyses the dual nature of technical knowledge and of technical artifacts and closes with a brief discussion of the role of functional knowledge in engineering curricula.

### 1. Introduction

The design, development and production of technical artifacts require various kinds of knowledge and skill on the part of engineers.<sup>1</sup> Part of this knowledge and these skills are taught at engineering schools, and part of it is acquired during engineering practice. For structuring engineering curricula it is, of course, interesting to know what kinds of knowledge and skills are involved in engineering practice. One of the few attempts to analyze and classify the various kinds of knowledge used by engineers can be found in a very interesting book by a

---

<sup>1</sup> Note that in the following we will restrict ourselves to technical artefacts whose functioning is dependent upon some physical/chemical construction. So we exclude from consideration software and biological technical artefacts.

former aeronautical engineer, Walter Vincenti, entitled: *What engineers know and how they know it: Analytical studies from aeronautical history* (1990). On the basis of detailed case studies about what kind of problems engineers had to face in the design and development of early airplanes, what knowledge and skills they needed to solve these problems and how they acquired this knowledge and these skills, Vincenti arrives at the following categories in his anatomy of engineering knowledge (1990, p. 207 ff):

- (1) Fundamental design concepts; this type includes knowledge of operational principles of technical artifacts and their normal configurations.
- (2) Criteria and specifications; this type includes knowledge of how to translate qualitative goals into specific requirements in terms of the hardware to be designed.
- (3) Theoretical tools; knowledge of mathematical methods and scientific/engineering theories.
- (4) Quantitative data; knowledge of physical properties of materials etc. and of quantities referred to in formulas of mathematical methods and theories.
- (5) Practical considerations; knowledge derived from experience in practice, for instance, about the most feasible way to produce a part.
- (6) Design instrumentalities; this category includes knowledge of procedures and of ways of thinking and the judgmental skills needed to solve (design) problems.

Although Vincenti has developed this classification of types of engineering knowledge primarily on the basis of studies into aeronautical practice, its categories are so general that it seems to be applicable to other engineering disciplines as well.

Vincenti's anatomy of engineering knowledge does not contain a separate category for knowledge of technical functions, nor does it bring to the fore the distinction between structural and functional knowledge.<sup>2</sup> It goes without saying that knowledge of structural properties of technical objects is of paramount importance for engineering practice. Consider a car. It has all kinds of structural properties that are technically relevant, such as its weight, the amount of fuel consumption per kilometer, its shape, its air resistance, its breaking power, the shape of its combustion chambers, the temperature and pressure in the combustion chamber during a combustion cycle etc. Knowledge of these properties, of how they hang together and of the physical/chemical processes taking place in, for instance, the engine of the car during operation, is part and parcel of standard technical knowledge of cars.

However, the idea that engineering knowledge consists of knowledge of structural properties of technical artifacts only, leaves out a kind of knowledge that is indispensable for engineering practice, namely knowledge of what things are for, that is, of their functional properties.<sup>3</sup> Apart from knowing that a certain object has a round shape, is made of steel etc., engineers also know that it is a steering wheel, i.e. that it performs a certain function in a car. In fact, most parts of a

---

<sup>2</sup> Note that in the following the notion 'structural' will be used as opposed to the notion 'functional'; the structural properties of technical artifacts include their geometrical, physical and chemical properties and behavior.

<sup>3</sup> In the following, when speaking about knowledge of the function of a technical artefact, we intend knowledge of its proper function and not its accidental functions (for instance, the proper function of a screwdriver is to fasten or loosen screws, but it may also perform all kinds of accidental functions, such as being used as a can opener or as a paper weight).

car are characterized in a functional way. Car designers, mechanics and users express at least part of their knowledge about technical objects, like a car, with the help of functional concepts. They claim for instance that object X has function Y, and assume that, just as a claim about a structural property, such a claim about object X may be true or false. And for explaining the operation of a car or why a specific car malfunctions, they often refer to functions of constituent parts.

The distinction between structural and functional knowledge of technical artifacts cuts right across Vincenti's different categories of engineering knowledge. Knowledge of functions is implicitly contained in the first category where it is related to the notion of normal configuration, and in the second category 'criteria and specifications', since lists of specifications are to a large extent determined by the function to be performed. Also in the category of fundamental design concepts functions do play a role. It contains operational principles that explain how a device works, that is, how it achieves its function or purpose. Thus knowledge of fundamental design concepts involves knowledge of functions and purposes. For two reasons, however, knowledge of functions deserves, in our opinion, a category of its own in any anatomy of engineering knowledge. In the first place, knowledge of functions is of principal importance for engineering practice; one can hardly imagine engineering practice without the use of functional concepts. And secondly, knowledge of functions has some features that set it apart from knowledge of structural properties of technical artifacts.

Vincenti seems to be aware of this last point. According to him, operational principles provide "an important point of difference between technology and science" (Vincenti 1990, p. 209). Functional concepts play no role in the physical sciences because they refer to how objects ought to behave, whereas these sciences restrict themselves to a description of how objects *de facto* behave. Here, indeed, he touches upon an important difference between knowledge of functions and knowledge of structural properties. Knowledge of functions has a normative aspect that is lacking in structural knowledge. This comes to the fore most clearly when claims are made about the malfunctioning of technical artifacts. From a purely scientific point of view it makes no sense to claim that an object is malfunctioning. Vincenti does not, however, analyze systematically the features that distinguish knowledge of functions from knowledge of structural properties.<sup>4</sup>

We will argue that engineering knowledge, or more generally, technical knowledge has two faces: it consists not only of statements concerning the structure of technical artifacts, but also of statements concerning their functions. Furthermore, we will show that this dual nature of technical knowledge is related to the dual nature of technical artifacts themselves. But first we will illustrate the importance of and difference between functional and structural descriptions of technical artifacts by having a brief look at engineering design practice.

---

<sup>4</sup> In fact, in epistemology a systematic analysis of the specific nature of knowledge of functions and how this type of knowledge is related to knowledge of structural properties of objects is still lacking; see Houkes (2005).

## 2. Engineering design

When we take a closer look at engineering design practice, the dual nature of technical knowledge is easily recognized. The engineering design process may be characterized schematically as a process that starts with the description of the expected behavior of the object of design (what it is supposed or ought to do), and ends with the description of an object with a structure that realizes that expected behavior. The description of the expected behavior is nothing else than the description of the function of the technical artifact to be designed. In other words, in the engineering design process a *functional* description is translated into a *structural* description, that is, a description that specifies, for every relevant detail, the geometrical and all other physical and chemical properties of the technical artifact. What is relevant in the description is primarily determined by the function of the technical artifact; anything that has a direct bearing on the performance of the function is relevant. As the outcome of a design process, a structural description is intended to be a blueprint for production, and therefore in principle it should be possible to make the object of design on the basis of the structural description.

The functional description of the object of design may be represented in terms of a ‘black box’, which transforms a certain input into a desired output (figure 1).<sup>5</sup> How this input is transformed into the output is left in the dark. It is precisely the aim of the design process to come up with a viable proposal for how this actually may be achieved. Depending on the case at hand, the input and output may be described in a more qualitative or quantitative way. For instance, in the ASM Handbook *Materials Selection and Design* (1997, p. 22 ff) the function of a fingernail clipper is described as “Remove excess length on fingernails” and the inputs and outputs of this function are specified in terms of energy, material and signal as follows:

	<i>Input</i>	<i>Output</i>
Energy	Finger force Kinetic (hand motion)	Sound Kinetic energy in nail
Material	Fingernail Hands, Debris	Cut nail, hands Debris
Signal	Long nail, hang nail Rough nail	Good appearing nail

Table 1 Input and output of fingernail clipper

In certain cases, the relation between input and output may be partly represented by a mathematical function, for instance the relation between input and output signal of an electronic circuit. Note, however, that in these cases the mathematical function is not to be confused with the technical function of the electronic circuit. The mathematical function can only *partly* represent the technical function because it does not capture the normative aspect of

<sup>5</sup> See, for instance, Dym (1994, p. 134-6).

the technical function (that is, that the device ought to, or is intended to realize this specific mathematical relation between input and output signal).

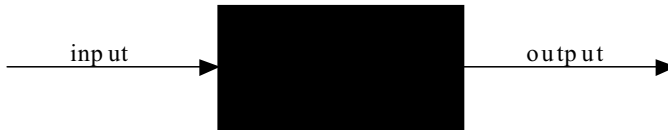


Figure 1 Black box representation of function

A purely functional description is opaque with regard to the structure of the object that realizes the function. This is due to the fact that a functional description is the result of viewing the object from a means-end perspective. What matters primarily from this perspective is that some object, irrespectively of its specific constitution, can be used as a (effective and efficient) means to achieve a certain end. This is typically the perspective of the user of a technical artifact.

When we turn our attention to structural descriptions of technical artifacts, the situation reverses: just as a functional description is opaque with regard to the structure that realizes the function described, a structural description of an object is opaque as regards the function performed by that object. To illustrate this, imagine that the fingernail clipper of figure 2 drops out of an airplane and lands before the feet of the chief engineer of an as yet undiscovered tribe in the Amazon forest. She carefully studies the structural properties of this to her totally unknown object and its behavior under various circumstances and comes up with all kinds of input-output schemes, that is, with all kinds of possible functions. If she is lucky, the input-output scheme of table 1 will be among these. But even then, how is she to determine which one of the many input-output schemes is the intended one and corresponds to the function of this object? In principle this is not possible on the basis of a structural description of the object; even the most detailed description of all structural properties of the object and of its physical/chemical behavior will not enable the engineer to deduce that it is a fingernail clipper.<sup>6</sup> One of the reasons is that such a deduction involves some form of naturalistic fallacy: from a logical point of view it is problematic to derive statements about how an object ought to behave, i.e., statements about its function, from its actual physical/chemical properties and behavior. Thus, from a functional point of view, a structural description is also a black box description. The situation is in fact symmetric in the sense that each mode of description black boxes the other one.

Purely structural descriptions of technical artifacts are typically of interest in the context of the production of technical artifacts. Such descriptions provide all information necessary for

---

<sup>6</sup> Such situations may also occur in ‘reverse engineering’, in which technical products are taken apart in order to analyse their working and the functions of their parts. Sometimes it may not be possible to reconstruct the function of a part on the basis of its physical properties and its place in the whole artefact.

making a technical artifact; for this it is in principle not necessary to know the function of the object to be made. Examples of purely structural descriptions of technical artifacts that underscore their importance for engineering practice may be found in ISO norms for standardized technical objects. In order to ensure that these standardized technical objects are in practice replaceable by any other item of the same kind, these norms fix minutely every relevant structural detail.



Figure 2 A 'physical object' with various input-output relations

In engineering design practice we also come across descriptions of technical artifacts that are of a mixed type; in fact, they seem to be the most common type of descriptions. Familiar examples are exploded views of technical objects, showing the geometrical form of all its parts (and how they fit together) together with a brief description of the function of these parts.<sup>7</sup> They describe technical artifacts in terms of their functional and structural properties. From the point of view of engineering design this kind of description is of particular interest. The function and structure of technical artifacts are intimately related to each other; not any kind of physical object can perform a certain function. These mixed descriptions are often precisely intended to convey how structure and function are related to each other. They are used to explain functional features of technical artifacts in terms of their structural features and vice versa.

The foregoing makes clear that the use of structural and functional properties for the description of technical artifacts is *de facto* indispensable for engineering practice. Functional and structural descriptions by themselves do not present 'complete' descriptions of technical artifacts: either physical/material aspects or functional aspects are ignored. Structural and functional descriptions may be considered to be complementary to each other and in many practical contexts an adequate description of a technical artifact will have to comprise both functional and structural properties. From the way engineers describe technical artifacts, we may conclude that they conceive of technical artifacts as (physical) structures with a function. In the following section we will argue that this 'structure-function' conception of technical artifacts is a reflection of the dual nature of technical artifacts.

---

<sup>7</sup> See, for example, Ullman (1992, p. 18).

### 3. The dual nature of technical artifacts

The structure-function conception implies that technical artifacts are not simply physical objects, since physical objects as such have no functional properties.<sup>8</sup> It also implies that technical artifacts are different from social objects like a ten-euro bill, or a law. Such objects have a function, even a practical function, but unlike technical artifacts the function of social objects is not realized by a specific physical structure (as is testified by the fact that various kinds of physical objects can and have been used for money). It is the intentional behavior of agents that realizes and sustains the functions of these social objects. The notion of intentional behavior refers to the fact that the behavior is based on beliefs and desires and that this kind of behavior is explained in terms of reasons and not in terms of physical causes. Technical artifacts are neither physical objects, nor social objects, but appear to have a kind of hybrid, dual nature. On the one hand they are physical constructions that may be used to perform a certain function. On the other hand they are intentional (social) objects since it is the function of a technical artifact that distinguishes it from physical objects and this function only has meaning within a context of intentional human action. Before presenting this dual nature view on technical artifacts, we will briefly discuss Herbert Simon's theory of artificial things as exposed in his classic *The sciences of the artificial* (in the following text, page numbers refer to this book). It proves to be a nice steppingstone to the dual nature view.

For Simon, the engineer and more in particular the designer is, in contrast to the scientist, "concerned with how things *ought* to be – how they ought to be in order to *attain goals*, and to *function*" (p. 4-5). This refers to the normative aspect of functions that we already mentioned above. One of the striking features of technical artifacts is precisely that they can be characterized in terms of functions and goals. Simon analyses functions and goals in the following way (p. 5):

Let us look a little more closely at the functional or purposeful aspect of artificial things. Fulfilment of purpose or adaptation to a goal involves a relation among three terms: the purpose or goal, the character of the artifact, and the environment in which the artifact performs.

Take for instance a clock; its purpose is to tell time, its character refers to its physical makeup (gears, springs etc. for a mechanical clock) and its environment is important because not every kind of clock is useful in every environment; sun dials can only perform their function in sunny climates. Figure 3 contains a schematic representation of Simon's analysis of artifacts.

According to Simon a technical artifact is a kind of 'interface' between "an 'inner' environment, the substance and organization of the artifact itself, and an 'outer' environment, the surroundings in which it operates" (p. 6). This distinction between inner and outer environment runs more or less parallel to the two different ways of describing technical artifacts discussed above. Looked at from the outer environment, the technical artifact presents itself primarily as something, whatever its inner environment, that fulfils a certain goal,

---

<sup>8</sup> This section is partly based on Kroes (2002).

purpose or function; the inner environment remains a black box. Looked at from the inner environment, the artifact is described as some kind of physical structure; from this perspective, the goal that it fulfils in the environment remains a black box. These two different ways of characterizing artifacts, in terms of their inner and outer environment, correspond closely to what we call the dual nature of technical artifacts to which we will now turn.

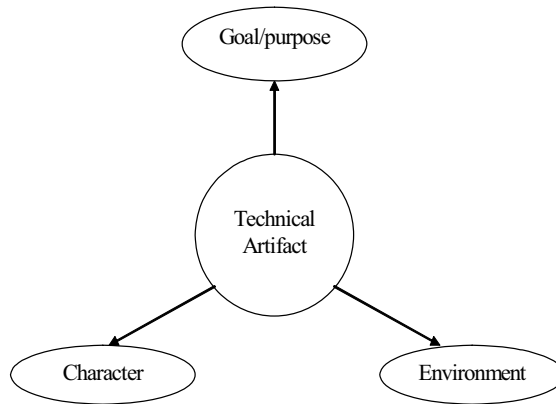


Figure 3 Simon's conception of a technical artifact

The view that technical artifacts have a dual nature is more or less a direct consequence of the structure-function conception of technical artifacts and the fact that the notions of structure and of function belong to two different conceptualizations of the world. On the one hand, we see the world as consisting of physical objects interacting through causal connections. This 'physical' or 'structural' conceptualization is employed by the physical sciences. On the other hand, we see the world as partly consisting of agents (primarily human beings), who intentionally represent the world and act intentionally in it, and whose behavior is partly explained in terms of reasons (and not causes). This is the 'intentional' conceptualization of the world, which underlies most of the social sciences. One aspect of this latter conceptualization is that certain activities are interpreted in terms of realizations of goals and that functions are attributed to certain objects or activities. The existence of these two different conceptualizations poses a fundamental problem, namely how these two conceptualizations can be integrated into one coherent conceptualization.

How do technical artifacts, as (physical) structures with a (intentional) function, fit into these two conceptualizations of the world? Looked upon as merely physical objects, technical artifacts fit into the physical conceptualization of the world; the way the artifact works can be explained in terms of causal processes. But as a mere physical object, it is not a technical artifact. Without its function, the object loses its status as a technical artifact. This means that technical artifacts cannot be described exhaustively within the physical conceptualization, since it has no place for its functional features. But neither can it be described exhaustively within the intentional conceptualization since its functionality must be realized through an



appropriate physical structure and the intentional conceptualization has no place for the physical features of a technical artifact. Hence the conclusion that technical artifacts have a dual nature: on the one hand they are physical, on the other intentional objects.

According to the above line of thought, the notion of technical artifact is related to three key notions, namely the notion of a physical structure, of a (technical) function and of a context of intentional human action (see figure 4).

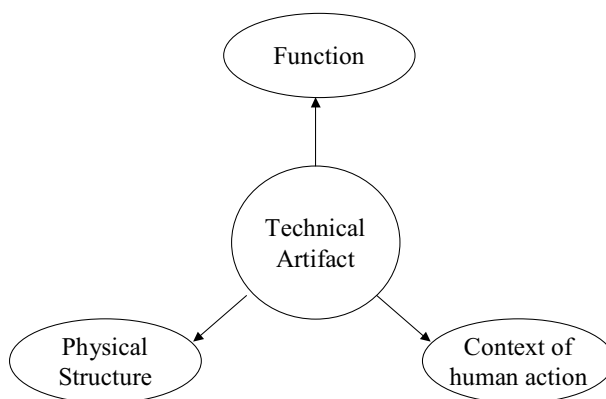


Figure 4 The various notions involved in the notion of a technical artifact

The context of human action has to be included in the analysis of technical artifacts because it makes no sense to speak about technical functions without reference to such a context. Functional discourse is part of the intentional conceptualization of the world; it is meaningless to speak about technical functions without a context of intentional (human) action. (This can be expressed in an ontological way by saying that some context of human action is constitutive for a technical function.) Thus, in figure 4 function and context of human action are intimately connected; they both belong to the domain of the intentional. Technical artifacts have a dual nature since they are at the same time part of the domain of the physical and of the intentional (see figure 5).

It is precisely the inclusion of the context of human action that marks one of the most notable differences between our analysis of technical artifacts and Simon's. We have replaced Simon's notion of goal or purpose by the notion of function. This may seem an insignificant move, but it is not because we may attribute functions to technical artifacts, but not goals (in the sense of an aim or an end (*telos*)). That notion has its place in a context of intentional human action; within such a context a means used to achieve a goal (end, aim) is attributed a function. Thus, Simon's analysis implicitly refers to a context of human action by referring to goals and purposes. Furthermore, the notion of environment has been replaced by the notion of context of human action. This change is important because it shows that not any kind of environment is relevant for the analysis of technical artifacts; only references to environments comprising a

context of human action are appropriate. In his example of the sun dial, for instance, Simon interprets the environment in a physical way (sunny climates are the required environment for sun dials). But this is problematic. It is not this physical environment that turns the object involved, a stick which casts a shadow on a surface, into an artifact of the type sun dial. Only within a context of human action (e.g. of ordering events or comparing time intervals) this physical system acquires a function and becomes a technical artifact (a time keeping device or clock).

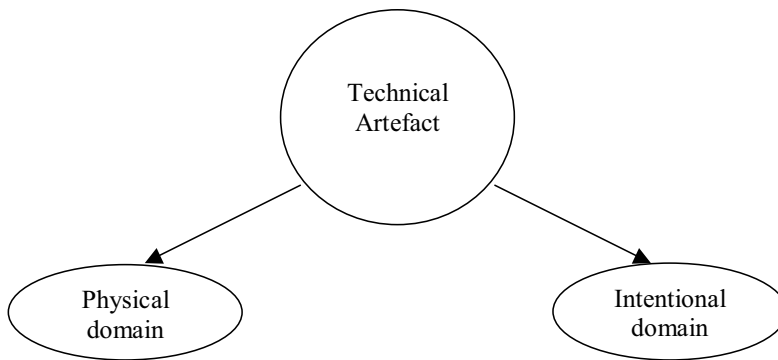


Figure 5 The dual nature of technical artifacts

The main difference between Simon's analysis and ours is that the latter gives a much more prominent and explicit place to the context of human action in analyzing the nature of technical artifacts. The advantage of this is that it brings much more into the open the dual nature of technical artifacts: we cannot make sense of technical artifacts without taking into consideration their physical structure, but also not without their context of intentional human action. Within Simon's analysis this dual nature stays more implicit and is related to the two different perspectives on technical artifacts, namely the perspective of the inner environment and the perspective of the outer environment. As soon as it is realized that these two environments are conceptualized in different ways, the dual nature of technical artifacts becomes manifest.

#### 4. Discussion: functional knowledge and engineering curricula

Knowledge of technical artifacts, we have argued above, involves, due to their dual nature, knowledge of physical structures and of technical functions. However, if we take a look at the content of engineering curricula, and we restrict our attention to engineering disciplines such as physical, chemical, mechanical, electrical, and aeronautical engineering, then knowledge of structures seems to be the dominant kind of knowledge taught in these curricula. Future engineers are taught the language of the physical sciences; this enables them to describe as precisely as possible the structural properties of physical objects and phenomena that are relevant for their engineering discipline. More in particular, they are well trained in analyzing

physical and chemical properties and phenomena that play a major role in the paradigmatic technical artifacts in their field and have to master all kinds of mathematical techniques for predicting the physical (chemical) behavior of these artifacts.

The situation with regard to the teaching of knowledge of functional properties of technical artifacts looks very much different. There is no general language, comparable to the language of the physical sciences that enables us to specify precisely the functional properties of technical artifacts.<sup>9</sup> Qualitative descriptions of functions, relying on the use of often vague concepts from natural language, such as the description of the function of the fingernail clipper above, appear to be more the rule than the exception. Furthermore, there are few formal techniques for analyzing technical functions. One of these techniques, important in the context of engineering design, is functional decomposition, which is used to decompose the overall function of the object to be designed into sub-functions, if possible down to the level of elementary functions. But from a formal point of view this technique is still ill understood. It is assumed that the overall function is the 'sum' of all the sub-functions. Formally, however, it is not clear at all what the expression 'sum of sub-functions' means. Similar remarks may be made with regard to formal techniques for representing and analyzing the notion of malfunctioning.

Thus, a general language for unambiguously expressing and analyzing knowledge of technical functions is missing. This may be one of the main reasons why the engineering curricula mentioned above show such a bias for structural knowledge. The danger of this situation, however, is that it gives a distorted picture of the importance of functional knowledge for engineering practice. We will illustrate this importance very briefly with the help of two examples from the history of technology; both concern the problem of expressing (properties related to) functional requirements in objective ways.

The first example concerns the development of early steam technology in the eighteenth century. In so far as this development is treated in engineering text books, its story is often told in terms of the steam engines involved: the steam engine of Savery, working without a piston, the Newcomen engine with piston and the improvements made by Watt (such as the introduction of a separate condenser). These 'nuts and bolts' histories of steam technology tell, however, only half of the story of steam technology. They completely neglect that engineers had to solve all kinds of problems, not about the technical design and making of steam engines, but about specifying the function of steam engines and that they developed specific knowledge and methods for this. Moreover, it took them more than a century to do so. The main function of the early steam engines was to drive pumps for draining mines. When ordering a steam engine, it was quite common for mine owners to specify the function (or 'duty') of the engine in terms of the number of horses or in terms of the type and dimensions of the waterwheel it would have to replace. But how was an engineer to determine the design parameters of a steam engine on the basis of such qualitative information? Physical notions like work and power still did not exist and so engineers had to come up with solutions of their own. They started to

---

<sup>9</sup> This is, for instance, a real obstacle for representing functional knowledge in CAD systems; see, for instance, Dym and Brey (2000).

compare the work done by different kind of horses, and finally ended up with the introduction of a standardized horsepower. Similar kinds of problems emerged when it came to comparing the efficiency of steam engines of different types working under different circumstances (e.g., fueled by coal or by wood). In this case too, engineers had to develop a lot of knowledge that was directly related to the function of steam engines in specific contexts of use. This kind of knowledge, which concerns the function of steam engines in daily practice and not so much their physical makeup, turned out to be of crucial importance for the development of steam technology.<sup>10</sup>

The second example is taken from Vincenti's work.<sup>11</sup> It concerns a similar problem, namely the translation of vague user requirements in clear, preferably quantitative, specifications. Vincenti has analyzed in detail how engineers managed to establish clear design requirements with regard to flying-qualities for airplanes. He starts his analysis with the following anecdote about a test pilot reporting that an airplane he had been testing was (Vincenti, 1990, p. 51):

...“tail heavy longitudinally.” He went on to add that “the tail heaviness is not tiresome because of the lightness of the controls.” A designer, reading these words at the time, might have had some idea of what caused the tail heaviness; he would have been hard pressed to know, however, how the mitigating “lightness of controls” had been achieved – or, indeed, just what the phrase meant.

Vincenti describes how an extensive research program was started, that took about a quarter of a century, to investigate how flying qualities and subjective pilot needs could be translated into specifications that could be related to design parameters of airplanes. Although knowledge about how to specify flying-qualities is not straightforwardly knowledge about functions of airplanes (which in general terms may be characterized as transportation of persons or goods), it is strongly function related in the sense that it aids or enables pilots to realize the function of airplanes.

This kind of functional or function-related knowledge, which concerns the context of use of technical artifacts, or what Simon calls their outer environment, is of great importance for the development of technology. Similar stories as above can be told for many fields of technology (from attempts to specify the image quality of television sets, the user-friendliness of software, to the sustainability of cars). This by itself would already warrant a more prominent place of this kind of knowledge in engineering curricula. But it would be a mistake to assume that functional knowledge is only relevant for engineers for establishing the right specifications for their objects of design. Functional knowledge is also an indispensable element in their understanding of how technical artifacts work, i.e., in their understanding of how the sub-functions of parts contribute to the realization of the overall function of the technical artifact. In other words, a purely structural description of all processes taking place in a car engine may provide a physical and chemical understanding of what goes on in the car engine, but it would not furnish the engineer with a technical understanding of how that engine works (or why it

---

<sup>10</sup> For more details about this kind of knowledge, see Kroes (1991).

<sup>11</sup> See Vincenti (1990), ch. 3.

malfunctions, whenever that is the case). Due to the dual nature of technical artifacts, functional concepts, just as structural ones, play a truly basic role in the thinking and doing of engineers.

## References

1. Vincenti, W.G., 'What engineers know and how they know it: analytical studies from aeronautical history' (John Hopkins U.P., Baltimore, 1990).
2. Houkes, W., 'Knowledge of artefact functions', *Studies in History and Philosophy of Science Part A*, to appear 2006.
3. Dym, C.L., 'Engineering design; a synthesis of views' (Cambridge University Press, Cambridge, 1994).
4. ASM Handbook Volume 20, 'Materials Selection and Design' (ASM International, 1997)
5. Ullman, D.G., 'The mechanical design process', (McGraw-Hill, New York, 1992).
6. Kroes, P.A., 'Design methodology and the nature of technical artifacts', *Design Studies* **23** (2002) 287-302.
7. Simon, H.A., 'The sciences of the artificial', (The MIT Press, Cambridge (Mass.), 1996) (third edition).
8. Dym C.L. and Brey P., 'Languages for engineering design: empirical constructs for representing objects and articulating processes', in 'The empirical turn in the philosophy of technology', Research in Philosophy and Technology (series editor C. Mitcham), Vol. 20, P.A. Kroes and A. Meijers (eds.), (JAI (Elsevier Science), Amsterdam, 2000) 119-148.
9. Kroes, P.A., 'Steam engines and the concept of efficiency; characteristics of technological knowledge', *Methodology and Science* **24** (2) (1991) 79-97.



## University teaching standards and evaluating teaching and pedagogy

Paul Ramsden  
Higher Education Academy, United Kingdom

### Abstract

There are now over 2 million students in UK higher education. Issues of improving student learning and the student experience have gained new prominence. Although British universities enjoy an enviable reputation for the quality of their teaching, learning and student support, pressures of time and resources have intensified.

Moreover, new challenges have become evident. These include an increased focus on accountability to students for the quality of the education and services they receive, the growing importance of e-learning, and increased competition from overseas providers.

The prime strategic focus of the new Higher Education Academy is to help UK universities and colleges and their staff to meet these challenges by providing the best possible learning experience for their students. I will describe some ways in which we intend to do this.

Underlying all the Academy's work is a fundamental conviction that the best learning outcomes occur when universities and their staff focus on the student *experience of learning* rather than *teaching performance* alone. I will outline some research evidence that supports this principle of a 'student-focused' approach to university teaching.

A student-focused approach is compatible with the idea of university teaching as inspiring learning and imaginatively imparting knowledge. It is also consistent with the very ancient belief that, if they are to deliver the best research and educational outcomes, universities should be free to secure their own destinies.

As an example of how the principle can be applied in practice, I will discuss models of university teaching standards and how these can be used to stimulate interest in improving teaching, recognise and reward faculty performance – both in individual universities and nationally.





## **Investigations of the Properties of SCC: a Method for Measuring Thixotropy and Viscosity**

Raissa P. Douglas<sup>(1)</sup>, Amedeo Gregori<sup>(2)</sup>, Zhihui Sun<sup>(1)</sup> and Surendra P. Shah<sup>(1)</sup>

<sup>(1)</sup> Center for Advanced Cement-Based Materials, Northwestern University, U.S.A.

<sup>(2)</sup> Department of Structural Engineering, University of L'Aquila, Italy

### **Abstract**

Over the last decade, research has been conducted at The Center for Advanced Cement-Based Materials (ACBM) in order to improve the understanding of the properties of SCC and to provide information that could be used towards the commercialization of such a concrete. The studies have been focused on the fresh state properties of SCC, specifically from gaining an understanding of the rheological properties of SCC. Investigation of mix-proportioning methods led to the development of a paste rheology model that was based on the minimum paste volume theory. This model works as a linkage between segregation and flow and extension of this model also led to design of fiber-reinforced SCC. Studies were conducted on steel reinforced and polypropylene reinforced specimens in order to evaluate flexural strength, compressive strength, fracture energy and shrinkage. Currently, research efforts at ACBM have been focused in two major areas: developing a field friendly device to measure viscosity and determining the relationship between formwork pressure and rheology.

### **1. Introduction**

Since the introduction of self-consolidating concrete (SCC) in Japan during the late 1980's, acceptance and usage of this concrete in the construction industry has been steadily gaining momentum. Major highlights in the development of SCC are shown in Figure 1. SCC differs from normally vibrated concrete (NVC) because of its characteristics in the fresh state, and ideally, once it sets it should behave as any other NVC. The fresh state properties of SCC are attributed to its rheological properties and hence this has been the focus of the research program at ACBM.

The rheological properties of SCC strongly depend on the methodology that is used to develop the SCC. NVC typically have yield stress values ranging from 500 to several thousands Pa, whereas SCC typically have yield stress values ranging 0 to 60 Pa. The viscosity of SCC mixtures range from 20 (incorporation of fines) to 200 Pa•s (incorporation of VMA) [1]. The matrix phase is an important factor in determining the stability of SCC; hence, being able to predict the characteristics of SCC from the rheological properties of the matrix saves time,

money, effort, and materials. Saak, Jennings, and Shah [2] developed a methodology for designing SCC through its matrix phase by incorporating the concept of a “self-flow zone” and modeling the segregation resistance of one spherical particle suspended in the cement paste. In 2001, the model was expanded to include the effect of particle interaction [3]. This model is based on the assumption that there is a minimum flow, minimum apparent viscosity, and optimum flow-viscosity ratio needed in order to produce a good quality SCC with satisfactory deformability and resistance to segregation. Therefore, there is a “window of opportunity” or satisfactory zone for obtaining a good performing SCC (see Figure 2). It was also shown that segregation resistance is affected by aggregate diameter. Hence the average aggregate diameter ( $D_{av}$ ) and average aggregate spacing ( $D_{ss}$ ) were used as parameters to account for aggregate influence. In 2002, it was shown that the density difference between the aggregate and the paste is an important parameter for the model and that minimum paste rheology model is accurate for concrete mixes with similar density differences [4].

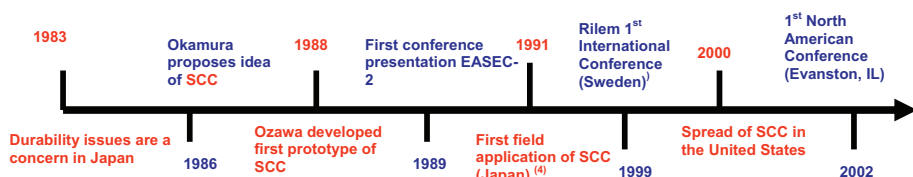


Figure 1: Timeline of SCC highlights

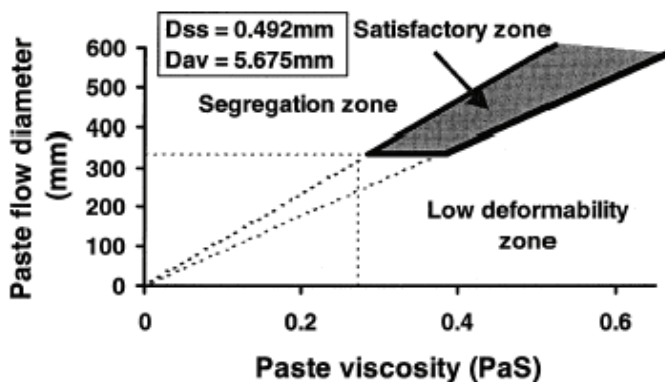


Figure 2: Window of Opportunity Shaded in grey (from Bui, 2002)

In 2003, researchers at ACBM also conducted studies investigating the properties of fiber-reinforced SCC (FRSCC). FRSCC combines the benefits of SCC and the properties of fiber reinforced concrete in hardened state in order to produce a concrete that is high performance in both the fresh and hardened state. In total, six non-fiber mixes and eighteen fiber self-

consolidating mixtures were evaluated. Two different fibers (steel and polypropylene) were used at two different fiber volumes (0.5 and 1%, by volume). In addition, matrix composition was also changed by using three different gravel-to-total aggregate ratios and three different water-to-cement ratios. It was determined that fiber type had a significant effect on paste requirements. For the same volume of fibers, the polypropylene fiber mixes required higher paste volumes than the steel fiber mixes. In addition, fiber type and fiber volume were the most significant factors in determining the flexural strength and toughness. The experimental program will be expanded to look at optimizing mix proportions and designing new fiber types to control FRSCC behavior.

Current work on SCC is focused on developing an inexpensive field device to measure viscosity, characterizing the effect of mixture ingredients on the thixotropy, and formwork pressure evaluations. The next section will provide an overview of the current work at ACBM.

## **2. Current Research Programs**

### **2.1 Field Friendly Viscometer**

#### **2.1.1 Introduction**

Determination of the viscosity and yield stress of concrete can be obtained by a number of indirect and direct techniques. One of the most common indirect techniques is the slump test. It was found that the viscosity is related to the time when the flow spread reaches 50cm in diameter,  $T_{50}$  [5], and the yield stress is best correlated to the final flow diameter of the concrete [6, 7]. The slump flow test is a simple and convenient test; however, the relationship between viscosity and the results obtained from slump flow test are difficult to interpret. The direct method is the approach in which the rheological properties of concrete are measured with a rheometer or viscometer. Commercial concrete rheometers cannot be used to evaluate the viscosity of cement paste due to the different size of the suspended particles in paste and concrete systems. Similarly, a paste rheometer should not be used for concrete. In addition, a study conducted at the National Institute of Standards and Technology (NIST) showed that the obtained value of viscosity depends on the rheometer [8].

Viscometers based on the movement of a spherical body into fluids have already been proposed for various fluids. In 1960, Scott et.al devised a rolling-sphere viscometer to investigate thixotropic fluids [9]. Falling ball rheometers have also been used on opaque systems [10, 11]. However, these systems are more difficult to study than transparent fluids (such as water or glycerin) since the position of the ball can not be detected visually. Thus, the major difference among the different falling ball rheometers is often the technique used to measure the speed of the moving ball. X-ray radiography, eddy current measuring system [10], acoustically tracked translating ball [12] are examples of position detections methods that have already been proposed but are not suitable for field usage in concrete construction applications due to cost or usability. Recently, the movement of a falling-ball, monitored by means of electromagnetic induction, has been proposed as a quality control test for SCC on site [13]. However, it must be noted that in the case of highly concentrated suspensions, such as concrete, the falling ball may stop prior to completing the drop and thus the test can not be performed only under action of the gravitational force on the ball. Stauber Greenwood et.al

used an Atwood machine to control the movement of the falling ball [11], but the number of repetitions needed to obtain a complete flow curve makes this approach time consuming and impractical for field usage. The objective of this part of the research program is to design an inexpensive falling ball viscometer that can be used in the laboratory and in the field.

### 2.1.2 System Configuration

A falling ball viscometer was designed at ACBM at Northwestern University. A scale with accuracy equals 0.001g, an elastic tensile spring, and steel balls are the major components of this viscometer (Figure 3).

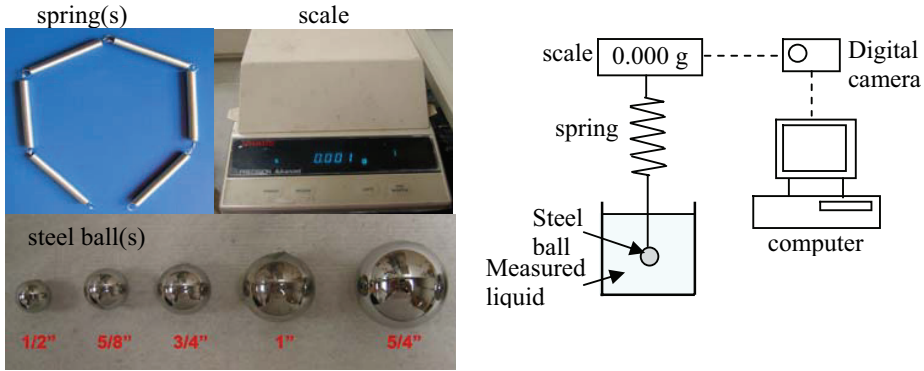


Figure 3: The Falling Ball Viscometer

When the steel ball is suspended by the spring, the forces acting on the ball can be resolved into four components: gravity ( $W$ ), tensile force ( $T$ ), buoyancy ( $B$ ), and drag force ( $D$ ) (see figure 4). The gravitational force and buoyant force can be directly determined based on the mass and volume of the steel ball and the density of the liquid. Thus, only the tensile force and drag force are unknown. During the measurement, the spring is hooked to a sensor that is located at the bottom of the scale. By suspending the steel ball with the spring, the tensile force in the spring during the downwards movement of the ball can be recorded exactly by reading the numbers shown on the scale. Once the tensile force is known, the displacement of the ball can be computed and this allows for the calculation of the velocity and acceleration of the ball. The only force left to be determined is the drag force, and it can be solved using the equation of motion shown in Figure 4. In steady state condition and when Reynolds number ( $R_n$ ) is less than 0.5, the drag force can be linearly related to the velocity by applying Stoke's Law [14] for a spherical particle as shown in equation 1.

$$D = 6\pi\eta rv; \quad R_n = vr\eta / \rho \quad (1)$$

where:

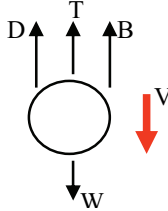
$\eta$  is the viscosity of the measured liquid;

$r$  is the radius of the ball

$v$  is the velocity of the ball

$\rho$  is the density of the liquid

Thus we see that the drag force is a function of the viscosity of the liquid, and hence the viscosity of the liquid can be determined.



Equation of motion:

$$\Sigma F = W - B - T - D = ma$$

Figure 4: Free Body Diagram of The Falling Ball

### 2.1.3 Experimental Results

When the viscosity is known, the drag force can be determined using equation 2, where  $K_{th}$  is the slope of the line when the drag force is plotted as a function of the velocity for a Newtonian Fluid. The subscript “th” denotes “theoretical value”.

$$D = K_{th}v; \quad K_{th} = 6\pi\eta r \quad (2)$$

Using the falling ball viscometer an experimental value,  $K_e$ , can be determined based on the concept described in Section 2.1.2. However,  $K_e$  was found to be different from  $K_{th}$  and this indicates that to obtain an accurate measurement of viscosity, a calibration for the system is necessary. In order to calibrate the viscometer, steel balls with various diameters were used for the same standard oil and a linear relationship between the difference of  $K_{th}$  and  $K_e$  was found as a function of the radius of the steel ball. Two other Newtonian fluids (a standard oil and honey) were also evaluated. The linear relationship  $K_{th}$  and  $K_e$  was still apparent and the slope of this linear relationship was regarded as a function of viscosity (see Figure 5). Once the system is calibrated, it is quite easy to use this falling ball viscometer to measure the viscosity of Newtonian fluids. For a given material and a given steel ball, the parameter  $K_e$  can be evaluated from the linear relationship between the measured drag force and the ball velocity. It is supposed that the calibration will be valid for non-Newtonian fluids, if the material behaves according to Bingham model. For a Bingham material, drag force is linearly related to the velocity of the moving ball, however, the linear line has an intersection with the y axis as shown in Figure 6, where  $D_0$  can be correlated to the yield stress of the material. The solid line in the figure can be shifted down until intersects with the origin. This implies that the calibration of the system should also be valid for a Bingham fluid. Based on this concept, the falling ball viscometer was used to evaluate cement paste. The cement paste was also tested using a commercial rheometer in order to compare the results. The viscosity results obtained with the two methods are plotted in Figure 7. Although the absolute values of viscosities that

obtained with the two devices are different, the trend is similar. The falling ball viscometer gives higher values of viscosities and the reasons for this are under investigation.

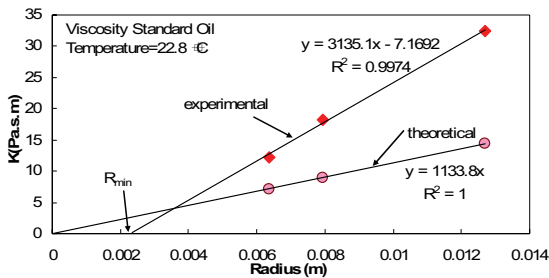


Figure 5: Relationship between K and Radius of the Ball

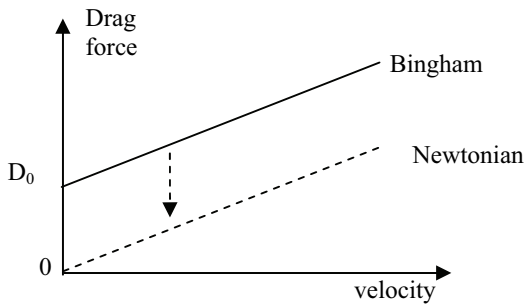


Figure 6: Validity for Bingham Material

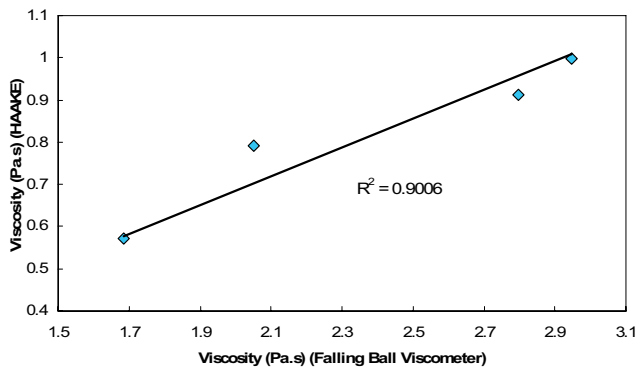


Figure 7: Comparisons of Viscosity

## **2.2 Formwork Pressure and Rheology**

### **2.2.1 Introduction**

Due to the highly flowable nature of SCC, one of its major advantages is that it speeds up the construction process because casting can be conducted at higher rates. However, increasing the casting rate can also have a negative consequence since it leads to higher lateral pressure against the formwork [15] and if not properly accounted for, these high pressure can lead to formwork failure. Hence, SCC formworks are often designed with the assumption that full liquid pressure head will be achieved and the forms are constructed using more structural ties or heavier steel-framed gang forms than those constructed for vibrated concrete [16, 17]. However, studies have shown that not all SCC achieve hydrostatic pressures [17-20] and the conservative assumption of hydrostatic pressure for all SCC's can lead to unnecessary costs due to the construction of over-dimensioned formworks. In 2001, Billberg conducted full scale tests using wall forms to evaluate the effect of different SCC compositions on formwork pressure [17]. The results indicated that casting rate strongly influenced pressure development, and that mix composition was not a significant factor affecting form pressures. However, an extensive laboratory study conducted by Assaad, Khayat and Mesbah showed that mix composition was another key factor affecting formwork pressure [21]. This was attributed to the belief that mix composition affects the kinetics of a structural build-up phase and thixotropy. Thixotropy is defined as "a decrease [in time] of... viscosity under constant shear stress or shear rate, followed by a gradual recovery when the stress or shear rate is removed" [22]. This "recovery" of viscosity affects the workability of the concrete, and hence directly affects a number of construction processes, e.x. mixing, transporting, pumping, casting, and formwork pressure development. While concrete is in motion (i.e. mixing, pumping, and placing) it behaves as a liquid, however at rest it is able to rebuild internal structural bonds and this can lead to a reduction in the pressure development.

However, although numerous researchers agree that thixotropy influences formwork pressure [18, 23, 24], it is still uncertain to what degree. Generally, the phenomenon of thixotropy is not well understood and often overlooked. Nonetheless, thixotropy plays a major role, and as stated by Mewis "[t]ogether with the related effect of yield stress, it constitutes probably the major remaining problem in theoretical rheology" [25]. Even a simple action, such as pouring, induces shearing which breaks down the structure and hence accurate experimental characterization of thixotropy has been difficult. Thixotropy in cementitious materials is even more difficult to measure due to the fact that the material experiences physio-chemical changes with time. Presently, there is no standard method to measure thixotropy but typical thixotropic experiments often consist of hysteresis loops or flow curves [22]. In 1940, Pierce devised an instrument to measure the gel strength of oil well cement slurries [26]. His apparatus consisted of immersing a thin metal plate inside of cement slurry and then measuring the force necessary to pull the plate from the slurry. However, this method is more measurement of yield strength. Assaad et. al developed a method to evaluate thixotropy using structural breakdown curves and using the area between the peak yield stress and equilibrium stress value to quantify thixotropy [21]. However, this approach is evaluating the amount of energy that is needed to breakdown the sample. For most materials (paints, polymers, etc) thixotropy is a reversible process in which the breakdown and rebuilding kinetics are independent of the specimen age. However,

cementitious materials also undergo a hydration reaction which makes thixotropy dependent on age. Thus, there is no reason to assume that the breakdown energy is equivalent to the rebuilding energy.

The objective of this research study is to determine the effect of material constituents on the thixotropy of cement paste because the aggregates are believed inactive in the thixotropic phenomena. A new protocol consisting of hysteresis loops and energy methods was developed at ACBM. This protocol quantifies the amount of thixotropic rebuilding in the paste matrix.

### 2.2.2 Protocol

The degree of thixotropy of different cementitious materials will be evaluated by comparing the rate of rebuilding. Each sample is brought to an equilibrium state under constant shear rate. Then, the sample is allowed to rest for a specific time interval, and then a hysteretic loop is applied. The area between the up curve of the hysteretic loop and the initial equilibrium line (in the plane of shear stress versus shear rate) is used as a measure of energy (see Figure 8). This area represents the power needed to shear a constant unit volume of paste. The process of allowing the sample to rest for a specific time interval and applying hysteretic loops is repeated nine times. A plot of the rebuilding energy (as a function of the area) versus time is used to determine the rate of thixotropy by looking at the slope of the graph. A higher slope indicates a faster rate of rebuilding which means higher thixotropy (see Figure 9).

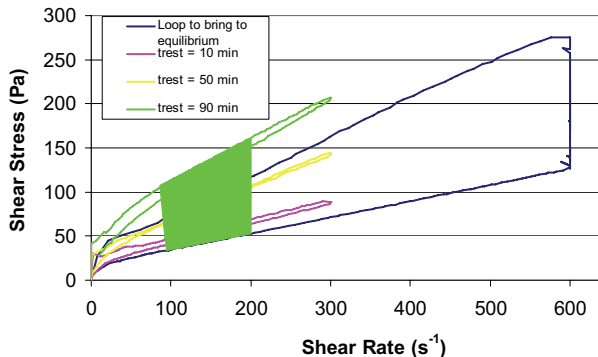


Figure 8: Rebuilding Area for a given  $t_{\text{rest}}$

### 2.2.3 Experimental Results

Initial studies showed that the degree of thixotropy is related to the initial slump flow diameter of the cement paste. Decreasing the slump flow was shown to increase the rate of thixotropy. It is well known that slump flow is correlated to yield stress; hence it appears as if yield stress influences thixotropy. In order to eliminate this factor, thixotropic comparisons were conducted on mixes having the same initial slump flows (i.e. yield stress).

Two different superplasticizers, polycarboxylate (PC) and polynaphthalene sulphonate (PNS), were used in order to investigate the effect of superplasticizer type on thixotropy. Keeping



constant the water-to-cement ratio, the dosage of each superplasticizer type was varied in order to achieve the target slump flow. In this study 9.25 inches (23 cm), 11 inches (28 cm), 12.5 inches (32 cm), and 14.5 inches (37 cm) were selected as the target slump flow diameters.

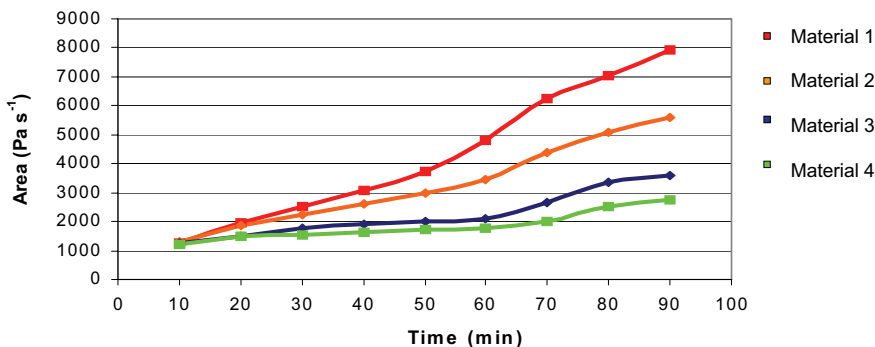


Figure 9: Rebuilding Area versus  $t_{\text{rest}}$

As shown in Figure 10, there is no significant difference in thixotropy between the mixes made with the PC and PNS superplasticizers for the low slump flow diameter (9.25 inches) target. A similar effect was noticed for a paste flow diameter of 11 inches. However, for a slump flow diameter of 14.5 inches the paste with PC superplasticizer appears more thixotropic than the paste made with PNS superplasticizer (see Figure 11). A similar effect was noticed for a slump flow diameter of 12.5 inches.

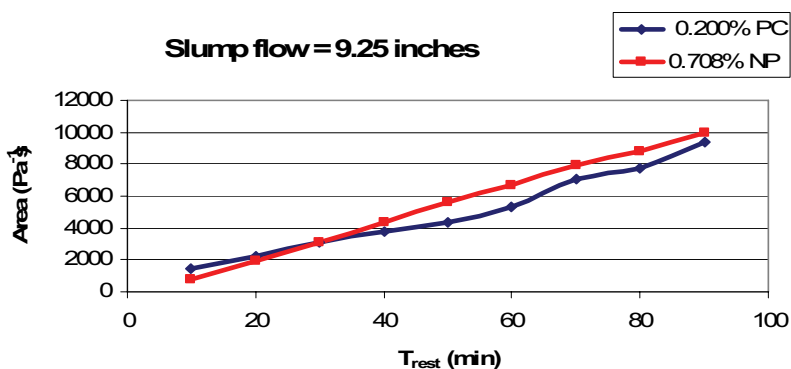


Figure 10: Effect of HRWR at low workability

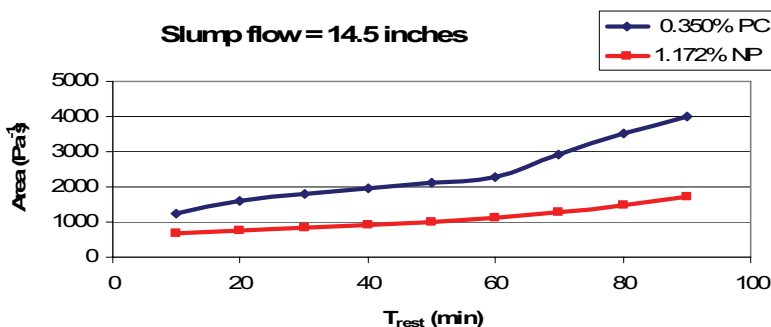


Figure 11: Effect of HRWR at high slump flow

### 3. Conclusions and Future Work

Investigations of quality control methods lead to the development of the penetration apparatus which provides a rapid indication of segregation resistance of SCC. Researchers at ACBM are developing a falling ball viscometer which can be used in the field. Preliminary results indicate that the system can provide valid information about viscosity, and it is suitable for a wide range of viscosities. Compared to commercial viscometers the system is inexpensive and easy to operate. Additional experiments will be conducted in order to improve the reliability of the equipment for Non-Newtonian fluids such as mortar and SCC.

Investigations are underway in order to correlate SCC rheology and formwork pressure. Thixotropy is believed to influence formwork pressure and a new protocol to evaluate the rebuilding kinetics of thixotropy was developed. This protocol can provide useful information about the effect of mixture ingredients on thixotropy of cementitious materials. Preliminary testing has shown that superplasticizer type can influence thixotropy and this indicates that it may be possible to control the thixotropy of cement paste through the mix design. Further investigations will focus on determining the effect of mineral admixtures, cement types, and viscosity modifying agents. Once the effect of the different constituents is understood, then thixotropic degree of SCC can be controlled in order to optimize its behavior in the fresh state. This can eventually lead to the design of SCC mixes that develop lower formwork pressure.

### References

1. Wallevik, O.H. *Rheology - A Scientific Approach To Develop Self-Compacting Concrete*. in *3rd International RILEM Symposium*. 2003. Reykjavik, Iceland: RILEM Publications S.A.R.L.

2. Saak, A., *Characterization and Modeling of Rheology of Cement Paste: With Applications Toward Self-Flowing Materials*, in *Material Science and Engineering*. 2000, Northwestern University: Evanston. p. 249.
3. Bui, V.K., Y. Akkaya, and S.P. Shah, *Rheological Model Self-Consolidating Concrete*. ACI Materials Journal, 2002. **99**(6): p. 549-559.
4. Douglas, R.P., et al., *Properties of Self-Consolidating Concrete Containing Class F Fly Ash: With a Verification of the Minimum Paste Volume Method*. ACI Special Publications, In Press.
5. Ferraris, C.F., H.O. Karthik, and R. Hill, *The influence of mineral admixtures on the rheology of cement paste and concrete*. Cement and Concrete Research, 2001: p. 245-255.
6. Tattersall, G.H. and P.F.G. Banfill, *The Rheology of Fresh Concrete*. First ed. 1983, Marshfield: Pitman Publishing Inc. 356.
7. Grunewald, S. and J.C. Walraven. *Rheological Measurements on Self-Compacting Fibre Reinforced Concrete*. in *3rd International Symposium on Self-Compacting Concrete*. 2003.
8. Ferraris, C. and L. Brower, *Comparison of Concrete Rheometers: International Tests at LCPC*. 2000, National Institute of Standards: Nantes, France.
9. Blair, G.W.S. and J.C. Oosthuizen, *Rolling-sphere viscometer for structured liquids*. British Journal of Applied Physics, 1960. **11**: p. 332-334.
10. Powell, R.L., et al., *Development of a Falling Ball Rheometer with Applications to Opaque Systems: Measurements of the Rheology of Suspensions of Rods*. The Society of Rheology, Inc., 1989. **33**(7): p. 1173-1188.
11. Greenwood, M.S., et al., *Using the Atwood Machine to Study Stokes' Law*. American Journal of Physics, 1986. **54**(10): p. 904-906.
12. Tran-Son-Tay, R., et al., *Magnetically driven, acoustically tracked, translating-ball rheometer for small, opaque samples*. Review of Scientific Instruments, 1988. **59**(8): p. 1399-1403.
13. Buchenau, G. and B. Hillemeier. *Quality-Test to Prove the Flow Behavior of SCC on Site*. in *3rd International Symposium on Self-Compacting Concrete*. 2003. Reykjavik, Iceland: RILEM Publications S.A.R.L.
14. Tran-Son-Tay, R., et al., *Magnetically Driven, Acoustically Tracked, Translating-Ball Rheometer for Small Opaque Samples*. Review of Scientific Instruments, 1988. **58**(8): p. 1399-1401.
15. Gardner, N.J., *Pressure of Concrete on Formwork--A review*. ACI Materials Journal, 1985: p. 744-753.
16. Nasvik, J., *Formwork for Self-consolidating concrete*. Concrete Construction, 2004.
17. Billberg, P. *Form Pressure Generated by Self-Compacting Concrete*. in *3rd International Symposium on Self-Compacting Concrete*. 2003. Reykjavik, Iceland: RILEM Publications S.A.R.L.
18. W. Brameshuber, S.U. *Investigations on the formwork pressure using self-compacting concrete*. in *3rd International Symposium on Self-Compacting Concrete*. 2003. Reykjavik, Iceland: RILEM Publications, S.A.R.L.
19. Fedroff, D. and R. Frosch, *Formwork for Self-Consolidating Concrete*. Concrete International, 2004: p. 32-37.

20. Assaad, J., *Formwork Pressure of Self-Consolidating Concrete-Influence of Thixotropy*, in *Departement de genie civil*. 2004, Universite de Sherbrooke: Sherbrooke (Quebec), Canada. p. 445.
21. Assaad, J., K. Khayat, and H. Mesbah, *Assessment of Thixotropy of Flowable and Self-Consolidating Concrete*. *ACI Materials Journal*, 2003. **100**(2): p. 99-107.
22. Barnes, H.A., *Thixotropy-a review*. *Journal of Non-Newtonian Fluid Mechanics*, 1997. **70**: p. 1-33.
23. Khayat, K., M. Saric-Coric, and F. Liotta, *Influence of Thixotropy on Stability Characteristics of Cement Grout and Concrete*. *ACI Materials Journal*, 2002. **99**(3): p. 234 - 241.
24. Leemann, A. and C. Hoffmann. *Pressure of Self-Compacting Concrete on the Formwork*. in *3rd International Symposium on Self-Compacting Concrete*. 2003. Reykjavik, Iceland: RILEM Publications, S.A.R.L.
25. Mewis, J., *Thixotropy--A general review*. *Journal of Non-Newtonian Fluid Mechanics*, 1979. **6**: p. 1-20.
26. Pierce, C.H., *Thixotropy of Oil Well Cement Slurries*, in *Department of Mining Engineering*. 1940, Stanford University. p. 75.

## A Blocking Criterion for Self-compacting Concrete

Lars N. Thrane<sup>(1)</sup>, Henrik Stang<sup>(2)</sup> and Mette R. Geiker<sup>(2)</sup>

<sup>(1)</sup>Concrete Centre, Danish Technological Institute, Denmark

<sup>(2)</sup>Department of Civil Engineering, Technical University of Denmark, Denmark

### Abstract

To benefit from the full potential of Self-Compacting Concrete (SCC) prediction tools for the form filling ability of SCC are needed. This paper presents a theoretical concept for assessment of the blocking resistance of SCC. A critical concrete flow rate above which no blocking occurs is introduced. The critical flow rate takes into account the mix design, the rheological properties of the matrix and concrete, and the geometry of the flow domain.

### 1. Introduction

SCC does not require vibration for compaction. This is a major advantage in sections of the formwork that are not easily accessible i.e. due to the form geometry or because of a high reinforcement density. However, it is a challenge to design a mix and select a casting technique and sequence that allows flow into confined zones and past reinforcement bars to ensure a proper form filling ability and a homogeneous SCC. The two terms “passing ability” and “blocking resistance” will be applied to describe the two different situations of SCC flow near reinforcement bars. The definitions used in this paper are;

- Passing ability is the ability of the concrete to pass reinforcement bars, e.g. retained material will include both aggregates and matrix
- Blocking resistance is resistance to accumulation of aggregates behind reinforcement bars thus leaving the concrete inhomogenous after flow.

Figure 1 illustrates the meaning of passing ability and blocking resistance. It shows flow of SCC past reinforcement bars in a simple flow domain. The situation to the left illustrates a low passing ability where the concrete remains stable but it is not possible to obtain a complete filling of the flow domain. The situation to the right illustrates a low blocking resistance where the aggregates tend to accumulate behind the reinforcement bars which result in variations in the particle volume fraction throughout the flow domain. Separation by blocking may result in

variations in properties such as strength, shrinkage, air void distribution, and bond between concrete and reinforcement.

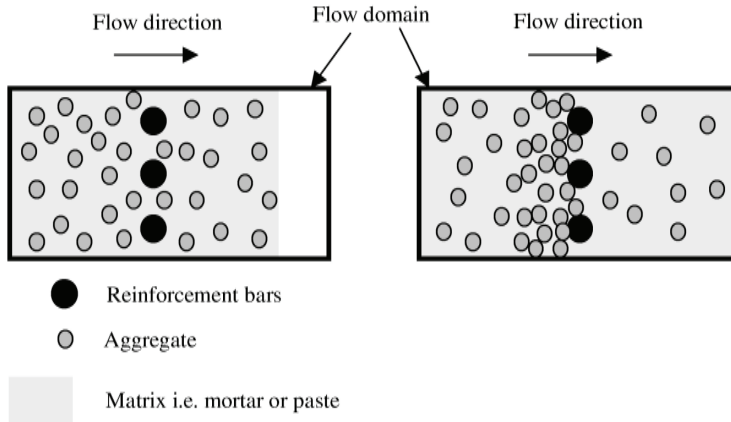


Figure 1 - Illustration of the terms "Passing ability" and "Blocking resistance". A low passing ability and blocking resistance is shown to the left and right, respectively.

Typically, the passing ability and blocking resistance are assessed experimentally. The L-box (1), J-ring (2), ring penetration test (3), and the passing ability tester (4) are examples of test methods to assess the passing ability and blocking resistance.

Tangtermsisikul et al. have proposed an empirical model on the blocking resistance (5). The model is based on the concept of a critical volume for each aggregate fraction. The critical volume is determined experimentally. For a given aggregate composition (grading and shape) this model may be used to assess a critical aggregate volume content.

A criterion for the blocking resistance based only on the mix composition may be referred to, as a static criterion i.e. the possible effect of dynamic behavior is not considered. However, as simulation of SCC flow is becoming an important tool in the assessment of the form filling ability, it is relevant to study the combined effect of mix composition and dynamic behavior on the blocking resistance. Especially, the dynamic behavior related to the macroscopic flow rate is expected to be relevant (see section 2).

Two different approaches to numerical simulation of form filling may be used, a single fluid or a two-phase flow approach such as mesoscopic discrete particle flow models.

Assuming that the rheological properties of SCC describe the flow properties, a single fluid simulation can be used to evaluate the passing ability of SCC e.g. the passing ability will depend on the combination of driving force (pressure drop and/or inertia) and the rheological properties of the fluid. Single fluid simulations may be used to assess the flow behavior during form filling e.g. flow patterns, dead zones, and no-fill zones. On the other hand, single fluid

simulations cannot describe the effect of dynamic behavior on the blocking resistance due to the absence of particles. However, assuming that a flow rate may be used as a criterion for the blocking resistance, a single fluid simulation offers the opportunity to investigate zones in the form where there is a risk of blocking.

Discrete particle flow modeling is a numerical tool for studies of movement and interaction of particles, including visualization of these phenomena. However, the computational costs are at present too high to be used for simulations of full-scale castings.

Numerical mesoscopic particle flow models have been proposed for simulation of concrete; the Dissipative Particle Dynamics (DPD) <sup>(6)</sup>, the Distinct Element Method (DEM) <sup>(7, 8)</sup>, and the Viscoplastic Suspension Element Method (VSEM) <sup>(9)</sup>.

Martys et al. have made a few studies of monodisperse spheres passing reinforcement bars under the influence of gravity <sup>(6)</sup>. The results show blocking when particle diameter to bar spacing is below 1/5. The effect of flow rate is not evident from these simulations. Also, there is still a need to improve models to include a wider range of particles sizes and shapes as well as to test and verify the models experimentally.

Experimental and numerical modeling have been undertaken, however, these have focused on a static blocking criterion based on bar spacing and mix composition - in particular aggregate size and volume fraction. In this paper the concept of a flow rate criterion is investigated taking into account the mix design, the rheological properties of the matrix and concrete, and the geometry of the flow domain.

## 2. Hypotheses of a Flow Rate Criterion for Blocking

The hydrodynamics of suspension flow is discussed in this section. The suspension is assumed to consist of two phases, a particle phase and a matrix phase. Suspension flow is a combination of matrix and particle flow. It is assumed that the particles move due to drag forces exerted by the matrix on the particles. The drag force,  $F_{\text{drag}}$ , is the resultant viscous force exerted on a particle by the matrix. Factors like slip in the interface between the matrix and the particle may affect the magnitude of the drag.

For suspensions to flow homogeneously the drag forces must overcome particle interactions,  $F_{p-p}$  and in confined (finite) domains also the interaction between particles and fixed solid boundaries,  $F_{p-b}$ . Figure 2 illustrates in principles these forces divided into their normal and tangential components  $F_{p-p,n}$ ,  $F_{p-p,t}$ ,  $F_{p-b,n}$ , and  $F_{p-b,t}$ .

As the flow domain narrows, the total resistance to flow results increasingly from interaction between the particles and the boundaries. Because the solid boundaries are fixed in space it is expected that the risk of initiating blocking increase for decreasing flow domain.

It is assumed that by increasing the flow rate a higher drag is generated thereby decreasing the risk of blocking. The drag force is a function of the matrix viscosity and the strain rate at the matrix-particle interface, which depends on the distance between particles. This again is a function of the particle volume fraction, size and shape. Concerning the effect of particle shape it is assumed that spherical particles require less drag to avoid blocking due to the ball bearing effect and the small contact area between particles and between particles and solid boundaries.

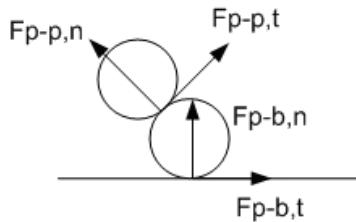


Figure 2 – Forces acting between particles and between particles and solid boundaries. These forces must be overcome for the suspension to flow homogeneously.

Thus, a critical flow rate is assumed to exist below which homogeneous suspension flow competes with separation by blocking.

Flow rate dependent phase separation has been observed in studies of concentrated and highly viscous pastes in a squeeze flow test by Poitou et al. (10) and in ram extrusion of high solid volume microcrystalline cellulose pastes by Rough et al (11). The phenomena observed in both test differs from blocking in the way that the main cause for separation is not particle restraint due to boundary interactions. In the squeeze flow test migration of particles occurs due to strain rate gradients and in ram extrusion water migration is a result of the compaction process and the development of pore pressures in the liquid phase.

Poitou et al. have developed a numerical scheme to describe the squeeze flow test (10). Conservation laws of mass and momentum were written for each phase and the suspension (particle) rheology were modeled using a shear-thinning power law expression while the matrix followed that of Newtonian liquid. The numerical scheme seems to simulate the behavior observed in the experiments. Furthermore, a qualitative analytical expression was developed to estimate a critical squeeze flow velocity below which migration of particles occurs. It is based on an energy criterion dividing the total viscous dissipation into an intrinsic viscous dissipation caused by friction between particles (particles and matrix move at the same velocity), and interaction dissipation due to the viscous drag (particles and matrix does not move at the same velocity). The concept of a critical velocity is based on the assumption that particles migrate to zones where the intrinsic viscous dissipation is low, i.e. where the solid shear rate is low. It is assumed that a critical velocity may be estimated when the viscous dissipation due to friction and drag are equal. For a quantitative estimate they select a matrix velocity relative to the particles  $v_p - v_f$  where  $v_p$  is the particle velocity,  $v_f$  the fluid velocity, and that  $v_p$  is approximately equal to the squeezing velocity.



A one-dimensional model was proposed by Rough et al. to describe the compaction and ram extrusion of highly concentrated pastes exhibiting high yield stresses (11). This type of material deforms as a stiff suspension where the particle stress is responsible for the deformation of the particles whereas the liquid stress (pore pressure) is the driving force for the flow of the liquid phase. The model includes several estimates of material parameters, which is based on existing results in the solids and soils literature. An important feature of the model is the use of experimentally determined parameters for the extrusion work parameters, the solids compressibility and reference particles permeability.

In the present work, a two-phase approach to suspension flow somewhat similar to the ones applied by Poitou et al. and Rough et al. is applied to assess the existence of a critical flow rate for the blocking resistance of suspension flow in narrowing gaps. The pressure drop required for the suspension to flow in the two situations; homogenous flow and heterogeneous flow is investigated. The procedure will be independent on the specific choice of the fluid velocity relative to the particles. Different studies on the rheological properties of SCC, mortar, and paste has shown a Bingham behavior with a yield stress,  $\tau_0$ , and plastic viscosity,  $\eta_{pl}$ . This will be applied to both the suspension and matrix phase.

Evidence that blocking may occur above a critical flow rate has been shown for colloidal particles arriving at a pore entrance (<sup>12</sup>). At high velocities the hydrodynamic forces acting on the particles at the pore entrance can overcome the inter-particle colloidal repulsion and result in the particles flocculating and plugging the pore. This indicates that the assumption of blocking occurring at velocities below the critical velocity is only valid when flow is controlled by hydrodynamic interactions and not interactions such as repulsion between colloid particles.

### **3. Determination of a Critical Flow Rate based on Macroscopic Pressure Drop in a Single Fluid and Two-Phase Approach to Flow**

The principles of a single fluid and two-phase approach for simulation of blocking are illustrated in Figure 3. A constant flow rate,  $Q_0$ , is imposed in the x-direction on a suspension consisting of monosized spherical particles at a volume fraction,  $\phi_p$ , submerged in a matrix phase. At the outflow the suspension is restrained in the flow direction by obstacles in this case illustrated by bars. The average suspension velocity in the x-direction is given by  $v_{s,i}$  and the particle and matrix velocities by  $v_{p,i}$  and  $v_{m,i}$ , respectively. The index  $i = 1, 2$  denotes flow in and out of the control volume.

The situation to the left illustrates homogeneous suspension flow in which

$$v_{s,i} = v_{p,i} = v_{m,i} \quad (1.1)$$

The situation to the right illustrates heterogeneous flow due to blocking. At the outflow blocking is a result of change in velocity,  $\Delta v_p$ , between the particle velocities coming in and out of the control volume. The magnitude of the velocities at time,  $t_0$ , will be given by

$$\begin{aligned}
 v_{s,1} &= v_{p,1} = v_{f,1} \\
 v_{p,2} &= v_{p,1} - \Delta v_p \\
 v_{p,2} &< v_{s,2} < v_{f,2}
 \end{aligned}
 \tag{1.2}$$

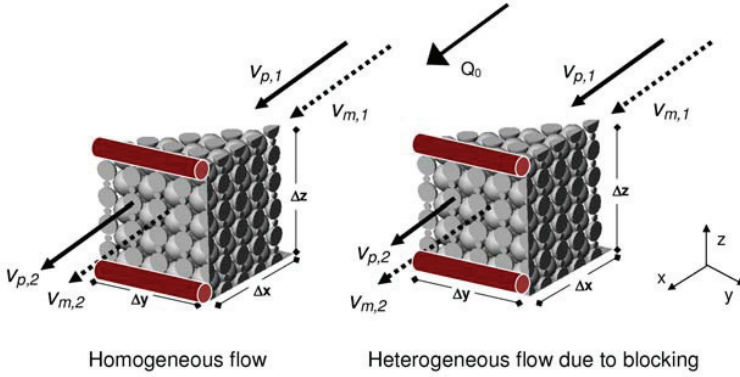


Figure 3 - Principles of particle and fluid velocities in and out of a control volume in the two situations; homogeneous and heterogeneous flow.

It is assumed that a critical flow rate may be estimated from the pressure drop required to retain a constant flow rate,  $Q_0$ , in the two situations, homogenous suspension flow,  $\Delta P_{sus}$ , and heterogeneous flow,  $\Delta P_{sep}$ . Blocking is initiated at a flow rate where the pressure drop in heterogonous flow is less than that of homogenous suspension flow. Therefore,

$$\begin{aligned}
 \Delta P_{sep} &> \Delta P_{sus} : \text{No blocking} \\
 \Delta P_{sep} &< \Delta P_{sus} : \text{Blocking} \\
 \Delta P_{sep} &= \Delta P_{sus} : \text{Critical flow rate}
 \end{aligned}
 \tag{1.3}$$

Particle accumulation continues if the pressure drop of heterogeneous flow at all times remains less than that required for the system to flow as a homogenous suspension. Complete blocking is obtained when the particle volume fraction reaches its maximum value,  $\phi_p^*$ .

In homogenous suspension flow the pressure drop depends on the rheological properties of the suspension. This again depends on the particle volume fraction,  $\phi_p$ , and the matrix viscosity. In two-phase flow the particle volume fraction at time  $t_1=t_0+dt$  is given by  $\phi_p(t_1) = \phi_p(t_0)+d\phi$  and it is assumed that the macroscopic pressure drop consists of a suspension part,  $\Delta P_{sep,sus}$ , and a capillary part,  $\Delta P_{sep,cap}$ . The suspension part refers to the part in which the matrix move

at the same velocity as the particles,  $v_{p,2}$ , over the surface area  $\Delta y \Delta z$ . The pressure drop of the suspension part is determined for the particle flow rate at time  $t_1$ ,  $Q_{p2}(t_1)$ .

The capillary part refers to the part in which the matrix moves at a velocity  $\Delta v_{pf,2}$  ( $= v_{p,2} - v_{m,2}$ ) higher than the particles over the surface area  $(1-\phi_p)\Delta y \Delta z$ . It is assumed that the matrix flow takes part in linear capillaries and modified capillary theories have been applied to estimate the number and dimension of linear capillaries in which matrix flows (13).

The suspension part and capillary part is illustrated in Figure 4.

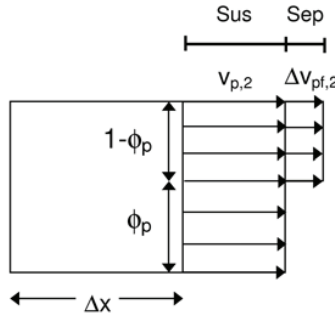


Figure 4 - Illustration of the suspension part (sus) and capillary part (sep) in heterogeneous flow.

Studying blocking is of interest in finite flow domains where solid boundaries play a significant role. Therefore, to study the pressure drop-flow rate relation one of the existing analytical expressions for well-defined flow domains are chosen. In this paper, it is decided to consider the volume rate of flow in a circular tube of a Bingham fluid where the pressure drop – flow rate relation is given by the Buckingham-Reiner equation

$$Q_0 = \frac{\pi R^3 \tau_R}{4 \eta_{pl}(\phi_p)} \left( 1 - \frac{4}{3} \frac{\tau_0(\phi_p)}{\tau_R} + \frac{1}{3} \left( \frac{\tau_0(\phi_p)}{\tau_R} \right)^4 \right) \quad (1.4)$$

where  $\tau_R = \frac{\Delta P \cdot R}{2L}$ , and  $R$  is the tube radius and  $L$  the tube length (14,15).

As indicated in equation 1.4 the yield stress  $\tau_0$  and plastic viscosity  $\eta_{pl}$  are functions of the particle volume fraction  $\phi_p$ . In order to include the effect of change in particle volume fraction, a rheological composite model is applied. Einstein was the first to propose such a model for a suspension of hard spheres, however, for very low particle volume fractions ( $\phi_p < 0.03$ ) ( ).

Another example is the so-called Krieger-Dougherty equation, which is a general empirical expression for suspensions of particles of spherical or other shape given by

$$\eta = \eta_m \left( 1 - \frac{\phi_p}{\phi_p^*} \right)^{-[\eta]\phi_p^*} \quad (1.5)$$

where  $\eta$  is the suspension viscosity,  $\eta_m$  the matrix viscosity and  $[\eta]$  the intrinsic viscosity which is 2.5 for spherical particles.

To illustrate this modeling concept, the Krieger-Dougherty relation (1.5) is applied to both the plastic viscosity and yield stress. Therefore, in stead of viscosities  $\eta$  and  $\eta_m$  in equation 1.5, these are replaced by the plastic viscosities  $\eta_{pl}$  and  $\eta_{pl,m}$  and for the yield stress by  $\tau_0$  and  $\tau_{0,m}$ .

The matrix pressure drop – flow rate relation is determined by combining the modified capillary theories and equation 1.4 where the rheological properties of the matrix are applied ( $\tau_{0,m}$  and  $\eta_{pl,m}$ ), independent on the particle volume fraction.

Initially, it is investigated whether it is possible to obtain heterogeneous flow consisting of combined suspension and matrix flow at a lower pressure drop than that required for homogeneous flow. Imposing a constant flow rate  $Q_0$  the criterion will be given by

$$Q_0 (\Delta P_0, \phi_0, \tau_0, \eta_{pl}) = Q_s (\Delta P_0 - \Delta P_{0-p}, \phi_0 + d\phi, \tau_0 + d\tau_0, \eta_{pl} + d\eta_{pl}) + Q_m (\Delta P_{0-p}, \phi_0 + d\phi, \tau_{0,m}, \eta_{pl,m}) \quad (1.6)$$

Figure 5 illustrates the meaning of  $\Delta P_{0-p}$  and  $\Delta Q_{0-p}$ . The figure shows the pressure drop – flow rate relation for suspension flow at an initial particle volume fraction  $\phi_p$ . Introducing a infinitesimal particle velocity gradient,  $d\mathbf{v}_p/dx$ , and infinitesimal time,  $dt$ , this results in an increase in the particle volume fraction,  $d\phi$ . Again the pressure drop – flow rate relation for suspension flow may be written at a particle volume fraction  $\phi_p + d\phi_p$ .

A parameter study shows that for  $d\phi \rightarrow 0$  equation 1.6 is fulfilled only at the intersection point between the flow curve of homogenous flow and matrix flow. At higher flow rates, the combined pressure drop corresponding to initiation of blocking will be higher than that of the homogenous suspension flow to keep a constant flow rate  $Q_0$ . This indicate that either homogeneous or matrix flow will occur depending on the flow rate. Furthermore, once blocking is initiated particles will continue to accumulate because the resistance to homogeneous flow increases more rapidly as a function of the particle volume fraction than does the resistance to matrix flow. This is a result of the suspension rheology being more dependent on the particle volume fraction than the dimension and numbers of capillaries for matrix flow.

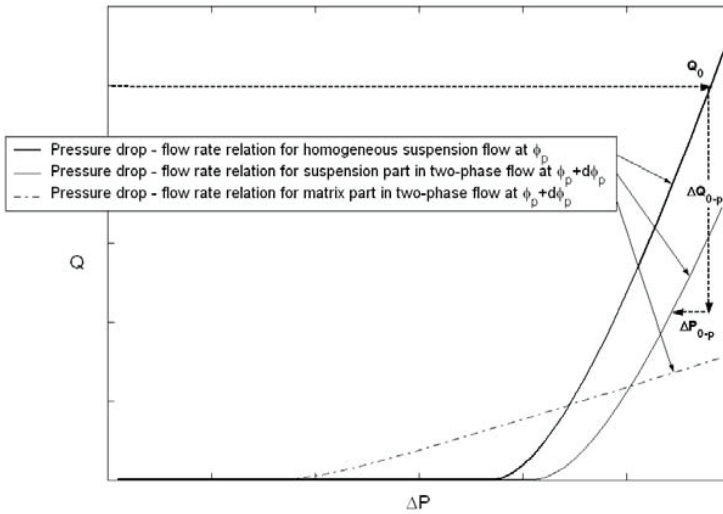


Figure 6 – Illustrations of the pressure drop – flow rate relation for suspension flow at particle volume fraction  $\phi_p$ , suspension flow at  $\phi_p + d\phi_p$ , and matrix flow at  $\phi_p + d\phi_p$ .

An example of the model is illustrated in Figure 7.

It illustrates the matrix velocity relative to the suspension,  $v_m - v_s$ , as a function of the aspect ratio (pipe radius over particle radius), pressure drop gradient,  $\Delta P/L$ , and the particle volume fraction,  $\phi_p$ , whenever

$$v_m - v_s > 0 \quad (1.7)$$

where  $v_s$  is the homogeneous suspension velocity. This corresponds to matrix flow dominating over homogeneous suspension flow and blocking is initiated. If  $v_m - v_s \leq 0$  it corresponds to homogeneous suspension flow dominating over matrix flow and initiation of blocking. This is indicated by  $v_m - v_s$  values of zero.

Comparing the 4 figures at a given particle volume fraction  $\phi_p$  it is observed that the critical velocity increases when the aspect ratio decreases as a result of the resistance to homogenous flow increasing more rapidly than the resistance to capillary flow taking into account the dimensions of the finite domain. Also, the it is observed that the transition zone between homogeneous flow and matrix flow occurs at a lower particle volume fraction when the aspect ratio decreases.

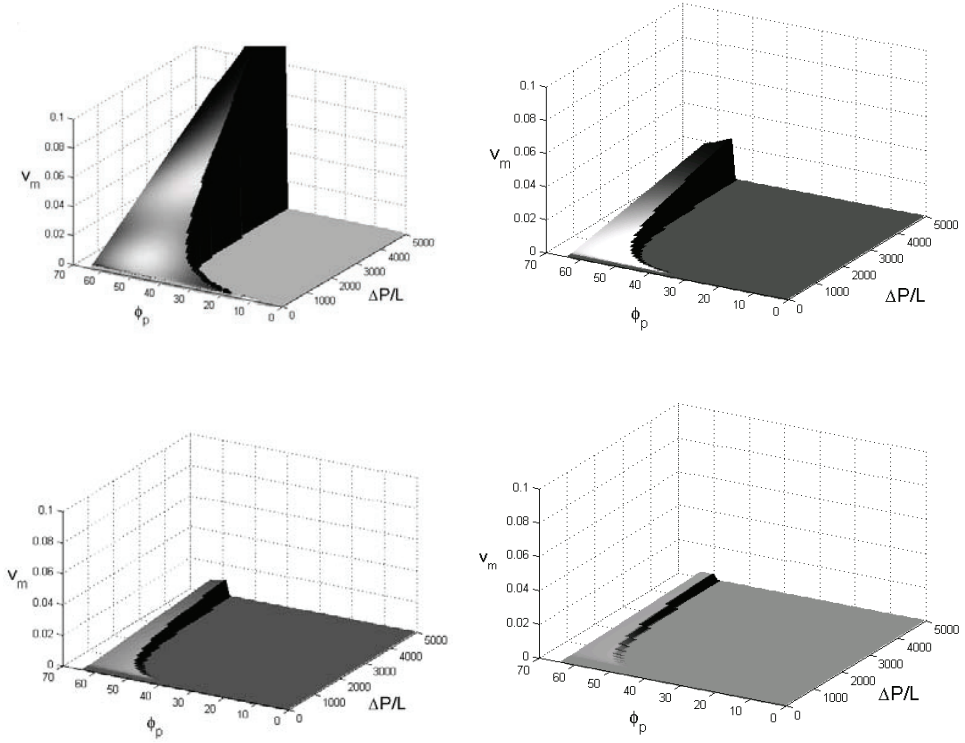


Figure 7 – Illustration of matrix velocity relative to the suspension,  $v_m - v_s$ , when  $v_m - v_s > 0$  corresponding to matrix flow dominating over homogeneous suspension flow resulting in initiation of blocking. If  $v_m - v_s \leq 0$  homogeneous suspension flow dominates over matrix flow which is illustrated by  $v_m = 0$ . It is shown as a function of the aspect ratio,  $A$ , particle volume fraction  $\phi_p$ , and pressure drop gradient,  $\Delta P/L$ . The aspect ratios applied are 2 (upper left), 4 (upper right), 6 (lower left), and 10 (lower right).

#### 4. Conclusion

A theoretical model for assessment of the blocking resistance of SCC has been introduced. The model proposes a flow rate criterion determined on the basis of a comparison of the macroscopic pressure drop needed to retain a constant flow rate in the two situations, homogenous flow and heterogeneous flow. A single fluid and two-phase approach to flow has been applied to assess the macroscopic pressure drop in these two situations. A composite model relates the mix composition and rheological properties of the suspension and modified capillary theories have been applied for assessment of the number and size of capillary pores available for matrix flow.

In relation with the current model, a flow rate criterion may be applied in a single fluid approach to simulation of form filling with SCC to estimate and identify locations in the formwork where there is an increased risk of blocking. By this approach, it is possible to retain the accuracy of a single fluid approach for simulation of form filling on a larger scale, and reduce the need for computer capacity compared to a discrete particle flow approach.

## References

1. Billberg, P. "Self-Compacting Concrete for Civil Engineering Structures - the Swedish Experience". CBI Report 2:99 (1999).
2. Efnarc publications "Specification and Guidelines for SCC", [www.efnarc.org](http://www.efnarc.org) (2002).
3. Kurokawa, Y. Tanigawa, Y., Kim, W. J., Teranishi, K., "Evaluation Method of High-Fluidity Concrete", Transactions of the Japan Concrete Institute, Vol. 17 (1995).
4. Noguchi, T., Oh, S. G., Tomosawa, F., "Rheological Approach to Passing Ability between Reinforcement bars of Self-Compacting Concrete", Proceedings of the First International Rilem Symposium, Stockholm, Sweden (1999).
5. Tangtermsisikul, S., Bui, V. K., "Blocking Criteria for aggregate phase of self-compacting high performance concrete", Proceedings of the Regional Symposium on Infra-Structures Development in Civil Engineering, Bangkok, Thailand, pp. 58-65 (1995).
6. Martys, N., Ferraris, C. H., "Simulation of SCC flow", Proceedings of the First North American Conference on the Design and Use of Self-Consolidating Concrete, Chicago (2002).
7. Petersson. Ö., Hakami, H., "Simulation of SCC—Laboratory Experiments and Numerical Modelling of Slump flow and L-box Tests", Proceedings of the Second International Symposium on SCC, Tokyo (2001).
8. Noor, M.A., Uomoto, T., "Three-Dimensional Discrete Element Simulation of Rheology Tests of Self-Compacting Concrete" Proceedings of the 1<sup>st</sup> International RILEM Symposium on SCC, Stockholm, Sweden, pp. 35-46 (1999).
9. Mori, H., Tanigawa, Y., "Simulation Methods for Fluidity of Fresh Concrete", Memoirs of the School of Engineering, Nagoya University, Vol 44, pp. 71-133 (1992).
10. Poitou, A. Racineux, G., "A Squeezing Experiment showing Binder Migration in Concentrated Suspensions", Journal of rheology, 45 (3), pp. 609-625 (2001).
11. Rough, S. L., Wilson, D. I., and Bridgwater, J., "A Model describing Liquid Phase Migration Within an Extruding Microcrystalline Cellulose Paste", Institution of Chemical Engineers, Trans Icheme, Vol 80, Part A (October 2002).
12. Ramachandran, V., Venkatesan, R., Tryggvason, G., Fogler, H. S., "Low Reynolds Number Interactions between Colloidal Particles near the Entrance to a Cylindrical Pore", Journal of Colloid and Interface Science 220, 311-322 (2000).
13. Carmen, P. C., "Fluid flow through Granular Beds", Trans. Inst. Chem. Engrs., London, (1937).
14. Buckingham, E., Proceedings. ASTM, 177, pp. 1154-1161 (1921).
15. Bird, R. B., Stewart, W. E., Lightfoot, E. N., "Transport Phenomena", Wiley, New York, pp. 48-50 (1960).

16. Larson, R. G., “The Structure and Rheology of Complex Fluids”, Oxford University Press (1999).



## **Plastic Shrinkage of Self-Compacting Concrete**

Bertil Persson

Division Building Materials, Lund Institute of Technology, Lund, Sweden

### **Abstract**

This paper emphasis a description of research on plastic shrinkage of Self-Compacting Concrete including the close related early shrinkage, strength development and self-desiccation. The major part of the research contains concrete with low water-cement ratio. The research was performed in environmental controlled conditions, sealed specimen, wax treated or drying specimen. Generally the research was performed short-term with a final measurement of strength and RH at 28 days' age. Unique measurement technique was used in the tests with measuring of the shrinkage profile all up to the surface of the concrete together with parallel measuring of the plastic crack width. In order to obtain low plastic crack width it was an advantage to use Self-Compacting Concrete with large aggregate size. A tendency of gap grading of the particles in the fresh concrete provided more bleeding water which in turn decreased the development of plastic cracking as compared with ideal, linear logarithmical distribution of the particles. In case of plastic cracking the size of the cracks were limited by early strength development. Plastic shrinkage before the final setting time of the concrete became a great part of the total shrinkage, even though autogenous shrinkage first was subtracted. Wax treatment had no/little influence on plastic shrinkage at low water-cement ratio.

### **1. Introduction and objective**

Concrete that does not require any drying time influencing on the construction time of the building has from obvious reasons attended a great interest from the market especially when it is cast without any vibrating tools, so called self-compacting concrete, SCC. However, as for ever and a day, some problems remain unsolved such as early age performance, especially in the surface zone, and measurement for moisture, for self-compacting concrete without construction moisture to be generally introduced. The objective of the research, with the developed unique measurement technique, was concentrated on measurement on the shrinkage profile all up to the surface of the concrete, and, in parallel, measurement of the plastic shrinkage width. The concrete for the research was manufactured in one batch in order to avoid time differences at the start of testing. Two fans were used in a wind tunnel at test of plastic shrinkage in order to decrease the variations of the wind speed. The following parameters were essential:

- Bleeding water
- Evaporation
- Water-cement ratio, w/c
- Wind speed

## 2. Experience of plastic shrinkage

### 2.1 General

The mechanism behind plastic shrinkage is the under-pressure that is created in the pore water meniscus, mainly due to evaporation from the surface of the concrete, but also due to chemical shrinkage of the hydrated water [1]. Plastic shrinkage may be divided into three stages [1]:

- The surface of the concrete is still wet due to bleeding and no plastic shrinkage occurs.
- The surface dries and a system of menisci is created between aggregate and cement particles. The radius of the meniscus decreases and the under-pressure increases.
- After few h the concrete final set and the plastic shrinkage ceases.

The under-pressure and the plastic shrinkage was measured, Figure 1 [2]. The pressure measurement was performed with a 0.38-mm needle into the fresh concrete. Calibration of the pressure device was performed in water at the same depth from the surface as the measurement in concrete, 10 mm and 40 mm. The following parameters affected the under-pressure [2]:

- w/c
- Additives and admixtures
- Curing conditions
- Type of cement

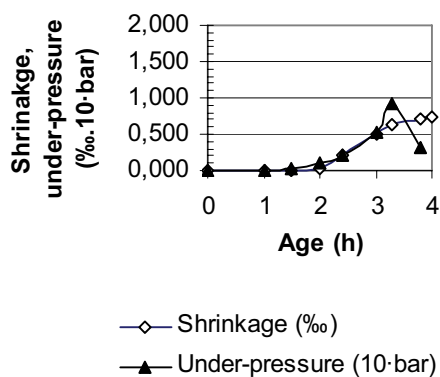


Figure 1 –Under-pressure in pore water and plastic shrinkage of concrete [2].

Figures 2 and 3 show the age and the maximum under-pressure of cement paste with different w/c and two cements either Degerhamn low-alkali cement, D (specific surface = 305 m<sup>2</sup>/kg) or Slite normal-alkali cement, S (specific surface = 364 m<sup>2</sup>/kg). The size of the under-pressure was also dependent of the depth from the surface, Figure 4 [2]. It was also observed that plastic shrinkage was substantially larger for SCC than for normal concrete, more than twice as large, Figure 5 [3]. Field studies confirmed the problems with plastic shrinkage of SCC especially during windy conditions and with rapid hardening cement, SH (specific surface = 475 m<sup>2</sup>/kg), Figure 6 [4].

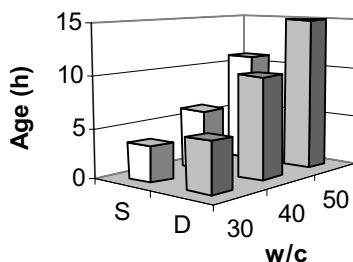


Figure 2 – Age at maximum under-pressure [2]. D= Degerhamn. S = Slite.

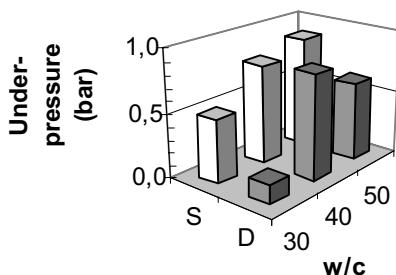


Figure 3 –Maximum under-pressure. D= Degerhamn cement. S = Slite cement [2].

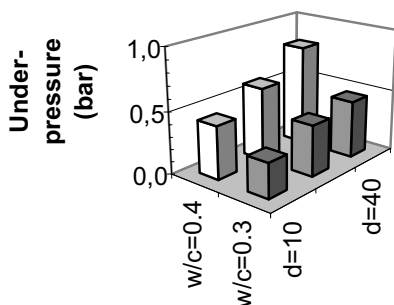


Figure 4 –Maximum under-pressure at different depth, d (mm) [2]. Cement D.

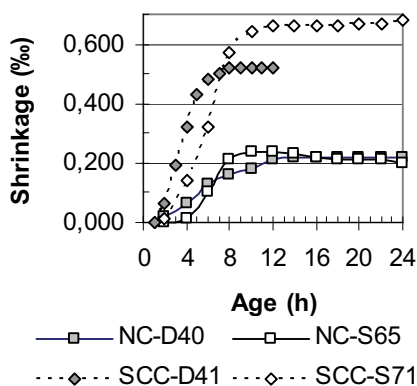


Figure 5 – Shrinkage of normal and SCC. 40= w/c (%). D= Degerhamn. S = Slite [3].

## 2.2 Cracking due to plastic shrinkage

Cracking due to plastic shrinkage is dependent on the following ambient conditions [5]:

- Ambient conditions such as air speed, temperature and relative humidity, RH

- External restraint such as geometry of mould, friction to mould and mould restraint
- Internal restraint such as concrete mix proportions, thickness of slab and cast-in reinforcement.
- Size of concrete slab.

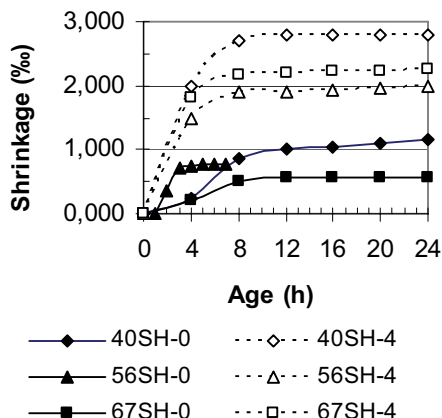


Figure 6 – Shrinkage of SCC with SH cement [4]. 4= 4 m/s wind, 40= w/c (%)

A great risk of plastic shrinkage cracking appears when the evaporation is larger than  $1 \text{ kg/m}^2\text{h}$  but cracking may occur at  $0.1 \text{ kg/m}^2\text{h}$  [6]. Figure 7 shows the evaporation rate at different air speed [7]. There is also a correlation between the bleeding rate and the evaporation, Figures 8-9 [8]. In Figure 8 two types of cement were investigated at  $\text{RH} = 50\%$ , Portland cement, PC, and trass cement, PKC. As soon as the evaporation rate exceeds the bleeding rate the plastic cracking takes place provided than the slab is restraint from movement, Figure 9 [8]. A combination of Figures 7 and 8 gave a substantial influence of temperature on the evaporation rate, the experiments of Figure 7 performed at  $20^\circ\text{C}$  and of Figure 8 at  $28^\circ\text{C}$ , Figure 10 [7,8].

### 2.3 Effect of fibres

A study with the objective to diminish the risk of plastic shrinkage cracking of concrete with fibre additives was performed, both of polypropylene, ppf and steel, sf [9]. For testing a newly developed test method was used [10]. Figure 11 shows the evaporation rate of concrete with and without fibres, both ppf and sf [9]. It seemed like the evaporation rate increased with ppf which ought to give a greater risk of cracking than for concrete without ppf. The reason for larger evaporation with ppf than without ppf is probably that fine channels are formed parallel to the fibres. The channels lead the water from the inner part of the concrete to the surface of the concrete [9]. Figure 12 shows the risk of plastic cracking at 4 m/s air speed with different amounts of sf [9]. About 0.5% sf was needed to limit the plastic crack width to 0.4 mm. The following risk equation was developed [9,11]:

$$S = (1.4 \cdot sf - 0.132) \cdot d^2 - (1.84 \cdot sf + 0.641) \cdot d - 0.669 \cdot sf^3 + 0.995 \cdot sf^2 - 0.345 \cdot sf + 1.08 \quad (1)$$

d denotes plastic crack width (mm)  
sf denotes steel fibre (%)  
S denotes probability for plastic cracking (-)

Steel fibres were clearly effective in order to limit the plastic shrinkage of concrete [9].

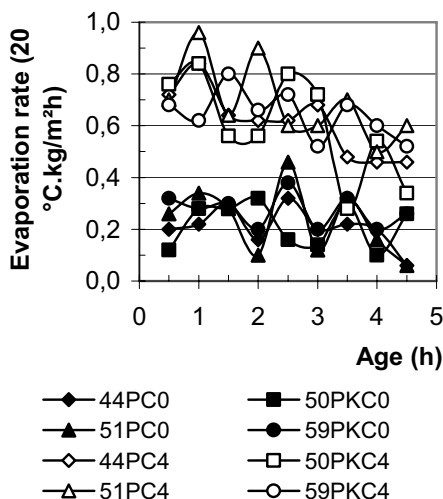
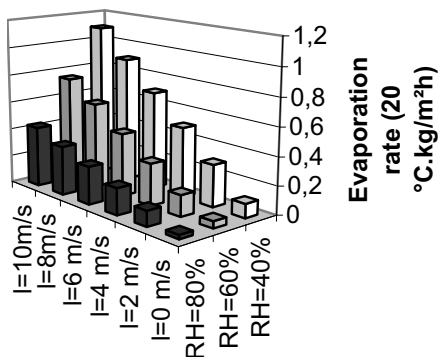


Figure 7 - Evaporation rate at different air speed, l [7]. RH= relative humidity.

Figure 8 - Evaporation rate [8]. PC= Portland, 4= 4 m/s air speed, 44= w/c.

### 3. Experimental methods

#### 3.1 Materials

Ten concrete were studied with mix proportions as shown in Table 1. The material was at first mixed dry for ½ min. and then with water and superplasticiser for 2½ min.. Slump flow, density and air content was then measured. The concrete was cast in a 20-°C climate chamber either two slabs, 0.1x0.36x0.56 m³, three beams 0.1x0.1x0.4 m³ or twelve cube, 0.1x0.1x0.1 m³, Figure 13 [11]. The slabs had 60 mm high edge-formed anchors at 0.19 m centre distance in the slab. Curing took place either in the air (RH = 60%), sealed with plastic foil and aluminium foil or with vax treatment (0.25kg/m²). The specimens were all placed in a tunnel with double fans providing an air speed of 4 m/s.

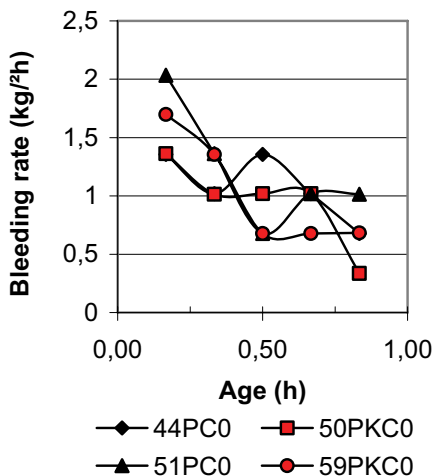


Figure 9 – Bleeding rate vs age [8]. ]. PC= Portland, 0= 0 m/s air speed, 44 = w/c.

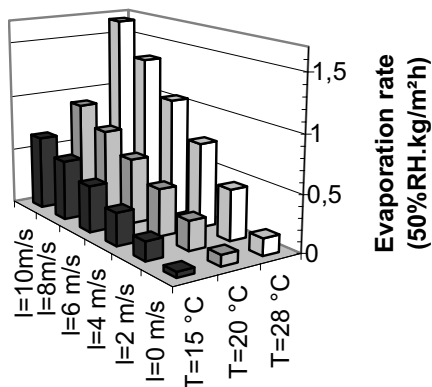


Figure 10 - Influence of temperature on the evaporation rate [7,8]. l= air speed.

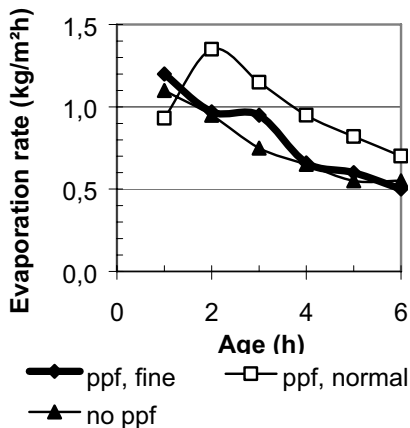


Figure 11 - Evaporation rate of concrete with and without fibres, ppf or sf [9].

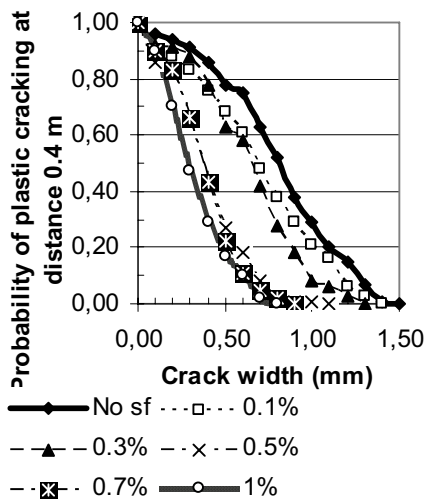


Figure 12 - Probability of plastic cracking at distance 0.4 m vs crack width [9].

Table 1 – Mix proportions and properties of studied concrete (kg/m<sup>3</sup>, etc.)

w/c (%) - max particle size (mm) /Material	35 m2	35 m8	38m8	38 m8id	38 m18	38 m18id	40m8	43 m18	53 m18	53m 18 extra
Crushed gneiss 11-18					643	385		631	639	631
Crushed gneiss 4-8			747	952	178	538		174	251	248
Gravel 0-2	1733									
Pea gravel 4-8		475					472			
Crushed gneiss 2-4		206					205			
Sand 0-4		627					621			
Sand 0-2			712	662	695	695		683	537	531
Sand 0-1			146	76	186	98		183	320	317
Sand 0.1-1		303					302			
Glass filler			78		59			58	61	60
Limest. filler (40µm)		140					158			
Blended cement		466					443			
Byggcement Slite			494	510	432	484		424	357	353
NORCEM cement	524									
Water	183	168	188	194	186	184	177	182	189	187
Superplasticiser	10.4	9.1	12.9	13.3	12.1	12.6	16.4	14.2	10	10
Viscosity agent							5.1			
Density	2442	2388	2369	2398	2383	2388	2384	2339	2357	2330
Cement + filler	524	606	572	510	491	484	601	482	418	413
Aggregate ratio, by weight dry mtrl	0.77	0.73	0.74	0.77	0.78	0.78	0.73	0.78	0.81	0.81
Superplast (%/cem)	2.0	2.0	2.6	2.6	2.8	2.6	3.7	3.3	2.8	2.8
Slump flow (mm)		740	665	750	635	720	740	670	670	670
Strength (28d,MPa)	59	113	67	68	77	67	88.5	63	43	56
RH (sealed,28d,%)	89.5	79	87	90.5	85.5	85	-	89	94	94

d= days, id = ideal distribution of particle in fresh concrete, x = twin extra mix.

### 3.2 Methods

The following measurements took place:

- Air speed in tunnel
- Crack width in slabs, Figure 14.

- Deformation at 20-mm and 70-mm depth of beams at one moveable gable which gave the possibility to extrapolate the shrinkage of the surface.
- RH of concrete peaces after strength tests, Figure 15.
- Strength of cubes
- Temperature, ambient, surface and centre of specimen.



Figure 13 – Overview of specimens cast in a RH=60% climate chamber [11].



Figure 14 – Plastic cracking of slab [11].



Figure 15 – RH measurement on concrete pieces from strength tests [11].



## 4. Results

### 4.1 Evaporation, self-desiccation and strength

The evaporation rate from a free water surface in the tunnel was slightly dependent on the position of the fan, Figure 16. From the tests and from previous experience the following equations for evaporation from a free water surface were estimated [4,7,11]:

$$E_{T=20\text{ }^{\circ}\text{C}}=0.15\cdot(1.07\cdot\text{RH})\cdot W+0.019\cdot\text{RH}^{-1.76} \quad (2)$$

$$E_{\text{RH}=50\%}=(0.00104\cdot T^{1.48})\cdot W+0.16\cdot\ln(T)-0.38 \quad (3)$$

$$E_{\text{RH}=80\%}=(0.00155\cdot T^{1.13})\cdot W+0.064\cdot\ln(T)-0.16 \quad (4)$$

E	denotes evaporation (kg/m <sup>2</sup> h)
RH	denotes relative humidity (-)
T	denotes temperature (°C)
W	denotes air speed (m/s)

Due to the air movement in the tunnel the temperature raise became minor, about 2½ °C, and then had little influence on RH and measured shrinkage. Even though temperature movement were taken into account with 0.01 %/°C. The development of RH was correlated to strength at 1 month' age, Figure 17-18, equations (5) – (7) (100-mm cube strength,  $f_c$  (MPa), RH (%)):

$$f_c = 16000\cdot(w/c)^{-1.46} \quad \{35 < w/c < 55\% \} \quad (5)$$

$$\text{RH} = 28.6\cdot(w/c)^{0.30} \quad \{35 < w/c < 55\% \} \quad (6)$$

$$\text{RH} = 200\cdot(f_c)^{-0.19} \quad \{40 < f_c < 120 \text{ MPa} \} \quad (7)$$

### 4.2 Plastic cracking

Figure 19-20 show plastic cracking width of concrete with different w/c versus age, air-cured or with vax. With w/c = 0.43 and 0.53 no plastic cracking took place. At w/c = 0.38 the largest cracking was measured for concrete with ideal, continues grading of the particles in the fresh mix. Concrete in the air mixed with gap grading obtained less than half the crack size as compared with the crack size with ideal grading of the particles in the fresh mix. An ideal grading of the particles in the fresh mix is used to obtain the best workability, but, obvious gives larger plastic shrinkage than a concrete with gap grading. Most probably a concrete with gap grading provides more bleeding water which delays the time of surface drying and, in turn, a condition for plastic shrinkage. For concrete with w/c = 0.38 and vax treatment cracking became smaller and was avoided for one concrete with gap grading and large maximum size of the aggregate, 18 mm, instead of 8 mm, which confirms the results with air curing and also indicate that larger aggregate size gives less risk for plastic shrinkage than smaller aggregate size. Possibly larger aggregate size more acts as crack-preventing reinforcement than smaller aggregate size does.

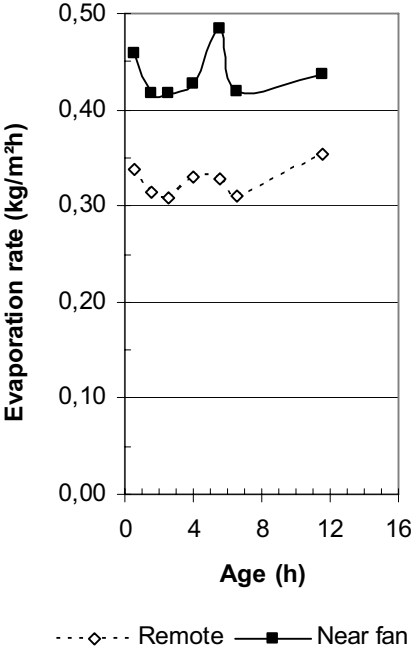


Figure 16 – Evaporation rate in tunnel.

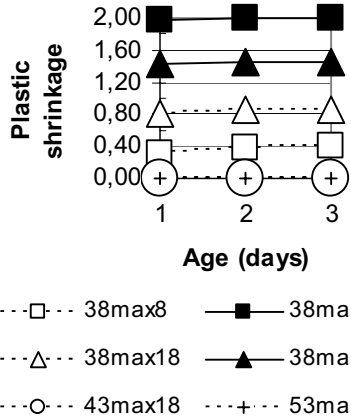


Figure 19 – Plastic shrinkage cracking with air curing [11].

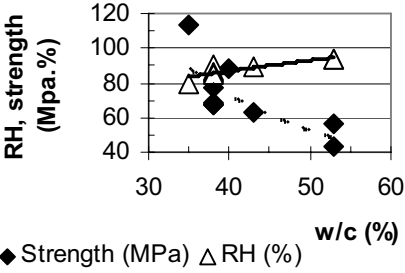


Figure 17 – RH, strength at 1-month' age.

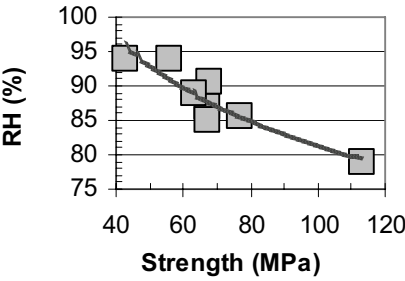


Figure 18 – RH vs strength, 1 month' age.

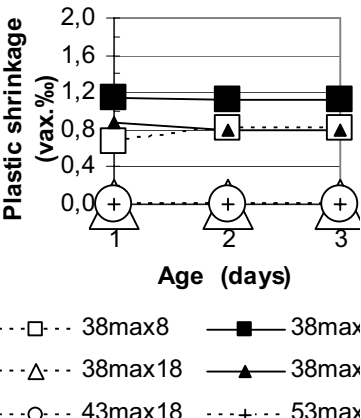


Figure 20 – Plastic shrinkage cracking with vax curing [11].

## 5. Analysis

### 5.1 Effect of strength and RH

Total shrinkage that was measured for SCC the first days after casting was large as compared to the shrinkage that is obtained for normal concrete after 1 day's age. Total shrinkage of normal concrete that is cured in the air varies between 0.4‰ and 0.7‰ while SCC in this study obtained twice as large shrinkage before 1 day's age. This observation is partly due to fact that shrinkage normally is measured from 1 day's age, partly that SCC contain an increased amount of paste, i.e. cement, filler and water, as compared to normal concrete. SCC contains a lower part of aggregate in order to prohibit shrinkage than normal concrete (aggregate does not shrink). Figure 21 shows shrinkage as a function of the one-day strength,  $f_1$ . Autogenous (sealed) shrinkage,  $\varepsilon_{s1}$ , was withdrawn from total shrinkage in order to obtain plastic shrinkage (plastic shrinkage is due to evaporation) with the following relationship (‰):

$$\varepsilon_{s1} = 0.018 \cdot f_1 - 0.59 \quad (8)$$

For shrinkage in the air at 1 day's age,  $\varepsilon_{a1}$  (RH = 60%), the following result with the one-day strength,  $f_1$ , was obtained (‰):

$$\varepsilon_{a1} = 0.046 \cdot f_1 - 0.57 \quad (9)$$

Plastic shrinkage thus became un-proportional to the one-day strength (‰):

$$\varepsilon_{p1} = -0.087 \cdot f_1 + 4.36 \quad (10)$$

A minimum strength was required to obtain any plastic shrinkage,  $f_1 >$  about 25 MPa. Early rapid strength development gave less plastic shrinkage cracking since hardening occurred at an earlier time with rapid strength development. A retarded strength development for example with too much superplasticiser in the concrete therefore gave larger plastic shrinkage crack width [11]. Lower plastic shrinkage at higher strength therefore became a logical explanation why no relationship exists between free shrinkage and plastic shrinkage. For vax treated concrete somewhat lower shrinkage was obtained after one day,  $\varepsilon_{v1}$ , as related to the one-day strength (‰):

$$\varepsilon_{v1} = 0.058 \cdot f_1 - 1.09 \quad (11)$$

- $f_1$  denotes the 1-day strength (MPa)
- $\varepsilon_{a1}$  denotes shrinkage in the air after 1 day (‰)
- $\varepsilon_{p1}$  denotes plastic shrinkage after 1 day (‰)
- $\varepsilon_{s1}$  denotes sealed shrinkage after 1 day (‰)
- $\varepsilon_{v1}$  denotes shrinkage with vax after 1 day (‰)

Since relationships exist between strength and RH also relationships were obtained between shrinkage and RH, Figure 22 (‰):

$$\varepsilon_{s1} = -3.55 \cdot RH + 3.27 \quad (12)$$

$$\varepsilon_{a1} = -9.695 \cdot RH + 9.675 \quad (13)$$

RH denotes relative humidity (-)  
 $\varepsilon_{a1}$  denotes shrinkage in the air after 1 day (‰)  
 $\varepsilon_{s1}$  denotes sealed shrinkage after 1 day (‰)

Shrinkage decreased at higher RH which is well-known. Plastic shrinkage mainly occurred before 1 day's age. No relationship was possible to obtain to RH (RH then was not measurable).

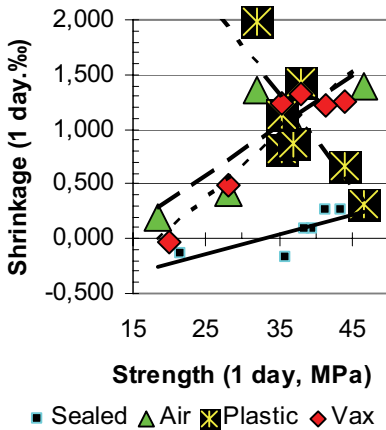


Figure 21 – Shrinkage vs 1-day strength.

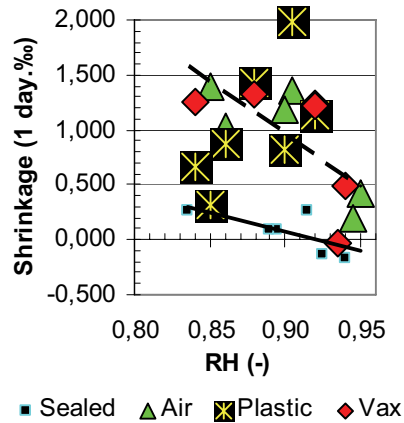


Figure 22 – Shrinkage vs 1-day RH [11].

## 5.2 Effect of mix proportions of concrete on plastic shrinkage

### 5.2.1 Sealed curing (autogenous shrinkage)

Figure 23 shows sealed shrinkage versus age. Figure 24 shows the particle distribution of the fresh concrete. Concrete 35max2 was a special one with other type of aggregate so this concrete was not taken into consideration. For the remaining types of concrete the following conclusions were drawn:

- Concrete with  $w/c \leq 0.38$  obtained large autogenous shrinkage before final set.
- Concrete with  $w/c > 0.38$  obtained autogenous expansion before final set.
- Concrete with larger amount of fines or larger tendency of gap grading obtained larger autogenous shrinkage before final set.
- After final set the increasing rates of shrinkage (development) were more or less equal of all concrete types.

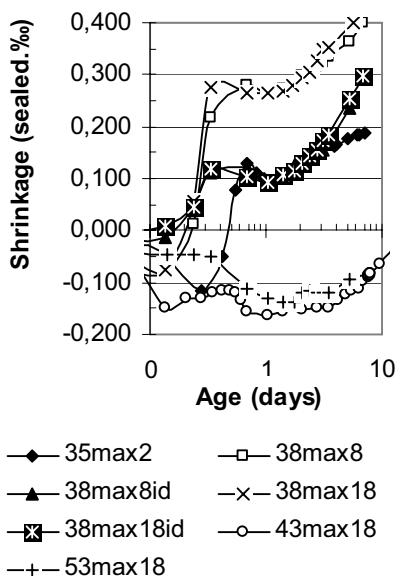


Figure 23 – Sealed shrinkage versus age. id = ideal fresh particle distribution, max 18 = 18-mm aggregate. 35 = w/c (%).

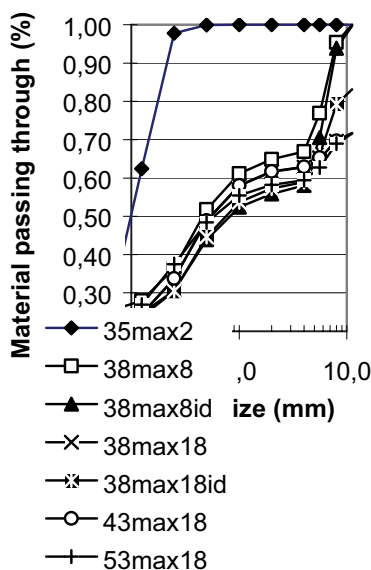


Figure 24 – Particle distribution of fresh concrete. id = ideal distribution, max 18 = 18-mm aggregate. 35 = w/c (%).

### 5.2.2 Plastic and drying shrinkage

Figure 25 shows shrinkage in the air versus age. w/c had a major effect on the plastic shrinkage. The plastic shrinkage before final set at about 8 hour's age, as shown in Figure 25, became a great part of the total shrinkage, about 1.1‰ for concrete with w/c = 0.38 provided that the autogenous shrinkage as shown in Figure 23 was subtracted at first. For concrete with w/c = 0.43 the plastic shrinkage became about 0.5‰ and for w/c = 0.53 about 0.25‰ since autogenous expansion as shown in Figure 23 first had to be added. For concrete with w/c = 0.38 larger shrinkage was obtained for concrete with maximum aggregate of 8 mm than for concrete with maximum aggregate of 18 mm, which well-known also for normal concrete [12]. w/c of the concrete also affected shrinkage of concrete with vax treatment [11]. Accordant Figure 26 the plastic shrinkage at final set at about 8 hour's age became a great part of the total shrinkage, about 1.1‰ for concrete with w/c = 0.38 provided that the autogenous shrinkage as shown in Figure 23 was subtracted at first. For concrete with w/c = 0.43 the plastic shrinkage became about 0.5‰ since autogenous expansion as shown in Figure 23 first had to be added. For concrete with w/c = 0.53 and vax treatment no plastic shrinkage was observed since the vax to some extent prohibited the moisture losses from the surface which precisely compensated for autogenous expansion of concrete with w/c = 0.53 [11]. Measured plastic shrinkage crack width was larger than measured plastic shrinkage both for air curing and for concrete with vax treatment since the crack was only measured in the surface. The plastic shrinkage was measured at

20-mm and 70-mm depth and then extrapolated linearly to the surface. In reality the shrinkage profile probably consisted of a more polynomial profile towards the surface which explained the difference (the polynomial profile giving larger shrinkage in the surface than a linear one). The explanation for this is the RH-distribution towards the surface which turn out to be polynomial. The only way to confirm this hypothesis is to construct a end block of the measurement rig that is divide into three part in turn connected to three measurement devices instead of the one-piece block and the two measurement devices that were used in this experiment [11].

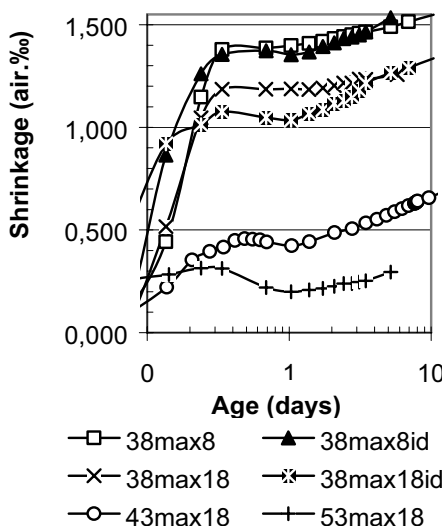


Figure 25 – Shrinkage in the air. id = ideal fresh particle distribution, max 18 = 18-mm aggregate.35 = w/c (%) [11].

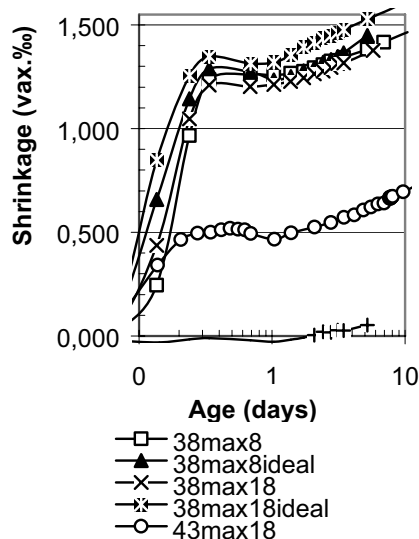


Figure 26 – Shrinkage with vax. id = ideal fresh particle distribution, max 18 = 18-mm aggregate.35 = w/c (%) [11].

## 6. Summary and conclusions

Experiments on plastic shrinkage of Self-Compacting Concrete were performed including the close related early shrinkage, strength development and self-desiccation. The major part of the research contains concrete with low water-cement ratio. The research was performed in environmental controlled conditions, sealed specimen, wax treated or drying specimen. Generally the research was performed short-term with a final measurement of strength and RH at 28 days' age. Unique measurement technique was used in the tests with measuring of the shrinkage profile all up to the surface of the concrete together with parallel measuring of the plastic crack width. The following conclusions were drawn:

- To obtain low plastic crack width it was an advantage to use Self-Compacting Concrete with large aggregate size.

- A tendency of gap grading of the particles in the fresh concrete provided more bleeding water which in turn decreased the development of plastic cracking as compared with an ideal, linear logarithmical distribution of the particles.
- In case of plastic cracking the size of the cracks were limited by early strength development.
- Plastic shrinkage before the final setting time of the concrete became a great part of the total shrinkage, even though autogenous shrinkage first was subtracted.
- Wax treatment had no/little influence on plastic shrinkage at low water-cement ratio

## Acknowledgement

The project was financed by the Swedish Development Found for Building Construction, SBUF, and by PEAB Sweden Ltd which hereby is gratefully acknowledged.

## References

1. Wittmann, F., 'On the action of capillary pressure in fresh concrete', *CRR* **6** (1976).
2. Radocea, A., 'Pore-water conditions for young cement paste, methods, preliminary models and parameter studies', Publication, P-91:5, Div. Building Materials, Chalmers University of Technology, Gothenburg (1991) 139 pp.
3. Gram, H.-E., 'Properties of SCC - especially early age and long term shrinkage and salt frost resistance', *First international RILEM symposium on SCC*. Stockholm. Ed.: Skarendahl och Peterson (1999) 211-226.
4. Friberg, P., 'Plastic shrinkage of SCC', Report TVBM-5051, Lund university (2002) 60 pp.
5. Rohde, M., Nilsson, L.-O., 'Cracking due to plastic shrinkage', Working report, Chalmers University of Technology, Gothenburg 2002).
6. Ljungkrantz, C. et al, § 6.1, § 9.1, § 9.2, Concrete Handbook Material, Svensk Byggtjänst (1994).
7. Byfors, J., 'Plain Concrete at Early Ages', Report FO 3:80, The Swedish Cement and Concrete Research Institute, CBI. Stockholm (1980).
8. Topçu, I.B., Elgün, V.B., 'Influence of concrete properties on bleeding and evaporation', *Cement and Concrete Research* (2003).
9. Qi, C., Weiss, J., 'Improving the Plastic Shrinkage Cracking Resistance of Concrete through Using Fiber Reinforcement', ACI Fall Meeting, Phoenix (2002).
10. ASTM C09.42.XX, 'Standard Test Method for Evaluating Plastic Cracking of Restrained Concrete' (2002) 17 pp.
11. Persson, B., 'Plastic shrinkage of concrete without building moisture', Report TVBM-7176, Lund university, Lund (2003) 60 pp.
12. Neville, A., Brooks, J.J., '*Concrete Technology*', Longman, Singapore (1987).





## Measurements of Radon Exhalation Rate for Monitoring Cement Hydration

Konstantin Kovler

Faculty of Civil and Environmental Engineering, Technion - Israel Institute of Technology,  
Haifa, Israel

### Abstract

The paper deals with one of the physical methods, which can be used for monitoring hydration of cementitious materials: radon exhalation method. The experiments with two types of hydrating cement paste (made at water to cement ratios of 0.25 and 0.33) are described. The kinetics of shrinkage deformation and hydration heat development is discussed. Different mechanisms influencing radon exhalation rate  $E$  from cement and hydration products are considered. The initial  $E$ -values determined in the beginning of the tests were 0.01-0.02 mBq kg<sup>-1</sup> s<sup>-1</sup> for the cement pastes made at water/cement ratios of 0.25 and 0.33, respectively. In 3 days both pastes showed  $E = 0.04$  mBq kg<sup>-1</sup> s<sup>-1</sup>. However, the most important finding seems to be the dramatic increase of the radon exhalation rate up to the maximum observed in a few hours after mixing with water (0.66 and 0.58 mBq kg<sup>-1</sup> s<sup>-1</sup> for 0.25 and 0.33 pastes, respectively). It was registered in the radon chamber within the time period usually classified as set. The test results showed a strong correlation between radon exhalation rate and deliberation of hydration heat. Peaks of the radon exhalation rate coincide with those of temperature measured on the surface of the cement paste. Analysis of the literature data shows that heating of the materials weakens physical adsorption of radon gas atoms on newly formed solid surfaces and can enhance the radon exhalation rate by several times. However, the performed experiment shows that the radon exhalation rate drastically increases (by dozens of times), and then decreases again. Such a dramatic growth can be explained by a synergy between temperature effect and two more phenomena: (a) intensive formation of microstructure with an extremely high specific surface area, when cement sets and while porosity is still high and (b) intensive flow of water, which traps radon from the newly formed solid surfaces of C-S-H to the sample surface and enhances radon emanation power.

### 1. Introduction

Cement hydration is a very complicated process, and its physical and chemical mechanisms are still under investigation. In general, the term "hydration" is used to describe a range of reactions between cement and water to produce a hardened product. A cement clinker particle is a multiphase solid having calcium silicate grains in a matrix of interstitial aluminate and

ferrite. They each have specific reactions with water to produce a range of hydration products which produce a dense, strength developing solid. The rates of reaction are important and depend on mineralogical composition of cement, its specific surface area, presence of chemical and mineral admixtures, environmental/curing conditions and geometry of the cast element. The  $C_3A$  reaction is fastest and generates most heat, but does not contribute much to ultimate strength of the cementitious material, although it contributes significantly to early strength. The principal contributors to longer term strength are the calcium silicates.  $C_3S$  is most reactive, giving early strength but  $C_2S$  has a better longer term contribution. The C-S-H produced is the principal binding phase in Portland cements and is quantitatively the most significant hydration product. The ferrite reactions are intermediate in rate between the  $C_3S$  and  $C_2S$  reactions but have an important long term contribution to strength and durability.

Usually the process starts as dissolution of cement particles with formation of new crystals. Several stages can be distinguished. First, the production of ettringite, a period of almost no reaction (dormant period), the production of C-S-H (calcium silica hydrate), the conversion of calcium sulfoaluminate into calcium-mono-sulfate and the formation of calcium sulfoferrite.

To follow the various stages of hydration one can utilize the chemical, physical and mechanical properties. Microstructural transformations occurring in the course of cement hydration can be represented by the changes of these properties. Numerous methods are used for monitoring the hydration of cement. Some of them are based on chemical measurements of the composition in the pore solution. Some others use electrical methods, which determine the dielectric properties, conductivity, or the magnetic properties. Additional group of methods is based on the wave propagation in the hardening material by means of generation of sonic or ultrasonic waves or registering acoustic emission. Very popular method is measuring the heat of hydration. Observation of the microstructural transformation under environmental scanning electron microscope in real time is known.

The present paper deals with one more physical method, which can be used for monitoring cement hydration: *radon exhalation method*. In recent years interest in radon has become a focus in research in environmental physics and built environment. However, the unique properties of radon as a noble gas can be also used as for monitoring cement hydration and microstructural transformations in cementitious system. Radon contained in trace amounts in hardening material, as other inert gases, does not interact with the surrounding media chemically, and hence does not interfere chemical reactions accompanying cement hydration.

## 2. Radon basics

Radon is one of the elements in the decay series of uranium that occurs as a trace element in almost all natural materials. All rocks contain some uranium, although most contain just a small amount - between 1 and 3 parts per million (ppm) of uranium. While uranium has a half-life of 4.4 billion years, the half-life of radon ( $^{222}\text{Rn}$ ) is only 3.8 days. This means that 50 % of a given volume of radon will decay in 3.8 days to form decay products like polonium, bismuth and lead. When we inhale high concentrations of radon, the gas molecules may decay to the

above mentioned elements, which may stick to the epithelial cells of the lung. The presence of these elements in high concentrations may eventually cause lung cancer.

The direct predecessor of radon in the decay series of uranium is radium which is often incorporated in the solid matrix of the cement particles. Before radon can enter the pore space of the material and become available for transport to the indoor environment, it has to escape the solid matrix of the particle. Radon is released from mineral grain via alpha recoil. As each radium atom decays by ejecting an alpha particle, the newly formed radon atom recoils in the opposite direction. By recoiling the radon atom may then enter the pore space between grains in a fractured rock. At the same time, the radon atom could also recoil towards the interior of the grain and not enter the pore space. If the material containing radium is stable (i.e. no structural changes and chemical reactions take place), the release of radon is controlled by two main mechanisms responsible for this escape: recoil and diffusion through the solid matrix.

### **3. Radon emanation from cement and its constituents**

Not all radon produced in the particle enters in the pore space. The ratio of escaped radon to radon produced is called emanation coefficient (or emanation power), which depends on the microstructure and morphology of the solid particles. For example, cement studied in the current work, was Portland cement EN 197.1 - CEM I 52,5 N, and had an emanation coefficient of 7.6% [1]. At the same time, if coal fly ash (FA) is added to the clinker, or dosage of gypsum as a set retarder in the clinker changes, the emanation coefficient will be different, depending on the emanation properties of the fly ash and gypsum particles, their dosage and specific surface of the clinker particles, which is defined by grinding. Fig. 1 shows typical values of emanation coefficient for Portland cement, fly ash (both – reported in [1]) and gypsum measured by means of the same procedure described in [1]. They are close to those known from other literature sources. For example, Stoulos et al. [2] determined the emanation power for gypsum as ~30%, regular Portland cement as 5-7%, and fly ash as less than 1%. Bossew [3] reported a similar value of emanation coefficient for gypsum (30%), and obtained significantly lower emanation power for quartz sand (6%) and mineral slag (0.8% only). As Fig. 1 shows, the emanation abilities of gypsum and FA differ by almost two (!) orders of magnitude, representing opposite ends of the emanation scale.

The emanation power of radon is thus strongly dependent on the microstructure and morphology of solid particles. It is well known, for instance, that fly ash has a dense glassy structure with most of the mass concentrated in the particle shell, preventing radon atoms from escaping the material. In addition, fly ash particles are known for their ideally spherical shape having the minimum surface to volume ratio among all possible particles geometries. In contrast, gypsum crystals usually are of longitudinal (fibroid) shape with well-developed surface area and have lower density. The typical "layered" structure of gypsum crystals is relatively weak (for example, it easily disintegrates under heating, resulting in the formation of calcium sulfate hemihydrate crystals of high specific surface area, up to 10 m<sup>2</sup>/g). All these features make the process of radon release easy.

It is known from the literature that the specific surface area of granular materials is another important factor influencing radon emanation. In general, the higher is surface to volume ratio of a granular material, the higher is its emanation power [4]. For example, Abumurad and Al-Tamimi [5] observed that for 1 basalt sample and 6 samples of different sedimentary rocks (chalk, silicified limestone, phosphate limestone, bituminous chalk, chert limestone, and bituminous chalky marl) the emanation coefficient decreased from 3.33% to 0.15%, when the particle size increased from 0.1 mm to 2 mm, not depending on type of the rock studied.

However, Portland cement is multiphase granular material and contains grains of different mineralogical composition, internal porosity, morphology and size. For example, it is known that specific surface areas for ordinary Portland cement and FA are similar. However, as shown in Fig. 1, their emanation properties differ significantly. In view of this, the general observation, that the radon emanation factor is inversely proportional to grain size [4], seems to be too simplified. It does not take into account other influencing factors, and therefore is not observed in direct comparison of emanation power values characterizing cement and FA.

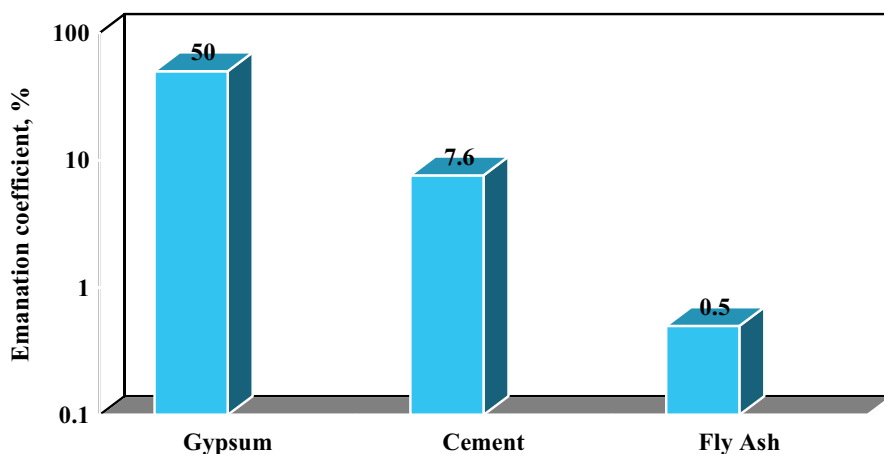


Figure 1. Radon emanation coefficient of cement, fly ash and gypsum.

#### 4. Radon exhalation from hardening cementitious materials

Once emanated in the pore space of the material, diffusion and advection are responsible for its transport and thus release. The macroscopic parameter that contains the combined information on radon generation and transport is the radon release (or exhalation) rate.

The works of Balek and his coworkers [6 - 8] attributed the changes in radon exhalation rate, mainly, to the changes in surface area and microporosity occurring in the hardening material during hydration. The first attempt to use radon as an indicator of microstructural changes occurring during cement hydration was made in Czechoslovakia by Balek and Donhálék in 1983 [6]. Their method was called REM (Radiometric Emanation Method). The authors suggested labeling the sample of cement powder before hydration by the parent isotopes of radon, such as  $^{228}\text{Th}$  or  $^{224}\text{Ra}$ . The atoms of  $^{220}\text{Rn}$  (one of radon isotopes called thoron, with a half-time of 56 seconds) are formed in this case by spontaneous decay:  $^{228}\text{Th} \xrightarrow{\alpha} ^{224}\text{Ra} \xrightarrow{\alpha} ^{220}\text{Rn} \xrightarrow{\alpha} .$

The labeling was made by impregnation of cement powder with a non-aqueous (acetone) solution containing  $^{228}\text{Th}$  or  $^{224}\text{Ra}$  in the concentration of  $10^{11} \text{ Bq m}^{-3}$ . The radionuclides were adsorbed on the surfaces of cement particles and the non-aqueous solution was evaporated. Balek and Donhálék found also that the specific activity of the cement samples labeled was  $10^6 - 10^7 \text{ Bq kg}^{-1}$ . The initial specific activity of the cement samples was not reported.

In our experiments [1] the total effective specific radioactivity (so called radium equivalent activity) of the tested cement was about  $10^2 \text{ Bq kg}^{-1}$ . This value is close to those reported in the literature [4]. In other words, the labeling made by Balek and Donhálék [6] increased radioactivity of the cement samples tested by 5-6 orders of magnitude, and obviously enhanced the sensitivity of their method. Knowing the recoil energy of 85 keV/atom every atom gains, when its parent decays, Balek and Donhálék estimated that the atoms of  $^{228}\text{Th}$  or  $^{224}\text{Ra}$  penetrated into the cement particles to a maximum depth of 120 nm. They also found that the concentration of radium and radon atoms in the labeled cement particles decreased practically linearly from the surface towards the center.

At the same time, working with very high radioactivity concentrations requires specific safety precautions. In addition, the labeling introduces one more factor, which can influence the quantitative results of such monitoring, because the cement particles size distribution is not even. Usually, the particle sizes change in the range between 1 and 100  $\mu\text{m}$ , with a median size of 10-20  $\mu\text{m}$ . The hydration rate strongly depends on the particle size. It is generally agreed that cement particles larger than 45  $\mu\text{m}$  are difficult to hydrate and those larger than 75  $\mu\text{m}$  may never hydrate completely. In view of this, labeling cement particles by the radon parents for a certain depth, of up to 0.1  $\mu\text{m}$ , which is independent of cement particle size, can lead to uncertainty with the interpretation of the monitoring results, especially when the effect of cement fineness is studied.

The results of radon measurements were reported by Balek and Donhálék as time dependence of a qualitative non-dimensional parameter called "emanating power" and compared with the curves of penetration resistance determined by Vicat needle, compressive strength, capillary porosity, and ultrasonic pulse velocity. The advantages of the REM method, in comparison with other methods, where the hydration is stopped, which can change the microstructure, surface area or porosity, have been emphasized.

In the 9 years following the publication of this pioneering paper, Balek and Donhálék published another paper, in which the same technique was used for monitoring cement hydration under different temperatures, simultaneously with measuring penetration resistance [7]. When the environmental temperature increased from 35°C to 85°C, the peak of radon activity in the time axis shifted, similarly to that of penetration resistance, to the early ages (from one hour to 6-7 minutes).

This shift, in particular, was used by Balek and Beckman [8] as a parameter in the mathematical model simulated morphology changes during hydration of Portland cement under isothermal conditions. Other factors considered by this model were different size of  $C_3S$  grains and increasing concentrations of  $Ca^{2+}$  due to  $C_3S$  hydrolysis. In this and other works by Balek and his coworkers, the increase of radon exhalation rate during cement hydration is attributed to the increase of the surface area, whereas the decrease of radon release rate is explained by closing pores and decrease of surface area. A new name of the method was also suggested: ETA (Emanation Thermal Analysis). The authors mention that "porosity changes in the nanometer scale comparable to the radon atom size, i.e. 0.38 nm, can be investigated, under 'in situ' conditions of the sample treatment of ETA" [8].

One more factor, which can influence radon exhalation rate in cementitious materials, is changing of relative humidity in the pore air. This factor has not been adequately studied yet for hardening systems.

In parallel to consolidation of the system, when cement paste, especially made at low water/cement ratios, start overcoming self-desiccation and, consequently, autogenous shrinkage, the air relative humidity in the pores can drop. There are some data available in the literature about this effect. For example, such a drop was observed by Bentz et al. [9] in cement paste made at water/cement ratio of 0.3, from a complete water saturation to relative humidity of 80%, within the period of 15-50 hours after mixing cement with water. As a result, radon trapping ability of water weakens, and emanation power is expected to decrease.

At the same time, the changes in moisture influence the radon diffusion also. This is counteracting to the effect of emanation power described before. Tanner gave the following explanation to this effect: if the pores are filled with water, radon must diffuse through the water, but radon diffusion coefficient for water is only  $10^{-5} \text{ cm}^2 \text{ s}^{-1}$  compared to the diffusion coefficient of about  $10^{-2} \text{ cm}^2 \text{ s}^{-1}$  for air [10].

Stranden et al. [11] found that the increase in emanation due to moistening will more than compensate the reduction in diffusion coefficient until a level where the pores have some liquid water, but are not completely filled with water. When the pores are completely filled with water, the reduced diffusion will reduce the radon dramatically. They discovered that the effects of moisture are rather dramatic and a factor of about 20 between the highest and lowest exhalation rate could be found in several cases.

## 5. Experimental part

Concentration of radium  $^{226}\text{Ra}$  in Portland cement was  $64.2 \pm 2 \text{ Bq kg}^{-1}$ . It was determined in cement powder sample by gamma-ray spectroscopy, using NaI detector (NPP Doza). The sample was dried at  $105^\circ\text{C}$  for 24 hours before testing. Cement was measured as a sample of  $200 \text{ cm}^3$  volume in sealed cylindrical polyethylene container after 30 days, to achieve secular equilibrium of the  $^{226}\text{Ra}$  progeny.

Cement paste specimens were mixed in a pan mixer, cast in the plastic forms of 1.5 liter and introduced uncovered in the radon chamber of 5.3 liter for testing radon. Such a small chamber enabled to obtain high radon concentrations within a short time of the test, which was important from the viewpoint of improving the sensitivity and reliability.

The radon concentrations in the closed chamber were measured by means of continuous radon gas monitor RAD-7, DurrIDGE Company Inc. The duration of each test was a few days. Experimental set-up allowed simultaneous testing of two samples (Fig. 2).



Figure 2. Experimental set-up for simultaneous measuring of radon exhalation rate in two adjacent chambers.

The method of determination of radon exhalation rate of the building material via radon concentration measured in the closed chamber is described by Kovler et al. [1]. We have to take into account that the concentration is not a characteristic of the material, because it increases with time until achieving a constant value  $C_\infty$  corresponding to the saturation condition. Maximum radon concentration in a hermetically closed space under saturation at infinite time,  $C_\infty (\text{Bq m}^{-3})$  is related to radon concentration  $C(t)$  at a given time  $t$  (s) as follows:

$$C(t) = C_{\infty}(1 - e^{-\lambda t}) \quad (1)$$

After measuring the radon concentration at a given time  $C(t)$  and calculating  $C_{\infty}$ , the radon exhalation rate  $E$  can be determined by formula:

$$E = C_{\infty}\lambda V/M \quad \text{or} \quad E = C_{\infty}\lambda V/S \quad (2)$$

where

$M$  and  $S$  - mass (kg) and surface area ( $\text{m}^2$ ) of the source, respectively,

$V$  - volume occupied by air (volume of the chamber minus volume of the specimen,  $\text{m}^3$ ),

$\lambda$  - radon decay constant ( $2.1 \cdot 10^{-6} \text{ s}^{-1}$ ),

$E$  - radon exhalation rate of the source, per unit surface area or mass ( $\text{Bq m}^{-2} \text{ s}^{-1}$  or  $\text{Bq kg}^{-1} \text{ s}^{-1}$ ).

Formula (2) assumes that the decay rate is negligible compared to the diffusion rate. For hydrating materials, which change their microstructure in time, the radon exhalation rate  $E$  should be time-dependent, so the formula is modified:

$$E(t) = \frac{V}{S} \left[ \frac{dC}{dt} + \lambda C(t) \right] \quad \text{or} \quad E(t) = \frac{V}{M} \left[ \frac{dC}{dt} + \lambda C(t) \right] \quad (3)$$

## 6. Radon exhalation of hydrated cement paste vs. unhydrated cement

At first, the radon exhalation of unhydrated cement was compared with that of hydrated cement paste, made with water to cement ratio of 0.25. Masses of the cement and cement paste samples were 1,420 and 2,481 g. The radon concentrations of both materials were measured at  $20^{\circ}\text{C}$ . In order to compare the measurements data, the relative radon concentrations (per 1 kg of cement) were calculated. These values are presented on a logarithm scale in Fig. 3. The low-value range is a characteristic of unhydrated cement. The radon concentration curve for hydrating cement paste starts from zero (background) concentrations, similarly to unhydrated cement. However, the relative radon concentrations developed within 3 days in the test chamber containing cement paste were  $\sim 20$  (!) times higher than those of cement. This fact clearly proves the importance of microstructural transformations taking place in the process of cement hydration, in comparison with cement grain, which is a time-stable material.

To explain this enormous difference in amount of radon atoms exhaling from the same amount of radium contained in cement, we have to take into account several important mechanisms occurring in the course of cement hydration. For this reason, it would be convenient to distinguish between three main stages, which are readily seen in Fig. 3 and correspond with stages in cement hydration and microstructural development: stage I (dormant period), stage II responsible for setting, when intensive microstructural transformations occur, and stage III (the densification of the structure and drying).



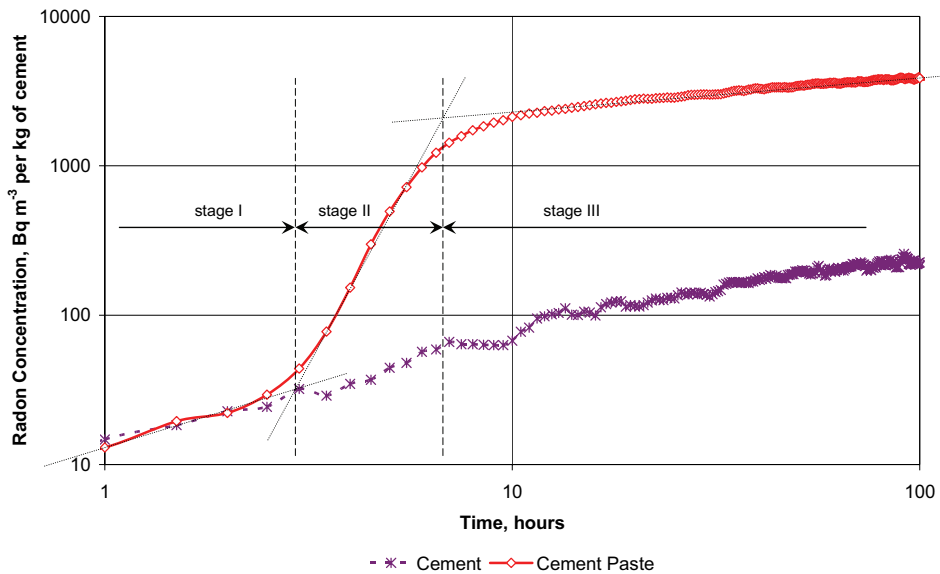


Figure 3. Dependence of relative radon concentration in the chamber (in  $\text{Bq m}^{-3}$  per 1 kg of cement) vs. time for cement and hydrating cement paste made at water/cement ratio of 0.25.

#### Stage I (dormant period)

In the very beginning of the test, when cement paste is still plastic, radon atoms are easily trapped by water surrounding cement particles, transport to the surface of the sample (mainly, by diffusion) and exhale in the air. It is known that the radon emanation coefficient under saturated conditions is smaller than that under dry conditions, whatever is the building material [12]. This behavior stems from the fact that the recoil distance of the radon atoms in air is about 900 times higher than in water. Thus, water traps the recoiled radon atoms more easily than air. A thin water film, which continuously engulfs cement particles, would be sufficient to stop the recoiled atoms in the water.

At the same time, the presence of water in a porous medium is known to dramatically influence radon diffusion. For example, Fournier et al. [12] found recently that radon diffusion coefficient in cement decreases from  $\sim 1 \cdot 10^{-2}$  (dry material) to  $\sim 2 \cdot 10^{-6} \text{ m h}^{-1}$  (saturated material).

These two tendencies seem to be counteracting in the fresh cement paste, because there was almost no difference in radon concentrations observed between cement and cement paste in the first 3 hours of the test. It has to be emphasized, that the scatter of radon measurements by Rad-7 monitor taken with relatively short cycle of exposure (15-30 minutes) cannot be better than  $30\text{-}40 \text{ Bq m}^{-3}$ , which is not far from the mean radon concentrations measured in this period of time.

#### Stage II (setting, intensive microstructural transformations)

Approximately 3.5 hours after mixing cement with water, the radon concentration curve of the cement paste deviates from that of the unhydrated cement, and the concentrations dramatically grow. This fact can be a result of the fast microstructural formation occurring in the hydrating paste. It is also well-known that calcium silicate hydrates (C-S-H) formed by cement hydration, have very fine structure. C-S-H is not a well-crystallized material. In fact, it is very nearly amorphous. As a result, it develops as a mass of extremely small irregular particles of indefinite morphology. As a consequence, hydrated cement paste has very high surface areas. For example, measurements using physical adsorption of water vapor on D-dried calcium silicate pastes indicate that C-S-H has surface area of  $250\text{--}450\text{ m}^2\text{ g}^{-1}$ , which is 3 orders of magnitude higher than in the unhydrated cement [13]. Winslow and Diamond [14] used low-angle X-ray scattering - the technique, which allows surface area measurement at different moisture states; they revealed areas of about  $800\text{ m}^2\text{ g}^{-1}$  for saturated samples; these areas are reduced at lower relative humidity. In other words, the extremely high surface area of the newly formed C-S-H, while porosity is still high, should significantly promote radon exhalation, as can be seen from the measurements on hardening cement paste.

#### Stage III (hardening, slow microstructural transformations and drying)

Finally, one might expect a reduction in radon exhalation rate at later ages. Indeed, as can be seen from Fig. 3, the slope of the radon concentration curve significantly reduces in further. It can happen due to the following reasons: reduction in the porosity and changing of the moisture.

It is well-known, that the radon diffusion coefficient depends on the porosity. When the cement paste structure is consolidating and densifying, radon exhalation rate should decrease.

We cannot exclude some influence of moisture change as well, although this factor does not seem to be a decisive one resulting in slowing down the exhalation rate.

### **7. Radon exhalation of hydrated cement pastes made of different water/cement ratios**

The radon exhalation kinetics of hardening cement pastes made at water/cement ratios of 0.25 and 0.33, has been studied in parallel with their shrinkage and temperature development (Figs 4-5). Shrinkage strains were measured on parallel sealed specimens having a form of triangle prisms, with right-angle legs of 50 mm and length of 100 mm. Air temperature and relative humidity were measured in parallel samples made from the same cement pastes and tested in the radon chamber, above the surface of the specimens, by means of the small-size (35 x 54 x 15 mm) datalogger OM-CP-PRHTEMP101 (Omega Engineering Inc.).

Fig. 4 shows the curves of temperature developed in the course of exothermal reaction of cement hydration vs. shrinkage deformation. It can be seen that the paste made at lower W/C (0.25) hydrates faster and develops larger heat of hydration. It achieves the maximum temperature in 4.8 hours, in comparison with 6.0 hours for 0.33 paste. The thermal effect observed in the small-size radon chamber was quiet impressive. Initial expansion of the

samples until the maximum (within 1-2 first hours) can be explained by reabsorption of bleed water. The temperature effect can be observed also in the shrinkage tests, by a slight deviation of the strain curve in the vicinity of the temperature peak.

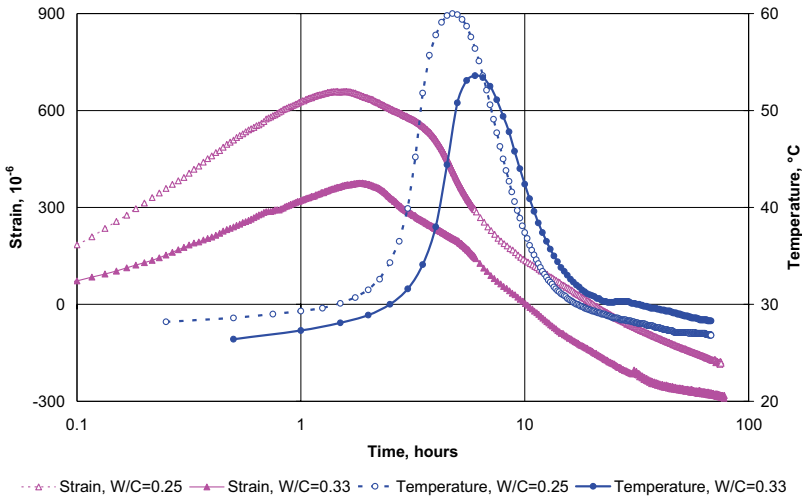


Figure 4. Time dependences of temperature in the chamber and free shrinkage for hydrating cement pastes made at water/cement ratios of 0.25 and 0.33.

Fig. 5 shows the development of radon concentration in the chamber in comparison with temperature measured above the same paste specimens. Masses of the pastes were close: 2,800 g for W/C=0.25 paste, and 2,700 g – for W/C=0.33 paste, so practically there was need for normalization. We have to take into account also that the typical error of the radon concentration measurement is about 5%.

As expected, the relative humidity in the chamber started to increase immediately after introducing the specimens into the chamber and sealing it (Fig. 6). This effect can be explained by continuous water vapor flow to the surface and evaporation in the ambient air of the chamber during the entire test. Most of the time the RH-value measured in the bottom of chamber was kept higher than 80%-90%. However, during the dramatic deliberation of heat, when cement paste set (see the temperature curves), RH measured on the surface of the sample decreased to ~60%, but then returned to the high values again, in spite of the fact that the air pumped through the circle of the radon monitor Rad-7 was continuously dried by anhydrite drierite column of the monitor to the RH-values not exceeding 3%.

Fig. 7 shows the results of the calculation of radon exhalation rate in both pastes using Eq. (3). The initial E-values determined in the beginning of the test were 0.01-0.02 mBq kg<sup>-1</sup> s<sup>-1</sup>, for the cement pastes made at water to cement ratios of 0.25 and 0.33, respectively. These values are close to those of unhydrated cement known from the literature, e.g. [1].

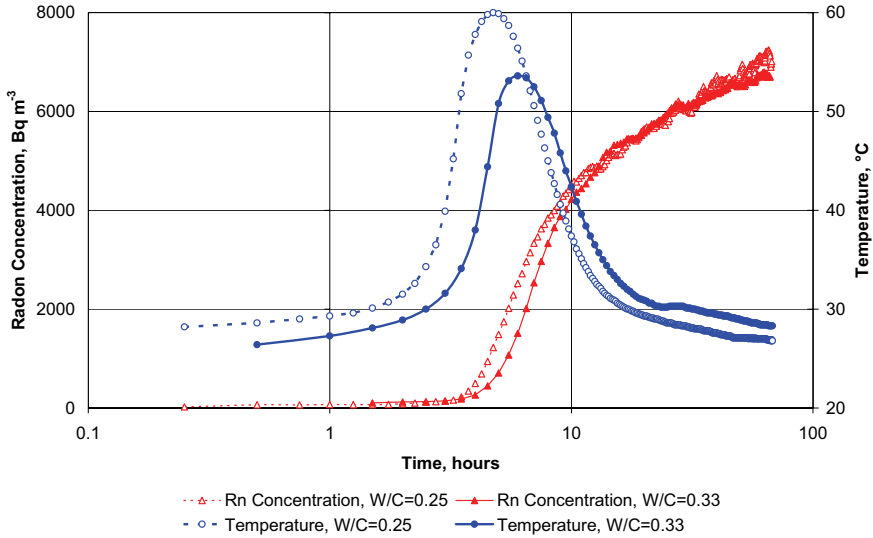


Figure 5. Time dependences of radon concentration and temperatures in the chamber for hydrating cement pastes made at water/cement ratios of 0.25 and 0.33.

The tail parts of the concentration curves (after 18 hours) can be approximated as following logarithmic dependences:  $C = 1292 \cdot \ln(t) + 1720$ , and  $E = 971 \cdot \ln(t) + 2757$ , for the 0.25 and 0.33 pastes, respectively (here  $C$  is in  $\text{Bq m}^{-3}$  and  $t$  is in hours). Accordingly, the approximated tail parts of the exhalation curves are drawn (they are almost overlapping). Comparing with the initial values of  $E$  determined in very beginning of the tests ( $0.01\text{--}0.02 \text{ mBq kg}^{-1} \text{ s}^{-1}$ ), the end  $E$ -values obtained in the end of the test are higher ( $0.04 \text{ mBq kg}^{-1} \text{ s}^{-1}$  in 3 days for both pastes). Possible reasons for this have been discussed before. The  $E$ -values measured in 3 days are close to those in 7 days reported before [15].

However, the most important finding seems to be the sharp increase of the radon exhalation rate up to the maximum observed in a few hours after mixing with water ( $0.66$  and  $0.58 \text{ mBq kg}^{-1} \text{ s}^{-1}$  for the 0.25 and 0.33 pastes, respectively). Such extremely high values of radon exhalation rate significantly exceed all  $E$ -values known from the previous literature dealing with radon exhalation from cementitious materials. They can lead to the development of very high radon concentrations in construction sites at closed spaces, although within a short time. Whether this phenomenon is of radiological concern for workers, which are employed in casting concrete in the work places with poor ventilation, will be estimated in the next paper.

It can be clearly seen, that the peaks of radon exhalation rate correspond well to those of temperature by time. As a consequence, the effect of temperature seems to be very important and has to be addressed, when interpreting the test results.

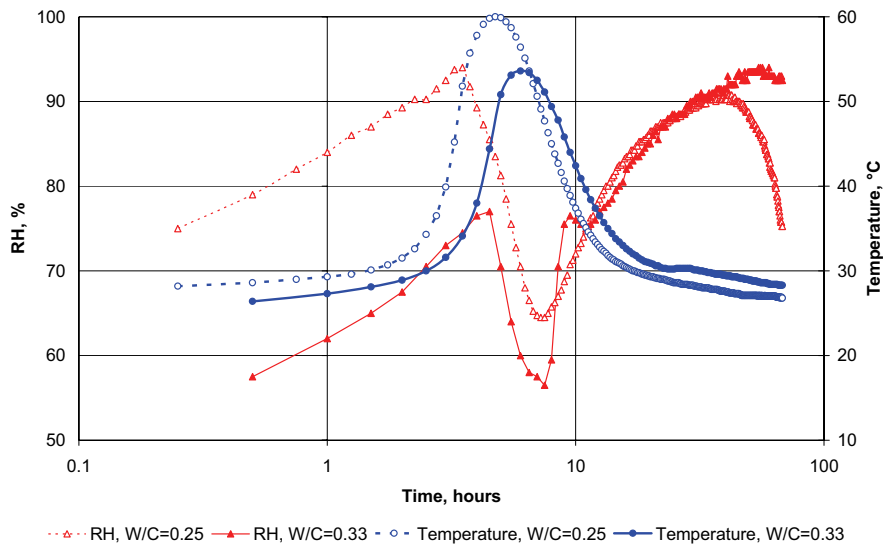


Figure 6. Time dependences of relative humidity and temperatures in the chamber for hydrating cement pastes made at water/cement ratios of 0.25 and 0.33.

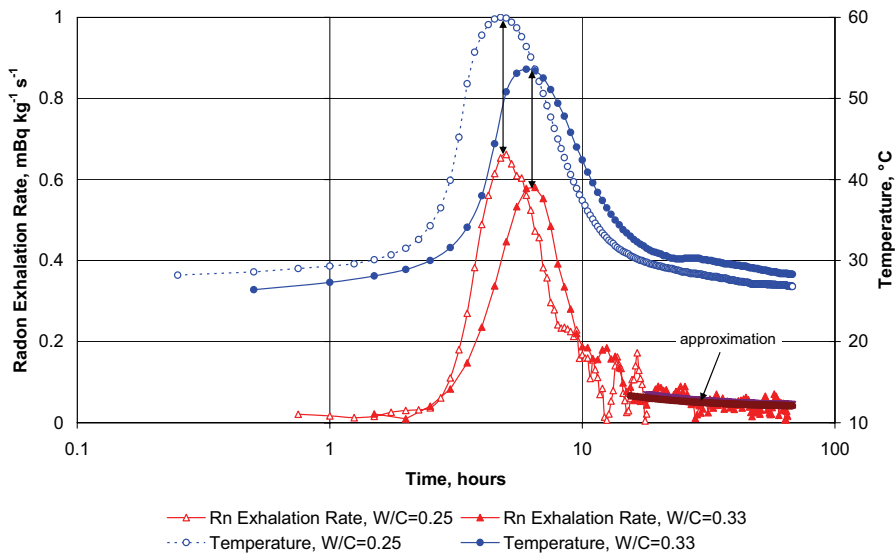


Figure 7. Time dependences of radon exhalation rate and temperatures in the chamber for hydrating cement pastes made at water/cement ratios of 0.25 and 0.33.

## 8. Effect of temperature

The correlation dependences for the two cement pastes made at water/cement ratios of 0.25 and 0.33 are shown in Fig. 8. It can be seen that the values of radon exhalation rate  $E$  ( $\text{mBq kg}^{-1} \text{s}^{-1}$ ) and the temperatures  $T$  ( $^{\circ}\text{C}$ ) are closely correlated by linear dependences:  $E = 0.0178 \cdot T - 0.496$  and  $E = 0.0188 \cdot T - 0.510$ , for the 0.25 and 0.33 cement pastes, respectively. The  $E$ -values increased by 20-40 times (!), when temperatures raised from  $\sim 30^{\circ}\text{C}$  to almost  $60^{\circ}\text{C}$ . Is the temperature effect alone capable to explain such a dramatic growth in radon release? Let us remind first what is known from the available literature sources about the temperature effect.

The significant increase of radon exhalation rate obtained in our tests was much higher than that discovered in the previous works dealt with temperature effect. For example, Stranden et al. [11] showed that the exhalation rate of concrete cubes heated from  $22^{\circ}\text{C}$  up to  $50^{\circ}\text{C}$  increased by 2-4 times only. At the same time, we have to recall that Stranden et al. worked with hardened concrete cubes, and not with hardening cement paste transforming from liquid to solid state by exothermal hydration reactions, so direct comparison of the results is difficult.

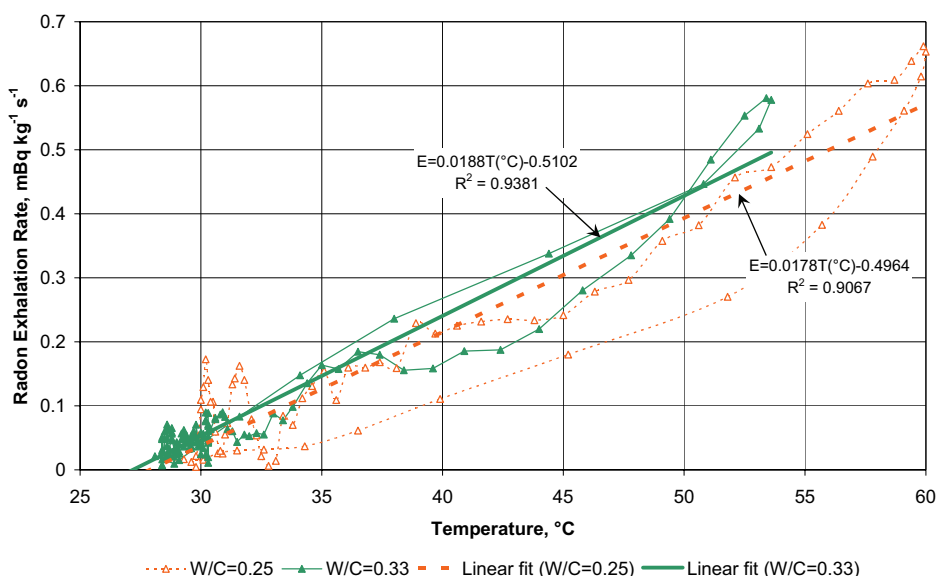


Figure 8. Correlation between radon exhalation rates and temperatures.

It is known that physical (or Van der Waals) adsorption of gases on solids weakens under heating. By cooling rock samples down to  $-80^{\circ}\text{C}$ , Baretto [16] discovered a very sharp decrease in radon exhalation; this fact suggests a strong adsorption at low temperatures.

Another effect, resulting in so intensive radon release in the pastes, in addition to the temperature effect, could be an active water vapor flow out of the samples. In fact, this flow took place in the experiments, because the RH-values were kept high during the test, in spite of the continuous circulation of the dry air through the drierite column of the radon monitor. At the same time, this water flow occurred immediately after sealing the samples in the chamber. Why we list this factor as one of the important? We suppose that the rate of this flow achieves maximum during the setting. However, additional tests are needed to justify this hypothesis.

Therefore, the most reliable explanation of this phenomenon seems to be a synergy of the three main effects:

- (1) sharp heat deliberation as result of exothermal hydration reaction of cement weakened physical adsorption radon gas on the solid surfaces;
- (2) intensive microstructural formation, when cement sets producing an extremely high specific surface area and exposed radon to free emanation, while porosity is still high;
- (3) intensive flow of water, which trapped radon from the newly formed solid surfaces of C-S-H to the sample surface.

## 9. Conclusions

It is shown that the radon exhalation  $E$  determined in the beginning of the test, were  $0.01\text{--}0.02\text{ mBq kg}^{-1}\text{ s}^{-1}$ , for the cement pastes made at water/cement ratios of 0.25 and 0.33, respectively. At the age of 3 days both pastes showed higher result:  $E = 0.04\text{ mBq kg}^{-1}\text{ s}^{-1}$ . However, the most important finding seems to be the dramatic increase of the radon exhalation rate up to the maximum observed in a few hours after mixing with water ( $0.66$  and  $0.58\text{ mBq kg}^{-1}\text{ s}^{-1}$  for 0.25 and 0.33 pastes, respectively). It was registered in the radon chamber within the time period usually classified as set. Such extremely high  $E$ -values significantly exceed all those known from the literature for cementitious materials.

The current research showed a strong correlation between radon exhalation rate  $E$  and deliberation of hydration heat. Peaks of the radon exhalation rate coincide perfectly with those of temperature measured above the surface of the cement paste. Analysis of the literature data shows that heating of the materials weakens physical adsorption of radon gas atoms on newly formed solid surfaces and can enhance the radon exhalation rate by several times. However, the performed experiment shows that the radon exhalation rate can increase by dozens of times, and then decreases again. Such a dramatic growth can be explained by a synergy between temperature effect and two more phenomena: (a) intensive microstructural formation produced an extremely high specific surface area, when cement sets and while porosity is still high, and (b) intensive flow of water, which traps radon from the newly formed solid surfaces of C-S-H to the sample surface and enhances radon emanation power.

At the moment, it is still difficult to conclude about the degree of contribution for each of these mechanisms in obtaining extremely high radon exhalation rate, when cement sets, but it is very important that all of these three mechanisms took place simultaneously, and a synergetic effect is quite possible. For determining of the contribution of heating alone in comparison with other possible accompanying effects, it is a need in execution of the additional study. Results of this

study, which has been started recently in the Technion – Israel Institute of Technology, will be reported in the next paper.

## Acknowledgements

The author thanks Eng. Andrey Perevalov and Eng. Pavel Larianovsky for the help in the experimental work. The useful comments and advices of Dr. Victor Steiner and Prof. Eugen Rabkin are highly acknowledged. The experimental work has been supported by the Foundation of Promoting Research in the Technion and by E. and J. Bishop Research Fund.

## References

1. Kovler, K., Perevalov, A., Steiner, V. and Metzger, L.A. 'Radon exhalation of cementitious materials made with coal fly ash: Part 1 – scientific background and testing of the cement and fly ash emanation', *J. of Environmental Radioactivity* (2005), **82** (2005) 321–334.
2. Stoulos, S., Manolopoulou, M. and Papastefanou, C., 'Measurement of radon emanation factor from granular samples: effects of additives in cement', *Applied Radiation and Isotopes* **60** (2004) 49–54.
3. Bossew, P., 'The radon emanation power of building materials, soils and rocks', *Applied Radiation and Isotopes* **59** (2003) 389–392.
4. United Nation Scientific Committee on the Effects of Atomic Radiation (UNSCEAR), 'Report to the General Assembly of the United Nations', 2000, Annex B. United Nations Sales Publication E.00.IX.3. United Nations, New York.
5. Abumurada, K.M. and Al-Tamimi, M., 'Emanation power of radon and its concentration in soil and rocks', *Radiation Measurements* **34** (2001) 423–426.
6. Balek, V. and Donhálék, J., 'A new method for investigating cement hydration by radioactive indicators', *Cem. & Concrete Res.* **13** (1983) 1-6.
7. Balek, V. and Donhálék, J., 'Radiometric emanation method for monitoring morphology and porosity changes during radwaste cementation', *Cem. & Concrete Res.* **22** (1992) 459-464.
8. Balek, V. and Beckman, I.N., 'Theory of emanation thermal analysis. X. Characterization of morphology changes during hydration of cementitious binders', *J. of Thermal Analysis and Calorimetry* **67** (2002) 37-47.
9. Bentz, D.P., Geiker, M.R. and Hansen, K.K., 'Shrinkage-reducing admixtures and early-age desiccation in cement pastes and mortars', *Cem. & Concrete Res.* **13** (1983) 1-6.
10. Tanner, A.B., 'Radon migration in the ground: a review', in 'Natural Radiation Environment', Eds. J.A.S. Adams and W.M. Lowder (Chicago, Univ. of Chicago Press, 1964) 161-190.
11. Stranden, E., Kolstad, A.K. and Lind, B., 'Radon exhalation: moisture and temperature dependence', *Health Physics* **47** (1984) 480-484.



12. Fournier, F., Groetz, J. E., Jacob, F., Crolet, J. M. and Lettner, H., 'Simulation of radon transport through building materials: influence of the water content on radon exhalation rate', *Transp. Porous Med.* **59** (2005) 197–214.
13. Mindess, S. and Young, J.F., 'Concrete' (Prentice-Hall, Englewood Cliffs, NJ, USA, 1981).
14. Winslow, D. and Diamond, S., 'Specific surface area of hardened Portland cement as determined by SAXS', *J. Am. Ceram. Soc.* **57** (1974) 193–197.
15. Kovler, K., Perevalov, A., Levit, A., Steiner, V. and Metzger, L.A. 'Radon exhalation of cementitious materials made with coal fly ash: Part 2 – testing hardened cement – fly ash pastes', *J. of Environmental Radioactivity* (2005), **82** (2005) 335–350.
16. Baretto, P.M.C., 'Radon-222 emanation characteristics of rocks and minerals', in 'Radon in Uranium Mining', Panel Proceedings (Vienna, IAEA, 1975) 129-148.



## **Volume Change Mechanisms in Concrete: new Directions for Modeling**

Zachary C. Grasley, David A. Lange and Yi-Shi Liu  
University of Illinois at Urbana-Champaign, USA

### **Abstract**

The mechanisms that cause non-load induced volume change in concrete have been the subject of research for many years. Recently, models have been developed that incorporate these mechanisms, their associated stresses, and material elastic properties to predict volumetric deformations. There is ample evidence that the solid microstructure of concrete exhibits viscoelastic behavior, implying that creep may occur under internal stresses that are associated with volume change mechanisms. Newly developed models may improve on existing theoretical models for predicting volume change due to internal stresses by incorporating the viscoelastic properties of cement paste.

### **1. Introduction**

The equilibrium volume of concrete or cement paste is, in general, unstable even in the absence of external loading. Often, the volume change in these cases is termed “material” induced volume change. These dilatational deformations include the following:

- Drying shrinkage
- Autogenous shrinkage
- Carbonation shrinkage
- Thermal dilation

Historically, these deformations have often been treated as material properties (i.e. unique, independent parameters defined by the material) as a simplified means to compare material performance. However, these volumetric deformations are at least partially the result of a response to internal stresses that is dependent on the constitutive properties of the material. The purpose of this paper is to discuss the mechanisms of volume change in concrete and to suggest new avenues of research that treat traditionally termed material properties instead as time-dependent responses to the internal state of stress in the material. Some implications of this approach on modeling will be discussed.

## 2. Shrinkage

A brief discussion of shrinkage mechanisms is included in the following sections. For a more thorough review, see [1].

### 2.1 Drying Shrinkage

Drying shrinkage is generally attributed to three primary mechanisms that occur as pore water first evaporates and then diffuses to the surface of the concrete: pore fluid capillary surface tension, disjoining pressure, and solid surface tension [2]. Each of these mechanisms involves pressure changes in the pore fluid inducing compressive stress in the solid microstructure that results in bulk shrinkage [3]. Whether a particular mechanism is active is determined by the internal relative humidity (RH). Pore fluid capillary surface tension is active above ~45% since capillary menisci are not stable below that level (pore fluid underpressure overtakes the tensile strength of water). Disjoining pressure may be active over the whole range of RH, and solid surface tension is generally believed to be active at low RH.

### 2.2 Autogenous Shrinkage

The term “autogenous shrinkage” is used due to the popularity of the term, although the deformation to be discussed here is, more specifically, self-desiccation shrinkage. In sealed concrete, moisture is still removed from pores. However, instead of diffusing to the surface of the specimen through the drying process, water is removed only through hydration. This occurs in all hydrating cementitious materials. In addition, since the reaction products of cement and water are less voluminous than the reactants, there is the creation of empty porosity in all cementitious materials. In materials with a low enough w/c ratio, all of the water in the capillary pores over about 50 nm may be consumed by self-desiccation. To continue feeding the hydration process, water is then removed from the smaller pores, resulting in the development of the same shrinkage stresses that occur in drying shrinkage.

### 2.3 Recent modeling work

While drying and autogenous shrinkage have historically been modeled phenomenologically or as material properties, recent work has been dedicated to modeling shrinkage as an elastic response to internal stresses. Bentz et al. [4] used the elastic solution for strain in a solid with spherical pores (in which a pressure is exerted in the pores) to calculate the shrinkage of elastic Vycor glass. The model accurately predicted shrinkage at relatively high RH.

Lura et al. [5] used the same model as Bentz et al. to predict the autogenous shrinkage of cement paste specimens. It was discovered that the model dramatically under-predicted the measured shrinkage. Lura suggested that this could be a result of creep of the solid microstructure. Figure 1 provides evidence for the viscoelastic response of cement paste to changes in pore fluid pressure. The specimen whose data are shown in Figure 1 was a sealed, 0.33 w/c mortar, with rectangular cross section. Shrinkage was measured using an externally mounted LVDT, and RH was measured with an embedded capacitive-type RH sensor located in the center of the specimen. Note that after internal RH equilibrates, shrinkage continues, albeit at a slightly reduced rate. Changes in the stress state induced by any of the generally accepted shrinkage mechanisms must be accompanied by a corresponding change in the

internal RH, which implies that the specimen was exposed to a constant state of stress after RH equilibration. Assuming that the data are accurate, this leaves two possibilities: either another RH-independent shrinkage mechanism is active, or viscoelastic/viscoplastic deformation (creep) is occurring at a constant stress.

Figure 2 shows the shrinkage of 3 mm thick portland cement paste bars exposed to various constant RH environments. Weight loss of the specimens was finished within 1 d after exposure, implying a constant internal RH after that time. After the initial deformation, a slower, time-dependent deformation follows. The additional shrinkage after 1 d exhibited by the specimen in a vacuumed environment (to eliminate carbonation) likely indicates a viscous response. There is additional evidence in the literature that the solid microstructure of portland cement paste is viscoelastic. For example, Acker [6] has measured the rate of viscous flow of the hydration products, and has stated that shrinkage should be considered as a viscoelastic deformation [7,8].

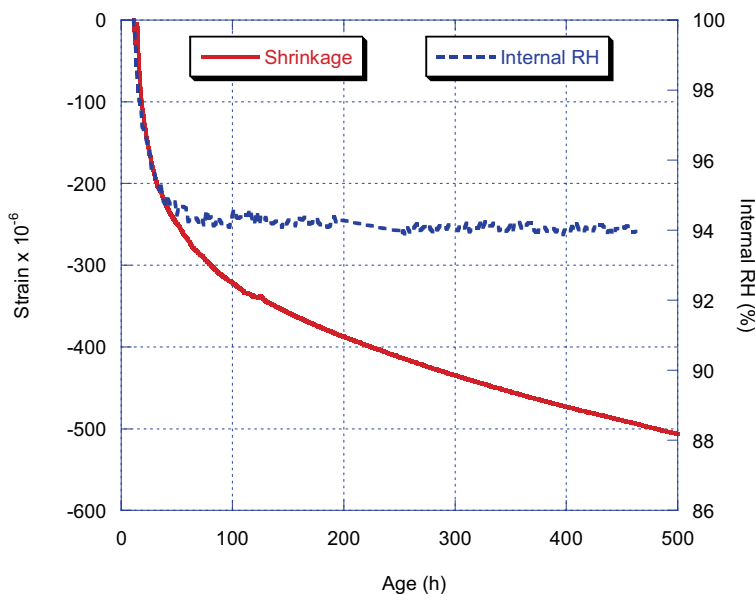


Figure 1. Illustration of cessation of self-desiccation accompanied by continued autogenous shrinkage in a portland cement paste mortar.

#### 2.4 Implications of modeling approach

Recent research suggests that shrinkage may be modeled as a response to internal stress rather than a material property. Superposition of shrinkage strains and external load induced strains (elastic and creep) has been shown to be invalid for drying specimens. A third strain component, called drying creep, is required to account for the deviation between superposition and measured strains. Two conditions associated with internal stresses might be present which

make superposition invalid. First, if the constitutive properties of the material are nonlinear, then the total stress on the microstructure (shrinkage stress and external load induced) may result in total strain that does not equate with the addition of strains calculated independently. This statement is equivalent to Pickett's explanation for the occurrence of drying creep [9]. Second, it is possible that the application of external loads actually influences the internal stresses associated with pore fluid pressure reductions. For example, if external loading causes changes in pore structure through elastic or permanent deformations, the pore radius at the meniscus location may be altered, leading to a change in the state of stress. Bazant et al. [10], however, have denounced this possibility. It is interesting to note that both of the interactions described above, if existent, should hold true for sealed specimens undergoing self-desiccation, implying that drying creep should also be considered in those cases. The presence of drying creep in sealed specimens has been noted in literature [11].

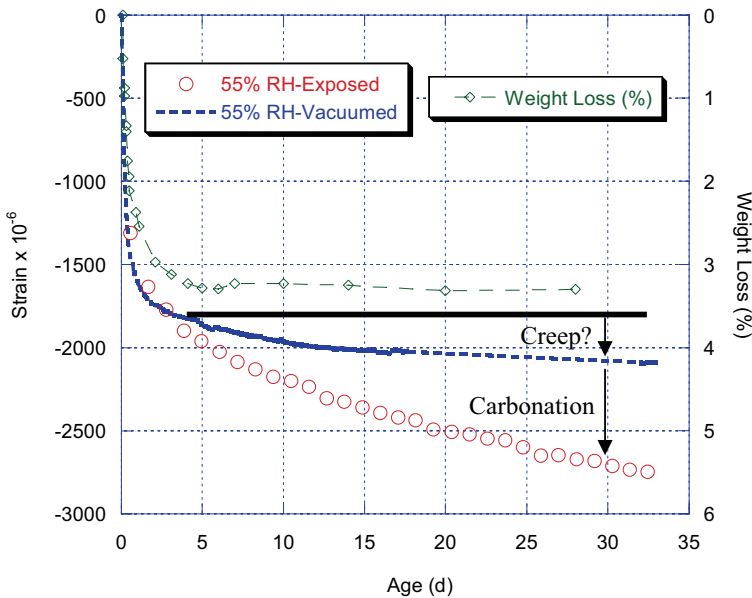


Figure 2. Drying shrinkage of 3 mm thick 0.4 w/c cement paste bars. Shrinkage continues after weight loss ceases.

If the constitutive properties of the solid microstructure of cement paste are viscoelastic, then the response of the solid microstructure to internal stress is time dependent even *after* moisture equilibration has occurred. This statement has important implications including:

- There is no unique solution to the moisture content versus shrinkage curves or the RH versus shrinkage curves that have been included in numerous publications since the 1930's. For example, Mills noted in 1966 [12] that when concrete specimens were dried to the same percent weight loss over a period of 15 months or in an oven over a

period of 7 d, the slowly dried specimens exhibited more than *double* the shrinkage of the rapidly dried specimens.

- The term ultimate shrinkage is a misnomer. The final shrinkage of any specimen is dependent on the loading history, i.e. the internal RH history. Again, the work of Mills applies here. Oven dried shrinkage is not necessarily the *ultimate shrinkage*. By drying a specimen more slowly, the duration of time that stresses are imposed on the solid microstructure is extended, allowing more time for creep to occur. Since the pore structure and mechanical properties of cementitious materials are also time dependent, the aging effect must also be considered.

## 2.5 Shrinkage stresses and scale

A dilemma is encountered when one considers the stress in the solid microstructure related to shrinkage. On the microscale, the zero stress state can be defined as the point the solid microstructure has percolated (“set”) prior to the onset of underpressure in the pore fluid. Once underpressure develops in the pore fluid, compressive stresses develop in the solid microstructure and shrinkage results. It is well known that applying a tensile restraint-type loading induces cracking in most concrete or cement paste specimens. Therefore, it seems necessary that when a bulk tensile stress is applied at least a portion of the material is under significant tensile stress. This is plausible since there must be bridging links between the zones of material under hydrostatic compression. These bridges will be under tension, in particular in zones near water that is located in areas of hindered adsorption (water exerting disjoining pressure) [10]. It appears as though the microstructure and pore fluid distribution are random such that determining the precise distribution of stresses is virtually impossible with current research tools. This necessitates some form of stress averaging across the microstructure for modeling purposes.

The preceding discussion reveals a complexity in modeling stress development associated with shrinkage. To link bulk scale stress development with the nanoscale mechanisms, one must make a leap between scales. This leap generally requires the redefinition of the zero stress state. That is, on the nanoscale, the zero stress state is associated with zero shrinkage, whereas on the bulk scale, the zero stress state is generally defined as the unrestrained state (the free shrinkage state). The presence of moisture gradients “muddies the water” even further. In this case, the free shrinkage state is dependent on the distance from the drying surface so additional stresses are developed [13].

## 2.6 Carbonation shrinkage

There is evidence that several mechanisms are active in carbonation shrinkage. The carbonation process involves carbon dioxide from the environment reacting with dissolved calcium in the pore fluid [14]. This reaction results in dissolution of CH, followed by decalcification of other hydration products once CH is consumed. Powers [14] suggested that dissolution of CH that is under pressure results in measurable shrinkage. The pressure exerted on the CH is caused by compressive stresses in the solid microstructure induced from drying or self-desiccation. Powers explanation for the carbonation shrinkage mechanism agrees well with measured data that suggests that carbonation shrinkage following moderate drying is much greater in magnitude [16]. A similar mechanism has been suggested to explain some of

the increased autogenous shrinkage observed in low  $w/cm$  cement paste when silica fume is utilized [16]. Since carbonation occurs in materials void of CH, other mechanisms may also be active.

If consumption of CH under stress is the primary mechanism for carbonation shrinkage, the deformation cannot be modeled using constitutive properties of the solid microstructure. Consumption of CH must therefore be considered as a separate phenomenon to drying and autogenous shrinkage.

### 3. Thermal Dilation

Thermal dilation of concrete is dependent on the thermal dilation of the cement paste and the aggregate. Since aggregates generally account for about 70% of concrete volume, the aggregate thermal dilation properties tend to dominate the behavior for typical concrete. The thermal dilation of cement paste can be subdivided into three distinct components [18,19]

1. dilation of the solid microstructure, just as thermal dilation of any solid material
2. additional dilation that is caused by changes in pore fluid pressure related to changes in internal RH. Increasing temperature decreases the surface tension of water and causes water to expand, resulting in a *reduction* in the pore fluid *underpressure* (i.e. increase in pressure) and additional expansion of the bulk material. This additional dilation is only seen in partially saturated materials, and is most apparent between about 50-80% internal RH [20].
3. delayed dilation that occurs in the opposite direction of the initial dilation. The mechanism of delayed dilation is dependent on whether the material is fully saturated or partially saturated. In the fully saturated case, as temperature changes the increased coefficient of thermal dilation (CTD) of the water results in pore fluid pressure that contributes to the initial measured dilation. Water then flows from high pressure zones to low pressure zones (or out of/into the material) causing a time dependent dilation with the rate controlled by the permeability of the material [21]. For partially saturated materials, the mechanism behind the delayed dilation is not as clear. It has been suggested that thermally induced differences in energy between physically bound water and free capillary water cause flow from one state to the other, resulting in changes in disjoining pressure [18].

Component number 2 is caused by a change in the same stresses that cause autogenous and drying shrinkage. As a result, thermal dilation and shrinkage are inextricably linked, and researchers may consider combining the phenomena in future models for thermal dilation. A first step in that direction is discussed in [22]. Since component number 2 is based on the same mechanism as that associated with shrinkage, it is also a time dependent deformation dependent on the viscoelastic properties of the solid microstructure.

### 4. Creep

If the solid microstructure of cement paste is considered as a viscoelastic material, then a discussion of volume change induced by internal stresses must also include creep. The



suggestion that creep and drying shrinkage are linked is not new [23, 18]. However, many creep mechanisms have been presented, not all of which are relevant for internal loading conditions.

Creep is often subdivided into basic and drying creep. Basic creep is creep that occurs in the absence of drying (and perhaps self-desiccation that leads to meniscus development). The primary proposed mechanisms for basic creep include:

- Powers suggested that creep could be caused by the seepage of physically bound water into the capillary water, induced by the increased stress in the physically bound water caused by the external load [24]. This is commonly called the seepage theory.
- Feldman [23] hypothesized that creep occurs when C-S-H gradually crystallizes and forms new interlayer space. This can be referred to as the interlayer theory.
- The sliding of C-S-H globules [25] or layers [26] that occurs under localized nanoscale shear stresses may contribute to creep. This theory is called the viscous shear theory.
- Another creep mechanism involves the redistribution of capillary water under load. This was proposed by Sellevold et al. [27], and occurs over a short time scale. This mechanism was later verified by Scherer [28].

A summary of many of the proposed creep mechanisms is included in [29].

Drying creep has also been attributed to many different sources. The phenomena was first recognized by Pickett [9], and is therefore often referred to as the Pickett effect. Some of the primary proposed explanations include:

- Pickett proposed that non-linearity of the stress-strain relationship led to additional strain when the stresses due to drying shrinkage and external load were superimposed.
- The stress induced shrinkage mechanism [30] suggests that when external loads are combined with drying (capillary menisci are present), the external load influences the shrinkage stresses, leading to an increase in shrinkage under compressive load.
- Another possible mechanism for drying creep is the development of microcracking due to high stresses induced by drying gradients. The presence of microcracks may increase the creep rate [30,9].
- Bazant et al. [10] have recently proposed the microprestress-solidification theory that explains both drying creep and the aging of creep properties (in addition to aging caused by hydration). It is suggested that the presence of disjoining pressure, which is always under compression due to its location in areas of hindered adsorption, forces balancing tension in bridging nanostructure. As the material ages, those bridges slowly creep, break, and reform. The relaxation of the tensile stresses in the bridging nanostructure results in aging viscous properties. At the same time, it is proposed that the rate of creep of the bridging nanostructure increases with decreasing internal RH, thus causing drying creep.

It is generally believed that some combination of the suggested sources are active in both compressive and tensile drying creep.

Many of the mechanisms for basic creep described above would be active on the scale that would allow viscoelastic response to internal stresses. Table 1 summarizes the primary basic

creep mechanisms, and assesses the potential for each mechanism to be active in creep of the solid microstructure subjected to internally applied stresses.

Table 1. Summary of proposed creep mechanisms and their likelihood of occurrence under internally applied stresses to the solid microstructure.

Proposed creep mechanism	Active scale for mechanism	Likely participant in creep of microstructure under internal load?
gel water seepage	nm	Maybe
capillary flow	$\mu\text{m}$	No
microcracking	nm– $\mu\text{m}$	No
sliding of C-S-H (globules or layers)	<nm	Yes
crystallization of C-S-H	<nm	Yes

## 5. Initial modeling work

A model has recently been developed at the University of Illinois at U-C for predicting the autogenous shrinkage of portland cement paste as a viscoelastic response to pore fluid pressure induced by self-desiccation [Grasley and Lange to be published, 2005]. The model is an extension of the elastic model used by Lura et al. [5], modified to account for creep of the solid microstructure. Internal RH measurements are used to calculate the internal stress history, and creep measurements under hydrostatic pressure allow calculation of the dilatational compliance. A novel experiment has also been developed that allows the measurement of an important parameter in the model, the bulk modulus of the solid microstructure [31]. While validation of the model is still ongoing, some initial results shown in Figure 3 look promising.

## 6. Summary

Many of the dilatational deformations in concrete that are often considered as material properties are actually mechanical responses to internal stresses. Many of these deformations, including thermal dilation, autogenous shrinkage, drying shrinkage, and creep are mechanistically linked. Recently, researchers have taken steps to develop models that link physicochemical mechanisms with elastic micromechanical response to predict autogenous shrinkage, drying shrinkage stresses, and thermal dilation. However, there is ample evidence that the solid microstructure exhibits a viscoelastic response to internal stresses. A new direction in modeling involves improving on these recently developed models by incorporating viscoelastic material properties. Work on such a model has been initiated, but additional efforts are needed to fully validate the model.

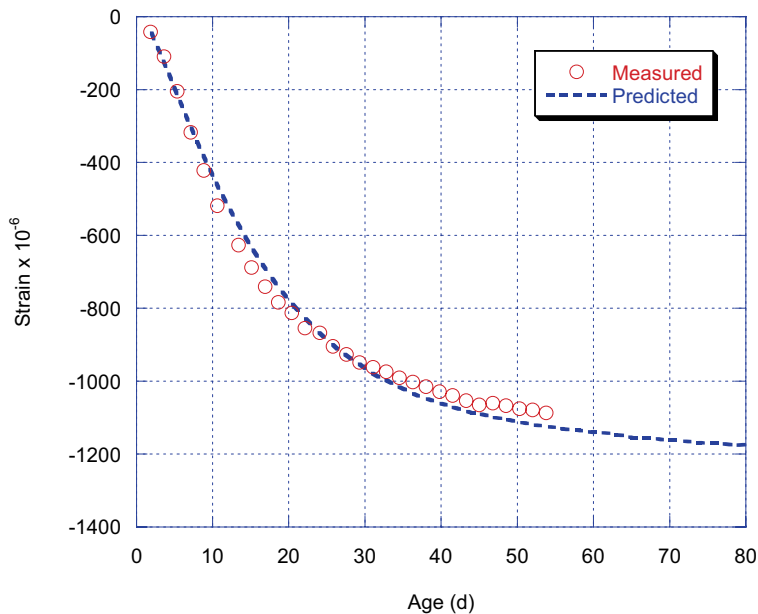


Figure 3. Comparison of measured versus predicted autogenous shrinkage using viscoelastic model.

## References

1. Grasley, Z.C., Lange, D.A., D'Ambrosia, M.D., 'Drying stresses and internal relative humidity in concrete', in 'Materials Science of Concrete VII', J. Skalny, Ed. (2004).
2. Mindess, S., and Young, J.F., 'Concrete', (Prentice-Hall, Inc, Englewood Cliffs, NJ, 1981).
3. Bissonette, B., Marchand, J., Charron, J.P., Delagrave, A., Barcelo, L., 'Early age behavior of cement-based materials', in 'Materials Science of Concrete VI', J. Skalny, Mindess, S., Ed., (2001).
4. Bentz, D.P., E.J. Garboczi, and D.A. Quenard, 'Modelling drying shrinkage in reconstructed porous materials: application to porous Vycor glass', *Modelling and Sim. in Mat. Sci. and Eng.*, 1998. **6**(3): p. 211-36
5. Lura, P., Guang, Y.E., van Bruegel, K., 'Effect of cement type on autoegenous deformation of cement-based materials', *ACI SP 220* (4) (2004) 57-68.
6. Acker, P., 'Micromechanics analysis of creep and shrinkage mechanisms', in 'ConCreep 6' (MIT, Elsevier, 2001).

7. Acker, P., 'Why does ultrahigh-performance concrete (UHPC) exhibit such low shrinkage and such low creep?', *ACI SP-220* (2004) 141-154.
8. Hua, C., P. Acker, and A. Ehrlacher, 'Analyses and models of the autogenous shrinkage of hardening cement paste: I. Modelling at macroscopic scale', *Cem. and Concr. Res.*, **25** (7) (1995) 1457-1468.
9. Pickett, G., 'The Effect of Change in Moisture Content on the Creep of Concrete Under a Sustained Load', *ACI J.* **38** (1942) 333-355.
10. Bazant, Z.P., S. Baweja, and F.-J. Ulm, 'Microprestress-solidification theory for concrete creep. i: aging and drying effects. *J. of Eng. Mech.* **123** (11) (1997) 1188-1194.
11. Lange, D.A. and S.A. Altoubat, 'The pickett effect at early age and experiment separating its mechanisms in tension', *Mat. and Struct.* **34** (248) (2002) 211-218.
12. Mills, R.H., 'Effects of sorbed water on dimensions, compressive strength and swelling pressure of hardened cement paste', in 'Symp. on Structu. of Portland Cem. Paste and Concr.' **SR 90** (Highway Research Board, 1966).
13. Grasley, Z.C. and D.A. Lange, 'Modeling drying shrinkage stress gradients in concrete', *Cem. Concr. and Agg.* **26** (2) (2004) 115-122.
14. Bary, B. and A. Sellier, 'Coupled moisture - carbon dioxide-calcium transfer model for carbonation of concrete', *Cem. and Concr. Res.* **34** (10) (2004) 1859-1872.
15. Powers, T.C., 'Hypothesis on carbonation shrinkage', *Portland Cem. Assn. - Res. and Development Lab. -- Journal* **4** (2) (1962) 40-50.
16. Verbeck, G.J., 'Carbonation of hydrated portland cement', in *ASTM Cem. & Concr. STP* **205** (1958).
17. Jensen, O.M. and P.F. Hansen, 'Autogenous deformation and change of the relative humidity in silica fume-modified cement paste', *ACI Mat. J.* **93** (6) (1996) 539-543.
18. Bazant, Z.P., 'Delayed thermal dilatations of cement paste and concrete due to mass transport', *Nuc. Eng. and Des.* **14** (2) (1970) 308-18.
19. Sellevold, E.J. 'Thermal expansion coefficient (CTE) of cement and concrete: effect of moisture content' in 'Advances in Cement and Concrete', Engineering Conferences International, Copper Mountain, CO (2003).
20. Grasley, Z.C., Lange, D.A. 'Thermal dilation and internal relative humidity in hardened cement paste', in 'International Symposium of Advances in Concrete through Science and Engineering', Evanston, IL, (2004).
21. Scherer, G.W., 'Thermal expansion kinetics: method to measure permeability of cementitious materials. I. Theory', *J. Am. Ceram. Soc.* **83** (11) (2000) 2753-61.
22. Grasley, Z.C. and D.A. Lange, 'Early-age concrete stresses induced by drying shrinkage and thermal dilation', in '5th Int. PhD Symp. in Civil Eng' (Delt, The Netherlands, 2004).
23. Feldman, R.F., 'Mechanism of creep of hydrated portland cement paste', *Cem. & Concr. Res.* **2**(5) (1972) 521-5400.
24. Powers, T.C., 'Study of creep of concrete (Interpretation des essais de fluage sur le beton)', *RILEM Bulletin* **34** (1967) 73-85.
25. Jennings, H.M., 'Colloid model of C-S-H and implications to the problem of creep and shrinkage', *Mat. and Struct.* **37** (265) (2004) 59-70.

26. Ruetz, W. 'A hypothesis for the creep of hardened cement paste and the influence of simultaneous shrinkage', in 'International Conference on the Structure of Concrete' (Cement and Concrete Association, London, 1968).
27. Sellevold, E.J. and C.W. Richards, 'Short-time creep transition for hardened cement paste', *J. Am. Ceram. Soc.* **55** (6) (1972) 284-9.
28. Scherer, G.W., 'Measuring permeability of rigid materials by a beam-bending method: I, Theory', *J. Am. Ceram. Soc.* **83** (9) (2000) 2231-2239.
29. Tamtsia, B.T. and J.J. Beaudoin, 'Basic creep of hardened cement paste. A re-examination of the role of water', *Cem. and Concr. Res.* **30**(9) (2000) 1465-1475.
30. Bazant, Z.P. and Y. Xi, 'Drying creep of concrete: Constitutive model and new experiments separating its mechanisms', *Mat. and Struct.* **27** (165) (1994) 3-14.
31. Grasley, Z.C., Valenza, J.J., Scherer, G.W., Lange, D.A., 'Measuring permeability and bulk modulus of cementitious materials', in 'ConCreep 7' (Nantes, France, 2005).



## **The Effect of Admixtures on the Fresh and Consolidated Behaviour of ECC**

GPAG van Zijl and H. Stander

Department of Civil Engineering, University of Stellenbosch, South Africa

### **Abstract**

In the development and application of high performance fibre reinforced cement-based composites (HPFRCC), repeatable mechanical response to all types of mechanical loading that are experienced by structural applications of these advanced materials, is imperative. Only if such repeatability is attained, confident prediction of structural behaviour, based on predictable material behaviour, can be made. Such repeatability depends on objective test methods, but also on quality control on the material processing itself. In this regard fibre dispersion is the dominant factor.

This paper reports on a systematic study of the influence of additives in the form of super plasticiser (SP) and viscous agent (VA) on a particular engineered cement-based composite (ECC) developed at the University of Stellenbosch. Indirect measures of fibre dispersion are reported, in the form of mechanical response to direct tensile, as well as flexural (three point) loading. The roles of fibre dispersion in (i) successfully achieving strain hardening and (ii) ensuring repeatability cannot clearly be distinguished. Nevertheless, by achieving both, clear evidence of good fibre dispersion is indicated.

### **1. Introduction**

Achieving improved performance of structural concrete, is of utmost importance. Fibres are added to cement-based material, primarily to alter the post-cracking behaviour. ECC as a subclass of HPFRCC is defined by mechanical properties such as pseudo strain hardening (in excess of three percent), deflection hardening, crack width limitation, compatible deformation with reinforcement. These attributes are of great importance to attain structural durability.

In this paper a systematic study of the influences of admixtures on cement-based composites, which have superior tensile behaviour in terms of ductility to normal concrete, is described. The primary focus is on the influence these admixtures have on the fresh state of ECC, and the impact of the fresh state properties on the consolidated behaviour of ECC. The influences are

measured and quantified in terms of flow table test results conducted on fresh ECC and mechanical response of the consolidated ECC to direct tensile and flexural testing.

It is well-documented that cement-replacement materials, especially fly-ash (FA), may improve fresh properties, in terms of flow-ability (Neville 1996, Chang 2004), and durability of the hardened product (Mindess et al 2003) of concrete. The beneficial influence of FA on fluidity is particularly true, attributed to its well-rounded spherical particles. A particular beneficial influence of FA in ECC containing polyvinyl alcohol (PVA) fibres is the enhanced bridging function of PVA fibres through reduced bond (Peled and Shah 2003), whereby fibre breakage and associated brittle fracture is prevented. Through inclusion of FA, the interfacial zone between fibres and the matrix is modified, whereby pullout along this interface becomes the main mechanism of fibre-matrix interaction. This means that a cohesion type failure occurs in the matrix, which entails pullout of the fibre and the surrounding interfacial zone matrix. The role of FA has also been exploited to counteract matrix densification by extrusion of PVA-ECC. These qualities, as well as cost reduction have motivated the use of 50% cement replacement by FA in this study.

In addition to balanced fibre strength and matrix-fibre interfacial properties, it is essential that the fibres are well dispersed in the matrix. Multiple cracking and the associated tensile ductility and strain hardening require a uniform spatial distribution of the fibres. Due to differences in density a good mixing procedure does not suffice to achieve proper dispersion in the final product. It has been argued that good workability or fluidity of the fresh material improves fibre dispersion, encouraging the use of workability enhancing agents in ECC to the point that it has become usual to add super-plasticiser (SP). However, Stahli and van Mier (2004) point out the danger of fibre segregation in too fluid mixes. To stabilise the rheology of the mix, viscosity modifying admixtures, or viscosity agents (VA), are commonly added in ECC.

This paper reports the study of SP and VA content in a particular PVA-ECC. A composite for casting is investigated, which requires good workability properties to ensure a uniform spreading of the constituents, especially the fibres, but also ease of placement during the casting process. A single fibre volume of  $V_f = 2\%$  PVA fibres of length 12mm and diameter 40  $\mu\text{m}$ , and a single W/B ratio of 0.4 are used.

## **2. Admixtures**

Admixtures are chemicals that are added to the concrete immediately before or during the mixing procedure, which may significantly alter the fresh, early age and consolidated state to economic and physical advantage. Only small quantities are usually required, typically 0.1 to 2 percent by mass of the binder.

The functions of the admixtures used in this research are to ensure better fibre dispersion and a workable composite (high flow-ability), optimal for placement in the intended application.



## 2.1 Superplasticiser

Superplasticisers, also called workability aids, are polymeric dispersion agents which overcome Van der Waals forces, whereby the fluidity or workability of cement paste or concrete is increased. In this study Premia 100 was used, termed a high-range water reducing agent. It has a high molecular weight and is manufactured to high standards of purity and can therefore achieve substantially greater primary effects without significant undesirable side-effects, like air entrainment.

The mode of action of SP is that it causes a combination of mutual repulsion and steric hindrance between cement particles, thus creating less friction when the particles move.

The behaviour of any particular combination of SP and cement will depend on several factors other than the admixture type, including the binder composition, the binder fineness and the water/binder ratio.

Substantially increased performance can be obtained if the SP is added a short time (1-2 minutes) after the first contact of the mix water with the binder (Domone and Illston 2001). If the SP is added at the same time as the water, a significant amount is incorporated into the rapid  $(\text{CaO})_3\text{Al}_2\text{O}_3$ /gypsum reaction, hence reducing that amount available for the workability action. The SP action only occurs for a limited time period.

## 2.2 Methyl Cellulose (Chryso Aquabeton ZA)

Chryso Aquabeton ZA is a powder additive which prevents wash out and segregation of concrete constituents in the fresh state. VA causes an increased viscosity through entanglement of its polymer chains. This is a mechanism of stabilisation of the matrix, as it decreases or prevents segregation (Lachemi et al. 2004). In combination with SP it can lead to good workability with resistance to segregation. Thereby, it assists in uniformly dispersing fibres in the matrix. The uniform dispersion of fibres is critical for achieving the multiple crack phenomenons and associated ductility. However, due to the increased viscosity, as well as cost, the amount of VA should be optimised. The minimum amount of VA which ensures matrix stability, in combination with the SP content which optimally disperses the fibres, is sought. An additional requirement is ease of placement, for practical casting of the material.

## 3. Experimental programme

An ECC mix of proportions shown in Table 1 was used for the study. Similar mixes, with the shown high FA content, have been shown to produce ductile, strain hardening tensile response (Gao Song and Van Zijl 2004). The varying amounts of additives shown in Table 2 form a matrix of mix designs, which are the basis of the systematic study.

Dog bone specimens for direct tensile testing were prepared for all mixes shown in Table 2. In addition, plate specimens for flexural testing were prepared from mixes 5, 8 and 9. Four specimens for each tensile test and three specimens for the flexural were prepared and tested, totalling 48 dog bones and 9 plates. Directly after casting, all specimens were kept in a

temperature control room at 23° C prior to demoulding 48 hours later. After demoulding the specimens were placed in water curing tanks at 23° C for the next 12 days. The specimens were tested on 14 days in a temperature control room at 23° C. All specimens were tested in the fully saturated state.

Table 1: Mix design for specimens

<b>Constituent</b>	<b>Mass</b>
<b>Water / Binder</b>	0.4
<b>Binder:</b>	
Cement	0.4
Fly Ash	0.5
Slag	0.1
<b>Aggregate / Binder</b>	0.5
<b>PVA Fibres (by volume )</b>	2%

Flow table testing was performed on the fresh ECC to study the flow-ability of the composite. The process is depicted in Figure 1, where an amount of the fresh ECC is placed in a cone on the table. The cone is lifted so that the ECC stays in that form on the table. The table has a sling and when it is turned the table top is lifted to fall free over a short distance, this counts as one hit of the table. Circular lines are visible on the round table and are used to measure the average spread of the fresh ECC after ten hits and again at 20 hits. The lines are spaced 1cm from each other and numbered from the outside inward, thus a lower value indicates a higher spread.

Table 2: Admixture ratios specimen set by weight of the binder

<b>Admixture</b>	<b>1</b>	<b>2</b>	<b>3</b>
<b>SP</b>	0.5%	1.0%	2.0%
<b>VA</b>	0.05%	0.05%	0.05%
	<b>4</b>	<b>5</b>	<b>6</b>
<b>SP</b>	0.5%	1.0%	2.0%
<b>VA</b>	0.10%	0.10%	0.10%
	<b>7</b>	<b>8</b>	<b>9</b>
<b>SP</b>	0.5%	1.0%	2.0%
<b>VA</b>	0.30%	0.30%	0.30%
	<b>10</b>	<b>11</b>	<b>12</b>
<b>SP</b>	0.5%	1.0%	2.0%
<b>VA</b>	0.50%	0.50%	0.50%

In addition to quantification of flow-ability, segregation of the mix can be visualised on the flow table, as the example in Figure 1 indeed shows. No quantified measurement of segregation in terms of bleeding or otherwise was made, other than visual observation of the phenomenon.



Figure 1: The flow table testing procedure, showing a mix exhibiting segregation

Direct tensile testing was performed on dog bone shaped specimens, as shown in Figure 2. The specimens were tested under displacement control in a Zwick Z250 Materials Testing Machine at a fixed displacement rate of 0.5 mm/minute. An HBM extensometer (DD1) was used to measure displacement between the extensometer ends, up to the extensometer limit of 2.2 mm lengthening over the 80 mm gauge length. Beyond this value, which represents a 2.75% tensile strain, only the crosshead measurement of displacement is available.

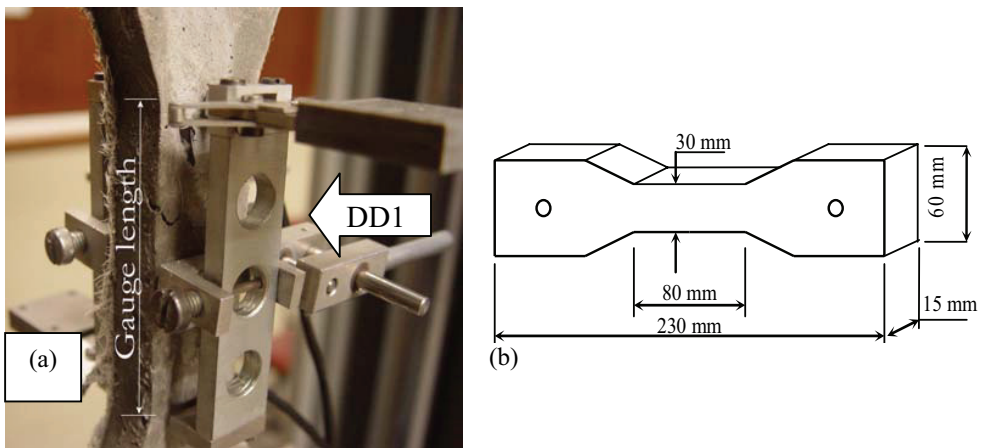


Figure 2: (a) Direct tensile testing of (b) dog bone shape specimen

Three point bending tests were conducted on plate specimens with a nominal thickness of 15 mm, under displacement control in a Zwick Z250 Materials Testing Machine. The nominal displacement rate used was 3 mm/min. The distance between the outer supports is 400 mm. The setup is shown in Figure 3.

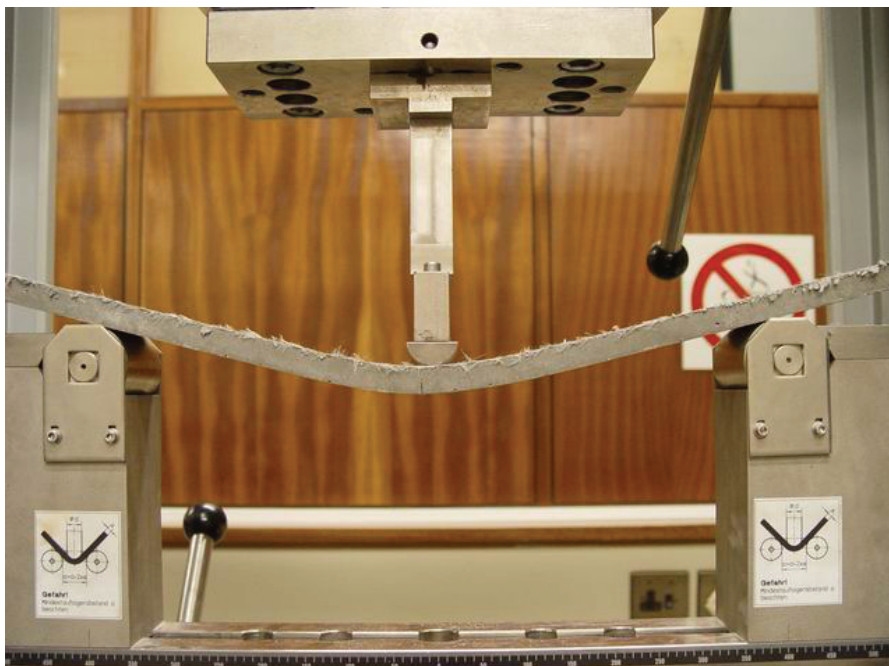


Figure 3: A three point bending test specimen

## 4. Test results

### 4.1 Flow table tests

The flow table test is a simple and straightforward procedure for studying both segregation and workability of a mix design. All mixes in Table 2 were tested on the flow table.

The basic result of increased flow-ability with SP content is confirmed by the flow table results. Also, reduced flow-ability with increased VA content was measured. Of interest is, however, the combined effect of these two additives. The influence both the additives have on the flow-ability of the mix design can be seen in Figure 4. This figure indicates equal flow-ability for different ratios of the two admixtures, thus indicating compensation by both sides for the extreme result caused by the other.

To study the influence of the additives on fibre dispersion, and in particular the correlation between workability/fluidity and fibre dispersion, the response of the hardened material is measured in direct tension and flexure. It is argued that the mechanical response of ECC reveals symptoms of fibre dispersion; ductile, strain hardening response indicates good fibre dispersion and vice versa. This indirect method is enforced by lack of visualisation method of the polymeric fibres.

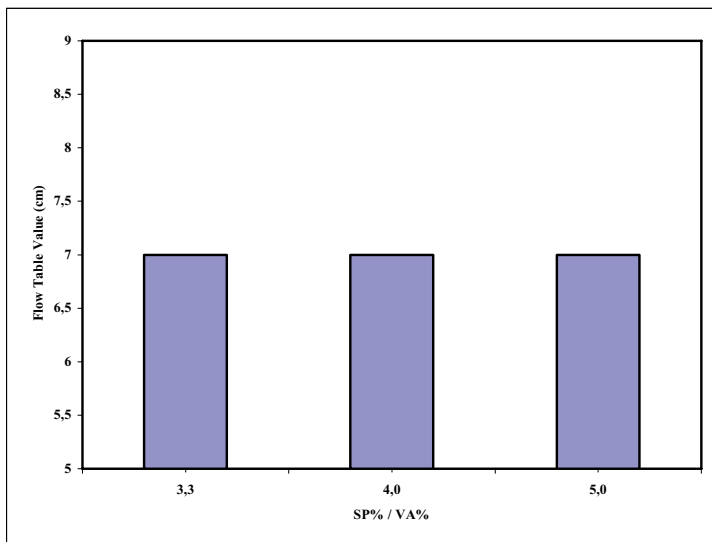


Figure 4: Equal flow table values for different ratios of the admixtures

#### 4.2 Mechanical response

The results from these tests indicate strain-hardening and acceptable repeatability of some mixes, while large scatter is considered a symptom of wrong dosage, either through segregation, or too low workability and associated disconnection in the specimen through inadequate compaction and dispersion. In Figure 5 the three-point flexural and direct tensile responses of the three combinations of SP and VA are shown. From the direct tensile responses it is clear that the additives determine whether strain-softening or hardening occurs. For the strain-hardening cases (predominantly combinations 7-9), multiple cracking was observed, as shown in Figure 6. Such behaviour is considered an indication of superior fibre dispersion, as well as optimal fibre-matrix interfacial bondage properties.

In disseminating the mechanical test results, the ultimate strain is quantified for each specimen tested in direct tension. This value is taken as the strain coinciding with the stress in the strain-softening branch of the value 80 percent of the ultimate tensile stress. The reason for using this measure is that some of the specimens only had strain-softening beyond the first crack.

In Figures 7 the averaged ultimate strains are shown as function of the SP and VA contents. Also shown in Figure 7 are the coefficients of variation (COV) of the ultimate strain ( $\epsilon_u$ ). It appears that the ductility is most sensitive to the amount of VA used. Independent from the amount of SP used, the ductility achieved by an optimum amount of VA, is unrivalled. Nevertheless an optimum combination is apparent from Figure 7, namely 0.3% VA and 1% SP. This is also reflected in the COV, with the lowest value associated with the highest ductility. This indicates that an optimum rheology exists, brought about by an optimum combination of additives, which results in superior ductility, as well as repeatability.

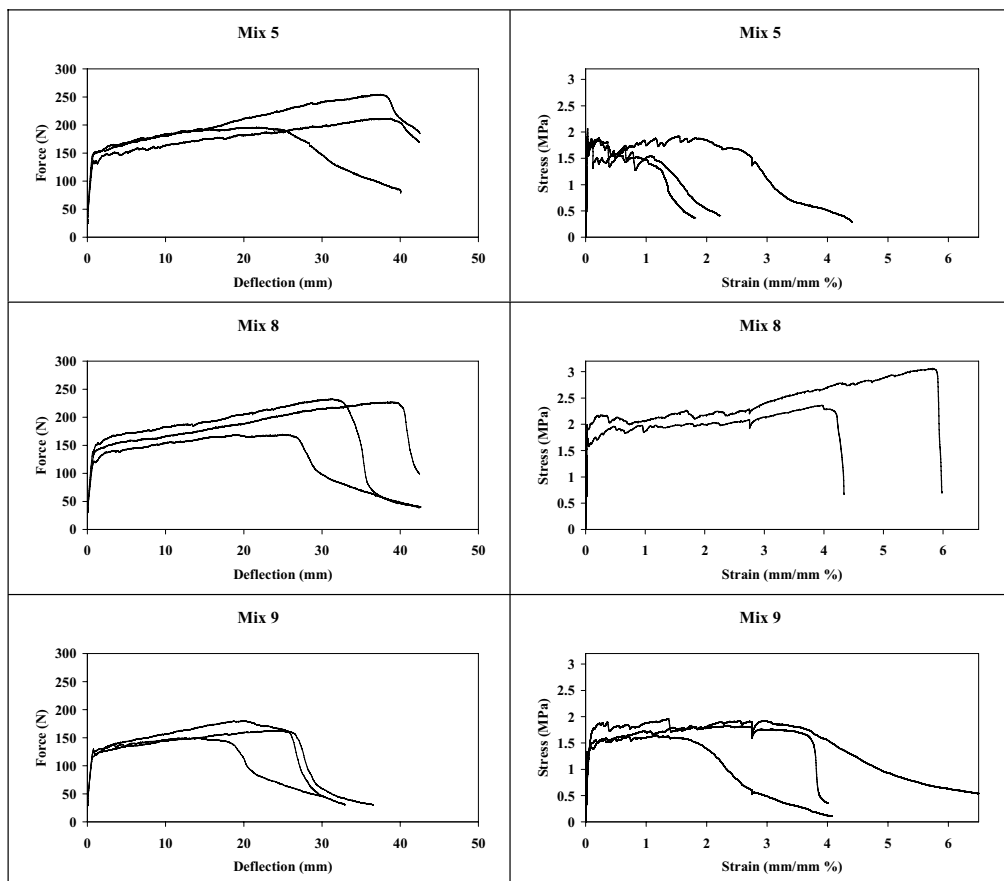


Figure 5: The bending and tensile test results for mix designs 5 (SP = 1%, VA = 0.1%), 8 (SP = 1%, VA = 0.3%) and 9 (SP = 2%, VA = 0.3%),



Figure 6: Multiple cracks depicted by white lines on a tensile specimen

The left side Figure 7 indicates that too little SP causes inferior workability that results in poor mixing conditions for the constituents, causing low ductility and associated poor fibre dispersion, but also matrix disconnection and irregularities. The upper range in SP content leads to lower ductility, indicating poor fibre dispersion caused by segregation.

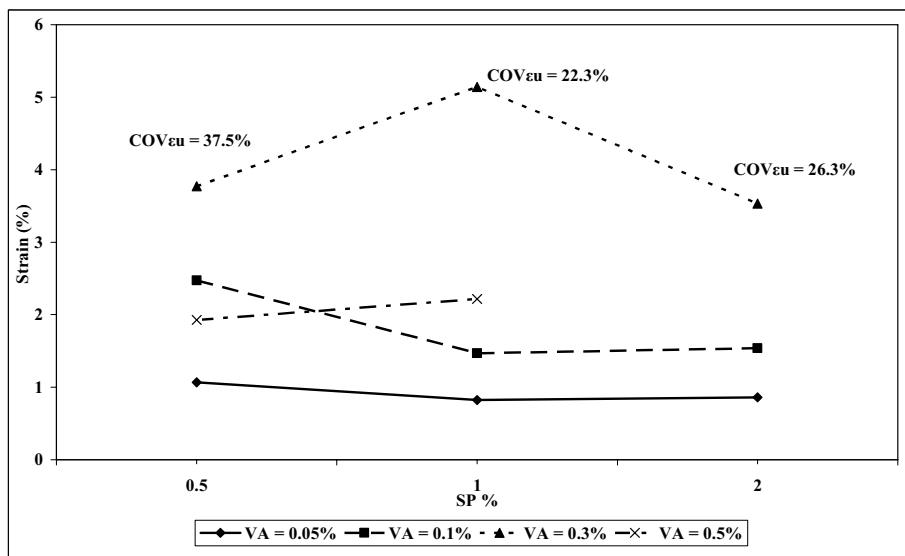


Figure 7: The effects of the varying amounts of SP on the ductility achieved

In Figure 8 the ultimate stresses are shown as functions of the SP and VA contents. The optimum VA and SP content in terms of ultimate strength coincides with the 0.3% VA and 1.0% SP for optimal ductility. This is not a coincidence, but is believed to be a clear indication of superior fibre dispersion, which leads to superior ductility, accompanied by strain-hardening to a maximum ultimate tensile strength. Contrary to the strain results, the ultimate strength showed larger variability (COV=18.7%) than the other SP contents, which needs further investigation.

The mean values of first cracking stress and strain; and ultimate stress and strain are connected with straight lines in Figure 9 for illustration purpose. Also, average tension-softening branches are drawn using approximately average measured gradients. The numbered arrows indicate, in sequence, the different areas of the curve: firstly, the linear elastic part, secondly the non-linear strain-hardening part and lastly the tension-softening failure part. With an increase in the amount of SP used, a decrease of the first crack strength becomes apparent, which indicates a prolonging effect on the strength development of the material (retardation). The second most notable influence is the differing strain-hardening gradients, the largest gradient correlating with the greatest ductility and tensile strength. Another observation is the correlation between the amount of strain-hardening and the gradient of tension-softening branch, which depicts the rate of failure. An increase in strain-hardening results in a more rapid rate of failure.

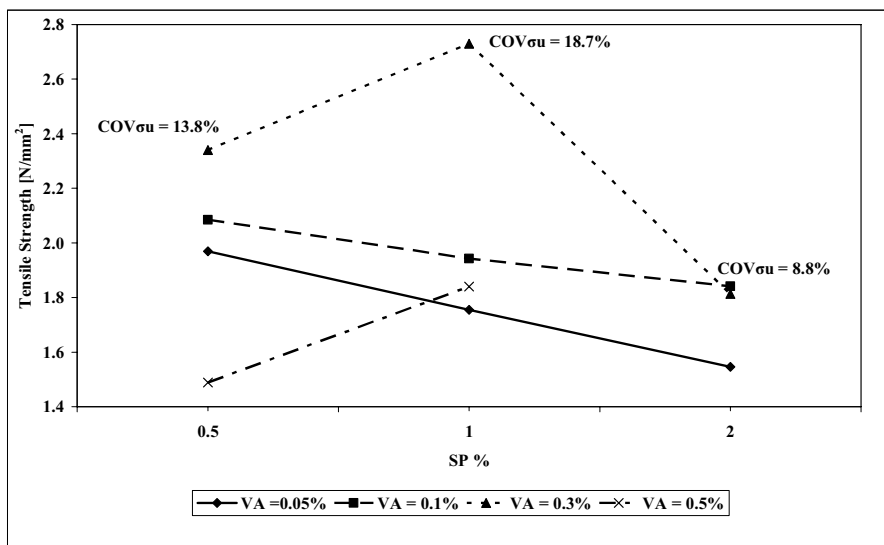


Figure 8: The effects of the varying amounts of SP on the tensile strength achieved

The mean values of the stress-strain curves for the varying sets of VA with the optimum amount of SP are depicted in Figure 10. Here it becomes apparent that the amount of VA used has a defining influence on the strain-hardening gained. A higher amount of the VA results in a steeper gradient of strain-hardening, as well as greater ductility. The fact that greater ductility leads to a more rapid rate of failure, is confirmed. Once again an optimum VA content is clear. Too low amounts of VA cause inferior dispersion of fibres in the fresh state and too high amounts result in poor workability which leads to premature failure.

### 4.3 Three point bending tests

The results of the three point bending tests indicate that the optimum mix design for mechanical behaviour in tensile and bending tests, do not correlate. Figure 5 illustrates the mechanical behaviour for mix designs 5, 8 and 9. The left column contains the bending test results and the right column the tensile test results for the same mix design.

In Figure 11 the averaged trends are illustrated, in similar fashion as Figures 9 and 10. A doubling of the SP content, affects the bending test results severely. The larger amount of SP causes segregation of the material constituents in the fresh state, confirmed by the flow table test observations. The result is poor ductility.

The optimum ultimate strength and ductility is found for flexure at VA = 0.1% as opposed to 0.3% for direct tension. The ultimate modulus of rupture (MORu) is at a peak for mix design 5, but is closely followed by that of mix design 8. Mix design 8 demonstrates the best repeatability with the deflection coefficient of variance ( $COV_{def}$ ). The gradients of strain-hardening are not affected by the amounts of additives used.



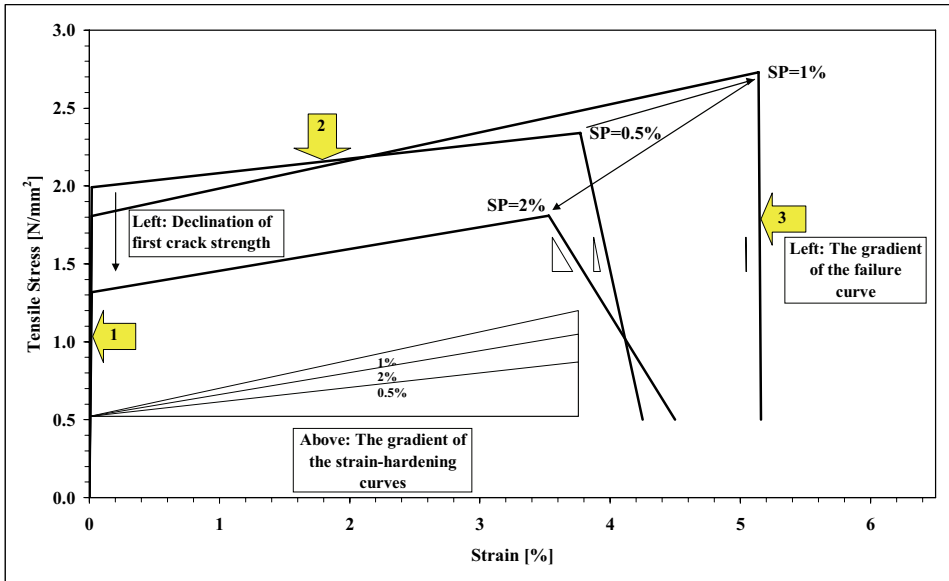


Figure 9: The average stress-strain curves for the optimum VA and varying sets of SP

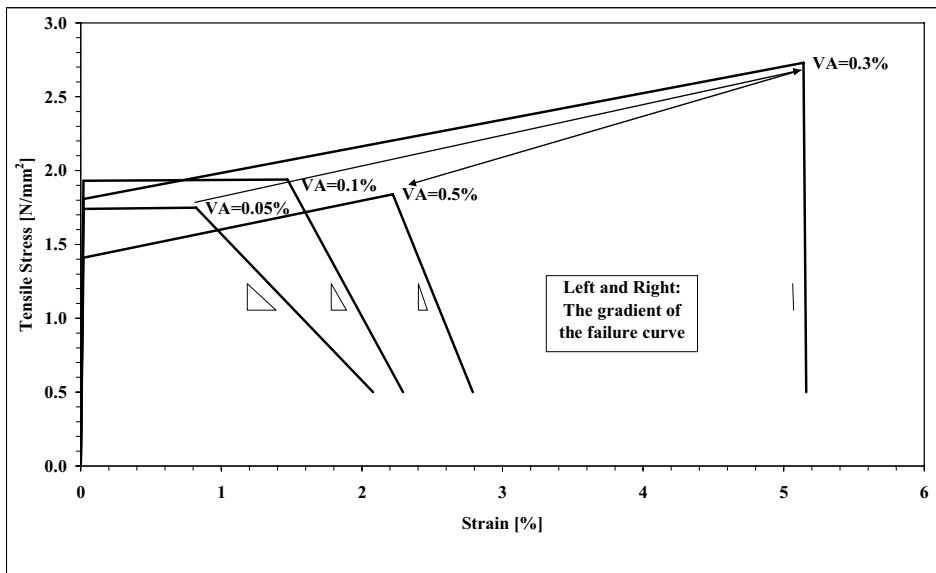


Figure 10: The average stress-strain curves for the optimum SP and varying sets of VA

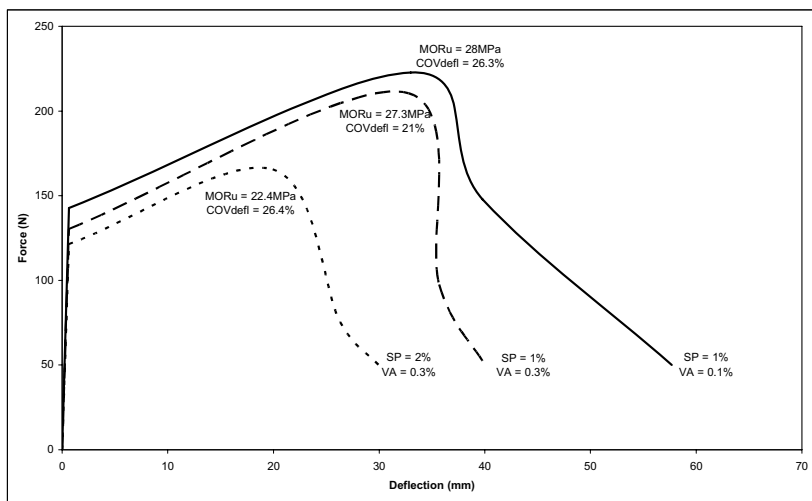


Figure 11: The average bending test results for mix designs 5, 8 and 9

## 5. Workability vs ductility / fibre dispersion

When the correlation between workability and ductility is investigated, it becomes obvious that superior ductility indicates an optimum workability along with the optimum dispersal of fibres. Figure 12 illustrates this optimum workability point for this systematic analysis. It is observed that for the first part of the graph that a higher viscosity results in poor ductility and for the latter part that higher flow-ability results in poor ductility as well. It is of great importance that when preparing a mix design of ECC for a casting application, the optimum workability point is allocated. A higher viscosity causes poor dispersion, matrix disconnections and surface irregularities, which result in premature failure, thus poor ductility. Higher flow-ability causes segregation of the specimens along with floating of PVA fibres, which results in poor fibre dispersion, thus poor ductility.

## 6. Conclusions

The effects of admixtures on the fresh and consolidated behaviour of ECC have been quantified in terms of flow table, tensile and bending parameter sensitivity to these ingredients. It has been postulated that good fluidity of the fresh mix, without segregation, results in well dispersed fibres, which leads to superior mechanical response either in direct tension or in flexure. This has been confirmed, by correlating flow table results with tensile and flexural ductility and ultimate strength:

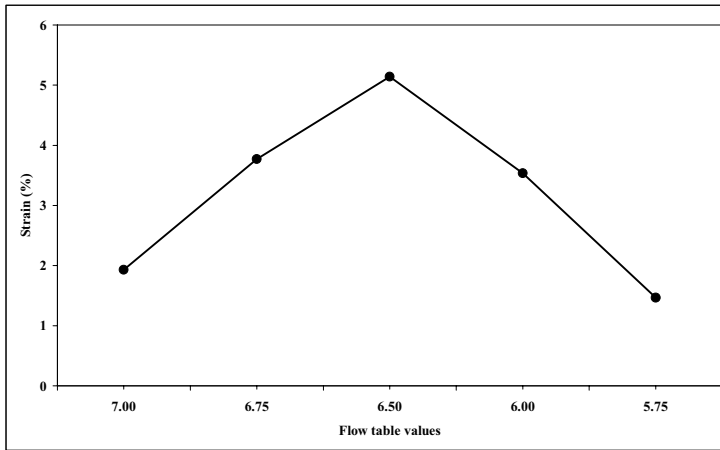


Figure 12: The influence of workability on the ductility achieved

1. Superior ductility in direct tensile testing was obtained for specimens with admixture content and mixture which caused an optimum workability in the fresh state, i.e. the highest flow ability without segregation. Specimens made of mixes with higher flow ability, resulting in segregation of the constituents, and those with lower flow ability were found to have lower tensile strength and ductility.
2. The dominating factor for achieving supreme ductility is the amount of VA used; unrivalled performance is illustrated with the optimum amount of VA and this is relatively insensitive to the amount of SP used in combination, within the range in quantity studied.
3. Improved workability not only led to superior mechanical response in terms of strength and ductility, but also improved repeatability, expressed by lower coefficients of variation in ultimate strength and strain.
4. Higher tensile strength for the same matrix design is only possible when strain-hardening occurs, for which good fibre dispersion is required to ensure multiple cracking. The maximum strain hardening gradient was found for mixes of optimal flow ability, which is further validation of the postulation that optimal flow ability causes optimal fibre dispersion. The largest gradient for the strain-hardening correlates with the greatest ductility and tensile strength.
5. The optimum amounts of additives differ slightly for mechanical behaviour in direct tensile testing from that in flexure. This needs further investigation.

## Acknowledgements

The support of this research by the South African Cement and Concrete Institute, Infraset Infrastructure Products, as well as the Technology and Human Resources in Industry Programme of the South African Ministry of Trade and Industry is gratefully acknowledged. The supply of PVA fibres by Kuraray Co. Ltd. is appreciated.

## References

1. Neville, A.M., *Properties of Concrete*, Wiley, New York, (1996) 243-255.
2. Chang, P.K., An approach to optimizing mix design for properties of high-performance concrete, *Cement and Concrete Research*, 34, (2004) 623-629.
3. Mindess, S., Young, J.F. and Darwin, D., *Concrete*. Prentice Hall, New Jersey, (2003) 99-114.
4. Peled, A. and Shah, P.S., Processing effect in cementitious composites: extrusion and casting, *Journal of Materials in Civil Engineering*. Vol. 15, No.2, (2003) 192-199.
5. Shah, SP, Srinivasan, R and DeFord, D., The use of extrusion rheometry in the development of extruded fibre-reinforced cement composites, *Concrete Science and Engineering*, Vol. 1, (March 1999) 26-36.
6. Stahli, P. and van Mier, J.G.M., Rheology Properties and Fracture Processes of HFC, *Proceedings of BEFIB*, (2004) 299-308.
7. Domone, P.L.J. and Illston, J.M., *Construction Materials – Their Nature and Behaviour*, Spon Press, London and New York, (2001), 112
8. Lachemi, M., Hossain, K.M.A., Lambros, V., Nkinamubanzi, P-C. and Bouzoubaa, N., Self-consolidating concrete incorporating new viscosity modifying admixtures, *Cement and Concrete Research*, 34, (2004) 917-926.
9. Gao Song and Van Zijl G.P.A.G., Tailoring ECC for commercial application. *Proceedings 6th Rilem Symposium on Fibre reinforced Concrete (FRC)*, Varenna, Italy, (2004) 1391-1400.

## **Investigation of early age deformation in self-compacting concrete**

Oskar Esping and Ingemar Löfgren

Dep. of Civil and Environmental Engineering, Chalmers University of Technology, Sweden.

### **Abstract**

Autogenous deformations and early age shrinkage due to evaporation ('plastic shrinkage') are two main driving forces for early age cracking. In this work, autogenous deformation at early ages (< 24 h) was accurately measured by linear displacements using a specially developed digital dilatometer. The method and equipment is described and a number of different mix compositions have been investigated: e.g. w/c-ratio from 0.38 to 0.67, coarse aggregate content, silica fume, fly ash and the effect of different admixtures (accelerator, retarder, shrinkage reducer, superplasticizer dosage). The significant influence of different mix parameters on the autogenous deformation is clearly demonstrated. In addition, in some specimens, the capillary pore pressure and temperature have been measured and the relationship between autogenous deformation is discussed.

### **1. Introduction**

As the use of high-performance and self-compacting concrete has increased, early age shrinkage and cracking have become a cause of great concern. Conditions as reduced maximum aggregate size, increased amount of fines, presence of retarding admixtures, increased binder content and deficient covering and curing all contribute to this problem. Early age cracking due to evaporation (often referred to as 'plastic shrinkage cracking') occurs when the concrete is in its 'plastic stage'. In traditional concretes it is mainly caused by the loss of water from the fresh concrete, e.g. by evaporation of water from the surface or by suction of water by the formwork material or by the sub-base. The loss of water from the paste generates negative capillary pressures, this cause the paste to contract (see Wittman [1]), which, in turn, can lead to cracks. To avoid this type of cracks, care has to be taken to protect the surface against drying. However, experience with the use of low w/b concretes have revealed that severe cracking may occur in spite of proper protection (curing membrane, plastic sheets, etc). Furthermore, self-compacting concrete seems to be especially susceptible to early-age cracking since there is no segregation and bleed water on the surface. However, there are also other internal effects that could be contributing. These include: retardation due to admixtures, suction of water by the fine material (e.g. lime filler) and the increased chemical shrinkage and autogenous deformation in the early age when the concrete is setting and starting to harden. As

the cracking tendency in the initial phase is a product of several factors, it is important to separate the mechanisms into those that are dependent on environmental conditions (e.g. evaporation of water from the surface) and those that occur without moisture transfer to the environment and which are associated with the autogenous deformation of the material. The former may be controlled by an appropriate curing while the latter has to be tackled by proper mix design.

In an ongoing study, initiated by AB Färdig Betong and financed by SBUF, the cracking tendency of self-compacting concrete has been investigated by means of the NORDTEST method "Concrete: Cracking tendency – Exposure to drying during the first 24 hours " NT BUILD 433. In addition, the autogenous deformation has been measured in a specially developed concrete digital dilatometer and the capillary pore pressure has been measured. In this study a number of different mix compositions have been investigated (e.g. w/c-ratio from 0.38 to 0.67, coarse aggregate content, silica fume, fly ash) and the effect of different admixtures (accelerator, retarder, shrinkage reducer, superplasticizer dosage) have been studied. This paper mainly deals with the autogenous deformations, for more information on the study see [2]. In the present investigation only deformation taking place in a sealed specimen at constant ambient temperature is considered and will be termed autogenous deformation. Moreover, in this study early age is considered as the time from mixing up to 24 hours after mixing.

## 2. Background

The hydration of Portland cement is a complex sequence of overlapping chemical reactions between clinker components, calcium sulphate, and water, leading to setting and hardening. Immediately after mixing cement and water reactions starts to occur and which generates an outburst of heat (Stages 0 and I in Figure 1). After these initial stages an induction period, or dormant period, is entered (Stage II). During the induction period not much hydration takes place, but this does not mean that the paste is 'dormant' with respect to volume changes. Setting (Stage III) is defined as the onset of rigidity in fresh concrete and the period of fluidity, preceding setting, corresponds to the induction period (Stage II), see *Figure 1(a)*. The setting process is the consequence of a change from a concentrated suspension of flocculated particles to a viscoelastic skeletal solid capable of supporting an applied stress. As long as the concrete is fluid there will be a linear relationship between the linear shrinkage and the volumetric chemical shrinkage. However, once the self-supporting skeleton starts to form the chemical shrinkage will mainly result in internal voids and the linear deformation diverges from the chemical shrinkage and it has been suggested (e.g. by Barcelo [3]) that when measuring the linear deformation the setting will be manifested as a change of the slope of the deformation, see *Figure 1(b)*. Furthermore, once the internal voids are created it leads to the development of a capillary underpressure in the skeletal structure, see *Figure 1(b)*, which leads to an external deformation of the hardening concrete. It can be argued that the deformation occurring when the concrete is plastic may have little consequence for the risk of cracking while the shrinkage taking place when the concrete is semiplastic is considerably more detrimental as the concrete at this stage has poorly developed mechanical properties (low tensile strength and strain capacity).

### 3. Experimental program

#### 3.1 Materials and mix design

The mix design and its constituents, used in this study, comprises of typical materials and compositions for self-compacting concrete (SCC) in Sweden. The properties of the dry materials and admixtures are listed in *Table 1*, *Figure 1* and *Table 2*. The concretes were prepared in batches of 40 liters, mixed in a BHS-60 twin-shaft paddle mixer for 4 minutes after water was added to the premixed dry materials. The admixtures were added directly after the water.

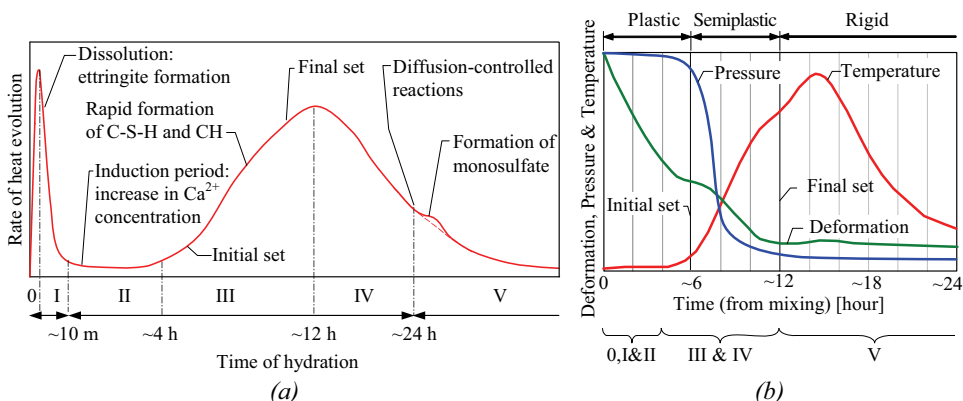


Figure 1. (a) Schematic representation of heat evolution during hydration of cement (based on [4]) and (b) Schematic representation of the early age linear autogenous deformation of concrete and the corresponding development of temperature and capillary pore pressure (from [2]).

Table 1. Properties of dry materials (cement, pozzolans, filler and aggregate).

ID	Product name	Supplier	Type	Density [kg/dm <sup>3</sup> ]	Area by BET [m <sup>2</sup> /kg]
C	Byggcement Std PK Skövde	Cementa	CEM II/A-LL 42.5R	3 080	2 000 (N <sub>2</sub> )
SF	Microsilica	ELKEM	Silica fume	2 250	~20 000 (N <sub>2</sub> ) 21 440 (H <sub>2</sub> O)
FA	EFA-Füller BF 1	BauMineral	Fly ash - type 2	2 270	~3 000 (N <sub>2</sub> ) 3 230 (H <sub>2</sub> O)
F	Limus 40	NordKalk	Grounded limestone	2 670	1 400 (N <sub>2</sub> ) 1 410 (H <sub>2</sub> O)
A 0-4	Sjögärde	Färdig Betong	Natural	2 670	3 010 (H <sub>2</sub> O)
A 0-8	Hol	Färdig Betong	Natural	2 650	1 750 (H <sub>2</sub> O)
A 8-16	Kungälv	Färdig Betong	Crushed	2 700	90 (H <sub>2</sub> O)

The mixes were designed to have a water to filler ratio by volume of one,  $w/f=1.0$  [5], where all solid material smaller than 0.125 mm was included as filler.

In order to evaluate the effect of constituent type and dosage, following SCC mixes were made:

1. Reference concretes; w/c 0.38, 0.45, 0.55 and 0.67 (see Table 3 and Figure 3)
2. Coarse aggregate content; w/c 0.55 with 20%, 30%, 40% (REF) and 50% A 8-16 of total volume of aggregate. The changes were replaced by equal volume of A 0-8.
3. Water content; 6 and 12 liters extra water (W) was added to w/c 0.67. The extra water corresponds to approximately 0.5% and 1.0% incorrect gravel moisture content. The changes were replaced by equal volume aggregate.
4. Fly ash; 25% FA by cement weight was added to w/c 0.45, 0.55 and 0.67. The FA reduced the C content with an efficiency factor of 0.4, so the water to binder ratio (w/b) was equal to w/c in the reference. The surplus of the FA was adjusted by reduced F content.
5. Silica fume; 5% and 10% SF by cement weight was added to w/c 0.55. The C was reduced by the corresponding addition of SF volume. No efficiency factor was used (w/b of 0.58 and 0.61 with a factor of 2.0)
6. Superplasticizer dosage; w/c 0.67 with 0.6%, 0.8% (REF) and 1.0% SP dosage of C weight.
7. Accelerator and retarder; 1.5% ACC and 0.2% RE by C weight was added to w/c 0.67.
8. Shrinkage reducing admixture; 1.0% and 2.0% SRA by C weight was added to w/c 0.45, 0.55 and 0.67.

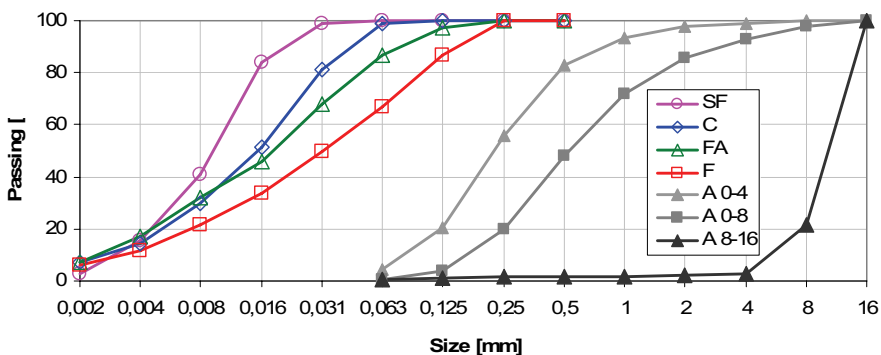


Figure 2. Dry materials size distribution.

### 3.2 Test methods

There is no standardized method of measuring early age deformation as there is for long term shrinkage, which could be explained by the difficulty in making accurate measurements of a sealed concrete prior to setting, as the readings must be started immediately after casting without disturbing the concrete mould.



In this study, autogenous linear deformation was monitored by a new test method, the concrete digital dilatometer (CDD), developed in order to start measure before setting when concrete is fresh, as well as for the hardening concrete. The method is a modification of the CT1 digital dilatometer for pastes and mortars [6]. The CDD sample consists a concrete specimen, cast in a steel coil reinforced 0.4 mm thick vapour proof flexible polyurethane (PU) tube with inner diameter of 82 mm and specimen length ~400 mm, sealed with a pair of hose clamps and 30 mm thick PVC end-caps equipped with O-ring sealing. The mould was placed in a mechanical stable measuring rig, where the unrestrained, time-depending, linear bulk deformation was recorded by a digital gauge (543-450B from Mitutoyo with an accuracy of 0.003 mm and resolution 0.001 mm) and logged every 5 minute using a data transducer (DMX8/2 from Mitutoyo). In order to reduce the friction between the sample and rig, and two layers of teflon coated paper was applied. The test was performed in a thermo stable room at 20°C, where the measurement recording was started at 30 minutes from water addition, and stopped after 72 hours. Main equipment and apparatus for a typical test was tree complete CDD set-up, consisting of PU-tube, end-caps, fixture, hose-clamps, measuring rig and digital gauge as shown in Figure 4. One of the specimens was, in some cases, equipped with sensors for recording the concrete temperature development.

Table 2. Properties of admixtures.

ID	Product name	Supplier	Type	Density [kg/dm <sup>3</sup> ]	Dry content [weight%]
SP	Sikament 56	SIKA	Superplastisizer (polycarboxylate ether based)	1 100	37%
ACC	SikaRapid-1	SIKA	Accelerator (sodium based)	1 200	37%
RE	SikaRetarder	SIKA	Retarder (polyalkyl ether based)	1 200	27%
SRA	SikaControl-40	SIKA	Shrinkage reducing admixture (polymeric glycol based)	1 000	-

Table 3. Recipe of reference mixes.

	w/c 0.38	w/c 0.45	w/c 0.55	w/c 0.67
Id	m <sub>drv</sub> [kg/m <sup>3</sup> ]	m <sub>drv</sub> [kg/m <sup>3</sup> ]	m <sub>drv</sub> [kg/m <sup>3</sup> ]	m <sub>drv</sub> [kg/m <sup>3</sup> ]
C	420	380	340	300
W	160	171	187	200
A 0-4	0	0	81	155
A 0-8	1021	998	879	771
A 8-16	694	678	651	628
F	40	100	160	220
SP	7.6 (1.8%C)	5.7 (1.5%C)	4.1 (1.2%C)	2.4 (0.8%C)

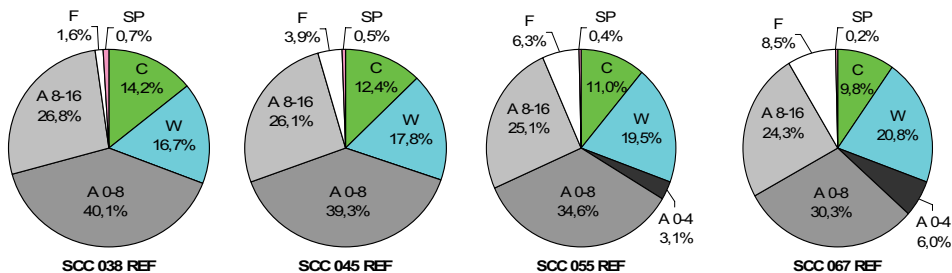


Figure 3. Reference mixes constituents distribution by volume.

Complimentary tests were also performed, on a few series of sealed specimens, where the evolution of temperature and capillary pore pressure was measured. The temperature was measured with thermo tread, type k, and the pore pressure was measured with a pressure transducers (Model AB 0-15 PSIG from Data Instruments – range 0-100 kPa, overload pressure 200 kPa), connected to de-aired water filled system with a 50 mm long needle with an external/internal diameter of 0.7/0.4 mm. The test was performed according to a procedure developed by Radocea [7]. The data was logged every minute using a data logger (PC-logger3100i from INTAB). For further description of the test equipments and procedures, see [2].

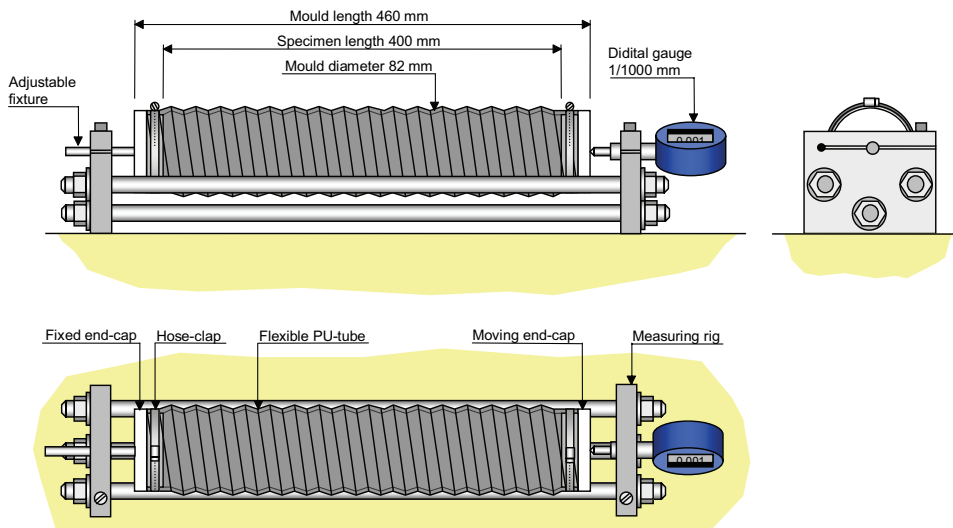
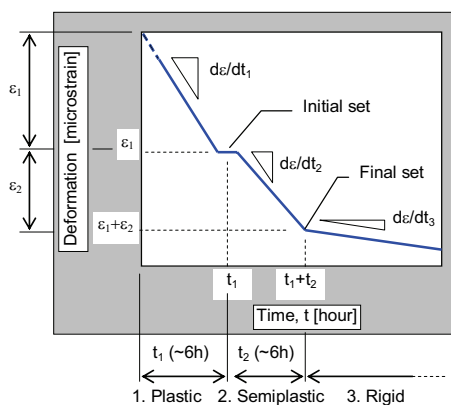


Figure 4. Test arrangement of the Concrete Digital Dilatometer (CDD) for linear autogenous deformation measurement.

### 3.3 Data presentation and interpretation

The results from the measures of linear autogenous deformation by the CDD is presented both graphically and as a number of deformation factors, evaluated by a model presented in *Figure 5*. The pattern of deformation comprises three stages which are rheologically defined as: 1. *Plastic*, 2. *Semiplastic* and 3. *Rigid* period. In the *plastic* and *semiplastic* period the rate of deformation ( $d\epsilon/dt_1$  and  $d\epsilon/dt_2$ ), period time ( $t_1$  and  $t_2$ ) and deformation ( $\epsilon_1$  and  $\epsilon_2$ ) is evaluated from the deformation/time graph. In the *rigid* period (3) the rate of deformation ( $d\epsilon/dt_3$ ) is evaluated between 48 to 72 hours from water addition. The transition from *plastic* to *semiplastic* ( $t_1$ ), corresponding to the initial set, takes place  $\sim 6$  hours after water addition. The transition to *rigid* period ( $t_1 + t_2$ ), corresponding to the final set, takes place at  $\sim 12$  hours. Compared to traditional vibrated concrete without addition of superplasticizer, the self-compacting concrete (SCC) tends to be retarded for about one hour. The time ( $t$ ) is relating to the point where the mixing water was added to the premixed solid material (including the cement). As the measures starts after 30 minutes, the curve is extrapolated to the time zero. From the test results, initial setting was defined as the point when the initial slope of the deformation changed, see e.g. Barcelo [3], and final setting was defined as the point when the deformation levelled out, occurs slightly ahead of the temperature peak. No other method was used to determine the setting.



$\epsilon_1$ :	Plastic deformation (to initial set) [μstrain]
$\epsilon_2$ :	Semiplastic deformation (from initial to final set) [μstrain]
$t_1$ :	Plastic time (to initial set) [h]
$t_2$ :	Semiplastic time (from initial to final set) [h]
$d\epsilon/dt_1$ :	Plastic rate of deformation (to initial set) [μstrain/h]
$d\epsilon/dt_2$ :	Semiplastic rate of deformation (between initial and final set) [μstrain/h]
$d\epsilon/dt_3$ :	Rigid rate of deformation (after final set, <72h) [μstrain/h]

Figure 5. Model of how the deformation parameters are defined and evaluated from the linear autogenous deformation measurements, where the deformation is divided into plastic/semiplastic/rigid period.

It ought to be pointed out that:

- ❑ Linear measurements of autogenous deformation on a concrete mix before setting are very sensitive and associated with a large scatter.
- ❑ The setting is a gradual change, without distinct transition from plastic to semiplastic to rigid state.

- ❑ It is not fully correct to define the fresh concrete deformation as linear, since the length cannot be defined for a fluid system. Start of the linear measurement should coincide with setting, but exact determination of the plastic to rigid transition is difficult and subjective.
- ❑ As the coefficient of thermal expansion changes considerable during the hydration no attempts have been made to adjust the measured deformations.
- ❑ Due to greater stiffness in the radial than in the longitudinal direction of the mould, when the concrete is in the fluid state, the flexible mould transforms some of the volumetric deformation into a linear deformation. As the concrete undergo transition from a fluid to a rigid state, the deformation becomes isotropic. The ratio between linear and volumetric deformation is shown in *Figure 6*.

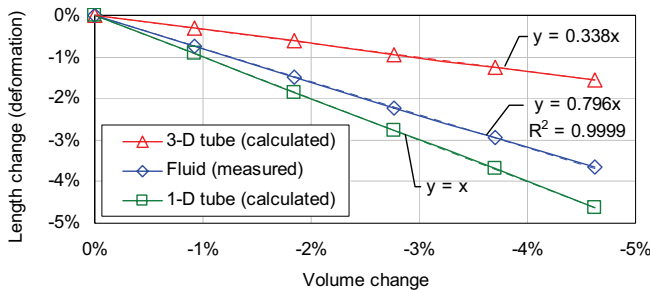


Figure 6. The ratio between linear and volumetric deformation for the mould (ø82 mm / L400 mm). When filled with a Newtonian fluid the ratio follows the measured ratio, but as rigid isotropic the ratio will follow the calculated 3-D deformation. With an infinite radial stiffness the ratio would follow 1-D length change.

#### 4. Results and discussion

The results of the autogenous deformation measurements for the reference concretes are presented in *Figure 7*. In *Figure 8* the evaluated deformation factors ( $\varepsilon$ ,  $d\varepsilon/dt$  and  $t$ ), for each period (1 to 3), are presented. The results tendency is expected and significant, and shows that:

- ❑ Increased cement content (lower w/c) increases both the total chemical shrinkage and the rate of it and thereby the total autogenous deformation ( $\varepsilon_1$ ,  $\varepsilon_2$ ,  $d\varepsilon/dt_1$ ,  $d\varepsilon/dt_2$  and  $d\varepsilon/dt_3$ ).
- ❑ Increased cement content (lower w/c) increased the autogenous deformation and the rate of it in the semiplastic period (between initial and final set,  $\varepsilon_2$  and  $d\varepsilon/dt_2$ ).
- ❑ Increased superplasticizer addition had a delaying and retarding effect on the hydration and thereby extends all the times for the periods ( $t_1$  and  $t_2$ ).

The results of the autogenous deformation measurements for the concrete with varying coarse aggregate content is presented in *Figure 9(a)*. It should be noted that the content of coarse aggregate had a large impact on the rheology, which can be deduced from the aggregate packing. An improved packing governs the flowability as more water is made available for dispersing the particles. The results indicate that:

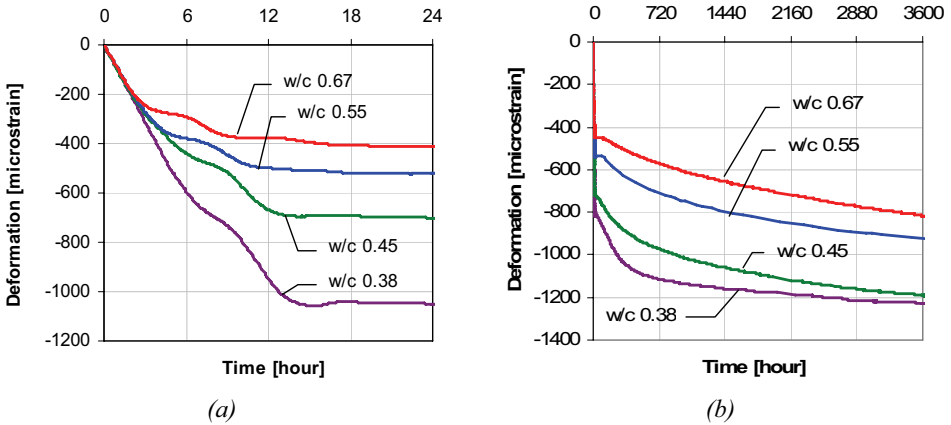


Figure 7. Autogenous deformation of self-compacting concrete with w/c from 0.38 to 0.67: (a) early age deformation (up to 24 hours); and (b) long term deformation (up to 150 days).

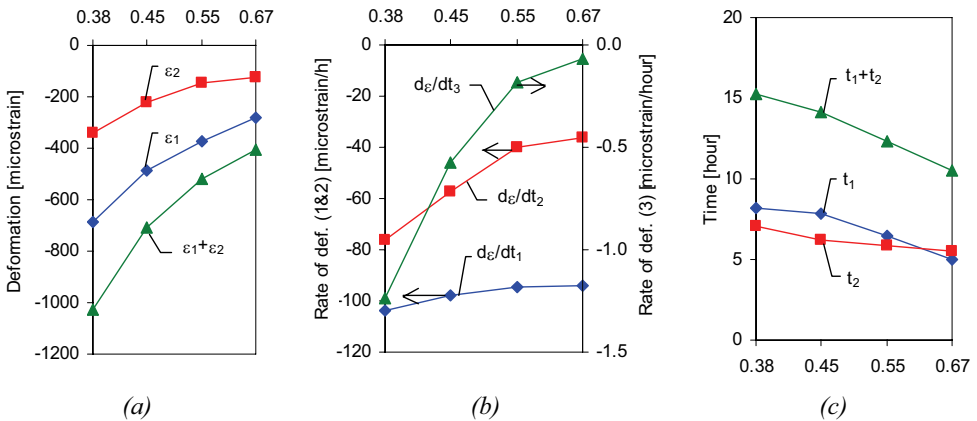


Figure 8. Autogenous deformation factors by w/c at the plastic (1), Semiplastic (2) and rigid (3) period. In (a) the total deformation for each period is presented, in (b) the rate of deformation is presented, and in (c) the times for the periods.

- ❑ Increased coarse aggregate content decreased both the magnitude and rate of autogenous deformation ( $\epsilon_1$ ,  $\epsilon_2$ ,  $d\epsilon/dt_1$ ,  $d\epsilon/dt_2$  and  $d\epsilon/dt_3$ ). The effect was more apparent at higher content of coarse aggregate, which might be explained by the coarser particles ability to create a restraining matrix.
- ❑ As the packing improves, water is made available and parallels can be made to increased water content, in Figure 9(b), where more water decreases the magnitude and rate of autogenous deformation.

- No significant changes in times ( $t_1$  and  $t_2$ ) could be observed, but an increased content of coarse aggregate tended to delay the rigid (3) period.

To investigate the effect of changes in water content, 6 and 12 liter extra water was added to the reference mix with w/c 0.67. The extra water can be viewed as a simulation of incorrect gravel moisture content by 0.5% respective 1.0%. The results of the autogenous deformation measurements are presented in *Figure 9(b)*. The tendency is significant and indicates that:

- Increased water content decreased both the magnitude and rate of autogenous deformation ( $\varepsilon_1$ ,  $\varepsilon_2$ ,  $d\varepsilon/dt_1$ ,  $d\varepsilon/dt_2$  and  $d\varepsilon/dt_3$ ), which can be explained by better dispersed fine particles and increased interparticle distances (decreases the interparticle forces). At w/c 0.67 the larger surplus of water will probably have small or no effect on the cement hydration.
- No large significant changes in times ( $t_1$  and  $t_2$ ) could be observed, but an increased water content tends to delay the rigid (3) period.

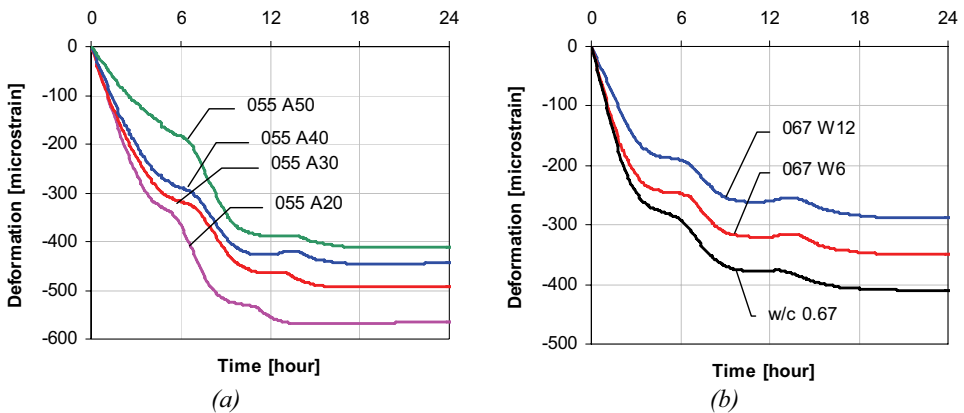


Figure 9. Autogenous deformation: (a) effect of coarse aggregate content (from 20% to 50% of total aggregate content) for concrete with w/c 0.55; and (b) effect of additional water (6 and 12 litres) for concrete with w/c 0.67.

The results of the autogenous deformation measurements for the concretes with fly ash (FA) are presented in *Figure 10(a)*. With this type of specific chemical composition and physical properties of the cement and FA, the results show the common tendency:

- The addition of FA caused the concrete to swell drastically in the *plastic* period. In the *semiplastic* period the deformation ( $\varepsilon_2$  and  $d\varepsilon/dt_2$ ) were similar to those without FA. The effect of FA at the *rigid* period is not clear, but at high w/c the FA seemed to have a reducing effect of the rate of deformation ( $d\varepsilon/dt_3$ ), and at low w/c the opposite was observed.
- The early swelling increased with lower w/c. This can be explained by that the dosage of FA is based on the cement content, the FA addition increases with decreased w/c (86, 77 and 68 kg FA for w/c 0.45, 0.55 and 0.67).
- A small incensement of times ( $t_1$  and  $t_2$ ), when FA addition, could be observed. The lower w/c the higher effect was observed. It is well known that a concrete with FA addition

tends to be retarded at early stages (“dormant” period), especially at low w/c (see e.g. Langana et al. [8]).

The behavior with high expansion (swelling) at early ages may, possibly, be explained by a larger and faster rate of ettringite formation, see Ravina [9] and Hanehara & Yamada [10]. In addition to those from the cement, sulfates may also originate from the fly ash; where sulfates (alkali, and perhaps also calcium) have been found to be deposited on the surface of the fly ash particles and on those of unburned carbon (which have a high internal surface), from the vapor phase in the boiler, as the particles cool. The sulfates are fully soluble and, being freely available to the mix water in their deposited state, augment both the alkalies and sulfate brought into solution from the cement. However, the sulfate content of the fly ash was not measured

The results of the autogenous deformation measurements for the concretes with silica fume are presented in *Figure 10(b)*. The tendency is significant and indicates that:

- ❑ Addition of silica fume increased the magnitude and rate of autogenous shrinkage in all periods ( $\varepsilon_1$ ,  $\varepsilon_2$ ,  $d\varepsilon/dt_1$ ,  $d\varepsilon/dt_2$  and  $d\varepsilon/dt_3$ ), and the effect increased with the silica dosage.
- ❑ Addition of silica fume increased the autogenous deformation and the rate of it in the semiplastic period (between initial and final set,  $\varepsilon_2$  and  $d\varepsilon/dt_2$ ).
- ❑ Silica fume decreased the *plastic* time period ( $t_1$ ), and the effect increased with the silica dosage. No changes in *semiplastic* time ( $t_2$ ) could be observed.

It is well known that silica fume increases the autogenous shrinkage (see [11]), as well as it accelerate the early hydration and initiate the stiffness at earlier age. That silica accelerates the early hydration for concrete with w/c higher than 0.5 was also found by Langana et al. [8].

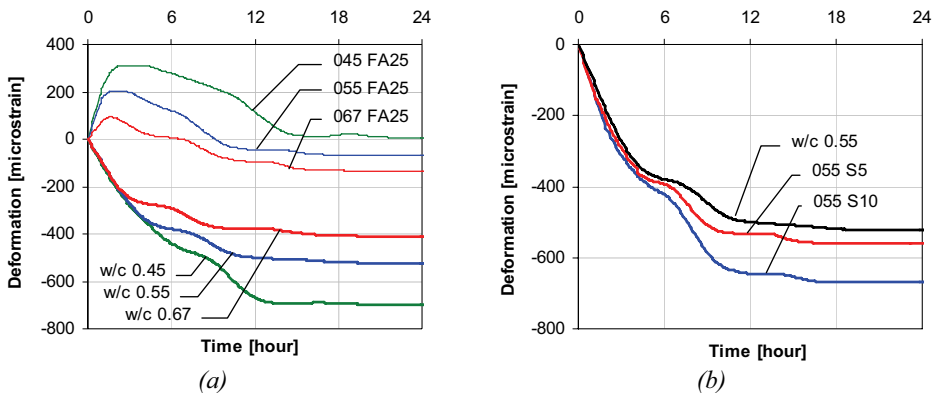


Figure 10. Autogenous deformation: (a) effect of fly ash (25%) on concrete with w/c 0.45, 0.55, and 0.67; and (b) effect of silica on concrete with w/c 0.55 (5% and 10% silica).

The results of the autogenous deformation measurements for the concrete with varying superplasticizer dosage (SP) are presented in *Figure 11(a)*. The results tendency is significant and indicates that:

- ❑ SP dosage increased the magnitude of autogenous shrinkage ( $\epsilon_1$  and  $\epsilon_2$ ).
- ❑ SP dosage increased the rate of shrinkage at the *plastic* and *semitplastic* period ( $d\epsilon/dt_1$  and  $d\epsilon/dt_2$ ). After setting, the effect was the opposite, where the rate of shrinkage ( $d\epsilon/dt_3$ ) decreased with SP dosage.
- ❑ SP dosage increased the *plastic* time period ( $t_1$ ). No changes in *semitplastic* time ( $t_2$ ) could be observed.

It is well known that SP retards the concrete, as it delays the early hydration and initiates the stiffness at higher age. The results clearly verify these phenomena. It has also been suggested that improved cement dispersion may lead to increased shrinkage, see e.g. [12]. For a well-dispersed cement system the average pore-radius should be smaller than for a system with cement particles agglomerating. A possible mechanism may be that improved dispersion leads to smaller pore radiuses as compared to a cement system where particle agglomeration occurs.

The results of the autogenous deformation measurements for the concrete with accelerator (ACC) and retarder (RE) are presented in Figure 11(b). The results tendency is significant and indicates that:

- ❑ In the *plastic* period (before initial setting), ACC increased the magnitude and rate of shrinkage ( $\epsilon_1$  and  $d\epsilon/dt_1$ ), and RE had the opposite effect, which could be expected.
- ❑ In the *semitplastic* period, ACC and RE showed no significant effect of magnitude and rate of shrinkage ( $\epsilon_2$  and  $d\epsilon/dt_2$ ).
- ❑ In the rigid period, both ACC and RE increased the rate of shrinkage ( $d\epsilon/dt_3$ ).
- ❑ ACC and RE showed no significant effect on the time of the periods ( $t_1$  and  $t_2$ ), but RE tended to delay the time to initial setting ( $t_I$ ).

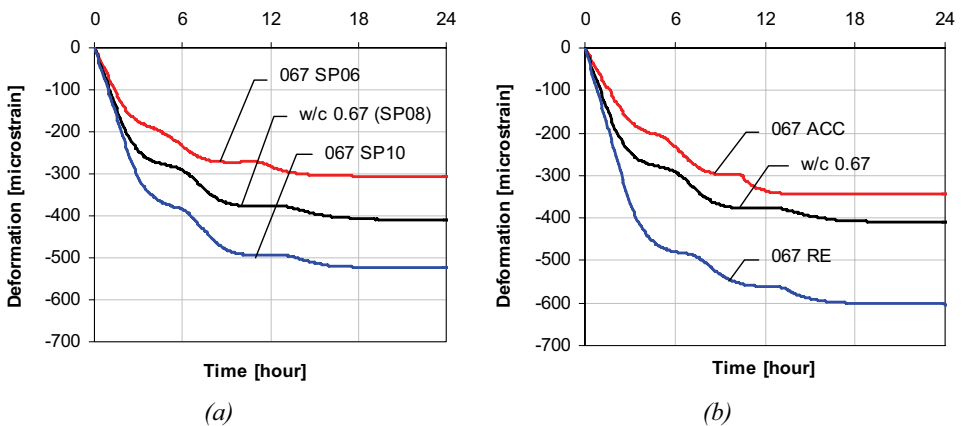


Figure 11. Autogenous deformation of concrete with w/c 0.67: (a) effect of superplasticizer dosage (SP) 0.6%, 0.8%, and 1.0%; and (b) effect of accelerator (ACC) and retarder (RE).

According to the supplier (SIKA) will RE have a small delaying effect at early hydration (to initial setting), and ACC will have no effect in the same time of period. The results in this study showed the same tendency.



The results of the autogenous deformation measurements for the concrete with shrinkage reducing admixture (SRA) are presented in *Figure 12*, and the evaluated deformation factors ( $\varepsilon$ ,  $d\varepsilon/dt$  and  $t$ ), for each period (1 to 3), are presented in *Figure 13*. The results tendency is significant and indicates that:

- Addition of SRA decreased the magnitude and rate of autogenous shrinkage for all concretes ( $\varepsilon_1$ ,  $\varepsilon_2$ ,  $d\varepsilon/dt_1$ ,  $d\varepsilon/dt_2$  and  $d\varepsilon/dt_3$ ), and the effect increased with increased SRA dosage.
- In the *semiplastic* period the effect of SRA was not as pronounced as in the *plastic* and *rigid* period.
- SRA showed no effect on the times of the periods ( $t_1$  and  $t_2$ ).

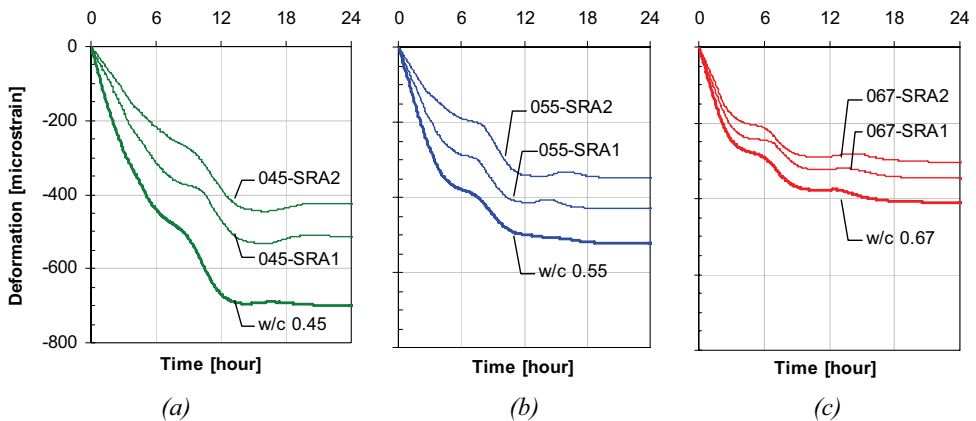


Figure 12. Effect of shrinkage reducing admixture (SRA) 1% and 2% on autogenous deformation: (a) for concrete with w/c 0.45; (b) for concrete with w/c 0.55; and (c) for concrete with w/c 0.67.

The results for the complementary measurements - where temperature, capillary pore pressure, and autogenous deformation were measured - can be seen in *Figure 14*. The relationship between the change in capillary pore pressure, deformation, and temperature (the initial temperature rise was a result of the concrete having a lower temperature than the climate room) can be seen in *Figure 14*, where the measurement results from two of the reference concretes are presented (w/c 0.45 and 0.67). As can be seen, as long as the concrete is plastic the deformation develops with almost a linear relationship and, during this period, the temperature and capillary pore pressure undergoes only small changes, which are linear. However, at one stage (at about five hours for w/c=0.67 and seven hours for w/c=0.45) the rate of the deformation is slowed down, indicating 'setting' of the concrete, and a knee point is reached. At this point in time, it can be seen that both the capillary pore pressure and the temperature reach an accelerating phase, which indicates that the dormant period is ended and that the cement hydration accelerates. Final set is reached at about 10 hours for w/c=0.67 and 13 hours for w/c=0.45, which for the deformation is manifested in a plateau slightly a head of the temperature peak.

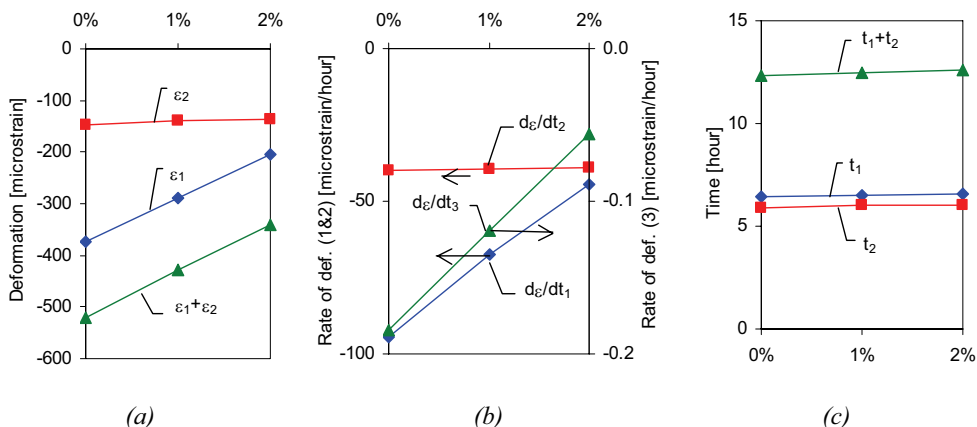


Figure 13. Autogenous deformation factors for w/c 0.55 with addition of 1% and 2% shrinkage reducing admixture (SRA). In (a) the total deformation for each period is presented, in (b) the rate of deformation is presented, and in (c) the times for the periods. The tendency for w/c 0.45 and 0.67 was similar.

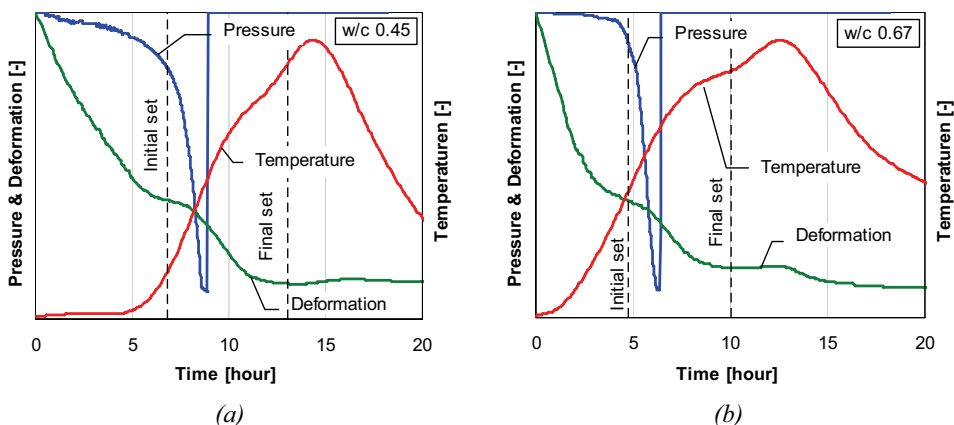


Figure 14. Comparison of development of temperature, capillary pore pressure, and the autogenous deformation (the axes have been normalized against maximum values): (a) for concrete with w/c 0.45; and (b) for concrete with w/c 0.67.

## 5. Conclusions

An experimental investigation of early age deformation and cracking tendency was made on a number of self-compacting concretes, with w/c-ratio between 0.38 and 0.67, and the influence of various mix parameters was investigated. Autogenous deformations were measured and in some specimens temperature and pore pressure was measured. When combining the measurements of linear autogenous deformation, capillary pore pressure, and temperature (see

Figure 14) it could be seen that as long as the concrete is plastic the deformation develops with almost a linear relationship and, during this period, the temperature and capillary pore pressure undergoes only small changes, which are linear. However, at one stage the rate of the deformation is slowed down, indicating 'setting' of the concrete, and a knee point is reached. At this point in time, it can be seen that both the capillary pore pressure and the temperature reach an accelerating phase, which indicates that the dormant period is ended and that the cement hydration accelerates. Final set is reached at about 10 to 13 hours (depending on the mix composition), which for the deformation is manifested in a plateau slightly ahead of the temperature peak.

The results from the measurements of linear autogenous deformation by the CDD show that:

- ❑ Increased cement content (lower w/c) increases the rate of and total chemical shrinkage and thereby the autogenous deformation.
- ❑ Increased coarse aggregate content decreased the magnitude and rate of autogenous deformation. The effect was more apparent at higher content of coarse aggregate, which might be explained by the coarser particles ability to create a restraining matrix. As the packing of the concrete was improved, water was "released" to the mix and parallels can be made to increased water content where more water decreases the magnitude and rate of autogenous deformation.
- ❑ Increased water content decreased the magnitude and rate of autogenous deformation, which can be explained by better dispersed fine particles and increased interparticle distances (decreases the interparticle forces). At w/c 0.67 the larger surplus of water probably had only a small or no effect on the cement hydration. No large significant changes in times could be observed, but an increased water content tends to delay the rigid period.
- ❑ The addition of FA caused the concrete to swell drastically in the plastic period. In the semiplastic period the deformation were similar to those without FA. The effect of FA in the rigid period is not clear, but at high w/c the FA seemed to have a reducing effect of the rate of deformation, and at low w/c the opposite was observed. The early swelling increased with lower w/c, which can be explained by that the dosage of FA is based on the cement content, the FA addition increases with decreased w/c. Moreover, it is well known that a concrete with FA addition tends to be retarded at early stages ("dormant" period), especially at low w/c.
- ❑ Addition of silica fume increased the magnitude and rate of autogenous shrinkage in all periods, and the effect increased with increased silica dosage. Silica fume decreased the plastic time period, and the effect increased with increased silica dosage. No changes in semiplastic time could be observed.
- ❑ Increased SP dosage increased the magnitude of autogenous shrinkage, which can be explained by the better cement dispersion. SP dosage increased the rate of shrinkage at the plastic and semiplastic period. After setting, the effect was the opposite, where the rate of shrinkage decreased with SP dosage.
- ❑ In the plastic period (before initial setting), accelerator (ACC) increased the magnitude and rate of shrinkage, and retarder (RE) had the opposite effect, which could be expected. In the semiplastic period, ACC and RE showed no significant effect of

magnitude and rate of shrinkage. ACC and RE showed no significant effect on the time of the periods, but RE tended to delay the time to initial setting.

- Addition of shrinkage reducing admixture (SRA) decreased the magnitude and rate of autogenous shrinkage for all concretes, and the effect increased with increased SRA dosage. In the semiplastic period the effect of SRA was not as pronounced as in the plastic and rigid period. SRA showed no effect on the times of the periods.

## References

1. Wittmann, F.H.: On the Action of Capillary Pressure in Fresh Concrete, Cement and Concrete Research, Vol. 6 (1976), pp. 49–56.
2. Esping, O. and Löfgren, I.: Cracking due to plastic and autogenous shrinkage - Investigation of early age deformation of self-compacting concrete. Publication No. 2005:11, Dep. of Civil and Environmental Engineering, Chalmers University of Technology, 2005.
3. Barcelo, L., Moranville, M., and Clavaud, B.: Autogenous shrinkage of concrete: a balance between autogenous swelling and self-desiccation, Cement and Concrete Research, Vol. 35 (2005), pp. 177–183.
4. Gartner, E.M., Young, J.F., Damidot, D.A., and Jawed, I.: Hydration of portland cement. Chapter three in Structure and performance of cements (ed. Bensted and Barnes) Spoon Press, London, (2002).
5. Okamura H.: Self-compacting high-performance concrete, Concrete International, vol 19 (7) (1997), pp 50-54.
6. Jensen O.M., Hansen F.: A dilatometer for measuring autogenous deformation in hardening Portland cement paste, Mat. and Structures, Vol 28 (181) (1995), pp. 406-409.
7. Radocea, A.: A Study on the Mechanisms of Plastic Shrinkage of Cement-Based Materials, doctoral dissertation, CTH Göteborg, Sweden, 1992, 125 pp.
8. Langan, B.W., Wengb, K., and Ward, M.A.: Effect of silica fume and fly ash on heat of hydration of Portland cement, Cement and Concrete Research, Vol. 32 (2002), pp. 1045–1051.
9. Ravina D.: Early longitudinal dimensional change of fly ash mortar exposed to drying conditions, Cement and Concrete Research, Vol 16 (1986), pp 902-910.
10. Hanehara, S. and Yamada, K.: Interaction between cement and chemical admixture from the point of cement hydration, absorption behaviour of admixture, and paste rheology, Cement and Concrete Research 29(1999), pp. 1159–1165.
11. Neville, A.M.: Properties of Concrete, fourth edition. Pearson Education Limited (2000).
12. Holt, E.E.: Early age autogenous shrinkage of concrete. Technical Research Centre of Finland, VTT Publication 446 (2001), Espoo, 184 p.

## Measuring Techniques for Autogenous Strain of Cement Paste

Pietro Lura and Ole Mejlhede Jensen  
Technical University of Denmark, Denmark

### Abstract

Volumetric measurement of autogenous strain is frequently performed by placing the fresh cement paste in a rubber membrane submerged in water. The volume change of the cement paste is measured by the amount of water displaced by the submerged sample. Volumetric and linear measurements of autogenous strain should in principle give identical results. However, the measuring results from the volumetric method are typically 3-5 times higher than the results from the linear technique. In this paper, water uptake from the buoyancy bath through the rubber membrane is identified as the principal artefact of the volumetric method. Water absorption is driven by a lowering of the water activity in the cement paste due to dissolved salts in the pore fluid and to self-desiccation. From the moment of casting, significant water uptake was registered in all experiments. This water uptake influenced the volumetric measurements by the same order of magnitude as the autogenous strain itself. By performing the measurements in a paraffin oil bath instead of a water bath, this artefact was eliminated. Furthermore, volumetric measurements performed in paraffin oil gave almost identical results as linear measurements performed on the same cement pastes.

### 1. Introduction

Measurements of autogenous strain of cement paste have been carried out in two fundamentally different ways: measurement of volumetric strain and measurement of linear strain. Volumetric measurement of autogenous strain is frequently performed by placing the fresh cement paste in a rubber membrane submerged in water. The change in volume of the cement paste is measured by the amount of water displaced; for example, by measuring the weight change of the submerged sample [1, 2] or the water level in a capillary tube [3, 4]. Linear measurement of autogenous strain is frequently performed by placing the cement paste in a rigid mould with low friction. The length change of the cement paste may be recorded by a displacement transducer at the end of the specimen [5].

Both experimental methods have been extensively used in parallel for more than 50 years [6, 7]. The two methods should in principle give identical results; however, the volumetric method

typically indicates 3-5 times higher strain than the linear technique [4]. Surprisingly few researchers have tried to find the reason for this disagreement [4, 8-10].

One fundamental reason for the inconsistency between volumetric and linear autogenous strain measurements after setting is transport of water through the rubber membrane, occurring when the buoyancy liquid used is water [11]. After setting, penetrated water may partially fill the internal voids produced by chemical shrinkage, causing an increase of the submerged weight or a decrease in water level that is interpreted as volumetric shrinkage. Concurrently, water penetration mitigates the shrinkage of the sample.

Rubber membranes normally used in the volumetric method are not waterproof. For example, condoms filled with water and exposed to air at low relative humidity lost about 0.5% of their water content per day [10, 12]. Despite this, some authors [10, 13] state that the influence of the permeability of the membrane on the volumetric measurements is insignificant until marked self-desiccation occurs in the cement paste, a few days after casting. Self-desiccation would then cause a relative-humidity gradient across the membrane and drive water from the water bath into the sample.

However, significant water transport through the condom does not start after some days, but instead occurs right after casting [11]. A difference in water activity across the membrane exists from the very start of the measurements, due to dissolved salts in the pore fluid. This difference in water activity constitutes a driving force for osmosis of water through the membrane into the paste. To examine this effect, Marciniak [12] measured the water uptake of condoms filled with synthetic pore solution, submerged in a distilled water bath. The weight of the condoms filled with pore solution increased by 0.1% per day, while condoms filled with distilled water did not show any appreciable weight change. Similarly, Beltzung and Wittmann [14] observed a mass increase of cement paste samples submerged in water and attributed this phenomenon to water diffusion through the latex membrane due to osmosis. Douglas and Hover [15] also measured a substantial weight change of condoms filled with cement paste and mortars submerged in a water bath. Barcelo [16] tested different latex membranes and observed that all allowed water transport.

The present study aims at investigating the phenomenon of water uptake of the samples in the volumetric method. In particular, its driving mechanisms need to be ascertained and its influence on the measured strain quantified. It is examined if it is possible to compensate for the water uptake by means of a calculation, or to modify the volumetric technique as to exclude this artefact. To verify the results of the volumetric measurements, linear autogenous strain is measured on the same cement pastes with a technique based on corrugated moulds [17]. A more detailed description of the measuring techniques and of the results presented in this paper is provided in a report [18].

## 2. Materials

### 2.1 Salt solutions

Two different salt solutions were produced: 1) A synthetic pore solution based on the compositions reported by Page and Vennesland [19]: 0.4 mol/l  $\text{Na}^+$ , 0.4 mol/l  $\text{K}^+$ , 0.002 mol/l  $\text{Ca}^{2+}$ , 0.724 mol/l  $\text{OH}^-$  and 0.04 mol/l  $\text{SO}_4^{2-}$ ; 2) A solution with half the ionic strength obtained by 1:1 dilution with demineralised water. This solution is referred to as 50% diluted, synthetic pore solution.

### 2.2 Cement pastes

Three cement pastes with widely different properties were investigated: A: w/c 0.30, 20% silica fume addition; B: w/c 0.30, 20% silica fume addition + 0.6% superabsorbent polymer, SAP, by weight of cement; C: w/c 0.35, 0% silica fume.

The cement used is a low-alkali Danish white Portland cement produced by Aalborg Portland, with Blaine fineness 420  $\text{m}^2/\text{kg}$ . The Bogue-calculated phase composition (in wt.%) is:  $\text{C}_3\text{S}$ : 66.1,  $\text{C}_2\text{S}$ : 21.2,  $\text{C}_3\text{A}$ : 4.3,  $\text{C}_4\text{AF}$ : 1.1,  $\text{CS}$ : 3.5, free  $\text{CaO}$ : 1.96,  $\text{Na}_2\text{O}$  eq.: 0.17.

The silica fume in pastes A and B was added as a dry powder at a rate of 20 wt.% of cement. The specific surface of the silica fume is 17.5  $\text{m}^2/\text{g}$  (BET method). The chemical composition (in wt.%) is:  $\text{SiO}_2$ : 94.1,  $\text{Fe}_2\text{O}_3$ : 1.00,  $\text{Al}_2\text{O}_3$ : 0.13,  $\text{MgO}$ : 0.71,  $\text{SO}_3$ : 0.43, and  $\text{Na}_2\text{O}$  eq.: 1.09.

In mixtures A and B, a naphthalene-based dry powder superplasticizer was added at a rate of 1.0 wt.% of cement+silica fume.

The SAP used in mixture B is a suspension-polymerized covalently cross-linked acrylamide/acrylic acid copolymer [20]. The spherical particles have diameters about 100-150  $\mu\text{m}$  in the dry state. The size of the swollen SAP particles in the cement pastes and mortars is about three times larger due to pore fluid absorption. The SAP was added at a rate of 0.6 wt.% of cement. In mixture B, extra mixing water was added in an amount sufficient to saturate the SAP particles. This amount corresponds to an entrained w/c of 0.075 [20].

The cement pastes were mixed in a 5-l epicyclic mixer. Cement and all other admixtures, including the SAP in mix B, were put into the bowl. Mixing was done at low speed for 1 minute, while gradually adding about 3/4 of the demineralised water. Mixing continued at high speed for 1 minute, after which it was stopped and the paste was scraped off from the blade and the walls of the bowl for 1 minute. Mixing was resumed for 1 minute at low speed while the rest of the water was added; a last minute at high speed followed. The water was added in two steps to assure the homogeneity of the mix and the dispersion of the silica fume. Total mixing time from first water addition was 5 minutes. The temperature of the ingredients was approximately 20°C at mixing.

### 3. Methods

#### 3.1 Volumetric autogenous strain

Volumetric measurements of autogenous strain were performed by monitoring the sample weight of cement paste samples contained in elastic membranes and submerged in a buoyancy liquid, either distilled water or paraffin oil. The experiments took place in a climate room at  $20 \pm 0.2^\circ\text{C}$ .

100 to 150 g of fresh cement paste was poured into a membrane, either a latex or polyurethane condom. The latex condoms were of type 'Plan' by RFSU, with thickness 0.06 mm and without gliding crème or reservoir. The polyurethane condoms were of type 'Avanti' by Durex, with thickness 0.04 mm, gliding crème and reservoir. The gliding crème was removed from the external surface of the condom with a paper towel before filling the condom with cement paste.

The filled membrane was tightly closed with a knot; attention was paid to avoid entrapment of air bubbles. The excess part was then cut off and a 0.12-mm mono-filament Silicon-PTFE string (fishing line) was tied to the sample by means of a plastic strap. The string, about 400 mm long, was tied to a stainless steel hook at the other end. Typical samples are shown in Figure 1.

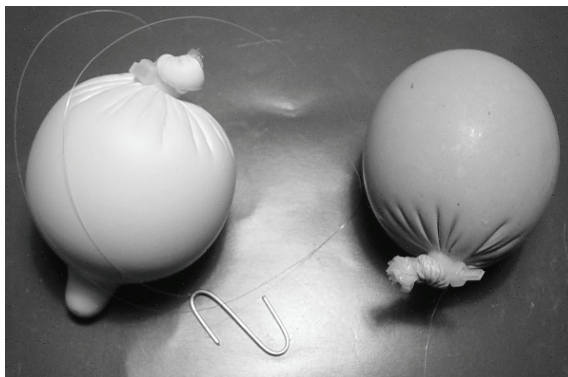


Figure 1: Polyurethane membrane with reservoir (left) and latex membrane without reservoir (right) filled with cement paste. The picture shows also the plastic strap around the knot, to which a thin string was tied, ending with a steel hook.

During the measurements, the samples hung from a hook beneath the balance plate. The balance was a Sartorius CP 225 D, with sensitivity 0.01 mg for weights below 80 g and 0.1 mg for weights until 220 g. All measurements were performed in the 220 g measuring range. The 0.1 mg accuracy in this range was fully sufficient for the measurements; in addition, this improves the stability of the readings from the balance. The 0.1 mg weighing accuracy results in a nominal accuracy on the measured strain of  $0.4\text{--}0.8\ \mu\text{m/m}$ , considering typical sample sizes, different buoyancy liquids, and isotropic deformations. The actual uncertainty on the



measured strain is significantly higher, being dominated by a number of factors, including temperature oscillations and drift of the balance. The balance was placed on a 100-kg concrete weighing table to minimize vibrations. The table was provided with a 110-mm circular hole through which the string passed. The test setup is shown in Figure 2.

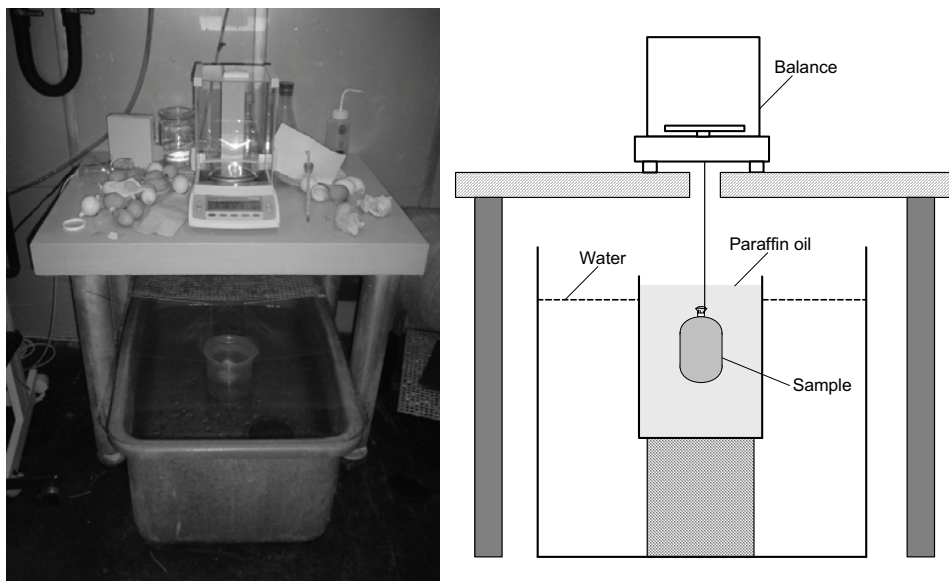


Figure 2: Setup for volumetric measurement of autogenous strain of cement paste. A Sartorius CP 225 D balance is placed on a massive weighing table. The sample is suspended to the balance by means of a string, passing through a hole in the table. The sample is submerged in a buoyancy bath, either water or paraffin oil.

In the case of measurement in water, the sample was submerged in a water bath, consisting of a container of dimensions  $0.5 \times 0.8 \times 0.4$  m, holding about 100 l of distilled water. Water circulation in the bath, was avoided to improve the stability of the weight measurements. Most of the surface of the bath was covered with a Plexiglas lid to reduce evaporation; this was done to avoid changes in the water level and thermal gradients. In the case of measurements in paraffin oil, a smaller cylindrical container ( $\varnothing$  130 mm, height 200 mm) was filled with paraffin oil; the container was submersed in the larger container filled with water to help keep the sample temperature constant. Temperature measurements by means of thermocouples showed a maximum temperature increase of  $0.5^\circ\text{C}$  in the samples measured in the water bath; the maximum temperature increase of the samples measured in the paraffin oil bath was  $1.5^\circ\text{C}$ . In both cases, the temperature peak occurred at 8 h from water addition and the temperature equilibrated at 24 h.

The submerged weight of the sample was measured and recorded automatically at regular intervals by controlling software. Measurements were generally recorded every 10 minutes

from about 30 minutes after water addition up to about 2 weeks. Upon submersion of the sample in the buoyancy liquid, air bubbles attached to the upper, external part of the membrane were gently removed. The first measurement immediately after submersion was discarded because of the influence of oscillations of the sample on the measurements. Another source of error was represented by drops of buoyancy liquid attached to the string. However, these fell into the bath within the first minute of the experiment and did not lead to further errors.

The cement pastes studied showed no noticeable bleeding. Therefore, no rotation of the specimens was necessary, as applied in other studies [15].

### 3.2 Linear autogenous strain

Linear autogenous strain of cement pastes was measured by a special measuring technique, where the cement paste is encapsulated in thin, corrugated polyethylene moulds with length:diameter ratio of approximately 300:30 mm. The technique ensures insignificant restraint of the hardening cement paste and permits measurements to start 30 minutes after water addition. The cement paste was cast under vibration into the moulds; the specimens were then placed in a dilatometer equipped with automatic data-logging and electronic linear displacement transducers (Figure 3). The dilatometer with samples was submerged into a temperature-controlled glycol bath at  $20 \pm 0.1^\circ\text{C}$ . Two samples were tested simultaneously in the dilatometer, with a measuring accuracy of  $\pm 5 \mu\text{m/m}$ . A separate sample with an embedded thermocouple registered the temperature evolution; a maximum temperature increase of  $0.5^\circ\text{C}$  occurred at 8 h from water addition and the temperature equilibrated at 24 h. Measurements were performed every 15 minutes and started 30 minutes after water addition. A detailed description of the measurement technique can be found in the literature [17].

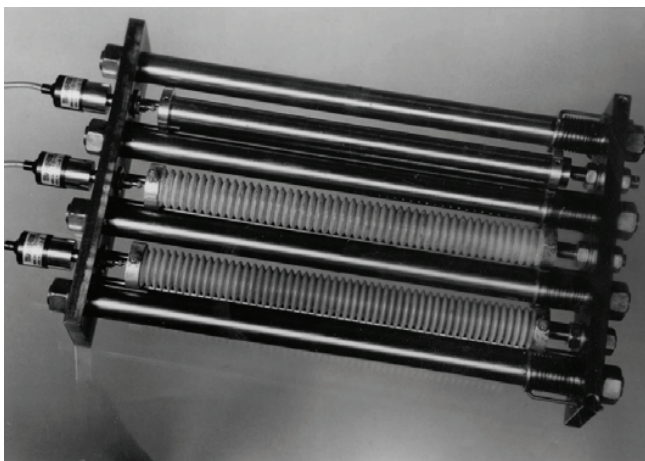


Figure 3: Dilatometer with corrugated moulds for measurements of linear autogenous strain of cement pastes.

### **3.3 Water-uptake measurements**

To test water uptake of buoyancy liquid through the different membranes used, a series of mass measurements was performed on different samples. Membranes filled with either salt solutions or cement pastes were submerged in the buoyancy liquids and their mass was recorded at regular intervals. Before every measurement, the samples were removed from the bath and the outer surface of the membranes was gently and thoroughly wiped with a paper towel to remove the attached film of water or paraffin oil.

## **4. Results and discussion**

### **4.1 Water uptake through solution-filled membranes**

To quantify the influence of osmosis on the volumetric measurements, rubber membranes filled with either synthetic pore solution, 50% diluted, synthetic pore solution, or demineralised water, were submerged in a demineralised water bath and their mass was monitored. Both latex and polyurethane membranes were tested. The membranes contained amounts of solutions varying from 70 to 140 g. Figures 4 and 5 show the results of the experiments. Water diffusion through the condoms was proportional to the solute concentration. In particular, the mass of condoms filled with synthetic pore solution increased by 0.4% per day, while the mass of the condoms filled with 50% diluted, synthetic pore solution increased at about half the rate. The mass of membranes filled with demineralised water remained almost unchanged. No substantial differences in rate of water uptake were observed between latex and polyurethane membranes. However, after a few days in the water bath, the polyurethane membranes started leaking and lost weight. Examination of the polyurethane membranes revealed extensive degradation. The scatter between identical membranes filled with similar quantities of synthetic pore solution was quite substantial, as shown by the standard deviation bars in Figures 4 and 5. The main reason is believed to be variability in thickness between the membranes and possibly presence of  $\mu\text{m}$ -sized pinholes in individual membranes.

### **4.2 Water uptake through cement paste-filled membranes**

Latex membranes filled with cement paste were submerged in a demineralised water bath about 30 minutes after mixing and their mass was measured until about 3 weeks of age. In the first day, the specimens were weighed every few hours, with the first measurement taken at about 2 h after mixing. Results of this experiment are shown in Figure 6.

Pastes A and B are expected to have similar permeabilities throughout the hydration process, since the presence of SAP should have only limited impact on the transport properties of the paste [21]. Therefore it is possible to analyze the water uptake of the two pastes in terms of the driving forces only. Long-term water uptake in cement paste B with SAP is lower than in paste A, whereas the water uptake in the first hours after mixing is quite similar. Osmosis is expected to dominate the water uptake of the samples in the first hours. Osmotic forces depend on the concentration of the pore solution, which should be similar in pastes A and B because the same cement and admixtures have been used. At a later age, self-desiccation occurs in paste A and becomes the dominant driving force for water uptake. This explains the higher water uptake of paste A at later ages. It is noticed that water transport into the sample due to osmosis in the first

hours occurs at a very high rate compared to later ages. In fact, high porosity and low tortuosity of the cement paste pore system at early age facilitate transport of water into the cement paste. Moreover, at early age the transport of water into the sample is entirely liquid-based, instead of the slower, combined liquid-gas transport that occurs when pores in the cement paste have been partially emptied by self-desiccation. Whereas at early ages the permeability of the elastic membrane is the limiting factor of the transport process, at later ages the reduced permeability of the cement pastes becomes dominant.

Paste C shows a high water uptake in the first hours after casting, but is close to paste A in the following days, indicating that self-desiccation does influence water uptake. Comparison of paste C with the other two pastes is complicated, because the water uptake is influenced also by the transport properties of the paste. In particular, paste C, with higher w/c and no silica fume, will have a much higher permeability than pastes A and B at any time.

A simple calculation confirms that the water uptake in the first half a day might be caused primarily by osmosis. The rate of water uptake of latex membranes filled with synthetic pore fluid is about 0.4% by weight per day (Figure 4). The cement pastes studied have initial water to solids volume ratio close to 0.5. The absorption in the first day may, therefore, be estimated as  $0.4\% \times 0.5 = 0.2\%$  by weight of cement paste. This value is close to the measured, initial absorption rate, around 0.15-0.20 wt-% per day (Figure 6).

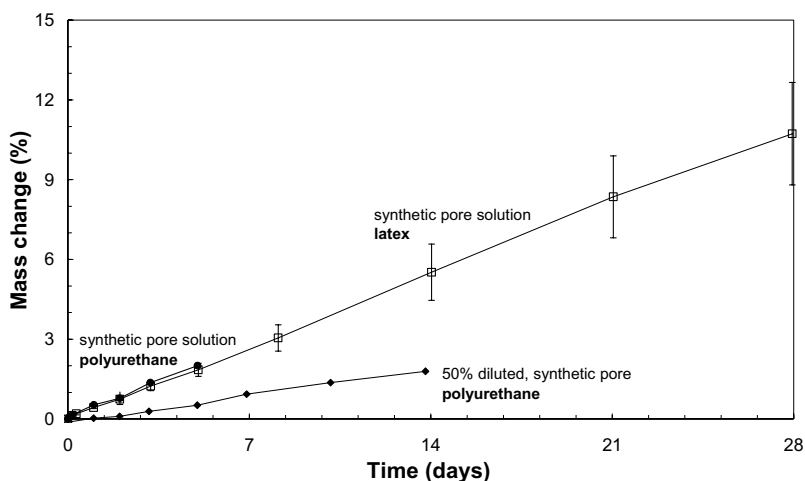


Figure 4: Mass change of solution-filled membranes submerged in a demineralised water bath at 20.0°C. The average and the standard deviation of 3 samples is shown in the case of the latex membranes filled with synthetic pore solution and of 2 samples in the case of the polyurethane membranes with synthetic pore solution. For the polyurethane membranes with 50% diluted, synthetic pore solution, measurements on only one sample are shown.

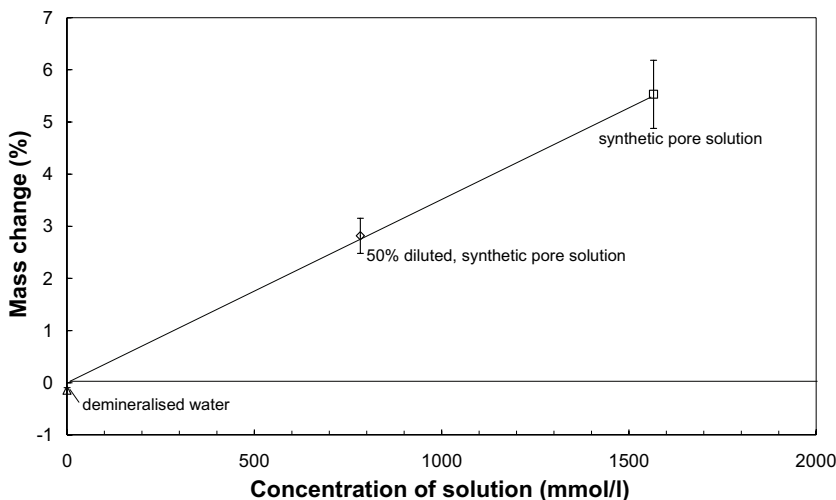


Figure 5: Mass change of membranes containing synthetic pore solution, 50% diluted, synthetic pore solution, and demineralised water, submerged for 21 days in a demineralised water bath at 20.0°C. Each measurement shows the average and the standard deviation based on 3 samples.

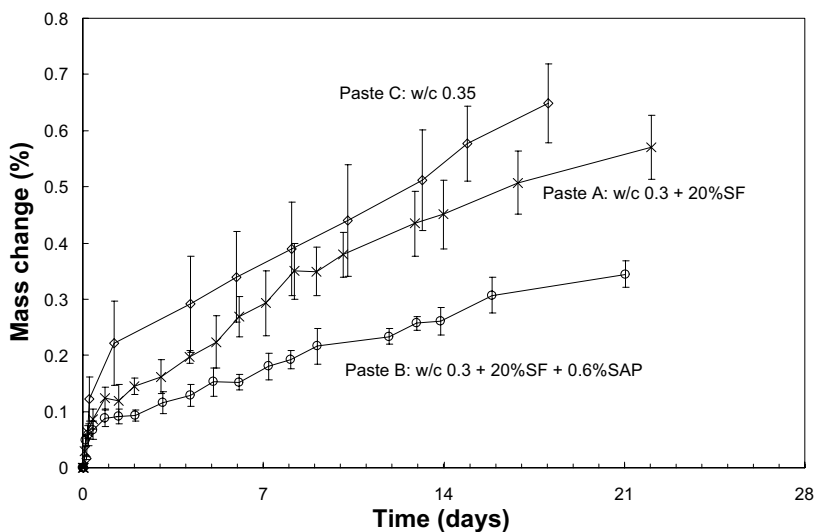


Figure 6: Mass change of cement paste-filled latex membranes submerged in a water bath at 20°C. The average and the standard deviation of 5 samples are shown for pastes A and B, while 3 samples were measured for paste C.

In Figure 7, the estimated error on volumetric autogenous strain measurements that would result from the weight change of the submerged samples is shown. The error was calculated based on the assumption that all the water absorbed into the sample filled voids produced by chemical shrinkage. This is a questionable assumption, especially before setting, when no voids are present in the pastes and the absorbed water might instead contribute to raise the w/c of the pastes. In a volumetric measurement, water absorbed into the sample increases the submerged weight of the sample, which is interpreted as shrinkage. The error has been converted to linear shrinkage, assuming isotropic deformation. This facilitates comparisons with linear measurements in the following sections of this paper. Figure 7 shows that absorption of water from the bath produces a fictitious shrinkage after 3 weeks of 2000  $\mu\text{m/m}$  for paste B, 4000  $\mu\text{m/m}$  for paste A and about 5000  $\mu\text{m/m}$  for paste C. Already at 1 day after casting, the measuring error is substantial, varying from 500 to 1500  $\mu\text{m/m}$  for the 3 pastes.

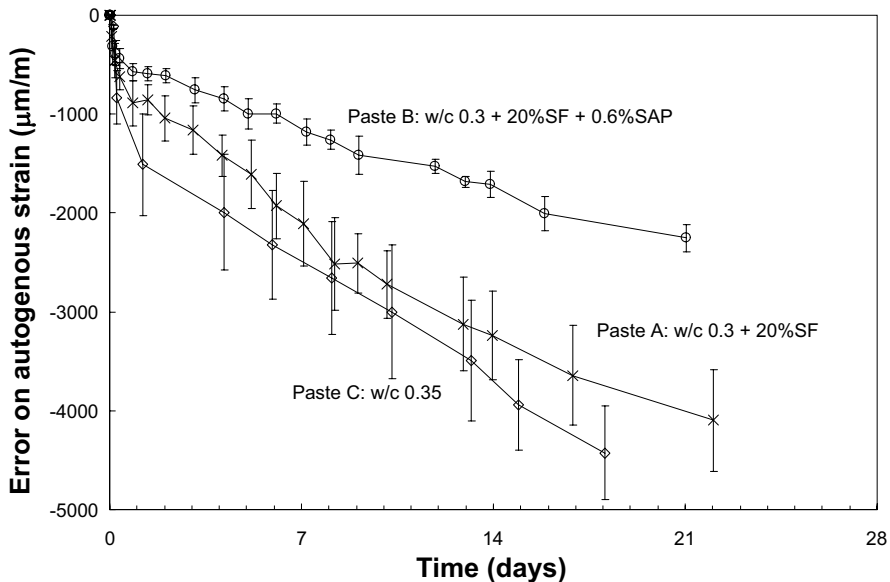


Figure 7: Error on the measured autogenous strain due to water uptake of cement paste in latex membranes submerged in water bath at 20°C. Linear strain was calculated assuming isotropic behaviour; shrinkage is plotted as negative strain. The average and the standard deviation of 5 samples are shown for pastes A and B, while 3 samples were measured for paste C.

Besides the previously described artefacts, water uptake from the bath affects the curing conditions of the sample, which will not be autogenous. To perform measurements of autogenous strain, the cementitious system must be: 1) sealed, 2) kept at constant temperature, and 3) not subjected to external forces [22]. Therefore, when water penetrates the membrane, the measured strain is not autogenous strain. Barcelo [16] describes the effect of water absorbed into the sample as an increase of the average w/c of the cement paste; with this assumption, he concludes that the effect of water uptake on self-desiccation is negligible in the

first week of hydration. However, it is misleading to assimilate the absorbed water to an increase of w/c: the situation is more similar to a cement paste with a given w/c cured with an external supply of water. This external supply of water will have a much greater influence on the autogenous shrinkage of the paste than if it was supplied initially as mixing water [20, 21].

Some authors [13, 23] state that water uptake through the elastic membrane is a slow process and its impact on the volumetric measurements can be neglected in short-term measurements; therefore, use of the volumetric technique is justified for measurements in the first day after casting. However, no data on water uptake of volumetric samples was published by these authors to confirm their hypothesis. On the contrary, Figure 7 in this paper shows that the impact of water uptake from the buoyancy bath on the volumetric measurements is great enough to compromise the whole measurement from the time of casting, since an error on the measured strain of 500-1500  $\mu\text{m/m}$  in 1 day is of the same order of magnitude as the true strain itself.

In theory, it is possible to eliminate this artefact by stopping the water uptake through the elastic membrane. The most obvious way is to choose an impermeable membrane. With this aim, Barcelo [24] measured a number of latex membranes but found that they all were permeable. Douglas [25] tested a number of different latex, polyurethane and neoprene membranes and all were permeable to water. Also in the present research, latex and polyurethane membranes were found to have similar permeabilities to water (Figure 4). The lack of tightness of the membranes is due both to their intrinsic permeability and to the presence of defects such as pinholes. Pinholes are especially significant to increase water uptake at early ages, while their importance at later ages are lowered by the reduced permeability of the cement paste. Making the membrane thicker, while improving the tightness, will also increase its stiffness and restrain the cement paste, especially around setting time [8]. It is not excluded that a satisfactory balance between stiffness and tightness of the elastic membrane can be achieved; however, this is not the case with the type of membranes used in the volumetric measurements in the last 15 years, i.e. latex condoms.

Another approach to eliminate the water uptake of the samples in the volumetric test is to substitute the buoyancy liquid. Measurements of mass change of polyurethane condoms filled with different cement pastes and submerged in paraffin oil were performed: the mass gain in the first week of submersion was about 0.005%, which is roughly 1/30 to 1/70 of the mass change observed in the same period on latex condoms filled with cement paste and submerged in a water bath, cf. Figure 6. This mass change would lead to an error on the measured autogenous strain of less than 50  $\mu\text{m/m}$  in one week. Polyurethane was preferred to latex because latex does not tolerate oils and swells up in a matter of hours. An expansion is erroneously measured as a result of this.

#### **4.3 Measurements of autogenous strain on cement pastes**

On the same pastes tested for weight change underwater, the autogenous strain was measured with three different methods:

- 1) Measurements of submerged weight of cement paste samples cast in latex condoms and submerged in a water bath;

- 2) Measurements of submerged weight of cement paste samples cast in polyurethane condoms and submerged in a paraffin oil bath;
- 3) Measurement of length changes of samples cast in corrugated moulds in the dilatometer [17].

In all cases, the mass of the samples before and after testing was measured. Mass change of the samples was generally negligible in the case of measurements of type 2) and 3), whereas the mass gain of samples tested in a water bath confirmed the findings in the previous section (Figure 6).

In Figures 8-10, measurements of autogenous strain with the three techniques are presented. For comparison, also calculated curves are shown based on addition of the error due to water uptake (Figure 7) to the measurement in paraffin oil

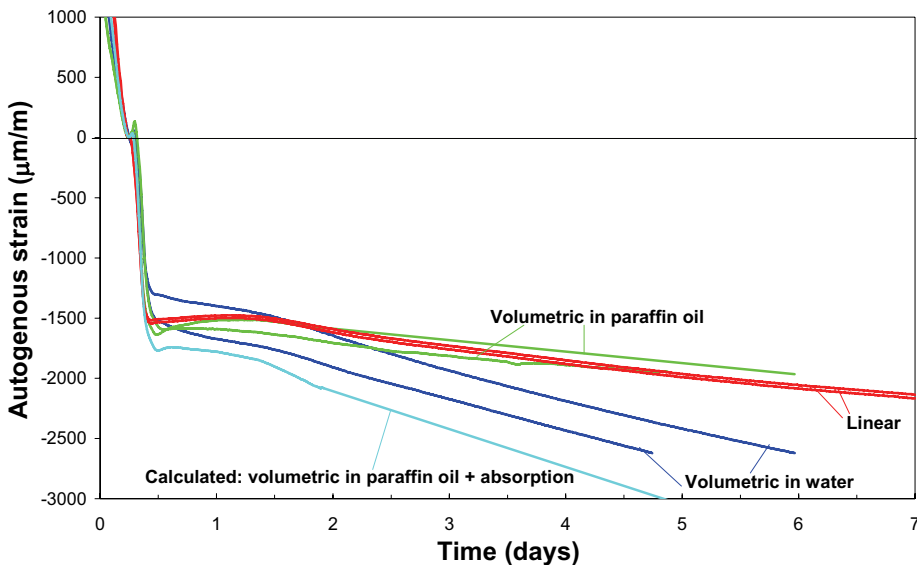


Figure 8: Measurements of autogenous strain with different techniques at 20°C on cement paste with w/c 0.3 and 20% silica fume addition (paste A). Conversion from volumetric to linear strain assumes isotropic behaviour; the curves are zeroed at setting, 6 h after casting, shrinkage is plotted as negative strain.

Measurements in Figures 8-10 show a number of common features. Linear measurements performed with the dilatometer [17] and volumetric measurements in paraffin oil fundamentally agree, after some differences in the first few hours. Moreover, both linear measurements and volumetric measurements in paraffin oil are quite reproducible and show little scatter throughout the measuring period. This good agreement, obtained for 3 cement pastes with completely different autogenous strain behaviour, confirms the overall validity of



these two techniques. However, the volumetric technique is experimentally more laborious than the linear and it is sensitive to a number of artefacts, including pressure exerted by the membrane and reabsorption of bleeding water and entrapped air into the sample [10, 15, 18].

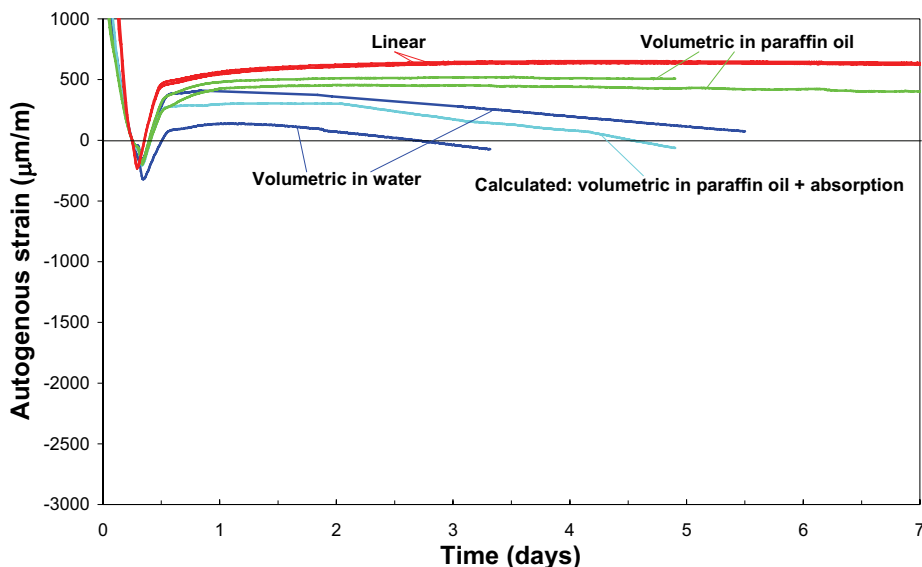


Figure 9: Measurements of autogenous strain with different techniques at 20°C on cement paste with w/c 0.3, 20% silica fume addition and 0.6% superabsorbent polymers (SAP) by weight of cement (paste B). Conversion from volumetric to linear strain assumes isotropic behaviour; the curves are zeroed at setting, 6 h after casting; shrinkage is plotted as negative strain.

On the contrary, the volumetric measurements in water fundamentally disagree with the other two types of strain measurements. The measured shrinkage is systematically higher than for the other two techniques. This confirms previous data in the literature about the volumetric technique in water bath [4, 9]. As discussed in the previous paragraphs, water uptake of the samples through the elastic membrane is a principal cause of this discrepancy [16, 25]. Water uptake causes an increase of the submerged weight of the sample that is erroneously interpreted as shrinkage in the volumetric measurements. A way to verify this assumption is adding the error due to water uptake (Figure 7) to the volumetric measurements in paraffin oil, and comparing the results with the volumetric measurements in water. Results of this calculation are also shown in Figures 8-10. These calculated curves have strong similarities with the volumetric measurements in water bath. In particular, a very close agreement is obtained with the shrinkage rate after a couple of days: this shows that a dominant part of the shrinkage measured with the volumetric method in water is an experimental artefact due to water uptake

through the rubber membrane. Moreover, volumetric measurements in water show a poor reproducibility in the first few hours, while the strain rate at later ages is more similar between the samples. Similarly, mass gain of the samples stored in water showed a high scatter especially in the first period, which may be due to different permeabilities of the elastic membranes. The high initial scatter in the volumetric measurements in water is another consequence of the water uptake through the membrane, which varies from sample to sample especially in the first hours.

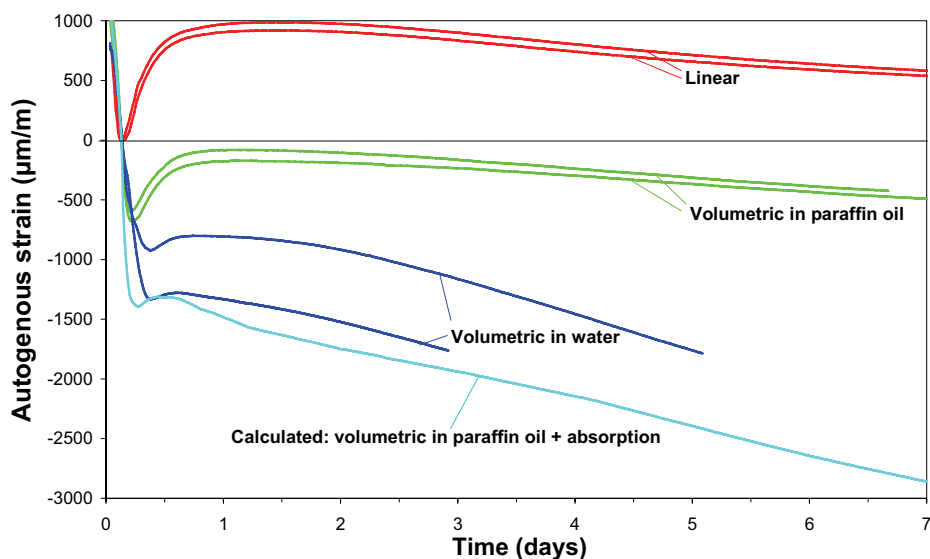


Figure 10: Measurements of autogenous strain with different techniques at 20°C on cement paste with w/c 0.35 (paste C). Conversion from volumetric to linear strain assumes isotropic behaviour; the curves are zeroed at setting, 3.5 h after casting; shrinkage is plotted as negative strain.

Barcelo and Douglas [16, 25] have suggested correcting the volumetric measurements in a water bath based on the average measured absorption. This approach is not recommendable. In addition to the unnecessary experimental trouble, the results will be influenced by a high scatter and furthermore they will be corrected for the effect of water absorption only in part.

## 5. Conclusions

Water uptake from the buoyancy bath through the elastic membrane is a principal artefact of the volumetric method for measuring autogenous strain. Water uptake of the samples is driven by a lowered water activity in the cement paste, due to dissolved salts in the pore fluid and self-desiccation. Water is absorbed into the cement paste sample at a high rate from the moment of submersion; the error it produces on the measured strain is of the same order of magnitude as

the autogenous strain itself. It is practically impossible to correct the measurements from water uptake through the membrane.

Water uptake through the membrane can be avoided by using paraffin oil as buoyancy liquid. The volumetric autogenous strain measured in this way is in good agreement with measurements performed with a linear, dilatometric technique. This confirms the overall validity of these two techniques. Some minor differences between the two measuring techniques in a couple of hours around setting should be the object of further research.

## Acknowledgements

This paper is part of a 3-year project dedicated to examine measuring methods for autogenous strain. The funding by the Danish Technical Scientific Research Council (STVF) is gratefully acknowledged.

## References

1. Yamazaki, Y., Monji, T., and Sugiura, K., 'Early age expanding behaviour of mortars and concretes using expansive additives of  $\text{CaO-CaSO}_4\text{-4CaO}\cdot\text{3Al}_2\text{O}_3\cdot\text{SO}_3$  system', 6<sup>th</sup> Int. Conf. on the Chemistry of Cement, Moscow, September 1974, Stroyizdat, Moscow **III-5** (1976) 192-195.
2. Justnes, H., Van Gemert, A., Verboven, F., and Sellevold, E., 'Total and external chemical shrinkage of low w/c ratio cement pastes', *Adv. Cem. Res.* **8** (31) (1996) 121-126.
3. Yates, J.C., 'Effect of calcium chloride on readings of a volumeter inclosing Portland cement pastes and on linear changes of concrete', *Highway Research Board Proc.* **21** (1941) 294-304.
4. Barcelo, L., Boivin, S., Rigaud, S., Acker, P., Clavaud, B., and Boulay, C., 'Linear vs. volumetric autogenous shrinkage measurement: Material behaviour or experimental artefact?', 2<sup>nd</sup> Int. Res. Sem. on Self-desiccation and its Importance in Concrete Technology, Lund, Sweden (1999) 109-125.
5. Buil, M., 'Studies of the shrinkage of hardening cement paste', D.Eng. thesis, Rapport de recherche LPC No. 92, Laboratoire Central des Ponts et Chaussées, Paris (1979).
6. Davis, H.E., 'Autogenous volume changes of concrete', Proc. 43<sup>rd</sup> Annual Meeting, American Society for Testing Materials, Philadelphia **40** (32) (1940) 1103-1112.
7. Wuerpel, C.E., 'Laboratory studies of concrete containing air-entraining admixtures', *ACI Journal* **42** (4) (1946) 305-359.
8. Baron, J., and Buil, M., 'Comments on the paper "Mechanical features of chemical shrinkage of cement pastes" by N. Setter & D.M. Roy', *Cem. Concr. Res.* **9** (4) (1979) 545-547.
9. Charron, J.-P., Marchand, J., Bissonnette, B., Pigeon, M., and Zuber, B., 'Comparative study of the effects of water/binder ratio and silica fume on the volume instability of hydrating cement pastes at early age', 3<sup>rd</sup> Int. Res. Sem. on Self-desiccation and its Importance in Concrete Technology, Lund, Sweden (2002) 39-50.

10. Hammer, T.A., Bjøntegaard, Ø., Sellevold, E.J., 'Measurement methods for testing of early age autogenous strain', in: A. Bentur (ed.) Early age cracking in cementitious systems, RILEM TC 181-EAS Committee, RILEM, Cachan (2002) 234-245.
11. Lura, P., and Jensen, O.M., 'A discussion of the paper: "On the measurement of free deformation of early age cement paste and concrete" by Ø. Bjøntegaard, T. A. Hammer and E. J. Sellevold', *Cem. Concr. Comp.* **27** (7-8) (2005) 854-856.
12. Marciniak, S., 'Autogenous deformations and relative humidity change: experimental studies, MSc thesis, Department of Building Technology and Structural Engineering, Aalborg University, Aalborg (2002).
13. Bjøntegaard, Ø., Hammer, T.A., and Sellevold, E.J., 'On the measurement of free deformation of early age cement paste and concrete', *Cem. Concr. Comp.* **26** (5) (2004) 427-435.
14. Beltzung, F., Wittmann, F., 'Influence of cement composition on endogenous shrinkage', 3<sup>rd</sup> Int. Res. Sem. on Self-desiccation and its Importance in Concrete Technology, Lund, Sweden (2002) 113-125.
15. Douglas, K.S., and Hover, K.C., 'Measuring non-drying bulk shrinkage of cement paste and mortar using Archimedes' principle: Part I', in: O.M. Jensen, D.P. Bentz & P. Lura (eds.) Autogenous deformation of concrete, ACI SP 220, American Concrete Institute, Farmington Hills, Michigan (2004) 39-51.
16. Barcelo, L., 'Influence des caractéristiques des ciments sur la structuration et le comportement dimensionnel des matériaux cimentaires au jeune âge', PhD thesis, Ecole Normale Supérieure de Cachan, Cachan, France (2001).
17. Jensen, O.M., Hansen, P.F., 'A dilatometer for measuring autogenous deformation in hardening Portland cement paste', *Mater. Struct.* **28** (181) (1995) 406-409.
18. Lura, P., and Jensen, O.M., 'Volumetric measurement in water bath - an inappropriate method to measure autogenous strain of cement paste', Technical report, Technical University of Denmark, February 2005, 29 pp.
19. Page, C.L., Vennesland, Ø., 'Pore solution composition and chloride binding capacity of silica-fume cement pastes', *Mater. Struct.* **16** (91) (1983) 19-25.
20. Jensen, O.M., and Hansen, P.F., 'Water-entrained cement-based materials – II. Implementation and experimental results', *Cem. Concr. Res.* **32** (6) (2002) 973-978.
21. Jensen, O.M., and Hansen, P.F., 'Water-entrained cement-based materials – I. Principles and theoretical background', *Cem. Concr. Res.* **31** (4) (2001) 647-654.
22. Jensen, O.M., and Hansen, P.F., 'Autogenous deformation and change of the relative humidity in silica fume-modified cement paste', *ACI Mater. J.* **93** (6) (1996) 539-543.
23. Baroghel-Bouny, V., Mounanga, P., Khelidj, A., Loukili, A., and Rafai, N., 'Autogenous deformations of cement pastes: Part II. W/C effects, micro-macro correlations, and threshold values', *Cem. Concr. Res.* (2005), in press.
24. Barcelo, L., personal communication, January 2005.
25. Douglas, K.S., 'Non-drying Bulk Shrinkage of Cement Paste and Mortar: Application to Pneumatic Transport Mixing of Sand and Cement', MSc thesis, Cornell University, Ithaca, New York (2002).

## **Cement Hydration: Building Bridges and Dams at the Microstructure Level**

Dale P. Bentz

Building and Fire Research Laboratory, National Institute of Standards and Technology, USA

### **Abstract**

The concurrent goals of cement hydration are to percolate (bridge) the original cement particles into a load-bearing network and to depercolate (dam) the original water-filled capillary porosity. The initial volume, particle size distribution, and flocculation/dispersion state of the cement particles have a large influence on both hydration rates and microstructure development. Likewise, the capillary porosity as characterized by its pore size distribution, percolation state, and saturation state also influences both hydration kinetics and microstructure. In this paper, experimental techniques and computer modeling are applied to further understanding several of the critical connections between these physical parameters and performance properties. First, the setting or bridging process is explored via a combination of needle penetration and rheological measurements, in concert with three-dimensional microstructural modeling. Second, low temperature calorimetry is shown to be a valuable indicator of the percolation state or damming of the water-filled pores with various size entryways in the three-dimensional microstructure. Porosity percolation (or depercolation) is shown to be strongly influenced by both curing conditions and the alkali content of the cement pastes. Finally, it is proposed that future efforts in this field be directed towards a greater understanding of the (nano)structures of cement hydration products, particularly the calcium silicate hydrate gel, and their influence on performance properties.

### **1. Introduction**

As with all materials, the microstructures of cement pastes, mortars, and concretes provide the bridges between materials processing and engineering properties. Unlike many other materials, however, cement-based materials exhibit a highly dynamic (micro)structure that is extremely sensitive to initial conditions, processing, and environmental exposure. There are few materials where water plays such a critical role in processing, microstructure development, performance, and durability. In cement-based materials, water is the liquid that provides flowability to the raw materials, serves as a vehicle for and participant in the numerous and complex cement hydration reactions, exerts forces on the solid components of the porous microstructure during self-desiccation, drying, freezing, alkali-silica gel formation, and

exposure to fire, and provides the pathways for the ingress of deleterious ions. From a geometrical/structural viewpoint, the characteristics of both the **porosity** where the water resides and of the **particles** initially present in the mixing water are critical influences on hydration rates, microstructure, and performance properties. In analogy to large scale construction, cement hydration can be viewed as the process of building *bridges* to connect cement particles and *dams* to disconnect the water-filled capillary pore space.

Because many of the cement hydration products form around the initial cement clinker particles, as shown in Figure 1, the initial configuration of these particles is crucial in providing a “scaffold” on which a network of (porous) solid bridges will form. Thus, the initial water-to-cement ratio ( $w/c$ ) [1], particle size distribution [2-4], and dispersion/flocculation state [5] of the particles all exert major influences not only on the developed microstructure (through and beyond setting) but also on the hydration kinetics. The bridging process can be conveniently explored via a coordinated experimental and computer modeling approach, as will be demonstrated in this paper.

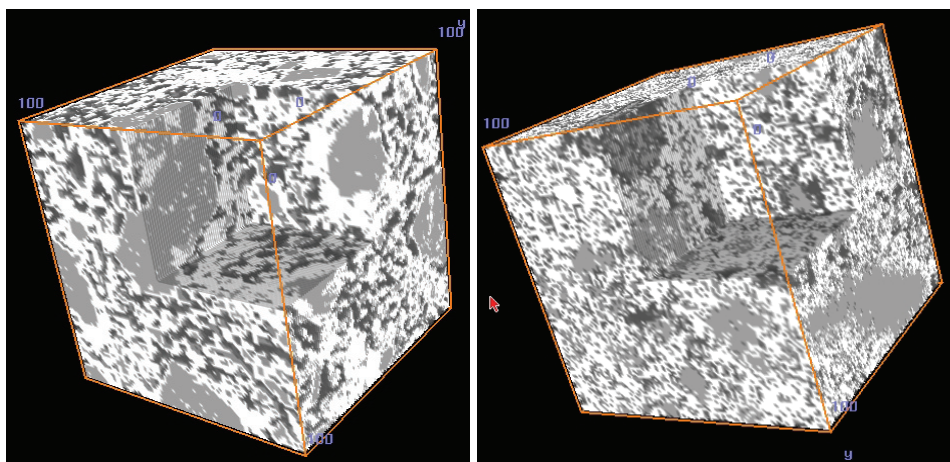


Figure 1: Greylevel-coded three-dimensional microstructures ( $100\ \mu\text{m} \times 100\ \mu\text{m} \times 100\ \mu\text{m}$ ) of real (left) and model (right) hydrating cement pastes of Cement and Concrete Reference Laboratory cement 133 with a  $w/c \approx 0.47$  and a degree of hydration of about 0.62. Light grey represents unhydrated cement particles, white hydration products, and dark grey capillary porosity. The real microstructure was captured by x-ray microtomography at beam line ID 19 of the European Synchrotron Research Facility in Grenoble, France, in September 2000 [6, 7].

While the microstructural bridges are critical for strength development and mechanical properties, the microstructural dams are more important for limiting transport and improving the durability of cement-based materials. As cement hydration connects the original cement particles together, it may also disconnect the water-filled capillary porosity, at least at the micrometer scale. Because there are nanometer-sized pores present in the calcium silicate hydrate gel (C-S-H) hydration product, the porosity always remains percolated at the

nanometer scale [8]. Although the capillary pores present in both the real and model microstructures in Figure 1 appear depercolated in two dimensions, in three dimensions, they are still highly connected. But, as first noted by Powers many years ago [9], for lower w/c pastes, sufficient hydration will result in depercolation of the initial water-filled capillary pores. Here, this depercolation, along with the role of curing conditions and cement alkali content, will be examined experimentally using low temperature calorimetry (LTC).

## 2. Experimental

Cement pastes were prepared using Cement and Concrete Reference Laboratory (CCRL) proficiency cement samples 140 [10] and 152 [11]. Since many of the experimental procedures have been provided in detail elsewhere [12-14], they will only be reviewed briefly here. Cement and water were mixed in a high speed blender using the following protocol: 30 s of low speed mixing while the cement powder is introduced into the mixing vessel that already contains the water, 30 s of high speed mixing, a rest of 150 s while the sides of the mixing vessel are scraped down, and 30 s more of high speed mixing to prepare the final product. The mixing water was either distilled water or a solution of alkalis (sulfates or hydroxides), prepared by dissolving the relevant potassium and sodium compounds in distilled water. The fresh paste was used for Vicat needle penetration [15] measurements at laboratory temperature (about 26 °C) and rheological measurements by the stress growth technique [16-18] at 20 °C, or cast into small ( $\approx 5$  g) wafers that were placed in capped plastic vials and cured under saturated (small amount of water on top) or sealed conditions in an environmental chamber maintained at 20 °C. Limited repeatability tests have indicated that the calculated values for the yield stress of the cement paste as measured by the stress growth technique have a standard uncertainty of 5 % [16-18]. At various ages, the specimens were removed from their vials, crushed using a mortar and pestle, and analyzed using loss-on-ignition (LOI) to assess the degree of hydration and/or LTC to investigate their pore structure. Based on a propagation of error analysis and assuming an uncertainty of 0.001 g in the mass measurements made initially and after heating at 105 °C and 1000 °C, the estimated uncertainty in the LOI-calculated degree of hydration was 0.004 [14]. For temperatures between -100 °C and 500 °C, the LTC equipment manufacturer has specified a constant calorimetric sensitivity of  $\pm 2.5$  % and a root-mean-square baseline noise of 1.5  $\mu$ W.

## 3. Computer Modeling

All simulations were conducted using the CEMHYD3D V3.0 computer programs [19]. Starting microstructures that matched the measured w/c, particle size distribution, phase composition, and phase distribution of cement 152 were created. Because no water-reducing agents were used in the experiment, the digitized spherical cement particles were flocculated, by randomly moving and aggregating together the individual cement particles prior to hydration [5]. Hydration simulations were conducted under sealed conditions and the percolation of the solids was monitored to compare to the physical measurements of setting [20]. During the percolation evaluation, two touching (flocculated) particles are not considered to be connected unless they are bridged by some volume of hydration products, specifically the C-S-H or one of the aluminate hydration products [2, 5, 20]. The volume fractions of the total

solids and of the connected solids, defined as those bridging from one side of the microstructure to the opposite one, averaged over the three principal directions, was recorded as a function of hydration cycles. For hydration at 25 °C, a conversion factor of 0.00035 h/cycle<sup>2</sup> was used to convert between hydration cycles (squared) and real time [13].

## **4. Results and Discussion**

### **4.1 Bridge Building: Percolation of Solids and Setting**

Several previous studies have shown a quantitative relationship between setting as measured by the Vicat needle method [15] and the percolation of the solids in a three-dimensional microstructural model [20, 21]. For the standard ASTM technique [15], the Vicat measurements are generally made on a rather low ( $< 0.3$ ) w/c cement paste. It is expected that the setting process would be a strong function of w/c [16-18], as the bridges being constructed to connect the particles together will generally need to be longer and/or fewer bridges per unit hydration of cement will be created when the w/c is increased.

Experimental and computer modeling results examining four different views of the “setting” process are provided in Figures 2 and 3. Figure 2 compares experimental measurements of the yield stress via stress growth measurements [16-18] with the computer modeled volume fractions of total solids, both as a function of hydration time for cement pastes with three different w/c (the stress growth measurement technique could not be applied to the w/c=0.3 cement pastes due to its high initial stiffness). As the cement particles flocculate together following mixing, they form a weak solid skeleton that is strengthened and reinforced by the cement hydration products. For a high enough w/c, this initial skeleton can not support itself under gravity so that settlement and bleeding will occur. In fact, minor bleeding was observed for the w/c=0.45 cement paste prepared with CCRL cement 152, and the initial yield stress values in Figure 2 are quite low. As the w/c is lowered to 0.4 and then to 0.35, the measured yield stress becomes higher as a greater applied stress is necessary to get the (greater number of) particles moving in the more concentrated suspensions. Initially, the model-predicted solids volume fraction and the measured yield stress track each other fairly closely, but for each w/c ratio, a point is reached where the measured yield stress climbs rapidly while the modeled volume fraction of solids continues to increase at a relatively constant and much slower rate. It is here that the percolation of the partially hydrated cement particles by the hydration products comes into play.

The bridges built by the hydration products are much stronger than the initial interparticle forces flocculating the particles together. As these bridges percolate the three-dimensional microstructure, a finite resistance to the penetration of the Vicat needle is developed, as shown in Figure 3. The time at which the needle resistance, equal to (40 mm – the needle penetration in mm), begins to increase from zero in Figure 3 is seen to correspond closely to the time when the measured yield stress begins to diverge in Figure 2. In Figure 3, the needle resistance measurements are seen to also be in general agreement with the modeled volume fraction of connected solids that characterizes the volume fraction of unhydrated cement clinker particles that are bridged by hydration products. All of this has occurred during the time when only the first 4 % to 8 % of the cement has hydrated. Already at this point, the solid skeleton is well in



place and the strength of the microstructure will continuously increase as new bridges are formed and existing ones are expanded.

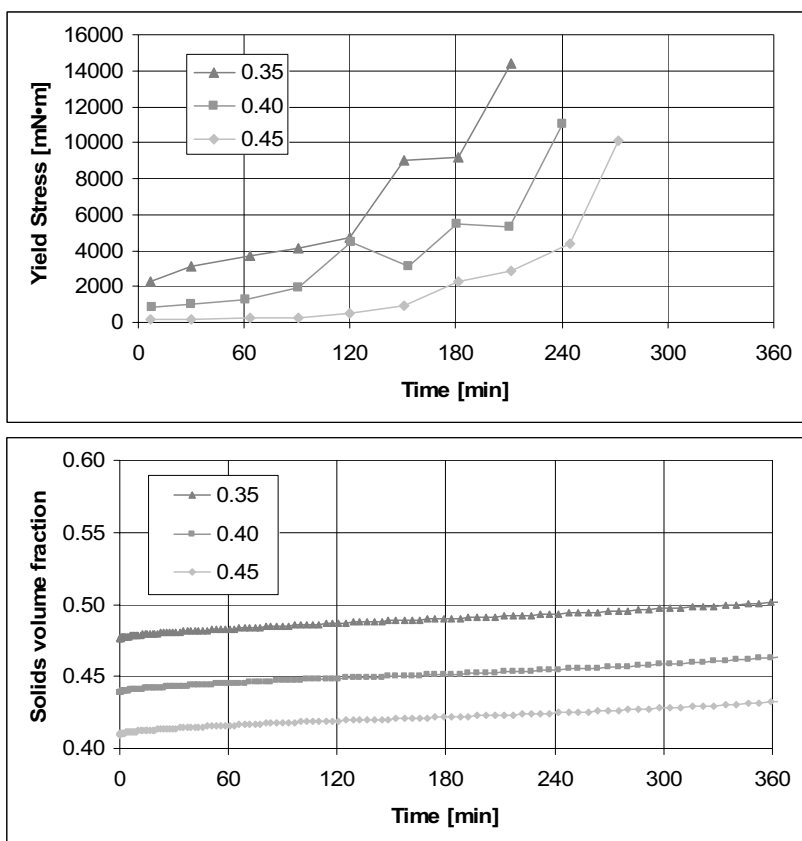


Figure 2: Two “views” of the setting process in cement paste as a function of w/c: yield stress by stress growth measurements (top) and total solids volume fraction (bottom).

#### 4.2 Dam Building: Depercolation of Capillary Porosity and Influences of Curing Conditions and Cement Alkali Content

While Powers first inferred depercolation of the capillary porosity in hydrating cement paste via measurements of permeability [9], the depercolation can also be observed based on chemical shrinkage measurements on pastes of various thicknesses [22] or via low temperature calorimetry scans [23-25]. A cooling scan in an LTC experiment is basically equivalent to a mercury porosimetry intrusion scan [23], but with the advantage that no drying of the specimen is required. Generally, a percolated **water-filled** capillary pore structure is indicated by a peak around -15 °C [25]. Thus, the presence or absence of this peak can be used to infer a percolated or depercolated capillary pore structure, respectively.

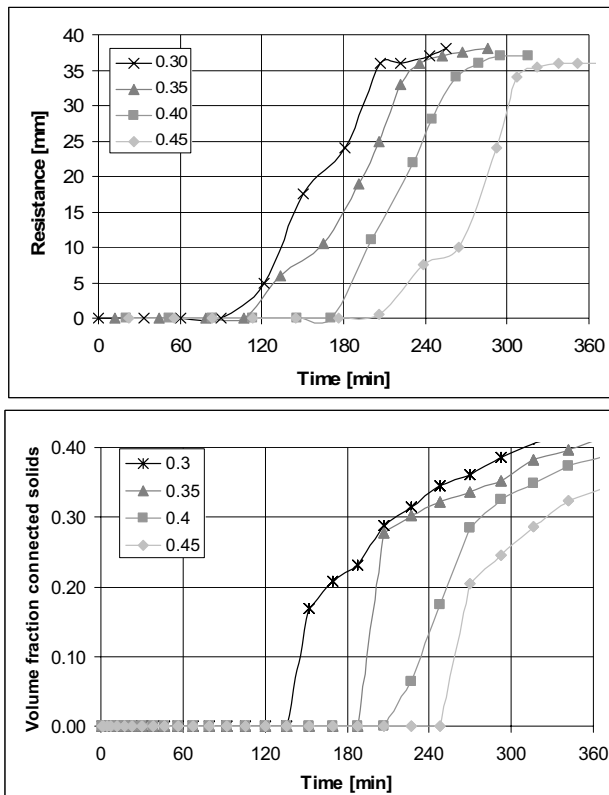


Figure 3: Two more “views” of the setting process in cement paste as a function of w/c: needle resistance (top) and connected solids volume fraction (bottom).

Figure 4 provides representative LTC scans of a w/c=0.35 cement paste cured under saturated or sealed conditions, along with scans on the pastes cured under sealed conditions after 24 h or more of resaturation. The w/c=0.35 is low enough that depercolation of the capillary pores would be expected to occur during the first week of curing [9]. For the various scans in Figure 4, basically three different peaks are observed corresponding to percolated capillary pores (freezing at about -15 °C), open gel pores (freezing at -25 °C to -30 °C), and dense gel pores (freezing at -40 °C to -45 °C) as defined in [25]. For saturated curing, the capillary pores are observed to depercolate between 3 d and 4 d of curing. Initially, a similar depercolation is observed for the capillary pores in the specimens exposed to sealed curing conditions. After a few weeks of curing, the open gel pores generally also depercolate, so that only pores accessible via the dense gel pores are detected via LTC. Specimens cured under sealed conditions are consistently seen to have smaller peaks for the capillary and open gel pores, as these larger pores are the first to empty due to chemical shrinkage and self-desiccation [12, 26].

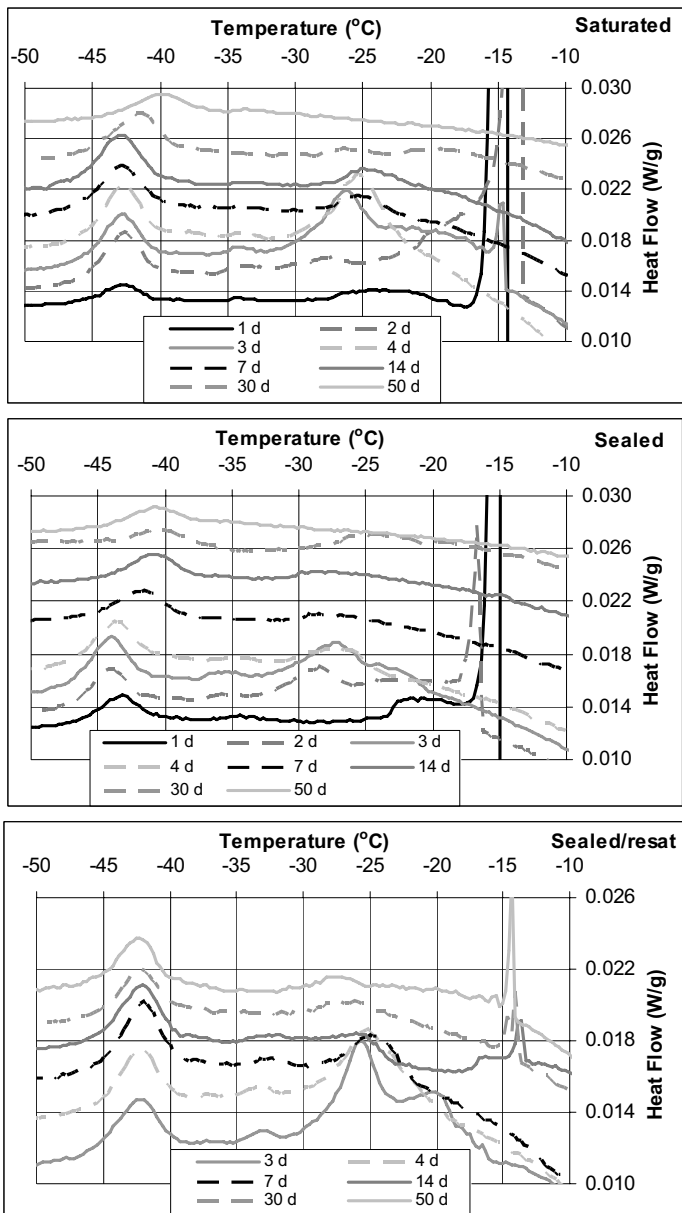


Figure 4: LTC results for CCRL cement 152 specimens ( $w/c=0.35$ ,  $20\text{ }^{\circ}\text{C}$ ) at various ages, cured under saturated (top) and sealed (middle) conditions and for specimens cured under sealed conditions for the indicated number of days and then resaturated (bottom) [12].

Interestingly, resaturation of the sealed specimens reveals a change in the percolation of the capillary pores that is not observed for the specimens cured under saturated conditions. For sealed conditions, while the capillary pores do initially depercolate, by 14 d, when resaturated, the specimens exhibit a re-percolated set of capillary pores (bottom plot for Figure 4), most likely due to the autogenous stresses and strains placed on the three-dimensional microstructure due to self-desiccation [26]. Similar effects have been observed by Bager and Sellevold upon exposing well-hydrated cement pastes to drying/resaturation [23]. Drying, whether external or internal (self-desiccation), results in the creation of a percolated set of capillary pores (or perhaps microcracks). As shown by the scanning electron micrographs in Figure 5, the specimens cured under sealed conditions definitely contain a set of large capillary pores relative to those present in the paste specimens cured under saturated conditions. Thus, a plausible explanation for the behavior observed for the sealed/resaturated specimens is that the autogenous shrinkage of the C-S-H gel reopens the entryways of the previously depercolated capillary pore network. Still, it can not be ruled out that some microcracks could also participate in either re-percolating the capillary pores or creating their own percolated network of porosity.

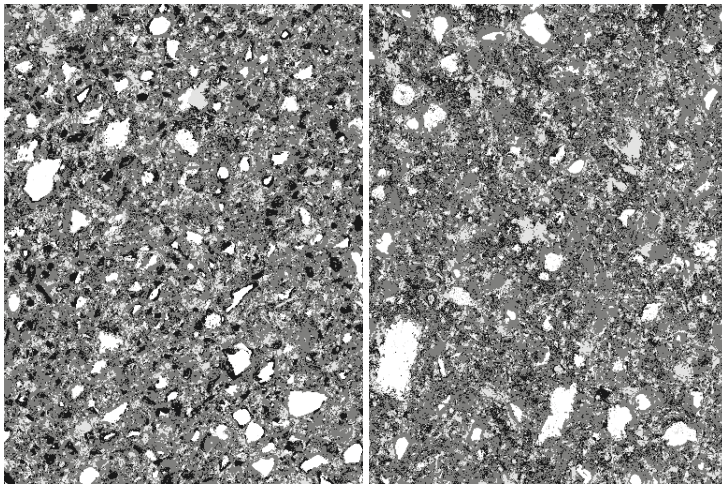


Figure 5: Ninety-two day (92 d) segmented scanning electron microscopy (SEM) images for CCRL cement 152,  $w/c=0.35$  cement paste specimens cured under sealed (left) and saturated (right) conditions [12]. Unhydrated cement particles are white, calcium hydroxide is light grey, C-S-H and other hydration products are dark grey, and capillary pores are black. Images are 384  $\mu\text{m}$  by 512  $\mu\text{m}$ .

While sealed curing appears to be detrimental in terms of microstructure (specifically pore structure) development for  $w/c=0.35$  pastes, for  $w/c=0.435$  pastes, as illustrated by the LTC cooling scans in Figure 6, it may actually be beneficial. As self-desiccation occurs during sealed curing, the largest water-filled pores in the three-dimensional microstructure will empty first [12, 26]. Since cement hydration products will generally not precipitate and grow in air

(or water vapor)-filled pores, hydration product formation will tend to be concentrated in the remaining smaller pores and pore entryways, where it should be more effective in depercolating the (water and vapor-filled) capillary pores [12], as supported by the experimental results in Figure 6. Thus, if curing to minimize transport and maximize durability, for an intermediate range of  $w/c$  (e.g., 0.4 to 0.45), some type of sealed/saturated curing could be superior to maintaining saturated conditions throughout. Such a seemingly counterintuitive concept is not new, having been suggested by both Swayze [27] and Powers [28] over 50 years ago.

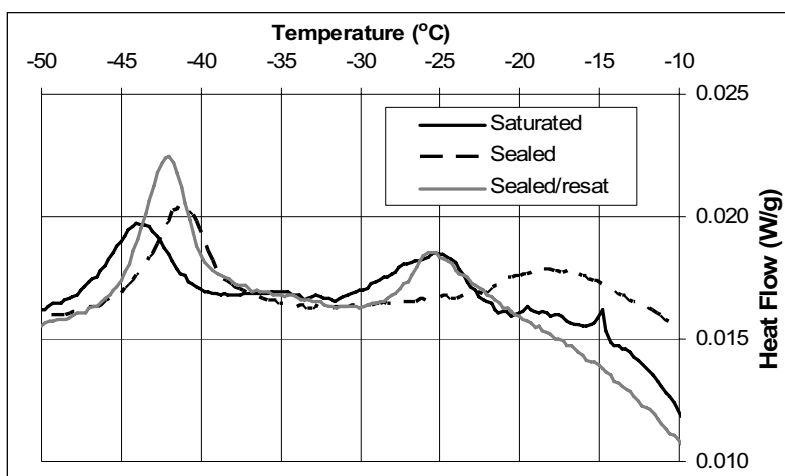


Figure 6: LTC results for CCRL proficiency cement 152 specimens ( $w/c=0.435$ ,  $20\text{ }^{\circ}\text{C}$ ) cured for 214 d [12].

Recently, it has been demonstrated that the percolation of the capillary porosity in hydrating cement paste can also be influenced by the level of alkalis in the cement paste [12, 14]. In the presence of sufficient alkali ions, the C-S-H has a tendency to form lath or plate-like nanostructures, with a higher degree of crystallinity [29]. Simple three-dimensional microstructure models have indicated that hydration products forming as needles or plates, as opposed to a random geometry, can be more efficient at depercolating the capillary pore space between the original cement particles [14]. In Figure 7, LTC cooling scans are provided for a set of hydrated cement pastes with and without additional alkalis, all of which have achieved nominally the same degree of hydration after 8 d of curing at  $20\text{ }^{\circ}\text{C}$  [14]. While the paste with no additional alkalis clearly contains both percolated capillary and open gel pore structures, only dense gel pores are identified in the pastes with either alkali sulfate or alkali hydroxide additions. For both additions, the same molar quantities of potassium and sodium ions (per unit mass of cement) were added to the mixing water and dissolved completely prior to the addition of the cement. This example illustrates one potential method for engineering the nanostructure of the dams formed during cement hydration.

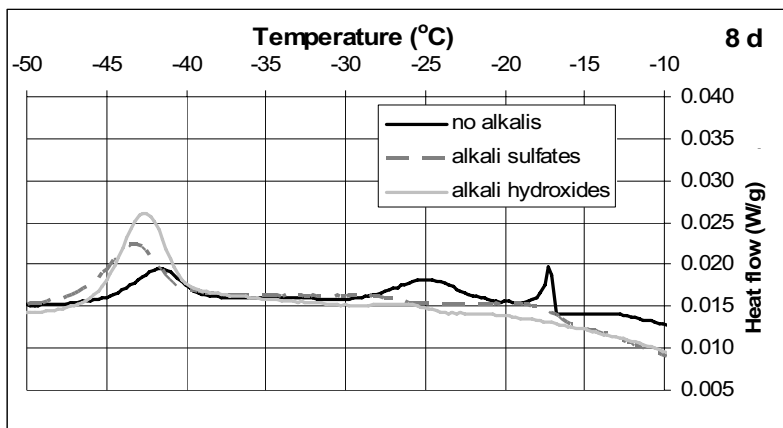


Figure 7: LTC results for CCRL cement 140 specimens ( $w/c=0.40$ , hydrated under saturated conditions for 8 d at 20 °C) with and without alkali additions (sulfates or hydroxides) [14]. All specimens have achieved basically the same degree of hydration, as measured using LOI [14].

#### 4.3 Prospectus for Future Research --- Migration from Microstructure to Nanostructure

In the future, the research focus will likely move from the microstructure created by the bridges and dams to the nanostructure of the bridges and dams themselves. For example, silica fume has a significant influence on the nanostructure of the dams, as illustrated by its large (up to 25X) influence on transport through the C-S-H gel [30]. As shown above, alkalis also definitely influence the nanostructure and crystallinity of the C-S-H gel. The nanostructure of the C-S-H gel is already being extensively studied, and atomic and nanostructure-level models are being advanced [29, 31, 32]. The ultimate engineering of the microstructure of cement-based materials will reach fruition only when the nanostructures of the bridges and dams comprising its building blocks are understood and predictable.

## 5. Conclusions

The construction of microstructural bridges and dams within hydrating cement paste has been investigated using a coordinated experimental/computer modeling approach. Bridge building is seen to be critical for the setting process, and of course also for the subsequent development of strength and mechanical properties. On the other hand, dam building is critical in depercolating the capillary porosity, leading to reduced transport coefficients and hopefully enhanced durability. Opportunities for engineering not only the nanostructure of the bridges and dams but also how they assemble at the microstructure level exist and will surely lead to innovative new materials and structures.

## Acknowledgements

The author would like to thank Dr. Chiara Ferraris and Mr. John Winpiger of BFRL/NIST for obtaining and processing the needle penetration and rheological data presented in this paper.

## References

1. Bentz, D.P., 'Influence of water-to-cement ratio on hydration kinetics: Simple models based on spatial considerations', accepted by *Cement and Concrete Research* 2005.
2. Bentz, D.P., Garboczi, E.J., Haecker, C.J., and Jensen, O.M., 'Effects of cement particle size distribution on performance properties of cement-based materials', *Cement and Concrete Research* **29** (1999) 1663-1671.
3. Knudsen T., 'The dispersion model for hydration of portland cement 1. General concepts', *Cement and Concrete Research* **14** (1984) 622-630.
4. Osbaeck B., and Johansen V., 'Particle size distribution and rate of strength development of portland cement', *Journal of the American Ceramic Society* **72** (2) (1989) 197-201.
5. Bentz, D.P., Garboczi, E.J., and Martys, N.S., 'Application of digital-image-based models to microstructure, transport properties, and degradation of cement-based materials', in 'The Modelling of Microstructure and Its Potential for Studying Transport Properties and Durability', Eds. H.M. Jennings et al. (Kluwer Academic Publishers, 1996) 167-186.
6. Bentz, D.P., Mizell, S., Satterfield, S., Devaney, J., George, W., Ketcham, P., Graham, J., Porterfield, J., Quenard, D., Vallee, F., Saltee, H., Bollor, E., and Baruchel, J., 'The visible cement data set', *Journal of Research of the National Institute of Standards and Technology* **107** (2) (2002) 137-148.
7. Bentz, D.P., 'Quantitative comparison of real and CEMHYD3D model microstructures using correlation functions', accepted by *Cement and Concrete Research* 2005.
8. Holzer, L., Gasser, Ph., and Münch, B., 'Three Dimensional Analysis of the Pore-Network in Cement Pastes Using FIB-Nanotomography,' submitted, 2005.
9. Powers, T.C., 'Capillary continuity or discontinuity in cement paste', *PCA Bulletin* **10** (1959) 2-12.
10. Cement and Concrete Reference Laboratory, 'Cement and concrete reference laboratory proficiency sample program: Final report on portland cement proficiency samples number 139 and 140', Gaithersburg, MD, March 2001.
11. Cement and Concrete Reference Laboratory, 'Cement and concrete reference laboratory proficiency sample program: Final report on portland cement proficiency samples number 151 and 152', Gaithersburg, MD, April 2004, available at <http://www.ccril.us>.
12. Bentz, D.P., and Stutzman, P.E., 'Curing, hydration, and microstructure of cement paste', submitted to *ACI Materials Journal* 2005.
13. Bentz, D.P., 'Modeling the influence of limestone filler on cement hydration using CEMHYD3D', accepted by *Cement and Concrete Composites* 2005.
14. Bentz, D.P., 'Influence of alkalis on porosity percolation in hydrating cement pastes', submitted to *Cement and Concrete Composites* 2005.
15. ASTM C191-04b, 'Standard Test Method for Time of Setting of Hydraulic Cement by Vicat Needle,' ASTM Annual Book of Standards, Vol. 04.01 Cement; Lime; Gypsum (American Society for Testing and Materials, West Conshohocken, PA, 2004).
16. Amziane, S., and Ferraris, C.F., 'Monitoring of setting evolution of cementitious materials by measurements of rheological properties and hydraulic pressure variations', submitted to *ACI Materials Journal* 2005.

17. Amziane, S., and Ferraris, C.F., 'SCC evolution of formwork hydraulic pressure and rheological properties', ACI Proceedings (New York), 2005.
18. Amziane, S., and Ferraris, C.F., 'Caractérisation de la prise des matériaux cimentaires', Proc. of the GFR convention, Mulhouse (France) October 2004 (in French).
19. Bentz D.P., 'CEMHYD3D: A three-dimensional cement hydration and microstructure development modelling package. Version 3.0', NISTIR **7232**, U.S. Department of Commerce, June 2005.
20. Haecker, C.J., Bentz, D.P., Feng, X.P., and Stutzman, P.E., 'Prediction of cement physical properties by virtual testing', *Cement International* **1** (3) (2003) 86-92.
21. Princigallo, A., Lura, P., van Breugel, K., and Levita, G., 'Early development of properties in a cement paste: A numerical and experimental study', *Cement and Concrete Research* **33** (2003) 1013-1020.
22. Geiker, M., 'Studies of portland cement hydration: Measurement of chemical shrinkage and a systematic evaluation of hydration curves by means of the dispersion model', Ph.D. Thesis, Technical University of Denmark, Lyngby, Denmark, 1983.
23. Bager, D.H., and Sellevold, E.J., 'Ice formation in hardened cement paste, Part II- Drying and resaturation on room temperature cured pastes', *Cement and Concrete Research* **16** (1986) 835-844.
24. Villadsen, J., 'Hærdetemperaturens indflydelse på hærdnet cementpastas porestruktur: Projekttrapport', The Technical University of Denmark, Lyngby, Denmark, 1989.
25. Snyder, K.A., and Bentz, D.P., 'Suspended hydration and loss of freezable water in cement pastes exposed to 90% relative humidity', *Cement and Concrete Research* **34** (11) (2004) 2045-2056.
26. Bentz, D.P., Jensen, O.M., Hansen, K.K., Oleson, J.F., Stang, H., and Haecker, C.J., 'Influence of cement particle size distribution on early age autogenous strains and stresses in cement-based materials', *Journal of the American Ceramic Society* **84** (1) (2001) 129-135.
27. Swayze, M.A., 'Early concrete volume changes and their control', *Journal of the American Concrete Institute* **13** (5) (1942) 425-440.
28. Powers, T.C., 'A discussion of cement hydration in relation to the curing of concrete', *Proceedings of the Highway Research Board* **27** (1947) 178-188.
29. Richardson I.G., 'Tobermorite/jennite- and tobermorite/calcium hydroxide-based models for the structure of C-S-H: Applicability to hardened pastes of tricalcium silicate,  $\beta$ -dicalcium silicate, portland cement, and blends of portland cement with blast-furnace slag, metakaolin, or silica fume', *Cement and Concrete Research* **34** (2004) 1733-1777.
30. Bentz, D.P., Jensen, O.M., Coats, A.M., and Glasser, F.P., 'Influence of silica fume on diffusivity in cement-based materials. I. Experimental and computer modeling studies on cement pastes', *Cement and Concrete Research* **30** (2000) 953-962.
31. Nonat, A., 'The structure and stoichiometry of C-S-H', *Cement and Concrete Research* **34** (2004) 1521-1528.
32. Cong, X., and Kirkpatrick, R.J., ' $^{29}\text{Si}$  MAS NMR study of the structure of calcium silicate hydrate', *Advanced Cement-Based Materials* **3** (1996) 144-156.



## **Strength Development and Microstructure of Fly Ash-Cement Mixes at Early Age**

Kiyofumi Kurumisawa and Toyoharu Nawa  
Graduate school of engineering, Hokkaido University, Japan

### **Abstract**

Strength development of fly ash-cement mixes is strongly influenced by early age curing. Strength development of cementitious mixes is essentially related to their microstructure. However, there have been few reports concerning effects of initial curing on strength development and microstructure of fly ash-cement mixes. In this study, the influence of curing condition on compressive and bending strength development of fly ash-cement mixes and their microstructures at early ages, were investigated using strength testing and the backscattered electron image method. From the results, it was evident that the relationship between strength development and microstructure was greatly dependent on the type of cement mixed with fly ash.

### **1. Introduction**

Fly ash is increasing in Japan as the amount of thermal power generation increases. The disposal of fly ash becomes a problem because the majority is disposed by reclaiming. Therefore, it was thought that it would be very useful to use fly ash as a concrete mixture material. However, while fly ash has the advantage of improving the long-term strength development and fluidity etc. when using it as a mineral admixture material for concrete, there is the disadvantage of the delay in initial strength development. If the initial strength development of concrete with fly ash is improved, then it can be used more effectively. Therefore, the curing temperature is raised to solve the problem, and the method of mixing the additives for activating the reaction of fly ash is examined<sup>1)-6)</sup>. However, the influence of the microstructure on initial strength development is not well clarified. In this study, initial strength development of cement-based materials with fly ash was examined from the microstructure point of view.

## 2. Material and experimental

### 2.1 Specimen preparation

#### (1) Cement

Ordinary portland cement (OPC), low heat portland cement (LHC) and rapid hardening portland cement (RHC) were used in this study. Chemical compositions of the cements are shown in Table 1. The result of calculating their potential Bogue composition is shown in Table 2. OPC and RHC have almost the same mineral composition. The amount of Belite in LHC is larger than that of Belite in OPC and RHC.

Backscatter electron images (BEI) of OPC, LHC and RHC particles are shown in Figs.1 – 3. The shapes of the cement particles were different depending on the type of cement.

#### (2) Fly ash

The properties of fly ash are shown in Table 3. The fly ash used in this study was of low calcium content.

#### (3) Mixture proportions

Mixture proportions of the mortars prepared in this study are shown in Table 4. In the mortars, the water to solid ratio of all the specimens is 145% by volume, and the sand to paste ratio is 1.4 by volume. Mortar was used for measuring strength. The water to solid ratio of the cement paste is also 145% by volume. Mixing time was 3 minutes. Cement paste was used for measuring BEI. Cement paste and mortar underwent sealed curing at 20°C until the measuring time.

Table 1 Chemical composition of cement

	Chemical composition (%)					
	SiO <sub>2</sub>	Al <sub>2</sub> O <sub>3</sub>	Fe <sub>2</sub> O <sub>3</sub>	CaO	MgO	SO <sub>3</sub>
OPC	21.5	5.5	2.9	64.3	1.9	1.8
RHC	20.4	4.8	2.5	64.4	2.3	3.2
LHC	25.9	3.2	3.7	63.1	0.1	2.4

Table 2 Mineral compositions

	OPC	LHC	RHC
Alite (%)	51.99	26.5	62.26
Belite (%)	22.71	54.31	11.82
Aluminate (%)	9.83	2.25	8.51
Ferrite (%)	8.72	11.25	7.48
Gypsum (%)	5.1	6.95	9.12

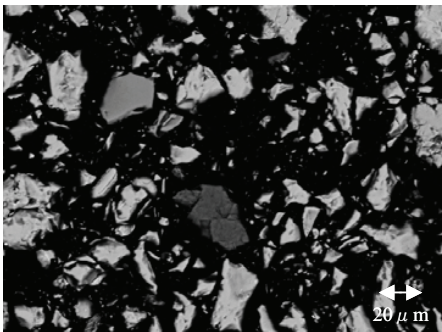


Fig.1 BEI of OPC particles

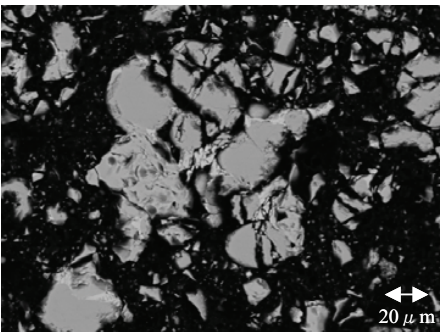


Fig.2 BEI of LHC particles

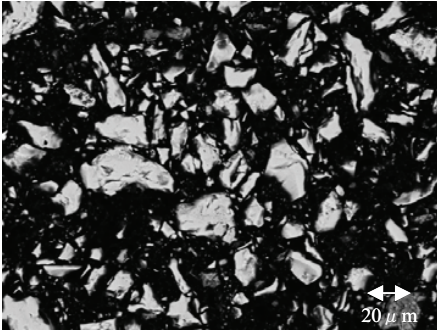


Fig.3 BEI of RHC particles

Table 3 Properties of fly ash

Ignition loss	(%)	2.0
SiO <sub>2</sub>	(%)	72.53
Al <sub>2</sub> O <sub>3</sub>	(%)	16.72
Fe <sub>2</sub> O <sub>3</sub>	(%)	2.95
CaO	(%)	1.63
MgO	(%)	1.23
Na <sub>2</sub> O	(%)	0.29
K <sub>2</sub> O	(%)	0.96
SO <sub>3</sub>	(%)	0.20
TiO <sub>2</sub>	(%)	0.68
MnO <sub>2</sub>	(%)	0.02
Surface area	(cm <sup>2</sup> /g)	3900
density	g/cm <sup>3</sup>	2.11

Table 4 Mix proportion of mortar

	Replacement ratio of Fly ash	Cement	W/S		Sand/Paste	
			by volume	by mass	by volume	by mass
OPC	0	OPC	145	45.9	1.4	1.964
LHC	0	LHC	145	44.8	1.4	1.931
RHC	0	RHC	145	46.3	1.4	1.977
OPC-fly ash	15	OPC	145	48.3	1.4	2.034
LHC-fly ash	15	LHC	145	47.2	1.4	2.003
RHC-fly ash	15	RHC	145	48.7	1.4	2.045

## 2.2 Measurements

### (1) Strength test

For compressive and bending strength tests three measurements were performed for each mixture and averaged to obtain the mean strength values. The dimensions of the specimens for compression tests were 400×400×400 mm and for the four-point-bending tests were 400×400×1000 mm at 3,7,28 and 91day.

### (2) BEI measurement

5mm thick cubes of pastes were prepared and immersed in acetone for approximately 24 h to remove most of the water by solvent exchange. D-drying was applied to the specimens to remove most of the acetone. They were then immersed in a low viscosity epoxy resin under

vacuum at room temperature. After the impregnated resin was hardened, the surface of specimens was polished first with sand paper and then with diamond paste. Finally, a carbon coating was applied. The specimens were examined at 15 KeV by SEM with BSE detector. The degree of hydration of cement ( $\alpha$ ) is calculated by this equation<sup>7)8)</sup>,

$$\alpha = 1 - \frac{UH_i}{(UH_0 * (1 - V_{RS}))}$$

UH<sub>0</sub>: initial area fraction of unhydrated cement particles  
UH<sub>i</sub>: area fraction of unhydrated cement particles at the age of t<sub>i</sub>  
V<sub>RS</sub>: area fraction of gypsum in the original cement powder.

3. Results

3.1 Results of strength tests

(1) Compressive strength tests

Fig.4 shows results of compressive strength tests of the mortars. Strength of all specimens is increasing with age. At early age, the strength of LHC is lower than that of OPC and RHC but the strength of LHC at 91days is higher than that of OPC.

Fig.5 shows results of compressive strength tests of mortars mixed with fly ash. These results are similar to those of the mortars without fly ash. However, the strength of LHC-fly ash at 91days is higher than that of the other cements. Furthermore, the development of strength of the mortar using low heat cement from 7days to 28days is considerably larger.

(2) Bending strength tests

The results of bending tests are shown in Figs.6-7. The results for bending strength are different from the results for compressive strength. It is observed that the strength of LHC after 28days was higher than the other cements. In the mixtures with fly ash, a similar tendency was shown. Bending strength of fly ash mortar using low heat cement increases

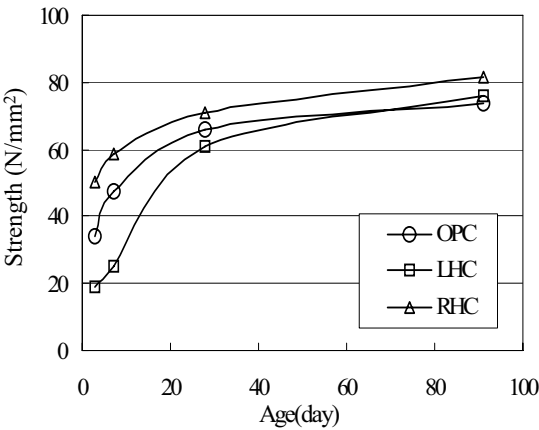


Fig.4 Results of compressive strength test

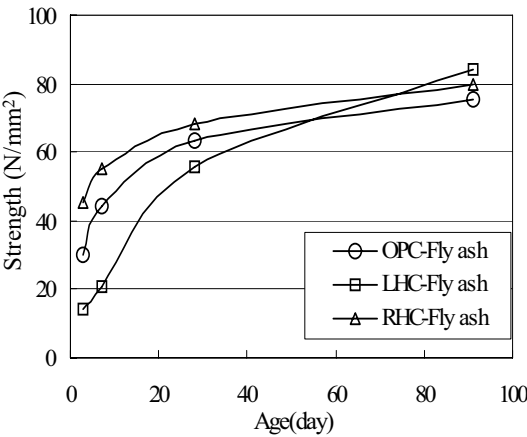


Fig.5 Results of compressive strength

gradually after 28days though the strength of the fly ash mortar using other cements hardly increases.

(3) Results of BEI

BEIs of hardened cement paste with fly ash are shown in Figs.8-10. High brightness pixels show unhydrated cement particles. Brighter grey shows calcium hydroxide and darker grey shows CSH. Also, a part of grey is fly ash in the circle and black pixels show pores. Each image is from a 28-day specimen observed at a magnification of 500X. Unhydrated cement particles in OPC-fly ash and RHC- fly ash are rarely seen. However, larger unhydrated cement particles are seen in BEI of LHC- fly ash and almost all of the unhydrated cement particles are Belite. There is a large amount of calcium hydroxide area in OPC-fly ash and RHC-fly ash.

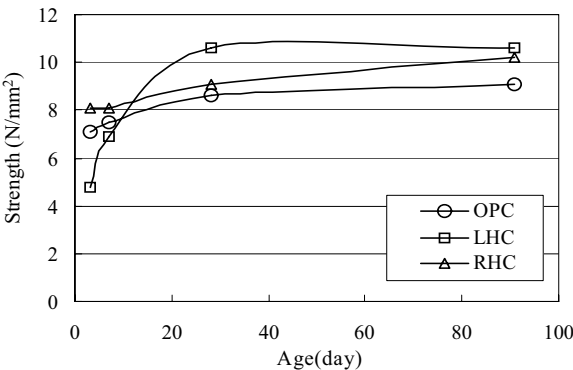


Fig.6 Results of bending strength test

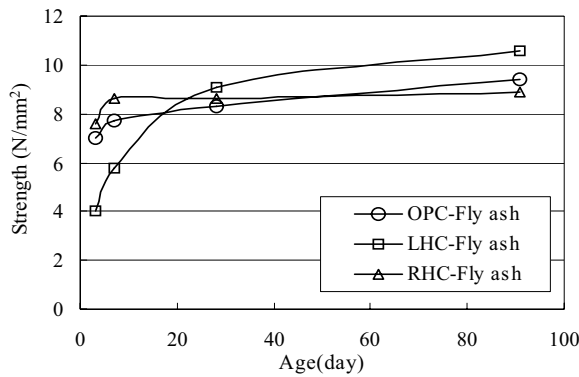


Fig.7 Results of bending strength test

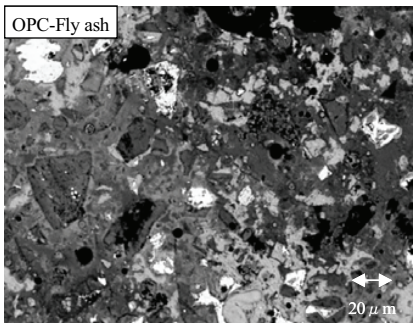


Fig.8 BEI of OPC-Fly ash paste  
(28days, x 500)

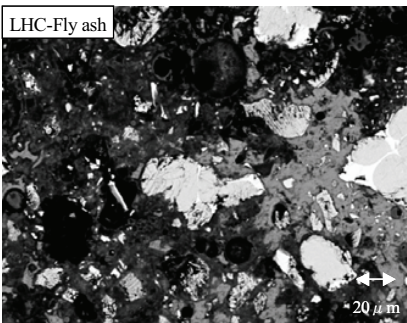


Fig.9 BEI of LHC-Fly ash paste  
(28days, x 500)

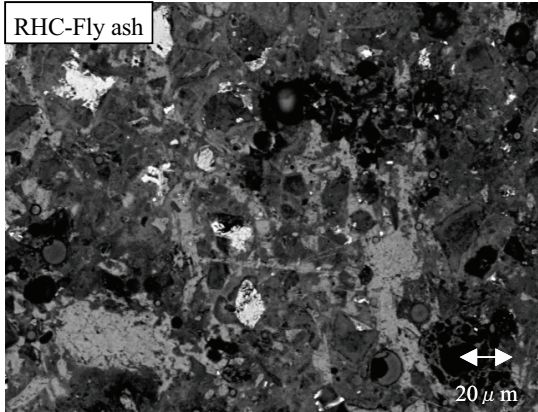


Fig.10 BEI of RHC-Fly ash paste (28days,  
x 500)

4. Discussion

The effect of the degree of hydration of cement on compressive strength is shown in Fig.10. Strength increases with an increase of the degree of hydration of cement. It is shown that it is greatly influenced by the hydration of cement. It is clearly indicated that the strength development at early age is dependent on the type of cement.

However, the same correlation was not seen for the relation between strength and the degree of hydration of LHC cement. This is because the degree of hydration of the hardened cement paste that uses the low heat cement from the 7<sup>th</sup> day to the 28<sup>th</sup> day could not be measured accurately. It will be necessary to examine this further in the future.

The effect of the degree of hydration for specimens mixed with different ratio of fly ash on compressive strength is shown in Fig.11. The strength of mortar mixed with 50%vol of fly ash increases regardless of the degree of hydration of cement after 7days. Moreover, the strength of the mortar that includes fly ash greatly depends on the

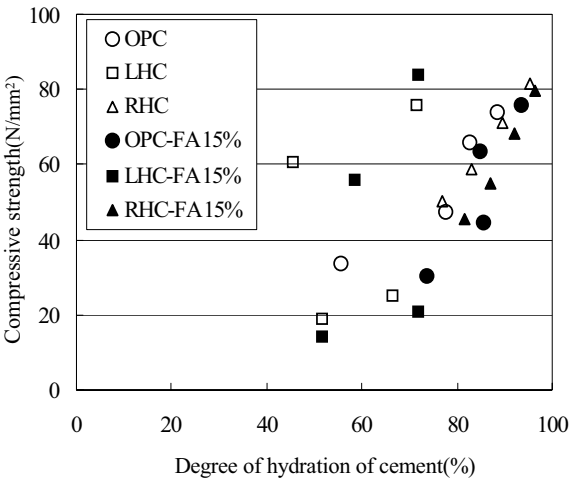


Fig.11 Effect of the degree of hydration of cement on compressive strength

strength of the cement in mixing up to 25% by volume.

The degree of hydration of cement increases when fly ash is mixed at 50%vol at early age. It is thought that this is because the hydration of the cement became more active by including fly ash.

It is reported the compressive strength is related the gel/space ratio<sup>9)</sup>. The result of calculation using the equation proposed by L. Lam<sup>9)</sup> is shown in Fig.12. There is a good relationship between the compressive strength and the gel/space ratio without specimens of LHC at 28 and

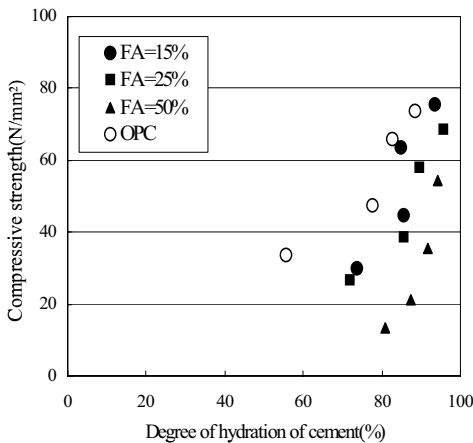


Fig.12 Effect of the degree of hydration of cement mixed with different ratios of fly ash on compressive strength

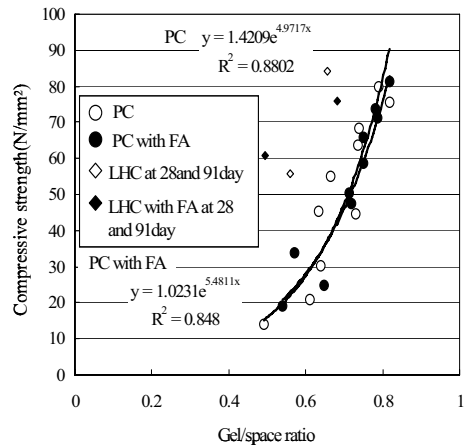


Fig.13 Relationship between the compressive strength and the gel/space

91day. However, there is no relationship between the strength and the gel/space ratio including specimens of LHC with longer age. It is thought that CSH gel formed from belite is different from that formed from alite.

## 5. Conclusions

In this study, the strength of LHC with fly ash at early age is lower than that of other cement with fly ash, but the strength of LHC with fly ash after more than 91days is higher than that of other cements with fly ash. Therefore, the type of cement is very important for the development of strength in fly ash-cement mortars at early ages.

## Acknowledgements

The authors would like to acknowledge support from the MAEDA ENGINEERING FOUNDATION. And the authors would like to thank Mr.Yamashiro and Mr.Saito for the preparation of samples and measurements of strength.

## References

1. H.Yazici, S.Aydin, H.Yigiter, B.Baradan: Effect of steam curing on class C high-volume flyash concrete mixtures, *Cement and Concrete Research*, in press
2. J. Payá, J. Monzó, E. Peris-Mora, M. V. Borrachero, R. Tercero and C. Pinillos: Early-strength development of portland cement mortars containing air classified fly ashes, *Cement and Concrete Research*, Vol. 25 (2), 1995, pp. 449-456
3. C. Shi and R. L. Day: Acceleration of the reactivity of fly ash by chemical activation, *Cement and Concrete Research*, Vol. 25 (1), 1995, pp. 15-21
4. C. Shi: Early microstructure development of activated lime-fly ash pastes, *Cement and Concrete Research*, Vol.26 (9), 1996, pp. 1351-1359
5. Y. Maltais and J. Marchand: Influence of curing temperature on cement hydration and mechanical strength development of fly ash mortars, *Cement and Concrete Research*, Vol. 27 (7), 1997, pp. 1009-1020
6. C. Y. Lee, H. K. Lee and K. M. Lee: Strength and microstructural characteristics of chemically activated fly ash–cement systems, *Cement and Concrete Research*, Vol. 33 (3), 2003, pp. 425-431
7. S.Igarashi, A.Watanabe and M.Kawamura: Evaluation of capillary pore size characteristics in high-strength concrete at early ages, *Cement and Concrete Research*, Vol. 35 (3), 2005, pp. 513-519
8. Personal communication with Dr. D.P Bentz of NIST
9. L. Lam, Y. L. Wong and C. S. Poon: Degree of hydration and gel/space ratio of high-volume fly ash/cement systems, *Cement and Concrete Research*, Vol. 30 (5), 2000, pp.747-756



## The Patch Microstructure in Concrete: Evidence that it is not an Artifact

Sidney Diamond<sup>(1)</sup> and Niels Thaulow<sup>(2)</sup>

<sup>(1)</sup>School of Civil Engineering, Purdue University, USA

<sup>(2)</sup>RJ Lee Group, Inc., USA

### Abstract

Cement paste in many mortars and concretes has been previously shown by backscatter SEM to contain dense patches with high contents of residual cement grains and little visible porosity adjacent to porous patches with few such residual cement grains and a large content of detectable pores. The latter include many hollow-shell grains as well as true capillary pores. It has recently been alleged that the dense patches are artifacts caused by polishing specimens so that areas exposed on the surface examined do not contain epoxy resin; these areas are alleged to show up as the dense patches. In the present paper we show that these allegations are incorrect. The normal specimen preparation system used at Purdue University achieves depths of epoxy penetration in excess of 6 mm, rendering such polishing artifacts most unlikely. Both backscatter and secondary electron SEM examination of areas of a specific concrete specimen known *not* to contain epoxy resin show the same dense and porous patches found on fully impregnated surfaces. In secondary electron examination the pores in the porous patches show the rim brightness effect expected for empty pores and the dense patches are seen to be in fact dense, and lack these features. Dense and porous patches are also readily observed in optical microscope imaging of thin sections of many mortars and concretes in the fluorescence mode. A possible origin of the patch structure in the fresh concrete paste is suggested.

### 1. Introduction

Recently the first-named writer has provided indications that much of the hardened cement paste in various mortars and concretes examined in backscatter-mode scanning electron microscopy (SEM) exhibits separate dense paste and porous paste patches (1-4). So-called *dense* patches were characterized as often having (1) a significant local content of *large residual unhydrated grains* embedded in a zone of 'outer product' C-S-H extending over an extensive contiguous area, (2) *comparatively few visible pores*, and (3) *a distinctly bright gray level*, indicative of the presence of few sub-micron pores. In contrast, porous patches were seen to show (1) *almost no residual cement grains* (2) *a high content of readily detectable pores*, and (3) *a lower gray level*, suggesting a higher content of unresolved pores. The readily detectable pores consist both of hollow-shell hydration grains and of detectable capillary pores, the latter typically smaller than the former. In high w:c field concretes exposed to

extensive leaching, the dense patches are almost fully hydrated and do not display much unhydrated cement, but the porosity differences remain. The sizes of individual patches vary somewhat but typically they were found to be on the order of 150 - 200  $\mu\text{m}$  across; thus examination at *low* magnification (ca. 100x or 150x) is helpful to recognize their existence. The boundaries between adjacent dense and porous patches were often found to be quite sharp.

The relative proportions of dense and porous areas seems to vary with w:c ratio. The pastes in many high w:c concretes examined were found to be mostly porous, and in some of them the porous patches formed a more or less continuous phase with only occasional dense patches; on the other hand, in relatively low w:c mortars and concretes, the porous patches are generally smaller and tend to be isolated. In such mortars and concretes there is a tendency for the porous patches to be associated with some of the sand grains, but in a manner quite different from the usual concept of an interfacial transition zone. Rather, the porous patches were seen to extend for distances of several hundred  $\mu\text{m}$  into the 'bulk' paste. Also, in contrast to the usual concept of the ITZ, a considerable proportion of the paste contact surfaces of many aggregates (and the entire paste contact surfaces of some sand grains) are seen to be in contact with dense patches of little apparent porosity.

One obvious hypothesis was that these patches represented the effect of inadequate mixing. In an experimental study (3), the first named author found that an "archetypical" conventional laboratory mixed concrete (w:c 0.5, dolomite coarse aggregate, river sand, ASTM Type I cement, no admixtures) mixed in an efficient pan mixer, retained clear evidence of the patch structure even after as much as 30 minutes of mixing. The concrete underwent progressive decreases in slump, and after 45 minutes became very stiff and had entirely lost its ability to exhibit slump. At this stage enough of the dolomite coarse aggregate was abraded into powder so as to provide the equivalent of a limestone-filled paste, and the patch effect was no longer visible. Nevertheless it was obvious that prolonged and effective mixing did not eliminate the patchy structure.

In a more recent study (4) it was found, somewhat surprisingly, that in a similar concrete evidences of the patch structure were retained despite the addition of a dose of superplasticizer sufficient to cause the fresh concrete to become completely fluidized, i.e. to "collapse" in the usual slump test. Thus the patchy structure does not seem to be related to the flocculated structure of cement paste that is present in most concretes.

Observations of the patchy structures in concretes have not been confined to backscatter SEM. Such structures have been routinely found by the second-named author in thin section observations of literally hundreds of concretes using optical fluorescence microscopy. In this mode of examination the boundaries between adjacent patches are not quite so definite, since the images observed reflect the integrated effect of the full depth of the 20  $\mu\text{m}$ -thick thin section rather than deriving entirely from a plane polished surface; nevertheless the existence of the dark and light-colored patches of dense and porous pastes is often readily apparent.

However, for reasons not clear to the present writers, Wong and Buenfeld (5) and Buenfeld and Wong (6) have challenged the existence of such dense and porous patches. These authors concluded that the patch structure described above is actually an artifact of backscatter SEM

due to improper specimen preparation. Specifically, they attributed its appearance to the effect of polishing the specimen surface so that parts of the surface being examined are beyond the depth of epoxy impregnation. Such local areas of unimpregnated paste were considered by these authors to artificially (or ‘artefactually’) induce the effect of the dense patches. To quote their conclusions from Ref. 5, “The appearance of these patches comes from paste areas that have been ground and polished beyond the epoxy resin intrusion depth. In a backscattered electron image, pores not filled with epoxy are not visible because the signal is generated from the base or side walls of the pores.”

In the present paper we provide evidence that this allegation is incorrect. In point of fact, in addition to its appearance in backscatter SEM, the patch structure is easily visible in both secondary electron mode SEM and in optical microscopy, neither of which would be subject to the supposed artifact. Furthermore, backscatter SEM examinations specifically and deliberately conducted in completely unimpregnated areas show the same patch structure as is seen on fully epoxy-impregnated surfaces.

Finally, we provide comments on the likely origin of the patch structure seen in hardened concretes and mortars.

## 2. Illustrations of the Patch Structure

In this section we provide illustrations of the patch structure as seen in backscatter mode SEM. Fig. 1 provides such an illustration, taken from (4).

Porous patches, especially in low w:c ratio concretes and mortars, are often seen to be associated with sand grains. The association, obvious in Fig. 1, is not equivalent to the usual idea of the existence of a porous ITZ structure. The individual porous patches often extend up to several hundred  $\mu\text{m}$  into the ‘bulk’ paste, and often only touch a portion of the contact surface of a given aggregate; some sand grains may be entirely in contact with dense paste.

Indeed, porous patches are found without visible connection to any sand or aggregate grain, at least on the plane of examination. An illustration is provided in Fig. 2, also taken from a 28-day old laboratory concrete similar to that of Fig. 1. Of course it is possible that the section shown lies above or below an aggregate that does not intersect the specimen surface.

In Fig. 3 we provide a very low magnification illustration of the paste structure in an approximately eight-year old field concrete of estimated w:c of about 0.65. The concrete was taken from a slab that has been exposed to contact with ground water and the consequent flow of water through it by advection. It is seen that the local dense paste patches are superimposed on a mostly porous paste microstructure.

Fig. 4 provides a higher magnification view of an extensive dense paste patch taken from the same backscatter SEM specimen as Fig. 3. The dense paste patch is seen to extend “wall to wall” from one sand grain to another without appreciable visible porosity. Note that, unlike the previously-shown 28-day old concretes, this concrete is almost fully hydrated. Even in the dense patch illustrated in Fig. 4, the only residual cement relics seen are small fragments of  $\text{C}_4\text{AF}$  and occasional bits of  $\beta\text{-C}_2\text{S}$ .

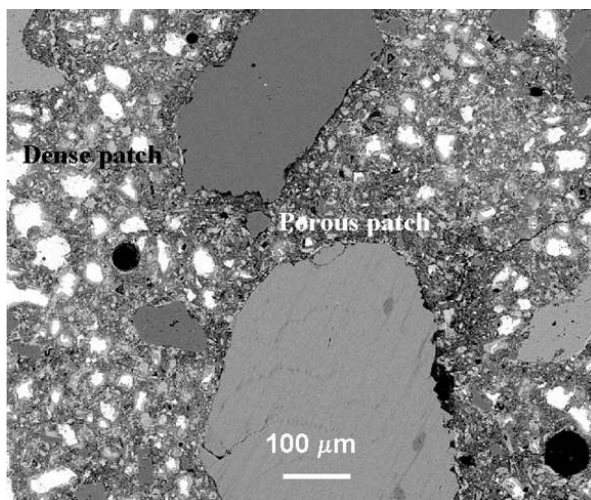


Fig. 1. Illustration of dense and porous patches as seen in a 28-day old laboratory-mixed w:c 0.50 concrete. Note the virtual absence of the residual cement grains and the darker gray level, indicative of higher porosity, in the porous patch areas.

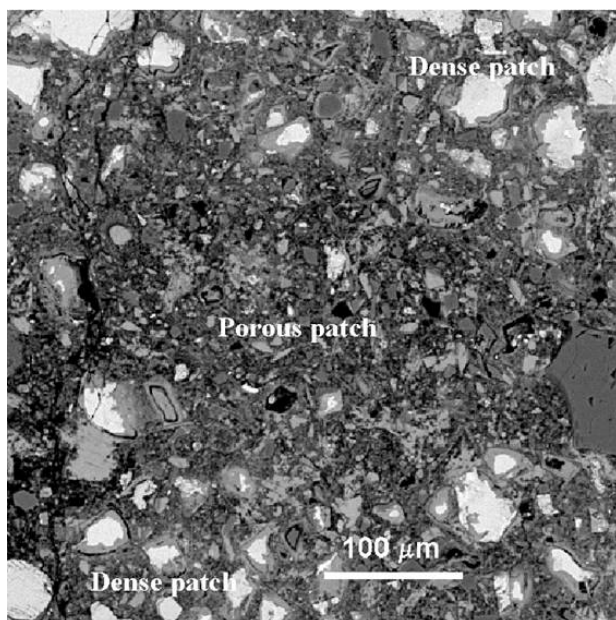


Fig.2. Porous patch without visible association to sand grains or coarse aggregate.

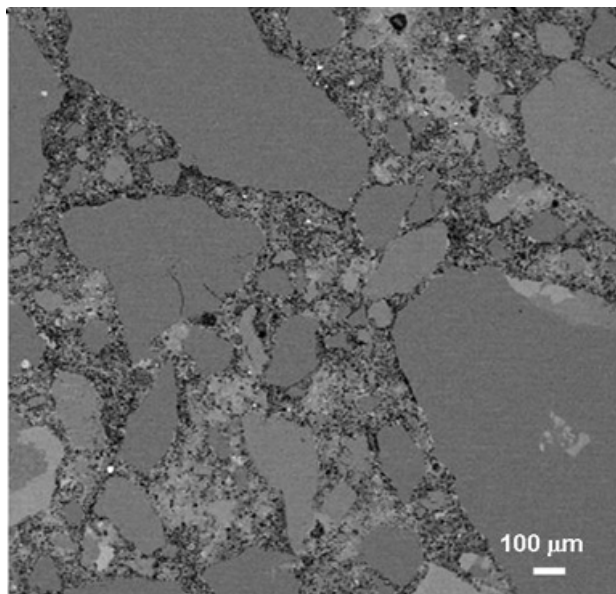


Fig. 3. Low magnification view illustrating the patch structure observed in a mature high w:c ratio field concrete.

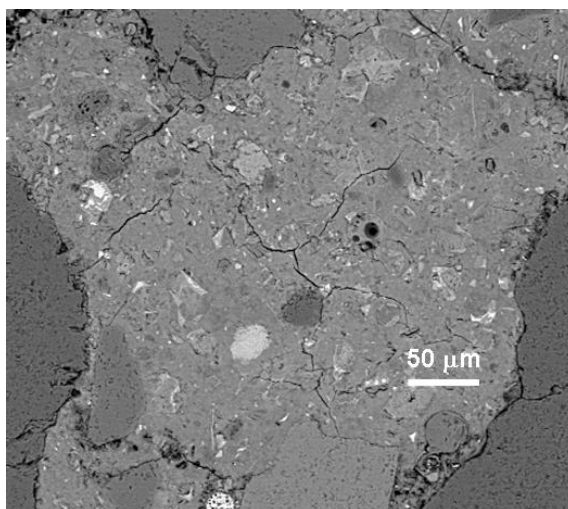


Fig. 4. Higher magnification view of an extensive dense patch from an area in same concrete specimen whose overall microstructure was illustrated in Fig. 3.

### 3. Epoxy Impregnation and Specimen Preparation at Purdue University

While laboratories vary somewhat in their specimen preparation procedures, nearly all use some variant of the impregnation procedure that was developed originally for preparation of epoxy-filled thin sections in the late 1950s. Such procedures typically use two-part epoxy systems consisting only of resin and hardener. A fluorescent dye was usually incorporated in the epoxy resin systems used for thin sections to provide for the examination in fluorescence microscopy, but is not commonly used for backscatter SEM preparations.

The epoxy mixes used vary in viscosity, but many, including the Araldite AY-103 resin used by Buenfeld [7], are extremely viscous, and have limited ability to intrude dense cement systems. Furthermore, many of these epoxies are designed to initiate autocatalytic reaction after a delay of ca. 30 or 40 minutes after the resin and hardener are mixed. This reaction quickly polymerizes the epoxy, thus rendering additional penetration into specimens impossible. In order to cope with this limited penetration, the usual procedure is to grind and roughly polish a flat surface, place the specimen in a desiccator, evacuate the air, and then introduce the epoxy over the prepared surface within the evacuated desiccator. Penetration is allowed to take place for a few minutes, and then air is admitted to provide pressure that is thought to induce further penetration. Only a few minutes of additional time is usually allowed for this further penetration. The depth of penetration achieved depends on the pore structure, and is extremely limited for dense, low w:c concretes. For example, Jakobsen et al. (8) reported penetration depths of ca. 150  $\mu\text{m}$  for a w:c 0.40 concrete; Kjellsen et al. (9) reported only ca. 120  $\mu\text{m}$  deep penetration into a w:c 0.40 cement paste. Despite this limited penetration, it is possible to prepare and polished surface specimens (and thin sections) entirely within the impregnated zone.

In contrast to these procedures, the procedure in use at Purdue University for many years takes advantage of the characteristics of a special four-component epoxy medium developed by A. R. Spurr (10). This special epoxy mixture is formulated to have an extremely low viscosity, but more importantly, to postpone polymerization indefinitely as long as the mix remains at room temperature. Heating to ca. 70°C is required to initiate polymerization. This property permits the time allowed for impregnation to be extended indefinitely, without being halted by the onset of polymerization.

As a practical matter, with this and non-self thickening epoxy, it is not necessary to prepare a flat surface to serve as a platform from which the limited penetration experienced in the usual impregnation method can take place. Rather, specimens (which are typically ca. 25 mm x ca. 15 mm) are simply dried, placed in a container surrounded by the epoxy mix, and then introduced into a desiccator. Evacuation is then started, and air is removed from the interior of the specimen at the same time as the low-viscosity epoxy resin penetrates from the exterior surfaces. Pumping is continued, and the effusion of air bubbles through the liquid epoxy goes on for about an hour. The active pumping is maintained for at least an additional three hours to permit further penetration; when convenient, it may be continued overnight. These processes are carried out at room temperature, and unlike many conventional epoxy systems, the Spurr's resin does not spontaneously give off noticeable heat. The specimen is then removed and

placed in an oven for several hours at 70°C for the intruded epoxy to become polymerized and hardened.

Penetration into even dense w:c 0.4 concretes is typically 6 or 7 mm – from the top down, from the bottom up, and from the perimeter inwards. Fig. 5 shows the penetration attained into a very dense w:c 0.40 mortar that was stored in limewater for seven years. A yellow fluorescent dye (Struer's Epodye) was added to the freshly mixed epoxy to mark the depth of penetration. The 'dark' area (in the black and white reproduction) is actually yellow.

Given this depth of penetration, it is not at all difficult to create a surface for backscatter SEM examination by sawing a slice approximately 1 or 2 mm from the top of the specimen, and then grinding the lower surface so created with fixed diamond plates of successively finer sizes, and finally polishing with successively finer diamond pastes down to  $\frac{1}{4}$   $\mu\text{m}$  in the usual manner.

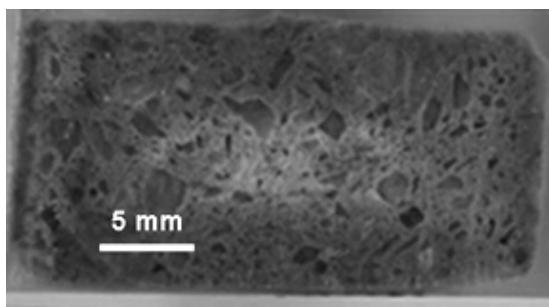


Fig. 5. Sawn cross-section of a seven-year old w:c 0.40 mortar showing a depth of epoxy impregnation of approximately 6 mm from all surfaces. Only the light-colored area in the center is unimpregnated.

It is obvious that with such a procedure there is no possibility of polishing through the remaining multi-mm thickness of epoxy-impregnated material so as to create the supposed artifact suggested by Wong and Buenfeld (5) and Buenfeld and Wong (6).

#### **4. Examination of Intruded and Unintruded Surfaces by Backscatter and Secondary Electron Mode SEM**

It was considered to be of interest to ascertain whether in fact the proposed artifact suggested by Wong and Buenfeld (5) and Buenfeld and Wong (6) would appear on a specimen that was polished so that definite areas of impregnated and unimpregnated surface were present.

The appearance of a normal, deeply impregnated polished specimen prepared at Purdue University using the Spurr's epoxy procedure described in the previous section is shown in Fig. 6a. The surface was examined in the secondary electron SEM mode and found to be almost perfectly smooth.

After a considerable search among a large collection of used and discarded specimens, two specimens were found in which apparently the polished surface was somehow cut near the center, i.e. at a depth below the general level of intrusion from the top of the specimen. In each case the outer portion of the polished surface was impregnated by penetration of epoxy inward from the perimeter of the specimen, but the central portion was unintruded. Fig. 6b shows one of them, with the obvious limit of epoxy penetration from the perimeter being marked by white arrows.

In the fully impregnated specimen of Fig. 6a, a typical area that shows dense and porous patches in backscatter mode SEM examination is shown in Fig. 7. Fig. 7 contains a low-magnification backscatter image of the area taken at 150x, a higher magnification view of the middle of this zone taken at 500x, and an energy-dispersive x-ray spectrum (EDS) taken in the ca. 10  $\mu\text{m}$  hollow shell pore marked by the white arrow. The EDS spectrum contains the elemental signature of the epoxy resin (C, O, and a weak Cl peak) clearly signaling the epoxy filling the hollow shell pore. Hydrated cement paste component peaks derived from the surrounding paste are also present. Larger voids generally show only the epoxy peaks.

In contrast to Fig. 7, Fig. 8 shows an area of the central, unintruded part of the specimen shown in Fig. 6B. The left-hand image was taken in backscatter mode SEM. The existence of both dense and porous patches is clearly seen, the dense patch occupying about the upper two-thirds of the image. Thus both dense and porous patches are visible and easily observed in backscatter SEM *despite the complete absence of epoxy impregnation*.

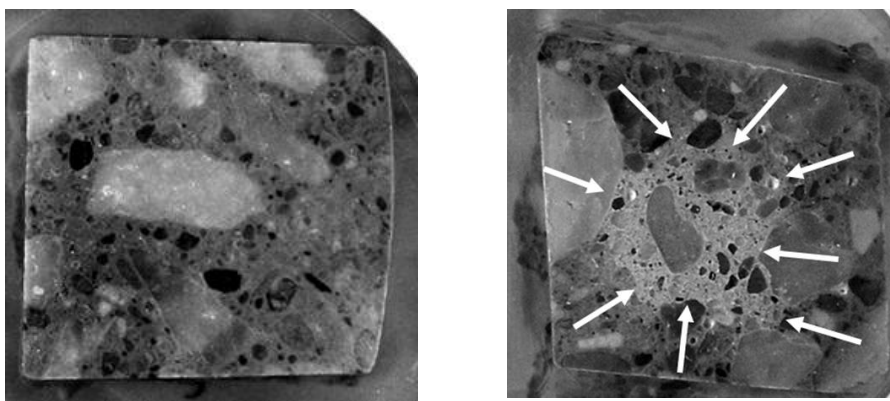


Fig. 6: A (left) Appearance of normally intruded polished specimen; B (right) A specimen inadvertently cut below the level of penetration (and discarded ).

The right-hand image of Fig. 8 was taken in precisely the same area as the backscatter SEM image, but using secondary electron SEM imaging. It is evident that the apparently dense area in backscatter SEM is in fact dense, as seen in the secondary electron mode as well. It is also



evident that the porous area revealed in backscatter SEM is indeed porous in reality. In secondary electron SEM examination, unfilled pores intersecting the specimen surface typically show characteristic rim brightness features induced by electron accumulation at the edges of the pores. These features are obvious here. These features are virtually absent in the dense patch, clearly signaling the absence of pores in the dense patch of this unintruded area of the specimen.

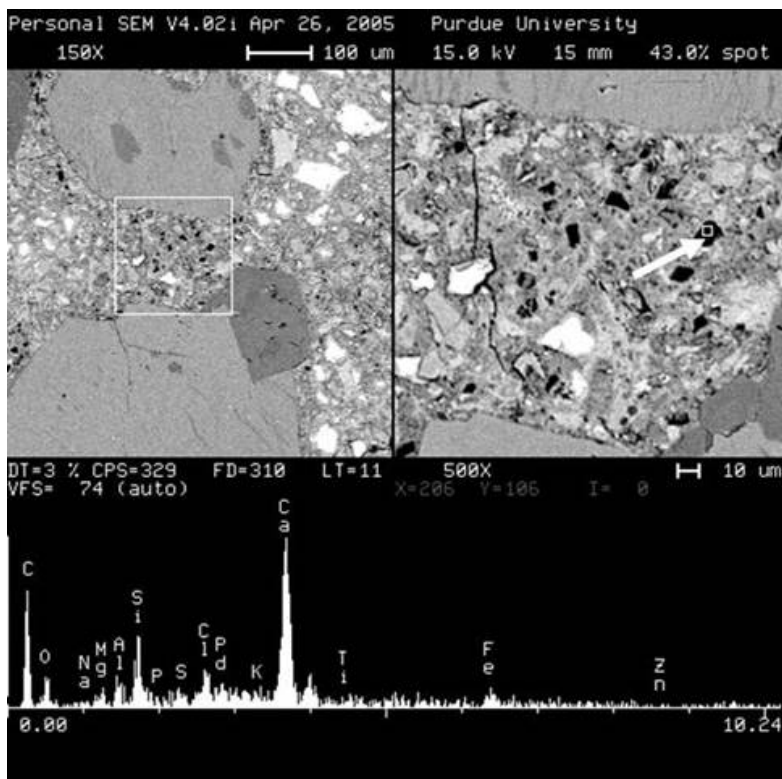


Fig. 7. Area examined in backscatter SEM from the specimen shown in Fig. 6A. Dense and porous patches are seen, with the porous patch shown at higher magnification. The EDS signal indicates that the hollow shell pore pointed to is impregnated with epoxy.

It is evident that the dense patches seen in backscatter SEM are in fact dense, and do not in any way reflect the supposed artifact alleged by Wong and Buenfeld (5,6). As expected, secondary electron imaging of the porous patches in the outer parts of this specimen that are intruded with epoxy do not show the bright rims around the pores seen in Fig. 8, since the pores in the epoxy intruded perimeter of the specimen are not empty.

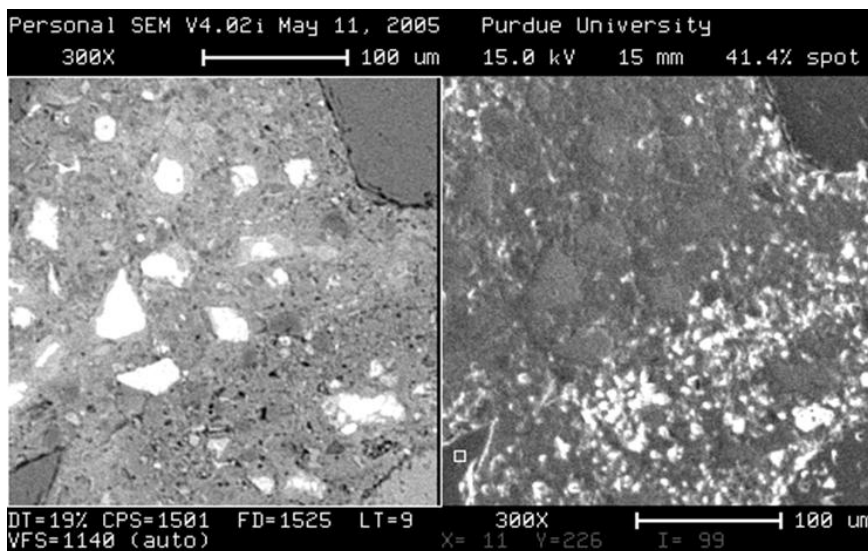


Fig. 8. Backscatter mode SEM image (left) and secondary electron mode image (right) taken in the central unintruded area of the specimen shown in Fig. 6B.

## 5. Dense and Porous Patches Observed in Fluorescent Optical Microscopy.

The second-named author has examined several thousand thin sections of various mortars and concretes prepared for examination in the fluorescent mode. Such specimens are impregnated using a standard two-component epoxy mix into which a 1% addition of Struer's Epodye is dissolved. In such preparations the specimen is dried at low temperature, a plane surface is prepared by grinding, the epoxy mix is applied to this surface after evacuation in a desiccator, and the exposed surface is impregnated. The specimen is then hardened at ca. 40° C, attached to a glass plate, and the impregnated surface is ground and polished. A cut is made to create a new surface parallel to the polished surface within the epoxy impregnated layer, and this second surface is also ground and polished, leaving the thin section at a uniform depth of 20  $\mu\text{m}$ . The fact that the entire thickness of the thin section is fully impregnated with the epoxy is checked by visual observation of the yellow color induced by the dye and then by microscopic examination using fluorescent illumination. The latter step is a recommendation of the Nordtest Build 361 standard (11) which provides guidance for the preparation of fluorescent thin section specimens for w:c ratio determination. Such determinations are routinely made in all thin sections examined at the RJ Lee Group laboratory. The entire procedure was described in detail by Jakobsen et al. (8).

The presence of dense and porous areas in many concretes is readily observed in the microscopic examination of thin sections. Dense paste patches are dark when observed in visible light illumination, and show only a low level of the green color induced in the epoxy-

filled paste by the fluorescent radiation in fluorescence examination. The common presence of residual cement grains in the dense patches is easily seen in the visible light illumination. The porous patches are easily distinguished by the bright green illumination induced by the fluorescent light passing through them.

The boundaries between dense and porous patches are relatively diffuse in optical microscope examination, since the signal intensity reflects the combined effects of the entire 20  $\mu\text{m}$  thickness of paste in the thin section. Backscatter SEM observations, in contrast, reflect only the polished surface of the specimen being observed.

Fig. 9 shows a fairly typical concrete specimen as it appears in both visible light illumination (left image) and fluorescent illumination (right image). The central area of cement paste in the field depicted is composed mostly of a dense patch; the peripheral area is a porous patch.

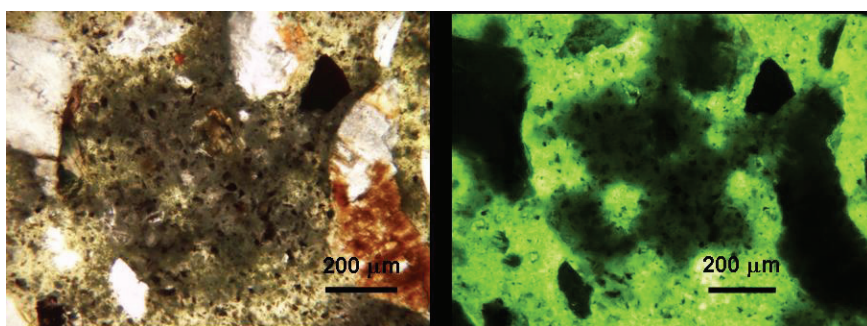


Fig. 9. Illustration of patch structure in concrete thin sections examined in visible light (left) and in fluorescent illumination (right). Most of the central area of the paste is a dense patch; the bright green areas are porous cement paste, and a number of sand grains are present.

In the fluorescent image care must be taken not to confuse sand grains with dense cement paste patches. The sand grains are easily distinguished in the accompanying visible light image.

Thin sections prepared at the RJ Lee Group laboratory are not covered by cover slips. This is done to permit subsequent backscatter SEM examination of the polished surface of the specimen. Such SEM examination of the upper polished surface of a thin section only requires application of a conductive coating. Single-surface polished specimens are also prepared at the RJ Lee Group laboratory directly for backscatter SEM examination. Such specimens omit the second cutting and polishing steps needed to produce thin sections, but are otherwise prepared in an identical manner.

The present writers have examined literally hundreds of both thin sections and impregnated polished specimens prepared only for SEM examination. The two types of specimens produce identical results in backscatter SEM; indeed it is not possible to tell which type of specimen was employed in generating a particular image without consulting the identification coding. The patch structure of cement paste is prominently displayed in many of the concrete specimens prepared by each of these methods.

## 6. Possible Origin of the Patch Structures

Recognition of the existence of the patchy structure in concretes is hardly original with the first-named author. More than 15 years ago, G. M. Idorn not only recognized the existence of the patchy structures, but provided a substantial clue as to their origin. Unfortunately, his description was contained as a small part of a general paper on marine concretes (12) which was of limited distribution, and was thus not conveniently accessible to the microstructure community. His examination was carried out on thin sections using the fluorescence mode as described previously.

Idorn's Figure 6 in Ref. 12 bore the legend "Photomicrograph of thin section of concrete with a cement paste which heterogeneously exhibits alternating dense partly hydrated, and diluted patches with very high permeability and diffusivity." His accompanying description indicated that the overall w:c ratio of the concrete was about 0.45, but that it was "on the microscale probably down to 0.2 in the coagulated parts of the paste, and towards 1.0 or more in the diluted regions."

Idorn also suggested that "This picture shows that the cement paste *in its original fresh state* has coagulated into very compact micropatches alternating with very diluted spaces." (italics and emphasis added by the present writers).

The idea that dense and porous patches seen in the hardened concrete are derived from corresponding local patches in the fresh state appears to be supported by observations made recently by K. O. Kjellsen (13). Kjellsen prepared w:c 0.40 mortar specimens incorporating fly ash, which were mixed according to the European cement standard EN 196-1 for determination of strength of cements. After a few minutes the freshly-mixed specimens were frozen in liquid nitrogen, the frozen water sublimed off, and the dried mortar impregnated with epoxy resin, then ground and polished. SEM examination suggested the existence of distinct areas of high local w:c ratio and few large cement grains, and other areas in which many large cement grains were closely spaced, thus suggesting that Idorn's supposition of the occurrence of "compact micropatches alternating with very dilute spaces" within the fresh pastes of some mortars and concretes may in fact be correct. Further investigations of this possible phenomenon are underway.

## 7. Conclusions

Conclusive evidence is presented that the patch structure as observed in many mortars and concretes by backscatter SEM is not an artifact of variable penetration of epoxy resin on the polished surface, as alleged by Wong and Buenfeld (5) and Buenfeld and Wong (6). The deep penetration of the Spurr's epoxy resin used at Purdue University (ca. 6  $\mu\text{m}$  into dense concretes and mortars) makes such an eventuality almost inconceivable except in the case of gross error in placing the location of the surface that is sawn in the specimen after epoxy penetration. Backscatter SEM examination of areas without epoxy in an aberrant specimen shows the same dense and porous patches seen in fully epoxy-intruded areas. Secondary electron SEM examination shows that the dense patches are indeed dense and the porous patches are indeed

porous. Dense and porous patches are also clearly observed in optical examination of thin sections, both in visible light and in fluorescent illumination.

The suggestion of Idorn (12) that the dense and porous patches seen in hardened concretes derive from predecessor dense and porous “micropatches” already present in the fresh concrete may indeed be correct, and is currently under investigation.

## Acknowledgments

The authors are particularly indebted to K. L. Kjellsen for providing us with his preliminary indication of what appear to be dense and porous patches in his freeze-dried freshly-mixed mortar preparations.

## References

1. Diamond, S., ‘Percolation due to overlapping ITZs in laboratory mortars? A microstructural evaluation’, *Cem. Concr. Res.* **33** (7) (2003) 949-955.
2. Diamond, S., ‘The patchy structure of cement paste in conventional concretes’, in ‘Concrete Science and Engineering: A Tribute to Arnon Bentur’, RILEM PRO 36, RILEM Publications S.A.R.L., Paris (2004) 85-94.
3. Diamond, S., ‘The patch microstructure in concrete: the effect of mixing time’, *Cem. Concr. Res.* **35** (5) (2005) 1014-1016.
4. Diamond, S., ‘The patch microstructure in concrete: the effect of superplasticizer’, submitted to *Cem. Concr. Res.* (2005).
5. Wong, H.S. and Buenfeld, N.R., ‘Patch microstructure in cement based materials: Fact or artefact?’ submitted to *Cem. Concr. Res.* (2005).
6. Buenfeld, N.R. and Wong, H.S., ‘Recent developments in backscattered electron imaging and image analysis of pores for predicting transport in concrete’, Proc. Of Conf. on Cementitious Materials as Model Porous Media: Nanostructure and Transport Processes, Monte Verità, Switzerland (July 2005).
7. Buenfeld, N.R. Personal communication, April 2005.
8. Jakobsen, U.H., Laugesen, P., and Thaulow, N. ‘Determination of water-cement ratio in hardened concrete by optical fluorescence microscopy, in: M. S. Khan (ed) ‘Water-cement ratio and other durability parameters, Techniques for determination’, SP-191, ACI International, Farmington Hills, MI (2000) 27-41.
9. Kjellsen, K.O., Monsøy A., Isachsen, K., Detwiler, R.J., ‘Preparation of flat-polished specimens for SEM-backscattered electron imaging and X-ray microanalysis – importance of epoxy impregnation’, *Cem. Concr. Res.* **33** (4) (2003) 611-616.
10. Spurr, R.A., ‘A low viscosity epoxy resin embedding medium for electron microscopy, *J. Ultrastructure Res.* **26** (3) (1969) 3-43.
11. Nordtest Method NT Build 361, “Concrete, Hardened: Water cement ratio” (1999).
12. Idorn, G.M., “Marine Concrete Technology – Viewed With Danish Eyes” in ‘International Experience With Durability of Concrete in Marine Environment’, Proc. of a Symposium Honoring Professor Ben C. Gerwick, Jr., P. K. Mehta, Ed., University of California Berkeley (1989) 28-48.
13. K. L. Kjellsen, personal communication, May 2005.



## **Progress towards quantitative understanding of cementitious microstructures**

Karen Scrivener  
EPFL, Lausanne, Switzerland

### **Abstract**

Cementitious microstructures are complex, with features ranging over several length scales. Consequently although we have a fairly good qualitative appreciation of their development, quantitative descriptions are often difficult to obtain and thus it is difficult to understand the microstructural mechanisms responsible for changes in behaviour. Progress in this direction and future challenges are discussed.

At EPFL we are working with two principal techniques – Backscattered electron (BSE) imaging of polished surfaces in the scanning electron microscope (SEM) coupled with image analysis and X-ray diffraction coupled with Rietveld analysis. These techniques enable a wide range of quantitative information to be obtained: the degree of reaction of the overall and individual anhydrous phases; the amounts, nature composition and distribution of the various hydration products.

The application of these techniques to various problems will be discussed. These include the effect of temperature on the strength development and microstructure of concrete.





## **Recent Developments of Standard Test Methods for Measuring the Fluid Penetration Resistance of Concrete and use in Performance Standards**

R.D. Hooton

Department of Civil Engineering, University of Toronto, Toronto, Ontario, Canada

### **Abstract**

In North America, until 2003, few standards existed for the measurement of the rates of fluid penetration and ion transport into concrete, regardless of the standards organization. The ones that did exist, did not cover all the transport mechanisms of interest and did not necessarily provide the data required for service-life modelling. Tests, such as the rapid chloride test (AASHTO T277 or ASTM C 1202) and the absorption test (ASTM C 642), while useful, just provide indirect indicators of concrete quality.

This paper describes the range of tests which are now available as well as providing an update on the current status of ASTM standardization efforts and how these tests are or might be used in performance specifications.

### **1. Introduction**

The cement paste matrix of concrete is porous at a macro level (eg. compaction voids, entrapped air), a micro level (eg. capillary pores) and a nano level (interlayer or gel pores). The properties of the pore system are also time-dependent due to interaction of the solids with the aqueous and gaseous fluids which occupy the various pore spaces.

From a durability perspective, it is the volume and the connectivity of the capillary pore network which allow penetration of aggressive fluids and ions and this pore system can be engineered using appropriate materials selection, mix proportions, compaction, and curing procedures. The chemical composition of the hydrated system also affects the interactions with transported ionic species. This paper is an update and modification of a previous paper on test methods (1).

## **2. Mechanisms of Ion and Mass Transport**

### **Sorptivity or Surface Absorption**

If the concrete surface is not saturated at the time it is exposed to water or solutions, then capillary tension will likely draw the solutions into a depth of between 5 and 15 mm in a matter of hours until the surface layer becomes saturated. This is the likely scenario with many structures. Even high performance concretes, with  $w/cm = 0.30$  and containing silica fume have been found to exhibit rapid chloride ingress due to sorptivity.

If the concrete surface is exposed to wetting and drying cycles and is intermittently exposed to chloride solutions, the capillarity will continue to absorb chlorides, concentrating them and building up an interior "surface" concentration at the depth of the convection zone (2). For de-icing salt exposure, the chloride concentration in the outer "convection zone" will build up during the winter and reduce due to rain washout in warmer weather (3). This is the scenario for bridge or parking decks subject to de-icer salts or for the tidal and splash zones in marine structures.

### **Diffusion**

When concrete is saturated, both surfaces are immersed in a fluid, and at least one surface is exposed to a chloride solution (for example), then a chloride concentration gradient exists between the surface and the pore solution and pure diffusion will result. The magnitude of the concentration gradient is the driving force for diffusion as solutions seek to come to an equilibrium concentration. When the external source of chlorides is constant, the surface concentration builds up rapidly. In the case of de-icing salts the surface concentration will build up slowly over many years and only then will the surface concentration become relatively constant.

In the laboratory, diffusion coefficients can be calculated using Fick's laws of diffusion by sealing a disk of concrete between two solutions, one of which has an elevated chloride concentration. Aliquots taken from the non-chloride solution are analysed at various time intervals. (In actual tests, it is important for both solutions to simulate pore solutions to avoid leaching.) When chlorides first "breakthrough" the sample thickness into the non-chloride solution, a diffusion coefficient can be calculated from the elapsed time. This "apparent" diffusion coefficient will be affected by any chloride binding that took place inside the sample as the chloride solution advanced. Also if the experiment is continued, the rate of increase in chloride concentration in the solution (ie the chloride flux) can also be used to calculate a steady-state diffusion coefficient. This is typically called an "effective" diffusion coefficient since it will not include a chloride binding term, since chloride binding was satisfied before the rate of increase in solution concentration was measured.

However, such static or steady state tests are very time consuming, so an electric potential is often simultaneously applied to accelerate the rate of chloride ingress. These have been termed migration tests and require use of the Nernst-Planck equation to determine the diffusion coefficients, but this will not be discussed in this paper. A review of these issues is given by Andrade (4), there is a standard test (5) and details of an improved test method given by

McGrath and Hooton (6). In addition, a non-steady state migration test was developed by Tang and Nilsson (7) which is rapid and uses a silver nitrate spray to colorimetrically determine the depth of chloride penetration. This rapid test was standardised as Nordtest NT Build 492, and was later studied and adapted by Stanish, Hooton and Thomas (8) as AASHTO standard TP 64 in the US.

Alternatively, Crank's solution (9) to Fick's second law can be used to determine the diffusion constant (Dc) of the concrete from chloride concentration profiles.

$$C(x, t) = C_s \left[ 1 - \operatorname{erf} \left( x / 2\sqrt{Dct} \right) \right] \quad \dots \text{Eqn. 1}$$

where  $C(x,t)$  = the chloride concentration at depth (x) and time (t)  
 $C_s$  = the chloride concentration at the concrete surface  
 $\operatorname{erf} [ ]$  = the error function for which values can be obtained from standard tables for various values of the number within the brackets.

Typically, chloride profiles are obtained from a particular concrete which has been exposed to a solution of known chloride concentration after a fixed length of time. Careful use of a milling machine can provide samples for chloride concentration profiles at 0.5 to 1 mm intervals (10,2). Such tests have been standardized as Nordtest NT Build 443 (11) and ASTM C 1556. By fitting an equation to the chloride profile obtained, the apparent or effective diffusion coefficient can be obtained. If water soluble chlorides are measured, then binding effects will be removed and an effective diffusion coefficient is obtained. If total or acid soluble chlorides are measured, then the bound chloride is included in the profile and an apparent diffusion coefficient is obtained. If cores taken from structures in service are taken, then the surface concentration could be lower than at the inside of the convection zone due to washing out of chlorides in some cases. Therefore, the surface values are not used to obtain the best fit line equation and the equation is extrapolated to the surface to obtain an estimate of  $C_s$ . An alternative approach for deeper levels of washout is to assume a pseudo-surface at the highest chloride concentration and then fit a diffusion profile to the interior portion of the concrete, making a correction for the thickness of the washed-out, convection zone (3). Some typical profiles from highway barrier walls, cored in the summer months, are shown in Figure 1.

One variable is whether acid soluble or water soluble chlorides are used in the calculations. It is far easier to dissolve samples in nitric acid and measure an approximation of the total chloride content. This will include chlorides that became bound. It is only the water soluble chlorides that will act to depassivate the steel reinforcement, however, the methods for obtaining water soluble chlorides are somewhat arbitrary and are difficult to define. As well, all materials contain some chlorides and there will be a background level of chloride throughout the concrete. For example, in Toronto and Chicago, the crushed limestone coarse aggregates typically contain significant chlorides, but unless the aggregate is crushed to powder, these chlorides are effectively insoluble inside the coarse particles. If the background chloride in concrete is effectively insoluble, then a correction should be made to subtract these background values when acid soluble chlorides are being determined.

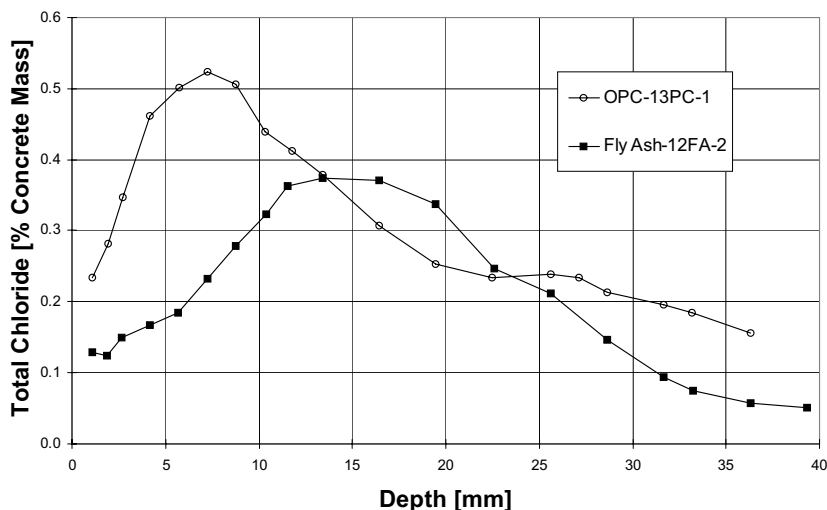


Figure 1. Chloride profiles from 9-year old Canadian highway barrier walls with  $w/cm = 0.41$ , one with 25% Class C fly ash (3)

Chloride diffusion rates are affected by temperature so a diffusion coefficient calculated from samples stored at an accelerated test temperature of say  $40^{\circ}\text{C}$  (12) will not be the same as values obtained at other temperatures. In addition, the response of diffusion coefficients to temperature are likely to vary with each concrete mixture especially when supplementary cementing materials (SCM) are used since each SCM will have different thermal sensitivity in terms of kinetics of hydration reactions. The precision of such a diffusion test also needs to be considered. In a specification for precast tunnel liners for the Sheppard Subway line in Toronto, a maximum limit of  $1.5 \times 10^{-12} \text{ m}^2/\text{s}$  was set using the above-mentioned 120 day,  $40^{\circ}\text{C}$  ponding procedure (12). The mixture was initially prequalified, then tests were performed on cores extracted from units after curing. The average value on 62 tests of production units was  $0.6 \times 10^{-12} \text{ m}^2/\text{s}$ , and the coefficient of variation was 38.7% (13). Therefore, in spite of this seemingly large variability, the 95% confidence limit was  $1.1 \times 10^{-12} \text{ m}^2/\text{s}$ , still lower than the specification limit. Wide variations on cast-in-place bridge decks meeting the same specification were also noted by Tikalsky et al (14)).

Another issue to consider is that the chloride diffusion coefficient for a particular concrete will be time dependent and will normally decrease with time as hydration products continue to form and alter the capillary pore system. The effect of this was considered by Maage et al (15,16) and Thomas and Bamforth (17) and a recent summary of different methods for calculating the time-dependent reduction coefficient has been made (18). Therefore, the age at chloride exposure and the length of chloride ponding are important parameters when  $D_a$  values are calculated.

### **Wick Action (Evaporative Transport)**

For relatively thin structural elements, if the concrete surface away from the water, sulfate, or chloride solution source is exposed to air at a relative humidity of less than 100% (e.g. in parking decks soffits or the inside of tunnel liners or slabs-on-grade where the subgrade is moist) then pore water will be drawn through the concrete toward this surface and evaporated. This will result in an increased chloride concentration inside the concrete. The effect of wick action will be to increase the rate of chloride ingress beyond that predicted by diffusion alone (12).

### **Permeation**

Permeability is the rate of ingress of a fluid when driven by a pressure gradient. While many practitioners refer to concrete permeability, pressure gradients are not that common except for fluid containing or offshore structures where hydrostatic pressure will increase with increasing depth of immersion. It may also be an issue for tunnel liners if the tunnel is well below the depth of ground water. Pressure driven fluid movement will increase the rate of water chloride ingress beyond that predicted by diffusion alone.

### **Construction Defects and Detailing**

If concrete is not compacted properly or if honeycombing or other defects such as cracking, occur during construction, then rates of chloride ingress calculated from tests on intact laboratory samples will become less meaningful (19). However, this is difficult to assess when developing standard test procedures and likely has to be addressed in modelling.

## **3. Recent ASTM Activities**

Prior to 1996, the C 1202 Rapid test (or Coulomb test) was under the jurisdiction of subcommittee C09.67 on Concrete's Resistance to the Environment, together with all the tests related to freezing and thawing and de-icer salt scaling. There were no other tests for measuring the transport properties of concrete. The C 1202 task group of C09.67 was initially chaired by D. Whiting, the developer of the test, and later by the writer.

In 1996, committee C09 on Concrete and Concrete Aggregates approved formation of a new subcommittee C09.66, on Concrete's Resistance to Fluid Penetration, under chairmanship of the writer. The scope of this subcommittee is "to develop and maintain standards related to ion and fluid penetration into hardened concrete". The jurisdiction of the C 1202 test was then transferred to this new subcommittee. In addition, the writer had previously initiated a draft test method to measure the initial rate of sorption, which was also put under jurisdiction of C09.66.

Within a short period of time, subcommittee membership grew to 50, and new task groups were formed to develop several new test methods including:

1. Initial Rate of Absorption (ASTM C 1585 was adopted in 2004)
2. Water Permeability (this task group was temporarily disbanded due to other priorities)
3. Bulk Chloride Diffusion (ASTM C 1556 was adopted in 2004)

4. A salt ponding test based on the AASHTO T259 90-day ponding test (ASTM C 1443 was adopted in 2003)
5. Resistivity (A one-minute conductivity test has been drafted)

In addition, in the near future work will be initiated on a rapid chloride migration test, a field rate of absorption test (20,21), and a test for water permeability. A description of these test development efforts is provided.

## **4. Test Methods**

### **1. ASTM C 1202:**

This well known, but sometimes controversial test method evolved from a FHWA study by D. Whiting (22), as AASHTO T277 in 1983 as a rapid index test in lieu of the AASHTO T259 90-day salt ponding test (described later). In this test, a saturated concrete disk is sandwiched between two cells (one filled with 0.3M NaOH and the other with 0.5M NaCl solution). A 60V DC potential is applied to electrodes in the two cells. The current is monitored and integrated over a 6-hour period to obtain the charge passed in coulombs.

The current level is due to conductivity, and both the current and the charge passed, are related to the connectivity of the saturated capillary pore system and to the conductivity of the pore fluid itself.

While this rapid test has become widely used as an index of concrete quality by highway and other specifying agencies, it has also been criticized.

Fundamentally, it is simply a conductivity or inverse-resistivity test and in spite of it often being referred to as the Rapid Chloride Permeability Test, it does not measure the “permeability” or “chloride diffusion” of concrete. Numerous researchers have pointed this out (4,23,24,25). Because current flow is affected by pore fluid conductivity, admixtures which result in large changes in conductivity are unfairly judged by this test (eg. calcium nitrate corrosion inhibitors) and this effect is noted in the standard.

Others have criticized it for apparent lack of relationship with salt ponding test data (26,27) and for the fact that high current flows will result in heating of the sample and solutions during the 6 h test, raising the measured conductivity. However, others have found that C 1202 test data, if corrected for temperature, do relate to salt ponding data (28,29,30,31) and that some of the lack of correlation found by others, is in large part due to poor sampling and analysis procedures used in salt ponding tests (ie. AASHTO T259---however, some of this had been improved in the ASTM C 1443 version of this test). This is demonstrated in Figures 2 and 3. In Figure 2, the integrated chloride content typically calculated from T259 test results is related to C 1202 data (30). In Figure 3, the depth of penetration of the 0.1% chloride front in T259 is related to temperature-corrected C 1202 data (30).

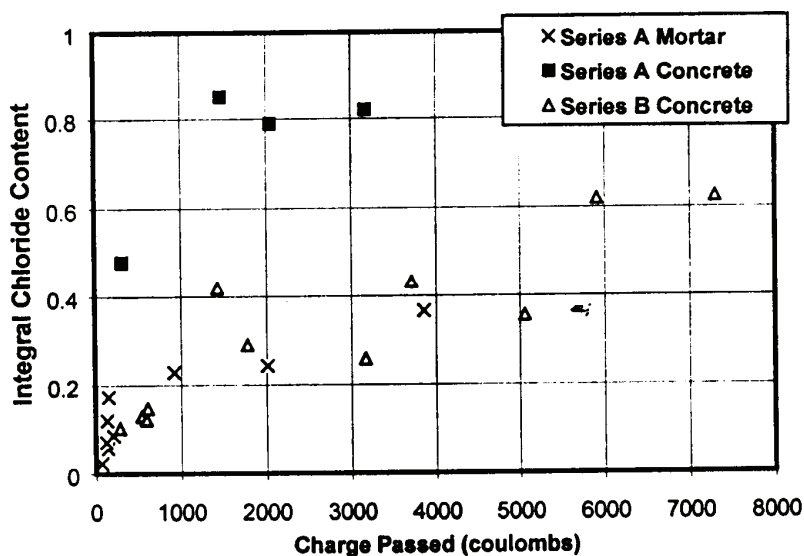


Figure 2. AASHTO T259 Integral Chloride Content vs. 6-Hour Rapid Chloride Permeability Test Number (after [30]).

Regardless, it is easy to envisage substitution of the C 1202 test with a simpler resistivity test or just to take the initial current reading in the C 1202 test to calculate a conductivity value (this is being done, as discussed later).

In spite of its shortcomings, after over 22 years of use, C 1202 test equipment is found in numerous highway department, commercial, and university laboratories in North America as well as in many countries internationally, and it continues to be specified for evaluating the quality of supplied and in-place concrete for both bridge decks, tunnel liners, and parking structures. For example, the 2004 version of Canadian standard CSA A23.1 includes a maximum 1500 coulomb limit at 56 days, for any concrete exposed to de-icer salts and freeze/thaw (35 MPa, max. 0.40 w/cm, air-entrained), and 1000 coulombs for similar concrete where extended service life is required (50 MPa, max. 0.37 w/cm, air-entrained). Therefore, in spite of other developments in test methods, it is likely that this test will remain in use for many years to come.

### Rate of Absorption Test

The original draft method was based on the procedures described by Hall (32). One face of a dried concrete disk with its sides sealed is placed in a shallow pan of water and its change in mass with time of exposure is recorded. The rate of absorption, or sorptivity, measures the capillary suction of the sample and is calculated from the slope of the volume of water uptake per unit area vs the square root of time plot. The sorptivity is related to the size and connectivity of the pore system (33) as well as the moisture state of the sample (34). If the

initial rate of absorption test of approximately 0.5 hour duration is extended to 2 or 3 days as in the Nordtest and ASTM C 1585 procedures (35), then the sorption capacity of the concrete can also be measured.

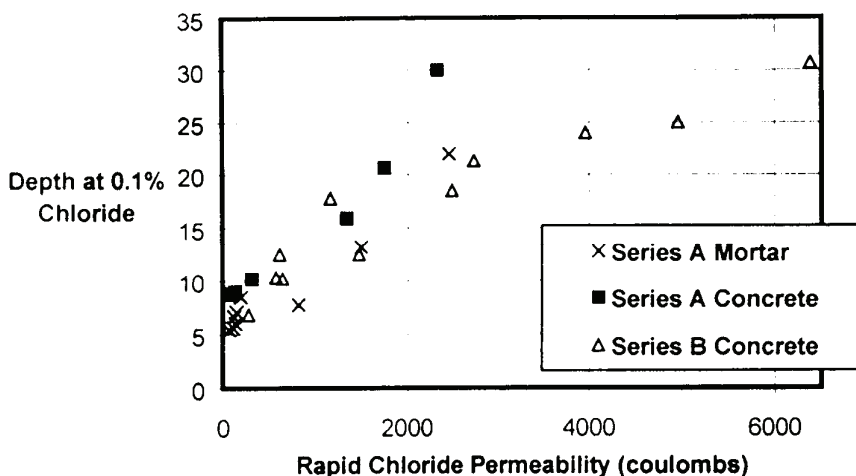


Figure 3: Modified Ponding Test Depth at 0.1% vs. 30-Minute RCPT Number (after [30]).

While the test is simple, and requires no elaborate equipment, standardization of the preconditioning of the concrete samples has been problematic. Drying at 110°C (as is the first step in the ASTM C 642, absorption and permeable voids test) serves to induce cracks, collapse the microstructure, and results in high sorptivity values. It also does not represent typical field conditions.

Solvent replacement, using isopropyl alcohol, and then evaporation of the alcohol works well to minimize cracking and microstructural collapse, but is very time consuming and messy (36). Drying for a fixed period (eg. 7 days) at 50°C is simple and does little damage, but the moisture condition in the sample when tested will not be uniform through its depth. Parrott (37) suggested that after an initial 3 day period of drying at 50°C, that the sample be sealed in a container at 50°C for 4 days, to allow the residual moisture in the sample to equilibrate in the pore system. This conditioning was adopted in several studies (38, 39) but resulted in sorptivity values that appeared to be poorly related to the quality of the concrete being tested. C. Ferraris and co-workers at NIST (40), had success conditioning samples to a constant relative humidity of 80% (which by the Kelvin equation is approximately when all of the capillary pores should be empty), so a practical version of this conditioning was added to the procedures (3 days at 80% rh and 50°C followed by storage in a sealed container for 14 days at 23°C). The test method was standardized in 2004 as C 1585.



### Chloride Bulk Diffusion Tests

The most common test methods for measuring the apparent diffusion coefficient of concrete, for both research and specification purposes have been bulk diffusion tests. This typically involves sealing all faces of a core or cylinder except one and immersing (or ponding) the specimens in a chloride solution of known concentrations for a fixed period of time. After removal from chloride exposure the concrete is profiled, (often in 1 mm increments). The powdered layers are digested in nitric acid, filtered, and titrated with  $\text{AgNO}_3$  to obtain the total chloride content (this includes both the bound and free chlorides in each layer). An equation can then be fitted to the resultant chloride depth profile to obtain both the surface concentration ( $C_s$ ) and the apparent diffusion coefficient ( $D_a$ ).

The equation normally used is the error function or Crank's solution to Fick's Second law:

$$C(x, t) = C_s \left[ 1 - \text{erf} \left( x / 2\sqrt{D_a t} \right) \right] \quad \dots \text{Eqn. 1}$$

where  $C(x,t)$  = the chloride concentration at depth ( $x$ ) and time ( $t$ )

$C_s$  = the chloride concentration at the concrete surface

$\text{erf} [ ]$  = the error function for which values can be obtained from standard tables for various values of the number within the brackets

Several bulk diffusion tests have been used, with the major variables being, 1) the age at ponding, 2) the period of chloride ponding, and 3) the temperature and concentration of chloride solution (41). Unfortunately, all of these variables influence the calculated  $D_a$  values, although on a relative basis, the ranking of  $D_a$  values is often the same (10)..

It was decided to adopt the Nordtest procedure (42) which uses a 2.8 M NaCl ponding solution at 23°C for a 35 day period or longer. The samples are immersed at a maturity level equivalent to 28 days at 20°C. The 23°C was thought to better represent normal conditions than 40°C (which has been used in several specifications) since some cementitious systems are activated at higher temperatures.

This test had also undergone interlaboratory testing in Scandinavia and had the precision data required for ASTM test methods. This test, with some minor modifications, was adopted by ASTM in 2004 as C 1556. Interlaboratory testing was conducted by ASTM committee members in 2004, but the data is still being processed.

### Water Permeability

Theoretically, Darcy's law can be used to calculate a permeability coefficient for concrete. However, because of its relatively low permeability and the fact that the permeating fluid will react with the concrete to some degree, a number of problems have to be overcome to obtain permeability coefficients (43, 44). In collaboration with the US Army Corps of Engineers, the writer helped develop the US Government Standard CRD-163, based on use of a high pressure triaxial cell. Later, El-Dieb and Hooton (45,46) refined the pressure application and measurement systems developed by Hearn and Mills (47), and were able to measure water

permeability of a mature concrete with  $w/cm = 0.29$ , and containing both silica fume plus slag down to a value of  $2 \times 10^{-16}$  m/s with good repeatability. Therefore, a task group will likely be reinstated to draft the CRD-163 standard into ASTM style and will consider the modifications suggested by El-Dieb and Hooton (45, 46).

Because of the interest in permeation of chloride solutions under pressure (ie: in underground tunnel liners) consideration needs to be made for the different density and viscosity of chloride solutions in the Darcy Equation.

### **Wick Action**

While evaporative transport of dissolved salts such as sulphates or chlorides is an important transport mechanism (especially with higher  $w/cm$  concretes having a continuous capillary pore structure), there is no current activity to develop a standard test method.

According to equations developed by Buenfeld et al (48), chloride deposition by wick action can be modelled by knowledge of a concrete's sorptivity and vapour diffusion coefficient. Work was later conducted at the University of Toronto (49) as well as elsewhere (50) to experimentally evaluate these equations. Further study of wick action is required since it is possible that wick action could also be modelled by permeability equations, using the pressure gradient between the saturated face and the meniscus pressure in the concrete at the location of evaporation (near the air-exposed face).

### **Chloride Migration**

Migration tests have been used by a number of researchers (6, 51) to measure an effective diffusion coefficient based on the steady-state flux of free chlorides through a concrete specimen. Such a test has been standardized as Nordtest NT Build 355 (5). The cell design of McGrath and Hooton (6) makes use of simulated pore solution in the cells with a superimposed chloride solution on one side. Luggin capillaries are also used to more accurately measure the potential across the specimens, rather than the applied potential. This minimizes errors due to voltage drops resulting from polarization at the electrodes and IR drops across the electrolytes.

ASTM subcommittee C09.66 is considering development of a standard migration test but in the near future, the Nordtest NT Build 492 rapid non-steady state migration test is the most likely candidate and a modification of it has been standardized as AASHTO TP64 as discussed below.

### **Rapid Migration Test**

A FHWA-funded project was completed at the University of Toronto (52), to develop an alternate rapid index test to ASTM C 1202 for chloride penetration resistance of concrete. The test which was recommended for standardization was based on the procedure developed by Tang and Nilsson (6) and adopted as Nordtest NT Build 492 (53).

This non-steady state migration test involves measurement of the depth of chloride ingress under an applied DC potential (the voltage and time of test are determined from an initial current measurement). The depth of penetration is measured by splitting the specimens open

after test and spraying with  $\text{AgNO}_3$  solution. Above about 0.07N chloride concentration, the  $\text{AgNO}_3$  will convert to  $\text{AgCl}_2$  and turn white in colour. The non-chloride areas will turn brown. A diffusion value can be calculated from the depth of penetration together with knowledge of the magnitude and period of the applied potential. An AASHTO test method (TP 64) was

adopted in 2004. In the AASHTO version of this test, a single test duration of 18 hours was selected, with voltage determined from an initial current measurement. Also, because the applicability of the theory behind the non-steady

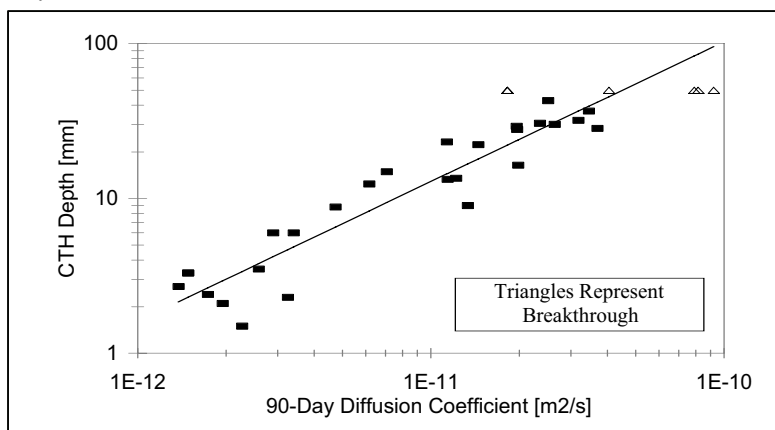


Figure 4. AASHTO TP 64 Rapid Migration Results Compared to ASTM C1556 Bulk Diffusion Results

state migration coefficient was questioned (54,55), this calculation was not adopted. Instead, the penetration of chlorides in mm/volt-hour was adopted for the time being. Results relate well to chloride bulk diffusion testing as shown in Figure 4.

The test is of similar rapidity to the ASTM C 1202 procedure but has the advantage that the results are not influenced by the pore fluid conductivity. This makes it applicable to concretes with for example, calcium nitrite corrosion inhibitor.

This test has also been modified to quantify the influence of curing on chloride diffusion rates with depth from a surface (56).

## 5. Use of Mass Transport Tests in Performance Specifications

One of the reasons that concrete durability is so difficult to specify, is that there is currently no single performance-related test which can be used to characterize durability performance. For characterizing physical performance, codes such as ACI 318, often make use of the

compressive strength test results and then use equations to estimate other properties such as elastic modulus and tensile or bending strength. For durability, most codes place prescriptive limits on allowable materials (eg. cement type) and mix proportions (eg. maximum water to cementitious materials ratio). Durability is not as simple as physical properties since there are many potential durability issues and exposure conditions to address. However, fundamental to almost all durability issues, is the resistance of a given concrete to ingress of aggressive fluids. Therefore a test which could provide a measure of, or an index of, a concrete's resistance to fluid ingress could provide a basic performance index for resistance to aggressive exposures. This may be complicated since although engineers often refer to concrete "permeability", there are many mechanisms of fluid ingress (ionic diffusion, capillary suction, wick action, and permeability due to pressure gradients) and complicating chemical processes (ionic binding, and time-dependent changes in the pore system due to hydration or alteration of hydrates). Therefore for a single fluid penetration resistance test to be universal, it would have to provide results which either relate to each of these mechanisms or at least relate to the results of tests for each of these specific penetration issues. Also, even if one were successful in developing a single standard penetration resistance test, some other durability issues, will still have to be addressed by placing limitations on materials, such as the maximum allowable level of reactive aluminates (typically  $C_3A$  of Portland cement) for sulfate resistance, and maximum alkali loading for resistance to deleterious effects due to alkali-aggregate reaction (or placing restrictions on the type of aggregate used).

Fueled by the National Ready Mixed Concrete Association's P2P (Prescription to Performance) initiative, there is a current interest in the US for developing concrete performance specifications, which will require adoption of test limits for fluid penetration resistance. Work on developing such a specification is being undertaken by the writer, together with J. Bickley, a Toronto consultant, and K. Hover of Cornell University.

Currently in North America, the main transport-related test used in standard specifications has been ASTM C 1202 (AASHTO T277). The results for this test do relate fairly well to those for both chloride diffusion (except for concrete containing calcium nitrite corrosion inhibitors) and water permeability, so its use can be justified. Other tests such as the ASTM C 1556 chloride bulk diffusion test have been used for input to service life models such as Life-365, but bulk diffusion tests take too long to be of practical use in specifications other than as a prequalification test. The Nordtest NT Build 492 or the AASHTO TP 64 rapid migration test could be used as an alternate to ASTM C 1202 in specifications.

In evaluation of concrete for performance, suppliers typically prequalify mixtures that meet the level of penetration resistance specified. In CSA A23.1, such limits exist for concretes to be used for bridge and parking decks as well as for extended service life in a chloride environment. However, the owner and the contractor typically also want to perform tests on the concrete as-delivered, to ensure that the prequalified concrete mixture is being delivered, so tests might be run on site-cast cylinders (this can also serve to protect the supplier). Lastly, the owner really wants to know the in-place performance of the concrete, and may require that cores be taken at various intervals, to ensure that the concrete performance is still met after being subject to placing and curing practices. Regardless of when such testing is performed, if

it is to be accepted by both specifiers and the industry, the tests need to be rapid and provide a reasonable index, or ranking, of concrete's resistance to fluid penetration.

As well, when specification limits are placed on the results of any tests, there needs to be an allowance for statistical variation in results due to the test precision. Therefore, if 1000 coulombs was specified using the ASTM C 1202 test, then that limit would be satisfactory for prequalification of a concrete mixture, but for identity testing as concrete is delivered, and for in-place testing of hardened concrete, as an example, an average maximum value of 1000 coulombs could be specified, but an upper limit for any single test result would have to be around 1400 coulombs (to account for the single laboratory coefficient of variation being 12%, and using a 95% confidence interval). This allowance for statistical variation has been used previously for air void spacing factors in the Canadian CSA A23.1 standard for concrete (There is a 230  $\mu\text{m}$  average maximum spacing factor, with no single test result exceeding 260  $\mu\text{m}$ ).

## 6. Summary

There is a need for a number of standard test methods related to fluid transport through concrete. ASTM subcommittee C09.66 has developed standards for a chloride bulk diffusion test (C 1556), a sorptivity test (C 1585), a water permeability test, and is nearing completion of a one minute conductivity test to augment the ASTM C 1202 rapid index (coulomb) test. In addition, work will soon be initiated on a rapid non-steady-state chloride migration test based on Nordtest NT Build 492 / AASHTO TP64, an in-place sorptivity test, and a water permeability test. With the exception of a few 100-year service life projects, where chloride diffusion limits have been specified, currently the only test commonly used in concrete specifications in North America is ASTM C 1202. Therefore, for performance specifications at this time, the C 1202 test is being adopted or being considered for adoption in various specifications and codes. This rapid index test may not be the best predictive test for long-term performance, but since it is wide available and the industry is familiar with it, this will help in adoption of performance specifications in the near term.

## References

1. Hooton, R.D., 'Development of Standard Test Methods for Measuring Fluid Penetration and Ion Transport Rates', Materials Science of Concrete: Fluid and Ion Transport Rates in Concrete, *A. Cer. S.*, Nov. (2001) 1-12.
2. Hong, K. And Hooton, R.D., 'Effects of Cyclic Exposure on Penetration of Concrete Cover', *Cement and Concrete Research* **29** (1999) 1379-1386.
3. Hong, K. and Hooton, R.D., 'Effects of Fresh Water Exposure on Chloride Contaminated Concrete', *Cement and Concrete Research*, **30** (2000) 1122-1207.
4. Andrade, C., 'Calculation of Chloride Diffusion Coefficients in Concrete from Ionic Diffusion Measurements', *Cement and Concrete Research*, **23** (1993) 724-742.
5. Nordtest NT Build 355, Chloride Diffusion Coefficient from Migration Cell Experiments, Nordtest Post Box 116, FIN-02151, Espoo Finland

6. McGrath, P.F. and Hooton, R.D. (1995) 'Influence of Voltage on Chloride Diffusion Coefficients from Chloride Migration Tests', *Cement and Concrete Research*, **26**, (1996), 1239-1244.
7. Tang, L. and Nilsson, L.-O., 'Rapid Determination of the Chloride Diffusivity in Concrete by Applying an Electrical Field,' *ACI Mat. J.*, **89** [1] (1991) 49-53.
8. Stanish, K.D., Hooton, R.D. and Thomas, M.D.A., 'Evaluation of Four Short-Term Methods for Determining Chloride Penetrability in Concrete', *Water-Cement Ratio and Other Durability Parameters: Techniques for Determination*, ACI SP-191 (2000) 81-98.
9. Crank, J., 'The Mathematics of Diffusion', 2<sup>nd</sup> Edn, (Clarendon Oxford), (1975).
10. McGrath, P.F. and Hooton, R.D., 'Effect of Binder Composition on Chloride Penetration Resistance of Concrete', Proceedings of the Fourth International Conference on Durability of Concrete, Sydney, ACI SP-170, **1**, Aug. (1997) 331-347.
11. Nordtest NT Build 443, Accelerated Chloride Penetration. P.O. Box 116, FIN-02151 Espoo Finland.
12. Wood, J.G.M., Wilson, J.R. and Leek, D.S., 'Improved Testing for Chloride Ingress Resistance of Concretes and Relation of Results to Calculated Behaviour,' Proceedings, 3rd International Conference on Deterioration and Repair of Reinforced Concrete in the Arabian Gulf. Bahrain Society of Civil Engineering and CIRIA, Oct. (1989) 15 pp.
13. Hart, J. Ryell, J., and Thomas, M.D.A., Proceedings, PCI/FHWA International Symposium on High Performance Concrete, New Orleans (1997).
14. Tikalsky, P.J., Pustka, D., and Marek, P., 'Statistical Variations in chloride Diffusion in Concrete Bridges', *ACI Structural J.*, **102**, May-June (2005) 481-486.
15. Maage, M. and Helland, S., 'Quality Inspection of Shore Approach High Strength Concrete', in Concrete Durability, *ACI SP 126*, **1**, (1991) 609-624.
16. Mangat, P.S. and Malloy, B.T., 'Prediction of Long Term Chloride Concentration in Concrete,' *Mat. and Structures*, **27**, (1994) 338-346.
17. Thomas, M.D.A. and Bamforth, P., 'Modelling Chloride Diffusion in Concrete: Effect of Flyash and Slag,' *Cem. and Concrete Res.*, **29** (1999) 487-496.
18. Nokken, M.R., Boddy, A., Hooton, R.D. and Thomas, M.D.A., 'Time-Dependant Diffusion in Concrete' *Cement and Concrete Research*, **35**, (2005) in press, available on-line, CEMCON3200, 8pp.
19. Garces Rodriguez, O. and Hooton, R.D., 'Influence of Cracks on Chloride Resistance of Concrete', *ACI Materials J.*, **100** [2] March-April (2003) 120-126.
20. DeSouza, S.J., Hooton, R.D. and Bickley, J.A., 'A Field Test for Evaluating High Performance Concrete Covercrete Quality', *Can. J. of Civil Engineering*, **25**, Dec. (1998) 551-556.
21. DeSouza, S.J. Hooton, R.D. and Bickley, J.A., 'Practical Quality Control Test Program for High-Performance Concrete in Precast Concrete Tunnel Liners', *Water-Cement Ratio and Other Durability Parameters: Techniques for Determination*, ACI SP-191 (2000) 99-114.
22. Whiting, D., 'Rapid Determination of the Chloride Ion Permeability of Concrete,' Final Report No. FHWA/JRD-371/1 19, Federal Highway Administration (1981).
23. Feldman, R.F., Chan, G., Brousseau, R.J., and Tumidajski, P., 'Investigation of the Rapid Chloride Permeability Test', *ACI Materials J.*, **91** [2] May-June (1994) 246-255.

24. Geiker, M., Thaulow, N. and Andersen, P.J., 'Assessment of Rapid Chloride Ion Permeability Test of Concrete with and without Mineral Admixtures,' *In Durability of Building Materials*, (eds. J.M. Baker, P.J. Nixon, A.J. Majumdar, H. Davis) E&FN Spon, London (1990) 493-502.
25. Julio-Betancourt, G.A. and Hooton, R. D., 'Study of the Joule Effect on RCPT Values and Evaluation of Related Electrical Properties of Concrete', *Cem. and Concrete Res.*, **34** (2004) 1007-1015.
26. Pfeifer, D.W., McDonald, D.B. and Krauss, P.D., 'The Rapid Chloride Permeability Test and Its Correlation to the 90-Day Chloride Ponding Test, *Prestressed/Precast Concrete Inst. J.*, **41** (4) (1994) 82-95.
27. Sherman, M.R., McDonald, D.B. and Pfeifer, D.W., 'Durability Aspects of Precast Prestressed Concrete Part 2: Chloride Permeability,' *Prestressed/Precast Concrete Inst. J.*, **41** (4) (1996) 76-95.
28. Hooton, R.D., Discussion, 'Rapid Chloride Permeability Test and Its Correlation to the 90-Day Chloride Ponding Test,' *J. Prestressed, Precast Concrete Inst.*, **42** [30] (1997) 65-66.
29. Ozyildirim, C., 'HPC Bridge Decks,' *ACI Concrete Internat.*, **21** (2) (1999) 59-60.
30. McGrath, P.F. and Hooton, R.D., 'A Re-Evaluation of the AASHTO T259-90 Day Salt Ponding Test,' *Cement and Concrete Res.*, **29** [8] (1999) 1239-1248.
31. Ozyildirim, C. 'Rapid Chloride Permeability Testing of Silica-Fume Concrete,' *Cement, Concrete and Aggregates*, CCAGPD, **16** [1] (1994) 53-56.
32. C. Hall, 'Water Sorptivity of Mortars and Concretes: A Review,' *Magazine of Concrete Res.*, **41** (147) (1989) 51-61.
33. Martys, N.S. and Ferraris, C.F., 'Capillary Transport in Mortars and Concrete,' *Cem. and Concrete Res.*, **27** (5) (1997) 757-760.
34. Ozyildirim, C. 'Rapid Chloride Permeability Testing of Silica-Fume Concrete,' *Cement, Concrete and Aggregates*, CCAGPD, **16** [1] (1994) 53-56.
35. Nordtest NT Build 368, Method for Capillary Absorption, Nordtest Post Box 116, FIN-02151, Espoo Finland (1991).
36. Hooton, R.D., Mesic, T. and Beal, D.L., 'Sorptivity Testing of Concrete as an Indicator of Concrete Durability and Curing Efficiency,' Proceedings, The Third Canadian Symposium on Cement and Concrete, Ottawa, Aug. (1993) 264-275.
37. Parrott, L.J., 'Moisture Conditioning and Transport Properties of Concrete Test Specimens,' *Mat. and Structures*, **27**, (1994) 460-468.
38. Hooton, R.D., Pun, P., Kojundic, T. and Fidjestol, P. 'Influence of Silica Fume on Chloride Resistance of Concrete,' Proceedings, PCI/FHWA International Symposium on High Performance Concrete, New Orleans, October (1997) 245-256.
39. Hooton, R.D., Gruber, K. and Boddy, A.M., 'The Chloride Penetration Resistance of Concrete Containing High-Reactivity Metakaolin,' Proceedings of the PCI/FHWA International Symposium on High Performance Concrete. New Orleans, Louisiana, October (1997) 172-183.
40. Bentz, D.P., Ehlen, M.A., Ferraris, C.F. and Winpigler, J.A., 'Service Life Prediction Based on Sorptivity for Highway Concrete Exposed to Sulfate Attack and Freeze-Thaw Conditions,' Pub. No. FHWA-RD-01-162, U.S. Dept. of Transportation (2002).
41. McGrath, P.F., *Development of Test Methods for Predicting Chloride Penetration into*

- High Performance Concrete*, Ph.D. Thesis, Department of Civil Engineering, University of Toronto, Toronto, Canada (1996).
42. Julio-Betancourt, G.A. and Hooton, R. D., 'Study of the Joule Effect on RCPT Values and Evaluation of Related Electrical Properties of Concrete', *Cem. and Concrete Res.*, **34** (2004) 1007-1015.
  43. Hooton, R.D., 'Problems Inherent in Permeability Measurement,' *Proceedings, Advances in Cement Manufacture and Use*, Engineering Foundation, N.Y. (1989) 143-154.
  44. Hooton, R.D., 'What is Needed in a Permeability Test for Evaluation of Concrete Quality', *Proceedings, Pore Structure and Permeability of Cementitious Materials*, Materials Research Society, 137 (1989) 141-150.
  45. El-Dieb, A.S. and Hooton, R.D., 'A High Pressure Permeability Cell with Improved Measurement Sensitivity for Saturated Water Permeability of High Performance Concrete,' *Cem. and Concrete Res.*, **24** [5] (1994) 854-862.
  46. El-Dieb, A.S. and Hooton, R.D., 'Water Permeability Measurement of High Performance Concrete Using a High Pressure Triaxial Cell,' *Cem. and Concrete Res.*, **25** [6] (1995) 1199-1208.
  47. Hearn, N. and Mills, R.H., 'A Simple Permeameter for Water or Gas Flow,' *Cem. and Concrete Res.*, **21** (1991) 257-261.
  48. Buenfeld, N.R., Shurafa-Daoudi, M-T. and McLoughlin, I.M., 'Chloride Transport due to Wick Action in Concrete,' in Chloride Penetration into Concrete, Proceedings of the RILEM International Workshop, St-Remy-les.Chevreuse, France, October (1995) 315-324.
  49. Nokken, M.R. and Hooton, R.D., 'Evaporative Transport of Chlorides in Concrete', Proceedings, Concrete Under Severe Environments, CONSEC'01, Vancouver, **1**, June 18-20 (2001) 357-364.
  50. Andrade, C., 'Calculation of Chloride Diffusion Coefficients in Concrete from Ionic Diffusion Measurements', *Cem. and Concrete Res.*, **23** (1993) 724-742.
  51. Aldred, J.M., Rangan, B.V., and Buenfeld, N.R., 'Effect of Initial Moisture Content on Wick Action Through Concrete', *Cem. And Concrete Res.*, **34** (2004) 907-912.
  52. Stanish, K.D., Hooton, R.D. and Thomas, M.D.A., 'A Rapid Migration Test for Evaluation of the Chloride Penetration Resistance of High Performance Concrete', Proceedings, PCI/FHWA/FIB International Symposium on High Performance Concrete, Orlando, (2000) 358-367.
  53. Nordtest NT Build 492, Method for Chloride Migration Coefficient from Non-Steady State Migration Experiments, (CTH Method), Nordtest Post Box 116, FIN-02151, Espoo Finland
  54. Stanish, K., Hooton, R.D., and Thomas, M., 'A Novel Method for Describing Chloride Ion Transport Due to an Electrical Gradient in Concrete, Part 1: Theoretical Description,' *Cem. and Concrete Res.*, **34** [1] (2004) 43-50.
  55. Stanish, K., Hooton, R.D., and Thomas, M., 'A Novel Method for Describing Chloride Ion Transport Due to an Electrical Gradient in Concrete, Part 2: Experimental Study,' *Cem. and Concrete Res.*, **34** [1] (2004) 51-58.
  56. Hooton, R.D., Geiker, M.R. and Bentz, E.C., "Effects of Curing on Chloride Ingress and Implications of Service Life", *ACI Materials J.*, **99** [2] (2002) 201-206.



## **Moisture Transport in Cementitious Materials – Theory and some Experimental Results**

Lars-Olof Nilsson

Laboratory of Building Materials, Lund Institute of Technology, Lund University, Sweden

### **Abstract**

Moisture transport is a significant parameter in describing the moisture conditions of a concrete that have a decisive effect on several properties and many aspects of deterioration processes. An overview is given on the various alternative theoretical treatment of moisture flow, including moisture flow under a temperature gradient. The moisture flow causing convection of ions is also discussed. Available data from literature and from recent experiments are presented and discussed.

### **1. Introduction**

The moisture conditions of a concrete structure have a decisive effect on several properties and many aspects of deterioration processes. Consequently moisture has a significant effect on the service-life of a structure. In this respect it is important to consider both material parameters and climatic parameters.

The moisture distribution in a concrete structure is determined by the concrete composition, curing and the microclimate in the different parts of the structure. A prediction requires access to data on the time-dependency of the binder reactions, moisture fixation and moisture flow, ambient temperature and humidity and computer software for the more complicated cases. A lot of research has been performed within these topics during the last decades. Today this knowledge can be applied in the design of structures.

This paper concentrates on moisture transport only; the mechanisms, theoretical descriptions and available data.

### **2. Moisture equilibrium conditions**

For the understanding and later references a few definitions and basic laws are first shown in this section.

## 2.1 Humidity and moisture in air and concrete

The moisture condition of air, also in the pore system of cementitious materials, is defined by the water vapour content  $v$  [ $\text{kg/m}^3$ ], the water vapour content at saturation  $v_s$ , constituting the relative humidity  $\varphi$

$$\varphi = \frac{v}{v_s} \quad (1)$$

To be exact, this relationship assumes that water vapour is an ideal gas. The original definition includes water vapour pressures.

The moisture content of concrete may be described in several ways:

- $w$  moisture content per volume [ $\text{kg/m}^3$ ]
- $u$  moisture content in per cent by weight [%]
- $S_{\text{cap}}$  degree of capillary saturation [-]

## 2.2 Local moisture equilibrium conditions

The water that is not chemically bound to the binder is physically bound in the pore system of the concrete. In the smallest pores the water is most firmly bound by adsorption in the reaction products. This water can dry out only at very low RH. The “equivalent” RH is a measure of the state of that water, its activity. In the capillary pores the water is bound by menisci, producing a very low, negative, pore water pressure. Since there is a relationship, assuming ideality, see equation (2), between the pore water pressure  $P_w$  and the relative humidity  $\varphi$  in the air above a meniscus, the RH can be used as a measure of the state of the moisture in concrete also for the liquid moisture<sup>[1]</sup>.

$$P_w = \frac{RT\rho_w}{M_w} \ln \varphi = \frac{RT\rho_w}{M_w} \ln \frac{v}{v_s} \quad (2)$$

where  $R$  is the gas constant,  $T$  the absolute temperature,  $\rho_w$  the density of water and  $M_w$  the molar weight of water. In this relationship one term including the water vapour pressure at saturation is neglected since it is significant only if RH is close to 100 %. Note that a second term must be added if the pore water contains dissolved ions.

The relationship between the total amount of evaporable water  $w_e$  [ $\text{kg/m}^3$ ] and the state of moisture RH can be calculated from available sorption curves, see the example in Fig 1.

The sorption properties depend mainly on the cement content  $C$ , the water-cement ratio  $w/C$ , the age or degree of hydration and the type and amount of silica-fume. They also vary to some extent with the type of cement, the temperature and the type and amount of other additives<sup>[3]</sup> such as fly ash and blast-furnace slag

The relationship is not totally independent of the temperature. A small temperature effect gives an increasing RH with increasing temperature at a constant moisture content of some 0.3-0.5 %RH/°C<sup>[4][5]</sup> depending on w/c and RH-level.

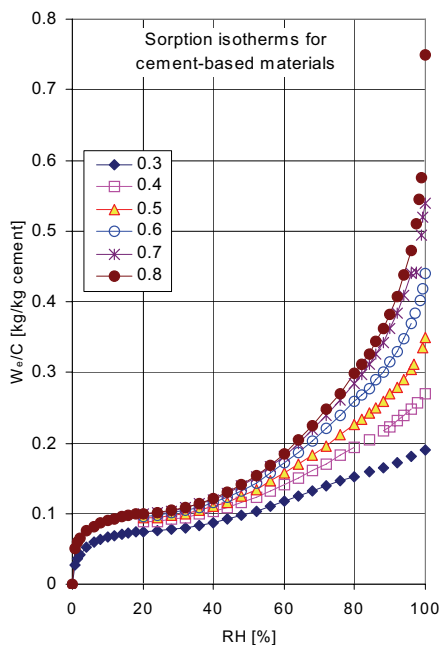


Figure 1 Desorption isotherms for OPC concrete with water-cement ratios 0.3-0.8<sup>[2]</sup>

The relationship also depends on the "moisture history", i.e. the extent of previous drying and wetting cycles. A clear, and large, hysteresis exists between the desorption and absorption isotherms, especially the 1<sup>st</sup> desorption isotherm, cf. Figure 2.

The equilibrium conditions during wetting and drying follow "scanning curves" between the desorption and absorption isotherms, cf. Figure 2.

Consequently, the local equilibrium between the content of moisture and the state of moisture is not a unique relationship. A certain moisture content may correspond to very different RH.

### 3. Moisture flow mechanisms and equations

Traditionally, the moisture flow in porous materials is regarded as a combination of vapour diffusion, with the vapour content as driving potential, and liquid flow with the pore water

pressure as potential. A description of the moisture flow  $J$  [kg/(m<sup>2</sup>·s)] with the vapour content  $v$  as a potential for the total flow and the vapour flow coefficient  $\delta_v$  is

$$J_v = -\delta_v \frac{\partial v}{\partial x} \quad (3)$$

The liquid flow depends on the pore water pressure gradients and the viscosity of water

$$J_l = -\frac{k_p}{\eta} \frac{\partial P_w}{\partial x} \quad (4)$$

where  $P_w$  is the pore water pressure,  $k_p$  the permeability and  $\eta$  the viscosity.

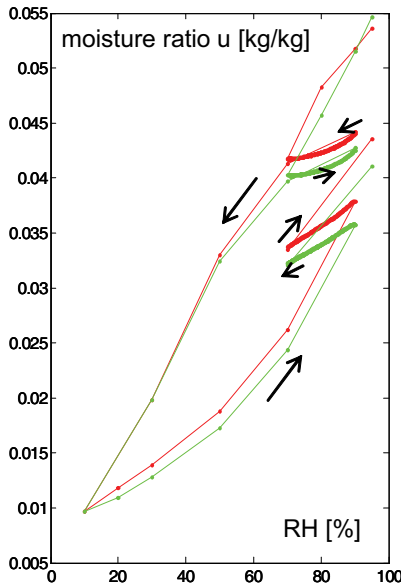


Figure 2 Desorption and absorption isotherms for an OPC concrete with water-cement ratio 0.36<sup>[6]</sup>. Absorption from 10 % RH. Scanning curves starting from the desorption and absorption isotherms, respectively.

All sorts of complicated descriptions of the total moisture flow have been used. Since measured data is lacking for the most complicated ones and the vapour flow and liquid flow usually occur in the same direction, and cannot be easily separated in an experiment, a simple description of the total moisture flow  $J$  can be used

$$J = J_v + J_l = -\delta_v \frac{\partial v}{\partial x} - \frac{k_p}{\eta} \frac{\partial P_w}{\partial x} = -\delta_v \frac{\partial v}{\partial x} - \delta_l \frac{\partial v}{\partial x} = -(\delta_v + \delta_l) \frac{\partial v}{\partial x} = -\delta \frac{\partial v}{\partial x} \quad (5)$$

The second term in equation (5) that includes  $P_w$  can be translated into a term in vapour content by using the relationship in equation (2), as long as the temperature remains constant or at least is independent of position  $x$ , i.e. no temperature gradient is present.

Another common alternative for the second term, since  $P_w$  is difficult to measure, is to use the moisture content  $w$  as a potential for liquid moisture flow.

$$J = -D_w \frac{\partial w}{\partial x} \quad (6)$$

In isothermal cases the gradients of vapour concentration and moisture content follow each other and the two terms can be combined into one. Equation (6) is then used for the total moisture flow.

However, the moisture flow description according to equation (6) has serious drawbacks for two reasons. Hysteresis causes a discrepancy in the  $w$ -RH relationship between points with different moisture history, e.g. if a part of the material has been rewetted. Differences or gradients in degree of hydration will create a similar discrepancy in the  $w$ -RH relationship. Of course, if two different materials are combined, equation (6) cannot describe the moisture flow over the interface.

What was said above referred to division of the total moisture flow into vapour and liquid flow only. Since there is no vapour or liquid in the reaction products, cf. figure 3, at least not at lower RH, equations (3)-(4) are not suitable. With equation (6) the adsorbed water flow can be regarded as a diffusion process with the concentration of water as the transport potential. However, the same drawbacks, already mentioned, of that equation are still applicable.

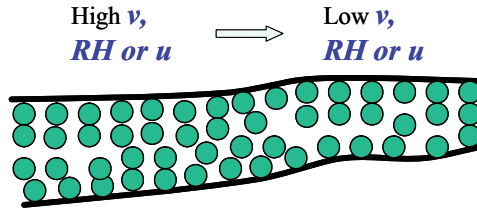


Fig. 3  
present.

Adsorbed water diffusion in a cementitious material, without vapour or liquid being present.

Because of that a description with RH as the state of adsorbed water should be most accurate, cf. equation (7). This is still not shown to be correct, however. For isothermal conditions it is not decisive but for non-isothermal cases it is crucial, see below.

$$J = -k_{RH} \frac{\partial \varphi}{\partial x} \quad (7)$$

A new way to describe the moisture flow through a, thin or thick, slice of a material with thickness  $\Delta x$  is the "fundamental potential"  $\Psi^{[7]}$

$$J = \frac{\Psi(\varphi_2) - \Psi(\varphi_1)}{\Delta x} \quad (8)$$

The fundamental potential  $\psi$  is the steady-state moisture flux times the thickness in an experiment where a specimen is exposed to  $\varphi_1$  and  $\varphi_2$  at the opposite sides. Consequently, it comes close to what is actually measured in experiments. No derivations or small differences will add to the uncertainty.

#### 4. Moisture dependency of moisture transport

Moisture transport coefficients are certainly not constants. Traditionally, the moisture dependency of the moisture flow is explained by the moisture transport mechanisms in porous materials being regarded as vapour flow or liquid flow, where the vapour flow is predominant at lower RH and liquid flow at higher, cf. figure 4.

At low RH the moisture flow is vapour diffusion because of a vapour concentration gradient. At increasing RH the adsorbate at the pore wall grows thicker which should somewhat reduce the available pore area for the diffusion of water vapour. When RH further increases, capillary condensation occurs in the narrowest pores. Here moisture now flows as a series of vapour diffusion and liquid suction. Eventually, the paths of liquid flow grow to fill most of the pore system. The moisture dependency of moisture transport, as a combination of vapour and liquid flow, in one pore is shown in principle in figure 5.

The slightly higher flow at very low humidity, because the adsorbate is thinner, has never been verified. In reality measurements always are done for a pore system with a combination of pore sizes and then this effect may be hidden.

In a pore system, moisture flow will occur in series and in parallel, in complicated combinations, cf. figure 6.

For a pore system, the moisture dependency of the moisture transport should be a "sum" of flows like in figure 5. The moisture dependency of the total moisture flow should look like figure 7, with a separation in vapour diffusion and liquid flow according to equation (5).

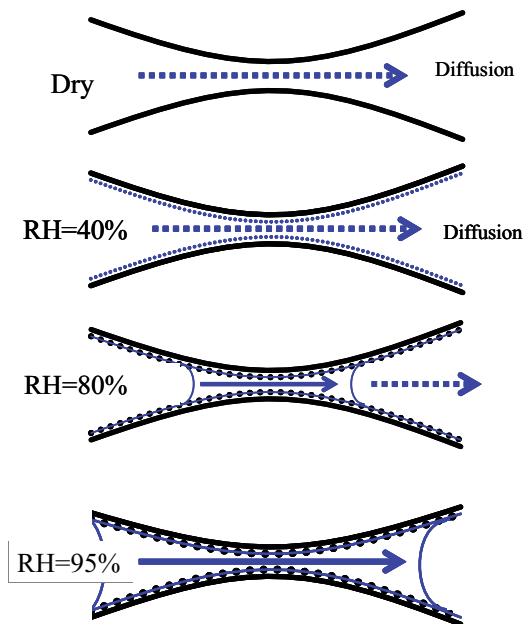


Fig. 4 Moisture flow in a pore as combinations of vapour diffusion and liquid suction at different levels of RH.

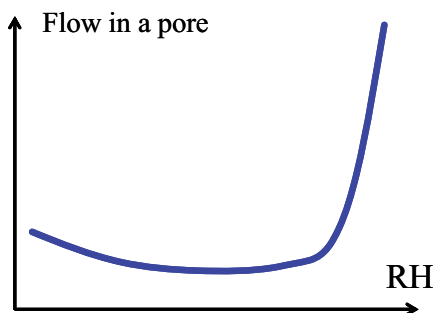


Fig. 5 Moisture transport in one pore as a combination of vapour diffusion and liquid suction.

As indicated in Figure 8, the relative proportion of moisture transport occurring as liquid flow tends to increase with an increase of RH. This is particularly true for materials with a high w/C. For the 0.4 w/C concrete, the moisture dependency seems to be very small. This should be due to a larger portion of moisture diffusion through the gel. That type of transport mechanism is only weakly influenced by the state of moisture in the material i.e. has a small moisture dependency.

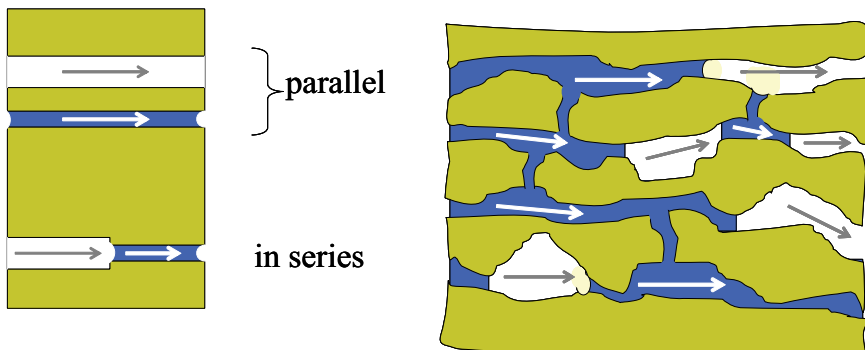


Fig. 6 Moisture flow through pore networks with vapour diffusion and liquid suction in various combinations.

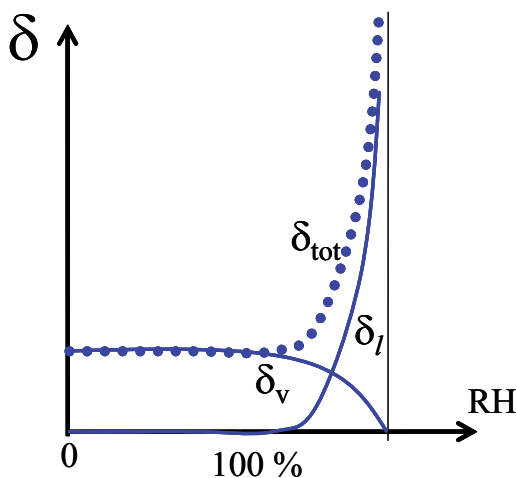


Fig. 7 Moisture transport in a pore system as a combination of vapour diffusion and liquid suction. Legends as in equation (5).

This is more or less what is seen in experiments. The moisture diffusion coefficient  $\delta$  is not at all a constant but a highly moisture-dependent parameter,  $\delta(\phi)$ , especially for concrete with w/C of 0.5 and higher, cf. Figure 8.

In Figure 9 a comparison is made to elucidate the moisture dependency of the average moisture transport coefficients  $\bar{\delta}(65,100)$  and  $\bar{\delta}(85,100)$  in two RH-intervals. With a significant moisture dependency for  $\delta(\phi)$  for high w/C concrete as in Figure 8, the moisture dependency of the average moisture transport coefficient  $\bar{\delta}(\phi_1, \phi_2)$  will strongly depend on the RH-interval limits.



With the same upper limit, here  $\varphi_2=100$  % RH, a lower low limit  $\varphi_1$  must give a much smaller average moisture diffusion coefficient since the interval is larger and the moisture dependency is strongly non-linear. This is also what Figure 9 shows, when comparing the two averages for  $\varphi_1$  equal to 65 and 85 % RH respectively.

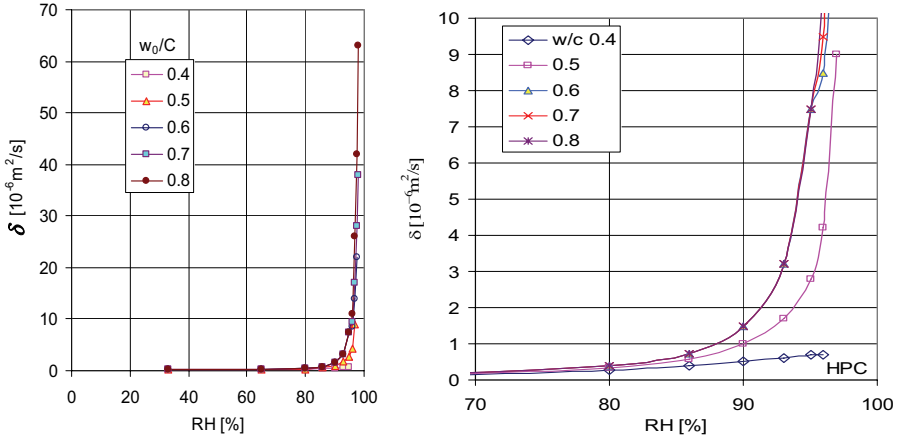


Fig. 8 Moisture diffusion coefficient  $\delta(\varphi)$  for concretes with different  $w/C$ <sup>[8]</sup>. The figure to the right is a portion of the lower right-hand corner of the left figure.

The moisture dependency, and the role, of adsorbed water flow in the reaction products of cementitious materials should be further investigated.

## 5. Relationships between moisture transport coefficients

Since there are unique relationships between the pore water pressure  $P_w$ , the state of moisture  $\varphi$  (RH), the moisture content  $w$  and the water vapour content  $v$ , any one of these parameters can be utilized to describe the total, isothermal, moisture flow  $J$  [kg/m<sup>2</sup>·s], combining all types of moisture flow, see Equation (9).

$$J = -\delta \frac{\partial v}{\partial x} = -\frac{k_p}{\eta} \frac{\partial P_w}{\partial x} = -k_{RH} \frac{\partial \varphi}{\partial x} = -D_w \frac{\partial w}{\partial x} \quad (9)$$

The relationships between some of these moisture transport coefficients are obviously fairly simple, see equation (10).

$$\delta_v = k_{RH} \frac{\partial \varphi}{\partial v} = k_{RH} \cdot v_s \quad (10)$$

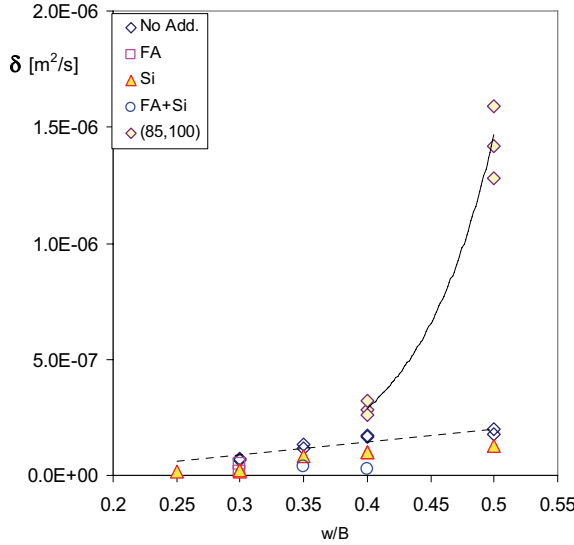


Fig. 9 Measured moisture diffusion coefficients  $\delta(65,100)$  and  $\delta(85,100)$  as averages in the RH-intervals 65-100% and 85-100% respectively. Data for  $\delta(85,100)$  from Hedenblad<sup>(8)</sup> and for  $\delta(65,100)$  from Nilsson<sup>10</sup>. The legend means no addition, fly ash, silica-fume respectively.

The relationship is much more complicated between the diffusivity and the others cf. equation (11).

$$D_w = \delta_v \frac{v_s}{\frac{\partial w}{\partial \phi}} = \frac{k_p}{\eta} \cdot \frac{1}{\frac{\partial w}{\partial P_w}} \quad (11)$$

where  $\frac{\partial w}{\partial \phi}$  is the slope of the sorption isotherm, and  $\frac{\partial w}{\partial P_w}$  is the slope of the suction curve, both called the “moisture capacity”.

Between the “diffusion coefficient”  $\delta$  and the moisture transport coefficient  $k_{RH}$  there is a plain proportionality with the vapour content at saturation as the proportionality constant, similar to the relation between the vapour content and the relative humidity. The moisture diffusivity  $D_w$ , however, has a non-linear relationship to the other flow properties, depending on the slope of the sorption isotherm. That slope is small in an RH-interval around 20-70 % but much higher at lower and higher RH, at least for concrete with w/C above 0.4, cf. Figure 10.

An extreme example of this “peculiar” moisture dependency of the moisture diffusivity  $D_w(w)$  is shown in figure 11 for aerated concrete. The maxima and the minima in figure 11 all correspond directly to the slope of the suction curve, cf. equation (11).

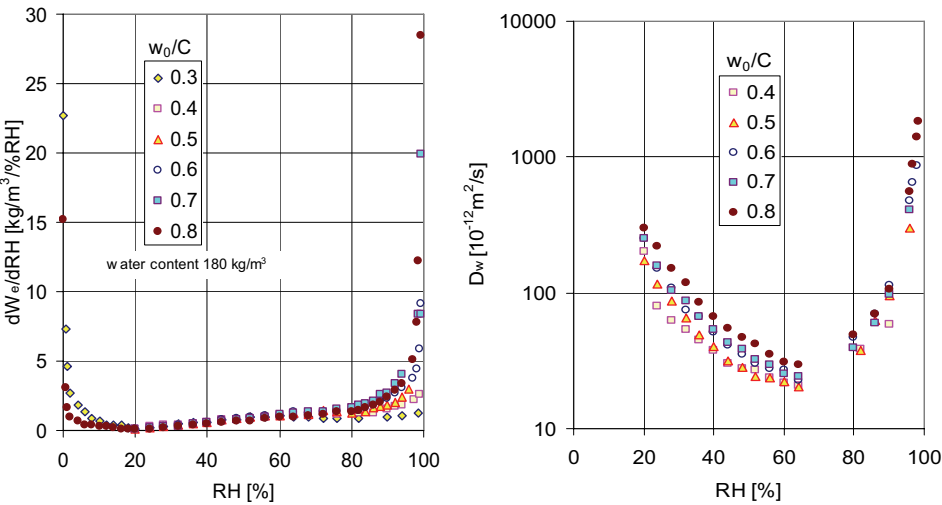


Fig. 10 The slope of the desorption isotherms in figure 1 (left) and the diffusivities  $D_w$  (right), for concretes with different  $w/C$ . Based on data in figure 8.

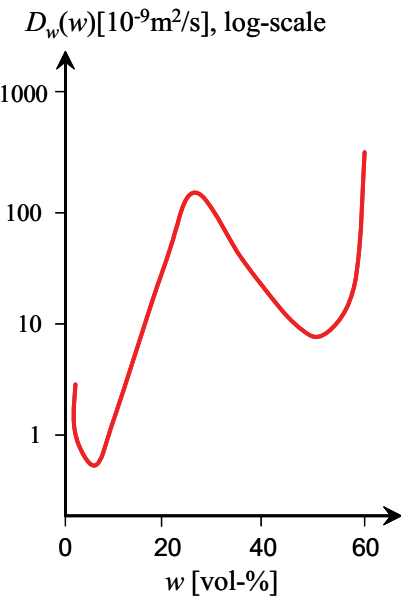


Fig. 11 Moisture diffusivity for an aerated concrete, van der Kooi (1971)<sup>[9]</sup>.

The fundamental potential  $\Psi$  is a direct measured flow in an experiment. Theoretically, it is the integral of  $\delta(RH)$ . Because of that it varies much less with the RH than  $\delta$  does, see Fig 12.

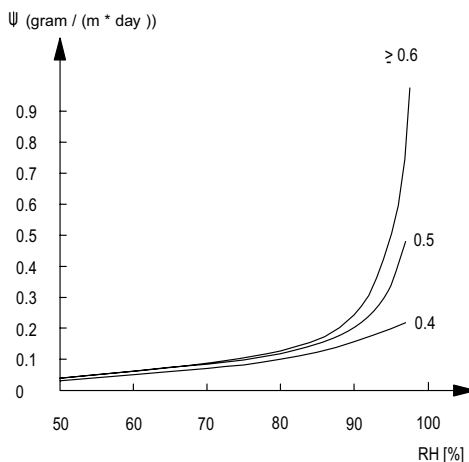


Fig 12. The fundamental potential  $\Psi$  for well cured concrete with water-cement ratios 0.4-0.8. Based on the same data as in figure 8.

## 6. Moisture transport properties versus concrete composition and structure

Moisture flow through concrete and mortar compared to moisture flow through a corresponding paste shows interesting results<sup>8</sup>. At low humidity, below some 70-80% RH, the flow through paste is larger than through concrete and mortar. The aggregate obviously acts as obstacles to the vapour flow. At higher humidity when the pore system is more saturated, the effect is the opposite. Flow through concrete is larger than through paste in spite of the aggregates as obstacles. The more porous interfacial zone along the aggregate grains may be one explanation. More micro cracks and higher small air void contents may be other explanations.

The air content is one significant parameter that influences the moisture flow. The larger air void system in mortar and concrete will always be air-filled. Moisture flow through the gel will take a “short-cut” through these large pores, as vapour diffusion. An example is shown in figure 13.

Closer to saturated conditions, at least for higher w/C, the air-filled voids will be obstacles for the liquid moisture flow. For low w/C the air pore system should still provide easier paths for the moisture flow, also close to saturation.

Consequently, in all experiments on moisture flow the air content must be considered. This is especially important when comparing paste with mortar and concrete.

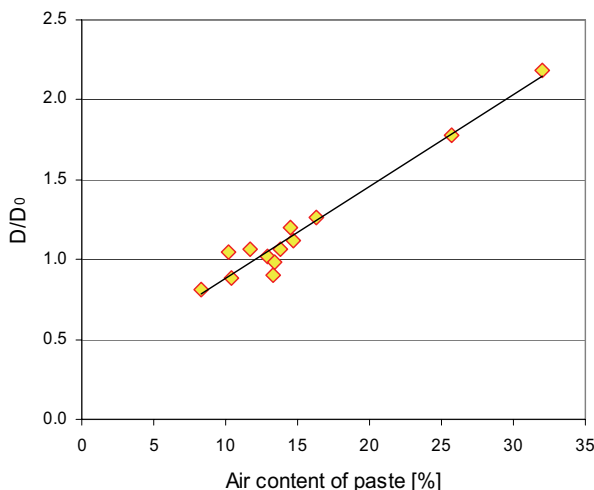


Fig. 13 Moisture diffusivity  $D_w$  for OPC mortar with  $w/C=0.6$  as a function of natural and entrained air content<sup>2</sup>, expressed as air content of the paste. Reference value  $D_0$  for a mortar with an average air content of 11.6 %. Mean values of four specimens.

The moisture flow coefficient  $\delta$  increases very much above 90 % RH, see Fig 8, since more and more of the flow is liquid flow. The properties are almost identical for concretes with various water-cement ratios. Only very close to saturated flow the  $w/C$  has an effect<sup>8</sup>. For HPC it is obvious that the pure liquid flow is negligible and, because of the large degree of saturation, pure vapour diffusion in air in the pores is only a part of the total flow. A significant portion of the transport paths for moisture should be diffusion of moisture through the gel, to some extent in series with diffusion in air, depending on the surrounding conditions. Wetter conditions should give less diffusion in air but more diffusion through the gel.

The average moisture transport coefficient  $\bar{\alpha}(65,100)$  measured<sup>(10)</sup> in the interval 65-100 % RH is shown in Figure 14. The effects of  $w/B$  and silica fume replacement are clearly visible. A factor of 1/10 to 1/20 is found when comparing  $w/B=0.5$  and 0.25. A cement replacement by 5-10 % silica fume and 10-20 % fly ash seems to give the lowest moisture transport coefficients, especially if silica fume and fly ash are combined. Silica fume has a very large effect at low  $w/B$ , 0.3 and lower, but the combination of fly ash and silica fume seems to work well also at  $w/B$  0.40.

As can be seen in Figure 15, the moisture transport coefficients  $\bar{\alpha}(65,100)$  are, at least to some extent, almost linearly influenced by the larger porosity of the concrete. The porosity  $p_{75}$  in the figure is the porosity corresponding to the pores that are emptied when concrete is dried to 75

% RH. Not surprisingly, however, the scatter is large since the pore volume says little about the connectivity between the pores.

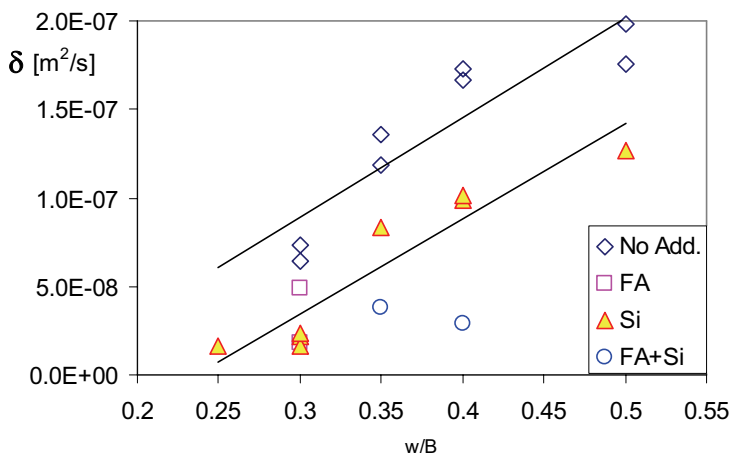


Fig. 14 Measured moisture diffusion coefficients  $\delta(65,100)$  at an age of 6.6 years, as averages in the RH-interval 65-100%, as a function of water-binder ratio<sup>[10]</sup>. The legend means no addition, fly ash, silica-fume respectively.

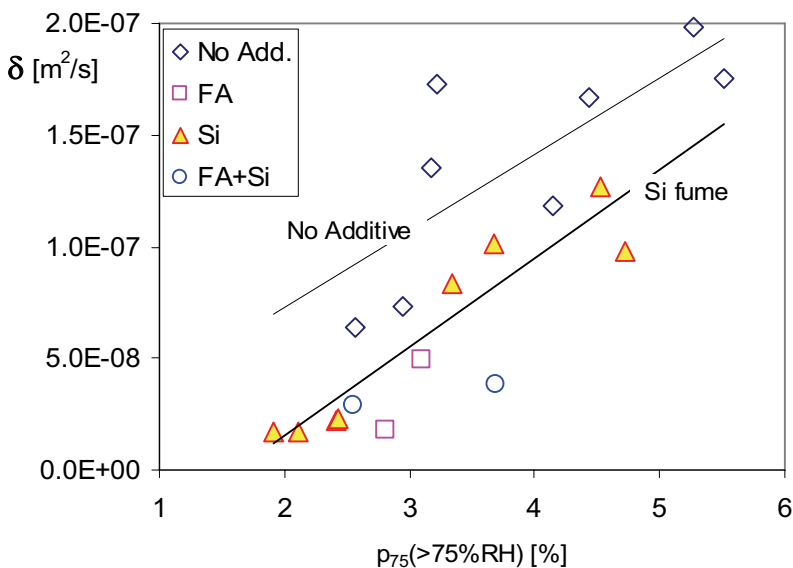


Fig. 15 Measured moisture diffusion coefficients  $\delta(65,100)$  at an age of 6.6 years, as a function of the part of the porosity that is filled above 75 % RH.

## 7. Non-isothermal moisture transport

In some rare cases cementitious materials are exposed to temperature conditions where temperature gradients occur for longer periods of time. Since ordinary concrete is an excellent heat conductor, temperature gradients normally vanish quickly and will have no significant effect on moisture flow.

These rare cases are of two types. Special concretes may have many times lower heat conductivity than ordinary concrete. That will create significant temperature gradients if a concrete structure is exposed to temperature differences. Another type of case is when concrete is exposed to special, large and constant temperature differences. One important example is concrete hydro-power dams, where the upstream side is very much warmer than the downstream side during winter. Another example is concrete slabs with cast-in heating pipes<sup>[11], [13]</sup>. A third is nuclear reactor containments<sup>[12]</sup>.

In such cases liquid flow and vapour diffusion may very well occur in different directions, because the vapour concentration gradient and the pore water pressure gradient could be of opposite signs. Consequently, the two terms in equation (5) can no longer be combined into one. Instead a description by using two terms, perhaps three, must be utilized. Alternative examples are given in equation (12).

$$J = -\delta_v \frac{\partial v}{\partial x} - \frac{k_p}{\eta} \frac{\partial P_w}{\partial x} = -\delta_{vT} \frac{\partial v}{\partial x} - D_{wT} \frac{\partial w}{\partial x} = -\delta'_{vT} \frac{\partial v}{\partial x} - D_T \frac{\partial T}{\partial x} \quad (12)$$

With a description by using the first alternative in equation (12), two terms containing the vapour and the pore water gradients respectively, is straightforward and easy to use. However, since it has not been possible to split the total moisture flow into these two terms, data is lacking for the two moisture transport coefficients  $\delta_v$  and  $k_p$ .

The significance of this lack of data is exemplified in figure 16, showing the predicted RH-distributions in a 200-mm thick concrete floor with OPC concrete with w/C=0.6 where heating pipes are cast in at a depth of 50 mm. Predictions are made with a finite difference model where moisture flow is described by the first part of equation (12). The first prediction (left) is made by assuming pure vapour diffusion only, i.e.  $k_p=0$ . The second prediction is made by “splitting” the total moisture flow into vapour and liquid flow according to the insert in the right part of the figure.

With a significant portion of the total moisture flow being liquid flow, the remaining moisture will be redistributed in such a way that RH will be almost constant at all depths and between the heating pipes. With vapour flow being more dominant (left) there will be a significant difference in RH between the pipes and between the top and bottom of the floor slab. Only careful measurements can tell which prediction is correct.

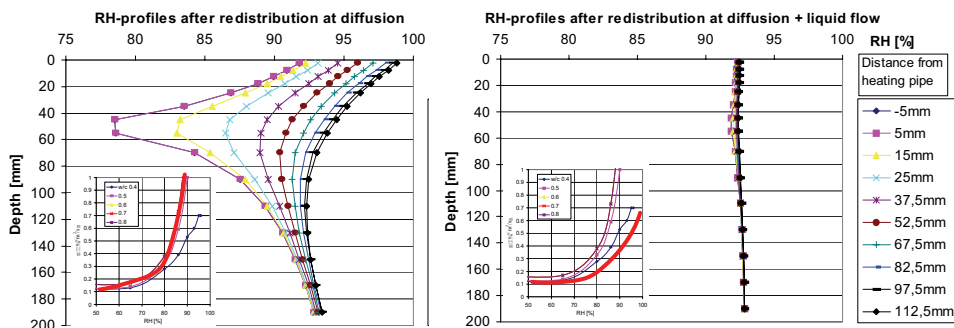


Fig 16. Predicted RH-distributions after redistribution of remaining moisture in a concrete floor slab with heating pipes<sup>[13]</sup>.

For application where moisture flows under temperature gradients we have to understand the moisture flow mechanisms much better. In cementitious materials a separation of the moisture flow into vapour diffusion, liquid flow and “bound water” diffusion might be most suitable.

## References

1. Bager, D. (ed.) “Water in Cement Paste & Concrete. Hydration and Pore Structure”. The Nordic Concrete Federation Workshop, Skagen, Denmark, 7 & 8 October 1999.
2. Nilsson, L-O (1980) *Hygroscopic moisture in concrete - drying, measurements and related material properties*. TVBM-1003, Building Materials. Lund Institute of Technology, Lund
3. Baroghel-Bouny, V., Mainguy, M., Lassabatere, T. and Coussy, O. (1999) “Characterization and identification of equilibrium and transfer moisture properties for ordinary and high-performance cementitious materials. Cement and Concrete Research 29, pp. 1225-1238.
4. Nilsson, L-O. (1988) *Temperature effects in relative humidity measurements on concrete - Some preliminary studies*. Nordic Symposium on Building Physics, Lund, August 1987, Document D13:1988, Swedish Council for Building Research, Stockholm
5. Radjy, F., Sellevold, E. J. & Kielsgaard Hansen, K. (2003) *Isosteric vapor pressure – temperature data for water sorption in hardened cement paste: Enthalpy, entropy and sorption isotherms at different temperatures*. Report R-057, BYG-DTU, Technical University of Denmark.
6. Åhs, M (2005) *Scanning sorption properties measured by a sorption balance*. Data from a first study, Building Materials. Lund Institute of Technology, Lund
7. Arfvidsson, J (1994) *Isothermal moisture processes in porous materials* (in Swedish). Report TVBH-1007. Building Physics, Lund Institute of Technology
8. Hedenblad, G. (1993) *Water vapour permeability of cement based materials*, rapport TVBM-1014, Building Materials. Lund Institute of Technology, Lund



9. van der Kooi, J. (1971) *Moisture transport in cellular concrete roofs*, Uitgeverij Waltman, Delft
10. Nilsson, L.-O. (2002) *Long-term moisture transport in high performance concrete*. Materials and Structures/Matériaux et Constructions, Vol. 35, December 2002, pp. 641-649
11. Leivo, V. & Rantal, J. (2005) *Moisture behaviour of a massive concrete slab with a low temperature floor heating system during the initial drying period*, Construction and Building Materials 19, pp. 297-305
12. Majumdar, P., Gupta, A. & Marchertas, A. (1995) *Moisture propagation and resulting stress in heated concrete walls*, Nuclear Engineering and Design 156, pp. 147-158
13. Sjöberg, A., Nilsson, L.-O. & Rapp, T. (2002) *Moisture measurements in floors with heating pipes. Part I.* (in Swedish) Publication P-02:1, dept. of Building Materials, Chalmers University of Technology, Göteborg 2002.



# **The Effect of PP fiber on the Compressive Strength and Water Permeability of Self-Compacting Concrete and High Performance Concrete**

G.Ye<sup>(1)</sup>, G. De Schutter<sup>(2)</sup>, L. Taerwe<sup>(1)</sup> and K. van Breugel<sup>(2)</sup>

<sup>(1)</sup>Microlab, Faculty of Civil Engineering and Geosciences, Delft University of Technology, Delft, The Netherlands.

<sup>(2)</sup>Magnel Laboratory for Concrete Research, Department of Structural Engineering, Ghent University, Belgium

## **Abstract**

This contribution aims to examine the influence of PP fiber on the compressive strength and permeability of high performance concrete and self-compacting concrete. The fiber content varies between 0 and 1 kg/m<sup>3</sup> (or 0 to 1.5 percent by volume content). The compressive strength and the water permeability measurements have been tested at age of 1 month, 3 months and 6 months. Meanwhile the microstructure of samples at the same age also has been determined by means of Mercury Intrusion Porosimetry (MIP) and Scanning Electron Microscopy (SEM). The role of PP fiber on the relation between permeability and pore structure has been investigated and analyzed.

## **1. Introduction**

The properties of High Performance Concrete (HPC) are a direct function of the characteristics of the constituents and mixture proportions. In general, the mechanical properties of HPC have attributes of truly high-performance because of its low unit water content, low water-cementitious materials ratio, low porosity, very dense and uniform microstructure, hence high durability. The invention of Self-Compacting Concrete (SCC) in the 1990's with its great workability and flowability, has receiving wide applications in infrastructures. Due to the higher content of filler used in SCC, the microstructure of SCC varied very much in comparison with traditional concrete and HPC. However, experiments [1] indicated that the pore structure of SCC is very similar to HPC concerning pore volume and pore size distribution.

Due to the dense microstructure of HPC and SCC, they risk a high probability of explosive spalling when exposed to high temperature. In general, the addition of PP fiber in concrete will reduce the spalling risk. This is due to the melting of the PP fiber, generating more pores. This enables moisture and heat to escape, thus leading to a lower pore pressure level in the concrete [2-5]. On the other hand, due to the addition of PP fiber, the mechanical properties and the permeability might change in the long term. This paper aims to examine the influence of PP

fiber on the compressive strength and permeability of high performance concrete and self-compacting concrete. The PP fiber content varies between 0 to 1 kg/m<sup>3</sup>. The compressive strength and water permeability measurements have been tested at curing age of 1 month, 3 months and 6 months. Meanwhile the microstructure of samples at same curing age also has been determined by means of Mercury Intrusion Porosimetry (MIP) and Scanning Electron Microscopy (SEM). The role of PP fiber on the relation between permeability and pore structure has been investigated and analyzed.

## 2. Experimental program

### 2.1 Materials

The SCC mixtures used in this study were prepared with Portland cement CEM I 52.5. Limestone powder, produced from carboniferous limestone of a very high purity (98% of CaCO<sub>3</sub> content), was added as filler. The chemical composition of cement and limestone filler is given in Table 1. The density of limestone powder was 2650 kg/m<sup>3</sup>. The Blaine value of the limestone powder and CEM I 52.5 are 526 m<sup>2</sup>/kg and 420 m<sup>2</sup>/kg, respectively. The aggregate was crashed carboniferous.

Table 1 Chemical composition of cement and limestone powder

	CEM I 52.5 (%)	Limestone filler (%)
CaO	63.95	-
SiO <sub>2</sub>	20.29	0.80
Al <sub>2</sub> O <sub>3</sub>	4.52	0.17
Fe <sub>2</sub> O <sub>3</sub>	2.35	0.10
MgO	2.22	0.50
K <sub>2</sub> O	0.94	-
Na <sub>2</sub> O	0.20	-
SO <sub>3</sub>	3.35	-
Cl <sup>-</sup>	0.015	0.002
CaCO <sub>3</sub>	-	98.00
C <sub>3</sub> S	59.0	-
C <sub>2</sub> S	12.60	-
C <sub>3</sub> A	8.01	-

The PP fiber has a length of 12 mm and a diameter of 18 µm. The characteristics of the PP fibers used in this study are given in Table 2.

### 2.2 Mixtures design and specimens casting

The mixture proportions of SCC and HPC without PP fiber are listed in Table 3. Table 4 lists the mix proportion of samples made with PP fiber at a dosage of 0.5 and 1 kg/m<sup>3</sup> in the SCC and HPC mixtures. Due to the PP fiber added in the SCC and HPC mixtures, the total amount of glenium and superplasticizer had to be increased in order to obtain the same workability as the SCC or HPC mixtures made without PP fiber. Fresh SCC mixtures are evaluated by U-box and slump flow in order to guarantee a good flowability.

Table 2 Characteristics of PP fiber

Density at solid state	0.93
Density at liquid state	0.85
Thickness (μm)	18
Width (μm)	150
Length (mm)	12
Melting temperature °C	171
Temperature at vaporization °C	341
Burning temperature °C	460
Thermal conductivity (w/m K)	0.15

Table 3 Mix proportions of SCC and HPC without PP fiber (kg/m<sup>3</sup>)

	SCC		HPC
	SCC01	SCC02	HPC
Portland cement CEM I 52.5	400	400	400
Water	165	192	132
Sand	853	782	650
Aggregate 4-8 mm	300	300	530
8-16 mm	400	340	720
Limestone powder	200	300	-
Glenium 51 (liter)	3.2	2.7	-
Superplasticizer Rheobuild	-	-	8.45
Total powder content	600	700	400
Water/cement ratio	0.41	0.48	0.33
Water/powder ratio	0.28	0.27	0.33

Table 4 Mix proportions of SCC and HPC with PPF (kg/m<sup>3</sup>)

	SCC				HPC	
	SCC01PPF05	SCC01PPF1	SCC02PPF05	SCC02PPF1	HPCPPF05	HPCPPF1
Portl. cement I 52.5	400	400	400	400	400	400
Water	165	165	192	192	132	132
Sand	853	853	782	782	650	650
Aggregate 4-8 mm	300	300	300	300	530	530
8-16 mm	400	400	340	340	720	720
Limestone powder	200	200	300	300	-	-
Glenium 51 (liter)	4.42	5.55	3.25	3.5	-	-
Superplasticizer	-	-	-	-	7.0	8.45
PP fiber	0.5	1	0.5	1	0.5	1
Tot powder content	600	600	700	700	400	400
Water/cement ratio	0.41	0.41	0.48	0.48	0.33	0.33
Water/powder ratio	0.28	0.28	0.27	0.27	0.33	0.33

Firstly, the aggregate, the sand, the cement and the PP fiber were mixed during half a minute in order to obtain a uniform distribution before water was added. After two minutes mixing with

water, the glenium or superplasticizer was added and the concrete was mixed for another three minutes. After mixing, the density of the concrete was determined, and the fresh concrete was tested by means of U-box and slump flow. When the fresh concrete reached the required flowability, the mixtures were immediately cast in 150×150×150 mm cube. After demoulding, the cubes were stored in an air-conditional room at 20°C ± 2 °C and at least 90% relative humidity until the testing age.

## 2.3 Test method

### 2.3.1 Compressive strength test

The compressive strength was determined according to standard test method (BS 1881-116:1983). Three specimens of each concrete were tested at each age of curing.

### 2.3.2 Permeability test

The water permeability was measured according to the German Standard DIN 1048 [6]. When testing the specimens, the following procedure is used:

The test specimen with a diameter of 100 mm and a height of 120 mm is sawn from the middle of a concrete cube 150 mm and is sealed with epoxy along the cylindrical surface. The tops of the specimen are carefully brushed with a steel brush to remove the surface skin and expose that area which is to be subjected to water pressure.

In each test, three specimens are clamped into the equipment. Then the specimens are exposed to a regime of three subsequent water pressures in 1 bar for 2 days, 3 bar for 1 day and 7 bar for 1 day. After 4 days, the three specimens are split, the water penetration profile is recorded, and the maximum penetration depth  $x_{\max}$  is measured.

According to the description in [7], assuming that Darcy's law applies for stationary, laminar flow of liquid water through circular pores in hardened concrete, the water permeability  $K$  can be calculated as follow:

$$K = \left( \frac{x_{\max}}{2^{\frac{1}{2}}(h_1 t_1 + h_2 t_2 + h_3 t_3)} \right)^2 \quad (1)$$

where,  $h_1$ ,  $h_2$  and  $h_3$  are three different pressure levels

$t_1$ ,  $t_2$  and  $t_3$  are different periods of time at three different pressure levels.

Mean water penetration depths and corresponding standard deviations were determined after 1, 2, 3, 5 and 6 month of curing age for both series of specimens.

### 2.3.3 Mercury porosimetry test (MIP)

MIP is used to determine the pore size distribution of pastes on samples dried at 105 °C till a constant weight (weight loss less than 0.01g/day). The measurements were made with a PMI automated porosimeter. The maximum pressure of PMI automated porosimeter is 420 MPa. In

order to avoid the influence of higher pressures damaging the CSH gel structure, the highest pressure used in this experiment was 212 MPa. According to the Washburn equation [8], with this pressure a minimum pore diameter of 0.0069  $\mu\text{m}$  was accessed.

### 2.3.4 BSE image acquisition and analysis

The scanning electron microscopy was used to observe the microstructure and the morphology of PP fiber on the polished specimens. In order to obtain high quality image use a backscattering scanning electron detector, the samples have to be prepared carefully, including epoxy impregnation, cutting, grinding and polishing. The procedure was extensively described in [9].

## 3. Results and discussions

### 3.1 The development of compressive strength

As shown in Figures 1 and 2 (left), as expected, with the increase of curing time, the compressive strength increases as well, regardless of the type of mixture. If HPC is compared with SCC01 at different curing stages as shown in Figure 2 (right), an almost identical compressive strength is found for both mixtures, although they have a different w/c ratio. The w/p ratio of SCC01 (0.28) was much lower than HPC (0.33). This finding can be explained by the effect of the high amount of limestone filler in the SCC samples, filling up the empty pore space.

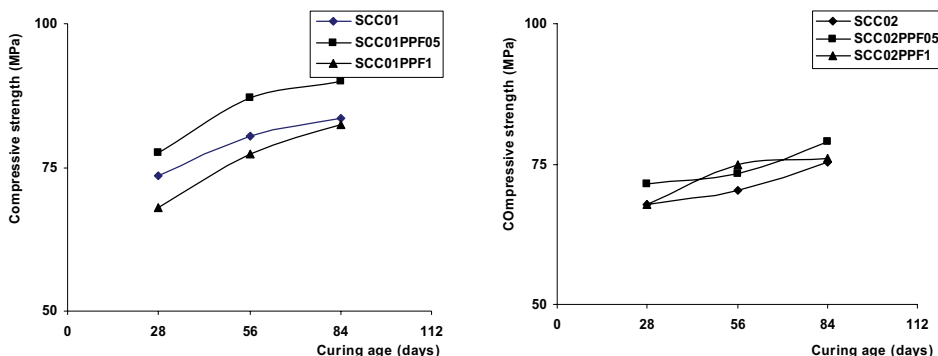


Figure 1. Compressive strength of SCC01 and SCC02 at curing age of 28, 56 and 84 days.

### 3.2 Effect of amount of PP fibers on compressive strength

The effects of amount of PP fiber on compressive strength are shown in Figures 3 and 4.

With increasing amount of PP fibers, the compressive strength is not always increasing. For an increasing amount of PP fiber from 0 to 0.5  $\text{kg/m}^3$ , the compressive strength also increases. However, the tendency slows down when the PP fiber content further increases to 1  $\text{kg/m}^3$ . Obviously, an optimal amount of PP fiber in concrete could be defined based on the

compressive strength, Due to the high surface area and low mechanical properties of PP fibers, the total amount of PP fiber in concrete is limited in order to gain a good compressive strength and workability. The optimization of the amount of PP fiber is between 0.5 to 1 kg/m<sup>3</sup>. An amount of PP fibers of 0.7 to 0.8 kg/m<sup>3</sup> in concrete can sufficiently avoid explosive spalling, as found in [5, 10]. This is consistent with the compressive strength evolution found in this study.

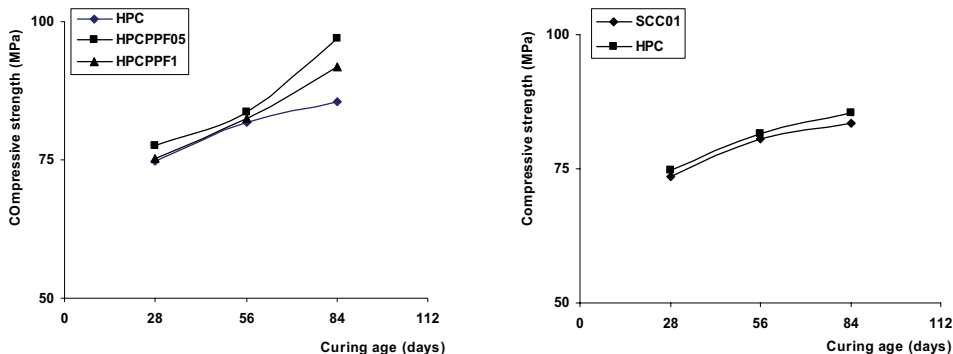


Figure 2. Compressive strength of HPC and the comparison of SCC01 and HPC at curing age of 28, 56 and 84 days.

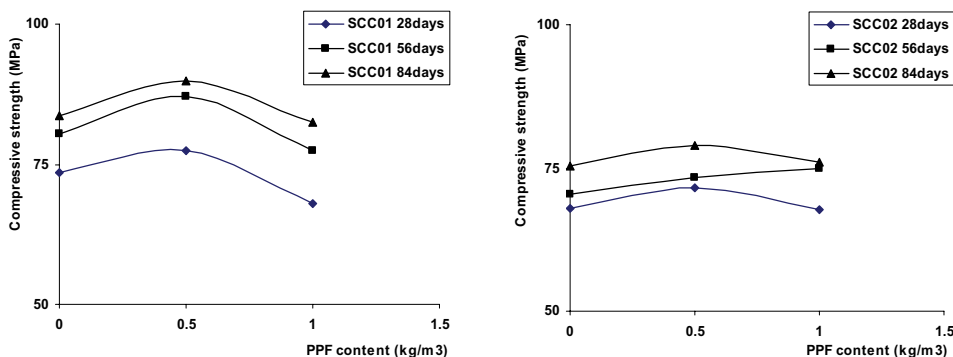


Figure 3. The effect of PP fibers on compressive strength of SCC01 and SCC02

### 3.3 Effect of amount of PP fibers on water permeability

The water permeability decreases with increasing curing age, regardless the type of mixtures and the amount of PP fiber content. However, the amount of PP fibers has a significant effect on the water permeability. As can be seen from Figure 6 (right), with increasing amount of PP fibers, the permeability increases, even at a curing age of 6 month. This is especially valid for the SCC sample with higher water/cement ratio (SCC02).



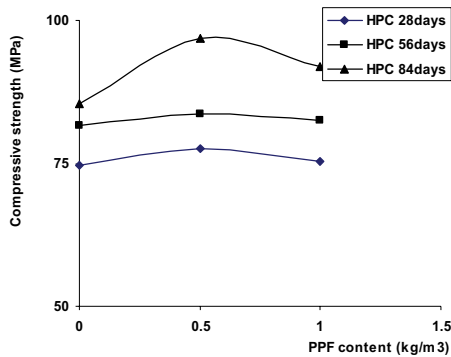


Figure 4. The effect of PP fibers on compressive strength of HPC

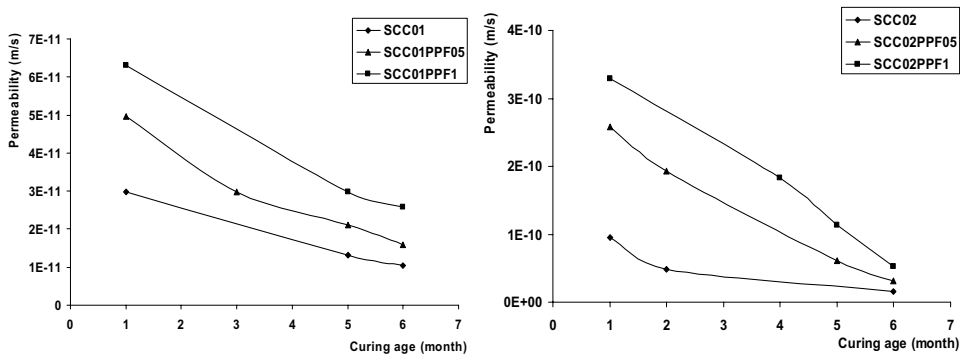


Figure 5. The effect of PP fibers on water permeability of SCC01 and SCC02

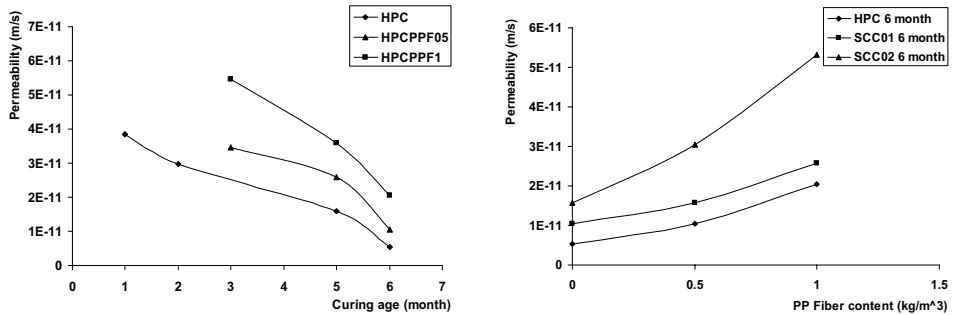


Figure 6. The effect of PP fibers on water permeability of HPC and the comparison of three mixtures at a curing age of 6 months

### 3.4 Effect of the microstructure on the permeability

With MIP, the total porosity and pore size distribution were measured for the samples with and without PP fibers at curing age of 1 month and 2 months. The MIP results at curing age of 2 months are presented in Figure 7 and Figure 8 (left).

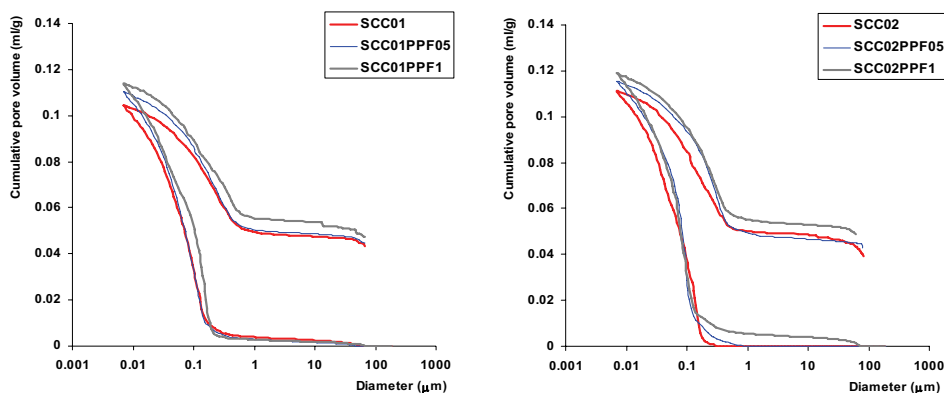


Figure 7. The total porosity and pore size distribution of SCC01 and SCC02 at curing age of 3 month.

From Figures 7 and 8 (left), it can be found that the presence of PP fibers in the mixtures leads to an increase of total porosity. This is due to the fact that for higher pressures mercury could access the space where the PP fiber exist. As also can be observed from the SEM image shown in Figure 8 (right), the presence of PP fibers and its interface together with capillary pores could form a path. This will increase the connectivity of capillary porosity, yielding an increasing water permeability, either for HPC or SCC. A preliminary computer tomography image (Figure 9) also shows an increase of connectivity in the sample when PP fibers were added.

## 4. Conclusion

From this study, it is concluded that the presence of PP fibers in concrete effects both on the compressive strength and the water permeability. When the amount of PP fibers changes from 0 to  $0.5 \text{ kg/m}^3$ , the compressive strength increases. The compressive strength shows a small tendency to decrease when the PP fiber content reaches  $1 \text{ kg/m}^3$ . The presence of PP fiber in concrete increases the connectivity of the capillary porosity which is indirectly observed from MIP measurements. This leads to higher water permeability, which probably also affects the long-term durability of concrete. An optimization of the amount of PP fibers  $0.7 - 0.8 \text{ kg/m}^3$  is beneficial for both compressive strength and fire spalling [5, 10]. This amount of PP fibers is also acceptable in the water permeability.

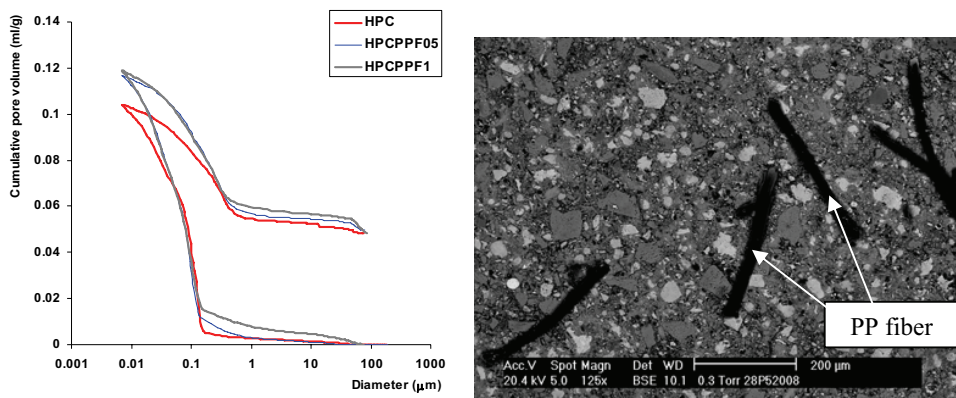


Figure 8. (left) The total porosity and pore size distribution of HPC at a curing age of 3 months (right) SEM image of SCC02, PP fiber content 0.5 kg/m<sup>3</sup> at a curing age of 28 days, (the dark parts are PP fibers).

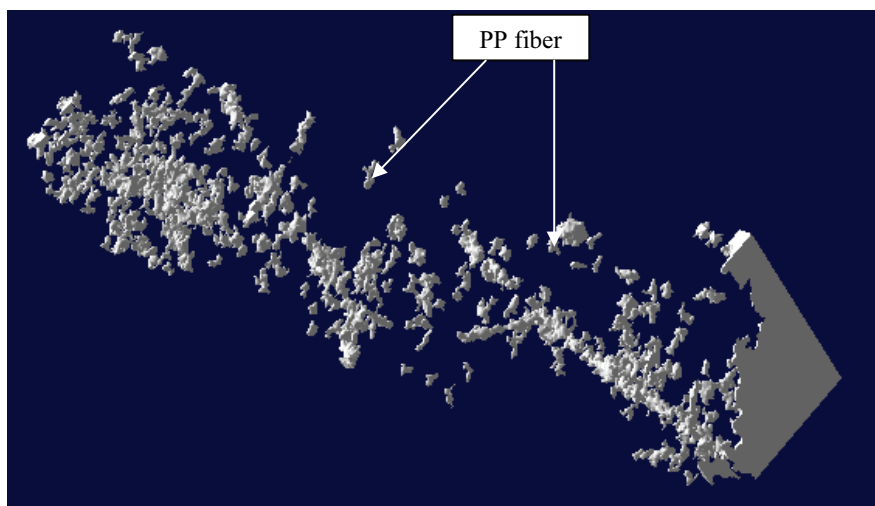


Figure 9. 3D computer tomography image of SCC02, PP fiber content 0.5 kg/m<sup>3</sup> at age of 28 days

## Acknowledgements

The research was financially supported by the Fund for Scientific Research - Flanders (Belgium) (FWO), this is gratefully acknowledged.

## References

1. Ye, G., Liu, X., De Schutter, D., Poppe, A. -M. and Taerwe, L., 'Hydration and microstructure studies on self-compacting cement paste containing limestone powder as filler', submitted to *Cem. Concr. Res.* (2005).
2. Bazant, Z.P., and Kaplan, M.F., 'Concrete at high temperatures', (Longman – Addison-Wesley, London, 1996).
3. Kodur, V.K.R., 'Spalling in high strength concrete exposed to fire — concerns, causes, critical parameters and cures', in Proceedings of ASCE Structures Congress, Philadelphia, PA, 2000 68-79.
4. Anderberg, Y., 'Spalling Phenomena of HPC and OC', in Proceedings of International Workshop on Fire Performance of High-Strength Concrete, NIST, Gaithersburg, MD, February, 1997 13-14.
5. Persson, B. 'Fire resistance of self-compacting concrete', *Mater. Struct.* **273** (37) 2004. 575-584.
6. Wasserundurchlässigkeit von Festbeton, DIN 1048, Blatt 1, Teil 4.7 (1972)
7. Hedegaard, S.E., Hansen, T.C., 'Water permeability of fly ash concretes', *Mater. Struct.*, **25** (1992) 381-387.
8. Washburn, E.W., in Proceedings of the National Academy of Sciences, PNASA, (1921) 7-21.
9. Ye, G. 'Experimental study and numerical simulation of the development of the microstructure and permeability of cementitious materials', *PhD thesis*, Delft University of Technology, The Netherlands, 2003.
10. Kalifa, P. Menneteau, F. D. and Quenard, D., 'Spalling and pore pressure in HPC at high temperatures', *Cem. Concr. Res.* **30** (12) (2000) 1915-1927.

## Prediction of Chloride Ingress and Binding in Concrete

Mette Geiker<sup>(1)</sup> and Erik Pram Nielsen<sup>(2)</sup>

<sup>(1)</sup>Department of Civil Engineering, Technical University of Denmark, Denmark

<sup>(2)</sup>AALBORG WHITE® Research and development Centre, Denmark

### Abstract

This paper summarizes recent work on an analytical model for predicting the ingress rate of chlorides in cement-based materials. A thermodynamic model for the phase equilibria in hydrated Portland cement based on the application of the phase rule was developed. The model's applicability to predict chloride binding in Portland cement pastes at any content of chloride, alkalis, sulfates and carbonate was verified experimentally and found to be consistent with data in the literature. The thermodynamic model for the phase equilibria in hydrated Portland cement was introduced into an existing Finite Difference Model for the ingress of chlorides into concrete accounting for its multi-component nature, and the composite theory was used for predicting the diffusivity of each ion based on the phases present, i.e. the phase assemblage, in the hydrated Portland cement paste. Agreement was found between chloride/calcium profiles predicted by the model and those determined experimentally on 0.45 water-to-powder Portland cement pastes exposed to 650 mM NaCl for 70 days. Measured chloride ingress was found to be a factor of five higher than predicted by the model. The effective diffusion rate of sodium and potassium was found more than 100 times lower than the effective diffusion rate of chloride.

### 1. Introduction

Service life prediction is becoming an inherent tool for design and redesign of reinforced concrete structures. For structures in marine environment and structures exposed to de-icing salt the risk of chloride induced reinforcement corrosion must be considered. For design purposes the service life of such structures is often divided into an initiation phase, i.e. the time to onset of corrosion, and a propagation phase [Tuutti 1982].

Corrosion rates for chloride-induced corrosion are generally high and the mechanisms and resulting effects are difficult to model. Therefore, service life is often modeled as the duration of the initiation period plus experienced based duration of the propagation period, e.g. in [Johnsen et al. 2003]. Modeling of the initiation period requires knowledge of the chloride ingress rate and the critical chloride concentration for initiation of reinforcement corrosion.

Predictive models, such as the DuraCrete model [Engelund et al 2000], Life-365 [Bentz and Thomas 2001], and the HETEK model [Nilsson et al. 1997], all make use of a combination of ingress models and experimentally based material parameters. Recently, it has been shown that the critical chloride concentration for initiation of reinforcement corrosion is strongly dependent on the amounts of interfacial defects [Buenfeld et al 2003], [Nygaard 2003]. However, this topic will not be dealt with in this paper.

The aim of a recent study [Nielsen 2004] was to provide an analytical model for predicting the ingress rate of chlorides in cement-based materials. A thermodynamic model for the phase equilibria in hydrated Portland cement based on the application of the phase rule was developed [Nielsen et al. 2005a]. This approach was extended to include the reactions resulting in the binding of chlorides and alkalis [Nielsen et al. 2005b]. The model's accuracy to predict chloride binding in Portland cement pastes at any content of chloride, alkalis, sulfates and carbonate was verified experimentally and found to be consistent with data in the literature [Nielsen et al. 2004]. Furthermore, the model was shown to be equally valid for the phases present, i.e. the phase assemblage identified in 25 years old Portland cement pastes exposed to sodium chloride [Nielsen 2004].

The thermodynamic model for the phase equilibria in hydrated Portland cement was introduced into an existing Finite Difference Model (FDM) for the ingress of chlorides into concrete. This model accounts for the multi-component nature of the pore solution. The composite theory was used for predicting the diffusivity of each ion based on the phase assemblage in the hydrated Portland cement paste. Agreement was found between chloride/calcium profiles predicted by the model and those determined experimentally on 0.45 water-to-powder (w/p) Portland cement pastes exposed to 650 mM NaCl for 70 days. Measured chloride ingress was found to be a factor of five higher than predicted by the model. The effective diffusion rate of sodium and potassium was found more than 100 times lower than the effective diffusion rate of chloride.

The present paper summarizes the modeling approach. For detailed information reference is given to the PhD thesis by Nielsen [2004] and work published in journals and conference proceedings by Nielsen et al. referred to in the text.

## **2. Estimation of phase assemblage in hydrated Portland cement without chloride and alkalis**

Portland cement clinker mainly consists of the clinker phases  $C_3S^1$  ( $3CaO.SiO_2$ ) and  $C_2S$  ( $2CaO.SiO_2$ ) and, to varying extents,  $C_3A$  ( $3CaO.Al_2O_3$ ) and  $C_4AF$  ( $4CaO.Al_2O_3.Fe_2O_3$ ). Upon grinding of the clinkers,  $CaSO_4$  is added to regulate setting of the finished cement. The  $CaSO_4$  may be present as a mixture of gypsum, hemihydrate and anhydrite. Portland cement is unstable in the presence of water, resulting in a solid matrix of reaction products after hydration.

---

<sup>1</sup> Cement chemistry notation is used

The relative content and composition of phases present in hydrated Portland cement can be calculated from the chemical composition of the cement and the water/cement ratio. How this can be undertaken is described in this section, which for simplicity starts out with a simple system,  $\text{CaO-SiO}_2\text{-H}_2\text{O}$ . Progressively, components are added until the complex cement paste system with all significant components is achieved. As the thermodynamic approach is not traditionally applied in civil engineering a short background for the estimation of phase assemblage in hydrated Portland cement is also given.

The number of independent variables describing the state of a system in equilibrium (degrees of freedom,  $F$ ) is given by the ‘phase rule’ of J. Willard Gibbs. For non-reacting systems the phase rule is;  $P + F = C + 2$ , where  $P$  is the number of phases and  $C$  is the number of chemical species or components [Putnis and McConnell 1980]. The phase rule for systems at constant temperature and pressure is reduced to;  $P + F = C$ . If the composition of all phases in the system are fixed and independent, the relationship becomes;  $P = C$ . A system obeying this relationship is said to be invariant.

Equilibrium is a static condition in which no changes occur in the macroscopic properties of a system with time. However, in engineering practice, the assumption of equilibrium is normally justified when it leads to results of satisfactory accuracy [Putnis and McConnell 1980].

## 2.1 $\text{CaO-SiO}_2\text{-H}_2\text{O}$

The phase diagram for the three-component system  $\text{CaO-SiO}_2\text{-H}_2\text{O}$  is given in Figure 1.  $\text{CaO}$  and  $\text{SiO}_2$  results from the dissolution of the clinker phases  $\text{C}_2\text{S}$  and  $\text{C}_3\text{S}$  (only  $\text{C}_3\text{S}$  is shown in figure 1) and, depending on the overall concentration of each species in solution, precipitate according to the diagram.

A fully hydrated paste of  $\text{C}_3\text{S}$  and  $\text{C}_2\text{S}$  in ratios as found in Portland cement paste is composed of a poorly crystalline calcium silicate hydrate phase ( $\text{C}_{1.75}\text{SH}_4$ ), calcium hydroxide ( $\text{CH}$ ) and the pore solution, corresponding to the lower lightly shaded region in Figure 1. As three phases are present in this region, the system is invariant according to the ‘phase rule’ ( $F=0$ ). Thus, as long as the overall composition of the system lies within the region the composition of each of these phases must be constant. The  $\text{Ca/Si}$  ratio of the  $\text{C-S-H}$  at 1.75 is in good agreement with observations in [Taylor 1997], [Richardson 2000], and [Famy et al. 2002].

If the relative content of  $\text{SiO}_2$  increases significantly, which would be the case of Portland cement pastes with large contents of silica fume,  $\text{CH}$  may become exhausted, resulting in the presence of only two phases in the subsystem; a  $\text{C-S-H}$  phase with  $\text{Ca/Si}$  molar ratio between 0.80 and 1.75 and the pore solution.

## 2.2 $\text{CaO-Al}_2\text{O}_3\text{-SO}_3\text{-(Fe}_2\text{O}_3\text{)-(CO}_2\text{)-SiO}_2\text{-H}_2\text{O}$

In this section further components ( $\text{Al}_2\text{O}_3$ ,  $\text{SO}_3$ ,  $\text{Fe}_2\text{O}_3$ ,  $\text{CO}_2$ ) are added to the  $\text{CaO-SiO}_2\text{-H}_2\text{O}$  system to resample the complex cement paste system. The main source of  $\text{Al}_2\text{O}_3$  is the clinker mineral  $\text{C}_3\text{A}$ , and the source of  $\text{SO}_3$  is the added  $\text{CaSO}_4$  (gypsum, hemihydrate or anhydrite) during grinding of the clinkers. These minerals, as well as  $\text{C}_3\text{S}$  and  $\text{C}_2\text{S}$ , react relatively fast

[Taylor 1997], which is why after a few months of hydration the phase assemblage of the hydrated part of the cement can be assumed to be metastable.

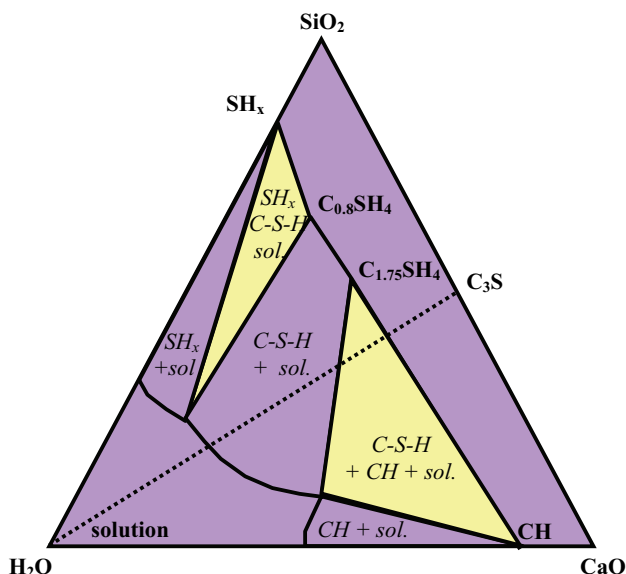


Figure 1 Phase diagram for the three-component system CaO-SiO<sub>2</sub>-H<sub>2</sub>O. Adapted from [Taylor 1997] in [Nielsen 2004]

The contents of  $\text{Al}_2\text{O}_3$  and  $\text{SO}_3$  in Portland cements are low compared to  $\text{CaO}$  and  $\text{SiO}_2$ . Thus, even a substantial amount of  $\text{CaO}$  combines with  $\text{Al}_2\text{O}_3$  and  $\text{SO}_3$ , the phase relationships in Figure 1 remain essentially the same. Some of the  $\text{Al}_2\text{O}_3$  and  $\text{SO}_3$  are incorporated in the C-S-H phase. Based on single point EDS<sup>2</sup> the following ratios were identified;  $\text{S}/\text{Ca} = 0.03$  and  $\text{Al}/\text{Ca} = 0.04$  [Nielsen et al. 2005a]. These values are in accordance with findings by Famy et al. [2002]. Thus, in hydrated Portland cement pastes the presence of  $\text{Al}_2\text{O}_3$  and  $\text{SO}_3$  would only result in a change in the relative amount of CH to C-S-H and the composition of C-S-H.

At ages less than one year or so the composition of the hydroxy-AFm<sup>3</sup> phase is most likely to be C<sub>4</sub>AH<sub>13</sub> (e.g. [Taylor 1997]) or C<sub>4</sub>AH<sub>18</sub> (e.g. [Kuzel and Pöllmann 1991]), but in older pastes the more stable phase hydrogarnet, C<sub>3</sub>AH<sub>6</sub>, is likely to occur instead [Taylor 1997], [Damidot and Glasser 1995].

Iron oxide ( $\text{Fe}_2\text{O}_3$ ) is likely to form a goethite-like hydrate;  $\text{FH}_3$  [Taylor and Newbury 1984]. Furthermore,  $\text{Fe}_2\text{O}_3$  appears to be incorporated to some extent in the C-S-H structure

<sup>2</sup> EDS: Energy dispersion Spectroscopy at 15 keV, 25  $\mu$ A and 40 s per point

<sup>3</sup> AFm is aluminum ferrite compounds with a single (mono) formula unit  $\text{CaX}_2$ .



corresponding to a Fe/Ca molar ratio of approx. 0.02. [Nielsen et al. 2005a], [Nielsen et al. 2005b]

Regarding the effect of carbonate (here represented by  $\text{CO}_2$ ), Damidot and Glasser [1995] concluded for the system  $\text{CaO-Al}_2\text{O}_3\text{-SO}_3\text{-Fe}_2\text{O}_3\text{-CO}_2\text{-SiO}_2\text{-H}_2\text{O}$  that hemiacarbonate ( $\text{C}_3\text{A} \cdot \frac{1}{2}\text{CaCO}_3 \cdot \frac{1}{2}\text{Ca(OH)}_2 \cdot 11\frac{1}{2}\text{H}_2\text{O}$ ) is only stable at low concentrations of carbonate and sulfate and high concentrations of calcium while monocarbonate ( $\text{C}_3\text{A} \cdot \text{CaCO}_3 \cdot 11\text{H}_2\text{O}$ ) is stable over a wider range of concentrations. They further suggested that monocarbonate preferentially forms in systems where alkalis are present.

### 2.3 Model for the phase equilibria in hydrated Portland cement

Portland cement paste typically has seven major components (i.e.  $\text{SiO}_2$ ,  $\text{Al}_2\text{O}_3$ ,  $\text{CaO}$ ,  $\text{Fe}_2\text{O}_3$ ,  $\text{SO}_3$ ,  $\text{CO}_2$ ,  $\text{H}_2\text{O}$ ). The phase assemblages described above are therefore relevant. Furthermore, from the aqueous phase diagram in Figure 2 it is observed that CH is stable in hydrated Portland cements with the assemblages described.

According to the phase rule, a maximum of seven phases (six hydrate phases and the pore solution) can be formed at constant temperature and pressure. Based on the above four assemblages are possible, see Table 1.

In a fully hydrated Portland cement, which as a first approximation is invariant at constant temperature and pressure, the relative contents of phases of known composition present can be calculated by solving 'n' equations for 'n' unknowns, where 'n' is the number of both components and phases. Since the system is invariant, the composition of each of the phases remains constant. Relevant physical properties of the phases described earlier can be found in the literature, e.g. [Taylor 1997] and [Lea 1970]. Values for the density and amount of evaporable water in C-S-H are proposed in [Nielsen et al. 2005a].

Table 1 Possible phase assemblages in Portland cement paste<sup>4</sup>.

1.	$\text{C}_4\text{AH}_{13}$ , monosulfate, monocarbonate, ...	$\text{C}_{1.75}\text{SH}_4$ , $\text{FH}_3$ , CH, Pore solution
2.	monosulfate, ettringite, monocarbonate, ...	
3.	Ettringite, monocarbonate, calcite, ...	
4.	Ettringite, calcite, gypsum, ...	

### 3. Estimation of phase assemblage in hydrated Portland cement with chloride and alkalies

This section summarizes the phase diagrams applicable for hydrated Portland cement paste exposed to chloride, sulfate and carbonate as well as findings on the pore solution composition.

<sup>4</sup> Phases not already mentioned in the text: Monosulphate:  $\text{C}_3\text{A} \cdot \text{CaSO}_4 \cdot 12\text{H}_2\text{O}$  Ettringite:  $\text{C}_3\text{A} \cdot 3\text{CaSO}_4 \cdot 32\text{H}_2\text{O}$ , Calcite:  $\text{CaCO}_3$

On this basis a model, for estimation of phase assemblage in hydrated Portland cement with chloride and alkalis, is provided.

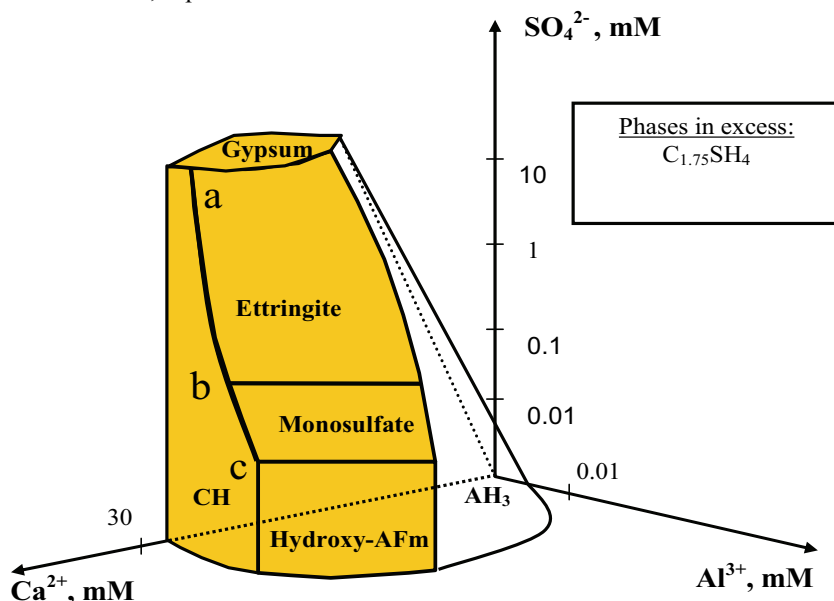


Figure 2 Aqueous phase diagram for the system  $\text{CaO-Al}_2\text{O}_3\text{-SO}_3\text{-SiO}_2\text{-H}_2\text{O}$ , for the case where  $\text{C}_{1.75}\text{SH}_4$  is stable. Adapted from [Damidot and Glasser 1993]. Invariant points a, b and c do not necessarily correspond to the scale given on the axes. [Nielsen 2004]

Figures 3 to 6 illustrate phase diagrams for relevant subsystems of the system  $\text{CaO-SiO}_2\text{-Al}_2\text{O}_3\text{-Fe}_2\text{O}_3\text{-SO}_3\text{-CaCl}_2\text{-CO}_2\text{-Na}_2\text{O-H}_2\text{O}$ , which are the main components in hydrated Portland cement. The subsystem  $\text{CaO-SiO}_2\text{-H}_2\text{O}$  is the same as that presented in figure 1. The composition of the pore solution as well as content of alkalis in the C-S-H can be calculated from the relationships given in Table 2.

The system  $\text{CaO-SiO}_2\text{-Al}_2\text{O}_3\text{-Fe}_2\text{O}_3\text{-SO}_3\text{-CaCl}_2\text{-CO}_2\text{-H}_2\text{O}$  (no alkalis) is thoroughly described in [Nielsen et al. 2003]. A solid solution between Friedel's salt and monocarbonate "AFmss"<sup>5</sup> was found, which introduce a degree of freedom to the system, see Figure 3. This permits the relative content of Friedel's salt to increase in the AFmss along with a simultaneous increase in the concentration of chloride ions in both the pore solution and in the C-S-H phase. The phase rule is satisfied as long as a single relationship exists for the distribution of chloride between all three phases. The distribution function for chloride between the C-S-H and the solid solution phase is independent of the alkali content, but is dependent on the iron content of the system.

<sup>5</sup> "ss" denotes solid solution

Sodium and potassium are considered to have the same properties and to show similar behavior, which is supported by the observation by Hong and Glasser [1999 and 2002]. The presence of sodium in a chloride containing cement paste system has to be defined by at least two additional components. In the solid phases it can be described by the element NaOH (which can be expressed by the relative contents of the components  $\text{Na}_2\text{O}$  and  $\text{H}_2\text{O}$ ), whilst the components  $\text{Na}_2\text{O}$ ,  $\text{NaCl}$  and  $\text{H}_2\text{O}$  must be defined in the pore solution in order to express the presence of  $\text{NaCl}$  and  $\text{NaOH}$  [Nielsen et al 2005b]. At low concentrations of chloride, the composition of the pore solution can be expressed by relative contents of  $\text{NaCl}$ ,  $\text{Na}_2\text{O}$ , and  $\text{H}_2\text{O}$ . Once all sodium is balanced by chlorides, any further addition of chlorides can be expressed by the increase in  $\text{CaCl}_2$  concentration, where  $\text{Ca}^{2+}$  is released from the solid phases [Nielsen et al 2005b].

The overall reaction, which takes place in hydrated Portland cement pastes exposed to chloride accounting for the total content of alkalis and the relative amount of solution to solid paste, is given in Table 2 (see [Nielsen et al 2005b] for details). The overall reaction is divided into two parts; one for the C-S-H which contains alkalis, the other for the alkali-free C-S-H. The overall reaction not only describes the distribution of chlorides between the C-S-H, AFms, and pore solution, but also for the change in  $\text{Ca}^{2+}$ ,  $\text{OH}^-$ , and alkali concentrations in the pore solution.

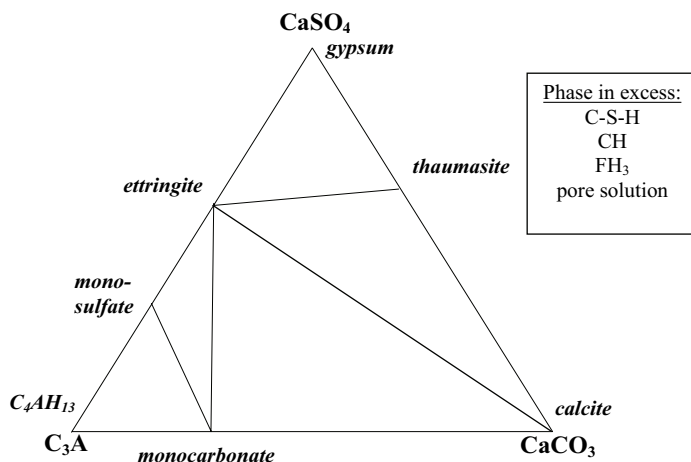


Figure 3 Subsystem  $\text{C}_3\text{A}-\text{CaSO}_4-\text{CaCO}_3$  of the system  $\text{SiO}_2-\text{Al}_2\text{O}_3-\text{SO}_3-\text{Fe}_2\text{O}_3-\text{CaO}-\text{Na}_2\text{O}-\text{CO}_2-\text{CaCl}_2-\text{NaCl}-\text{H}_2\text{O}$  for hydrated Portland cement.  $\text{C}_3\text{A}$  does not refer to the normative content  $\text{C}_3\text{A}$  in the clinker, but to the total  $\text{Al}_2\text{O}_3$ . From [Nielsen 2004].<sup>6</sup>

<sup>6</sup> Phases not already mentioned in the text: Thauмасite:  $[\text{Ca}_3\text{Si}(\text{OH})_6 \cdot 12\text{H}_2\text{O}](\text{SO}_4)(\text{CO}_3)$

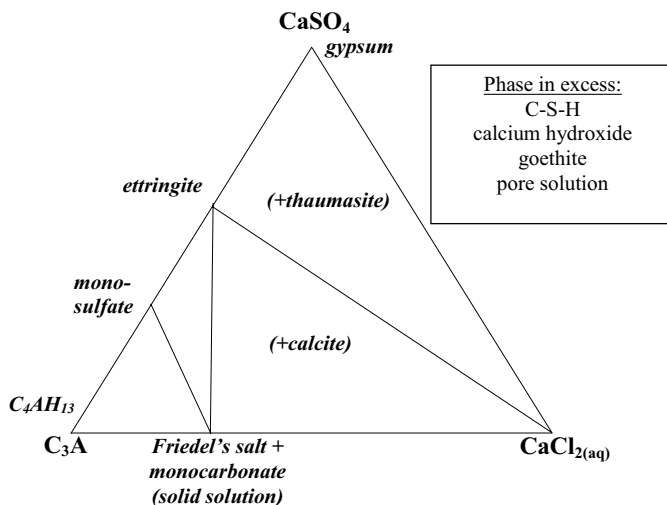


Figure 4 Subsystem  $C_3A$ - $CaSO_4$ - $CaCO_3$  of the system  $SiO_2$ - $Al_2O_3$ - $SO_3$ - $Fe_2O_3$ - $CaO$ - $Na_2O$ - $CO_2$ - $CaCl_2$ - $NaCl$ - $H_2O$  for hydrated Portland cement.  $C_3A$  does not refer to the normative content  $C_3A$  in the clinker, but to the total  $Al_2O_3$ . From [Nielsen 2004].

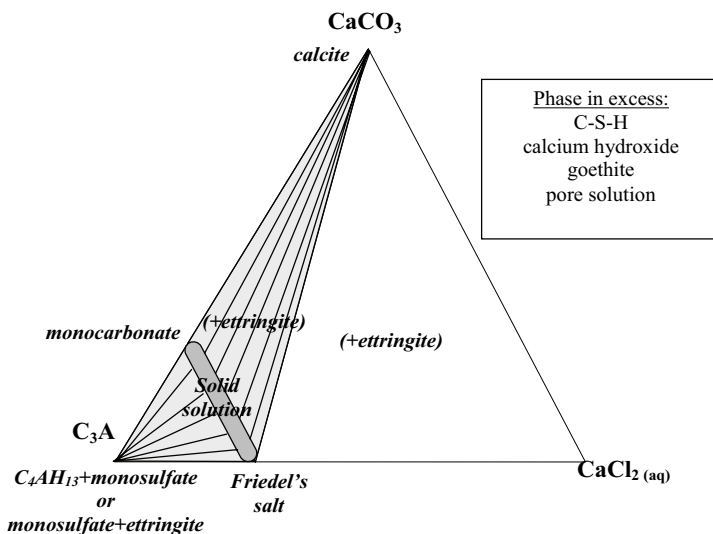


Figure 5 Subsystem  $C_3A$ - $CaCl_2$ - $CaCO_3$  of the system  $SiO_2$ - $Al_2O_3$ - $SO_3$ - $Fe_2O_3$ - $CaO$ - $Na_2O$ - $CO_2$ - $CaCl_2$ - $NaCl$ - $H_2O$  for hydrated Portland cement.  $C_3A$  does not refer to the normative content  $C_3A$  in the clinker, but to the total  $Al_2O_3$ . From [Nielsen 2004].<sup>7</sup>

<sup>7</sup> Phases not already mentioned in the text: Friedel's salt:  $C_3A.CaCl_2.10H_2O$

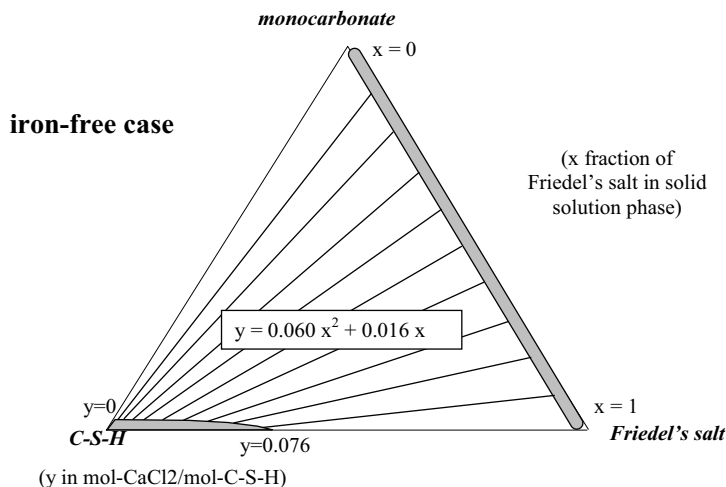


Figure 6 Pseudo ternary subsystem for “C-S-H – monocarbonate- Friedel’s salt” in the  $\text{SiO}_2\text{-Al}_2\text{O}_3\text{-SO}_3\text{-Fe}_2\text{O}_3\text{-CaO-Na}_2\text{O-CO}_2\text{-CaCl}_2\text{-NaCl-H}_2\text{O}$  system for hydrated Portland cement (notice: iron-free case; i.e. white Portland cement). C-S-H corner is not-to-scale. From [Nielsen 2004].

#### 4. Prediction of ingress rate

Based on a computation model for the diffusion of multi-species in solution [Truc 2000] a FDM for simulating the ingress of chlorides in cement-based materials was developed [Nielsen 2004]. This FDM model takes into account a) the phase assemblage present and b) the effect of capillary porosity of the hydrated paste on the effective diffusion coefficient. The FDM is based on the assumption of instantaneous binding reactions.

The model for phase assemblage was presented above, whereas the estimation of diffusion coefficients is described below. The effective diffusion coefficients for each species in solution during transport through a hydrated Portland cement paste can be estimated by application of the composite theory [Jensen 1999]. The procedure is e.g. described in [Nielsen and Geiker 2003], where the water-filled porosity was estimated by means of Powers’ model and sorption isotherms. However, Powers’ model does not take into account the difference in density of the various phases formed.

Table 2 Overall reaction describing the binding of chloride by the C-S-H and AFm phases, and the composition of the pore solution. From [Nielsen 2004]

<p><b>1.a)</b> Chloride binding in PC pastes in which Na is still present in the C-S-H, and no AFm phases other than monocarbonate are present.</p> $\mathbf{b} \cdot [\text{C}_3\text{A} \cdot \text{CaCO}_3 \cdot 11\text{H}_2\text{O}]_{(\text{s})} + \mathbf{a} \cdot [1.75\text{CaO} \cdot \text{SiO}_2 \cdot \mathbf{z}\text{NaOH} \cdot 4\text{H}_2\text{O}]_{(\text{s})} + ((\mathbf{k}+1) \cdot \mathbf{y} \cdot \mathbf{a} + \mathbf{b} \cdot \mathbf{x}) \text{CaCl}_2_{(\text{aq})} + 2 \cdot 0.83 \cdot \mathbf{k} \cdot \mathbf{y} \cdot \mathbf{a} \text{NaOH}_{(\text{aq})}$ $\downarrow$ $2 \cdot \mathbf{k} \cdot \mathbf{y} \cdot \mathbf{a} \text{NaCl}_{(\text{aq})} + \mathbf{a} [1.75\text{CaO} \cdot \text{SiO}_2 \cdot (\mathbf{z} - 0.34 \cdot \mathbf{k} \cdot \mathbf{y})\text{NaOH} \cdot \mathbf{y}\text{CaCl}_2 \cdot 4\text{H}_2\text{O}]_{(\text{s})} + \mathbf{k} \cdot \mathbf{y} \cdot \mathbf{a} \text{Ca}(\text{OH})_2_{(\text{s})} + \mathbf{b} [\text{C}_3\text{A} \cdot \text{CaCl}_2_{(\text{x})} \cdot \text{CaCO}_3_{(1-\text{x})} \cdot 11\text{H}_2\text{O}]_{(\text{s})} + \mathbf{b} \cdot \mathbf{x} \text{CaCO}_3_{(\text{s})}$ <p><b>1.b)</b> Chloride binding in PC pastes in which Na is still present in the C-S-H, and other AFm phases than monocarbonate are present</p> $\mathbf{b} \cdot [\text{C}_3\text{A} \cdot \text{CaCO}_3 \cdot 11\text{H}_2\text{O}]_{(\text{s})} + \mathbf{a} \cdot [1.75\text{CaO} \cdot \text{SiO}_2 \cdot \mathbf{z}\text{NaOH} \cdot 4\text{H}_2\text{O}]_{(\text{s})} + ((\mathbf{k}+1) \cdot \mathbf{y} \cdot \mathbf{a} + \mathbf{b} \cdot \mathbf{x}) \text{CaCl}_2_{(\text{aq})} + 2 \cdot 0.83 \cdot \mathbf{k} \cdot \mathbf{y} \cdot \mathbf{a} \text{NaOH}_{(\text{aq})}$ $\downarrow$ $2 \cdot \mathbf{k} \cdot \mathbf{y} \cdot \mathbf{a} \text{NaCl}_{(\text{aq})} + \mathbf{a} [1.75\text{CaO} \cdot \text{SiO}_2 \cdot (\mathbf{z} - 0.34 \cdot \mathbf{k} \cdot \mathbf{y})\text{NaOH} \cdot \mathbf{y}\text{CaCl}_2 \cdot 4\text{H}_2\text{O}]_{(\text{s})} + \mathbf{k} \cdot \mathbf{y} \cdot \mathbf{a} \text{Ca}(\text{OH})_2_{(\text{s})} + (\mathbf{b} + \mathbf{b}\mathbf{x}) [\text{C}_3\text{A} \cdot \text{CaCl}_2_{(\text{x})} \cdot \text{CaCO}_3_{(1-\text{x})} \cdot 11\text{H}_2\text{O}]_{(\text{s})}$ <p><b>2.</b> Chloride binding in Portland cement pastes with alkali-free C-S-H</p> $\mathbf{b} \cdot [\text{C}_3\text{A} \cdot \text{CaCl}_2_{(\text{m})} \cdot \text{CaCO}_3_{(1-\text{m})} \cdot 11\text{H}_2\text{O}]_{(\text{s})} + (\mathbf{b} \cdot \mathbf{x} + \mathbf{y} \cdot \mathbf{a}) \text{CaCl}_2_{(\text{aq})} + \mathbf{a} [1.75\text{CaO} \cdot \text{SiO}_2 \cdot (\mathbf{z} / 0.34 \cdot \mathbf{k})\text{CaCl}_2 \cdot 4\text{H}_2\text{O}]_{(\text{s})}$ $\downarrow$ $\mathbf{a} \cdot [(\mathbf{1.75} - \mathbf{y})\text{CaO} \cdot \text{SiO}_2 \cdot (\mathbf{z} / (0.34 \cdot \mathbf{k}) + \mathbf{y})\text{CaCl}_2 \cdot (\mathbf{4} - \mathbf{y})\text{H}_2\text{O}]_{(\text{s})} + \mathbf{y} \cdot \mathbf{a} \text{Ca}(\text{OH})_2_{(\text{s})} + \mathbf{b} \cdot [\text{C}_3\text{A} \cdot \text{CaCl}_2_{(\text{m} + \mathbf{x})} \cdot \text{CaCO}_3_{(1-\text{m}-\mathbf{x})} \cdot 11\text{H}_2\text{O}]_{(\text{s})} + \mathbf{b} \cdot \mathbf{x} \text{CaCO}_3_{(\text{s})}$ <p>Note: in eq.2, for each mol of CaCl<sub>2</sub> bound by the C-S-H, (PS/a)/75 mol CaCl<sub>2</sub> remain in solution, where PS denotes the amount of solution in millilitre (i.e. pore solution + exposure solution, if applicable).</p> <p>- ‘x’ denotes the fraction of Friedel’s salt in the AFm solid solution phase; ‘y’ denotes the content of CaCl<sub>2</sub> in the C-S-H, in mol/mol, and is related to ‘x’ as follows,</p> <p style="padding-left: 40px;">In the iron-free case (white Portland cement)</p> $\mathbf{y} = 0.0601 \mathbf{x}^2 + 0.0164 \mathbf{x}$ <p style="padding-left: 40px;">In the iron-containing case (grey Portland cement)</p> $\mathbf{y} = 0.0376 \mathbf{x}^2 + 0.0046 \mathbf{x}$ <p>- ‘a’ is the content of C-S-H, in mol; ‘b’ is the initial content of monocarbonate, in mol.</p> <p>- ‘z’ is the molar ratio of NaOH, in the chloride-free C-S-H, to C-S-H, i.e. in mol/mol. This can be calculated from the initial Rd, i.e. 0.65 (see the text), which is a general value, independent of water to powder ratio.</p> <p>- ‘k’ is defined as</p> $\mathbf{k} = \mathbf{z} \cdot (\text{PS}/\mathbf{a}) \cdot 25 / (0.83 \cdot 0.81 \cdot \mathbf{M}_{\text{w,C-S-H}} \cdot \mathbf{Rd}_0) = \mathbf{z} \cdot (\text{PS}/\mathbf{a}) \cdot 0.2354, \text{ where PS is the amount of solution in milliliter (i.e. pore solution + exposure solution, if applicable).}$ <p>- ‘m’ denotes the fraction of Friedel’s salt in the solid solution phase at the chloride content where all alkalis have been released to the pore solution from the C-S-H.</p>
--

#### 4.1 Estimation of effective diffusion coefficients

Based on an equation from Maxwell for the diffusion coefficient of a composite Jensen [1999] proposed an equation for the diffusion coefficient of the gel matrix,  $D_{gm}$ . The gel matrix was defined as the total volume of solid gel products, gel water, and unhydrated cement particles. According to the model described in section 2 the gel matrix corresponds to the volume fraction occupied by all phases in the hydrated Portland cement paste, excluding only the capillary porosity. Jensen [1999] assumed that CH and unhydrated cement particles are impenetrable by ions. Nielsen [2004] further assumed that also calcite, gypsum, goethite, and brucite are impenetrable for ions, i.e.;

$$D_{gm,i} = D_{gp,i} \frac{V_{gp}}{V_{gp} + \frac{3}{2}(V_{ce} + V_{CH} + V_{calcite} + V_{gypsum} + V_{goethite} + V_{brucite})}$$

where  $D_{gp}$  is the diffusion coefficient of the so-called gel proper (gel solid and gel water). Garboczi has proposed a diffusion coefficient of chloride ions in the gel proper corresponding to 1/400 of the diffusion coefficient through water-filled capillaries,  $D_{cw}$ . It is assumed as a first approximation that the same applies for all other species. Assuming phase symmetric crumbled foil composites, Fuglsang-Nielsen [2004] proposed the following equation for the diffusion coefficient through the cement paste,  $D_p$ ,

$$D_{p,i} = D_{gm,i} \frac{n + 2\sqrt{n} \cdot (1 + c \cdot (n-1))}{n + 2\sqrt{n} - c \cdot (n-1)}$$

where  $n$  is defined by the ratio of  $D_{cw}$  to  $D_{gm}$ , i.e. 1/400, and  $c$  is the total volume fraction of capillary porosity. Finally, if the aggregates are impermeable, the effective diffusion coefficient,  $D_{eff}$ , through a mortar or concrete can be predicted by the following equation proposed by Maxwell [mentioned e.g. in Jensen [1999],

$$D_{eff,i} = D_{p,i} \frac{1}{1 + \frac{\phi}{2}} (1 - \phi)$$

where  $\phi$  is the volume fraction of aggregates and air.

The effect of degree of saturation can be taken into account by assuming only part of the capillary pores to be water filled, see [Nielsen and Geiker 2003].

#### 4.2 Testing of the ingress model

To test the applicability of the ingress model the ingress of NaCl in hydrated Portland cement pastes (w/p 0.45) was studied at a maturity of 4.5 months [Nielsen 2004]. Here, results of ingress in a white Portland cement with 12 %  $C_3A$  are presented.

The samples were exposed to unidirectional ingress of a 650 mM NaCl solution for 70 days. The volume of exposure solution to volume of samples was high (approx. 36). Therefore, the pH of the exposure solution never exceeded 9.5 and the concentration of NaCl remained

constant within  $\pm 20$  mmol/l. Analyses of the composition as a function of depth were carried out by EDS. Perpendicular to the exposed surface three line-scans with spacing of approx. 4 mm were undertaken at step increments of 50  $\mu\text{m}$ <sup>8</sup>; these measurements are referred to as profiles in the following. Furthermore, parallel to the surface at depths of 2, 4, 6, 10 and 15 mm line-scans of 200 randomly located points were performed. The latter measurements were used to investigate the phase assemblage as a function of depth.

Measured vs. predicted molar ratios of Cl to Ca in the solid solution phase of monocarbonate and Friedel's salt (AFmss) at the depths of 2, 4, 6, 10 and 15 mm were compared, see Figure 7. The good agreement between predicted and measured Cl to Ca ratios supports the assumption of quasi-instantaneous binding.

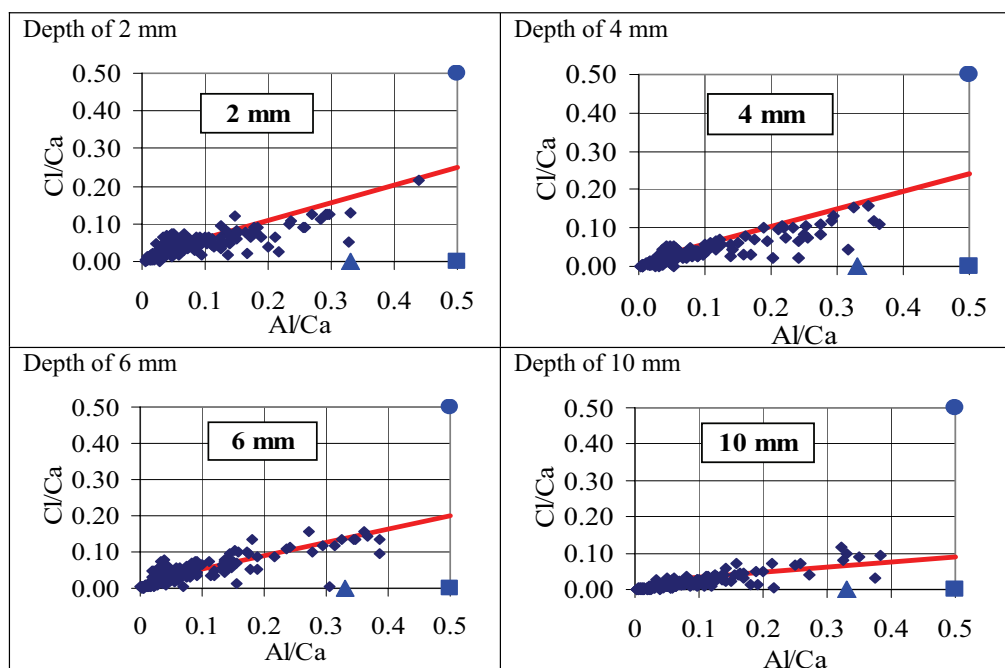


Figure 7: Measured vs. predicted molar ratio of Cl to Ca in the solid solution phase at different depths from the surface exposed to unidirectional ingress of 650 mM NaCl for 70 days at 20°C (w/p 0.45 WPC(12) paste with 1 wt. % replacement of powder by calcite. After [Nielsen 2004].  
▲ Ettringite, ■ Monocarbonate, ● Friedel's Salt

The ingress of sodium in the Portland cement pastes was much slower than the ingress of chloride. This does not agree with the multi-species theory, where chloride and sodium are expected to have similar ingress rates, if no reaction with the concrete took place, resulting

<sup>8</sup> Reduced measuring time at each point from 40 s to 14 s



from the electrical field between the ions in solution. The leaching of potassium was also observed to be much slower than expected. The observations are in accordance with that reported in [Volkwein 1995]. A possible explanation could be that the model is based on the assumption of instantaneous binding reactions. Hydroxyl could be more readily available from dissolution of CH than absorption and desorption of alkalis in the C-S-H, resulting in a faster ingress of chloride compared to that of sodium due to fast leaching of hydroxyl.

The measured molar ratio profiles for Cl to Si, Na to Si and K to Si were compared with profiles predicted by the model. In Figure 8 the intrinsic diffusion coefficients for alkalis were adjusted. The measured ingress profiles could be fitted by increasing all diffusion coefficients by a factor of 4.5 to include the effect of cracks or other defects expected and reducing the intrinsic diffusion coefficient of the alkalis by a factor of 100 (i.e.  $D_{Cl}$  scaled by 4.5,  $D_{Na,K}$  scaled by  $4.5/100$ ). The scattering of points for “Average of 3 ingress profiles (EDS)” is due to a combination of reduced measuring time and a single measuring point not being representative. The predicted ingress profiles agree with the measured (average of 200 EDS) profiles for Cl to Si, Na to Si and K to Si when the above mentioned corrections are made.

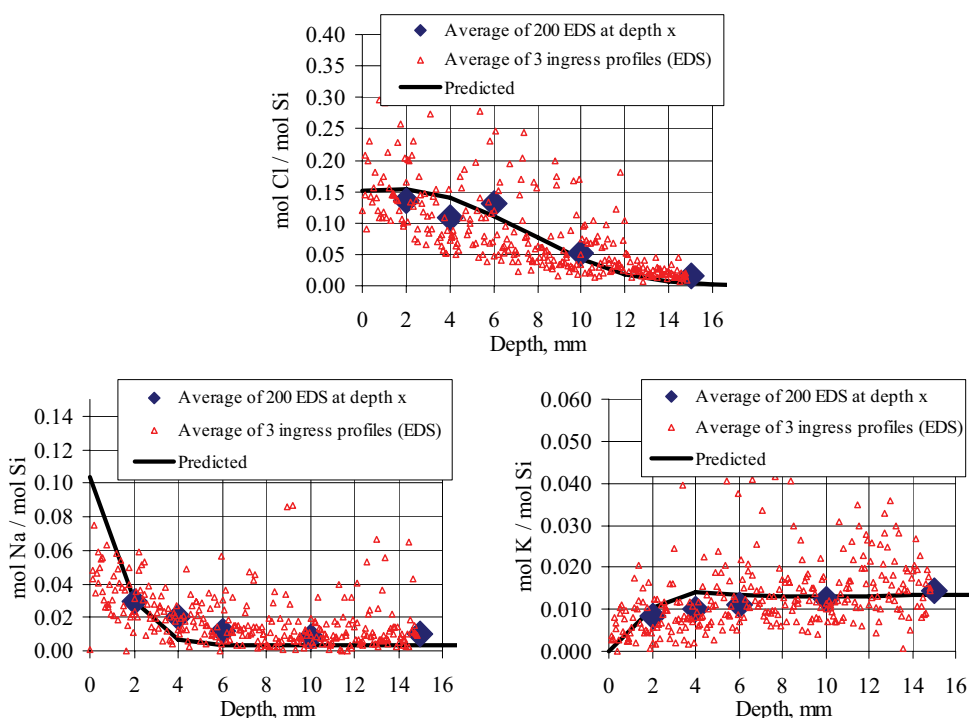


Figure 8: Measured vs. predicted profiles of Cl, Na and K after unidirectional exposure to 650 mM NaCl for 70 days at 20°C (w/p 0.45 WPC(12) paste with 1 wt. % replacement of powder

by calcite). Note;  $D_i$  for K and Na have been adjusted by 1/100 and  $D_i$  has been scaled by a factor 4.5 to account for imperfections. After [Nielsen 2004].

## 5. Selected observations

The applicability of the models is exemplified in the following. Based on the phase equilibria model the following observations were made:

- Chloride binding in Portland cement pastes is highly dependent on the content of alkalis; the higher content of alkalis the lower amount of bound chloride at any total content of chloride. Contrary to general agreement, the content of alumina was shown to only play a relative minor role in the overall extent of chloride binding, as the major part of chloride is bound by the C-S-H phase.
- The increased chloride binding capacity obtained by reducing the alkali content of the cement also reduces the ratio of chloride to hydroxyl ions in the pore solution<sup>9</sup> as long as the content of alkalis is low;  $\text{Na}_2\text{O}_{\text{eq}} < 0.30\text{-}0.35$ . This occurs even though the initial pH of the pore solution is also lower at these low alkali contents.
- As alkalis are transported at a much slower rate into concrete than chlorides, low-alkali Portland cements should be used in aggressive environments containing chlorides. Furthermore, owing to the minor effect of alumina on chloride binding, low-alkali low-aluminate Portland cements could arguably be recommended for aggressive marine environments providing maximum protection to both chloride transport and sulfate attack.
- At high degrees of carbonation or in cements with large amounts of limestone filler, more chloride becomes bound by aluminum bearing phases. This may be the reason why a strong influence by the  $\text{C}_3\text{A}$  content on the chloride binding of cements has been in many investigations.

## 6. Limitations of the models

Limitations of the phase equilibria model are among others;

- The model is restricted to Portland cement pastes with limited (see below) or without supplementary cementing materials at temperatures around 20°C
- The w/p of the cement paste matrix has to be high enough to ensure a residual capillary porosity at complete hydration, i.e.  $w/p > \text{approx. } 0.40$
- The model is only valid for hydrated Portland cement pastes where the reactions proceed at a slow rate (i.e. degree of hydration is high enough), i.e. metastable or stable systems
- The Ca/Si of the paste has to be high enough to ensure the presence of both  $\text{C}_{1.75}\text{SH}_4$  and CH in the stable assemblage. However, if the addition of  $\text{SiO}_2$  is high enough to use up the CH phase, the assemblage can still be calculated as being composed of a  $\text{C}_{1.75}\text{SH}_4$  and a  $\text{C}_{0.8}\text{SH}_4$  (in order to ensure as many equations as unknowns), where the actual C-S-H solid solution phase is of course in reality a mixture of the two end-member phases. This would require a study of the absorption properties of this C-S-H with respect to alkalis and chloride, to be able to calculate the composition of the pore solution.

Limitations of the model for estimation of effective diffusion coefficients include;

---

<sup>9</sup> Ratios at 0.50-0.60 are typically given as the chloride threshold value for reinforcement corrosion.

- The model does not include the the inhomogeneous pore structure of the cement paste, defects as e.g. microcracks, Interfacial Transition Zones between paste and aggregate, and tortuosity
- The model is based on the assumption of a quasi-instantaneous binding (justified for chlorides but not for sodium).

## 7. Conclusions

A Finite Difference Model (FDM) for simulation of the ingress of chloride and sodium/potassium in Portland cement based materials was developed taking into account a) the phase assemblage present and b) the effect of capillary porosity of the hydrated paste on the effective diffusion coefficient.

The FDM allows prediction of the (relative) performance of different types of Portland cement towards the ingress of chloride and sodium/potassium without having to carry out extensive and time-consuming experiments for calibration purposes.

Further research should be carried out to calibrate the model to chloride and sodium ingress measurements on concrete, determining the effect of imperfections. The effect of a possible layer, e.g. of carbonate or brucite, at the surface of the concrete should also be included to obtain realistic predictions.

## References

1. Bentz, E.C. and Thomas, M. D. A.: *Service life and life cycle analysis of reinforced concrete*, version 1.1 The program and manual were written under contract to a consortium consisting of W. R. Grace Construction Products, Master Builders, and the Silica Fume Association [2001]
2. Buenfeld, N. R., Glass, G. K., Reddy, B., and Viles, R. F. (2003). Process for the protection of reinforcement in reinforced concrete - United States Patent Application 20030075457. US Patent & Trademark Office. Johnsen, T. H., Geiker, M. R. and Faber, M. H.: Quantitative Condition Indicators for Concrete Structures. *Concrete International*, December 2003, pp. 47-54
3. Engelund, S., Edvardsen, C. and Mohr, L.: *General guidelines for durability design and redesign*, Report 15, Contract BRPR-CT95-0132, Project BE95-1347, [2000]
4. Damidot, D and Glasser, F.P., Thermodynamic investigation of the  $\text{CaO-Al}_2\text{O}_3\text{-CaSO}_4\text{-H}_2\text{O}$  system at 25°C and the influence of  $\text{Na}_2\text{O}$ . *Cement and Concrete Research* (23) no.6, pp. 221-238, 1993.
5. Damidot, D. and Glasser, F.P., Thermodynamic investigation of the  $\text{CaO-Al}_2\text{O}_3\text{-CaSO}_4\text{-CaCO}_3\text{-H}_2\text{O}$ , *Advances in Cement Research* (27), pp. 129-134, 1995.
6. Famy, C., Scrivener, K.L., Atkinson, A. and Brough, A.R., Effects of an early or a late heat treatment on the microstructure and composition of inner C-S-H products of Portland cement mortars. *Cement and Concrete Research* (32), pp. 269-278, 2002.

7. Fuglsang-Nielsen, L., Composite materials- mechanical and physical behaviour as influenced by phase geometry. Dep. of Civil Engineering, Technical University of Denmark, expected to 2004.
8. Hong, S.-Y. and Glasser, F.P., Alkali binding in cement pastes. Part I. The C-S-H phase. *Cement and Concrete Research* (29), pp. 1893-1903, 1999.
9. Hong, S.-Y. and Glasser, F.P., Alkali sorption by C-S-H and C-A-S-H gels. Part II. Role of alumina. *Cement and Concrete Research* (32), pp. 1101-1111, 2002.
10. Jensen, O.M., Chloride Ingress in Cement Paste and Mortar measured by Electron Probe Micro Analysis. Dept. of Civil Engineering. Technical University of Denmark. Series R No.51, Lyngby, 1999.
11. Johnsen, T. H., Geiker, M. R. and Faber, M. H.: Quantitative Condition Indicators for Concrete Structures. *Concrete International*, December 2003, pp. 47-54
12. Kuzel, H.-J. and Pöllmann, H., Hydration of C3A in the presence of  $\text{Ca}(\text{OH})_2$ ,  $\text{CaSO}_4 \cdot 2\text{H}_2\text{O}$  and  $\text{CaCO}_3$ , *Cement and Concrete Research* (21), pp. 885-895, 1991.
13. Lea, F.M., The chemistry of cement and concrete, 3rd edition, Edward Arnold Ltd Press, 1970.
14. Nilsson, L.O. Sandberg, P., Poulsen, E., Tang, L., Andersen, A., and Frederiksen, J.M.: A system for estimation of chloride ingress into concrete. Theoretical background. HETEK, The Danish Road Directorate, Report No. 83, 1997
15. Nielsen, E.P.: The Durability of White Portland cement to Chemical Attack. PhD thesis, Department of Civil Engineering, Technical University of Denmark, Report no. R-084, ISSN 1601-2917, ISBN 87-7877-147-1, 2004
16. Nielsen, E.P., Herfort, D. and Geiker, M.R: Phase equilibria of hydrated Portland cement. *Cement and Concrete Research* 35, (2005a) 109-115.
17. Nielsen, E.P., Herfort, D. and Geiker, M.R: Binding of chlorides and alkalies in Portland cement systems. *Cement and Concrete Research* 35, (2005b) 117-123
18. Nielsen, E. P. and Geiker, M.: Chloride diffusion in partially saturated cementitious material. *Cement and Concrete Research*, 33 (2003) 133-138
19. Nielsen, E.P., Herfort, D. and Geiker, M.R: Chloride binding in the  $\text{CaO-SiO}_2\text{-Al}_2\text{O}_3\text{-Fe}_2\text{O}_3\text{-SO}_3\text{-Na}_2\text{O-CO}_2\text{-H}_2\text{O}$  system for Portland cement. Proceedings, International Symposium on Advances in Concrete through Science and Engineering, Evanston, Illinois, 21-24 March 2004.
20. Nygaard, P.V.: Effect of steel-concrete interface defects on the chloride threshold for reinforced concrete. MSc Thesis, department of Civil Engineering, Technical University of Denmark, 2003
21. Putnis, A. and McConnell, J.D.C., Principles of mineral behaviour. Elsevier, New York, 1980.
22. Richardson, I.G., The nature of C-S-H in hardened cements. *Cement and Concrete Research* (29), pp. 1131-1147, 1999.
23. Taylor, H.F.W., Cement Chemistry, 2nd Edition. Thomas Telford Services Ltd., London, 1997.
24. Taylor, H.F.W, and Newbury, D.E., An electron microprobe study of a mature cement paste, *Cement and Concrete Research* (14), pp. 565-573, 1984.

25. Truc, O., Prediction of chloride penetration into saturated concrete – Multi-species approach, Doctoral Thesis, publication P-00:4, Department of Building Materials, Chalmers University of Technology, Göteborg, Sweden, 2000.
26. Tuutti, K. Corrosion of Steel in Concrete. Swedish Cement and Concrete Research Institute, Stockholm. Report no. CBI Research FO 4:82, 1982
27. Volkwein, A., Penetration of chlorides into concrete – Phenomena and consequences. Points of view based on 20 years research and site experience with deicing salts. Proceedings of the International RILEM workshop on Chloride penetration into concrete, St-Rémy-lès-Chevreuse, France, 1995



## **Integrated Structures and Materials Design**

Victor C. Li

Department of Civil and Environmental Engineering, Department of Materials Science and Engineering, University of Michigan, Ann Arbor, USA

### **Abstract**

This paper introduces the concept of Integrated Structures and Materials Design (ISMD). The development of ISMD is motivated by recent developments of performance based design codes for structures, and micromechanics based design for materials. An application example, material and structural design of a bridge deck link-slab, is used to illustrate the essential elements of ISMD. Broad implications of ISMD on educational approach, research collaboration, and next generation infrastructure development, are briefly discussed.

### **1. Introduction**

In recent years, structural design codes in many countries have moved or are moving towards performance based design concepts (see, e.g. [1]) in place of the classical prescriptive approach. The performance based design concept allows for greater flexibility, e.g., in dimensioning and reinforcement detailing by structural engineers. It also allows for a larger degree of freedom in construction material choice. To fully exploit this last aspect, it is desirable to have a larger repertoire of concrete materials, particularly those with properties drastically improved over the limitations of current concrete. Performance based design creates opportunities for collaboration between structural engineers and materials engineers.

In the last ten years, systematic engineering of ultra high ductility concrete containing short discontinuous fibers has proceeded at a rapid pace, to the point where such materials have been placed in full-scale structures (see, e.g. [2]). Worthy of note is that these materials and their tensile properties are deployed for enhancing structural functions. These include, for example, an ultra ductile concrete used in a super-thin composite steel/concrete bridge deck in Hokkaido, Japan, and in coupling beams for a tall building in central Tokyo in Japan. The successful development and application of such material relies heavily on the micromechanics based approach adopted in the material design process.

These two development trends, performance based structural design and the micromechanics based concrete material design, offer an interesting window of opportunity for structural engineers and material engineers to integrate their knowledge in order to attain structural

performance not feasible heretofore. This integrated approach remains largely unexplored, partly because both trends are relatively recent, but also partly due to the cultural gap between the structural engineering and materials engineering communities. Bridging the gap between these two communities can bring significant enrichment to the fields of structural engineering and materials engineering, and further the innovative development of both.

The primary objective of this paper is to present the concept of the integrated structural and materials design (ISMD) as a collaborative research platform. ISMD acknowledges material (macroscopic or composite) properties as the common link between structural engineering and materials engineering, and that these material properties are “designable” by suitable microstructure tailoring. In the following, the concept of ISMD is described. An example of a bridge deck link-slab is used to illustrate this concept. Elements of micromechanics tools employed in the ductile concrete design are highlighted. Finally, a discussion on the implications of ISMD on future research directions is given.

## **2. The Concept of Integrated Structures and Materials Design**

In the world of structural engineering, materials are shaped into structural elements that are then assembled into structural systems in order to meet targeted structural functions and performance goals. The performance goals are often stated in terms of ultimate limit states or serviceability limit states. Typically, design codes provide the structural design framework with respect to material selection, dimensioning, and in the case of reinforced concrete, reinforcement detailing. Embodied within design codes are deep knowledge developed from structural mechanics analyses and verified by extensive experimental investigations and experience. Structural analyses utilize mechanical properties of materials in the form of constitutive laws. Thus structural mechanics forms the basic analytic tool for structural engineers. This body of knowledge while not visible to the eye, is the fundamental reason why structures (in most instances) carry anticipated loads in a predictable way. The world of structural engineering, shaping materials into structural elements and joining them to form structural systems, with structural performance as the target, is depicted as the upper triangle in Figure 1.

In the world of materials engineering, raw ingredients are shaped into a composite through processing. Traditionally, raw ingredient selection is based on empiricism. In recent years, as knowledge of the impact the various phases in a composite have upon macroscopic properties increases, composite materials with specific desirable properties have been systematically designed. A particularly useful set of analytic tools for fiber reinforced cementitious composite design is micromechanics, which quantifies the mechanical interaction between fiber, matrix and fiber/matrix interface and relates this interaction to composite material properties. Micromechanics in this form can be considered analogous to structural mechanics where the fiber, matrix and interface serve as loading-carrying ‘members’, and the composite is regarded as the structural system. Naturally, the length scales are much smaller, and some mechanical or physical phenomena are unique to composite materials. Micromechanics can be a powerful tool to deliberately tailor the composite ingredients, such as fiber dimensions and surface coatings, along with sand particle amount and size. In addition, knowledge of material



processing and its effect on both fresh and hardened properties aids in composite design. Again, while not visible to the eye, this body of knowledge on micromechanics and processing allows systematic development of composites with properties not reachable heretofore. The world of materials engineering, with composite property as the target, is depicted as the lower triangle in Figure 1.

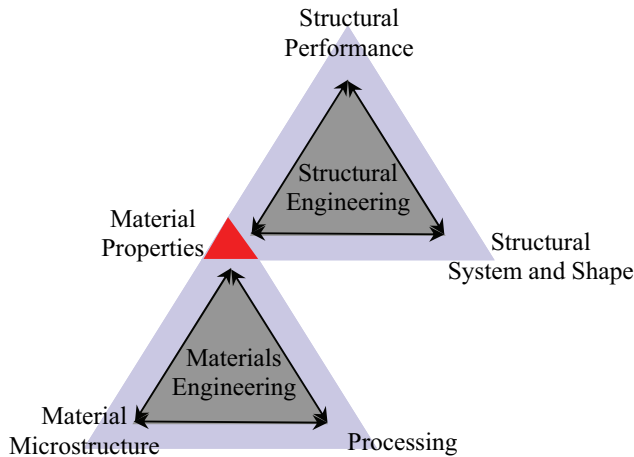


Figure 1: Integrated Structures and Materials Design – A Collaborative Platform for Structural Engineering and Materials Engineering

It is clear from the above discussion and from Figure 1 that the common link between structural engineering and materials engineering is composite properties. As pointed out previously, performance based design of structures provides flexibility and incentive to deliberately select composite materials with properties that efficiently meet the structural performance target. In turn, modern materials engineering provides the tools for intentionally tailoring material ingredients for desired composite properties. Thus, the integration of structural and materials design is a natural joining of these technical fields. In other engineering fields such as aerospace engineering, such integration has already been in practice for some time. In the discipline of civil engineering, this tighter integration can bring about innovative structural systems unattainable if chasms between the structural engineering and materials engineering fields remain.

In most universities, structural engineering and materials engineering are two sub-disciplines within civil engineering. Students in one sub-discipline may lack exposure to the other sub-discipline in their education. This trend unfortunately perpetuates the separation of the two fields as these students continue on as practicing structural or construction materials engineers. In this light, ISMD is not only a collaborative research platform, but also serves as an integrated education platform for future generations of engineers.

Although the concept of integrated structures and materials design is appealing, its implementation faces obstacles requiring attention from both the structural engineering and the materials engineering communities. A shift in mind-frame is needed. The list below is not intended to be exhaustive, but is considered fundamental:

- Material properties characterization should be carried out in such a way that the resulting information can be captured as parameters in constitutive models usable in structural analyses. While this may appear obvious, current standard material tests such as ASTM C1018 which measures toughness based on flexural beams, are of limited use for structural design. It is known that such test results depend on beam height, and are meant to serve only as indices for comparing the relative energy absorption of different fiber mixes.
- Structural performance should be translated into demands on composite material properties, and not on specific fiber types. This recognizes that it is the composite properties that govern the structural performance, and not the fiber type. It is understood that fiber type plays an important role in composite properties, but fiber type is only one of many ingredient parameters that govern composite properties. In other words, a specific fiber may give better or worse composite property depending on the interface characteristics and matrix composition.
- For ISMD to be successful, materials engineers need to view structural performance as the ultimate goal if materials engineering is to maximize its potential impact on the future practice of civil engineering. Structural engineers need to recognize that increasingly, (beyond dimensioning, and reinforcement type and detailing) concrete materials properties are readily designable, and that in many instances the global performance of a structure can be strongly governed by properties other than compressive strength of concrete materials.

Along these lines, the upper triangle in Figure 1 needs to embrace the lower triangle as an additional degree of freedom of structural design (beyond dimensioning, reinforcement detailing, and choice of concrete compressive strength), while the lower triangle needs to reach upward and embrace structural performance as the ultimate material design objective. These expanded mind-frames support meaningful interactions and collaboration between the two allied communities necessary for the common good of next-generation infrastructure systems which are safe, durable, and sustainable.

### **3. Illustration of the use of ISMD**

In this section, the use of ISMD is illustrated by using the structural design of a bridge deck link-slab as an example. This example is chosen because of its relative design simplicity, as well as the fact that it fully exploits ISMD. Another illustration of ISMD using a self-centering seismic moment frame can be found in [3]. ISMD typically involves three main steps: a) translation of targeted structural performance to desired material properties, b) design of composite material to meet the desired material properties, and c) design of the structure based on actual attainable composite properties. These three steps for the link-slab design are detailed below:

### 3.1 Translation of targeted structural performance to desired material properties

Conventional expansion joints of concrete bridge decks are needed to accommodate deck movements due to live load, temperature variations, and material shrinkage. Without expansion joints, random cracking and crushing of the deck would result from such mechanical and environmental loading. Unfortunately expansion joints often jam, resulting in leakage of aggressive agents through the deck, causing damage on beam-ends, and requiring expensive and frequent joint maintenance. One proposed solution to this problem is the use of reinforced link-slabs. Link-slabs are designed to replace the expansion joint and surrounding concrete while still accommodating movements of the adjacent spans so that the deck becomes continuous. The link-slabs, partially debonded from the girder, then serve as hinges over the simply supported beams and connected to the adjacent concrete slabs via steel reinforcements. A shortcoming of concrete link slabs is that they require heavy steel reinforcement to control the crack width in order to maintain durability. Success in crack control is sensitive to the correct design and placement of this steel reinforcement. Large steel reinforcement ratios result in stiffening of the link-slab, contrary to the desire of a flexible hinge.

Thus the performance target of a concrete link-slab can be summarized as:

- Adequate moment capacity to resist bending load caused by rotation of the adjacent slabs due to expected maximum live loads
- Maintain durability by controlling crack widths in the slab in the presence of deck movement due to temperature variations, live load and material shrinkage
- Maintain hinge action to comply as much as possible with the original simple span design

The first and second performance targets suggest high steel reinforcement ratios, while the third target suggests a low ratio. These contradictory requirements can be resolved if the crack width in the concrete can be self-controlled. This essentially decouples the need for crack width control from steel reinforcement required for moment capacity assurance. Indeed, as the link slab becomes more flexible with lower steel reinforcement ratios, the section stiffness and therefore the moment induced actually decreases so that the first performance target can also be met more easily. It is of course well known that normal concrete or even normal fiber reinforced concrete does not have the capability of self-controlled crack widths. Once cracked, concrete depends on steel reinforcement to control crack widths.

Assuming a link-slab of 5% the length of each adjacent deck slab as suggested by Caner and Zia [4], the imposed tensile strain related to imposed deformation by temperature, live load and shrinkage is calculated to be around 1.6%, adopting a factor of safety of two [5]. This implies that cracking in concrete link-slabs is inevitable since normal concrete has a tensile strain capacity of 0.01%. Furthermore, cyclic fatigue loading due to traffic movements may be expected to widen the width of concrete cracks over time [6].

According to previous ACI [7] and AASHTO codes [8], crack widths should be kept below 330  $\mu\text{m}$  as outdoor exposure limit for durability. Based on water permeability test data (e.g. [9]), concrete cracks below 100  $\mu\text{m}$  have the same coefficient of permeability as sound concrete. This stringent requirement is desirable but difficult, if not impossible to achieve with normal concrete. Gilani and Jansson [10] reported that the eight concrete link-slabs built in

Michigan between 2001 and 2003 generally perform well when carefully designed and constructed. In under-performing link slabs with inadequate amounts of reinforcement, crack widths of 250-500  $\mu\text{m}$  were found.

A new type of ductile concrete material is needed to optimally meet the specified structural performance target. Ideally this ductile concrete should have the following characteristics:

- A tensile strain capacity exceeding 1.6%, needed to meet all three structural performance targets with a minimum amount of steel reinforcement;
- Within this straining range, the material must not crack, or if it does crack, must have crack width self-controlled to below 100  $\mu\text{m}$ ;
- For the hinge action performance target, a low Young's modulus is preferred;
- The material should resist fatigue loading so that the crack widths, if any, should remain below 100  $\mu\text{m}$  during its service life; and
- To support traffic load acting on the link-slab, all other properties of normal concrete, including compressive strength (minimum of 35 MPa at 28 days), should be maintained.

This specification of the ideal material properties completes the translation of desired structural performance to desired material properties as represented in the upper triangle in ISMD (Figure 1). From hereon, this set of desired material properties becomes the target of composite material design by the materials engineer. Their responsibility is to tailor material ingredients so that the resulting composite can meet the above set of material characteristics, and be processed under field conditions typical of bridge deck construction or retrofit, as represented by the lower triangle in ISMD. For practical reasons, the material should be producible by regular construction equipment found in the field for current practices.

### **3.2 Design of composite material to meet the desired material properties**

To maintain physical and mechanical compatibility between the link-slab and the deck-slab, it is desired to use a Portland cement based composite for the link-slab. The high tensile strain capacity demand cannot be met by tension-softening fiber reinforced concrete. Although some continuous fiber reinforced mortar and cement composites with high fiber content may meet this demand, their difficult fabrication process prevent them from direct casting in the field for the purpose of bridge deck retrofitting. The high cost associated with high fiber content will make the material economically infeasible for field adoption. One possibility is to use an Engineered Cementitious Composite (ECC) [11] designed with 2% by volume of short, discontinuous PVA REC-15 fiber. This composite material can self-consolidate, making it very easy to cast. The mix composition detailed in Table 1, have been determined by applying micromechanics principles. For details of micromechanics theory behind this design, the reader is referred to Li and co-workers [12, 13].

As can be seen, ECC is made with many of the same ingredients found in normal concrete, less the coarse aggregates. The mortar containing fine silica sand (maximum grain size 250  $\mu\text{m}$ ; average size 110  $\mu\text{m}$ ) has a deliberately low fracture toughness to allow microcracks to grow out from mm-size initial defects such as air-voids when overloaded in tension. These microcracks are then immediately bridged by specially engineered fibers to control the opening

of the crack, resulting in what is known as steady state propagation of flat cracks [14]. The width of these flat cracks can be limited to less than 100  $\mu\text{m}$  by ‘proper’ fiber bridging behavior [15], via control of fiber and interface properties. Typically, fibers with small diameter, high stiffness and strength, and strong interfacial bond to the mortar, provide the best possibility of limiting the flat crack width. However, excessive interfacial bond leads to fiber breakage instead of debonding and slip, returning the composite to a tension-softening FRC. When steady state flat crack propagation prevails, and if a suitable amount and size of initial defects are available in the mortar matrix, multiple cracking and an overall ductile response of the composite result. Thus, it is clear that amongst other requirements, successful design of ECC requires a matrix with limited toughness and an appropriate flaw system, strong and stiff fibers, and suitable interface bonding. In this way, micromechanics theory allows for a systematic and holistic approach to quantitatively tailor the material ingredients. For example, tailoring of a 40  $\mu\text{m}$  diameter and 12 mm long PVA fiber (overall Young’s modulus 28.5 GPa) with a hydrophobic surface coating led to significant improvement in composite ductility [16]. The selection of matrix grain size and incorporation of Class F flyash in ECC also aids in achieving desirable rheological control of fresh properties for self-consolidating casting, while simultaneously limiting the matrix toughness to an appropriate level.

Table 1: Mix proportion of PVA-ECC (Mix M45)

Component	Proportion
Cement	1.0
Fly Ash	1.2
Sand	0.8
Water	0.58
Superplasticizer	0.013
Fiber (vol %)	0.02

It is expected that trade-offs between composite tensile strength and tensile ductility are needed. For example, higher composite strength may be reached by engineering the mortar matrix to have a higher toughness and/or smaller initial flaws, at the expense of ductility. The optimal mix of strength and ductility depends on the particular structural application. For the link-slab, it is clear that tensile ductility is more important to sustain the large imposed deformation, and is given priority over strength. The mix composition of the ECC described in Table 1 provides all the necessary properties required of the link-slab application [11]. In particular, the tensile strength  $\sigma_{ty}$  of 3.5 MPa, a yield strain  $\epsilon_{ty}$  of 0.02% (corresponding to a Young’s modulus  $E$  of 17.5 GPa), with a tensile ductility  $\epsilon_{tu}$  of 2% (minimum), and a steady state crack width  $w_{ss}$  of 60  $\mu\text{m}$ , meet the target composite property requirements specified above. A typical stress-strain curve of this material is given in Figure 2. These material properties have been obtained from a uniaxial tension test [13]. The 28-day compressive strength  $f_c$  and strain capacity  $\epsilon_c$  of this mix is about 75 MPa and 0.43%.

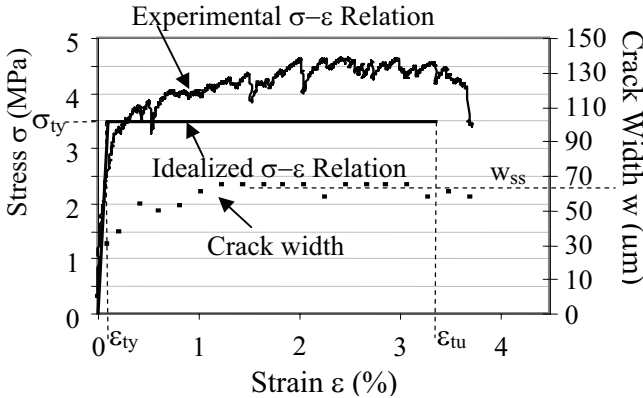


Figure 2: A Typical Stress-Strain and Crack Width Development Curve of ECC for Link-Slab Application.

To ensure that this ECC will meet the serviceability requirements of the link-slab which will be constructed in Michigan with severe winter conditions, standard freeze-thaw durability tests were conducted. These tests [17] confirm that ECC behaves equivalent to air-entrained concrete, even without deliberate air-entrainment. Additional tests include wear tests conducted by MDOT [17] which verified the suitability of this material to be used on bridge decks subjected to heavy traffic volumes. A comparative study of PVA-ECC versus polymer cement mortar subjected to high cycle fatigue loading also indicates the superiority of the fatigue resistance of ECC [18].

### 3.3 Design of the ECC-Link-slab

The design procedure of an ECC link-slab is detailed in Lepech and Li [19]. Experimental verification of the performance of ECC link-slab in accordance with this design is described in [5]. Here, a synopsis of the design aspects relevant to the present ISMD illustration is given.

The geometry of the link-slab and its connection to the deck slabs and the supporting girder is shown in Figure 3. The height of the length slab  $t_s$  is assumed the same as that of the adjacent concrete deck. The debond zone is the center section of the link slab in which all shear connectors between the girder and deck are removed to prevent composite action between girder and deck, so as to allow hinge action. Zia et al [20] found that up to 5% of each adjacent bridge deck may be debonded without affecting the simple span design assumption of the adjacent spans. The full length  $L_{ls}$  of the link slab includes portions connected to the girders via shear studs. This geometry moves the high stress concentration at the ends of the debond zone away from the potentially weaker interfaces between the link-slab and the deck slabs.

The moment induced  $M_{ls}$  must be met by the moment capacity  $M_{r-ls}$  of the link slab.  $M_{ls}$  can be obtained from the maximum (specified as allowable by different DOTs) end rotation  $\theta_{max}$  of the adjacent bridge spans, as

$$M_{ls} = \frac{2E_{ECC}I_{ls}}{L_{dz}} \theta_{max} \quad (1)$$

where  $E_{ECC}$  is the elastic modulus of ECC material and  $I_{ls}$  is the uncracked moment of inertia of the link slab.  $M_{ls}$  can be obtained from a non-linear section analysis of the link-slab. Figure 4 shows the X-section geometry, the typically assumed linear strain profile under bending load, and the corresponding stress profile in the section under negative moment. The linear elastic – perfectly plastic idealized tensile stress-strain curve shown in Figure 2 is adopted. Following [4], it is further assumed that the stress in the reinforcement is limited to 40% of steel yield strength,  $f_{y-steel}$ . This working stress design approach was originally intended to control concrete crack width, but becomes extremely conservative for ECC link-slab design as the ECC self-controls its crack width. Note that unlike concrete, ECC is allowed to carry tension equal to its “yield strength”  $\sigma_{ty}$ , as long as the tensile strain  $\varepsilon_T$  (at the outer-most fiber) does not exceed the tensile strain capacity  $\varepsilon_{tu}$ . The stress profile description is completed by specifying the yield strain  $\varepsilon_{ty}$  of ECC to be 0.02%, as shown in Figure 2.

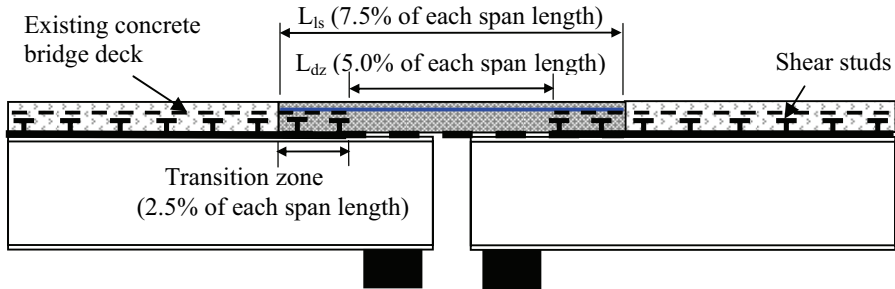


Figure 3: Schematic of ECC Link Slab

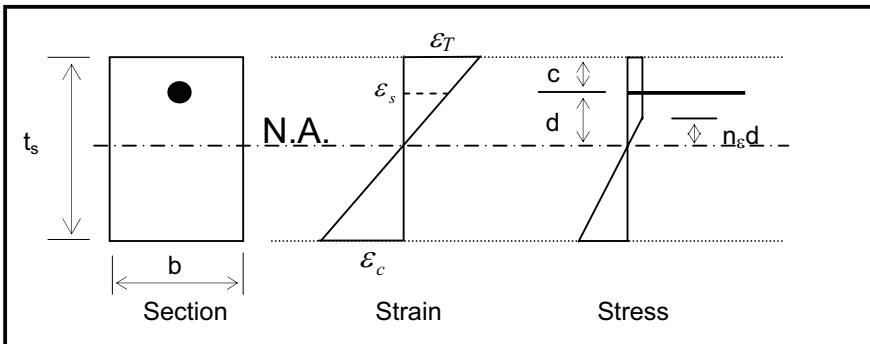


Figure 4: Stress and Strain Distributions in ECC Link Slab Cross-Section

The location of the neutral axis (represented by the unknown variable  $d$  measured from the reinforcement to the N.A. in Figure 4) can be determined by enforcing force equilibrium in the section. Subsequently,  $M_{r-ls}$  can be obtained by summing moments about the neutral axis, as

$$M_{r-ls} = T_{Steel} \cdot d + T_{ECC-2} \left( \frac{(1 - n_\varepsilon)d + c}{2} + n_\varepsilon \cdot d \right) + T_{ECC-1} \left( \frac{2}{3} \right) n_\varepsilon d + C_{ECC} \left( \frac{2}{3} \right) (H - d - c) \quad (2)$$

where

$$n_\varepsilon = \frac{\varepsilon_{ty}}{0.4 \varepsilon_{y-steel}} \quad (3)$$

and

$$T_{steel} = (0.4 f_{y-steel}) \rho_t s b \quad (4a)$$

$$T_{ECC-2} = \sigma_{ty} ((1 - n_\varepsilon)d + c) b \quad (4b)$$

$$T_{ECC-1} = \left( \frac{1}{2} \right) \sigma_{ty} n_\varepsilon d b \quad (4c)$$

$$C_{ECC} = \left( \frac{1}{2} \right) \sigma_{ty} \left( \frac{1}{n_\varepsilon} \right) \left( \frac{1}{d} \right) (t_s - d - c)^2 b \quad (4d)$$

where  $T_{steel}$ ,  $T_{ECC-1}$ ,  $T_{ECC-2}$ , and  $C_{ECC}$  are the tensile force in the steel, the tensile force carried by ECC before and after “yield”, and the compressive force carried by ECC in the compression zone, respectively.

By matching moment induced (1) to moment capacity (2), the amount of steel reinforcement  $\rho$  needed can be determined.

The most important design check is to assure that the expected tensile and compressive strains are below those of the strain capacities of ECC material. The total tensile strain  $\varepsilon_t$  is the sum of those induced by temperature  $\varepsilon_T$ , by drying shrinkage  $\varepsilon_{sh}$  and by live load  $\varepsilon_{LL}$ , i.e.

$$\varepsilon_t = \varepsilon_T + \varepsilon_{sh} + \varepsilon_{LL} \quad (5)$$

where



$$\varepsilon_T = \frac{\alpha_T \cdot \Delta T \cdot \beta \cdot L_{long}}{L_{dz}} \quad (6a)$$

and

$$\varepsilon_{LL} = \frac{0.4 \cdot \varepsilon_{y-steel} \cdot (d + c)}{d} \quad (6b)$$

where  $L_{long}$  is the length of the longer adjacent span, and  $\beta$  is a design value taken as 2.0 for joints with two roller bearings and 1.0 for all other joints. The compressive strain is given by

$$\varepsilon_{LL} = \frac{0.4 \cdot \varepsilon_{y-steel} \cdot (t_s - d - c)}{d} \quad (7)$$

The material check is then

$$\varepsilon_t < \varepsilon_{tu} \quad ; \quad \varepsilon_c < \varepsilon_{cu} \quad (8)$$

If these checks are not met, then modifications of the link-slab geometry (particularly lengthening  $L_{dz}$ ) and/or the ECC material with higher strain-capacity will be needed. Additional design considerations and checks can be found in [19]. Unlike concrete link-slab design, it is not necessary to check crack width since as mentioned before, the crack width for ECC is self-controlled to below 100 $\mu$ m.

With the selection of reinforcement ratio  $\rho$ , the moment capacity of the ECC link-slab is assured.

#### 4. Implications of ISMD

It can be observed from the ECC link-slab example described that the application of ISMD requires the following: The structural engineer, in consultation with the owner of the structure, sets the agenda, in the form of specifying the structural performance target, and translating that target into a set of required composite material properties. The materials engineer conducts materials design based on this set of required composite material properties. In addition, all material characterization must be performed so that the material property data is usable in the structural design process.

ISMD, as represented by the two triangles overlapping at the corner of material properties, serves as a collaborative platform between the structural engineer and the material engineer. Material property is their common “language”.

There are several broad implications of ISMD:

- ISMD encourages structural innovation via advanced materials development. It provides an additional degree of freedom for meeting structural performance targets through materials design, beyond structural element dimensioning, reinforcement detailing and choice of concrete compressive strength.
- ISMD encourages materials innovation with direct impacts on structural performance. It provides guidelines to proper material characterization, as well as incentives for developing tools for materials design.
- ISMD assists material suppliers to specify their material in a way meaningful to structural engineers. Robust material testing methods is also necessary.
- ISMD encourages students in structural and materials engineering to cross disciplinary boundaries so that they would be more effective in contributing to infrastructure development as future engineers.
- ISMD provides a meaningful platform of collaborative research between structural and materials researchers.
- ISMD supports the elevation of sustainability as a primary infrastructure design target, through integration of green material design and processing, and structural durability [21].

In civil engineering practice, day-to-day use of ISMD, at least in the current situation, is not yet practical. Greatly simplified methods of handshaking between structural engineers and materials engineers need to be developed. It is a major challenge to researchers to establish this handshaking methodology. In the future, structural engineers may be able to “dial up”, or map desirable material properties to appropriate material mix designs using a networked computer database that has embedded materials design knowledge.

## 5. Conclusions

This article describes the concept of ISMD, driven by the increasing prevalence of performance based design of structures, and by the recent development of micromechanics based tools for materials engineering. The concept of ISMD is illustrated with the design of a bridge deck link-slab. A specially engineered ECC material is adopted to meet the ductility and durability demanded by the specified structural performance target. ISMD has wide ranging implications. While ISMD provides an excellent collaborative research platform between structural engineers and materials engineers, the practical adoption of ISMD in the civil engineering profession will require investigation into establishing simple “dial-up” tools. Such dial-up tools will add a new degree of freedom in the pursuit of performance based structural design.

## Acknowledgments

The authors thank the Michigan Department of Transportation and the National Science Foundation for funding this research (CMS-0223971, CMS-0329416, and CMS-0070035). Helpful discussions with S. Billington, M. Lepech, J. Lynch and H. Stang are acknowledged.

## References

1. SEAOC, Vision 2000: A framework for performance based engineering of buildings, Structural Engineers Association of California, Sacramento, CA, 1995.
2. Li, V.C., "Strategies for High Performance Fiber Reinforced Cementitious Composites Development," in *Fiber Reinforced Concrete: From Theory to Practice*, Proc. N. American/European Workshop on Advances in Fiber Reinforced Concrete, Bergamo, Italy. Eds. S. Ahmad, M. di Prisco, C. Meyer, GA. Plizzari, and S. Shah, pp. 93-98, 2004.
3. Li, V.C., and Fischer, G., "Reinforced ECC - An Evolution from Materials to Structures," Proceedings of the First FIB Congress, Osaka, Japan, Oct. 2002, 105-122.
4. Caner, A., and Zia, P., "Behavior and design of link slabs for jointless bridge decks", *PCI Journal*, May-June (1998) 68-80.
5. Kim, Y.Y., Fischer, G., and Li, V.C., "Performance of Bridge Deck Link Slabs Designed with Ductile ECC," *ACI Structural J.*, **101** (6) (2004) 792-801.
6. Matsui, S. (1997). "Technology Developments for Bridge Decks - Innovations on Durability and Construction - (in Japanese)." *Kyouryou To Kiso*(8), 84-92.
7. American Concrete Institute, "Building Code Requirements for Structural Concrete (ACI 318-95) and Commentary (ACI 318R-95)", American Concrete Institute. Farmington Hills, MI. 1995.
8. American Association of State Highway and Transportation Officials "AASHTO LFRD Bridge Design Specifications: Second Edition." AASHTO. Washington, D.C., USA 1998. pp. 5-41.
9. Wang, K., Jansen, D, Shah, S., Karr, A., "Permeability Study of Cracked Concrete", *Cement and Concrete Research*, **27** (3) (1997) 381-393.
10. Gilani, A. and Jansson, P., "Link Slabs for Simply Supported Bridges." MDOT Report Number MDOT SPR-54181, Structural Research Unit, Construction and Technology Support Area, Michigan Department of Transportation. Lansing, Michigan, 2004.
11. Wang, S. and Li, V.C., "Polyvinyl Alcohol Fiber Reinforced Engineered Cementitious Composites: Material Design and Performances," in Proc., Int'l Workshop on HPFRCC Structural Applications, Hawaii, May, 2005.
12. Li, V.C., "On Engineered Cementitious Composites (ECC) – A Review of the Material and its Applications," *J. Advanced Concrete Technology*, **1** (3) (2003) 215-230.
13. Li, V.C., Wang, S., and Wu, C., "Tensile Strain-Hardening Behavior of PVA-ECC," *ACI Materials J.*, **98** (6) (2001) 483-492.
14. Li, V.C. and Leung, C.K.Y., "Steady State and Multiple Cracking of Short Random Fiber Composites," *ASCE J. of Engineering Mechanics*, **118** (11) (1992) 2246-2264.
15. Wang, S., "Micromechanics Based Matrix Design for ECCs," PhD Thesis, University of Michigan, Ann Arbor, April, 2005.
16. Li, V.C., Wu, C., Wang, S., Ogawa, A., and Saito, T., "Interface Tailoring for Strain-Hardening PVA-ECC," *ACI Materials J.*, **99** (5) 463-472, 2002.
17. Li, V.C., and Lepech, M., "Crack Resistant Concrete Material for Transportation Construction," in Transportation Research Board 83<sup>rd</sup> Annual Meeting, Washington, D.C., Compendium of Papers CD ROM, Paper 04-4680, 2004.
18. Suthiwarapirak, P., Matsumoto, T., and Kanda, T., "Flexural Fatigue Failure

- Characteristics of an Engineered Cementitious Composite and Polymer Cement Mortars,” *J. Materials, Conc. Struc. Pavements, JSCE*, **718** (57) (2002) 121-134.
19. Lepech, M. and V.C. Li, “Design and Field Demonstration of ECC Link Slabs for Jointless Bridge Decks,” ConMat’05, Vancouver, Canada, August, 2005, CD-documents/1-05/SS-GF-05\_FP.pdf.
  20. Zia, P., A. Caner, and El-Safte, A.K., “Jointless Bridge Decks, Research Project 23241-94-4,” Center for Trans. Engin. Studies, North Carolina State, 1995, pp. 1-117.
  21. Keoleian, G.A., A. Kendall, J.E. Dettling, V.M. Smith, R. Chandler, M.D. Lepech, and V.C. Li, “Life Cycle Modeling of Concrete Bridge Design: Comparison of Engineered Cementitious Composite Link Slabs and Conventional Steel Expansion Joints,” in ASCE *J. Infrastructure Systems*, (2005) 51-60.

## Calculation of Thermal Stresses in Concrete Pavements at Early age

Jun Zhang and Zhi Hua Li

Department of Civil Engineering, Tsinghua University, Beijing, P.R.China

### Abstract

In the present work, an analytical solution of thermal stress in concrete pavement at early age is derived. In the modeling, the nonlinear characteristic of temperature distribution along the slab depth is considered. The nonlinear temperature profile is first divided into three components, an average temperature component, a linear temperature component and a nonlinear temperature component, which all are functions of concrete casting time depending on the balance between heat generation from the cement hydration and heat exchange with its surroundings. Afterward, the thermal stresses resulted by each temperature component is calculated separately according to the temperature variation history. The total thermal stress is obtained by summing the three stress components together.

### 1. Introduction

The service life of a concrete pavement is determined by many factors including initial design, material properties, traffic, environment, salt application, presence and effectiveness of protective systems and maintenance practices among others. All these factors influence the development of cracks in concrete slabs during service. Cracking and joint openings in pavements may further lead to concrete spalling and punchouts. It has long been recognized that critical stresses which may leads pavement cracking results not only from the traffic loads, but also from the temperature changes and shrinkage of concrete. Concrete shrinkage and temperature changes and its gradients resulted stresses may be one of the major mechanisms leading to the initial crack formation in concrete pavements. The hydration of cement in a concrete mixture is a process that generates heat and the rate of heat generation is accelerated with increase of concrete temperature. During the hydration of cement under field conditions, the development of concrete temperature is determined by the balance between heat generation from the cement hydration and heat exchange with its surroundings. The surroundings may either be an additional heat source or at a lower temperature than the concrete. The typical developing model of concrete temperature after casting is that at beginning the temperature increases with time. After reaching to a peak, the temperature stars to decrease and finally goes into a stable

stage with surrounding endearments.

Fig. 1 presents a typical temperature-time diagram of a concrete pavement in the different locations since pavement construction [1]. From the figure shown above, first it can be concluded that the temperature change with time is quite significant. It is well know that as temperature rising, the slab expands and it contracts as the temperature dropping. If a concrete slab of moderate dimensions rests freely on its supports, it can contract to accommodate the shortening of its length produced by temperature decreasing. However, in pavements, concrete slab and supporting base are in contact with each other and the slab cannot contract freely. Thus, as concrete temperature decreases, a certain amount of tensile stresses will be developed in the slab. A rising in temperature has an effect similar to temperature dropping just resulting compressive stresses in pavement instead of tensile stresses. Second, the temperature difference between different locations in the same section and at the same time is also pronounced. The thermal stresses resulted by the temperature gradient along the slab depth must be significant also. Third, nonlinear characteristic of the distribution of temperature along the slab depth is distinct (three measured data can not be predicted with a single linear function) and the distribution law may obey different nonlinear function at different time. Therefore, the stresses caused by nonlinear thermal gradient must also be included in the thermal stress analysis.

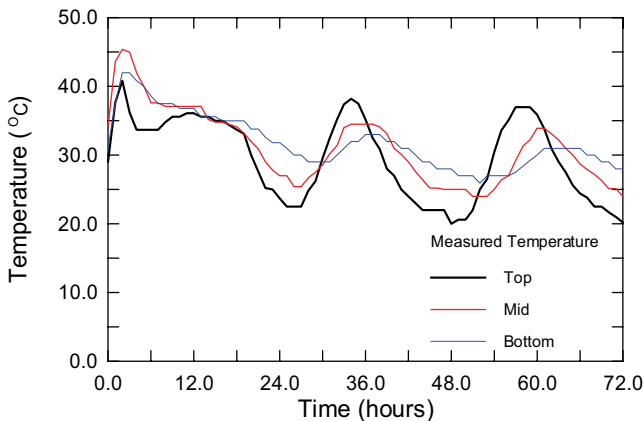


Fig. 1. Field measured temperature data at three typical locations and their variation with time

In this paper, an analytical solution of thermal stresses in concrete pavement is developed. In the modeling, the temperature distribution along the slab depth is divided into three components: a component of uniform temperature, a linear component and a nonlinear component. Afterward, the thermal stresses resulted by each temperature component are calculated separately according to the temperature variation history. The interfacial friction between slab and supporting base is recognized as the mechanisms leading to stresses in slab as concrete temperature uniformly changes. The problem is simplified as one dimension and a bilinear friction stress-slippage

relation is used. Second, the stresses resulted from linear and nonlinear components are analyzed with classical plate theory [2, 3]. The total thermal stress is then obtained by summing the three stress components together.

## 2. Thermal Stress Model

### 2.1 Thermal gradient components and mathematical modeling

In order to calculate the stresses resulted from temperature change with time and its nonlinear distribution throughout the pavement depth respectively, it is assumed that the cross section of the slab remains plane after bending. Thus, the slab can deform only in two ways: it can expand or contract along its axial direction or it can bend with the cross section remaining plane upward or downward. Based on above assumption, the temperature distribution in the slab along the depth can then be divided into three components accordingly: (1) a component of uniform temperature that causes the slab expand or contraction uniformly as the temperature rising or dropping; (2) a linear component that causes the slab bending; and (3) the nonlinear component that remains after the uniform and the linear temperature parts are subtracted from the total temperature distribution, see Fig. 2 [4].

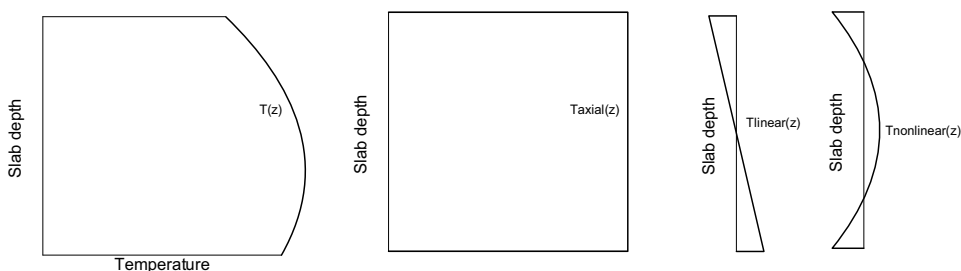


Fig.2. Schematic representation of the three temperature components in a given slab section.

To isolate the above temperature components, a mathematical model of a polynomial with two degree was used to simulate a temperature profile along the slab depth, i.e.

$$T = A + Bz + Cz^2 \quad (1)$$

Where  $T$  is temperature in degree and  $z$  is the vertical distance measured from middle of slab with  $z=h/2$  at surface and  $z=-h/2$  at the bottom.  $A$ ,  $B$ ,  $C$  are unknown coefficients to be determined from field measured temperature data. Thus, the uniform temperature component,  $T_{axial}$ , causing axial displacement can be determined by

$$T_{axial} = \frac{1}{h} \int_{-h/2}^{h/2} (A + Bz + Cz^2) dz = A + C \frac{h^2}{12} \quad (2)$$

It can be seen that for a given slab, the variation of  $T_{axial}$  with time is governed by the coefficients

of  $A$  and  $C$ . The linear component of the temperature distribution that causes bending of the pavement slab is

$$T_{linear} = \frac{6z}{h^2} \int_{-h/2}^{h/2} (T_{total} - T_{axial}) z dz = Bz \quad (3)$$

It should be noted that a positive  $B$  means that the temperature at top surface is higher than that at bottom. The difference between top and bottom fibers is equal to  $Bh$  which is the governing parameters of the magnitude of thermal stress produced by the linear component. Finally, the nonlinear temperature component is determined by

$$T_{nonlinear} = T_{total} - T_{axial} - T_{linear} = C \left( z^2 - \frac{h^2}{12} \right) \quad (4)$$

From the expression, we can see that the nonlinear temperature is distributed symmetrically along the slab depth. If the coefficient  $C$  is positive, the top and bottom portion of the slab would tend to expand and the middle portion would tend to contract. The situation is reversed in the case of the coefficient  $C$  is negative.

## 2.2 Thermal stresses resulted from the axial component

Similar with the method used for calculating shrinkage stress in concrete pavement [5], the uniform temperature variation resulted stresses in the slab can be obtained by follow. First it is assumed that the concrete slab behaves in a linear elastic manner and the base beneath the concrete slab is a rigid material and the deformation under action of the horizontal friction forces is ignored. Second the temperature change resulted axial stresses along slab length is sufficient to reflect the magnitude of stresses in the slab. This consideration allows the mathematical model to be considered a one-dimensional problem. A concrete pavement section with width  $W$ , height  $H$  and length  $L$  is modeled, as shown in Fig. 2.  $y$  is the direction perpendicular to the slab length,  $x$  is the direction parallel to the slab length. The ends of the slab are located at  $x=0$  and  $x=L$ , respectively. Due to the symmetry of the problem, only half of the slab is modeled.

Before derivation of the governing equations for the model, a law governing the slab/base interfacial friction stress-slippage relation needs to be given. A number of experimental studies had shown that the development of slab/base interfacial friction stress with slab slippage can be described by a bilinear function [6, 7]. The shear stress first almost linearly increases to a certain value (so called steady state value) with the increase of slab slippage. Then the stress stays at this value with further increase of the slab slippage. In the present work, friction stress acting on the slab surface is modeled as

$$\begin{aligned} \tau &= \frac{\tau_0}{\delta_0} |u| \quad \text{for} \quad 0 \leq |u| \leq \delta_0 \\ \tau &= \tau_0 \quad \text{for} \quad \delta_0 < |u| \end{aligned} \quad (5)$$



where  $u$  is the average slippage along thickness of slab relative to base at location  $x$ , which is given by

$$u(x) = u_e(x) + u_c(x) \quad (6)$$

where  $u_e$  is the displacement induced by concrete shrinkage.  $u_c$  is the displacement resulted from internal axial stress.  $\tau_0$  is the steady state frictional stress.  $\delta_0$  is the corresponding slippage as the frictional stress achieves  $\tau_0$ .  $\tau_0$  and  $\delta_0$  are normally governed by the type of base and they can be determined by sliding tests with a laboratory size slab cast on a given base.

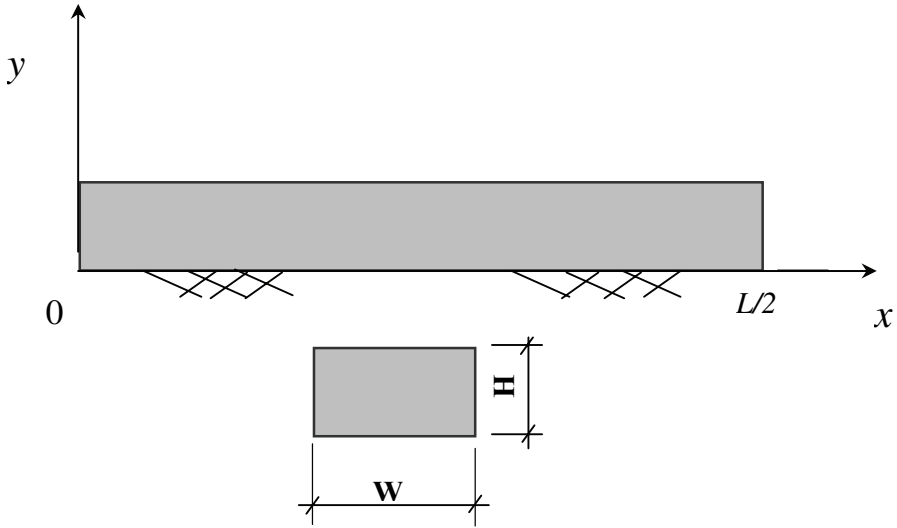


Fig. 3. Schematic diagrams showing the slab model used in analyses

When the slab is subjected to a temperature change ( $T_{axial} - T_{a0}$ ), where  $T_{a0}$  is the initial uniform temperature when the restraint from base start to act on the slab, based on the above assumptions, the axial force equilibrium for a slab length  $dx$  in the presence of a thickness average axial stress  $\sigma_c$  and slab/base interfacial shear stress  $\tau$  requires:

$$\frac{\partial \sigma_c}{\partial x} - \frac{\tau}{H} = 0 \quad (7)$$

From elasticity theory, the first derivative of  $\sigma_c$  with respect to  $x$  can be related to axial displacement  $u_c$  by

$$\frac{\partial \sigma_c}{\partial x} = E_c \frac{\partial^2 u_c}{\partial^2 x} \quad (8)$$

where  $E_c$  is Young's modulus of concrete. Replacing  $\frac{\partial \sigma_c}{\partial x}$  with (8) in (7) and noting that,

$\frac{\partial^2 u}{\partial^2 x} = \frac{\partial^2 u_c}{\partial^2 x}$  (  $\frac{\partial^2 u_c}{\partial^2 x} = 0$  ), the general equation governing the average axial displacement distribution in the slab,  $u$  is

$$\frac{\partial^2 u}{\partial^2 x} - \frac{\tau}{E_c H} = 0 \quad (9)$$

According to the magnitude of displacement, the slab may finally be divided into two sections on each of which a specific  $\tau$  should be applied.

Stage I:  $|u| \leq \delta_0$  at  $x=0$

In this case, the slab/base interfacial friction stress  $\tau$  linearly increases with the increase of slab slippage  $u$  and this linear friction stress-slippage relationship can be applied along the whole slab. Replacing  $\tau$  with the linear relation given by (5) in (8), we have:

$$\frac{\partial^2 u}{\partial^2 x} - \frac{\tau_0}{E_c H \delta_0} u = 0 \quad (10)$$

To solve this differential equation with boundary conditions that  $u=0$  at  $x=L/2$  and

$\frac{\partial u}{\partial x} = \frac{\sigma_{c0}}{E_c} + \alpha(T_{axial} - T_{a0})$  at  $x=0$ , yields (detailed derivation can be found in [5]):

$$\sigma_c = -E_c \alpha (T_{axial} - T_{a0}) \left[ 1 - \frac{\cosh \beta \left( \frac{L}{2} - x \right)}{\cosh \beta \frac{L}{2}} \right] + \sigma_{c0} \frac{\cosh \beta \left( \frac{L}{2} - x \right)}{\cosh \beta \frac{L}{2}} \quad (11)$$

Where  $\alpha$  is thermal expansion factor of  $\beta = \sqrt{\tau_0 / E_c H \delta_0}$  concrete and  $\sigma_{c0}$  is average axial stress at  $x=0$  along slab thickness. Here, we define  $\sigma_{c0}$  as negative if it compresses the slab and positive if it tensions the slab. Similarly, if  $\alpha(T_{axial} - T_{a0})$  is negative, the temperature change makes the slab shorter and if it is positive, it makes the slab longer. The sign of  $\sigma_c$  has the same meanings as  $\sigma_{c0}$ . When  $d\sigma_c/dx=0$ , we obtain  $x=L/2$ , so the maximum average stress in slab,  $\sigma_{cm}$  occurs at this location and it is given by

$$\sigma_{cm} = -E_c \alpha (T_{axial} - T_{a0}) \left[ 1 - \frac{1}{\cosh \beta \frac{L}{2}} \right] + \sigma_{c0} \frac{1}{\cosh \beta \frac{L}{2}} \quad (12)$$

Stage II:  $|u| > \delta_0$  at  $x=0$

In this case, the slab should be divided into two sections according to the displacement relative to base. Now assume  $u = \delta_0$  at  $x = x_0$ , for the section of  $0 \leq x \leq x_0$ , the slab/base interfacial friction stress is fully developed and the shear stress is a constant ( $\tau_0$ ), as shown in equation (1). Replace  $\tau$  with  $\tau_0$  in (8), the general governing equation of  $u$  can be rewritten as

$$\frac{\partial^2 u}{\partial^2 x} - \frac{\tau_0}{E_c H} = 0 \quad (13)$$

To solve this differential equation with boundary conditions  $\frac{\partial u}{\partial x} = \frac{\sigma_{c0}}{E_c} + \alpha(T_{axial} - T_{a0})$  that at  $x=0$  and  $u = \delta_0$  at  $x = x_0$ , yields:

$$\sigma_c = -E_c \alpha (T_{axial} - T_{a0}) \left[ 1 - \frac{\cosh \beta \left( \frac{L}{2} - x \right)}{\cosh \beta \left( \frac{L}{2} - x_0 \right)} \right] + \sigma_{c00} \frac{\cosh \beta \left( \frac{L}{2} - x \right)}{\cosh \beta \left( \frac{L}{2} - x_0 \right)} \quad (14)$$

$\sigma_{c00}$  is the thickness average axial stress at  $x = x_0$  and  $\sigma_{c00} = E_c \beta^2 \delta_0 x_0 + \sigma_{c0}$ . The length  $x_0$  can be numerically determined from (19) by setting  $x = x_0$  and  $u = \delta_0$ , i.e.

$$\delta_0 = -\frac{1}{\beta} \left[ \beta^2 \delta_0 x_0 + \frac{\sigma_{c0}}{E_c} + \alpha(T_{axial} - T_{a0}) \right] \tanh \beta \left( \frac{L}{2} - x_0 \right) \quad (15)$$

The above equation indicates that the length of fully developed zone of the slab/base friction stress,  $x_0$ , and the length of being development zone ( $L/2 - x_0$ ), are governed by the combined effects of  $\delta_0$ ,  $\beta$ ,  $\sigma_{c0}$  and  $\varepsilon_c$ . When  $d\sigma_c/dx=0$ , from equation (14), we obtain  $x=L/2$ . So the maximum thickness average stress,  $\sigma_{cm}$  at this stage occurs at this location and it is given by

$$\sigma_{cm} = -E_c \alpha (T_{axial} - T_{a0}) \left[ 1 - \frac{1}{\cosh \beta \left( \frac{L}{2} - x_0 \right)} \right] + (E_c \beta^2 \delta_0 x_0 + \sigma_{c0}) \frac{1}{\cosh \beta \left( \frac{L}{2} - x_0 \right)} \quad (16)$$

Due to the present work is focus on analyzing the development of thermal stresses in jointed concrete pavements at early age, so that  $\sigma_{c0}=0$  is used in the following analyses.

### 2.3 Thermal stresses resulted by linear component

A number of methods of determining the thermal stresses caused by the linear temperature distribution along the slab section were proposed [2, 3]. The general solution for an elastic slab subjected to linear temperature profile was given by Westergaard as

$$\begin{aligned} -\frac{\partial^2 w}{\partial x^2} &= \frac{12}{Eh^3} (M_x - \nu M_y) + \frac{\alpha \Delta T}{h} \\ -\frac{\partial^2 w}{\partial y^2} &= \frac{12}{Eh^3} (M_y - \nu M_x) + \frac{\alpha \Delta T}{h} \end{aligned} \quad (17)$$

Where  $x$ ,  $y$ ,  $z$  are the directions of slab length, width and thickness respectively.  $w$  is the displacement in the  $z$ -direction.  $\nu$  is Poisson's ratio of concrete.  $\Delta T$  is the temperature difference between top and bottom of the slab, which is equal to  $Bh$  in the present analysis. The right side of above equation represents the total curvature of the slab corresponding to the moment curvature in  $x$  and  $y$  direction and the curvature due to the linear temperature gradients respectively. The thermal stresses produced by the linear temperature difference can be obtained by solving above differential equation with appropriate boundary and external restrained conditions. In the present work, research is focus on the development of thermal stresses in concrete pavement during early age. The slab is normally relative long and the pavement joints have not been cut yet in this stage. The restrain action along the slab length is significant and we may assume that  $\partial^2 w / \partial x^2 = 0$ . Thus from (17), we have

$$\begin{aligned} M_y &= \frac{Eh^3}{12(1-\nu)} \left[ -\frac{\partial^2 w}{\partial y^2} - \frac{(1+\nu)\alpha \Delta T}{h} \right] \\ M_x &= \nu M_y - \frac{Eh^2 \alpha \Delta T}{12} \end{aligned} \quad (18)$$

In addition, the moment  $M_y$  can be related to the reflective force of base  $kw$  by

$$\frac{d^2 M_y}{dy^2} = kw \quad (19)$$

$k$  is the stiffness of pavement base. Replace  $M_y$  with (18) in (19), the general governing equation of  $w$  can be rewritten as

$$l^4 \frac{\partial^4 w}{\partial y^4} + w = 0 \quad (20)$$

Where  $l = \left[ \frac{Eh^3}{12(1-\nu^2)k} \right]^{\frac{1}{4}}$ . Solve the above differential equation with boundary conditions that

$M_y=0$  and  $dM_y/dy=0$  at  $y=\pm W/2$ ,  $W$  is the width of slab, yields:

$$w = w_0 \frac{2 \cos W_l \cosh W_l}{\sin 2W_l + \sinh 2W_l} \left[ (-\operatorname{tg} W_l + \tanh W_l) \cos \frac{y}{l\sqrt{2}} \cosh \frac{y}{l\sqrt{2}} + (\operatorname{tg} W_l + \tanh W_l) \sin \frac{y}{l\sqrt{2}} \sinh \frac{y}{l\sqrt{2}} \right] \quad (21)$$

Here  $w_0 = \frac{(1+\nu)\alpha\Delta T}{h} l^2$ ,  $W_l = \frac{W}{l\sqrt{8}}$ . Thus replace  $w$  in (19) with (21), we can obtain the expression of the stress distribution in  $x$  and  $y$  direction along the slab depth as

$$\sigma_{yz} = 2\sigma_0 \left\{ 1 - \frac{2 \cos W_l \cosh W_l}{\sin 2W_l + \sinh 2W_l} \left[ (\operatorname{tg} W_l + \tanh W_l) \cos \frac{y}{l\sqrt{2}} \cosh \frac{y}{l\sqrt{2}} + (\operatorname{tg} W_l - \tanh W_l) \sin \frac{y}{l\sqrt{2}} \sinh \frac{y}{l\sqrt{2}} \right] \right\} \frac{z}{h} \quad (22)$$

$$\sigma_{xz} = 2 \left[ \sigma_0 + \nu (\sigma_{yz} - \sigma_0) \right] \frac{z}{h}$$

Where  $\sigma_0 = \frac{E\alpha B h}{2(1-\nu)}$ , which is the stress as slab length and width are infinite and the deformation

produced by the temperature differences is fully restrained. It should be noted that positive  $B$  means that the temperature at top surface is higher than that at bottom and leads to a compressive stress at top surface and a tensile stress at bottom. The maximum stress produced by the linear temperature gradient will occur at the section with  $y=0$  in the direction of  $x$ -axial. The stress distribution in the section of  $y=0$  along  $x$ -direction,  $\sigma_{xz}$  can be expressed as

$$\sigma_{xz} = 2\sigma_0 \left[ 1 - \nu (1 - C_y) \right] \frac{z}{h} \quad (23)$$

And the maximum stress at slab top or bottom can be given by

$$\sigma_{xm} = \sigma_0 \left[ 1 - \nu (1 - C_y) \right] \quad (24)$$

Where  $C_y = 1 - \frac{2 \cos W_l \cosh W_l}{\sin 2W_l + \sinh 2W_l} (\operatorname{tg} W_l + \tanh W_l)$ , that is a function of slab width and depth

as well as stiffness of slab and supporting base. From equation (24), we can see that the maximum stress is a product between  $\sigma_0$ , which is the stress value as the slab is full restrained in both  $x$  and  $y$  directions, and a factor which reflects the influence of slab width in the case of the slab length is relative long.

## 2.4 Thermal stresses resulted by nonlinear component

According to the basic assumption that the cross section of the plane remains plane under the action of thermal load, the stresses caused by this nonlinear part can be calculated by

$$\sigma_{nonlinear} = -\frac{E\alpha T_{nonlinear}}{1-\nu} = -\frac{E\alpha C}{1-\nu} \left( z^2 - \frac{h^2}{12} \right) \quad (25)$$

Apparently, if the coefficient  $C$  is positive (the temperature at slab top or bottom is higher than that in the middle), the extreme fiber of the slab would tend to expand and cause compressive stresses at these positions and tensile stresses would result at middle of the slab. This condition is reversed if coefficient  $C$  is negative. The maximum tensile stress may occur at top or bottom and middle of the slab that depends on the sign of coefficient  $C$ . In the case of  $C$  is negative, the maximum tensile stress occurs at top or bottom surface and is given by

$$\sigma_{non-m} = -\frac{E\alpha Ch^2}{6(1-\nu)} \quad (26)$$

In the case of  $C$  is positive, the maximum tensile stress occurs at middle section and is given by

$$\sigma_{non-m} = -\frac{E\alpha Ch^2}{12(1-\nu)} \quad (27)$$

So far, the completed analytical solution of thermal stresses resulted by the corresponded three-temperature components is developed separately. The total thermal stresses can be obtained by summing the three stress components together as

$$\sigma_t = \sigma_{axial} + \sigma_{linear} + \sigma_{nonlinear} \quad (28)$$

## 3. Examples of Calculation

### 3.1 Material parameters for model input

In terms of stress development, the final set temperature is the temperature at which the concrete begins to resist the stresses resulted by volume change from shrinkage or temperature changes of concrete. This normally corresponds to the time that the concrete transitions from a plastic state to a solid state. The final set temperature is related to the temperature  $T_{a0}$  that is used in the uniformly axial thermal stress analysis in the present study. It should be note that also before final set, the concrete behaves a plastic material and no strength and stiffness developed and therefore there is no stress developed in the slab also in this stage even with a temperature variation. As discussed in the previous section, the temperature development in concrete pavement after placement is a complex process which may be affected by the temperature of concrete material at placement, the type and quantity of the cementitious material, curing temperature and solar radiation intensity and the boundary conditions of the slab. As a general conclusion, the temperature in pavement is greatly varied with time since placement, see Fig. 1. In order to accounting the effect of temperature variation on the development of concrete

strength, a concept called equivalent age [8] is used in the present work. The equivalent age represents the age of curing at the reference temperature that would result in the same fraction of the limited strength as would result from curing at other temperature. Based on the definition, the equivalent age  $t_{eq}$  can be expressed as

$$t_{eq} = \int_0^t \frac{K(T)}{K(T_{ref})} dt \quad (29)$$

Where  $t_{eq}$  is the equivalent age at the reference temperature  $T_{ref}$ .  $K(T_{ref})$  and  $K(T)$  are the rate constant at reference temperature  $T_{ref}$  and temperature  $T$ . According to the Arrhenius law, the rate constant can be expressed as

$$K(T) = ae^{-\frac{U_{aT}}{R(273+T)}} \quad (30)$$

Where  $U_{aT}$  is the apparent activation energy at temperature  $T$  (J/mol).  $R$  is the universal gas constant, 8.314J/molK and  $a$  is the proportional constant.  $T$  is temperature in Celsius ( $^{\circ}\text{C}$ ). Replace  $K(T)$  with (30) in (29) yields

$$t_{eq} = \int_0^t e^{\frac{1}{R} \left( \frac{U_{ar}}{293} - \frac{U_{aT}}{273+T} \right)} dt \quad (31)$$

Where  $T_{ref}=20^{\circ}\text{C}$  is assumed. A number of researchers have concluded that the apparent activation energy could not be considered as a constant independent of time except during the beginning of hydration of cement. Previous studies shown that the apparent activation energy changes slightly at early ages and decreases greatly at later ages [9,10]. In addition, the apparent activation energy of concrete cured at high temperature will decrease more quickly than that cured at normal temperature, means that it is not only a function of time, but also a function curing temperature. Based on these findings, the apparent activation energy of concrete can be calculated by the following equation [11]

$$U_a = U_0 e^{\alpha t} = (42830 - 43T) e^{(-0.00017T)t} \quad (32)$$

Where  $T$  is curing temperature ( $^{\circ}\text{C}$ ) and  $t$  is curing time in days. Due to the actual curing temperature  $T$  is varied with time, it is convenient to solve  $t_{eq}$  in the matrix form instead of integrating. If the curing time is divided into  $n$  sections and the temperature in each time interval is assumed to be a constant, then we have

$$t_{eq} = \sum_{i=1}^n e^{\frac{1}{R} \left( \frac{U_{ar}}{293} - \frac{U_{aT_i}}{273+T_i} \right)} (t_i - t_{i-1}) \quad (33)$$

Where  $U_{ar} = U_0 e^{\alpha_r t}$  and  $U_{aT_i} = \left( \frac{1}{i} \sum_{j=1}^i U_{0T_j} \right) e^{\left( \frac{1}{i} \sum_{j=1}^i \alpha_{T_j} \right) \sum_{j=1}^i t_j}$ .

The section number of  $n$  may depend on the required accuracy on the equivalent age and normally can be equal to the time intervals for temperature measurement. Further, it is well known that the setting time of concrete is affected by the hydration degree of cement, which is a function of the water/cement ratio [12]. If we define the hydration degree of cement as [13]

$$\alpha(t_e) = \exp - \left[ \ln \left( 1 + \frac{t_{eq}}{t_k} \right) \right]^\beta \quad (34)$$

Where  $t_k$  and  $\beta$  are adiabatic hydration shape parameters. According to Byfors [12], final set of concrete occurs at a specific degree of hydration, so called critical hydration degree, that is a function of water-cement ratio and can be predicted by

$$\alpha_c = k (w/c) \quad (35)$$

Where  $k$  is a constant and varied between 0.4 to 0.46.  $w/c$  is water cement ratio. Using (35) in (34), the setting time ( $t_0$ ) can be solved and corresponded temperature  $T_{a0}$  can then be determined according to the field temperature data. Accordingly, the development of elastic modulus of concrete with curing time under varied curing temperature can also be determined by [13]

$$E(\alpha) = E_l \left( \frac{\alpha - \alpha_c}{1 - \alpha_c} \right)^{1/2} = 1.05 E_{28} \left( \frac{\alpha - \alpha_c}{1 - \alpha_c} \right)^{1/2} \quad (36)$$

Thus, under varied curing temperature condition, all the necessary material parameters used for thermal stress calculation are properly predicted using the concept of equivalent age.

### 3.2 Examples of calculation and discussions

The temperature data obtained by Schindler et al [1] was adopted for the analysis of thermal stress development at early age since pavement construction. The pavement temperatures were measured by thermocouples positioned at three typical locations, 25 mm below the top surface, mid-depth and 25 mm above the bottom surface. The required parameters for thermal stress analysis of concrete slabs, including dimension of slab, concrete and base materials as well as slab/base interfacial properties are listed in Table 1.

To calculate the thermal stresses, the temperature distribution along the slab depth is determined first using the temperature distribution mode. For a given slab section with the measured temperature data at three different locations, it is easy to solve the parameters  $A$ ,  $B$  and  $C$ , which is a function of concrete casting time. The temperature distribution can then be obtained by replacing  $A$ ,  $B$  and  $C$  with the obtained values in equation (1). Using the parameters listed in Table 1 and the temperature distribution parameters ( $A$ ,  $B$ ,  $C$ ) as model inputs, the thermal stress distribution along the slab depth and its developing pattern with concrete age can be obtained. In the modeling, the average temperature along whole slab depth at different time after casting is used for solving the equivalent age  $t_{eq}$ . The model calculating results are shown in Figs 4 to 6.



Table 1 Input parameters for model calculation

Parameters	Slab
<b>Pavement parameters</b>	
Pavement width	3.7 m
Pavement thickness	230 mm
Pavement length	10.0 m
Subbase type	Cement treated
$\tau_0$	0.106 MPa
$\delta_0$	0.025 mm
<b>Concrete mix proposition</b>	
Cement	390 kg/m <sup>3</sup> (a)
Fly ash	-
Water	179 kg/m <sup>3</sup>
Sand	676 kg/m <sup>3</sup>
Stone	1115 kg/m <sup>3</sup>
<b>Properties of concrete</b>	
$\alpha_c$	0.18
$\beta$	-0.768
$t_k$	1.312 Hours
Modulus of elasticity	35 GPa (28 days)
Coefficient of thermal expansion	10.0 Micro strain/°C
Poisson's ratio	0.2
Modulus of subgrade	81 MN/m <sup>3</sup>

The typical temperature distributions throughout the slab depth at 5, 14, 26 and 35 hours after concrete casting along with three field measured temperature data are shown in Fig. 4. From the predicted temperature distribution diagrams, it can be seen that in the early age, due to the hydration of cement that generates heat, the temperature inside the slab is higher than that of top or bottom surfaces. The temperature differential in the slab tends to be negative in this stage. With increase of time, the heat generated by the hydration of cement is gradually reduced and the environmental effect gradually becomes the dominating factor which finally leads the temperature distribution varied periodically with time going. The nonlinearity of the temperature distribution in the slab is quite obvious and the variation of the temperature distribution with time is distinct also. Fig. 5 displays the thermal stress distribution along the slab depth at 5, 14, 26 and 35 hours after concrete casting. Based on the model results presented in the figure, we can see that the thermal stress is distributed nonlinearly. The maximum stress may occur at any location of the whole slab thickness that is governed by the sum of the stress components,  $\sigma_{axial}$ ,  $\sigma_{linear}$  and  $\sigma_{nonlinear}$ , which in turn are dependent on the temperature distribution characteristics, such as parameter  $A$ ,  $B$  and  $C$ .

As an example of calculation, the development of thermal stresses at top surface of the slab with time since concrete casting are presented in Fig. 6. The variations of axial temperature  $T_{axial}$ , parameter  $B$  and  $C$  with time are displayed along with the stress-time diagram also. From the results, we can see that the model can well predicting the development of thermal stresses in concrete pavement which subjected to a periodic variation of temperature. A peak stress can be observed approximately around an average temperature peak. For a given dimension of slab and

concrete material properties (listed in Table 1), the magnitude of the individual stress component,  $\sigma_{axial}$ ,  $\sigma_{linear}$  and  $\sigma_{nonlinear}$  principally governed by the variations of  $T_{axial}$ , parameter  $B$  and  $C$  respectively. In generally, small variation in temperature including both the average temperature change and the gradient throughout the slab depth will result in a low variation of thermal stresses.

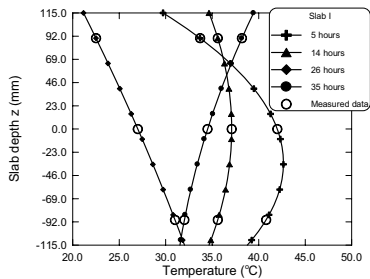


Fig.4. Temperature distribution along the slab depth at some typical age of concrete

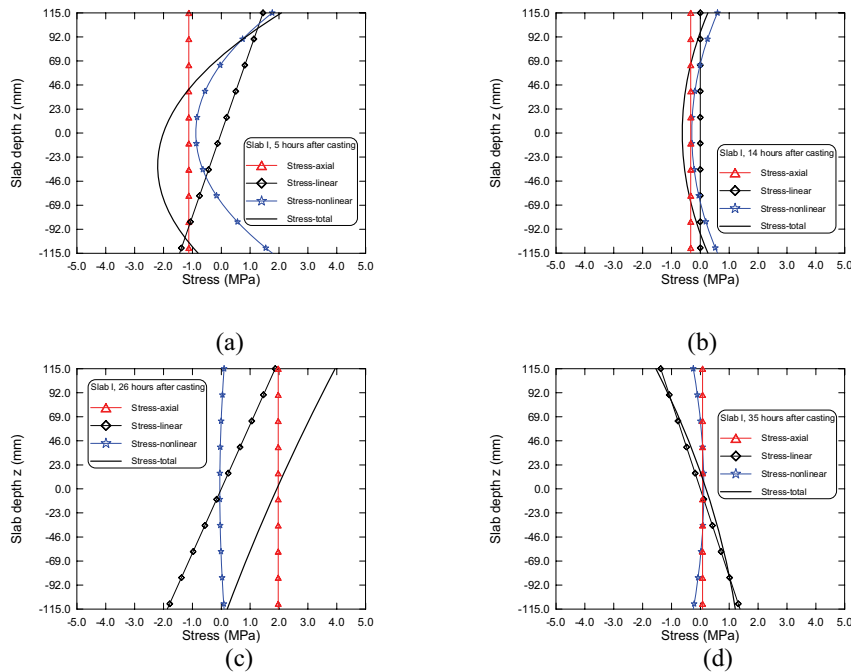


Fig.5. Stress distribution along the slab depth at some typical age of concrete

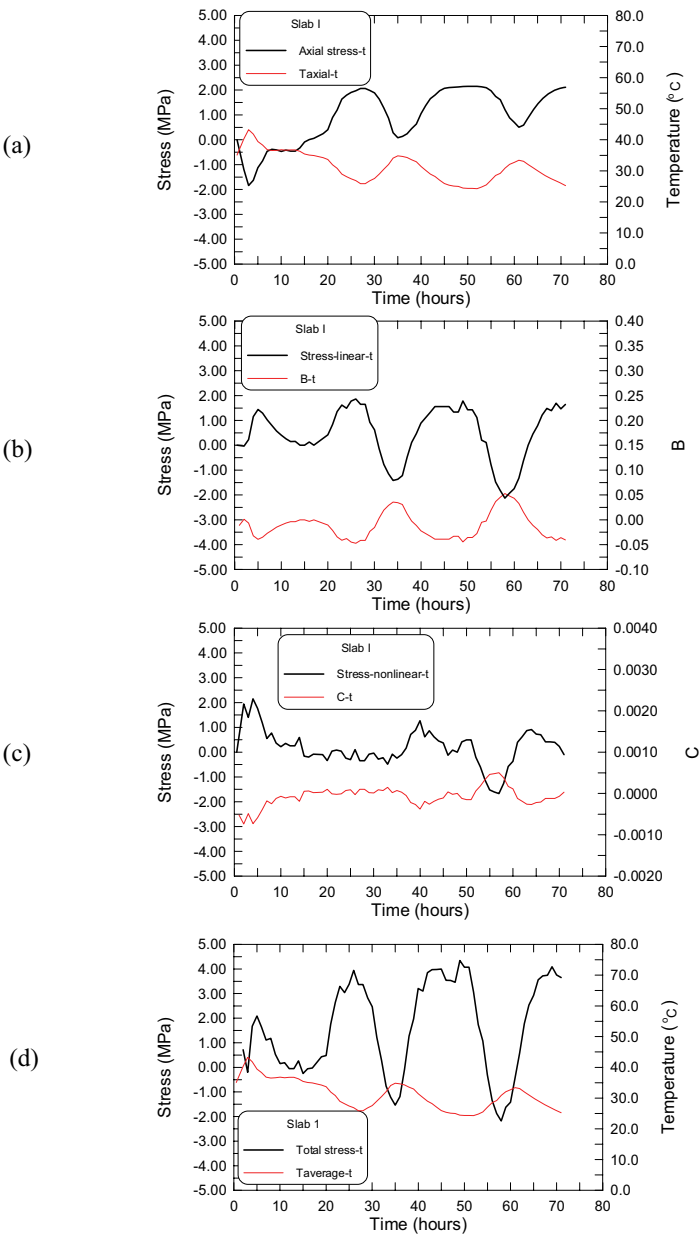


Fig. 6. The development of thermal stresses at slab top with concrete age in slab, (a) axial stress, (b) linear stress (c) nonlinear stress and (d) total stress

#### 4. Conclusions

The paper presents an analytical solution of thermal stresses in concrete pavement at early age. In the modeling, the temperature across the slab thickness is first modeled with two-degree of polynomial function based on measured temperature data at three different locations. Then the temperature distribution is divided into three components, an average temperature component, a linear temperature component and a nonlinear temperature component. After that, the thermal stress resulted by each individual component is calculated separately according to the temperature variation history in the slab. The total thermal stress is obtained by summing the three stress components together. The model is able to predict the stress distribution along the slab depth at a given time and the stress development with time since pavement construction. The model was used to field measured temperature data for thermal stress calculation. The model results shown that the temperature distribution along the slab depth is highly nonlinear and the variation of the temperature with time is distinct. As a result of the temperature variation with time, the axial stress resulted from this variation is significant. Due to the nonlinear temperature distribution, the thermal stresses are nonlinearly distributed along the slab depth also. The maximum stress may occur at any location of the slab depth that governs by the sum of the three stress components, which in turn are dependent on the temperature distribution characteristics as well as their variation with time. The model can be used in both, temperature induced cracking control and concrete pavement design.

#### Acknowledgement

This work has been supported by a grant from the National Science Foundation of China (No. 50178043) to Tsinghua University.

#### References

1. Schindler, A.K., Ruiz, J.M., Rasmussen, R.O., Chang, G.K. and Wathne, L.G., Concrete pavement temperature prediction and case studies with FHWA HIPERPAV models, Cement and Concrete Composites, 3.
2. Westergaard, H.M., Analysis of stress in concrete pavements due to variations of temperature. Proc., 6<sup>th</sup> Ann. Meeting, Hwy. Res. Board, Washington, D.C., 201-215, 1926..
3. Bradbury, R.D., Reinforced concrete pavement. Wire Reinforcement Institute, Washington, D.C., 34-41, 1938..
4. Choubane, B. and Tia, M., Nonlinear temperature gradient effect on maximum warping stresses in rigid pavements. Transportation Research Record, 1370, Transportation Research Board, Washington D.C., 11-19, 1992..
5. Zhang, J. and Li, V.C., Influence of supporting base characteristics on the shrinkage induced stresses in concrete pavements. ASCE Journal of Transportation Engineering, Vol. 127, Issue 6, pp. 455-462, 2001.

6. Wesevich, J.W., McCullough, B.F. and Burns, N.H., Stabilized subbase friction study for concrete pavements. Research Report 495-1, Center for Transportation Research, University of Texas at Austin, 1987.
7. Wimsatt, A.W., McCullough, B.F. and Burns, N.H., Methods of analyzing and factors influencing frictional effects of subbases. Research Report 495-2F, Center for Transportation Research, University of Texas at Austin, 1987.
8. Rastrup, E., Heat of hydration, Magazine of Concrete Research, 6(17), 127-140.
9. Kjellsen, K. and Detwiler, R.J., 1993. Later-age strength prediction by a modified maturity model. ACI Materials Journal, May-June (1994) 220-227.
10. Chanvillard, G. and Daloia, L., Concrete strength estimation at early age: Modification of the method of equivalent age. ACI Materials Journal, 94 (6), (1997) 220-227.
11. Kim, J.K., Estimation of compressive strength by a new apparent activation energy function. Cement and Concrete Research, 31(2) (2001) 217-225.
12. Byfors, J., Plain Concrete at Early Age. CBI, 1980.
13. Gutsch, A. W., Stoffeigenschaften jungen Betons-Versuche und Modelle. Doct. Th., TU Braunschweig, 1998.



## On the Application of Cohesive Crack Modeling in Cementitious Materials

Henrik Stang, John Forbes Olesen, Peter Noe Poulsen and Lars Dick-Nielsen  
Department of Civil Engineering, Technical University of Denmark

### Abstract

Cohesive crack models – in particular the Fictitious Crack Model – are applied routinely in the analysis of crack propagation in concrete and mortar. Bridged crack models – where cohesive stresses are assumed to exist together with a stress singularity at the crack tip – on the other hand, are used typically for multi scale problems such as crack propagation in fiber reinforced composites. Mortar and concrete, however, are multi-scale materials and the question naturally arises, if bridged crack models in fact are more suitable for concrete and mortar as well? A model for a centrally cracked sheet is established applying semi-analytical, bridged and fictitious crack modeling. The fictitious crack model is compared with a FEM analysis and it is demonstrated, that the standard fictitious crack implementation in FEM packages (in this case DIANA) provides a good approximation. Further, a quantitative condition is established indicating when a bridged crack model can be approximated with a cohesive crack model with smooth crack closure, in terms of the ratio between the energy dissipation associated with the crack tip and that of the process zone.

### 1. Introduction

Coarse mortar and concrete are typically characterized as quasi-brittle materials. Cement and fine mortars are sometimes considered brittle and sometimes quasi-brittle materials. The proper modeling of these materials has been under debate for more than 30 years. At this point in time, it is generally agreed that the cohesive crack model proposed by Hillerborg, [1], the so-called *Fictitious Crack Model*, FCM, provides a reasonably consistent framework for the modeling of mode I crack propagation in concrete and mortar. In particular this model has been used extensively in finite element models of problems where the crack path is known in advance.

#### 1.1 Cohesive crack models

The fictitious crack model resembles that of Barenblatt [2] somewhat. In the FCM non-constant closing stresses or cohesive stresses,  $\sigma_w(w)$ , are applied to the crack surface. These cohesive stresses depend on the crack opening,  $w$ , and vary from zero at a characteristic crack opening,  $w_c$ , to the tensile strength of the material,  $f_t$ , at zero crack opening at the tip of the

crack. It is assumed that the cohesive stresses close the crack smoothly, thus even when the un-cracked material is considered linear elastic – which is often the case in the modeling of cementitious materials – stresses are finite in the un-cracked material at the crack tip (on other words, during mode I crack propagation, the stress intensity factor  $K_I$  is zero) and the condition for crack propagation is that the stress at the crack tip has reached the tensile strength,  $f_t$ . The zone in which the cohesive stresses are present is originally called the *micro-cracked zone*, [1], and later the *process zone* or *fracture zone*, [3], when it was realized, that the cohesive stresses were due not only to stress transfer in micro-ligaments between micro-cracks, but also to frictional stresses in various bridging configurations by aggregates, fibers and other inhomogenities. Thus, the cohesive law implicitly contains information about the micro-structure of the material.

In the FCM there is no a priori assumption regarding the length of the process zone,  $l_p$ , there is no direct connection between the length of the process zone and the opening,  $w$ , of the process zone and in particular it is not assumed, that the fracture process zone is small compared to the pre-existing macro-crack, total crack length or a characteristic dimension of the structure in question. In order to maintain smooth crack closure the distribution of closing stresses along the crack faces is essential in the FCM, as pointed out by Karihaloo, [4]. The features described above distinguish the FCM from other well-known cohesive models. The Barenblatt model assumed characteristic cohesive stresses distributed over a short process zone, resulting in a model essentially equivalent to Linear Elastic Fracture Mechanics (LEFM) models, while the Dugdale model, [5] assumes a constant closing stresses. All three models reduce to LEFM only in the limiting case of small process zones (compared to total crack length and/or characteristic dimension of the structure in question).

In the original formulation it is implicitly assumed that for any given cohesive law,  $\sigma_w(w)$  – whether it is experimentally determined or theoretically assessed – the process zone length and opening can be adjusted in such a way that smooth crack closure, i.e. finite stresses at the crack tip, can be achieved. Otherwise the model formulation would break down and the crack propagation criterion would be inadequate. To the authors' knowledge it has never been rigorously proven that for any cohesive law, the process zone can always be adjusted to meet the smooth crack closure condition, however, implementations in practice supports the assumption, at least within a broad range of cohesive laws.

Implementations of the FCM are available in many commercial and research oriented Finite Element Method codes. In these implementations the cohesive law, i.e. the cohesive stress versus crack opening curve, is considered to be material input. The curve can either be user supplied, or the curve might be restricted to e.g. a linear or bi-linear softening curve. In all cases the length and the opening (and thus the cohesive stress) of the process zone is adjusted by iteration to meet the crack propagation criterion – expressed in terms of a finite stress – in the element ahead of the crack tip. In practice this turns out to be a robust process with little mesh size dependency and little dependency of the displacement field on which the elements are based, i.e. it



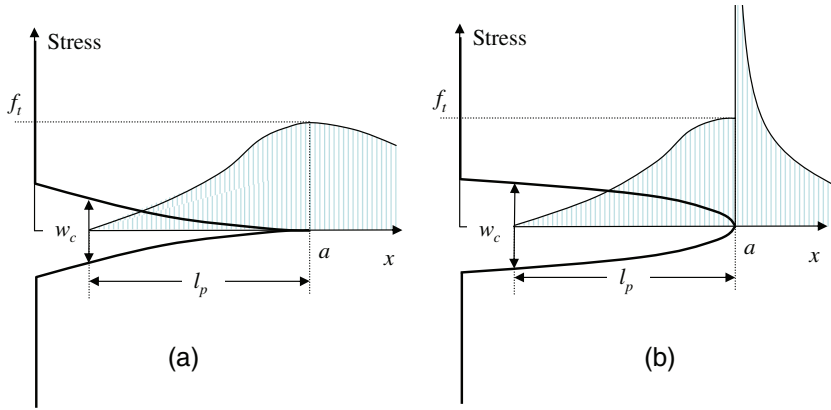


Figure 1: Sketch showing the process zone in (a) a cohesive law with smooth crack closure and (b) a bridged crack model.

seems that smooth crack closure is achieved without it being a specific requirement. Numerous FEM studies of crack propagation with the FCM have been referred to in the literature which all describe excellent convergence with mesh refinement.

This observation is also made in the original formulation by Hillerborg, [1]: *The analysis can be performed with a rather coarse mesh, ....., because there are no stress singularities and the amount of absorbed energy is not very sensitive to the mesh size.* Thus it appears that the standard, rather coarse numerical implementation ensures that the smooth crack closure condition is met with reasonable accuracy. This will be further substantiated in the present paper comparing a semi-analytical approach to the problem of propagation of a cohesive crack with a FEM based approach to the same problem.

## 1.2 Bridged crack models

The FCM or any other cohesive crack model with smooth crack closure can be considered as a special case of the more general *bridged crack model* according to Cox and Marshall, [6], see also Fig. 1, where cohesive stresses are assumed to exist together with a stress singularity at the crack tip, i.e. smooth crack closure is not required. In bridged crack models the crack propagation criterion is that  $K_I = K_{Ic}$  and in crack propagation problems the length and the opening (and thus the cohesive stress) of the process zone is adjusted so that this criterion is fulfilled in the un-cracked material at the crack tip.

Bridged crack models are formulated in order to deal with the fact that many crack propagation problems are in fact multi-scale problems as outlined in the following. Real materials are inhomogeneous with many size scales which makes crack propagation problems multi-scale problems with the atomic bond being the smallest scale and phenomena such as aggregate and

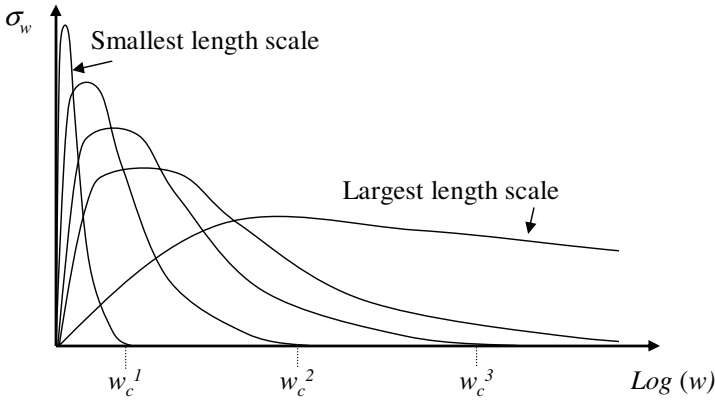


Figure 2: Schematic illustration of a multi-scale cohesive law. Note that the x-axis is logarithmic.

The concept of a multi-scale cohesive law is illustrated in Fig.2. On each scale the cohesive law for a cementitious material represents a characteristic mechanism reflecting the average nature of the bond including the presence of defects: atomic bond separation on the smallest scale, separation of grain interfaces, micro-crack ligament stress-transfer and aggregate or fiber bridging at the largest scale.

It follows that the magnitude of the cohesive stresses at the various length scales in general will be of different orders of magnitude. The significance of the cohesive law at the various length scales can be characterized based on the energy that it represents, i.e. the area under the curve at the various length scales. Thus, in general it is not possible a priori to disregard any part of the cohesive law. In practice, however, it is not possible to solve a crack propagation problem by taking detailed information about the cohesive law into account at all length scales because of the finite resolution of the solution for the displacement fields. Using a FEM approach to solve for displacements at all length scales would require an unreasonably large number of elements. This problem can be solved by lumping all energy corresponding to length scales smaller than a certain scale,  $w_c^i$ , corresponding to the resolution of the solution for the displacement field, into a single point. This corresponds to applying LEFM to those small scales and applying the cohesive law only to the larger length scales, i.e. applying the bridged crack model.

Thus, with this interpretation of the bridged crack model and assuming that LEFM is adopted for all length scales smaller than  $w_c^i$ , the crack propagation criterion is:

$$K_I = K_{Ic} \quad (1)$$

with

$$K_{Ic} = \sqrt{E' G_F^i} \quad (2)$$

and

$$G_F^i = \int_0^{w_c^i} \sigma_w(w) dw \quad (3)$$

while the cohesive law is enforced for  $w > w_c^i$ . Here,  $E'$  is Young's modulus,  $E$ , for the uncracked material in plane stress and  $E/(1-\nu^2)$  in plane strain, with  $\nu$  denoting Poisson's ratio.

It follows from the above that in principle all crack propagation problems in inhomogeneous materials should be solved using the bridged crack approach (except in the cases where the total crack length,  $a \gg l_p$  so that the LEFM can be used for all length scales). However, bridged crack models are more difficult to implement in numerical approaches than cohesive models. Further, bridged crack models require initial defects in order to initiate crack propagation and the models are sensitive to the length of these initial defects. Cohesive crack models on the other hand do not require initial defects to initiate crack propagation (since, as indicated above, the presence of defects is already included in the cohesive law in an average sense), and if initial defects are present, the stress needed to initiate their propagation is relatively insensitive to their size, [10].

Thus, from a computational point of view, it is very useful to know when a bridged crack model can be approximated with a cohesive crack. This must depend on the ratio between the fracture energy associated with the crack tip and the fracture energy associated with the cohesive law. This will be the second issue dealt with in the present paper applying a semi-analytical approach to the bridged crack and the cohesive model.

### 1.3 FCM for multi-scale materials

The bridged crack model can be approximated with the FCM by artificially adjusting the tensile strength and the first part of the cohesive law as indicated in Fig. 3, such that

$$(f_t' - f_t)w' \approx \frac{K_{Ic}^2}{E'} \quad (4)$$

where  $f_t'$  is the artificially increased tensile strength and where  $w'$  is the crack opening over which the cohesive stress is increased.

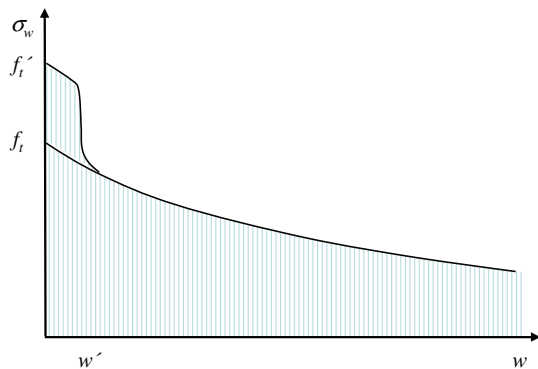


Figure 3: Schematic showing a cohesive law adjusted to take into account the scales smaller than the resolution of the solution for the displacement field.

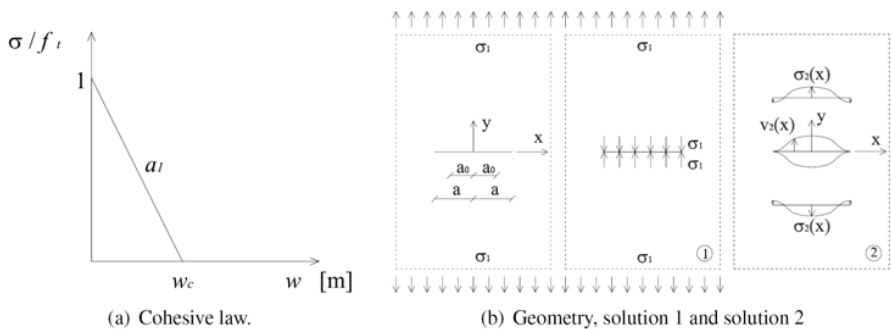


Figure 4: Center cracked sheet.

This observation is consistent with previous results indicating difficulty with differentiating between tensile strength and the initial slope of the cohesive law, [11], on the structural level.

It follows from the above that when a cohesive law is determined from experimental results using e.g. inverse analysis, the experimentally determined tensile strength will depend on the resolution of the solution for the displacement field and thus a certain mesh dependence of the tensile strength can be expected. This issue is not further dealt with in this paper.

## 2. Semi-Analytical Approach

As a generic example, the problem of a centrally cracked infinitely large sheet is considered, see Fig. 4. The un-cracked material is assumed to be linear elastic with Young's modulus  $E'$ , while a bridged crack model is governing fracture. Together with the crack propagation

criterion (1), a simple linear cohesive law is applied: the maximum stress is called the tensile strength,  $f_t$  and the cohesive stress decreases with the slope  $a_1$  as the crack opening increases, see Fig. 4(a). The area under the cohesive stress versus crack opening curve is interpreted as the fracture energy,  $G_F^i$ , according to equation (3).

In [10] a semi-analytical approach was suggested to solve the presented crack propagation problem in order to investigate the effect of initial crack length on first crack strength of cement mortar and paste assuming smooth crack closure. Here emphasis will be on the effect of the crack propagation criterion on crack length and opening profile in the bridged crack model assuming non-smooth crack closure. The approach will be briefly summarized here.

In the infinite sheet an initial stress free defect of length  $2a_0$  is present. The total length of the crack is  $2a$ , see Fig. 4(b). Note also the coordinate system with the x-axis in the crack plane and with origo at the center of the crack. The cohesive crack is assumed to propagate when the stress intensity factor  $K_I$  is equal to  $K_{Ic}$ . The solution for  $K_I$  and the crack opening displacement for a given crack length  $a$  and a given far field uniaxial tensile stress,  $\sigma_1$  can be found by superposition of two fundamental solutions as shown in Fig 4(b).

The first fundamental solution is trivial with  $\sigma_1$  on the crack surfaces,  $K_I \equiv 0$  and  $v_1 \equiv 0$  where  $v$  is the crack opening displacement on each crack face.

The second fundamental solution is a crack in an infinite sheet loaded only on the crack surfaces with the stress  $\sigma_2(x)$ . The stress intensity factor and the crack opening displacement is obtained by integration of the fundamental solution of two opposite forces on a crack surface, see [12]:

$$\frac{1}{2} w(x) = v_2(x, 0) = - \int_{-a}^a \frac{2\sigma_2(\xi)}{\pi E'} \cosh^{-1} \frac{a^2 - \xi x}{a|x - \xi|} d\xi \quad (5)$$

$$K_I = K_{I2}(\pm a) = - \int_{-a}^a \frac{\sigma_2(x)}{\sqrt{\pi a}} \frac{\sqrt{a^2 - x^2}}{a \pm x} dx \quad (6)$$

where  $\xi$  is an integration variable along the x-axis,  $w(x)$  is the total crack opening and  $E' = E$  for plane stress.

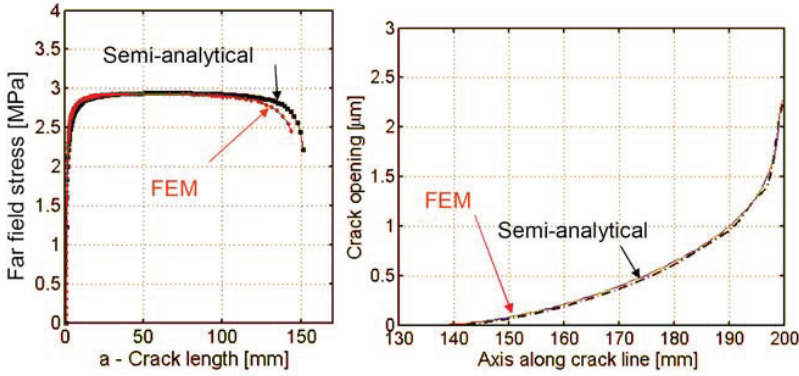


Figure 5: Comparison between FEM-Diana analysis and the semi-analytical calculation. On the top the far field stress is shown as function of the crack length and on the bottom the crack opening profile along the crack line is shown at peak load where  $a = 65$  mm (200 mm on the x-axis corresponds to the center of the specimen)

The stress free condition of the initial defect and the cohesive law of the propagating crack require that:

$$\sigma_2(x) + \sigma_1 = 0 \quad \text{for} \quad |x| \leq a_0 \quad (7)$$

and

$$\sigma_w(w(x)) = \sigma_2(x) + \sigma_1 \quad \text{for} \quad a_0 < |x| \leq a \quad (8)$$

Introducing Equation (5) in (8) this equation together with (7) determines  $\sigma_2$  and thus the crack opening displacement through Equation (5). The stress intensity factor can then be determined from Equation (6). Finally,  $K_I = K_{Ic}$  can be achieved by adjusting the crack length,  $a$ . As a result corresponding values for crack length and far field stress are obtained given the cohesive law and the crack propagation criterion  $K_I = K_{Ic}$ . The cohesive crack model is obtained from the special case  $K_{Ic} = 0$ .

### 3. FEM Approach to the Cohesive Crack Model

In order to compare the semi-analytical analysis outlined above for  $K_{Ic} = 0$  with a FEM-based cohesive crack model analysis, a FEM model for a centrally cracked finite sheet was build and analyzed. The sheet is 400 mm wide and 800 mm long with an initial (stress free) crack length  $a_0 = 1$  mm. The sheet is loaded in uniaxial tension in plane stress. A total of 6300 elements are used in the modeling, which comprises one quarter of the specimen. The applied element is an eight-node quadrilateral plane stress element. Appropriate convergence analysis

proved the mesh to be sufficient. The bulk material was assumed to be linear elastic. Interface elements were placed ahead of the crack allowing the crack to propagate in its own plane. A linear softening FCM was assigned to the interface elements. The material parameters employed in the analysis—corresponding to a typical cementitious mortar—are summarized in Table 1. The commercial Finite Element package 'DIANA' was used for the modeling.

$E$	$f_t$	$G_F$	$a_0$
20 GPa	3 MPa	50 Nm/m <sup>2</sup>	1 mm

Table 1: Material parameters used for the comparison between the FEM and the semi-analytical approach.

First, it was ensured by investigating the stress field in the sheet before crack propagation that the stresses were independent of the boundaries, i.e. that the cracked sheet effectively behaved like an infinite sheet. Thus, the present FEM geometry was shown to be equivalent to the geometry investigated in the semi-analytical approach in terms of initial crack propagation.

Next, the crack propagation problem was investigated and compared with the results from the semi-analytical approach. Typical results are shown in Fig. 5, where the far field stress versus crack length relationships obtained from the two approaches are shown together with the crack opening profile at peak load.

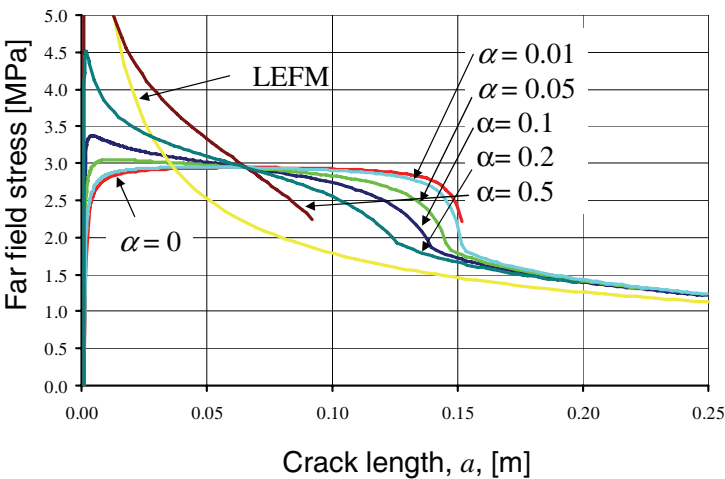


Figure 6: Far field stress versus crack length calculation for FCM ( $\alpha = 0$ ), bridged crack model with  $\alpha = 0.01, 0.05, 0.1, 0.2, 0.5$  and a LEFM analysis.

In general the comparison shows that very good agreement is obtained in the case analyzed. The far field stress needed for crack propagation is slightly overestimated by the FEM analysis in the beginning and underestimated after the peak stress ( $= 2.95$  MPa), which is reached at a crack length  $a = 65$  mm. The reason for this underestimation is the finite size of the sheet in the FEM analysis. The crack profiles at peak load show very good agreement. Thus it appears that the standard FCM implementation in FEM solves the crack propagation problem of a cohesive crack with smooth crack closure with good accuracy.

#### 4. Results for Bridged Crack Model

In order to investigate the effect of  $K_{Ic} \neq 0$  the bridged crack model is now investigated with the critical stress intensity factor equal to a fraction,  $\alpha$ , of the stress intensity factor corresponding to the fracture energy associated with the cohesive law,  $G_F$ :

$$K_{Ic} = \alpha \sqrt{EG_F} \quad (9)$$

A parametric variation is carried out for  $\alpha$  as shown in Fig. 6, where the far field stress is shown as function of the crack length for  $\alpha = 0, 0.01, 0.05, 0.1, 0.2, 0.5$ . The material parameters are as shown in Table 1. Furthermore a calculation based on Linear Elastic Fracture Mechanics with  $K_{Ic} = \sqrt{EG_F}$  is shown.

Clearly, as  $\alpha$  is increased the solution for the bridged crack model approaches the LEFM-solution. A significant deviation from the cohesive crack model is observed for  $\alpha > 0.1$  but already at  $\alpha = 0.05$  a significant deviation for the crack length at peak stress is observed.

#### 5. Discussion

The standard FEM implementation of the FCM corresponds very well to the cohesive crack model with smooth crack closure.

The FEM FCM solution is similar to the semi-analytical solution for a bridged crack model with  $\alpha \approx 0.01$ , i.e. apparently not completely smooth crack closure is obtained. This corresponds well with the observation that a FEM solution is not that sensitive to the applied mesh and the fact that even with a linear approximation of the displacement field – which will never reproduce smooth crack closure – reasonable results can be obtained.

Based on the above if experimental results are analyzed with a FEM-based FCM, a the tensile strength can be expected to be mesh dependent.

It is allowable to use FCM in multi-scale problems when the energy dissipation associated with scales less than the resolution of the solution for the displacements is less than 0.01-0.05 times the fracture energy  $G_F$  of the FCM, depending on the required accuracy. This makes FCM



applicable for mortar and concrete with reasonable accuracy, however the concept of a tensile strength is somewhat artificial.

Care should be taken when applying cohesive crack models with smooth crack closure to crack propagation problems in fiber reinforced composite materials where the fibers provide large scale bridging effects. The above investigation provides a quantitative condition for when the fracture energy of the matrix can be disregarded and a cohesive model applied.

## References

1. A. Hillerborg, M. Modéer and P.E. Petersson. Analysis of crack formation and crack growth in concrete by means of fracture mechanics and finite elements. *Cem Concr. Res.*, 6(6):773-782, 1976
2. G.I. Barenblatt. The mathematical theory of equilibrium cracks in brittle fracture. *Adv. Appl. Mech.*, 7:56-129, 1962.
3. A. Hillerborg. Analysis of fracture by means of the fictitious crack model, particularly for fibre reinforced concrete. *The Int. J. Cem. Comp.*, 2(4):177-184, 1980.
4. B. L. Karihaloo. *Fracture Mechanics & Structural Concrete*. Concrete Design and Construction Series. Longman Scientific & Technical, Harlow, Essex, England, 1995
5. D. S. Dugdale. Yielding of steel sheets containing slits. *J. Mech. Phys. Solids*, 8:100-104, 1960
6. B. Cox and D. Marshall. Concepts in the fracture and fatigue of bridged cracks. *Acta Metallurgical ET Meteriala*, 41:341-363, 1994.
7. A. Needleman. An analysis of tensile decohesion along an interface. *J. Mech. Phys. Solids*, 38:289-324, 1990.
8. V.C. Li and M. Maalej. Toughening in cement based composites. Part i: Cement, mortar and concrete. *Cement & Concrete Composites*, 18:223-237, 1996.
9. G. Bao and Z. Suo. Remarks on crack-bridging concepts. *Appl. Mech. Rev.*, 45(8):355-366, 1992.
10. L. Dick-Nielsen, P. N. Poulsen, H. Stang and J. F. Olesen. Semi-analytical cohesive crack model for the analysis of first crack strength of mortar. In *Proceedings of the 17<sup>th</sup> Nordic Seminar on Computational Mechanics*, pages 183-186. KTH Mechanichs. Stockholm, Swede, 2004.
11. H. Stang and J. F. Olesen. On the interpretation of bending tests on frc-materials. In *Fracture Mechanics of Concrete Structure. Vol. 1*, pages 511-520. Aedificatio Publishers, Freiburg, Germany, 1998.
12. H. Tada, P. Paris and G. Irwin. *The Stress Analysis of Cracks Handbook*. Paris Productions Incorporated, 226 Woodbourne Dr., St. Louis, Misssouri, USA, 1985.



## **Micro-mechanical Analysis of Fiber Reinforced Cementitious Composites using Cohesive Crack Modeling**

Lars Dick-Nielsen, Henrik Stang and Peter Noe Poulsen

Department of Civil Engineering, Technical University of Denmark, Lyngby, Denmark

### **Abstract**

This paper discusses the mechanism appearing during fiber debonding in fiber reinforced cementitious composite. The investigation is performed on the micro scale by use of a Finite Element Model. The model is 3 dimensional and the fictitious crack model and a mixed mode stress formulation are implemented. It is shown that the cohesive law for a unidirectional fiber reinforced cementitious composite can be found through superposition of the cohesive law for mortar and the fiber bridging curve. A comparison between the numerical and an analytical model for fiber pull-out is performed.

### **1. Introduction**

Fiber bridging, i.e. fibers bridging a propagating and opening matrix crack, is a fundamental mechanism governing the nonlinear behavior of fiber reinforced cementitious composites. The stresses carried across the crack by the bridging fibers are often described with an (average) cohesive law. When a cohesive law is applied for the matrix crack as well, an average cohesive law emerges describing the crack in the composite.

In [1] it was suggested to use a superposition scheme for the fiber bridging cohesive stresses and the matrix cohesive law (the fictitious crack model) in order to derive an average cohesive law for fiber reinforced concrete. In contrast to fiber reinforced concrete, Engineered Cementitious Composite (ECC) is a high performance fiber reinforced cementitious composite, which is characterized by its ability to undergo strain hardening in tension. Strain hardening is achieved through multiple cracking of the material. For strain-hardening to occur in an ECC material it is required, that the criteria for multiple cracking are satisfied. These criteria require that (1) the maximum fiber bridging stress is higher than the stress at which cracking is initiated and that (2) the cracks propagate in a steady state manner in an infinitely large specimen [2]. Both criteria can be expressed in terms of the average cohesive law for the composite. Thus, in order to engineer ECC materials it is essential to be able to predict the

average cohesive law for the composite. The cohesive law for the mortar can be found e.g. from a wedge splitting test and an inverse analysis [3]. A closed form solution for the total response of the fibers has been derived, see e.g. [4]. The approach in the derivation is first to derive an analytical solution for the fiber debonding and pull-out case and then integrate this solution over the crack surface for random orientation and position of the fibers. Having arrived at the cohesive laws for the matrix and the fibers respectively, the remaining question now is: can the cohesive law for the ECC material be found through a simple superposition of the two fundamental laws or will there be effects that make superposition invalid? Or in other words, is the debonding and pull-out case representative of the fiber bridging, which takes place in the composite?

One effect that might be able to cause superposition to be invalid is described by Cook and Gordon [5]. In their paper from 1964 they describe how a tensile stress field is formed in front of a crack tip and how this tensile stress field can cause debonding of a weak interface in front of the crack. If significant fiber-matrix debonding takes place before the crack tip reaches the fiber, the fiber pull-out case with an initially perfect fiber-matrix interface would not be representative of the fiber bridging case and a direct superposition would not be valid. In the present paper this effect will be denoted as the Cook/Gordon effect. Another effect possibly invalidating superposition could be matrix spalling taking place at the crack surface during inclined fiber debonding and pull-out. This effect, however, is not investigated here.

In the present paper the validity of the superposition scheme of the fundamental cohesive laws in order to obtain the average cohesive law for a typical ECC composite is investigated. To investigate whether superposition of the cohesive laws for the mortar and fiber bridging is valid, a Finite Element Model is set up. The three basic cases: debonding and pull-out of a straight fiber perpendicular to the crack face, crack propagation in pure mortar and crack propagation in a Representative Volume Element (RVE) with mortar and fiber are analyzed and a parameter study is performed. Finally, a comparison between the numerical and an analytical model for fiber debonding and pull-out is performed.

## **2. Model description**

### **2.1 Mesh**

To investigate crack propagation in a RVE, a Finite Element Model is used. Symmetry is assumed and the RVE is only representing one side of the crack (see Figure 1). The aim of the investigation is to determine whether superposition of the cohesive laws for the fiber and the mortar can be applied in order to find the cohesive law for the RVE. Particularly, it will be investigated how the initial fiber-matrix debonding takes place in the fiber pull-out case and in the model involving matrix cracking, respectively. Therefore only the first part of the fiber-matrix debonding is relevant and the height of the RVE is chosen so the debonding of the fiber will not reach the end of the model for relevant matrix crack openings. To control where the crack propagation starts a straight notch is introduced in the crack plane.

For modeling of the fiber, 15 node, wedge shaped, solid elements are used and for the mortar 20 node, cubic shaped, solid elements are used. The elements are based on quadratic interpolation and Gauss integration. Between the mortar and the fiber and in the symmetry crack plane 8+8 nodes interface elements are used. The model contains 3984 elements. The computation time was in the order of 14 hours on a computer with a 2.4 GHz Intel Xeon processor and 3 Gb RAM.

In the model the fiber is assumed to have a diameter of 40  $\mu\text{m}$  and the length of the sides in the (x,y)-plane are 251  $\mu\text{m}$ . This gives a fiber volume percent of 2, which is typical for ECC. The height of the RVE is 4 mm. The length of the PVA fibers are typically 12 mm but because the simulations end before the debonding of the fiber is completed only 4 mm is modeled.

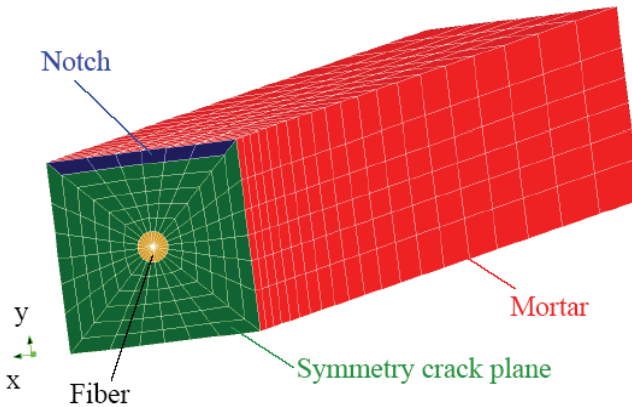


Figure 1. The mesh applied in the total model.

The model containing the fiber as well as the mortar crack (in the symmetry crack plane) is referred to as the total model. When the mortar crack is replaced with a free surface, the model can be used to simulate fiber debonding and pull-out. For convenience this model is referred to as the fiber pull-out model. Replacing the fiber by mortar and letting the mortar crack interface cover the entire bottom surface the model can simulate crack propagation in pure mortar.

## 2.2 Constraints

The displacements perpendicular to the end planes in the (x,y)-plane are constrained. This causes the load to be applied as a displacement load. The nodes in each side of the RVE in the (z,x)- and (z,y)-plane are tied together in the direction perpendicular to the plane. This causes the edges in the (x,z)- and (y,z)-planes to remain plane and result in a stress state throughout the RVE in average equal to plane stress.

## 2.3 Mixed mode cohesive crack model

The fiber-matrix interface crack as well as the mortar crack is modeled using a mixed mode cohesive model where the normal stresses,  $\sigma$ , and the shear stress,  $\tau$ , depend on both the displacement in the tangential  $\delta_t$  and the normal  $\delta_n$  direction [5].

$$\sigma = \sigma(\delta_n, \delta_n) \quad (1)$$

$$\tau = \tau(\delta_s, \delta_n) \quad (2)$$

In addition to the usual softening relations between normal deformation and normal stress and shear deformation and shear stress, softening of the cohesive normal stress law takes place due to a shear deformation and the same apply for the shear stress law and deformations in the normal direction. The model is incremental and has been implemented into the commercial finite element program DIANA.

#### 2.4 Deriving the average cohesive law from the RVE

The aim is to derive an average cohesive law ( $\sigma_w, w$ ) for the RVE. Here  $\sigma_w$  is the applied stress and  $w$  is the average crack opening. The average crack opening,  $w$  can be found by taking the total elongation,  $\delta$  of the RVE and subtract the elastic elongation (see figure below) where the total elongation is found from the FEM calculation.

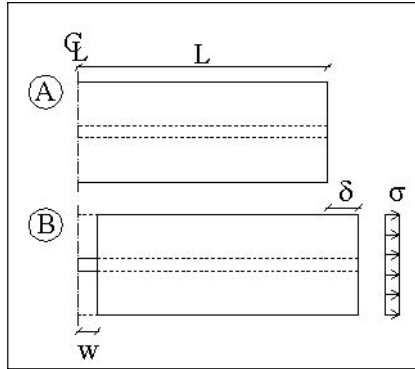


Figure 2. Relation between the average crack opening,  $w$  and the applied stress,  $\sigma$ .

The average crack opening,  $w$  can be found from the relation below, where the elastic strain,  $\varepsilon$  can be found from the applied stress,  $\sigma$  and the composite stiffness.

$$\delta = \varepsilon \cdot L + w \quad (3)$$

$$\delta = \sigma / (E_f \cdot \xi_f + (1 - \xi_f) \cdot E_m) \cdot L + w$$

$$w = \delta - \sigma / (E_f \cdot \xi_f + (1 - \xi_f) \cdot E_m) \cdot L \quad (4)$$

Here  $E_f$  and  $E_m$  are the plane stress elastic moduli for the fiber and the mortar respectively,  $\xi_f$  is the fiber volume concentration and  $\sigma$  is the average stress applied by the prescribed

displacement. This formulation enables the determination of an average crack opening without integrating over the actual crack opening profile.

Equation (4) is applied in the interpretation of the fiber pull-out model as well as the pure mortar model. This makes comparison between the obtained  $(\sigma_w, w)$ -relations from the different models consistent.

## 2.5 Material parameters

In the next section the results from the performed investigations are presented. First the results for one set of material parameters are presented and afterwards a parameter study is performed. Typical data from a PVA fiber ECC material are considered.

To perform the FEM calculation two sets of cohesive laws are needed for each calculation, one for the mortar crack and one for the interface between mortar and the fiber. The cohesive law for the mortar is based on experimental investigations on a typical ECC matrix [6] where a bi-linear cohesive law is determined from wedge splitting tests and inverse analysis [3]. The cohesive law for the interface between the mortar and the fiber is difficult to measure. Therefore values determined by Shao, Li and Shah [7] are taken as a basis for the mode II cohesive law, while the mode I cohesive law is estimated. To get a better understanding of the influence of these cohesive laws a parameter study is performed.

The mode I cohesive law for the mortar is assumed to be bilinear as shown in Figure 3. The following parameters were determined: the tensile strength  $f_t = 2.83\text{MPa}$ , the stress-separation constants  $a_1 = -156\text{ mm}^{-1}$ ,  $a_2 = -9.74\text{ mm}^{-1}$  and  $b_2 = 0.241$ , the fracture energy  $G_F = 14.1\text{ N/m}$ , the elastic modulus  $E = 31.0\text{ GPa}$  and the Poisson's ratio  $\nu = 0.2$ . The cohesive law for the shear stresses (mode II) in the mortar is not significant, since the crack will mainly propagate in a mode I. This is confirmed by calculations performed during the present investigation. The cohesive mode II law for the mortar is chosen as a linear relation:  $\tau_{max} = 3.0\text{ MPa}$  and the slope of the stress-separation curve  $a_I = -50\text{ mm}^{-1}$ .

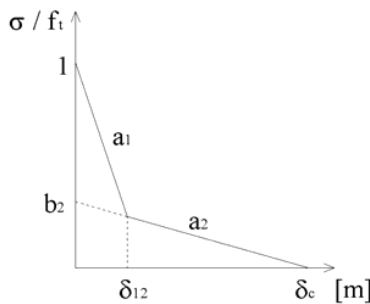


Figure 3. Bilinear stress-separation curve and the associated terminology.

The Young's modulus for the PVA fibers is  $E = 42.8$  GPa and the Poisson's ratio is chosen to  $\nu = 0.2$ . This Poisson's ratio is chosen in order to isolate the Cook/Gordon effect from any influence of a possible Poisson's effect. In the parameter study the effect of the Poisson's ratio will be investigated separately. The cohesive mode II law for the fiber-matrix interface is also bi-linear and has the following values: The shear strength  $\tau_{max} = 3$  MPa, constants  $a_1 = -222 \text{ mm}^{-1}$ ,  $a_2 = -19.6 \text{ mm}^{-1}$  and  $b_2 = 0.392$ . These values are based on [7], where a shear strength of 3 MPa was the largest measured. The mode I cohesive law for the fiber-matrix interface is estimated to vary linearly with a tensile strength of 0.5 MPa and a constant  $a_I$  of  $-1000 \text{ mm}^{-1}$ . Because of the difficulty in measuring the fiber-matrix cohesive law a parameter study will be performed.

### 3. Results

The approach now is to determine average cohesive laws in terms of stress-separation curves for the pure mortar model, the fiber pull-out model and total model. When these three curves are determined, the interrelationship between the curves is investigated and discussed.

#### 3.1 Stress-separation curves

In Figure 4 average cohesive laws for the mortar model, the fiber pull-out model and total model are shown. In addition to these curves a dotted curve made from superposition of the pure mortar curve and the fiber pull-out curve is shown. It appears from the figure that the average cohesive law from the total model can be found from a direct superposition of the pure mortar cohesive law and the fiber pull-out curve.

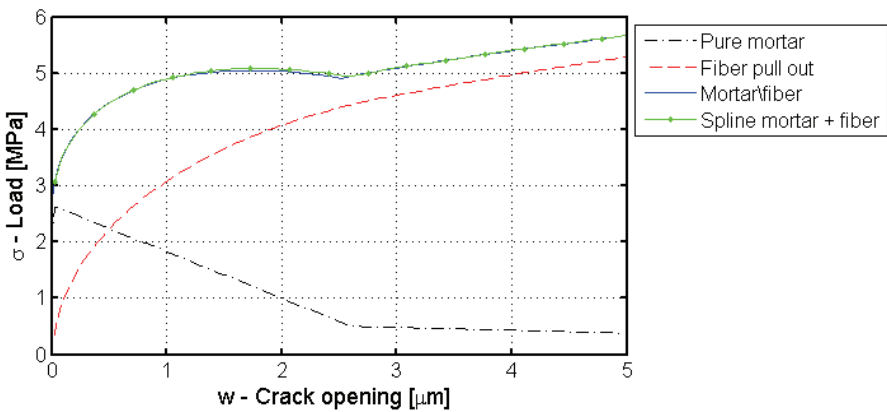


Figure 4. Average cohesive laws.



In the next sections some of the mechanisms that appear during the crack propagation and fiber debonding will be discussed. This will give a better understanding of why superposition is valid for the present choice of material parameters.

### 3.2 Crack propagation in symmetry plane

In Figure 5 the crack front in the mortar interface is plotted for different loading stages. For an applied stress of 2.32 MPa only the elements close to the notch are open.

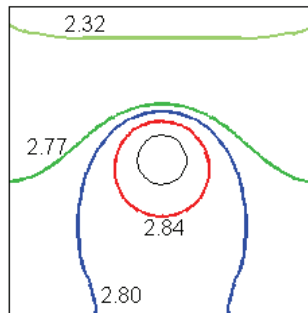


Figure 5. Crack front for different loading stages (Load in MPa).

In the figure it is shown that the crack does not propagate directly across the fiber with a straight crack front. When the crack front gets close to the fiber the crack starts to propagate around the fiber leaving a section behind the fiber closed. As the load is increased, the section behind the fiber opens but in the opposite direction than the rest of the crack. The crack opening is less than 10 nm after the crack has propagated through the entire cross section of the RVE.

### 3.3 Debonding along the fiber

The figure above illustrates how the crack propagates around the fiber in the mortar crack interface. Another interesting mechanism to illustrate is the mortar crack propagation versus the fiber debonding. In Figure 6 A) the lines at which the crack propagation in the mortar and the fiber debonding will be compared are marked with two fat lines. Figure 6 B) shows the crack propagation in the mortar compared with the debonding of the fiber for an applied stress of 2.80 MPa. In Figure 6 B) the deformations are scaled with a factor  $10^4$  and the opened nodes are marked with a circle.

The fiber starts to debond for an applied stress of 2.80 MPa, but debonding is only initiated at the node at the bottom. The debonding process continues when the crack in the mortar hits the fiber. At this point in time debonding has progressed 22  $\mu\text{m}$  along the front of the fiber. It is seen that the Cook/Gordon effect is present but insignificant for the present choice of material parameters.

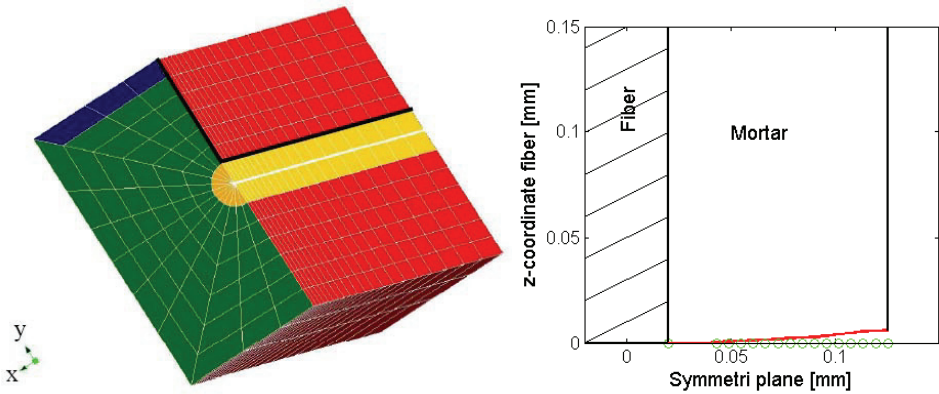


Figure 6. A) Cut in model. B) Debonding versus crack propagation.

### 3.4 Stresses along the fiber-matrix interface in the total model

In sections 3.4 and 3.5 the stresses along the fiber-matrix interface at the front of the fiber (where the matrix crack first meets the fiber) will be discussed for the total model and the fiber pull-out model respectively. The fiber front is marked with a thick line in Figure 6. Figure 7 A) shows the applied stress for the total model, Figure 7 B) the shear stresses along the fiber front and Figure 7 C) the normal stresses perpendicular to the fiber front.

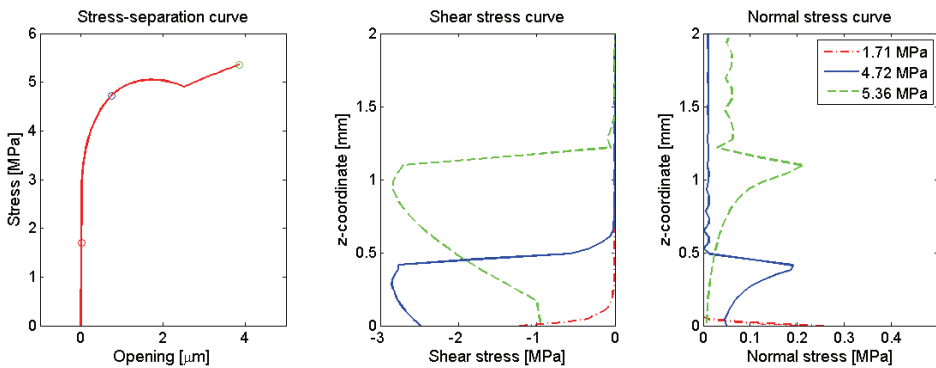


Figure 7. A) Applied stress. B) Shear stresses on fiber front. C) Normal stresses on fiber front.

The maximum normal and shear stress in the cohesive laws for the mortar/fiber interface are 0.5 MPa and 3.0 MPa, respectively. In the figures above it is seen that neither of the maximum stresses are reached due to the mixed mode material model applied to the interface. From the figures it is seen that debonding of the fiber in the total model is initiated by a combination of normal and shear stresses. But this mixed mode debonding process is not a phenomenon that is strictly related to the initiation phase of the debonding process. Early in the debonding process

a characteristic shear and normal stress profile are formed and these profiles then move up along the fiber. Further it should be noted that the Poisson's ratio in the fiber and the mortar in this calculation are identical. A separate investigation of the effect of different Poisson's ratio in the fiber and matrix is performed later.

### 3.5 Stresses along the fiber-matrix interface in the fiber pull-out model

In the previous section the stresses along the fiber front was discussed for the total model. In this section a similar investigation is performed for the fiber pull-out model. Figure 8 A) shows the applied stress for the fiber pull-out model, Figure 8 B) the shear stresses along the fiber-matrix interface and Figure 8 C) the normal stresses perpendicular to the fiber-matrix interface.

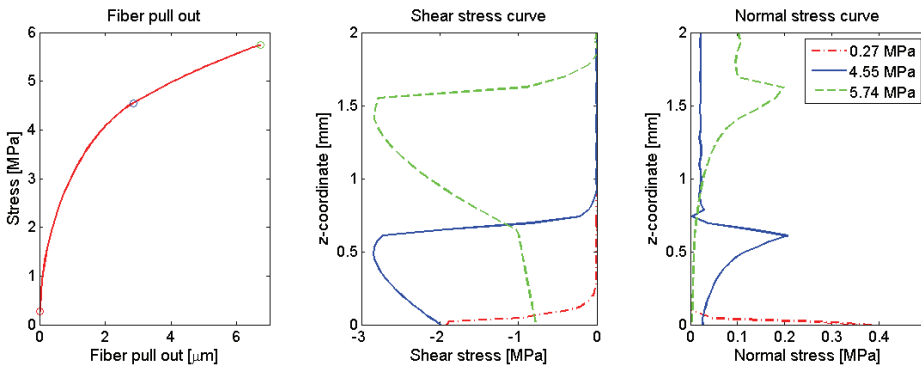


Figure 8. A) Applied load. B) Shear stresses on fiber front. C) Normal stresses on fiber front.

The results from the fiber pull-out model are very similar to the results obtained from the total model. Again the debonding is initiated due to a mixed mode stress combination. The tensile stress field in front of the debonding zone is not present in the analytical fiber pull-out model, which is the foundation for the derivation of the fiber bridging relation [4]. The influence of leaving out the tensile stress field in the derivation of the analytical fiber pull-out model will be discussed in section 3.9. As stated in the previous section these tensile stresses are present even without a difference in the Poisson's ratio in the fiber and the matrix.

The similarity of the stress profiles for the total model and the fiber pull-out model, together with the weak effect of the Cook/Gordon mechanism and the fact that the mortar crack propagates through the RVE without initiating significant debonding, explains why superposition between the stress-separation curves for the mortar and fiber is valid.

### 3.6 Comparison of the Cook/Gordon approach and the cohesive approach

In order to investigate the effect of the applied fracture mechanical approach on the significance of the Cook/Gordon effect, the stress field ahead of the crack model applied by Cook and Gordon [5] is compared with the stress field ahead of the cohesive crack applied in the present approach.

Cook and Gordon analyzed the stress state around a crack shaped as a flat ellipsoidal hole in an infinite sheet loaded in uni-axial tension. The ellipse has the semi-axes  $a$  and  $b$  resulting in a crack tip radius  $r$  ( $r = b^2/a$ ). They assumed that the crack tip radius is of molecular dimensions and that it remains constant during crack propagation in a brittle medium. In Figure 9 the stress state in front of the crack tip is plotted according to [5] for the ratio  $a/b = 100$ . In the figure  $\sigma_{xx}$  are the stresses parallel with the crack plane and  $\sigma_{yy}$  are perpendicular to the crack plane. Stresses have been normalized with respect to the maximum normal stress,  $\sigma_{yy}$ , which is identified as the tensile strength of the material.

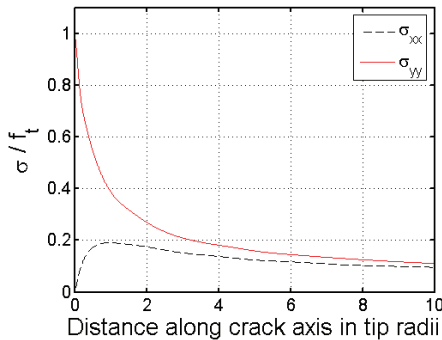


Figure 9. Stress state in front of crack tip according to Cook and Gordon, [5].

The magnitude of the crack tip radius is assumed by Cook and Gordon to be 0.2 nm. This means that the peak in the normal stresses parallel to the crack plane  $\sigma_{xx}$  will appear very close to the crack tip. The ratio between the two peak stresses is found to be just below 1/5. To relate these results to the cohesive approach a sheet with the width 0.6 m and the height 0.5 m is modeled using FEM. The sheet is loaded in uni-axial tension and contains a slit like stress free crack with the length 4 mm ( $2 a_0$ ). The dimensions are chosen such that the sheet can be regarded as infinite compared to the initial crack. The model contains an interface in which the crack can propagate. The model consist of  $20 \times 4120$  (height  $\times$  width) quadrilateral, 8 nodes plane stress elements. The element size increase with a factor 1.025 from the crack tip towards the edge along the width, and with a factor 3 from the crack towards the ends along the height. The material used is identical to the mortar described in section 2.5 ( $f_t = 2.83$  MPa). In Figure 10 A) matching values of the far field stress and the half crack length,  $a$  are plotted.

In Figure 10 B) the ratio between the two normal stresses at the crack tip in the cohesive approach is plotted for different crack lengths  $a$ . The ratio found in the cohesive approach is of the same magnitude as in the approach adopted by Cook and Gordon. For crack lengths in the micron scale the ratio the between the normal stresses found in the cohesive model are significant higher than predicted by Cook and Gordon. The Cook/Gordon effect is therefore more pronounced in the cohesive approach.

### 3.7 Parameter study of the cohesive laws

In sections 3.1-3.5, the cracking and debonding process for one set of material parameters have been investigated. In order to evaluate the sensitivity of the conclusions on the choice of material parameters, a parameter study is carried out. The parameters being varied are the parameters characterizing the mixed mode cohesive law for the mortar/fiber interface as shown in figure 11.

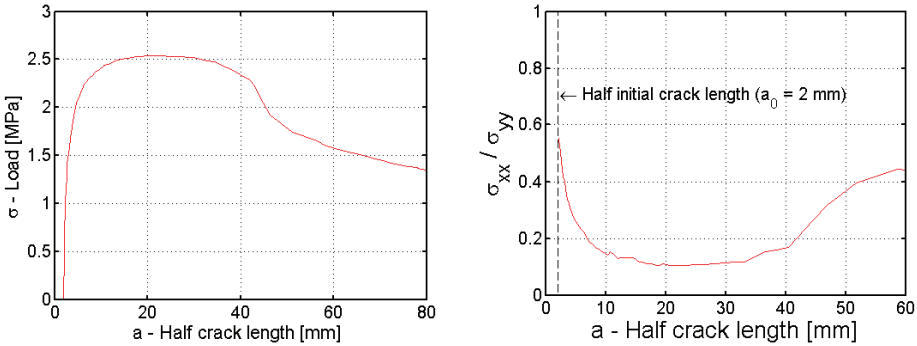


Figure 10. **A)** Matching values of far field stress and crack length. **B)** Ratio between the normal stresses at the crack tip. (The coordinate system from [5] is adopted here).

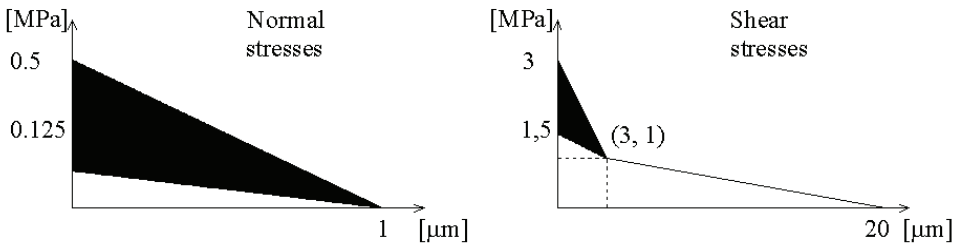


Figure 11. Cohesive laws for the mortar/fiber interface with indication of the parameter variation in the parameter study undertaken.

For the normal stresses the tensile strength is varied in the range from 0.125-0.5 MPa. For the shear stresses the slope of the first branch is varied. This is done by choosing the shear strength in the range from 1.5-3 MPa. In Table 1 below the performed calculations are listed.

The results obtained in this study are very similar to the ones obtained in the previous sections. The new results will therefore not be illustrated here.

An interesting combination was a low tensile strength (0.125 MPa) and a high shear strength (3 MPa). This could cause debonding in the total model to be initiated due to the Cook/Gordon

effect while debonding in the fiber pull-out model would be initiated mainly due to shear stresses. The analysis showed that the low tensile strength did in fact lower the shear stress needed to initiate debonding in the total model. But because the same was valid in the fiber pull-out model, superposition between the cohesive laws for the mortar and fiber pull-out was still valid.

		$\sigma_{\max}$ [MPa]		
		0.125	0.25	0.5
$\tau_{\max}$ [MPa]	1.5	x	x	x
	2	x	x	x
	2.5	x	x	x
	3	x	x	x

Table 1. The combination of material parameters is the parameter study carried out.

### 3.8 Parameter study of the Poisson's ratio

In the previous sections the fiber and mortar had the same Poisson's ratio. This was chosen in order to isolate the Cook/Gordon effect on the fiber debonding in the total model. In this section the fiber is given a more realistic Poisson's ratio of 0.35 in order to investigate the effect of the Poisson's ratio. For the present investigation four calculations are performed. The normal strength in the mode I cohesive law is varied from 0.125 MPa to 0.5 MPa (see table 1). Finally, a pure mode II calculation is performed. In all calculations the cohesive mode II law with a shear strength of 3 MPa is used (see section 3.7). The figures below illustrate the stresses on the fiber-matrix interface at the fiber front (see Figure 6) for the mode I law with a tensile strength of 0.5 MPa. The results from the calculation where the fiber has a Poisson's ratio of 0.35 are shown with thick lines and the corresponding results for at Poisson's ratio of 0.2 are shown with thin dotted lines.

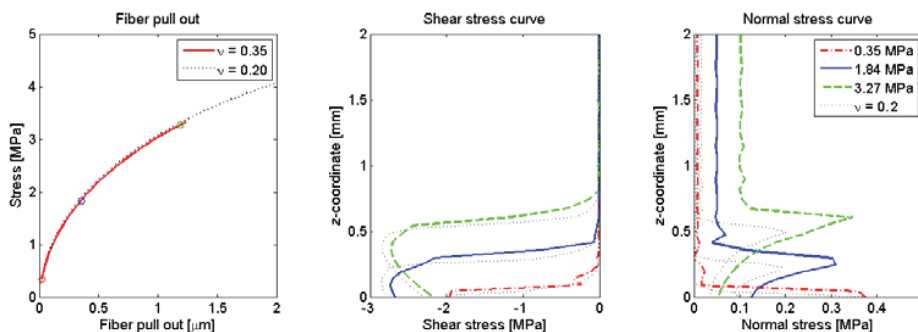


Figure 12. A) Applied load. B) Shear stresses on fiber front. C) Normal stresses on fiber front.

In the figures it is seen that increasing the Poisson's ratio in the fiber causes the normal stresses on the front of the fiber to increase as expected. Due to the mixed mode material model the increase in normal stresses causes the shear stresses to decrease. The shear stress profile for a

Poisson's ratio of 0.2 has a higher peak stress but is a little slimmer compared to the corresponding results for a Poisson's ratio of 0.35. In total the fiber pull-out curves for the two Poisson's ratios end up being very similar, with the curve for a Poisson's ratio of 0.2 slightly higher than the curve corresponding to a Poisson's ratio of 0.35.

In the figures below fiber pull-out curves are plotted to illustrate the effect of the Poisson's ratio for different mode I cohesive laws on the interface.

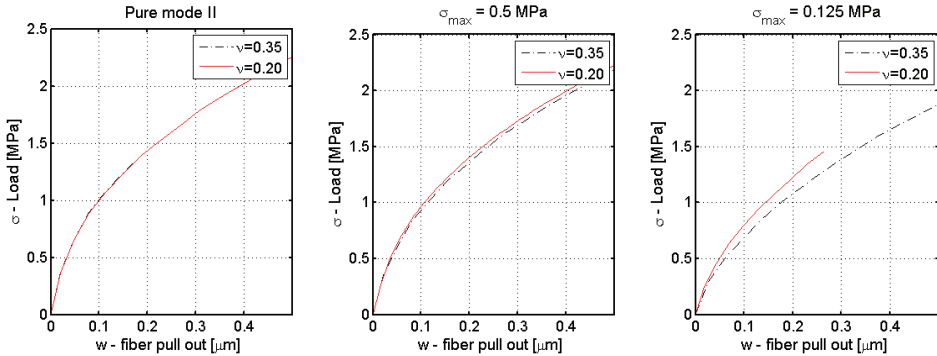


Figure 13. Fiber pull-out curves as functions of fiber Poisson's ratio for different mode I cohesive laws on the interface: **A)** Pure mode II. **B)** Tensile strength of 0.5 MPa. **C)** Tensile strength of 0.125 MPa.

In the extreme case where the mode I law is so strong that debonding will occur in pure mode II, the Poisson's effect can be neglected. When comparing Figure 13 A and B it is observed that a mode I law with a tensile strength of 0.5 MPa results in a fiber pull-out curve close to the one obtained in the pure mode II calculation. This explains why the Poisson's ratio has so little influence when applying a mode I law with a tensile strength of 0.5 MPa. For a mode I cohesive law with a tensile strength of 0.125 MPa the difference in Poisson's ratio between the mortar and the fiber is seen to have a significant influence of results. This is because the increase in normal stresses becomes significant compared with the tensile strength. The conclusion is that if the interface between the fiber and the mortar has a weak mode I cohesive law, it is important to include the effects introduced by the Poisson's ratio. In this investigation all fibers have been pulled out normal to the crack plane. Another relevant investigation is the Poisson's effect on pull-out of fibers inclined to the crack plane. When pulling out a fiber inclined to the crack plane, the Poisson's effect might be insignificant compared to the large contact pressure between fiber and crack face or possible spalling of the matrix.

### 3.9 Comparison of the analytical and numerical model for fiber pull-out

In this section a comparison is made between the present numerical model for fiber pull-out and the corresponding analytical model [4]. Three assumptions are made in order to derive the analytical model: (1) an aspect ratio larger than 100. (This is fulfilled for most fibers and this is

also valid for the present numerical model.) (2) The slip between matrix and fiber during debonding is negligible hence the shear stresses are constant,  $\tau_0$ . (This is not valid in the numerical model when applying a cohesive law. As illustrated in Figure 8 a shear stress profile is formed after debonding is initiated and as the debonding propagates the shear stress profile travels with the debonding.) The Poisson's effect is negligible. As shown in the previous section the Poisson's effect can be neglected, but only in the case where the mode I cohesive strength between fiber and mortar is strong. Apart from these three assumptions the analytical model does not take into consideration the tension stress field in front of the debonded zone, hence debonding in the analytical model is pure mode II. The relation between the pull-out force,  $P$ , and the relative displacement,  $\delta$ , between the fiber and the matrix in the analytical model is given by the expression below:

$$P = \sqrt{\frac{\pi^2 \tau_0 E_f d_f^3 (1 + \eta)}{2}} \delta + \frac{\pi^2 G_d E_f d_f^3}{2} \quad (5)$$

Here  $E_f$  and  $d_f$  are Young's modulus and diameter of the fiber respectively, and  $\eta = V_m E_m / V_f E_f$  where  $V_m$  and  $V_f$  is the volume fraction of mortar and fiber respectively. The chemical bond strength  $G_d$  is related to the fracture energy  $G_f$  of the mode II cohesive law, however in the analytical model,  $G_d$  is assumed to be dissipated in a point. Because of the difficulties in deciding which constant frictional bond strength,  $\tau_0$  correspond to the applied cohesive law, a direct comparison between the numerical model and the analytical model is not performed. Instead an investigation is performed with the numerical model on the effect of the mode I cohesive law, which is left out in the analytical model. This is done by comparing fiber pull-out curves obtained from applying a fixed mode II law with a shear strength of 3 MPa together with a variation of the cohesive mode I laws. The cohesive laws used are the ones shown in section 3.7. In Figure 14 the fiber pull-out curves are plotted for a Poisson's ratio in the fiber of 0.35.

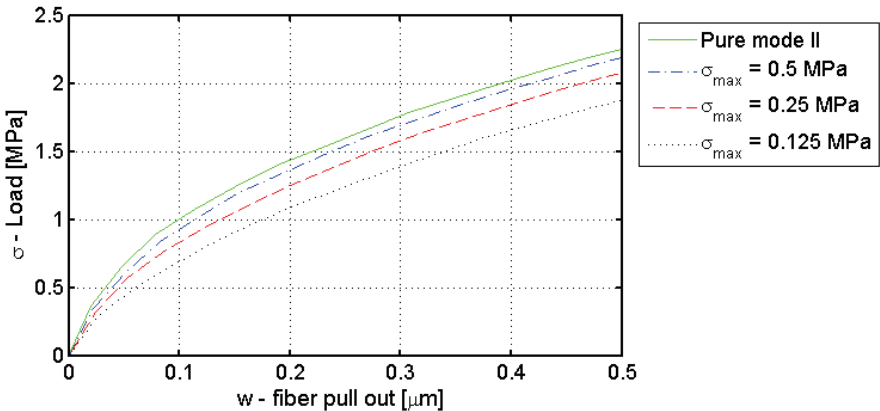


Figure 14. Fiber pull-out curves for different mode I cohesive laws and a fixed mode II law using the numerical model with a Poisson's ratio in the fiber of 0.35.



In the figure it is seen that the pull-out load decreases for a decreasing tensile strength in the mode I cohesive law. If the analytical model is calibrated with a fiber pull-out test, the influence of leaving out the mode I part is probably not that significant, because the constants will be affected by the mixed mode conditions. If on the other hand the fiber pull-out is model based on independently obtained mode II constants then a significant error can be made by leaving out the mode I part, particularly if the mode I properties are relatively weak.

#### **4. Concluding remarks**

In the present investigation it has been examined whether superposition of the average cohesive law for the fiber pull-out and the cohesive law for mortar was valid in order to find the average cohesive law for the total model. Special attention was given to the tensile stress field in front of the crack tip, possibly leading to the so-called Cook/Gordon effect, while the investigations were limited to the case of straight fibers arranged perpendicular to the crack surface. The present investigation showed that in general superposition is valid. Furthermore that a low mode I strength in the mortar/fiber interface did lower the shear stress needed to initiate debonding in the total model. However, because the same applied in the fiber pull-out model superposition of the cohesive laws was still valid.

The present investigation further showed that the mortar crack propagation and the subsequent fiber debonding and pull-out essentially are two separate mechanisms in the sense that the mortar crack propagated through the RVE without initiating any significant debonding; the mortar crack grows past the fiber and then gradually back towards the fiber before significant debonding begins.

The influence of a difference in the Poisson's ratio between mortar and fiber was examined. It was found that if the strength of the mode I interface between fiber and mortar was sufficient high, then the Poisson's ratio did not have any influence on the problem and the debonding would propagate in an almost pure mode II. If on the other hand the mode I strength was low, then the increase in normal stresses due to the Poisson's effect did lower significantly the force needed to pull-out the fiber due to the mixed mode condition.

Finally, a comparison between an analytical and numerical model for fiber pull-out was conducted. In the analytical model the mixed mode stress condition is not taken into consideration. The conclusion is that as long as the analytical model is calibrated with fiber pull-out tests then the influence of leaving out the mode I part is not significant, because the material constants then will be affected by the mixed mode conditions. If the mode I strength is low and the analytical model is not calibrated with tests then leaving out the mode I part can lead to overestimation of the load carrying capacity.

## References

1. Li, V.C., Stang, H. and Krenchel, H. 'Micromechanics of Crack Bridging in Fiber Reinforced Concrete', *Materials and Structures*, **26**, 486-494, 1993.
2. Li, V.C. and Leung, C.K.Y., 'Steady State and Multiple Cracking of Short Random Fiber Composites', *ASCE J. Eng. Mech.* **118**, 2246-2264, 1992
3. Østergaard, L., Olesen, J. F. Stang, H. & Lange, D. A., 'A simple and fast method for interpretation and inverse analysis of the wedge splitting test', *Submitted for publication*.
4. Lin, Z., Kanda, T. & Li, V. C., 'On interface property characterization and performance of fiber-reinforced cementitious composites', *J. Concrete Sci. & Eng.*, **1**, 173-184, 1999.
5. Cook, J., Gordon J. E., Evans, C. C. & Marsh, D. M., 'A mechanism for the control of crack propagation in all-brittle Systems'. *Proc. Roy. Soc.*, **2282 A**, 508-520, 1964
6. Wang, S. Private communication, DTU, 2004.
7. Shao, Y., Li, Z. & Shah, S. P., 'Matrix cracking and interface debonding in fiber-reinforced cement-matrix composites'. *Advn. Cem. Bas. Mat.* **1**, 55-66, 1993
8. Walter, R., Olesen, J. F. & Stang, H., 'Interface mixed mode model', *Proceedings of ICF 11*, Mixed mode 4628, 2005

# **A Preliminary Numerical Investigation on the Influence of Material Variability in the Early-age Cracking Behavior of Restrained Concrete**

Aleksandra Radlinska, Brad Pease and Jason Weiss  
Purdue University, West Lafayette, USA

## **Abstract**

Residual stresses arising from the restraint of drying, chemical, autogenous or thermal shrinkage can result in the development of tensile residual stresses. If the stresses that develop are high enough they may cause cracks to develop in the concrete. Substantial research has been focused on the development of test methods to assess stress development and the potential for cracking in concrete. In addition, these test methods frequently focus on the determination of material properties that can be used in deterministic computer programs to simulate stress development and cracking potential. While these models are a great step forward; variability is inherent in the material properties, the construction processes, and the environmental conditions (i.e., temperature and relative humidity). This paper presents results from a preliminary investigation aimed at investigating the effects of variability on the risk of cracking. A Monte Carlo method is described for assessing the anticipated material variability and the results of this approach are discussed.

## **1. Background**

Shrinkage cracking can be thought to occur when the stress that develops in response to the prevention of shrinkage (residual stress) exceeds the cracking resistance of the material (Figure 1). Determining whether cracks may develop in a concrete however is complicated by the fact that both the stress development and strength are time-dependent. Tensile strength, like other material properties, develops over time as it is related to the degree of hydration while residual stresses develop over time because shrinkage occurs in response to moisture loss, which is a slow, diffusion-controlled process. It should be noted that the residual stress that develops in concrete as a result of restraint can not be computed directly using the product of the free shrinkage and elastic modulus (i.e., Hooke's Law) since the concrete is sensitive to stress relaxation (creep).

The potential for shrinkage cracks to develop in concrete depends on several time-dependent factors including material stiffness, shrinkage rate, shrinkage magnitude, stress relaxation, and material toughness. A model has been formulated to estimate the potential for restrained

shrinkage cracking in concrete elements [1, 2]. Although this model is relatively basic and assumes uniform shrinkage throughout the element, previous research showed a favorable comparison between the model predictions and experimental observations [3]. Other models have been developed to predict shrinkage cracking as well as to consider the potential for thermal cracking [4, 5]. This approach has been used to illustrate implications associated with the use of higher strength concrete, to simulate the behavior of structures with imperfect restraint, and to illustrate the role of reducing the magnitude and rate of free shrinkage [3, 6].

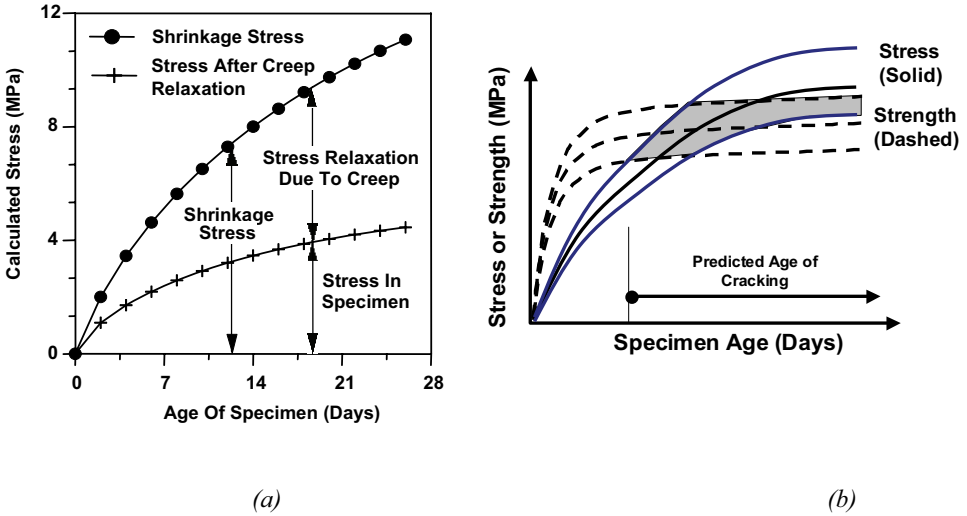


Figure 1. a) Stress and strength development in restrained shrinkage specimens (Weiss 1997) and b) a conceptual illustration of the role of variability on the predicted age of cracking

Previous work [1] has shown that Equation 1 may be used to estimate the stress development in a restrained concrete element.

$$\varepsilon_{Permit}(t) = \int_0^t \left[ \left( \frac{1}{E_{\sigma}(\xi)} + \frac{1}{E_c} \phi(t, \xi) \right) \frac{d\sigma(\xi)}{d\xi} + \alpha(\xi) \right] \cdot d\xi \quad (1)$$

where,  $\varepsilon_{Permit}(t)$  is the total strain that is permitted to develop in the actual restrained concrete (i.e., for complete restraint  $\varepsilon(t) = 0$  which will be assumed throughout this paper),  $E_{\sigma}(\xi)$  is the time dependent elastic moduli,  $E_c$  is a reference elastic modulus (i.e., a 28 day value),  $\phi(t, \xi)$  is the creep coefficient, and  $\alpha(\xi)$  is the differential shrinkage with respect to time (t) (i.e.,

$$\varepsilon_{Tot-Shr}(t) = \int_0^t \alpha(\xi) \cdot d\xi).$$

The ability to compute the residual stress enables these stresses to be compared with the tensile strength in an attempt to ascertain whether cracking may occur in a given concrete. While this allows complicated interactions between various material properties to be considered in relatively simple fashion it does not account for effects of moisture gradients in its current form and does not account for mesostructural scale issues like aggregate distribution or microcracking. While additional work is being performed to account for moisture gradients, aggregates, and microcracking [7, 8, 9], this paper addresses another very important issue. This paper provides preliminary results from an investigation to demonstrate how variability would influence the modeling predictions. A Monte Carlo approach has been used to include material variability in the model for the purpose of quantifying the level of uncertainty in the model predictions.

It is anticipated that this type of modeling approach will be able to be used to quantify the sensitivity of the model to variability in modeling inputs thereby enabling the most sensitive inputs to be determined. This could enable researchers to determine which inputs require the most significant scrutiny and could signal where new and more accurate standardized testing protocols are needed. In addition, it is also anticipated that this type of approach can be used by contractors to assess the risk associated with the selection of construction operations and constituent materials with greater confidence. This approach can also be used by specification developers to indicate how specifications based on anticipated construction variations can be written more effectively to minimize the risk of early-age cracking.

## **2. Uncertainty and Variability in Modeling Predictions**

While the aforementioned model assesses the influence of material properties on the early-age cracking susceptibility of a concrete, this model results in a deterministic solution for a single value of the time of cracking. It should be noted that variability exists in both the residual stress and tensile strength development. Figure 1b illustrates that as a result of this variability the predicted time of cracking may also vary. The variability can come from many sources including variations in the material properties (i.e., elastic modulus ( $E$ ), creep/stress relaxation ( $\phi$ ), shrinkage ( $\epsilon_{sh}$ ), and tensile strength/fracture resistance ( $f'_t$ )), variations in the environmental conditions (temperature or relative humidity), or variations in the degree to which the structure is restrained. While each of these variables can be thought to have some inherent variability, it is difficult to immediately determine which property may be the most significant. As a result, it appears that a probabilistic approach may have benefits in that it can quantify the extent of variability that may exist in cracking predictions. The following section describes the formulation of the problem as well as a series of preliminary simulations that were performed to better assess how variability influences the predicted age of cracking.

## **3. Time-Dependent Material Property Model Inputs**

The first step in performing a series of simulations to assess the sensitivity of the model is to describe how the material properties would develop over time. Rather than specifically considering a single material, this work will focus on describing general series of equations to describe material property development. There will be specific parameters in these equations

that can be varied and as such these equations can be used to simulate a wide range of material behaviors.

We will begin by describing the time-dependent modulus of elasticity using the equation described by McIntosh [10]

$$E_c(t) = E_\infty \frac{C_1(t-t_s)}{1 + C_1(t-t_s)} \quad (2)$$

where  $E_\infty$  is the theoretical maximum elastic modulus that would develop at a very late age,  $C_1$  is a material constant that describes the rate of elastic modulus development,  $t$  is the age of the specimen, and  $t_s$  is time of initial set. It should be noted that while this type of equation can generally be well fit to data from concrete specimens, current work is investigating whether this is the most appropriate equation for modeling very early-age behavior and it is anticipated that an equation that is capable of describing the transition from a liquid to a solid may be more beneficial for future model developments [11].

Second, a formulation for the time-dependent tensile strength will be considered that again is based on the hyperbolic equation proposed by McIntosh.

$$f_{ten(t)} = f_{ten-\infty} \frac{C_2(t-t_s)}{1 + C_2(t-t_s)} \quad (3)$$

where  $f_{ten-\infty}$  is the theoretical maximum tensile strength that would develop at a very late age and  $C_2$  is a material constant that describes the rate of tensile strength development. It should be noted that this formulation should remain somewhat flexible and as a result the constant is intentionally selected to be independent of the constant used in the equation for elastic modulus. This would be consistent with the suggestion of Rostasy [12] who has proposed that the elastic modulus develops at a much more rapid rate than the tensile strength. Recent work by Barde et al. [13] also demonstrated that different mechanical properties may have different rate constants due to the fact that in higher strength materials the tensile strength behavior could need to be modified to account for the transition in property development that occurs when cracks that propagated through the matrix and interfaces at early ages begin to propagate through the aggregate as well.

An expression should be included to account for the shrinkage that would develop over time. An equation of the form developed by Bazant [14] is an attractive option (Eqn. 4)

$$\varepsilon_{Shr-Dry}(t) = \varepsilon_{SH-\infty} (1 - RH_{AMB}^3) \tanh \left( \sqrt{\frac{t-t_{dry}}{T_{SH}}} \right) \quad (4)$$

where  $\varepsilon_{SH-\infty}$  is a parameter that describes a materials shrinkage,  $RH_{AMB}$  is a parameter that describes the relative humidity of the environment,  $t_{dry}$  is time of initial drying and  $T_{SH}$  is

a constant that accounts for the time it takes moisture to diffuse from the specimen (including both parameters for the materials diffusion and the size of the specimen).

This work chose to rewrite the shrinkage expression as seen in Eqn. 5 by considering the autogenous and drying shrinkage to be additive. While equation 5 provides an easy to use approach it should be noted that the additive behavior of drying and autogenous shrinkage is not strictly true.

$$\varepsilon_{Shr-Tot}(t) = \varepsilon_{Shr-Auto}(t) + \varepsilon_{Shr-Dry}(t) \quad (5)$$

The autogenous (Eqn. 6) and drying (Eqn. 7) shrinkage terms can be approximated initially using the forms proposed by Bazant [14] after introducing an internal humidity term ( $RH_{INT}$ ) and two constants to account for the time-dependent nature of the shrinkage ( $C_3$  and  $C_4$ )

$$\varepsilon_{Shr-Auto}(t) = \varepsilon_{SH-\infty} (1 - RH_{INT}^3) \tanh\left(\sqrt{\frac{t - t_{set}}{C_3}}\right) \quad (6)$$

$$\varepsilon_{Shr-Dry}(t) = \varepsilon_{SH-\infty} (RH_{INT}^3 - RH_{AMB}^3) \tanh\left(\sqrt{\frac{t - t_{dry}}{C_4}}\right) \quad (7)$$

In this paper the constants  $C_3$  and  $C_4$  were selected based on comparison with sealed and drying shrinkage specimens, however these constants as well as the choice of the hyperbolic tangent may need to be investigated more thoroughly in subsequent work. Finally, creep will be considered in accordance with the CEB-FIP model [15]. It should be noted that the elastic modulus used in the creep computations will be based on the time-dependent equation shown in Eqn. 2.

At this point it should be noted that the material shrinkage coefficient proposed by Bazant [14] can be estimated using neat paste specimens. Figure 2a illustrates the length change that was observed in neat paste specimens that were stored at various relative humidities in a  $CO_2$  free environment. Further details on the neat paste specimen preparation and measurement techniques are provided elsewhere [16], however to illustrate this approach Equation 8 was fitted to the data from those tests as shown in Figure 2a

$$\varepsilon_{Shr-\infty} = \beta_N (1 - RH_{AMB}^3) \quad (8)$$

where  $\beta_N$  is the shrinkage coefficient that can be thought of as a ‘coefficient of hygral length change’. Pickett [17] and L’Hermite [18] illustrated that the shrinkage of the paste can be linked to that of mortar and concrete using an equation of the form

$$\varepsilon_{Shr-\infty} = \beta_N (1 - V_F)^n (1 - RH_{AMB}^3) \quad (9)$$

where  $V_F$  is the volume fraction of the aggregate and  $n$  is a coefficient that describes the stiffness of the aggregate and paste which is typically between 1.2 and 1.7 for normal strength concretes.

At this point it is interesting to note that shrinkage-reducing admixtures (SRA's) have been proposed to reduce the shrinkage in cementitious materials by reducing the surface tension of the pore solution. Pease et al. [19] measured the surface tension of SRA-water solutions. Figure 2b illustrates that when the surface tension of the SRA-water solutions used in making the pastes is plotted against the shrinkage coefficient ( $\beta_N$ ) a linear relationship is obtained [19]. This suggests that since the surface tension of the SRA-water solution, and corresponding surface tension of the pore fluid in a cementitious material, can be controlled through the dosage of SRA that this reduction in surface tension may be able to be directly used to predict the shrinkage reduction that may be expected for a concrete.

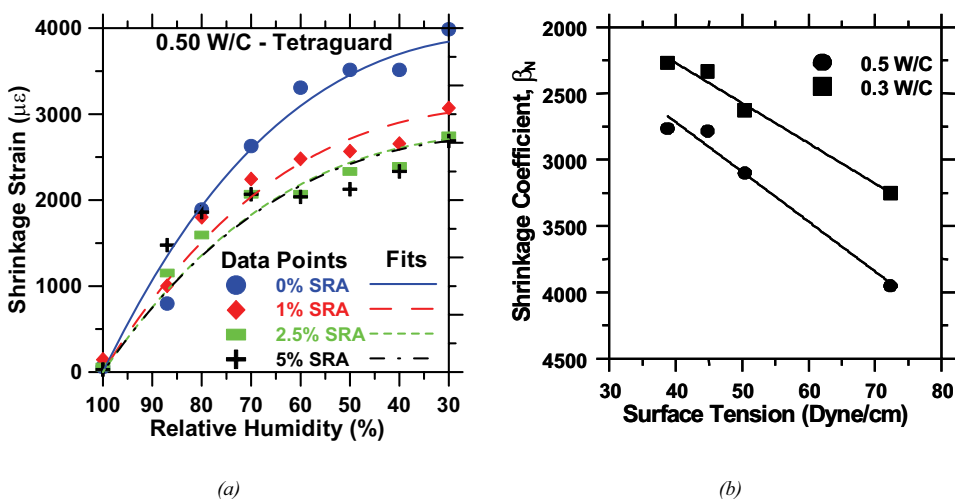


Figure 2. a) The shrinkage of neat cement pastes at various relative humidities with a water-to-cement ratio of 0.50 and varying amounts of SRA (Tetraguard) and b) the corresponding shrinkage coefficient for pastes with a water-to-cement ratio (w/c) of 0.30 and 0.50

The shrinkage behavior of mortar containing SRA was assessed using a mixture with 55% aggregate. The specimens consisted of three 50 mm diameter cylinders that were exposed to a 50% relative humidity environment at an age of 3 days. Figure 3 shows the relative shrinkage of these specimens by dividing the shrinkage of a specimen containing SRA with the shrinkage of a plain specimen. It can be observed that the influence of the SRA has two main effects. First, the SRA reduces the overall magnitude of the shrinkage and second the SRA substantially delays the rate of shrinkage. This is consistent with previous observations [20] and illustrates that the use of SRA may substantially reduce the potential for shrinkage cracking.



The aforementioned discussions on mixtures containing SRA demonstrate that it may be possible to control the shrinkage that may be experienced in a concrete mixture. This paper will illustrate that the deterministic model described in section 3 may be used to determine the threshold for shrinkage (assuming, creep, strength, and elastic modulus remain constant) that is necessary to cause residual stress levels to develop that are sufficient to cause shrinkage cracking. It will however be shown in the following section that variations in the material properties can result in a substantial risk for cracking even if the deterministic approach outlined in section 3 would not predict cracking. It is also possible to imagine that variations in the environmental conditions (i.e., temperature or relative humidity) or variations in construction practices (i.e., the time the concrete is exposed to drying or the specimen geometry) can also substantially alter the potential for cracking [21]. This paper provides an initial illustration of how this model can be used, however additional study is needed to quantify the variability in material properties, to quantify the extent of correlation between variability in these properties, and to improve the fundamental model inputs.

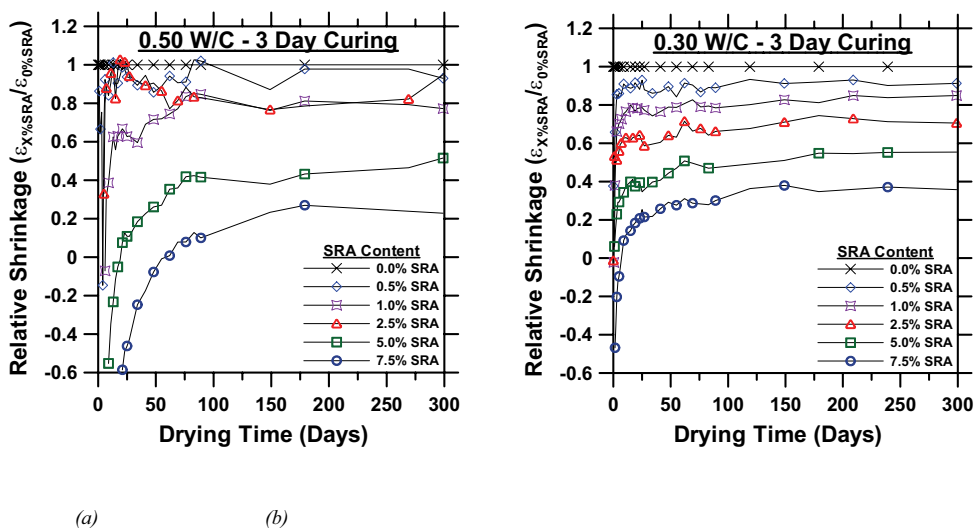


Figure 3. The relative shrinkage of mortars containing varying amounts of SRA (Tetraguard) with a) water-to-cement ratio of 0.50 and b) water-to-cement ratio of 0.30

#### 4. Model Simulations – Deterministic Predictions

The model described in section 2 was combined with the material property development equations described in section 3 and used to simulate the restrained shrinkage response of concrete under various conditions. The time-steps used in the model were 0.1 day increments for the first 8 days, 0.2 day increments to 14 days, 0.5 day increments to 28 days, 1 day increments to 56 days, 2 day increments to 90 days, and 4 day increments up to 350 days. A baseline condition was simulated that could be representative of a fairly typical concrete

with a compressive strength of 33 MPa. Table 1 provides a listing of the material inputs that were used in the baseline simulations.

**Table 1.** Baseline model inputs used for simulations described in this paper

$f_{comp}$	$E_{28}$	$f_{ten}$	$RH_{AMB}$	$RH_{INT}$	$\varepsilon_{SH-ULT}$	$C_1$	$C_2$	$C_3$	$C_4$	$t_{set}$	$t_{dry}$
MPa	GPa	MPa	%	%	$\mu\varepsilon$	1/day	1/day	1/day	1/day	day	day
33	27.5	5	50	95	600	2.0	0.3	15.0	30.0	0.25	1.00

Figure 4 illustrates the typical results from the model with Figure 4a illustrating the shrinkage, Figure 4b illustrating the elastic stress development and residual stress development, and Figure 4c illustrating the residual stress and tensile strength. The information from Figure 4c was used to determine the time of cracking which was simply determined to be the first age in the simulation where the residual strength exceeded the tensile strength of the concrete.

The model inputs were then kept constant except for the magnitude of the ultimate shrinkage strain (Equation 9) which was varied to illustrate how variations in the magnitude of shrinkage can influence the predicted time of cracking. Figure 4d illustrates that as the magnitude of shrinkage is reduced the time of cracking increases until a point at which cracking would no longer be expected to occur (i.e.,  $\varepsilon_{SH} \sim 550 \mu\varepsilon$ ).

## 5. Model Simulations – Considering Variability in Material Properties

The model described in section 4 was modified to consider variability in material properties using a Monte Carlo approach. To begin, only the magnitude of free shrinkage ( $\varepsilon_{SH-\infty}$ ) was varied assuming a normal distribution with a coefficient of variation of 10%. As a result it would be expected that only 5% of the shrinkage values would be below shrinkage of  $500 \mu\varepsilon$  while 95% of the shrinkage values would fall below shrinkage of  $700 \mu\varepsilon$ . If the deterministic model calculations are performed with shrinkage of approximately  $550 \mu\varepsilon$  cracking would not be predicted while cracking would be predicted at an age of 8.7 days for a specimen with shrinkage of  $700 \mu\varepsilon$ . It can therefore be expected that the model that incorporates variability would predict the majority of cracks to develop between 8.7 days and some very late age with some specimens (i.e., the specimens with a shrinkage of less than  $550 \mu\varepsilon$ ) not cracking at all.

A series of iterative simulations was performed with each simulation using a randomly selected shrinkage value in accordance with the normal distribution. The sampling was performed using the Latin Hypercube sampling procedure. In the simulations described in this paper 10,000 iterations were performed and the time of cracking that was determined from each iteration was saved and used to develop a cumulative probability distribution as shown in Figure 5a. It can be seen that the age of cracking predicted using the deterministic approach described in section 4 occurs at 27.5 days while the predictions of this model occur over a wider range and capture the fact that the age of cracking may not be predicted in some specimens. This type of approach can be used to better quantify the risk of cracking and to develop a plot like that shown in Figure 5b where the time of cracking is plotted along with a

probability that cracking would be experienced for different values for the average magnitude of shrinkage.

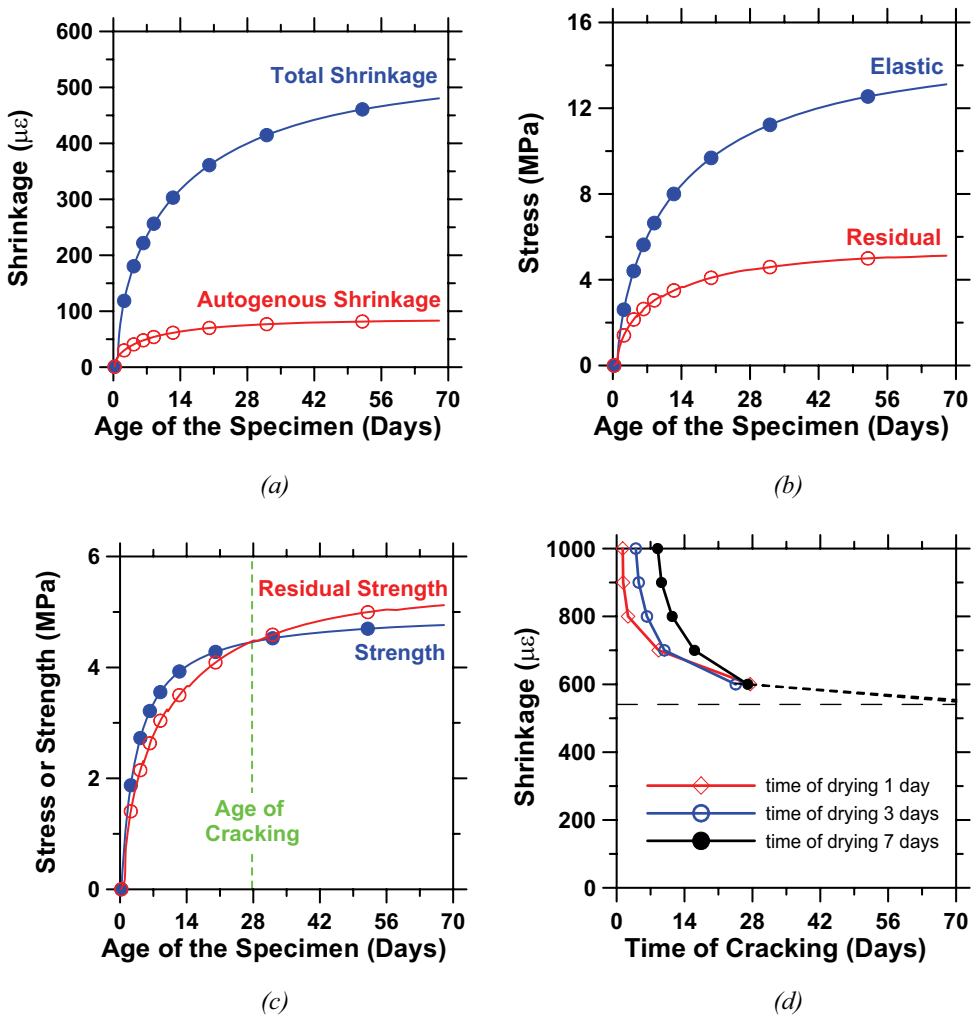


Figure 4. Results of simulations using the data in Table 1 to illustrate typical results: a) autogenous and total shrinkage, b) elastic and residual stresses, c) residual stress and tensile strength to illustrate the deterministic age of cracking, and d) the influence of variation in the ultimate shrinkage coefficient and on the predicted time of cracking

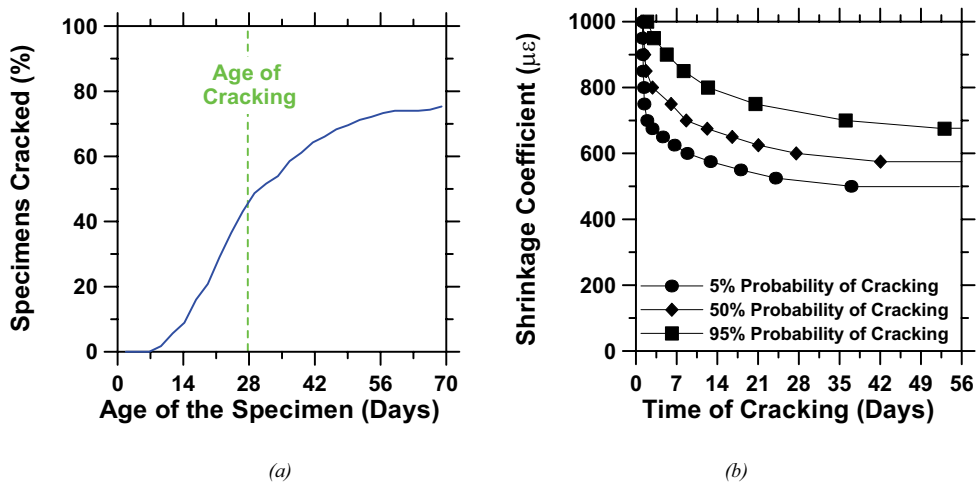


Figure 5. Results from simulations assuming only variability in shrinkage illustrating the cumulative age of cracking distribution and the age of cracking from the deterministic equations and b) 5%, 50% and 95% probability of cracking limits for specimens with different shrinkage coefficients

While information on variations of a single property is useful, the variability could be assessed directly in this case. The benefit of the Monte Carlo approach will be demonstrated later in this paper where more than one material property is varied. First however we should discuss the fact that simply having the results of the simulation form a probability distribution can make the results a bit more cumbersome to interpret. As a result, several different expressions were investigated to describe the probability of cracking using only a few parameters.

The expressions investigated to describe the probability of cracking included lognormal, gamma, and exponential distributions; however several common trends were observed from the functions that should be mentioned. The lognormal and exponential curves appeared to slightly underestimate low cracking probabilities (i.e.,  $< \sim 25\%$ ) while the log-logistic curve tended to underestimate the higher cracking probabilities (i.e.,  $> \sim 90\%$ ). In addition, the lognormal curves require the use of an error function that may make their application more difficult for several users. As a result, the cumulative probability of cracking curves were fit using a log-logistic distribution function which was modified to account for the fact that cracking may not always be observed in some mixtures. This modification came in the form of a factor ( $P_{Crack-\infty}$ ) which describes the probability of cracking after a long time period which in this cases it is assumed as the amount of cracking observed after 1 year when the simulation was stopped. Therefore the probability of cracking is described using Eqn. 10

$$P_{Crack-cdf} = P_{Crack-\infty} \frac{1}{1 + \left( \frac{\beta}{t - \gamma} \right)^\alpha} \quad (10)$$

where  $\alpha$  is the shape parameter,  $\beta$  is the scale parameter, and  $\gamma$  is a time-location factor. The derivative of Eqn. 10 provides an expression for the cracking probability density which is described in Eqn. 11

$$P_{Crack-pdf} = P_{Crack-\infty} \frac{\alpha t^{\alpha-1}}{\beta \left( 1 + \left( \frac{t - \gamma}{\beta} \right)^\alpha \right)^2} \quad (11)$$

which can be helpful for fitting and comparisons with probability histograms.

Figure 6a shows a simulation for the probability distribution function obtained from the simulation that was fitted using Eqn. 11 and a histogram of the results of the simulation. It can be noticed that the distribution function contains the most frequent ages of cracking before the time of cracking predicted using a deterministic model (i.e., 27.5 days). Integrating the probability density function over time yields the cumulative distribution shown in Figure 6b. Not surprisingly it can be seen that after a certain period of time the potential for additional cracking events decreases dramatically and the number of specimens that can be expected to crack begins to plateau (i.e., this plateau is the probability for a crack to occur,  $P_{crack-\infty}$ ).

While the predictions from the model show reasonable agreement with what one may expect, as discussed earlier, the real power of this approach will be to consider simultaneous variations in more than one property. Three material properties were considered including the magnitude of free shrinkage ( $\epsilon_{SH-\infty}$ ), elastic modulus ( $E_\infty$ ), and tensile strength ( $f_{ten-\infty}$ ). The material properties were assumed initially to have a normal distribution with a coefficient of variation of 10%. Further, the material properties were assumed for some trials to be uncorrelated with each other. Other trials however will assume that some correlation exists between the properties. It was assumed for this paper that an increase in shrinkage would likely be correlated to a decrease in elastic modulus and tensile strength. As such the same coefficient of variation was used between these properties to determine the variation in each material property (10% COV) in the correlated cases. For the remainder of the paper the data where the three variables were allowed to vary independently will be referred to as uncorrelated and the data in which the variations in material are related to one another (assuming elastic modulus and strength are positively correlated and elastic modulus and shrinkage are negatively correlated) will be referred to as correlated.

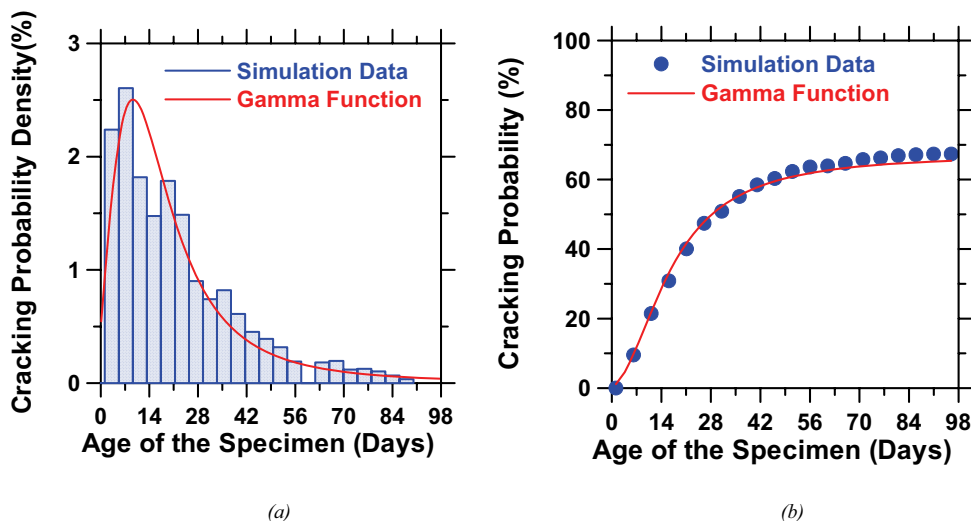


Figure 6. a) Cracking probability density for different ages of the specimen and b) cumulative distribution of cracking probability for different ages of the specimen

Results from one simulation are shown on Figure 7 while Table 2 provides the coefficients for Eqn. 10 that were determined from a series of simulations. It can be seen that the correlated outcomes tend to result in a later age of cracking. It should however be noted that there is a greater probability of observing a crack when the results are correlated. At this point it should also be noted that while the variability in each material property is assumed to have a similar coefficient of variation it is highly likely that each property will exhibit a different level of variation with modern quality control practices.

The difference in the results obtained from varying a) only shrinkage, b) shrinkage, elastic modulus, and tensile splitting strength assuming there are uncorrelated, and c) shrinkage, elastic modulus and tensile splitting strength assuming they are correlated has been shown in the Figure 8a. Since the initial distribution of material properties was assumed to be normal the 50% probability of cracking curves form a single line that is relatively consistent with the deterministic prediction. However, the 5% potential for cracking shows that when we assume all three components are correlated the spread of results occupies a larger range than for uncorrelated components. This is consistent with what one may expect as the data in uncorrelated results may tend to 'offset' one another while the data in the correlated results may tend to 'add together' creating a condition that is more likely to result in cracking.

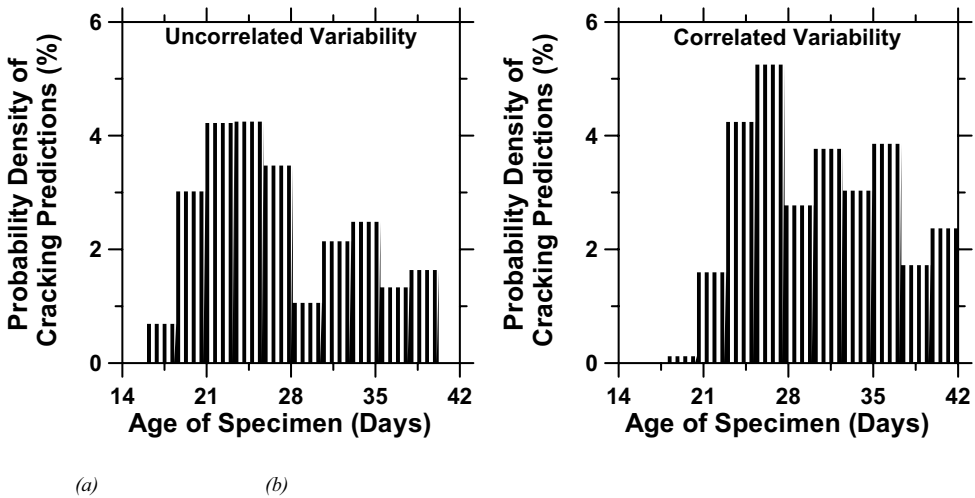


Figure 7. A comparison of the model simulation predictions for the age of the specimen at the time of cracking assuming a) uncorrelated variability in material properties and b) correlated variability in material properties

Table 2. Log-logistic simulation parameters considering variability due to: a) shrinkage only, b) shrinkage, tensile strength and elastic modulus assuming they are uncorrelated, and c) shrinkage, tensile strength and elastic modulus assuming they are correlated

Only Variation in Shrinkage [ $\epsilon_{SH}$ ]				
$t_{day}$	$P_{crack}$	$\alpha$	$\beta$	$\gamma$
1	60.90	2.98	22.54	0.32
3	58.90	2.58	17.33	4.80
7	57.20	2.59	14.94	10.94
Variation in Three Parameters [ $\epsilon_{SH}$ , $f_{ten}$ , $E$ ] Assumed Uncorrelated				
$t_{day}$	$P_{crack}$	$\alpha$	$\beta$	$\gamma$
1	67.40	2.05	17.70	-1.29
3	71.20	1.88	13.71	3.41
7	73.70	2.18	13.83	7.48
Variation in Three Parameters [ $\epsilon_{SH}(-)$ , $f_{ten}(+)$ , $E(+)$ ] Assumed Correlated				
$t_{day}$	$P_{crack}$	$\alpha$	$\beta$	$\gamma$
1	78.30	3.08	23.37	-0.14
3	83.90	2.65	17.78	4.26
7	85.90	2.45	14.42	10.98

Among the important factors that influence the predicted time of cracking is the time when drying was initiated. As can be read from Figure 8b the sooner the specimen is exposed to drying, the sooner it can be expected to crack (see also Figure 4d). It is interesting to note however that this may not result in a reduction in the overall potential for cracking to develop. It appears that the combination of increased elastic modulus and reduced creep in specimens that dry at a later age cause this increased probability of cracking at a later age.

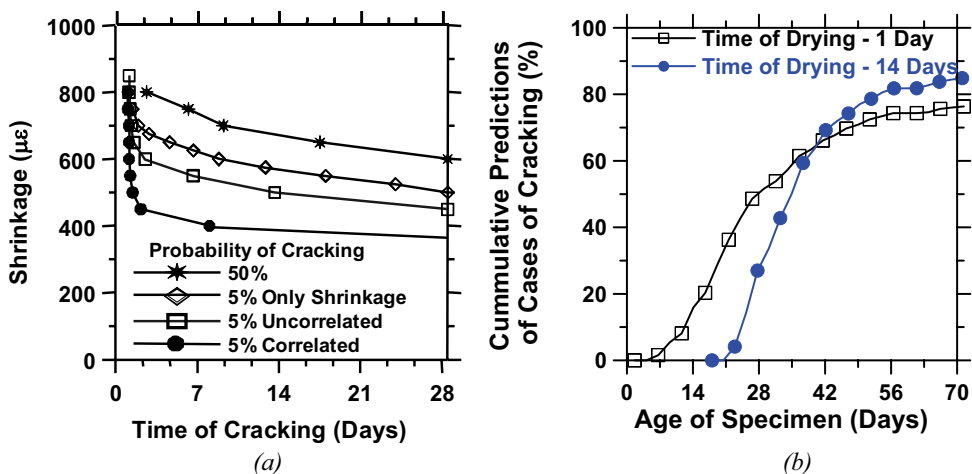


Figure 8. A comparison of the results for a) varying value of shrinkage, varying shrinkage, elastic modulus, and tensile strength (uncorrelated variability) and varying shrinkage, elastic modulus, and tensile strength (correlated variability) and b) an illustration of the influence of a delay in the time drying is initiated

## 6. Summary, Discussion, and Future Work

This paper has outlined a procedure for implementing variability into a predictive model for shrinkage cracking. Preliminary work has shown that:

- Even small amounts of variability result in substantial scatter in the predicted time of cracking. It is therefore suggested that a deterministic prediction of cracking alone may not provide sufficient information for the selection of material properties. Inherent material variability should be considered in specifying a limit on the magnitude of free shrinkage.
- While a normal distribution of variability in the material properties may be assumed, the time-dependent nature of material property development and the multiplicative nature of the variability results in a distribution of the time of cracking that is not a normal distribution. A log-logistic curve was initially used to describe this response since it appeared to describe low probability of cracking better than other models, however



this equation needed to be modified to account for the probability that cracking may not be observed.

- Three different approaches were considered in implementing this approach. The first considered only variability in shrinkage. The results from this approach appeared consistent with what one may expect from hand calculations. When multiple sources of variation are introduced a much higher variability in the results is observed.

While some resources describe the level of variability that may be expected in material properties [22], further research is needed to quantify both the level of variability and correlation in variability that may be expected in practical applications. Further information on the variability in environmental conditions and construction practices would also have great value for improving the information that may be obtained from these types of simulations. Further, it is hoped that over time this approach will be extended to models that are being developed to consider moisture gradients and fundamental physical mechanisms. It is believed that this approach may enable contractors to consider material variations, quality control practices, and environmental conditions which will enable them to minimize their risk of cracking.

## Acknowledgements

The authors gratefully acknowledge support phases of this research which has come from the Center for Advanced Cement Based Materials and the National Science Foundation (NSF) through Grant No. 0134272: a CAREER AWARD. Finally the last author wishes to express his gratitude to those at the Danish Technological University who invited him and worked with him as a Kund Højgaard Visiting Professor, this was truly a delightful opportunity.

## References

1. Weiss, W. J., "Shrinkage Cracking in Restrained Concrete Slabs: Test Methods, Material Compositions, Shrinkage Reducing Admixtures and Theoretical Modeling," MS Thesis, Northwestern University, Evanston, IL, 1997
2. Weiss, W. J., "Prediction of Early-Age Shrinkage Cracking in Concrete Elements." Ph.D. Dissertation, Northwestern University, Evanston, IL, 1999
3. Shah, S. P., Weiss, W.J., and Yang, W., "Shrinkage Cracking-Can It Be Prevented?" Concrete International, Vol. 20, No. 4, 1998
4. Schindler, A.K., Ruiz J.M., Rasmussen R.O., Chang G.K., Wathne L.G. (2004) "Concrete pavement temperature prediction and case studies with the FHWA HIPERPAVE models", Cement and Concrete Composites 26, 463-471
5. Schlangen, HEJG, Koenders, EAB and van Breugel, K (2004) "Multi-scale modelling of crack formation in the concrete cover zone," Advances in cement and concrete, eds. Lange, D.A., Scrivener, K.L., and Marchand, J., Illinois at Urbana-Champaign: Engineering Conferences International, pp. 281-291.

6. Parameswaran, S. (2004) "Investigating the role of material properties and their variability in the selection of repair materials" MS Thesis, Purdue University, West Lafayette, USA
7. Weiss, W. J., and Shah, S. P., "Restrained Shrinkage Cracking: The Role of Shrinkage Reducing Admixtures and Specimen Geometry," RILEM International Conference on Early-Age Cracking in Cementitious Systems (EAC'01), eds. K., Kovler, and A. Bentur, March 12-14, Haifa Israel, 2001
8. Moon, J. H., Rajabipour, F., and Weiss, W. J., "Incorporating Moisture Diffusion In The Analysis Of The Restrained Ring Test," Proceedings of the 4<sup>th</sup> International Conference on Concrete Under Severe Conditions: Environment & Loading, Vol. 2, ed. K. Sakai, O.E. Gjorv, and N. Banthia, 2004, pp. 1973-1980
9. J.-H. Moon, F. Rajabipour, B. Pease, and J. Weiss, "Autogenous Shrinkage, Residual Stress, and Cracking in Cementitious Composites: The Influence of Internal and External Restraint," Fourth International Seminar on Self-desiccation and Its Importance in Concrete Technology, Maryland, USA, 20 June 2005
10. McIntosh, J. D., "The Effects of Low-Temperature Curing on the Compressive Strength of Concrete," Proceedings of the RILEM Symposium on Winter Concreting, 1956
11. Weiss, W. J., Borischevsky, B. B., and Shah, S. P., "The Influence of a Shrinkage Reducing Admixture on the Early-Age Behavior of High Performance Concrete," Fifth International Symposium on the Utilization of High Strength/High Performance Concrete, Sandefjord, Norway, Vol. 2, 1999
12. Olken, P., and Rostasy, F. S., "A Practical Planning Tool for the Simulation of Thermal Stresses and For the Prediction of Early Thermal Cracks in Massive Concrete Structures," Thermal Cracking in Concrete At Early-Ages, Ed. R. Springenschmid, EF Spon London 1994, pp. 289-296
13. Barde, A., "Early Age Flexural Behavior of Cementitious Systems and Factors Affecting Maturity Based Predictions," MS Thesis, Purdue University, West Lafayette, IN, 2004
14. Bazant, Z. P., "Mathematical Modeling of Creep and Shrinkage of Concrete," John Wiley & Sons, Inc, 1989
15. Muller, H.S., "New Prediction Models for Creep and Shrinkage of Concrete", Creep and Shrinkage of Concrete: Effect of Materials and Environment eds. M.A. Daye and C.C.Fu, American Concrete Institute, Detroit, Michigan, 1992
16. Pease, B. J., "The Role of Shrinkage Reducing Admixtures on Shrinkage, Stress Development, and Cracking," Master's Thesis, Purdue University, West Lafayette, IN, 2005
17. Pickett, G., "Effect of Aggregate on Shrinkage of Concrete and Hypothesis Concerning Shrinkage," Journal of ACI, Vol. 52, January 1956, pp. 581-590
18. L'Hermite, R. G., "Volume Changes of Concrete," Fourth International Symposium on the Chemistry of Cement, Washington, D.C., 1960, pp. 659-694
19. Pease, B. J., Shah, H. R., and Weiss, W. J., "Shrinkage Behavior and Residual Stress Development in Mortars Containing Shrinkage Reducing Admixtures (SRA's)," ACI SP 227 - Shrinkage and Creep of Concrete, eds. Gardner, N. J. and Weiss, W. J., 2005

20. Weiss, W. J., Borischevsky, B. B., and Shah, S. P., "The Influence of a Shrinkage Reducing Admixture on the Early-Age Behavior of High Performance Concrete," Fifth International Symposium on the Utilization of High Strength/High Performance Concrete, Sandefjord, Norway, Vol. 2, 1999a, 1418-1428
21. Schindler, A.K., Ruiz J.M., Rasmussen R.O., Chang G.K., Wathne L.G. (2004) "Concrete pavement temperature prediction and case studies with the FHWA HIPERPAVE models", Cement and Concrete Composites 26, 463-471
22. Osterle, R.G., Refai, T.M., Weiss W.J. (1994) "Variations in calculated movements of jointless bridges using Monte Carlo simulation", Construction Technologies Laboratories



## Experimental Study of Crack Healing of Early Age Cracks

Nynke ter Heide, Erik Schlangen and Klaas van Breugel  
Delft University of Technology, CITG, Microlab, The Netherlands.

### Abstract

An experimental study is performed on crack healing in hydrating concrete. The aim of the research is to investigate under which conditions cracks that are formed in concrete at very early age can heal again when the cement hydrates further. To study this phenomenon, three-point-bending tests are performed on prismatic concrete specimens at early age to create cracks with a specified crack opening. After the test the specimens are matured further under water with and without compressive loading to close the cracks. Several weeks after the first test the specimens are tested again to investigate the amount of healing and further development of mechanical properties. From the tests it can be concluded that the mechanical properties of the concrete are almost fully recovered for cracks made after 20 hours of hydration and loaded in compression afterwards. If the degree of hydration of the specimens is higher at the moment of cracking, the strength gain is less.

### 1. Introduction

Self-healing is a phenomenon that can “repair” cracked concrete. Although reinforced concrete is designed to crack, in some circumstances cracking should be avoided. Major reasons for requiring crack-free structures are liquid tightness and enhanced durability of concrete structures. Self-healing can help to realize structures without cracks. Within self-healing we actually can distinguish two mechanisms:

- *Self tightening*: the crack is blocked with small particles from the crack faces or small parts present in fluids that flow through the crack.
- *Self-healing*: a chemical reaction takes place connecting the two crack surfaces. The reaction can be continuing hydration of the cement or a chemical reaction that occurs after hydration (like the formation of calcium carbonate).

An overview of research on self-healing mechanisms is given in [1]. All of the studies described in [1] focus actually on self tightening of old cracks and the formation of calcium carbonate in these cracks. Continuation of the hydration process, because of un-hydrated cement particles present, is believed not to happen. Reason for this is that the distance between the two crack faces is generally too large to be bridged by hydration products. Recently a study

of temperature influence on crack healing was reported in [2]. From this research it was found that with lower crack widths and at higher temperatures, crack healing is more likely to take place. In self-healing research attention is always focussed on blocking of the cracks and increasing the permeability of the material. The recovering of mechanical properties of the material is almost never investigated. An exception on this is given in [3], where an experimental study is described of self-healing of a cementitious composite containing hollow glass fibres carrying air-curing chemicals. The self-healing effectiveness is confirmed by measurement of the elastic modulus of the composite. The elastic modulus is found to regain its original value in a repeat loading subsequent to damage in a first load cycle. An other way to actively create a crack healing environment in a crack is by using micro-organisms [4,5]. These organisms have to be injected into an already formed crack and are able to induce calcite precipitation in the cracks, and in such a way realize blocking of the crack path and increase stiffness and strength.

In massive concrete structures often surface cracks develop already during the first day of hydration [6,7]. With continuation of the hydration process and cooling down of the interior of the structure the surface is loaded in compression. The cracks are closed due to this compressive stress. The question is whether the cracks can heal in this situation. Hydration is still in process and the crack faces are touching each other again. Probably an environment is created in which the cracks can heal. To study this an experimental investigation is started which is described in this paper. The next paragraph describes the tests performed and the variables studied. This will be followed by the first results of the experiments and discussion and preliminary conclusions of the research.

## **2. Experimental Program**

### **2.1 Description of test set-up**

In order to study the effect of crack healing in early age concrete, first cracks have to be made in the concrete in a controlled way. For this a three-point-bending test is chosen on prismatic concrete specimens. The specimens are cast in steel moulds and have dimensions of 40x40x160mm. The distance between the loading points is 105 mm (see figure 1a). The reaction force is in the centre. The deformation is measured with two LVDT's (at front and back) fixed at the bottom of the specimen (in the centre). The measuring length is 55 mm. The deformation measured with these LVDT's give a bending strain at the bottom of the specimen. If the crack localizes this value is a measure (although not exact) for the crack opening. The specimen is loaded in a special 3-point-bending frame (see figure 1b) in an Instron 8872 servo-hydraulic loading device. In the 3-point-bending frame the load is applied to the concrete via pendulum bars to minimize friction at the loading points.

The test are performed in deformation control using the average signal of the two LVDT's as feed back signal. The speed of loading was set to 0.02  $\mu\text{m/s}$  at the start of the test. In the descending branch of the measured softening curve (at a crack mouth opening of 20  $\mu\text{m}$ ) the speed was increased by a factor of two. A typical load-deformation curve of a specimen tested at an age of 1 day is plotted in figure 2. In this test the loading is stopped at a crack mouth

opening of 50  $\mu\text{m}$ . The specimen is unloaded and taken out of the machine. The crack opening decreases after unloading but the crack will not completely close.

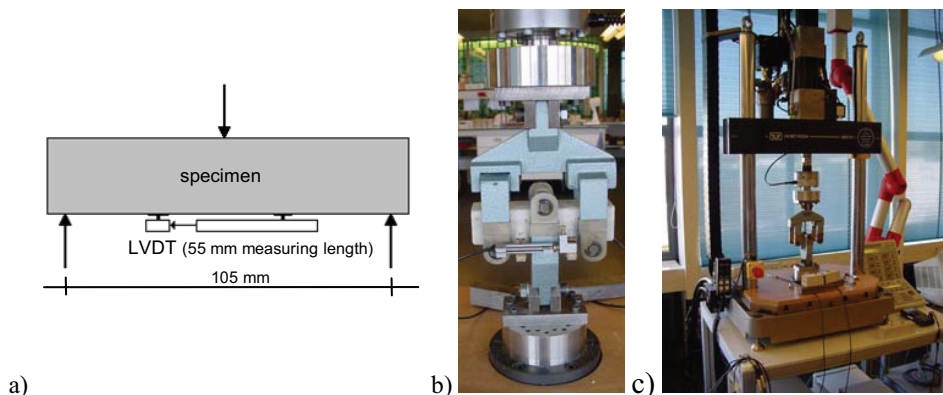


Figure 1. Specimen dimension (a) and 3-point bending loading device (b) in Instron 8872 (c).

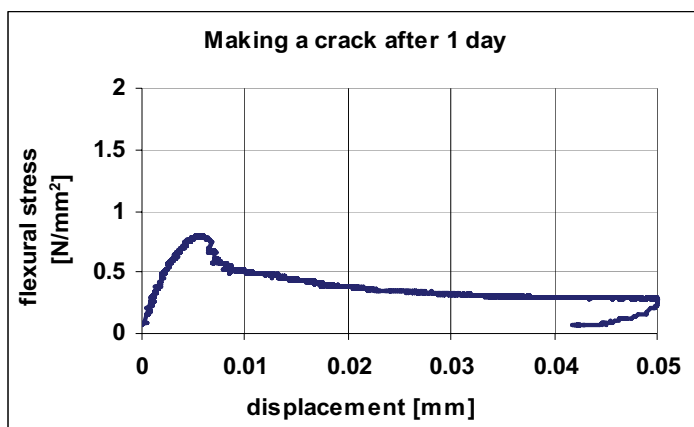


Figure 2. Flexural stress plotted versus displacement for a specimen loaded in 3-point-bending at an age of 1 day.

At this moment the specimen is put in a compression loading device to apply a compressive force to close the crack. This force is measured by means of the deformation of calibrated steel spring. The amount of compressive force is varied in the tests. In figure 3 the compressive loading devices are shown with specimens subjected to 0.5, 1 and 2  $\text{N/mm}^2$  compressive stress.

The specimens are then stored for a specific period at a certain temperature and relative humidity (or under water) to undergo crack healing. Due to creep of the concrete, the applied

load will decrease in time. This is checked during the healing process by measuring the deformation of the spring. It turned out that the decrease in load was smaller than 1 %, so no adjustments were needed. Next to healing of the crack the concrete will also have further hydration. This means that the mechanical properties of the material itself will also improve. To test the mechanical properties of the healed crack the specimens are, after a certain period of healing, again tested in three-point-bending. To be able to judge the recovering of mechanical properties of the crack, the results have to be compared with cracks that are not healed and with cracks that are made after the healing process. Therefore virgin specimen stored at the same environment and with the same age as the healed specimens were tested. A typical example of the obtained load-displacement response for a virgin specimen tested at an age of 2 weeks is given in figure 4.

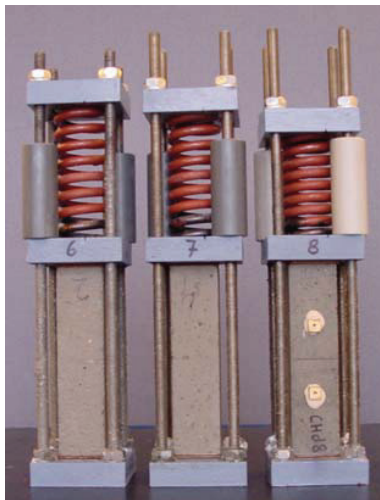


Figure 3. Compression loading devices with specimen loaded with (from left to right) 0.5, 1 and 2 N/mm<sup>2</sup> respectively.

The specimen is first loaded in deformation control up to a displacement of 50  $\mu\text{m}$ . Then the specimen is unloaded and again tested. The maximum load reached in the second stage of the test can be seen as a maximum flexural stress for a specimen with an unhealed crack at an age of 2 weeks. Question is however whether the crack has the same length in a specimen tested at an age of 1 day (27.5 hours) and at 2 weeks when in both cases the crack opening has reached a value of 50  $\mu\text{m}$ . To be able to answer this, the specimens have been vacuum impregnated with a fluorescence epoxy after the test. The cracks can then be visualised under UV-light. An example of this is given in figure 5, where a specimen is shown tested after 1 day up to 50  $\mu\text{m}$ . The crack has developed to a depth of about 17 mm into the specimen. The specimen is still very porous at an age of 1 day. The epoxy enters the pores in the material at the surface but also from the crack as can be seen in figure 5. Only a few specimens have been tested in this way up till now. The scatter in the crack length that is observed is rather large. To investigate this better, more specimens will be impregnated in the future tests.



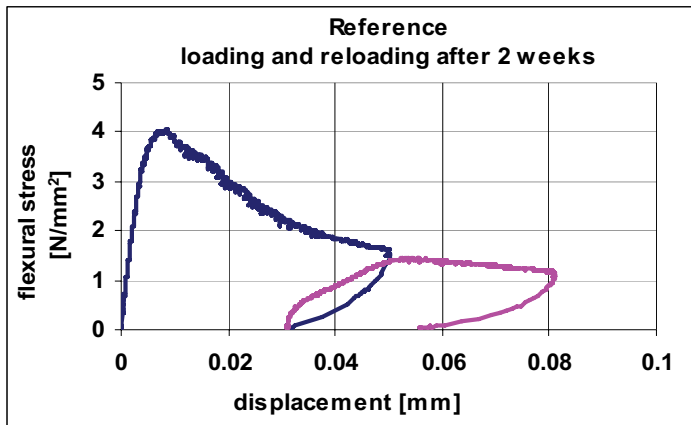


Figure 4. Flexural stress versus displacement of virgin specimen tested at age of 2 weeks.

In order to get insight into the reaction products or other material formed inside the crack during the crack healing mechanism, the cracked and healed specimens are investigated in the ESEM.

## 2.2 Description of tested variables

In the experiments several parameters are varied. The experimental work is still ongoing at the moment of compiling this paper. The parameters that are discussed in this paper are:

- the amount of compressive force applied during healing. The variation of this parameter is 0.0, 0.5, 1.0 and 2.0 N/mm<sup>2</sup>.
- the moment of creating the first crack in the specimen. The cracks are made at an age of 20, 27.5 (further named 1 day), 48 and 72 hours. The age at loading has some variation, since the specimens are cast at the same time, but for testing only one machine is available. Each test, including preparation, takes about 45 minutes.
- the crack (mouth) opening of the crack. Initial crack openings of 20, 50, 100 and 150  $\mu\text{m}$  are discussed in this paper.

Always one parameter is varied. The default parameters in the tests are 1.0 N/mm<sup>2</sup> compressive stress, crack made at age of 1 day and crack opening of 50  $\mu\text{m}$ . All the tests are performed at least three times.

In the experiments that still have to be performed also the time of healing will be varied. Now only a healing time of 2 weeks is tested. In the remaining tests healing times up to 3 months will be performed. Another variation is the relative humidity during crack healing. In all the tests presented here the specimens were stored under water. In [8] also results will be presented for specimens stored at different relative humidity's. Furthermore the concrete mix will be varied in these tests. In the experiments described here only a mix with a blast-furnace-slag cement is used. In table 1 the mix composition of the concrete is given. In the remaining tests also a faster reacting Portland Cement will be used.

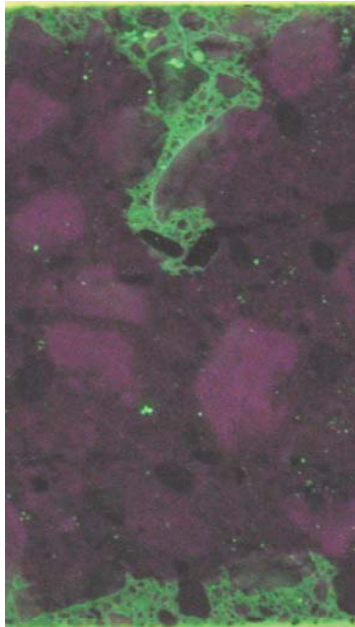


Figure 5. Example of crack development in a specimen tested at age of 1 day.

Table 1. Mix composition of the concrete used in the tests.

Cement	CEM III/b 42,5 LH HS	375 kg/m <sup>3</sup>
Water		187.5 kg/m <sup>3</sup>
River gravel	8 - 4 mm	540 kg/m <sup>3</sup>
	2 - 4 mm	363 kg/m <sup>3</sup>
	1 - 2 mm	272 kg/m <sup>3</sup>
	0.5 - 1 mm	272 kg/m <sup>3</sup>
	0.25 - 0.5 mm	234 kg/m <sup>3</sup>
	0.125 - 0.25 mm	127 kg/m <sup>3</sup>

### 3. Experimental Findings

#### 3.1 Influence of compressive stress

The first parameter that is investigated is the compressive stress on the specimen during the crack healing. The specimens are tested at an age of 1 day up to a crack opening of 50  $\mu\text{m}$  as shown in figure 2. Then a compressive force is applied to the specimens and they are stored for 2 weeks under water and tested again. In figure 6 the flexural stress is plotted versus displacement for the reloading test after 2 weeks healing for a test with (1 N/mm<sup>2</sup>) and without (0 N/mm<sup>2</sup>) compressive stress. Furthermore the graph is shown of the specimen without

healing. The latter is the reloading part of the curve shown in figure 4, which is the virgin specimen tested at an age of 2 weeks. The graph shows that when the crack is not closed (the compressive stress is  $0 \text{ N/mm}^2$ ) the recovery of strength is minor. However with a compressive stress of  $1 \text{ N/mm}^2$  both the stiffness and the strength of the specimen is recovered and shows values close to the reference specimen.

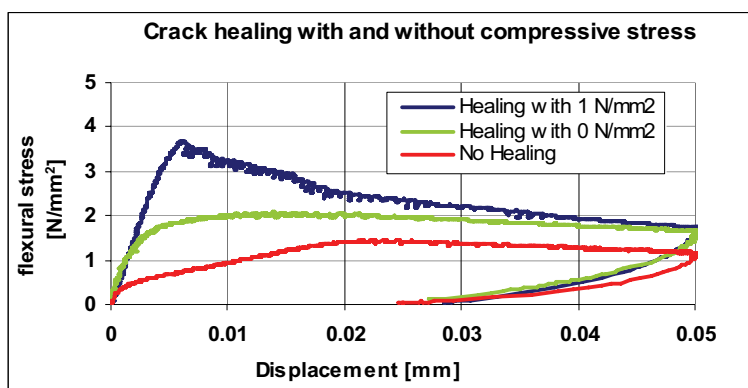


Figure 6. Stress-displacement curve of specimen with and without compressive stress during healing, compared with unhealed cracked specimen.

Figure 7 gives the relative strength of the specimen after healing for different amount of compressive stress applied during healing. The relative strength is given in percentage of the strength of the un-cracked virgin specimen tested at an age of 2 weeks (see figure 4, peak in first loading part). In the figure also a line is shown (with vertical bars showing the scatter) which represents the strength of the material of the unhealed specimen (see figure 4, peak in reloading part). The figure shows clearly that almost no increase in strength is obtained when the specimen is not loaded in compression ( $0 \text{ N/mm}^2$ ). Furthermore it can be seen that, in case a compressive loading is applied to close the crack, the amount of compressive stress is not really influencing the strength gain.

### 3.2 Influence of age when the first crack is produced.

The second parameter that is investigated is the moment of cracking or the age of the specimen when the first crack is produced. In figure 8 the stress-displacement curves are shown for the specimens tested at different age. In these test the crack is opened up to a crack mouth opening of  $50 \mu\text{m}$ . Subsequently, the specimens are loaded in compression with a compressive stress of  $1 \text{ N/mm}^2$  and stored under water for 2 weeks. The strength after healing (relative to the strength of the virgin specimen) is plotted in figure 9 for the various ages of making the first crack. The reference test is for each series always performed at the same age. So this means that for instance the strength of the specimen tested for the first time at 72 hours and subsequently healed for 2 weeks is compared with the strength of a specimen loaded for the first time at an age of 17 days. Although the difference in strength of the virgin material

between an age of 14 and 17 days is very small. A clear decrease in strength recovery is observed with increasing age of the specimen when making the first crack.

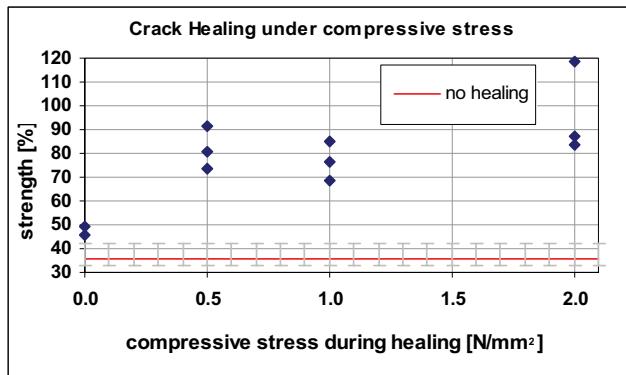


Figure 7. Resulting relative strength after crack healing for various compressive stress values.

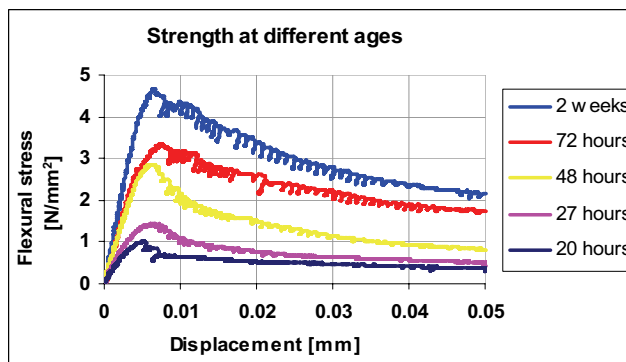


Figure 8. Flexural stress versus crack opening displacement for specimens loaded (first loading) at different age.

### 3.3 Influence of crack width on strength recovery.

The last parameter discussed in this paper is the influence of the width of the crack that is made in the specimen on the healing mechanism. In these tests the specimens are loaded at an age of 1 day and the compressive stress during healing is equal to  $1.0 \text{ N/mm}^2$ . A larger crack mouth opening will result in a longer crack which has propagated further into the specimen. The load that can be carried at a larger crack opening will be smaller. This can be seen from the line showing the residual strength of the reference specimen without healing in figure 10. This is the line that corresponds to the peak load of the reloading part in the load-displacement diagram of the virgin specimen tested at an age of 2 weeks up to different crack openings. In figure 10 the various results for different initial crack openings are plotted. There is quite some

scatter, but there seems to be no influence of crack opening on the strength recovery after healing.

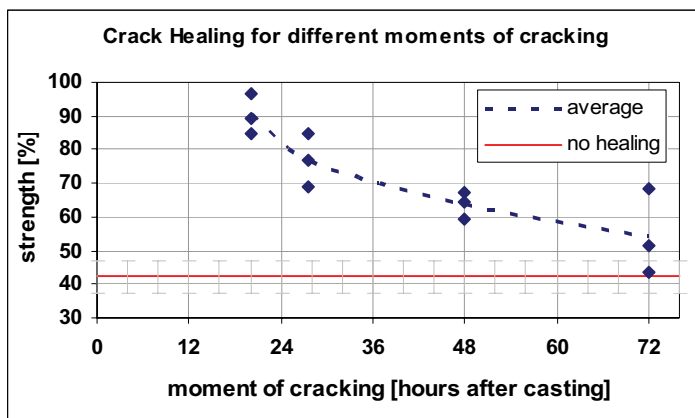


Figure 9. Strength recovery as function of age of specimen when the first crack is made.

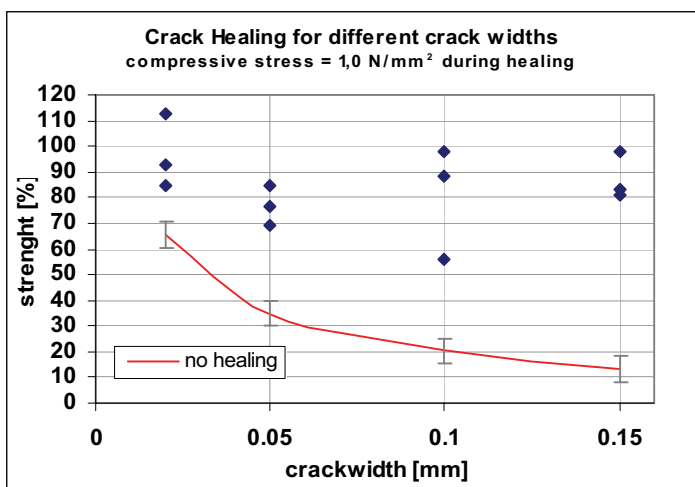


Figure 10. Strength recovery after healing as function of initial crack opening.

#### 4. Discussion of Results and Conclusions

This paper discusses the first outcome of an experimental investigation recently started at the Microlab of Delft University on crack healing of cracks in early age concrete. Prismatic specimens are at a certain age cracked in 3-point-bending after which they are subjected to a compressive load and stored under water to heal.

The variables in the research that are investigated and discussed in this paper are:

- amount of compressive stress during healing.
- age of specimen when making the first crack.
- crack mouth opening of the crack.

From the experimental results it can be concluded that:

- Cracks do heal under the conditions that the cracks are made at an early age and the cracks are closed again (a compressive stress is applied) and the specimens are stored under water.
- The amount of compressive stress does not seem to influence the strength recovery. The results indicate that a compressive stress is needed to close the crack, but once the two crack faces touch each other again, or the distance between the crack faces is small enough, crack healing can happen.
- With increasing age of the specimen at the moment the first crack is made, a decrease in strength recovery is found. The age of the specimen when the first crack is made determines the degree of hydration. With that also the amount of hydration that still can take place is fixed. The amount of strength recovery is therefore also limited when the concrete has already reached a higher degree of hydration when the crack is made.
- The width of the crack does not seem to influence the strength recovery due to healing. The tests with different crack mouth openings show all a similar amount of strength recovery.

The authors believe that ongoing hydration is the mechanism for crack healing that leads to the strength recovery in this investigation. This mechanism only works when the crack is closed again. It has been shown that the crack healing does take place when enough humidity is present. The specimens are stored under water. However, tests with specimens stored at other humidity's are published in [8]. The strength recovery of the material in the crack is actually more than the strength increase (during the healing period) of the concrete itself. Probably this can be explained by the fact that the material in and around the crack has sufficient water available. This makes full hydration (degree of hydration equal to 1) possible. In the bulk concrete this will not be reached.

The question remains what kind of products are formed inside the crack. First observations in ESEM indicate that the cracks are (for a large part) filled with reaction product. Also needle type products are observed, most probably ettringite. Some ESEM pictures of a crack that has healed for 2 weeks and is reloaded afterwards are shown in figure 11. Further results on this as well as observation from thin section analysis are published in [8].

For the practical situation of early age surface cracks in (massive) concrete structures, which are a concern from a durability point of view, this investigation shows some promising results. It indicates that these surface cracks can disappear again, at least under the right conditions as discussed in this paper.

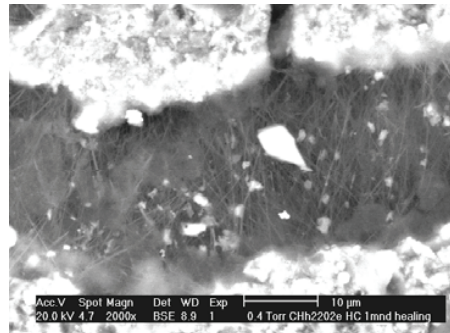
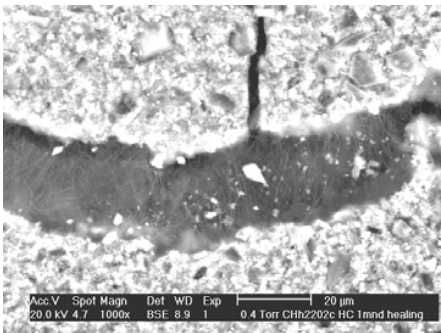
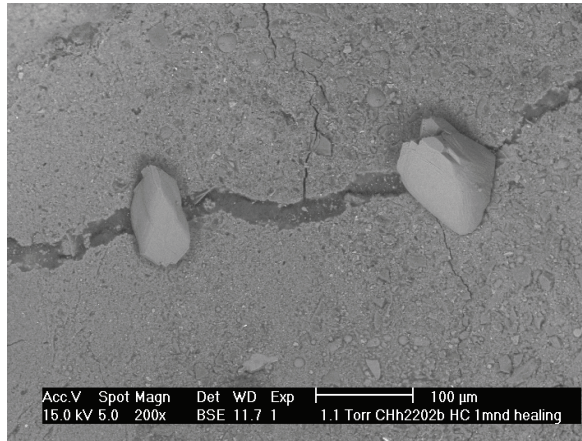


Figure 11. ESEM images at different magnifications of healed crack.

### Acknowledgement

The authors would like to thank mr. G. Timmers and mr. R. van Maasackers for assisting with the experiments and the ESEM work. Furthermore, the authors acknowledge in depth discussions on the subject with Dr. M.R. de Rooij, Dr. E.A.B. Koenders and Ms. J. Bouwmeester.

### References

1. Edvardsen, C.K. Water permeability and self-healing of through cracks in concrete, Deutscher Ausschuss für Stahlbeton, Heft 455, 1996 (in German).
2. Reinhardt, H-W. & Joos, M. Permeability and self-healing of cracked concrete as a function of temperature and crack width, C&CR 33, 2003, 981-985.
3. Li, V.C., Lim, Y.M. and Chan, Y-W. Feasibility study of a passive smart self-healing cementitious composite. Composites Part B 29B (1998) 819-827.

4. Bang, S.S., Galinat, J.K. & Ramakrishnan, V. Calcite precipitation induced by polyurethane-immobilized *Bacillus pasteurii*, *Enzyme and Microbial Technology* 28 (2001) 404–409.
5. Rodriguez-Navarro, C, Rodriguez-Gallego, M., Chekroun, K.B. and Gonzalez-Munoz, M.T. Conservation of Ornamental Stone by *Myxococcus xanthus*-Induced Carbonate Biomineralization, *Applied and Environmental Microbiology*, Apr. 2003, p. 2182–2193.
6. Salet, T. and Schlangen, E. Early-age crack control in tunnels. In *Proc. Euromat 97*, Sarton, L. and Zeedijk, H. (eds), Maastricht, 1997, Vol 4, 367-377.
7. Thermal Cracking in Concrete at Early-Ages, *Proceedings of the International Rilem symposium*, no.25, E and FN Spon, London, 1994.
8. Ter Heide, N. Crack healing in hydrating concrete. MSc-thesis, Delft University of Technology, The Netherlands, 2005.



## Cracking, Damage and Fracture in Four Dimensions

E.N. Landis<sup>1</sup>, T. Zhang<sup>2</sup>, E.N. Nagy<sup>1</sup>, G. Nagy<sup>2</sup> and W.R. Franklin<sup>2</sup>

<sup>1</sup>University of Maine, USA

<sup>2</sup>Rensselaer Polytechnic Institute, USA

### Abstract

Concrete and cracking are nearly synonymous despite our best efforts and intentions. Relationships between cracking and the stress states that lead to cracking can be instructive. In an effort to better understand these relationships, x-ray microtomography was used to make high-resolution three-dimensional digital images of small concrete specimens under load. Using 3D image analysis, quantitative measurements of internal crack growth were made that include effects of crack tortuosity, branching and microcracking. Successive images at different levels of cracking and damage provide us with a detailed picture of internal crack progression. When coupled with load-deformation response, bulk material properties such as fracture toughness or damage variables can be quantitatively linked with cracking. Measurements to date have shown distinct fracture regimes linked to crack formation and propagation. In addition, the crack measurements offer a way to provide a physical basis for a scalar damage variable.

### 1. Introduction

The role of cracks and flaws in materials has been central to our understanding of strength and failure in materials for nearly a century. Since the work of Griffith and the subsequent birth of fracture mechanics, cracks have been the focus of our strength and damage theories. Continuum damage theory further established the role of distributed crack systems on bulk stiffness degradation. Over the past 30 years this body of knowledge has been applied with great enthusiasm to problems of strength, toughness, durability, and overall performance of concrete and reinforced concrete systems. A problem, however, is that despite the substantial efforts of researchers around the world, surprisingly little progress has been made in truly quantitative relationships between crack parameters and bulk material parameters. Indeed, few if any fracture mechanics principles have made their way into building codes or standard design procedures, and after 30 years there is still no standard test to measure fracture toughness!

The theme of the work described in this paper, is that the problems just described ultimately may stem from a fundamental lack of understanding of crack systems in an extremely heterogeneous medium such as concrete. For years we have been thinking and modeling in terms of

elliptical cracks, penny-shaped cracks, wing cracks, crack normal vectors, crack shielding, fictitious cracks, fracture process zones, and so forth. While these concepts and idealizations are most certainly grounded in real phenomena, perhaps the direct application to a complex system such as concrete is too great a stretch.

Thus, in order to help improve our understanding of the complex cracking that occurs in concrete, we are employing high resolution 3D scanning coupled with quantitative 3D image analysis techniques. The goal is to characterize these crack systems in such a way that our dependence on simple geometric forms is minimized. Once this is done, we can make steps to relate crack parameters to bulk material properties. The implied assumption here is that improvements in our understanding of the physical processes involved in damage and fracture will lead to improvements in our ability to predict material performance.

## 2. Experimental Methods

The 3D scanning technique employed here is called x-ray microtomography [1]. It is similar in practice to computed axial tomography (CAT-scans) used in medical imaging in that a sequence of radiographic images made at different angles are mathematically reconstructed to produce a 3D map of an object's x-ray absorption, which in turn can be used to deduce the internal structure of the object. The difference is that microtomography uses extremely high intensity radiation from a synchrotron source. The synchrotron provides a collimated beam, high flux, and narrow bandwidth x-rays. When combined with an appropriate scintillator and digital image capturing system, 3D images with a spatial resolution approaching 1 micron are possible. Because of the synchrotron source, the images have very good dynamic range, and thus subtle variations in material structure can be detected. A schematic diagram of the microtomography system components is presented in Fig. 1. The rotation stage allows imaging of the specimen at different angles, while the microscope objective allows scans of variable magnification.

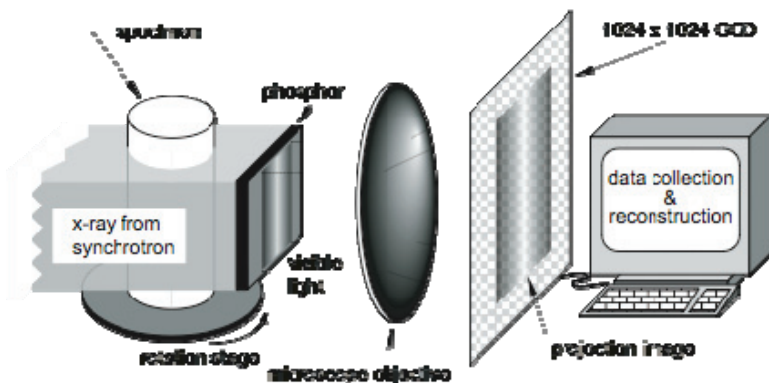


Fig. 1 - Illustration of microtomographic scanning set-up.

When applied to problems of concrete microstructure, microtomography provides a nice complement to our imaging toolbox. As such it has been used to image cement and concrete in a number of applications, including sulfate attack [2][3], porosity and pore structure, [4], and fracture [5][6]. While not as high resolution as electron microscopy, it does offer the advantage of providing true 3D data. Because it is nondestructive, microtomography can be used to scan the same specimen multiple times, allowing us to explore microstructural changes resulting from a number of different agents. This aspect was exploited in the research detailed below.

An example cross sectional “slice” image of concrete microstructure is shown in Fig. 2. In the figure one can see many of the important features of hydrated cement paste: unreacted cement grains (white flecks), pore space (dark spots), transition zones around aggregates, as well as a variable density within an aggregate particle. It should be emphasized that this is one slice out of the hundreds that are produced in a single scan.

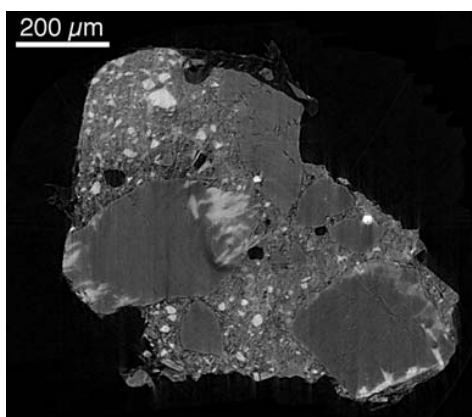


Fig. 2 - Example 2D “slice” image taken from 3D tomographic reconstruction.

## 2.1 In-situ Loading

As previously indicated, the technique was previously utilized in a study of concrete fracture mechanics [5][6]. For that study, a small compression testing frame was constructed so that tomographic scanning could take place while the specimen was under load. Thus, the same specimen could be scanned multiple times at progressively higher levels of damage. The frame was able to measure applied force and the resulting displacement while being nominally transparent to x-rays. It is illustrated in Fig. 3. The data presented in this paper resulted from those fracture studies.

The microtomographic scanning/loading protocol was as follows. An initial scan of an undamaged specimen was made prior to loading. Then the specimen was loaded to a prescribed deformation, and a subsequent scan was made. The specimen was then unloaded and reloaded for additional scans. This procedure was repeated for at least 4 cycles as illustrated in Fig. 4.

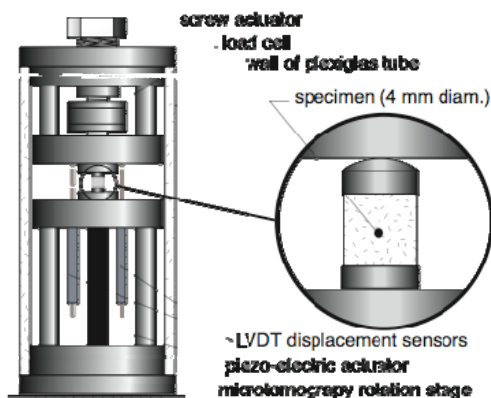


Fig. 3 - In-situ loading frame.

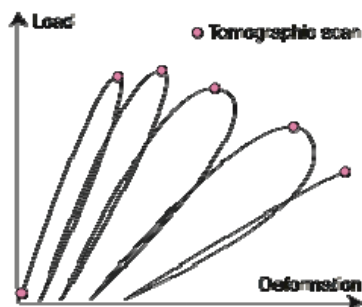


Fig. 4 - Load cycles and scanning.

Fig. 5 shows a sequence of images taken of a specimen loaded to different levels of damage. In this case the planes shown are perpendicular to the axis of loading. The sequence shows roughly the same plane in each of the scans. (Note that it is not possible to precisely match planes due to nonuniform deformation in the specimen.) The growth of crack networks is clearly shown. In subsequent images cracks grow longer, branch, and interconnect as the network extends. It is important to note the complexity of the network. Indeed, we must dispense with some of our traditional simplifications as it would be difficult to characterize such a crack network in terms of conventional plane geometry.

The specimens prepared for this study were small cylinders 4 mm in diameter by 4 mm in height. The small size was required by the constraints of the synchrotron beamline. However, the small specimen size led to a relatively high spatial resolution of 6 microns per voxel. The mix proportion of the specimens was (by mass) 1 part type I portland cement to 2 parts sand to 0.6 parts water. The maximum aggregate size was 0.425 mm. No air entraining or other admixtures were used.

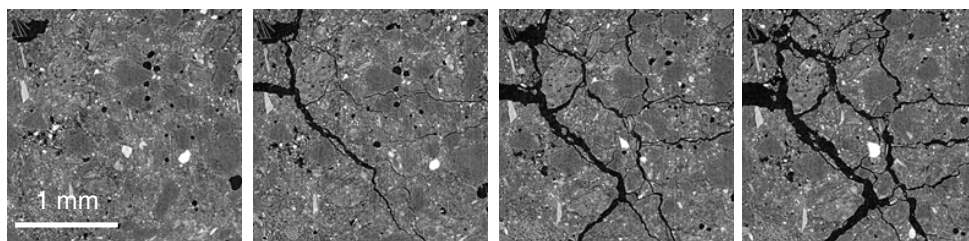


Fig. 5 - Images of specimen segment at different levels of damage.

### 3. 3D Image Processing

As the data produced by the tomographic scans is digital, we have at our disposal an extensive library of image analysis and image processing techniques. In the work described here, a variety of 3D analysis routines were developed in order to extract quantitative measurements from the acquired data. Specifically, we utilized routines to 1) segment images to separate void space from solid, 2) isolate the specimen, 3) isolate void objects, and 4) measure properties of void objects and displacement fields. Two different approaches were used to isolate crack objects, as is detailed below.

#### 3.1 Image Segmentation

Microtomography produces images where the voxel (3D pixel) intensity is roughly proportional to the density of the material at that point. A histogram of voxel intensities of a porous material such as concrete shows distinct peaks at intensities representing the solid material and the void space. As such, a simple way to separate the two is to establish a threshold intensity at the minimum between the two peaks [7]. Any voxel with an intensity above the threshold is considered solid, and is made white, while any voxel with an intensity below the threshold is considered void, and is colored black. Fig. 6 illustrates the effect applied to the image segments of Fig. 5. As can be seen in the images, void and crack space is clearly visible.

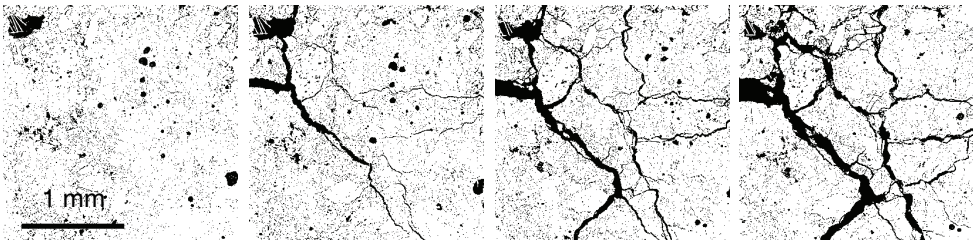


Fig. 6 - Black and white images where black indicates void space, white indicates solid.

#### 3.2 Specimen Isolation

Because the specimens used in this work were of an irregular shape, it became necessary to develop a routine to isolate the specimen from the surrounding background. In doing this, all subsequent image analysis could be focused exclusively on the specimen interior, rather than the entire field of view.

Two steps were used to separate interior void space from exterior space. First, a shrink wrapping algorithm [8] was used to define the boundary of the specimen, as illustrated in Fig. 7. The “wrapper” encloses the boundary of the specimen while preserving all the irregularities on the boundary. Second, the result of the shrink wrapping can be combined with the previously determined binary image to separate the internal void objects. As illustrated in Fig. 8, a logical ‘AND’ is applied to two images. The output from the shrink wrap is shown on the left as a solid object. Any voxel that is black in both the left image and the center black & white image

remains black in the right-hand image. The result is an image that includes only the internal void space. Thus, any subsequent analysis of void objects applies only to the internal objects. The use of a logical statement is much more computationally efficient than image coordinate arithmetic.

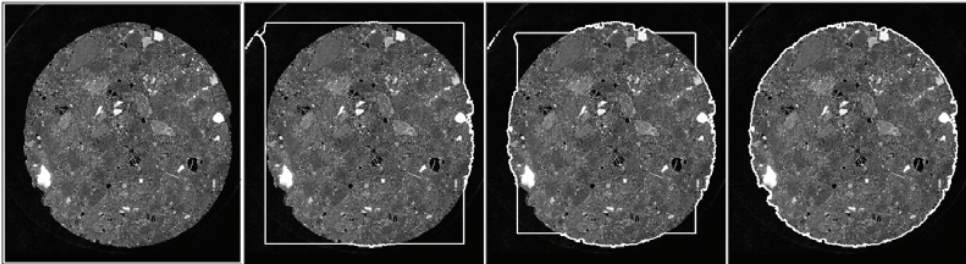


Fig. 7 - Application of shrinkwrap algorithm to isolate specimen from background.

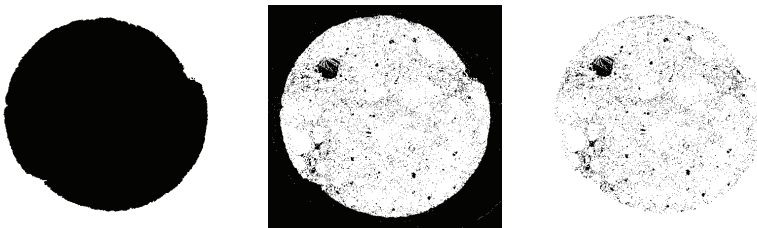


Fig. 8 - Logical 'AND' applied to two leftmost images. Any pixel that is black in both images becomes black in the resulting (right-hand) image.

### 3.3 Object Connectivity

In order to make measurements of different object properties, each individual void object must first be isolated and labeled. This is done by evaluating the connectivity of the black voxels. If two adjacent black objects share a face (6-connectivity), edge (18-connectivity), or corner (26-connectivity) they are considered as part of the same object. In this work, a fast, robust 3D connected components algorithm developed by Franklin [9] was used. This program returns (among other image statistics) the number of discrete objects, and the volume and surface area of each object. Volume is determined by the number of voxels in the object, while surface area is determined by the number of free voxel faces. (That is, black voxel faces that are in contact with white voxels.)

## 4. Crack Measurements

The measurements resulting from the connected components analysis is enlightening. Table 1 shows the measurement results from five different scans of the same specimen at successively higher levels of deformation. Even in the undamaged specimen (scan 1) there are over 3 mil-

lion void objects in a 4 mm diameter by 4 mm high cylinder. A majority of these are very small objects of 1 to 3 voxels ( $216$  to  $648 \mu\text{m}^3$ ) in volume. The total volume of the void space in the first scan corresponds to a porosity of roughly 5%, which is reasonable for the level of resolution in the scans. The higher levels of porosity typically measured using techniques such as mercury intrusion porosimetry result from a much finer resolution.

Table 1 - Measurements of void/crack system.

Scan	Total number of void objects	Total volume of void objects ( $\text{mm}^3$ )	Totals surface area of void objects ( $\text{mm}^2$ )
1	$3.12 \times 10^6$	2.56	554
2	$3.06 \times 10^6$	3.36	595
3	$3.09 \times 10^6$	4.17	680
4	$2.71 \times 10^6$	5.94	716
5	$2.54 \times 10^6$	6.86	733

Of particular interest in this work is the changes in void object measurements that occur as the specimen becomes progressively more damaged. For simplicity, any growth in cumulative object volume or surface area above that measured in the first (undamaged specimen) scan is hereafter referred to as cracks. The first item to note is that the total number of void objects actually *decreases* with progressive damage. While this is perhaps not intuitive, we must recognize that during damage growth many initially isolated void spaces become connected by the resulting cracks. Thus, void volume and surface area can increase while number of void objects decreases.

The relationship between the growth in volume and the growth in surface area provides additional insight. Initially, increases in both crack surface area and volume are significant, as judged by the relative increases seen in scans 2 and 3 in Table 1. This would be indicative of significant crack extension along with a corresponding crack opening. In the later stages of damage however, the incremental increases in surface area are relatively small, while the increases in volume are still significant. This is best illustrated in scan 4, where there is a 42% increase in crack volume corresponding to only a 5% increase in crack surface area. Clearly significant crack opening is taking place. This phenomenon likely explains the mobilization of fracture toughening mechanisms as discussed below.

## 5. Connections with Bulk Properties

The above measurements are particularly useful when used in conjunction with changes in bulk material properties. In work done to date, crack data has been used to calculate fracture energy

[5][6], and has been used in conjunction with changes in specimen compliance to relate crack properties to a scalar damage variable [10]. In both cases, crack properties are related to properties of the specimen load-deformation response. Relevant load-deformation properties are shown in Table 2.

### 5.1 Fracture Energy

The first chapter of any fracture mechanics textbook defines fracture energy in terms of the conversion of available strain energy to new crack surfaces. That is:

$$G_i = \frac{dU_i}{dA_i} \quad (1)$$

where  $G_i$  is the incremental energy required to grow a crack by an area of  $dA_i$ ,  $dU_i$  is the incremental change in strain energy. Thus one simply needs to measure the change in strain energy that accompanies an incremental growth in crack area. In the fracture mechanics text books, this relationship is traditionally followed by examples where the fracture energy can be calculated for idealized geometries: planar cracks in through-thickness 2D systems.

In this work, however, no geometric assumptions need be made. Changes in strain energy can be calculated using available load-deformation data. This can then be related to the corresponding change in crack surface area to produce the incremental fracture energy using equation (1). The cumulative net change in strain energy is plotted against the net increase in crack surface area for the specimen data presented in Table 2, along with that from a second specimen, in Fig. 9. The plot shows two clear fracture regimes: an initial linear section with a slope of about 90 J/mm<sup>2</sup>, and a second linear regime with a slope approaching 400 J/mm<sup>2</sup>. We have suggested that the initial segment represents fracture dominated by simple tensile cracking, while the latter segment represents the mobilization of a variety of toughening mechanisms, including friction, crack bridging and interlocking [6].

It is important to note that no assumptions about crack geometry were made in the above fracture energy calculation.

### 5.2 Scalar Damage Variable

Continuum damage mechanics is an elegant way to handle the gradual degradation in material properties due to diffuse cracking and void growth. However, in the usual approach, crack distributions are assumed to have a simplified geometry. The relationship between cracking and the resulting material stiffness degradation is based on either micromechanics-based arguments, or continuum representations of crack densities. In either case the relationships tend to ultimately boil down to averaging constants that may or may not have any physical reality.

In an effort to give a physical basis to a scalar damage variable, without making assumptions about the geometries of crack distributions, measured changes in specimen stiffness were related to changes in crack properties. The damage variable,  $D_i$ , was calculated from the changes in specimens stiffness as follows:



Table 2 - Changes in specimen and crack properties from initial condition.

Scan	Specimen elastic modulus (GPa)	Net Change in Strain Energy (J)	Damage variable, $D$	Net increase in crack object volume (mm <sup>3</sup> )	Net increase in crack object surface area (mm <sup>2</sup> )
1	20.7	0	0	-	-
2	20.5	0.0052	$9.7 \times 10^{-3}$	0.80	41
3	16.2	0.0115	0.22	1.61	126
4	9.73	0.0251	0.53	3.38	162
5	6.63	0.0324	0.68	4.30	179

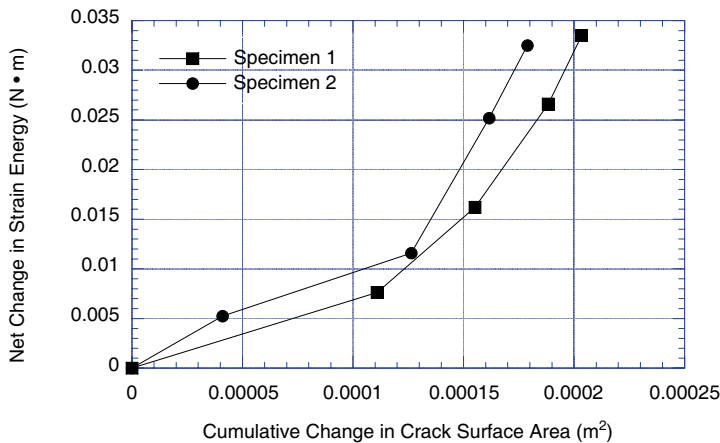


Fig. 9 - Plot of cumulative change in strain energy vs. crack surface energy.

$$E_i = E_1 (1 - D_i) \tag{2}$$

where  $E_1$  is the initial (undamaged) elastic modulus, and  $E_i$  is the subsequent (damaged) modulus.  $D_i$  was calculated by rearranging equation (2), and is presented in Table 2.  $D$  is plotted against the cumulative increase in crack surface area in Fig. 10, while Fig. 11 shows  $D$  plotted against crack volume.

Upon first glance these two plotted relationships might seem counter intuitive. Clearly there is known energy dissipation associated with crack growth that should in turn affect specimen compliance. It is likely however, that the apparent nonlinear relationship shown in Fig. 10 stems from the fact that the measured cracks have a wide, but not random, range of orientations, which might necessitate the need for a higher order anisotropic damage representation. A tensorial representation of the microstructure presented here might be challenging, as single crack objects are themselves multi-faceted and not amenable to traditional geometric descriptors such as crack normal vectors. The crack volume basis for a damage descriptor, while perhaps less appealing from first principles, offers several advantages. First, a reasonably linear relationship as shown here is always desirable for simplicity. Second, the prospects for an in-situ measurement of crack volume, while still not currently reliable, are at least foreseeable in that crack volume can be tied to porosity and pore size distribution, which may one day be readily measurable with techniques such as ultrasonic or electromagnetic imaging.

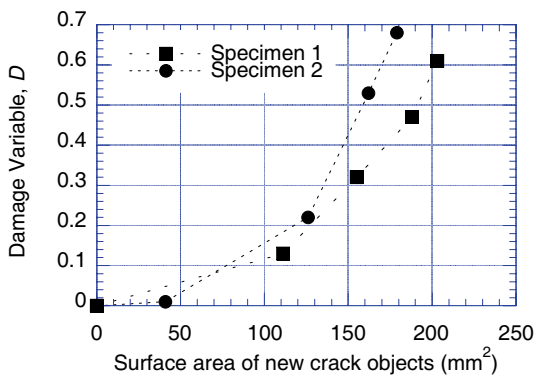


Fig. 10 - Damage variable plotted against cumulative increase in crack object surface area.

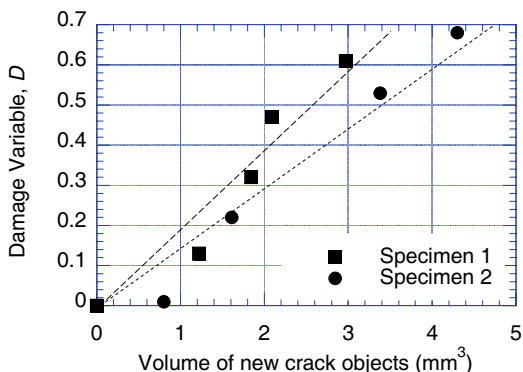


Fig. 11 - Damage variable plotted against cumulative increase in crack object volume.

## 6. Conclusions

The work presented in this paper represents a small, but deliberate first step in an attempt to wean ourselves from simple geometric descriptors of cracks and crack systems. Simple characterizations of 3D surface areas and volumes are a logical starting point, and indeed they provide useful insight into damage evolution in a relatively simple loading regime. The necessary next steps will be to develop more sophisticated descriptors of the crack systems: descriptors that can adequately represent the complexity and interconnectivity of the systems. Once these descriptors are developed, they may be used in material models that are based on a realistic physical picture of microstructure and all the associated mechanisms that affect material behavior.

## References

1. Flannery, B.P., Deckman, H.W., Roberge, W.G. and D'Amico, K.L., 'Three-Dimensional X-ray Microtomography', *Science* **237** (1987), 1439-1444.
2. Bentz, D.P., Martys, N.S., Stutzman, P.E., Levenson, M.S., Garboczi, E.J., Dunsmuir, J. and Schwartz, L.M., 'X-Ray Microtomography of an ASTM C109 Mortar Exposed to Sulfate Attack', in *Microstructure of Cement-Based Systems/Bonding and Interfaces in Cementitious Materials*, S. Diamond (ed.) (Materials Research Society, Pittsburgh, 1995).
3. Stock, S.R., Naik, N.K., Wilkinson, A.P. and Kurtis, K.E., 'X-ray microtomography (microCT) of the progression of sulfate attack of cement paste', *Cement and Concrete Research* **32** (10) (2002), 1673-1675.
4. Bentz, D.P., Quenard, D.A., Kunzel, H.M., Baruchel, J., Peyrin, F., Martys, N.S. and Garboczi, E.J., 'Microstructure and transport properties of porous building materials II: Three-dimensional X-ray tomographic studies', *Materials and Structures* **33** (2000), 147-153.
5. Landis, E.N., Nagy, E.N., Keane, D.T. and Nagy, G., 'A Technique to Measure Three-Dimensional Work-of-Fracture of Concrete in Compression', *Journal of Engineering Mechanics* **125** (6) (1999), 599-605.
6. Landis, E.N., Nagy, E.N. and Keane, D.T., 'Microstructure and Fracture in Three Dimensions', *Engineering Fracture Mechanics* **70** (7) (2003), 911-925.
7. Gonzalez, R.C. and Woods, R.E., 'Digital Image Processing' (Prentice Hall, Upper Saddle River, 2002).
8. Zhang, T., 'Identification of Structural Changes from Volumetric Image Sequence', PhD Thesis, Computer and Systems Engineering, Rensselaer Polytechnic Institute, Troy, NY, USA, (2004).
9. Franklin, W.R., Connect, <http://www.ecse.rpi.edu/Hompages/wrf/research/connect/index.html>, (1999).
10. Landis, E.N., 'Towards a Physical Damage Variable for Concrete', *Journal of Engineering Mechanics* (submitted) (2005).



## **Crack Sampling, Treatment and Analysis.**

Peter Laugesen  
Pelcon Materials & Testing ApS, Denmark

### **Abstract**

Cracks in concrete expose a vast variation in size, extent and influence. To allow for a thorough analysis of the cracks, it is of utmost importance that sampled specimens are representative and treated to reveal, but not modify, the cracks. Analysis of such specimens may facilitate an understanding of the causes of the cracks and hence their future prevention, if relevant.

The presentation is focussed on specimen sampling and preparation, applying a range of techniques including fluorescence impregnated sectioned cores, plane sections and thin sections. The presentation comprises the following issues:

- Sampling of cracks
  - Orientation and placing of cores
  - Coring
  - Cooling agents
  - Core extraction
  - In-situ core treatment
- Treatment of sampled specimens
  - Planning, placing and orientation of sub-specimens
  - Drying, Evacuation & Impregnation
  - Cutting / Grinding / Polishing
  - Cooling & heating
  - Cracks in hard/soft matrix
- Crack analysis

### **1. Detection of cracks**

Cracks in concrete structures are detected especially during drying after a rainy day, see figure 1. An alternative is to provide spray water with a dispenser during the inspection. Other

indications of cracks are precipitations, as the stalactites often seen under bridge-decks or ASR gel, or discolouration on walls e.g. white efflorescence of carbonated leached Portlandite or reddish from corroding reinforcement bars.

## 2. Influence of sampling on cracks

Coring squads are frequently drilling concrete structures to produce holes, not cores. This calls for special attention and instruction when coring structures for crack analysis, as rough handling of the specimens during coring, e.g. caused by the generated heat and (over) load from the drill, breaking-loose of the core or even dropping/throwing the core to the ground, introduces various new cracks to the sample. A typical surface damage is obtained when breaking loose of the core by hammer and screwdriver. When using an extraction tool transferring the load some 40mm from surface, the core can be safely sampled.



Figure 1. The visibility of cracks in concrete structures depends markedly on the weather.

Unavoidable stress release or stress changes in the concrete sample by the coring cause various strains. For cracks placed in relation to reinforcement bars, the crack width may change by such stress release. Another example comprises the pop-outs protruding on the cylinder surface of the concrete cores after some hours, sometimes even capable of lifting 5-10mm thick concrete slices by deeper lying ASR. A special case concerns the documentation of bonding quality, e.g. at casting joints, between concrete and reinforcement bars, and between concrete and spacers. For the latter case, the tensile capacity of the concrete surrounding the spacer is reduced with its reduced volume, causing radiating cracks from the corners of the spacer. This

furthermore generates de-bonding between spacer and concrete. The influence of the sampling in these cases may increase the width of bonding cracks or even introduce them.

Specimens representing the above examples will contain 'false' cracks or markedly enlarged cracks. Great attention and care must be paid to avoid confusing such cracks with the original/true cracks.

The coring sludge must be removed from the core faces by gently washing, to avoid a blocking of possible cracks and porous zones by the sludge, which will obscure the following fluorescence impregnation. Water-cooling normally applied for concrete coring must be expected to influence possible crack precipitations, such as chloride salts,  $\text{Ca}(\text{OH})_2$ , ettringite, gypsum and ASR-gel. This calls for use of other cooling agents or using dry cutting with a diamond blade.

### 3. Inspection of sample

At the initial inspection of the core/sample focus should be directed towards the location and orientation of cracks; scrutinising the sample during drying after application of a light water spraying is a fine help, see figure 2. At this point any influence from the sampling or transportation must be taken into account, frequently leading to the abandoning of the specimen as being non-valid!



Figure 2. Observation of the core during drying may reveal possible cracks.

Planning of the further specimen preparation includes placing and orientation of sub-samples and analysis planes and the possible use of multiple sectioning, multiple orientations and or various profile grinding options. A first understanding of the concrete type, casting and compaction methods and structural influence to the material in your hand will greatly help in the later analysis and assessment.

#### **4. Drying and vacuum impregnation by fluorescent epoxy**

Full-sample vacuum impregnation with fluorescent epoxy [1, 2, 3] has been adapted by the author during 20 years. The procedure has some obvious advantages:

- Weak specimens will be protected during the further laboratory treatment
- Precipitations in cracks and pores are protected against leaching during further lab. treatment
- Possible damages of the specimen caused by (wrong) laboratory handling can be detected
- All cracks or defects with connection to the specimen surface will be impregnated / filled with fluorescent epoxy and are easy to discriminate by aid of UV-light, see figure 5
- UV-analysis facilitates that sub-samples are placed in the most relevant places.

Prior to the impregnation the specimen is gently dried. To reduce the possible influence on the microstructure, this drying is carried out at standardised conditions, which has proven sufficient to remove water from open cracks. Exact procedures of drying and impregnation are given in boxes 1 and 2.

#### **5. Cutting**

After hardening of the epoxy the plastic bag is removed and all sample marks are transferred to the core, which is now ready for sectioning by diamond saw.

Cutting with water-cooled diamond saw of a Ø: 100mm specimen, with a pressure of  $\sim 1\frac{1}{2}$  kg, should provide a cutting speed of  $\sim 5$  cm per minute. If this is not obtained the saw blade must be 'sharpened' by aid of a grinding block to expose new diamonds; ultimately change the blade. Never increase cutting pressure in case of slow cutting speed, as this may damage the specimen. To achieve a uniform cutting pressure on the concrete material, the pressure must be lower at the start and end of the sectioning due to the reduced cross section. A typical damage is shown in figure 5.

Massive amounts of epoxy may be difficult to cut by diamond sawing, as it is too soft; one solution is to cool the impregnated specimen before sectioning. However this is normally not needed when the impregnation is carried out correctly with a minimum of surplus epoxy.

An adequate vacuum chamber, as seen in figure 3, allows for impregnation while the specimen is evacuated.



- Dry core in ventilated oven at 35°C for 16-24 hours
- Wrap core in plastic bag (0.1mm thick)
  - Blunt or cover sharp corners
  - Insert 4/6mm tube to bottom of core (+ ½m)
  - Strap with scotch tape
- Place upright in vacuum chamber
  - Upper part of 4/6mm tube through lid
  - Close tube squeezer
- Evacuation to ~ 10mBar vacuum for 60 minutes
- Mix and stir epoxy
- Place end of tube in epoxy
- Open tube-squeezer gently
  - Allow epoxy to de-gas on entering
  - Adjust tube-squeezer during impregnation
- Cover the specimen completely with epoxy
- Release vacuum gently after 5-10 minutes
- Cool wrapped sample in water
  - Avoid water in the epoxy
- Hardening in 16-24 hours at room temperature

Box 1. Procedure for vacuum impregnation of concrete samples.

- Constituents
  - Resin: BY 158
  - Hardener: HY 2996
  - Dye: Hudson Yellow
- Procedure fluorescence dye:
  - 1 w. % dye added to resin
  - Shake well
  - Magnetic stirred for 2 days
  - Store in darkness
- Procedure epoxy
  - Mix resin & hardener to proportions
  - Stir for 2 minutes
  - Never use last drops of resin
- Safety:
  - All epoxy work in laboratory hut
  - Certified staff required

Box 2. Details of the fluorescent epoxy applied.



Figure 3. Vacuum chamber.



Figure 4. Laboratory damage: Fracture at the lower side of an impregnated core, caused by too high cutting pressure, not adjusted to the reduced cross sectional area. The crack is formed after impregnation, since it is open and connected to the core surface. Image: 5 x 15mm.

## 6. Surfaces for analysis

The relevant faces of the sub-samples to be analysed may be just the cored surface, see figure 5.

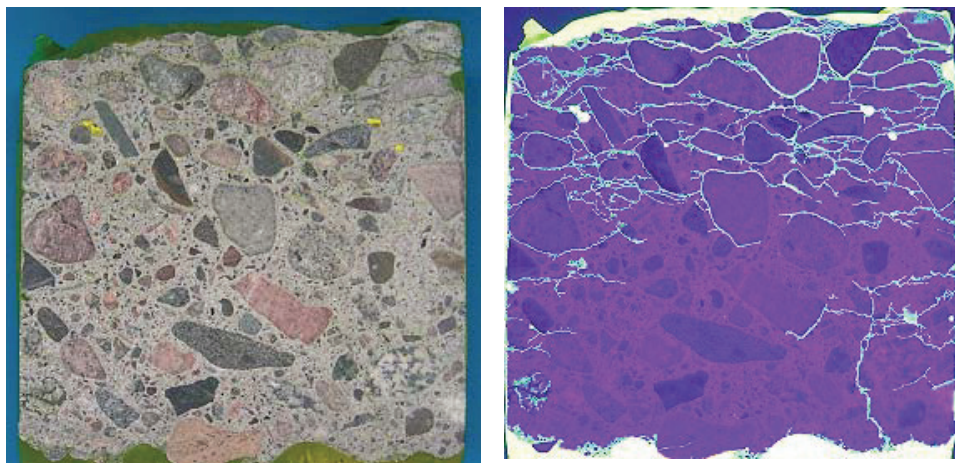


Figure 5. Fluorescence impregnated and sectioned core seen in normal light (left) and UV-light (right). The specimen represents a 30-years old concrete pavement deteriorated by freeze-thaw. Cross section: 150 x 150 mm. From [6].

For finer details a further grinding and perhaps even polishing is required. In this respect it is essential that grinding sludge is removed from the specimen, as e.g. by spray water and short time ultra-sound, yet without damaging the fragile details as non-impregnated crack faces and air void rims. Detailed crack analysis requires the use of fluorescence impregnated thin sections, which also allow for further analysis of the general microstructure. Fluorescence impregnated thin sections require that specialised equipment and procedures are followed, as described in [2, 4, 5].

## 7. Analysis

The limitation of the fluorescence impregnation method is that only open cracks are impregnated, whereas cracks blocked by e.g. ASR gel or massive precipitations of ettringite or  $\text{Ca(OH)}_2$  will not be impregnated. Hence the analysis must be made using both normal light and UV-light. Low-angle light, e.g. by cold-light lamps, is essential to evaluate the surface quality and to aid the detailed analysis.

The UV-light or ‘black-light’ is provided by use of e.g. ‘Philips TLD 18 W/08 H7’ lamps, and requires shading from normal light. The use of barrier filters isolating the fluorescent light enables a finer discrimination between the impregnated cracks and the surrounding concrete. Simple yellow filters for photo application are applicable, although LWP 515 filters ensures a better distinction.

Detailed UV-analysis of cracks may be blurred by transmitted light from deeper in the samples, especially in transparent aggregates, such as marble and light coloured granites. In this case fluorescent thin sections may be required.

Quantitative analysis of the crack systems comprising crack types (coarse, fine, micro), areal content, orientation, spatial distribution, dendritic length, average width and connectivity may be performed; details not described in the present paper.

To ensure that the crack analysis is assessed correctly, it is essential that the spatial extent of the cracks is taken into account; hence the third dimension must be included. Crack planes placed close to and semi parallel to the analysed surface may be overseen or mistaken for preparation defects.

The UV-analysis must be carried out in combination with normal light analysis to ensure that non-impregnated cracks are also included. Such cracks could be filled by other material, as already described or be without connection to the impregnated surface of the core. In these cases a second impregnation and re-grinding of the specimen surfaces may be required, as for impregnated plane sections [1, 3] of thin sections [2, 4, 5].

In case of multiple crack causes, a combination of specimen types of impregnated, cut sections, plane sections and thin sections are required. To understand the often complex nature of such crack systems, details must be assessed of the crack extent, phase-boundaries, irregularity, crack dislocation, carbonation depths, precipitation sequences, self healing, re-opening of cracks etc. Once the picture seems to be established it is viable playing 'the devils advocate', frequently exposing alternative solutions.

In the following a few examples are presented of various crack types and causes, see figures 6-10.

## References

1. Henrichsen, A. & Laugesen, P.: *Monitoring of Concrete Quality in High Performance Civil Engineering Constructions*, in S. Diamond et al.(ed): *Microstructure of Cement Based Systems / Bonding and Interfaces in Cementitious Materials*, MRS Volume 370, 1994, pp. 49-56.
2. Jakobsen, U.H., Laugesen, P. and Thaulow, N. 2000: *Determination of water to cement ratio in hardened concrete by optical fluorescence microscopy*. In: Khan, M.S. (ed) *Water-Cement Ratio and other durability parameters - Techniques for determination*, ACI SP-191, pp. 27-41.
3. Testing of Concrete, Hardened Concrete: *Production of fluorescence impregnated plane sections*. Danish test method DSF 423.39:1998.
4. Testing of Concrete, Hardened Concrete: *Production of fluorescence impregnated thin sections*. Danish test method DSF 423.40, 1998.
5. Nordtest Method, NT Build 361, 1991: Concrete, Hardened: *Water-cement ratio*
6. Peter Laugesen: Unpublished Pelcon reports.

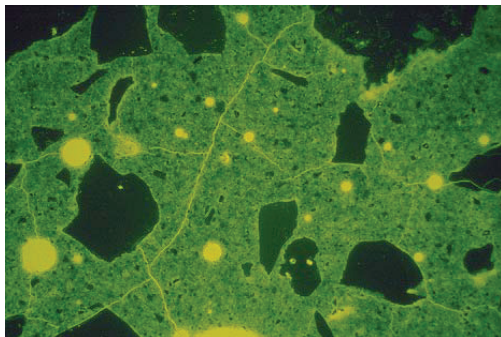


Figure 6. Micro cracks in concrete caused by chemical shrinkage during the hydration, due to too low sand content, i.e. too high ‘spacing factor’ of the sand grains. Thin section photo, 1 x 1.5mm. From [6].



Figure 7. Industrial concrete floor with map cracking. The upper 2-5mm delaminated due to excessive and late trowelling of the surface. Coring of such structures must be expected to cause some damaging of the fragile surface layer, unless initially sealed/injected with (fluorescent) epoxy. From [6].

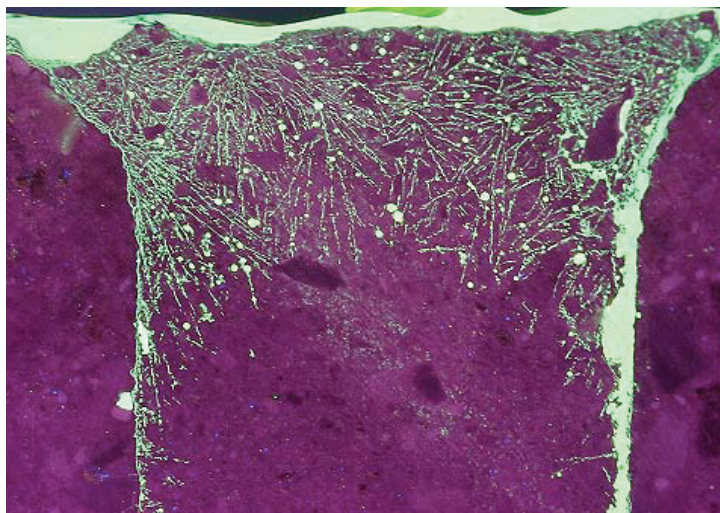
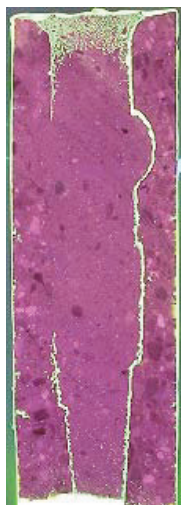


Figure 8. Left: Grouted joint between two floor elements, just visible in each side of the 300mm long core; Vertical lines mark de-bonding. Right: Close-up of upper part of grout showing numerous small cracks caused by freezing of very young concrete; hence the cracks are imprints after ice-wedges. From [6].



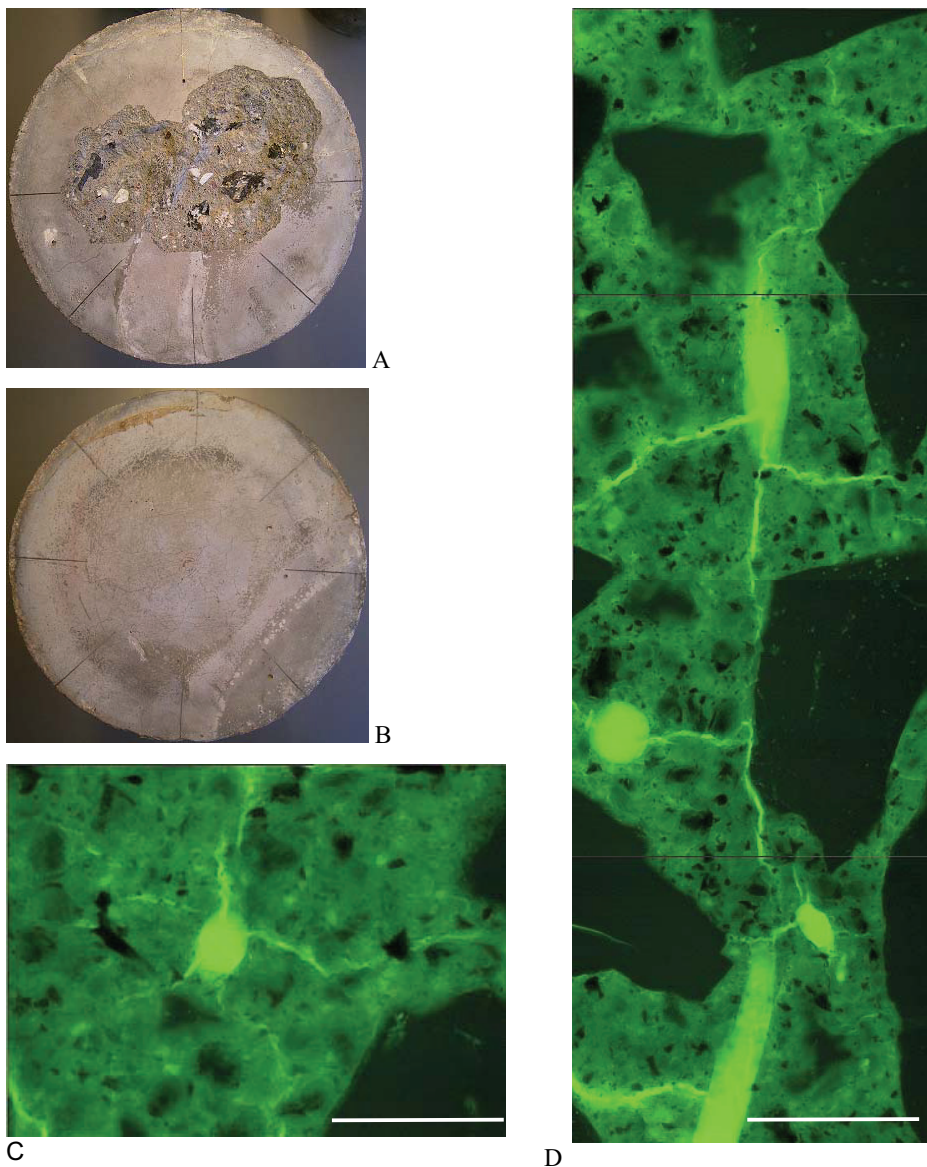


Figure 9. Fire tested concrete cylinders, Ø: 150mm, with different amounts and types of PP fibres. A: Marked explosive spalling. B: no spalling. C and D: Thin section photos from sample B, showing empty voids after PP-fibres, with radiating micro cracks; scale bar: 0.1mm. The thin sections cut the PP-fibres in both elongate and perpendicular. From [6].

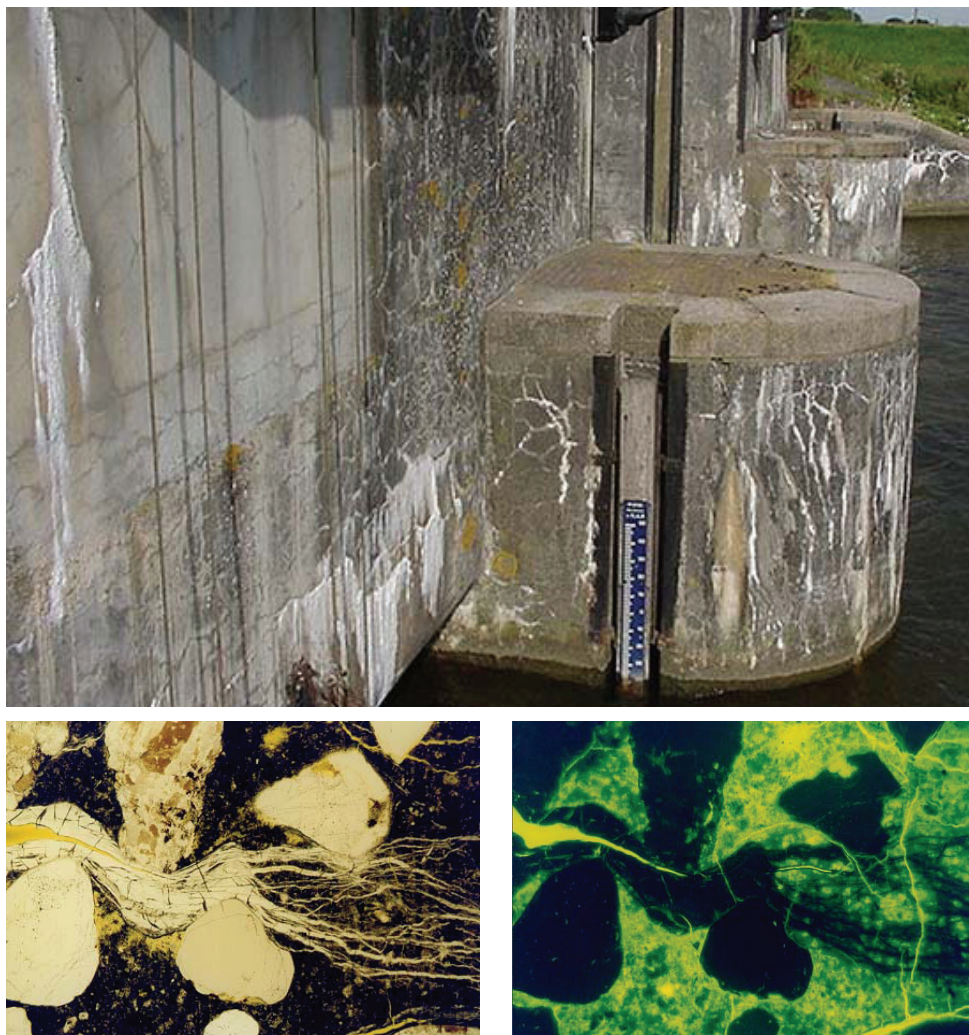


Figure 10. Upper: Water dam affected by marked crack development, mainly caused by ASR. Lower left: thin section photo from the same structure, showing multiple generations of gel-filled (white) radiating cracks from ASR grain (left of the photo). Image: 1 x 1.5mm. Lower right: same field of view, but seen in fluorescence light mode; the gel precipitations appear black, whereas open desiccation cracks formed in the laboratory by drying of the soaked concrete appear yellow-green. From [6].





## **The Modeling of Micostructure to Predict Service Life of Concrete Structures**

Kiyofumi Kurumisawa and Toyoharu Nawa  
Graduate school of engineering, Hokkaido University, Japan

### **Abstract**

A principal objective of “material science” is to establish relationships between processing techniques, microstructure, and properties of materials. The study of the microstructure is a relatively new field which has gradually evolved as an integral part of material science and is often considered to be the observation and description of matter in the scale ranging from atomic dimensions to engineering components such as structural members. The formation of microstructure of cement paste is influenced by the distribution of solid particles in solution phase as well as development of hydration of the cement. This presentation discusses these modelling of the microstructure and its relationship between microstructure and durability of concrete for civil engineering student to appreciate the importance of cement chemistry.



## **Dense and Porous Areas in Concrete: An Artifact?**

Sidney Diamond

School of Civil Engineering, Purdue University, U.S.A

### **Abstract**

In recent papers the writer has called attention to observations of perceived local inhomogeneity of hardened cement paste in concretes and mortars. In particular the distribution of locally porous and locally dense areas observed in backscatter SEM has been emphasized. Very recently, Wong and Buenfeld have challenged these findings, and consider that the apparent inhomogeneity is due to an artifact associated with failure of the epoxy to penetrate uniformly to the plane of observation created by grinding and polishing the SEM specimen. Results of ongoing investigations by the writer and others into this question will be reported.



## **A system of concepts to enhance the information content of online documents in concrete technology**

Jens Borrmann and Joachim Schwarte  
Institute of Construction Materials, University of Stuttgart, Germany

### **Abstract**

E-Learning is a frequently discussed topic and subject of today's activities in the development of modern information and communication technology (ICT) applications, not only in training on the job or the service industry but also in the scientific research at universities. The Institute of Construction Materials (IWB) at the University of Stuttgart worked on different kinds of e-learning projects like *WiBA-Net* [1], *100-online* [2] and *self-study online* [3] and is still learning from its experience of transferring knowledge with the aid of modern ICT. Additional projects like *BiM-Online* [4] which focused on the possibilities of knowledge transfer via the World Wide Web open up the technological possibilities of the upcoming Semantic-Web standards with its idea of machine readable metadata.

The results of both areas of activity, the e-learning part and the research on information technology using modern online standards, ended in thinking about a basic system of concepts to increase the information content of online documents dealing with terms of concrete technology. The main goal is to realise a data and content model which is able to enhance the readability and comprehensibility of online documents by presenting additional, context related information about concrete technology issues.

The paper will give an introduction to the technical aspects of this development as well as the possibilities to disseminate the results with the aid of modern online technologies of e-learning and W3C metadata standards.

### **1. Introduction**

Today the learning environment of a student at the university mainly consists of visiting lectures, doing practical exercises and, especially in the preparation towards the exam, intensive studying of technical literature e.g. the lecture notes. Within several research programmes and IT projects, which will be introduced in chapter 2, the Institute of Construction Materials at the University of Stuttgart was able to test different ways to impart knowledge not only in the field of higher education at the university but also in the daily usage

at civil engineering consultants. The fact that the projects were funded and financed by different organisations was quite an advantage, as the IWB was able to test and rate different approaches at the same time.

Overall it has to be said, that the production of online material is a very time-consuming work. Independent of the unique projects, all of the needed information has to be extracted and then be recorded with a suitable application. After realising a CD-ROM project which also uses online technologies, these circumstances were the decisive factors to develop the software application *LORe* (Learning Objects Repository [5]). *LORe* allows a database based collection of online content objects and additional metadata annotation in one single step. Furthermore, it is able to reference even the smallest information units like single statements to guarantee an efficient reuse of this content in future projects. The fact that this information is saved without any layout information, makes it possible to reuse and disseminate them in different views and different complexity.

These principles have shown the potential but also the raising problems of content repositories dealing with smallest content objects. The ongoing work will be the development of a data structure like a system of concepts which is able to cope with these problems and enhance the functionalities towards an open system.

## 2. Projects

### 2.1 BK:/3

In 2002 the publisher Ernst & Sohn released the multimedia CD-ROM *BK:/3* [6] that was intended to become the third part of a well-known two volume yearly publication called *Beton-Kalender*. In the framework of this project the IWB developed the part related to the field of concrete technology. The goal was to realise a framework that merges the new standards DIN EN 206-1 and its national extension DIN 1045-2 as well as delivers fundamental knowledge about the construction material concrete. This additional information was derived from essays published in the *Beton-Kalender 2002* [7].

Besides the chapter structure of the standard as well as of the related part of the *Beton-Kalender* and a full text search, there was also a list of keywords being implemented to help the users browsing through the content and finding the information they need within the whole hypertext system (Figure 1a). Each single term of the generated list was linked to the most relevant chapter. In the chapters lots of concrete technology terms are also highlighted to show the user that there is additional information in other parts of the system (Figure 1b).

### 2.2 100-Online

The e-learning programme *100-online* was founded by the University of Stuttgart in 2001 with the aim to launch projects which enable the usage of multimedia techniques within the local lectures. Therefore the main concern of the project *Werkstoffe im Bauwesen 2* (engl.: *Construction Materials 2*) was to digitise and structure the lecture materials in the same way they are presented in the lecture hall. At this time the development of a new software application called *LORe* was initiated at the IWB.



## 2.3 WiBA-Net

At the same time *100-online* was in progress, the IWB was involved in another e-learning project called *WiBA-Net*. *WiBA-Net* was financed by the funding programme “*New Media in Education*” which was announced by the Federal Ministry of Education and Research (BmBF) in 2001 and lasted until the end of 2003. Authors of different civil engineering institutes as well as architects took part as content authors. The development of the learning management system and the pedagogical consulting was managed by computer scientists and pedagogues. The objective of *WiBA-Net* was to realise an e-learning platform that contains all the learning content mentioned in the professors’ memorandum [8] and provides all the different facets of e-learning functionality like communicative and teaching components.

Besides commercial software tools like *Macromedia Dreamweaver*, *LORe* was also used by the IWB as an application to collect online e-learning content, to generate single screens for teaching paths and, with its ability to refer even single sentences, to realise the *WiBA-Net* glossary. In addition to the global access to the glossary with the aid of a search box presented on the *WiBA-Net* website (Figure 3a), the glossary was also implemented into the screen view in a very efficient way. With the internal structure of the database the system is able to embed context related definitions automatically (Figure 3b).

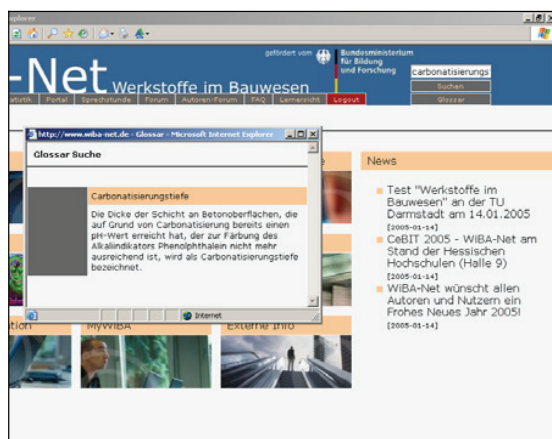


Figure 3a: WiBA-Net glossary

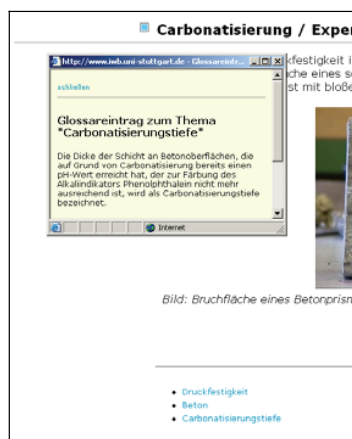


Figure 3b: LORe screen glossary

## 2.4 Self-Study Online

As a second step towards an “Online Campus” the University of Stuttgart started a new programme in 2003 called *self-study online*. The main goal of the projects launched within this initiative was to provide enhanced e-learning objects to the students to improve their knowledge without the need of visiting additional lectures at the present university. The learning material to the lecture “*Construction Materials 2*” which was already collected and implemented into the LORe database during the 100-online project, was enhanced with more detailed information about special subjects.



Therefore, a further application module was developed to organise and structure single screens and to combine them to bigger e-learning sequences, called stacks. At the beginning of the development, the functionality of these stacks was limited to display a linear combination of screens but the ongoing work ended in context based navigation mechanisms which make it possible to jump to content related screens of other courses without losing the way back to the starting point (Figure 4).

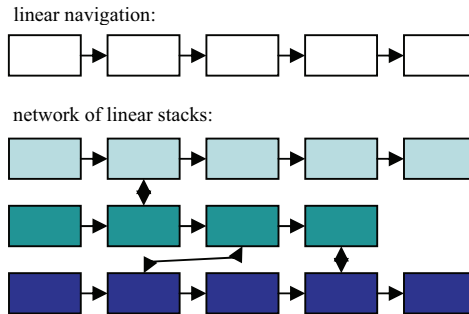


Figure 4: Navigation possibilities in the *self-study online* environment

### 3. Technical Solutions

To make online content reusable and therefore sustainable as well, it is essential to choose highly flexible technologies which are able to represent semantic relationships between single objects in a focused concrete technology domain. The *BK:/3* project has shown that the usage of static links between content units is indeed highly sustainable because of the approved and established technologies like HTML and JavaScript which were used. However, in the field of online accessibility the idea of reusability and portability is getting more and more important.

As a next step to a better reusability, LORe was developed and used in all of the following three e-learning projects to record and structure the needed content units and to provide them in a very fine granularity. LORe itself is an open source application using the online-database backend MySQL [9] and the scripting language PHP [10]. This choice was made to guarantee an economic development, a maximum of transparency and the benefit of a database backend to map all the needed content connections in a table structure.

The content collection and creation with LORe follows a very atomistic approach. This is necessary to reference and track even the smallest unit (asset) of information in the whole system. To do so, not only the size must be taken into account, but also the annotated metadata describing each single unit. The following different content types can be represented by LORe

- *terms*: To index the textual assets (e.g. statements)
- *Statements*: definitions, mnemonic sentences, text fragments
- *Global structure*: (= chapter headings of an as finest as possible structure which finds general approval)

- *Local structures*: (= chapter headings of an existing course structure or course compendium)
- *Asset URLs*: World Wide Web address of content resources (pictures, videos, textual documents, transparencies, etc.)
- *Asset-Captions*: multiple asset captions to describe assets in different contexts
- *Lokalmaterial-URLs*: URLs of resources (PDF documents, PowerPoint presentations, transparencies etc.) which should be presented to the local students but not to the whole system
- *Screens*: Arrangements of assets and statements and Assets, which can be disseminated in different layouts
- *Stack*: sequences of screens which are thematically linked to each other

To create a single screen, the authors have the possibility to browse through the asset collection, to mark each of the assets that should be shown in the screen and, as a final step, to arrange them in order to their appearance in the screen (fig. 5).

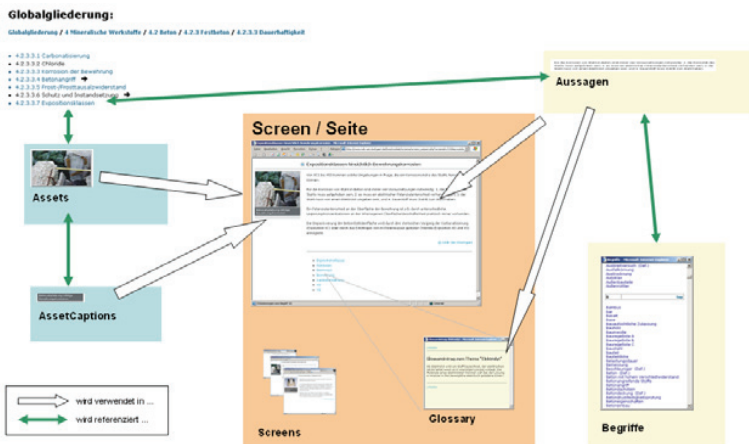


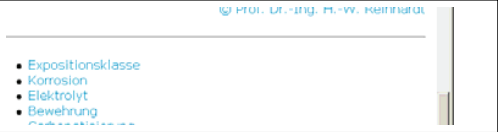
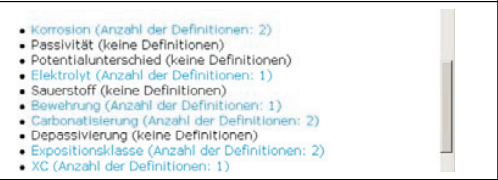

Figure 5: Dynamic compilation of a *LORe* screen about exposure classes for corrosion

This compilation of single assets is also stored in the database backend so that they can be displayed in different layouts. The circumstance that the system knows the appearance of each single text fragment in any situation at any time can be used to realise different intelligent software modules. One of these modules is the automatic screen glossary which displays all relevant terms in the screen automatically that had already been defined within the system.

The example in figure 5 “exposure classes for corrosion” is subject of a single screen generated by *LORe*. On this screen the following statement is displayed: “The loss of the passive film which protects the reinforcement in a concrete structure can be caused by the infiltration of chloride (exposure classes XD and XS) or by the loss of alkalinity due to carbonation (exposure class XC)”. While the author applies this sentence to the repository to refer it to the

screen, he also has to submit concrete relevant terms, like passive film, reinforcement, chloride, exposure class, XC, XS and so on. The application is now able to track the terms which are annotated to the statement. If there are already definitions of the terms in the system, they will be shown as a glossary entry in the screen with a link to these assigned definitions. Because of the dynamical compilation of the screens, *LORe* is able to control the visibility of the glossary links in different ways (Table 1).

Table 1: Possibilities of displaying a screen glossary

Glossary of relevant terms which were annotated to the screen statements and are already defined within the system.	
List of all terms related to the statements in the screen including information which term is already defined in the system and which is not. (authors' view to see the lack of definitions in the system)	
No glossary at all.	

Bigger learning objects which are called stacks are realised in the same way as screens. The composition is stored in the database and the layout comes with the displaying application. The only difference is that it is not a compilation of single assets, but a linear sequence of screens which can be stored in a table base as well. The author simply has to label the stack and relate the reference number of the needed screens to it. To define the correct order of the screens within the stack each of them has to be rated. With this information *LORe* is able to present a course providing all the needed navigation buttons and contents of the aggregated screens.

To guarantee an effective data transfer between different applications like *LORe* and the *WiBA-Info-Pool* [11], *LORe* was enhanced by an interface which generates XML-metadata documents based on the SCORM specification [12] (Figure 6). Besides the pedagogical and administrative metadata, like authors' name, date of creation, object type, MIME-type, aggregation level, there also are information to the content itself like keywords and the global structure of the *WiBA-Net* project.

In this case XML-documents are used as structured datasets. The inherent data is a result of a SQL-query which collects information about a single e-learning object over different relational database tables. That means that the module that creates the metadata set has to know about the structure of the database backend to build up a complete metadata-set and to compile a machine readable XML-document for exporting the information.

4. Cognition

Because of the different aims of each single project, it was possible to try several knowledge transferring facilities with regard to their suitability for daily use. The following table shows the different applications in relation to the projects and their use within this field.

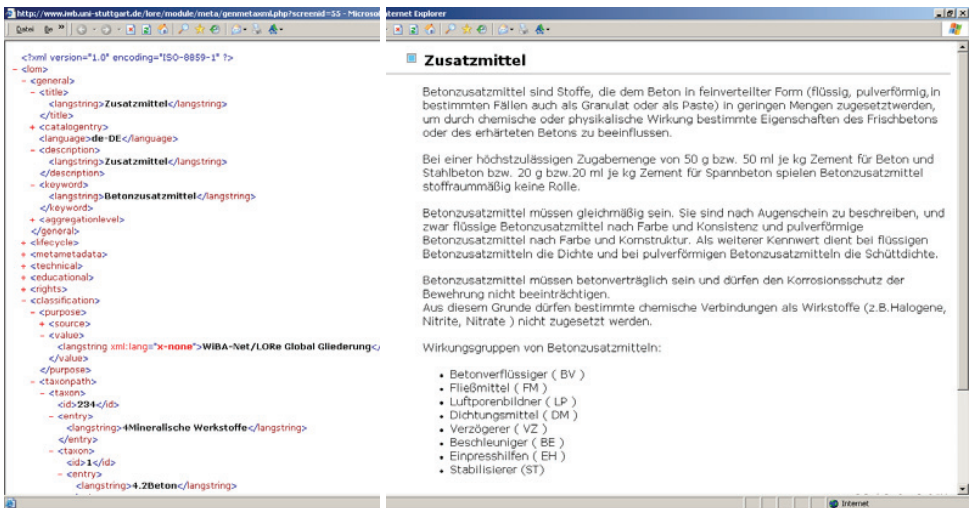


Figure 6: XML-metadata of a LORe screen about concrete additives

Table 2: Knowledge delivering applications and their usage in knowledge representation and structuring at the IWB

Application	Projects	Usage
WiBA-Net network	WiBA-Net	Collection and delivering of assets, webpages, and learning paths, metadata-editing
LORe	100-online	Collecting assets and text fragments, metadata-editing, generating list of terms
	WiBA-Net	Screen production, generating list of terms, generating a glossary
	Self-Study online	Screen and stack production and presentation, generating a list of terms

Regarding the knowledge transfer with the aid of a multi-authors environment which *WiBA-Net* is, it was obvious that the attractiveness of e-learning content for a student studying at a present university is related to the fact whether the content is quite close to the outline of the lecture or not. The internal user access statistics of *WiBA-Net* have shown that the number of students who logged in and activate learning paths even rose shortly after these paths were discussed in

the lecture hall. Furthermore, it was obvious that the students especially noticed the learning paths which were created at the universities they are registered at.

In all of the projects content extraction, digitalisation and metadata annotation became a very time intensive work, so that it has to be thought about the reusability of already recorded knowledge not only within the same application but also within other information systems dealing with the same domain. The first step has already been done by dividing larger learning objects into small assets and storing them in a relational database with the possibility to retrieve them in a quite comfortable way. The second step must be to provide mechanisms and data structures to make single assets available in different information environments.

## 5. Terms, Concepts, System of Concepts

The usage of keyword lists to browse through a known information system as well as glossaries to deliver additional information to existing documents dealing with concrete technology issues are mainly helpful in every situation where these documents are the basis of decisions between persons who do not have equal knowledge, not only in higher education but also in the daily work of civil engineering consultants.

To realise a needed data structure that has the potential to be used in different environments it has to be considered that the minimum of complexity of the single information objects like statements and definitions has to be bound to a semantic layer (Figure 7). Only if this semantic linking is expressive enough it can be expected that an information system can display additional information in a considered context. Therefore the semantic layer can be developed as a system of concepts.

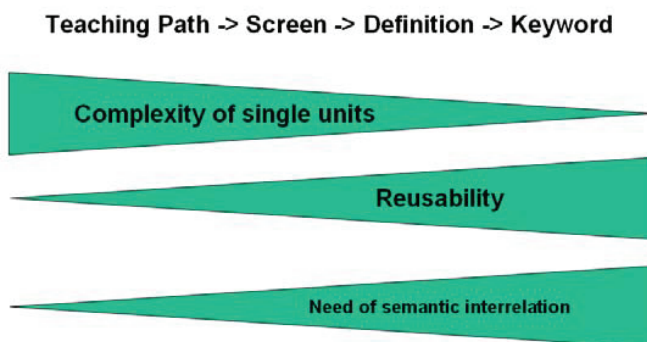


Figure 7: Correlations between complexity, reusability and therefore the need of semantic structures of different information units

To structure an unsorted list of terms like it has been collected within the *LORe* system or the *BK:/3* project, it is important to take different scientific disciplines into account. Besides fundamental knowledge of concrete technology, the developments of computer sciences, library science and semantics as a special field of linguistic as well as several national standards [13],[14] dealing with this subject have to be considered, too.

In semantics for example, it is strictly differentiated between terms and concepts to explain the process of the human way of thinking and understanding and expressing things in a dialogue. This matter of fact was manifested in the German national standard DIN 2330. It defines a concept as a unit which is in somebody's mind, whereas a term is a written or spoken representation of a concept. The relation and the difference between a term and a concept might be described with the semiotic triangle (Figure 8).

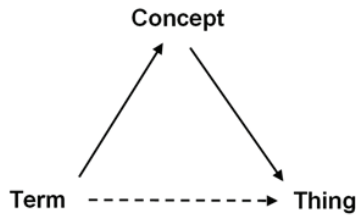


Figure 8: Semiotic triangle

A dialogue between two persons about a topic or thing in concrete technology for instance which can be material or immaterial, runs always over these two peoples' mind, their imagination of the real existing thing. This is the reason why misunderstanding can easily occur. The characteristics of a concept which defines the thing and separates it from other concepts depends on at least two things - the context a person makes up his mind on a thing and the knowledge a person has about a thing or an issue.

Talking about *dispersion* for example, a physicist is thinking about an optical phenomenon, the colour dispersion, but in the context of concrete technology it is a fluid-solid mixture. The other problem that might complicate a dialogue is the difference of knowledge between the two persons, especially if a person expects his partner to have the same level of knowledge. The physicist thinks of a homogeneous grey coloured construction while talking about a concrete wall but the authorised civil engineer wants to know the load to calculate the amount of steel within the construction. In a face-to-face dialogue, the engineer and the physicist will clear the blur if they realise that they talk about different things or rather talk on a different level of expertise. A technical information system that should enhance a document repository in an automatic way must have the ability to decide in which context which information should be present adequately. The direct link between a real item and a term without the idea of a concept can only be successful if the term is embedded in a clearly defined vocabulary like it is in mathematics for example. In the civil engineering sciences there's no such unambiguousness. Depending on the point of view "concrete" can represent totally different things. The term can even be an adjective like "precise".

To equalise the meaning of terms in a dialogue it is important to define a representative vocabulary and to use it consequently. A system of concepts would be a semantic basis to enhance documents by providing a semantic layer which is able to define the context of used

terms. DIN 2331 defines a system of concepts as a number of concepts which are linked to each other and thus getting a connected unit.

Systems of concepts themselves can be realised in different semantic complexities. The three bigger groups are classifications which are mostly structured hierarchically, thesauri and at last ontologies which have the most powerful semantic expressiveness (Figure 9).

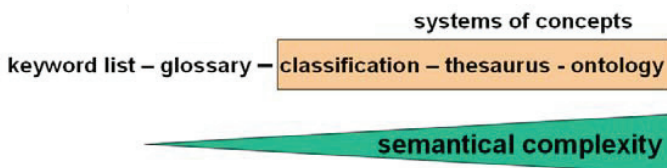


Figure 9: Knowledge representation systems

The previous projects have shown that the combination of relational database systems and serialised data streams provides a great potential to open up a closed system and delivers content to other applications. With the aid of the already approved technologies and the additional semantic web recommendations, a system of concepts can be developed that is not only a part of the *LORe* system but can also be adopted by other information systems because of the possibility of exchanging the semantic structure.

The needed compatibility can be guaranteed by using standardised web mark-up languages deriving from the semantic web activities of the World Wide Web Consortium [15]. These languages were developed to provide standards which have the needed functionality to serialise data structures like systems of concepts in a machine readable format, covering all the semantic relations. The already used XML-metadata files of the *SCORM* derived metadata sets don't suffice to cover this goal, because not the concepts themselves are being related to each other but the single learning objects. Furthermore, the relations in the existing metadata set can only be established by a hierarchical structure. The online technology OWL [16] seems to be even more suitable. OWL is an acronym for Ontology Web Language and became a W3C recommendation in February 2004. The main target of this language is to provide the technology to define systems of concepts up to ontologies which can describe knowledge domains in a machine readable way. OWL uses the RDF [17] syntax which was already proved in finished research activities [18].

## 6. Vision

A system of concepts representing the knowledge domain of concrete technology can be adopted in different fields. In a document repository it can be used as a controlled vocabulary to support the process of indexing documents, dealing with concrete technology issues like testing or inspection results of concrete constructions. The fact that each single concept is linked to another makes it possible to deliver additional information to the correlating documents in a semi-automatic way, even more if the single concepts have already been described in the semantic structure. This integrated approach can help to minimise

misunderstandings in the daily dialogue and also brings different documents in relation to each other. In companies it might be possible to merge existing data and knowledge islands by referring them to an integrative basis that has the possibility to combine further information presented even in the World Wide Web in a semantic manner.

## References

1. WiBA-Net Portal, <http://www.wiba-net.de>, 2005.
2. Universität Stuttgart, 100-online, <http://www.uni-stuttgart.de/100-online>, 2002.
3. Universität Stuttgart, self-study online, <http://www.uni-stuttgart.de/self-study/>, 2003.
4. BiM-Online Portal, <http://www.b-i-m.de/>, 2001
5. Learning Objects Repository – LORe, <http://www.iwb.uni-stuttgart.de/lore4lore/>, 2003.
6. Zilch, K.; Schmidhuber, C.; Quast, U.; Reinhardt, H.-W.; Koptik, J.; Schwarte, J.: BK:/3: Interaktive Beiträge aus dem Beton-Kalender. Berlin: Ernst & Sohn, 2002. - ISBN 3-433-02528-2
7. Reinhardt, H.-W.: Beton. In: Eibl, J. (Hrsg.): Betonkalender 2002, 91 Jg. Berlin: Ernst & Sohn, 2001.
8. Reinhardt, H.-W.; Franke, L.; Grübl, P.; Setzer, M. J.; Wittmann, F. H. (eds.): Hochschullehrer-Memorandum: Werkstoffe im Bauwesen – universitäre Lehre und Forschung. In: Bauingenieur 75(2000), Nr. 11, S. 723-729.
9. MySQL, <http://www.mysql.com>, 2005.
10. PHP – Hypertext Preprozessor, <http://www.php.net>, 2005.
11. Schwarte, J.; Borrmann, J.; Reinhardt, H.-W.: *Computer aided teaching in civil engineering materials science at the University of Stuttgart*: Proceeding of the Knud Højgaard Conference Advanced Cement-Based Materials – Research and teaching: Lyngby, 12-15 June 2005. – in print
12. Advanced Distributed Learning Initiative, Sharable Content Reference Model (SCORM) Version 1.2, The SCORM Content Aggregation Model, 2001 - <http://www.adlnet.org/>. 2003.
13. DIN 2330: Begriffe und Benennungen. Ausgabe 12.93. Berlin: Beuth Verlag.
14. DIN 2331: Begriffssysteme und ihre Darstellung. Ausgabe 04.80. Berlin: Beuth Verlag.
15. DIN 1463: Erstellung und Entwicklung von Thesauri. Ausgabe 11.87. Berlin: Beuth Verlag.
16. W3C: Semantic-Web: <http://www.w3.org/2001/sw/>. 2005
17. OWL Web Ontology Language Overview: <http://www.w3.org/TR/owl-features/>
18. RDF Resource Description Framework (RDF) / W3C Semantic Web Activity: [www.w3.org/RDF/](http://www.w3.org/RDF/). 2005
19. Schreyer, M.: met@BiM - Ein semantisches Datenmodell für Baustoffinformationen im World Wide Web (Anwendungen an Beton mit rezyklierter Gesteinskörnung). Mitteilungen des Instituts für Werkstoffe im Bauwesen. Bd. 2002/5. Dissertation. IWB. Universität Stuttgart, 2002.



## **Computer Aided Teaching in Civil Engineering Materials Science at the University of Stuttgart**

Joachim Schwarte, Jens Borrmann and Hans-Wolf Reinhardt  
Institute of Construction Materials, University of Stuttgart, Germany

### **Abstract**

During the past five years the Institute of Construction Materials at the University of Stuttgart (IWB) has participated in different projects concerning e-teaching. Amongst other efforts co-workers of IWB have created a set of virtual content concerning concrete technology within a German e-teaching network in civil engineering materials science called “WiBA-Net” ([www.wiba-net.de](http://www.wiba-net.de)).

The content of this network consists of teaching material that is organized at four different levels of granularity. At the most basic level single items (“assets”) are collected. At the second level such assets are arranged into single pages filling one screen. Several pages dealing with aspects of a single topic are ordered into a teaching path at the third level and finally a set of teaching paths forms an entire course at level four. Virtual searching methods are offered on all four levels depending on the state of the user. Besides the mentioned teaching material also virtual communication facilities are offered within the network. During the work on WiBA-Net, which consists of six German Universities, questions concerning the reusability of virtual content, metadata enhancement techniques and the concept of Blended Learning were focused. Educational and didactic aspects have been closely taken into account and quality assuring evaluation methods have been applied.

Meanwhile first experiences have been made in real life teaching and learning situations, which give us an idea of future needs and development in the field.

### **1. Introduction**

With its funding programme “New Media in Education” the German Federal Ministry of Education and Research aimed at the development of virtual teaching content using multimedia techniques and the World-Wide-Web (WWW). Equally important was the integration of E-Learning modules into real life curricula to be reused in the daily work of faculties and students [1]. In the years 2000 to 2004 more than 100 projects with a total of more than 500 single

project partners at German universities and other scientific institutions were supported with a total amount of more than 200,000,000 €.

## 2. WiBA-Net

One of the projects that have been funded within the mentioned framework has had the aim to cover the field of construction materials in civil engineering. This project is called WiBA-Net. Table 1 gives an overview of the participating project partners in the WiBA-Net project. WiBA-Net is the only system of its kind in Germany and has the goal to gather all e-learning activities concerning the covered topics.

Table 1: List of the initial WiBA-Net project partners [1]

University	Professor
Technical University of Darmstadt	Prof. Dr.-Ing. Peter Grübl
Technical University of Berlin	Prof. Dr.-Ing. Bernd Hillemeier
Technical University of Hamburg-Harburg	Prof. Dr.-Ing. Lutz Franke
University of Stuttgart	Prof. Dr.-Ing. Hans-Wolf Reinhardt
University of Duisburg-Essen	Prof. Dr. rer. nat. Dr.-Ing. habil. M. J. Setzer
University of Leipzig	Prof. em. Dr.-Ing. Dr.-Ing. e.h. Gert König

### 2.1 Basic Concept of WiBA-Net

WiBA-Net covers all topics in the field of civil engineering material science at the level of basic courses typically held at German speaking universities. In [2] almost all Professors working in this field in Germany had agreed on a catalogue of mandatory knowledge items for this purpose.

WiBA-Net is a network that may be useful for all levels of education and further education of civil engineers and architects. WiBA-Net offers interactive and multimedia content that can be integrated in almost all kinds of teaching and learning scenarios in the sense of the so called “Blended Learning” (Figure 1). This means that the traditional teaching framework is in the first instance not significantly changed but only supplemented by new virtual components.

### 2.2 Components of WiBA-Net

The central database of WiBA-Net is called the WiBA-Info-Pool. It is a collection of context-free assets and content aggregations that are composed by use of such assets. Any object in the database can be associated with one or more chapters of the general taxonomy. Agreement on this taxonomy was one of the first steps in the work on the WiBA-Net project. The taxonomy of the WiBA-Info-Pool contains more than 1600 chapters and subchapters on eight hierarchical levels.

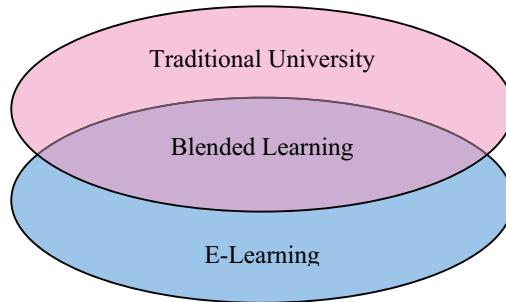


Figure 1: Blended Learning.

The user interface of WiBA-Net is a website (<http://www.wiba-net.de>). The portal of this website is accessible for the public and gives some general overview about construction materials and interesting buildings around the world as well as some background information concerning the project itself. From the portal page the non-public parts of the system may be entered by use of a login-id and a corresponding password. Figure 2 shows the WiBA-Net portal page.

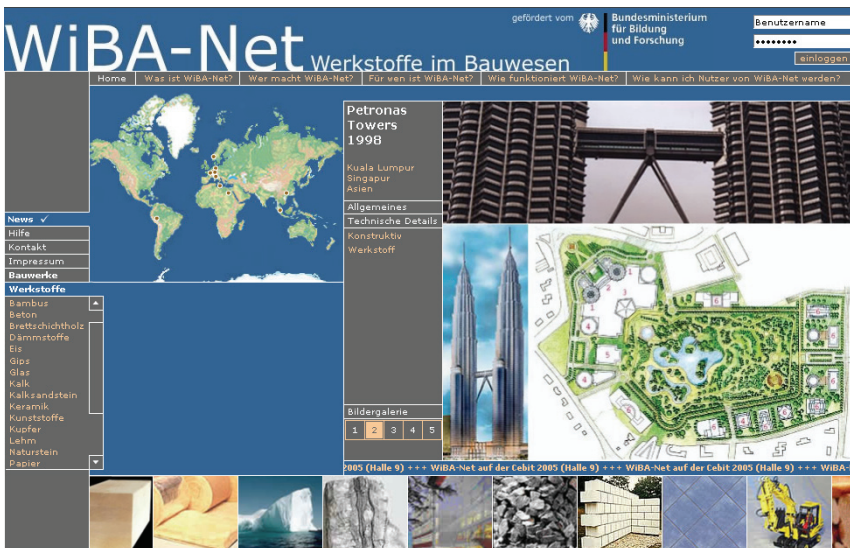


Figure 2: The WiBA-Net portal page ([www.wiba-net.de](http://www.wiba-net.de))

The user database of WiBA-Net recognizes two different groups of users: tutors and learners. Every user of the system is associated to one of the responsible professors.

On the basis of the WiBA-Info-Pool there are four groups of higher system components. These groups cover the

- competence imparting components,
- competence deepening components,
- communicative components and
- additive components.

The competence imparting system components have the purpose to deliver the knowledge to the users. Since learning processes are quite complex, different virtual teaching approaches like delivering smaller learning objects, which can be discovered in an unstructured way as well as guided teaching with the aid of larger learning paths had to be considered. These approaches meet different types of learning strategies like 'meaning oriented' or 'reproducing oriented' [3]. Also different previous and present curricula had to be taken into account.

The competence deepening components shall offer the possibility to extend the acquired knowledge of the users. This group of system components includes a pool of virtual exercises and multiple choice tests. Transcripts of examination questions of recent years are stored in this area as well.

For communication a simple bulletin board system and a chat room application are provided within WiBA-Net. The additive components offer interfaces to external information sources like websites of standardization institutions.

### **2.3 Content Levels**

The content objects in WiBA-Net are organized in four levels of different granularity. The lowest level consists of the assets that are stored in the Info-Pool (see above). This level may not be accessed directly by the learners. It is in fact restricted for the use of tutors during their work on more complex content items or on presentation material for the use during lectures.

Figure 3 shows one typical asset. In a simplified animation the procedures of drying and carbonation of concrete with steel reinforcement under different environmental conditions are illustrated.

The second level consists of single pages that are created on the basis of unified layout templates. Each of these single pages should cover only a single isolated topical item and should be presentable on typical computer devices entirely without the need of scrolling. Figure 4 gives an example of such a single page that is already embedded into a teaching path environment (see below). Such pages are compositions of assets that are given in the WiBA-Info-Pool and additional text elements. Larger assets like animations, movies or detailed figures may be reached via hyperlinks. If such a hyperlink is used, a new window that is significantly smaller than the page window, from which it is called, is created. Such windows are shown only temporarily and contain only a single linked asset without any comments.

The elements of the third level are called "teaching paths". The paradigm of these teaching paths is to act as a guide through the somehow unordered content of the Info-Pool. The

teaching paths are intended to help the learners to discern interrelation between the different items. At present there are more the 200 teaching paths available, which together include approximately 3000 single pages.

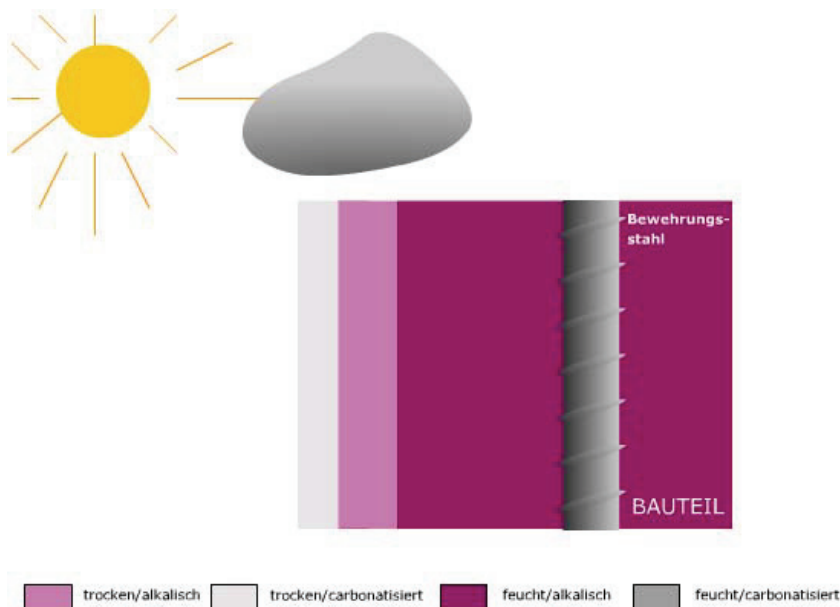


Figure 3: Animated asset to illustrate the procedure of carbonation of concrete

In Figure 4 navigation elements of the teaching path can be seen at the bottom. In this example the caption in the blue bar at the top gives the title of the whole learning path (“compressive strength of concrete”) whereas the headline with the light blue square on the left gives the name of the particular single page (“compressive strength”).

On the fourth level chapters and entire courses are offered. Such chapters and courses are hierarchically ordered lists of corresponding teaching paths. The main purpose of these levels is to be an aid for content navigation during self study.

## 2.4 Technical Aspects

Because reusability of the content of WiBA-Net shall be assured as far as possible, there must be little dependency on proprietary software products. On the other hand an acceptable level of technological quality of the content can only be assured if modern software solutions are adopted. For this reason compromises concerning these problems had to be found regarding the techniques to be used on the four different content levels.

On the lowest content level any file-type was decided to be admissible. Concerning digital pictures it was recommended to store multiple versions of different quality whenever necessary. Animations and interactive elements should be created preferably with Macromedia Flash, since this software product seems to be the leading application in its field.

**Betondruckfestigkeit**

**Druckfestigkeit**

Die Druckfestigkeit ist die wichtigste bautechnische Eigenschaft von Festbeton.

Zur Zeit werden Betone mit Druckfestigkeiten zwischen 10 und 85 N/mm<sup>2</sup> routinemäßig hergestellt.

Hochfeste Betone können, unter bestimmten Bedingungen, Druckfestigkeiten von 150 N/mm<sup>2</sup> erreichen.

Maßgebend für die Beurteilung der Betone ist die Druckfestigkeit nach 28 Tagen, sie liegt auch der Einteilung in Betonfestigkeitsklassen zugrunde.

© Prof. Dr.-Ing. H.-W. Reinhardt

- Druckfestigkeit
- hochfester Beton

BEENDEN      INHALT      ZURÜCK      WEITER

+ Betondruckfestigkeit / Einf...  
+ Einflüsse auf die Be...  
+ Betonfestigkeitsklassen  
+ Betondruckfestigkeitsprü...

Betondruckfestigkeit / Einf...  
Allgemeines zum Begriff der

Figure 4: First page of the learning path concerning the compressive strength of concrete

On the second level, which is the page creation level, it has to be differentiated between static HTML-pages and dynamic pages, that are build on the fly using some server side scripting solution and an appropriate database backend. For the creation of static HTML-pages generality any advanced HTML-editor may be used. The recommendation for this sector was the usage of Macromedia Dreamweaver. It is well known that static web pages have severe fundamental disadvantages in comparison to dynamic solutions. For this reason at IWB a special software solution was created on the basis of MySQL and PHP4. This application is called LORe. LORe has been successfully used within WiBA-Net and some other e-learning projects and is still under further development.

On the third level, which is the presentation level for teaching paths, a software product call L<sup>3</sup> ("lifelong learning") was used. L<sup>3</sup> is a predecessor of an authoring environment that has become a part of the product line "SAP learning solution". A client side JAVA-application is used for content creation. The structure of the learning paths is stored in XML documents. Storage and delivery is done by an associated server side content management system, which is

also based on JAVA. Because of the quite strict structures of WiBA-Net compliant learning paths not all features of L<sup>3</sup> were applicable.

The hierarchical order of the learning paths at content level four is stored in a server side database that was created on the basis of the software product MTS ("modular training system"), which was developed at the IGD in Darmstadt.

For authoring and evaluation of online quiz material like multiple choice tests the software system "Perception" by Questionmark is used.

## **2.5 Didactic Aspects**

The intention of didactic efforts is the processing of content in such a way, that it becomes possible and worth to be learnt by students of certain abilities. A teaching process is of high didactic quality when this aim is reached. This means, that the students shall be supported in their learning efforts and shall be motivated to deal deeply with the topic. Online systems like WiBA-Net may be a valuable part of a teaching concept in this sense.

It is of great importance, that learning targets are specified and available to the learners. For this purpose every learning path has a prefix page that performs this task. It is a fact that the time a learner has to spend using a virtual system in order to reach a specific target, must be bounded. This means that the time, necessary to work through any single teaching path, shall not exceed a certain period of time. As an absolute maximum duration thirty minutes of consecutive online work was determined.

## **2.6 Evaluation and Quality Insurance**

The main criterion for the success of any online system is the intensity of usage that is usually measured by means of hits or clicks per time period. For this purpose detailed statistical information concerning the usage of the system are provided to the tutors on a special web page. This usage statistic provides information on the total numbers of students that use the system. Furthermore it can be seen which teaching paths are visited and how many minutes the users spent visiting any single path on the average.

## **2.7 Metadata**

In order to reach a high level of reusability of the content so called metadata are also of great importance. In the field of e-learning different metadata standards are already available. One of the most well known and most important probably of these standards is SCORM [4].

For the content objects of different levels of granularity in WiBA-Net different SCORM-compliant metadata sets had to be defined. For the input process of all relevant metadata special editor functionalities were developed.

Figure 5 shows chapter 4.2.3 of the WiBA-Info-Pool which is entitled "hardened concrete" as an example. Available subchapters are "requirements", "properties", "durability" and "special types of concrete". In the displayed list there are besides the four subchapters also two references to single assets. The first is a page with the title "hardened concrete" the other one is

a JPEG-picture. For both items the corresponding metadata sets can be reached and updated by using the small hyperlinks that are attached to the names of the items.

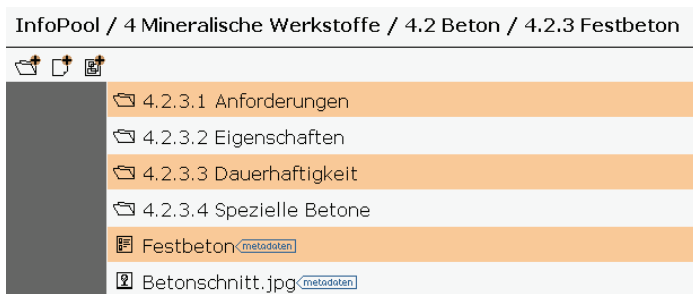


Figure 5: Part of the WiBA-InfoPool

### 3. Current Situation

At the University of Stuttgart a basic level lecture course called „Construction Materials I“ is part of the curriculum of the students studying civil engineering. The lectures are offered for students in the second and third semester with a total of 3 lecture hours per week.

The lectures are accompanied by exercises that are offered once a year in the winter semester. During these exercises the equipment and rooms of the local material research laboratory “Materialprüfungsanstalt Universität Stuttgart (MPA Stuttgart, Otto-Graf-Institut (FMPI))” are used. The here presented testing methods shall give a further knowledge on how to determine characteristic properties of the materials the lectures deal with. The basics of generally used measuring techniques and material testing are shown.

Participation in these exercises is obligatory for the students to take the examination. In accordance with the examination regulations, the exercises cover 2 lecture hours per week. For an efficient execution of the exercises, the students are divided into groups of manageable size of about 16 persons. Twice a week consultation hours are offered by a scientific co-worker of the institute. During the past two years digital videos and pictures of most of the presented experiments were produced and formatted for the use as assets in WiBA-Net.

#### 3.1 Live Presentations

The “teaching paths” of the WiBA-Net content are not intended to be used directly during the lecture hours. In some cases assets from the WiBA-Info-Pool have been integrated into the presentation material. When lectures take place in rooms with advanced technical equipment, it may be possible to store blackboard content and overhead sheets during the lecture directly into the WiBA-Info-Pool. A special system component of WiBA-Net called “digital lecture room” has been designed to assist such methods. Nevertheless it should be admitted that the necessary equipment is not available in most cases.



In Stuttgart the lecture courses were basically not changed with respect to the introduction of WiBA-Net. During the lectures the students are introduced to the WiBA-Net in detail and they are invited to use the system for pre- and postprocessing of the lecture hours, for their self-study and for communication purposes.

### **3.2 Self-Study**

Whether or not virtual systems will be used by students for their self study depends on several conditions like the availability and quality of traditional material like textbooks. If virtual systems and traditional material are competing against each other, the student will mostly prefer that solution that has a closer interconnection to the lectures and to the typical type of question in the examinations.

As one result of surveys that were carried out amongst the system users in the student body of the University of Stuttgart it can be stated that the majority has the opinion that usage of a system like WiBA-Net is too time consuming. One of the statements that the students had to rate within this survey was “I appreciate the existence of the e-learning system”. On the scale varying from 1 (strong agreement) to 7 (strong negation) the determined rating was 2.97, which is quite an agreement. The statement “I frequently use the offered e-learning system” on the other hand was not agreed to (rating = 5.38). This is apparently in contradiction to the common believe, that virtual techniques increase the effectiveness and speed of learning.

### **3.3 Communication**

It has been found out that the need for a special virtual communication tool within the WiBA-Net-system is very limited. The bulletin board is hardly used at all. For asynchronous virtual communication the versatile platform BSCW [5] is used in general. The students of civil engineering get used to that system during the first term, where it's use is obligatory during an introductory lecture course concerning information technology. Since there are some further advantages of BSCW in comparison with the WiBA-Net bulletin board it was recommended to us BSCW for communication purposes concerning the construction material lessons as well.

In the WiBA-Net chat room besides text dialogues also pictures and life drawing may be interchanged and discussed. Such graphically enhanced chat rooms are not very common. For certain purposes the use of such a online chat application is quite interesting. Figure 6 shows an example dialogue in the WiBA-Net chat room.

This advanced chat application is used mainly in a moderated mode on invitation by a certain tutor and only by students from a single university at one time. Different behaviour was not observed at all. Obviously there is no need for cross-university communication between the students that might be facilitated with a tool like the WiBA-Net chat room. Again the little acceptance of the offered communication systems can be explained with survey results (s.3.2). Potentially different behaviour of more advanced students, who are not the primary target group of the WiBA-Net system at the moment, should be object of further research.

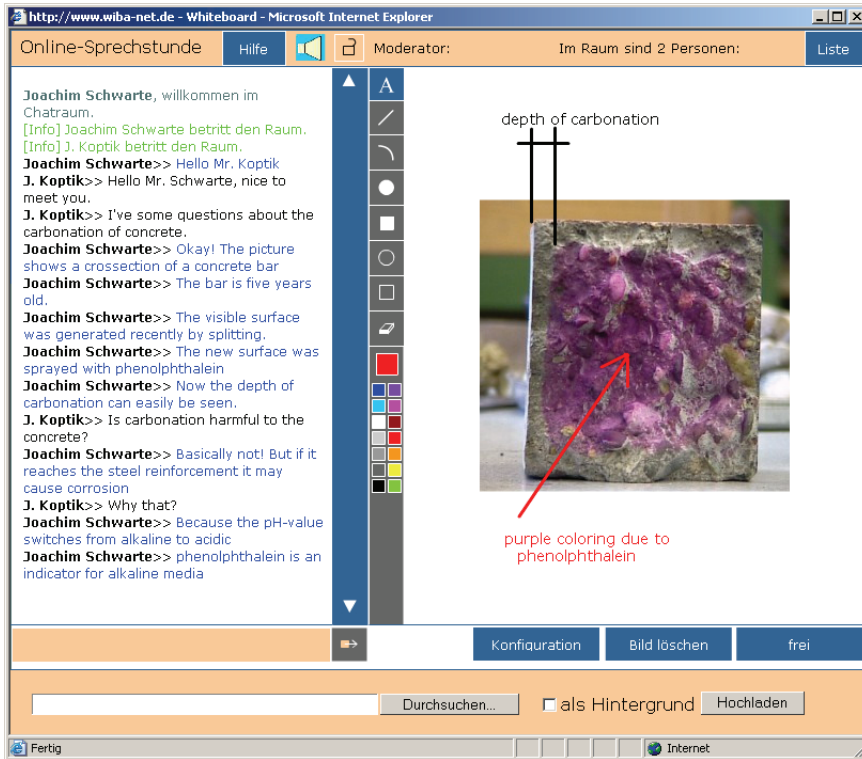


Figure 6: Example session in the WiBA-Net chat room

### 3.4 Blended Learning (?)

We do speak of blended learning but in fact we don't want to constrain the students in their choice, which learning instruments they should use. We do offer increasingly diversified material to the students. This development does not seem to be in too good accordance with the students needs. Especially in the first few terms most students prefer a situation in which there is a set of obligatory teaching resources, which is in total not too extensive. The extent of virtual content is often quite unclear. It has to be considered, that the burden a student has to carry in the first terms of his engineering studies is quite high. Only about ten percent of the entire content of the curriculum, that also contains time consuming courses in mathematics, technical mechanics etc., is covered by the system discussed here. This means that a very deep and long-lasting usage of optional learning resources like e-learning systems cannot be expected. In the mostly short periods of preparation for examinations the situation may be significantly different. Information on the students learning behaviour in such situations is not available so far.

#### 4. Future Needs and Development

Large virtual e-learning systems like WiBA-Net are not easy to maintain. Any changes in the technical standards and in the state of the art should be included quite contemporary. For this purpose a society has been incorporated that mainly is build by the initial project partners. This society is called “Friends of WiBA-Net” and will be formally the operating body of the system in future.

#### 5. Summary

With WiBA-Net a large and complete e-learning platform, that is available to all universities and institutions of higher technical education in Germany, was created. Initially the system was designed and promoted mainly for self study purposes of students studying civil engineering at one of the participating universities and it has been used mainly in this way so far. Different approaches for a closer integration into the teaching situation at some of these universities are still under investigation and may change the described behaviour of the learners in the future. Future maintenance and further development will be assured by a society founded by the project partners. Other universities are invited to become new users of WiBA-Net.

#### References

1. DLR-Projektträger - Neue Medien in der Bildung + Fachinformation (Ed.):
2. *Kursbuch eLearning, Produkte aus dem Förderprogramm*: Bonn, BmBF, 2004. - [http://www.bmbf.de/pub/nmb\\_kursbuch.pdf](http://www.bmbf.de/pub/nmb_kursbuch.pdf)
3. Reinhardt, H.-W.; Franke, L.; Grübl, P.; Setzer, M. J.; Wittmann, F. H. (Eds.): *Hochschullehrer-Memorandum: Werkstoffe im Bauwesen – universitäre Lehre und Forschung*. In: *Bauingenieur* 75(2000), Nr. 11, S. 723-729.
4. Wild, K.-P.: *Lernstrategien und Lernstile*. In: Rost, D. H. (Ed.): *Handwörterbuch – Pädagogische Psychologie*. Weinheim: Verlagsgruppe Belz, 2001, p. 424-428.
5. Advanced Distributed Learning Initiative, Sharable Content Reference Model (SCORM) Version 1.2, *The SCORM Content Aggregation Model*, 2001 - <http://www.adlnet.org/>. 2003.
6. Fraunhofer-Institut für Angewandte Informationstechnik FIT, *BSCW-Homepage*: <http://bscw.fit.fraunhofer.de/>, 2005.



## The Virtual Classroom

Per Møller<sup>(1)</sup> and Mette Geiker<sup>(2)</sup>

<sup>(1)</sup>Department of Management and Production, Technical University of Denmark, Denmark

<sup>(2)</sup>Department of Civil Engineering, Technical University of Denmark, Denmark

### Abstract

The process of undertaking educational classes or programs remotely from schools, campuses or physical institutions that provide them has become revitalized through the application of the internet as a means of communication. Real time online teaching offers at least the same level of effectiveness as traditional classes or workshops, but at a fraction of the costs. The success of training in the virtual classroom depends on the efficiency of the hardware and software platform as well as capabilities of the teacher to control and communicate via the platform.

### 1. Introduction

Distance Learning, i.e. “the process of undertaking educational classes or programs remotely from schools, campuses or physical institutions that provide them” [2], has become revitalized through the application of the internet as a means of communication. Therefore, Distance Learning is now also known as “Online Learning” or “elearning”<sup>1</sup> [2].

A recent issue of Newsweek brings three showcases of Distance Learning [2] arguing that Distance Learning allows you to obtain online qualifications wherever you are and whatever your schedule. This is what we will call “asynchronous elearning”. One of the showcases describes a highly interactive program; however from the webpage neither this program seems to be based on so-called “synchronous elearning”.

**Asynchronous learning** is a learning event where interaction between teacher and students occurs intermittently with a time delay. Examples are self-paced courses taken via the internet or CD-ROM, online discussion groups (usually through Bulletin Board Systems, BBS), and email. Thus, asynchronous learning is today’s variation of the classic letter course, which enlists the computer in the teaching process. [3]

---

<sup>1</sup> “elearning” is spelled in several other ways; “eLearning”, “ e-learning”, and “E-learning”. We have selected the spelling recently used by Newsweek.

**Synchronous learning** is a real-time, instructor-led online learning event in which all participants are logged on at the same time and communicates directly with each other. [3]

In the year 2000 a report was prepared by the American Senate headed by senator Bob Kerry [1] pointing out three major problems related to education;

1. Not enough money is spent on educational research
2. Educational research often does not support enhanced learning performance
3. Educational research often is not accessible to teachers or easily translated into practice

This report had a major influence on the development of online education at The Technical University of Denmark (DTU) as it inspired the first author to make his own experiences. Especially Bob Kerry's statements regarding the quality of research results from the many research activities in didactics emerging through the years without having any positive impact on the proliferation of learning made an impression.

Thus, in late 2003 two Departments at the DTU, Department of Management and Production and the Department of Civil Engineering, established an independent organisation, the "E-Learning Consortium", with the purpose of securing a solid platform for online education as well as carrying out the necessary education and training of future web-educators. In addition the E-Learning Consortium was to provide research funds for new initiatives in the field of elearning.

To reflect the wider perspectives of the platform, i.e. on-line web-based communication in global industrial organisations in addition to teaching, the activities of the E-Learning-Consortium were recently moved to an independent company, KnowledgeComm ApS<sup>2</sup>, located at DTU.

DTU has extensive experience with on-line elearning, including education of MSc-students in fundamental theories, individual learning activities for employees in industrial companies and interest groups, which require cost-effective and application oriented, operational learning, lecturing at meetings and conferences, and project meetings. As a European pioneer of on-line elearning, KnowledgeComm ApS participates in the ongoing development of the American state-of-the-art software platform.

This paper deals with the platform for synchronous elearning and the education of web-educators established at DTU.

---

<sup>2</sup> KnowledgeComm ApS offers web-instructor education, leasing of virtual rooms and consultancy in web-based communication, see <http://www.knowledgecomm.org/>. The actual elearning courses are offered by DTU professors and others.

## 2. Platform for synchronous elearning

Synchronous elearning platforms can facilitate learning sessions, which offer at least the same level of effectiveness as traditional classes or workshops, but at a fraction of the costs. The students are simply connected to the virtual classroom via a normal ADSL-line.

The possibilities are almost without limitations:

- Students can select long distance learning from the best universities with the most relevant courses and best teachers and thereby plan an optimal education
- Employees in companies with many geographical locations can work together on shared projects and development of common competencies
- Interest groups can collaborate on learning activities, independent of location.

A platform for synchronous elearning shall allow real-time on-line two-way communication between lecturer and students. In this **virtual classroom** setting, the instructor or a moderator maintains control of the class, with the ability to “call on” participants. In most platforms, students and teachers can use a whiteboard to see work in progress and share knowledge. Interaction may also occur via audio- or videoconferencing, VoIP or Webcasts. Newest forms include application sharing, where participants can collaborate in using the same software. [3]

After extensive research of various platforms the American Hotcomm-system based in Boston was selected as the educational platform. Reasons were numerous, but among the most important was that the dialogue and support were extremely good in spite of the distance. In addition the cost of establishing a server based in Denmark wasn't in any way prohibitive in order for the use to have the necessary capacity to explore the potential and interest at DTU.

## 3. Training of web-educators

It soon became apparent that a lot of the experiments in synchronous elearning outside DTU were based on random platforms, lack of technical insight, lack of understanding of the weak points of the software and poor abilities to work out academically competent educational material for use on the software platforms.

Education on the internet through synchroneous methods is a very demanding task. It is far more complex for the educator to communicate like this than by traditional means such as in a class or auditorium. It demands a higher degree of preparation, plan of instruction, and carefully prepared teaching materials.

If one is to compare it to other media, then this method of teaching has several similarities with communication of knowledge via audiovisual media such as TV. Actually one can regard the teacher as being a “host” on a TV-Station.

The reason for the limited profit was more a problem based on a lack of understanding of the multidisciplinary technique in didactics, phonetics, and academic competence required rather

than the educational potential of the medium. Thus, a program for training of future web-educators was set up.

The practical implementation of the program has been an interaction between the three elements of the course; 1) technical aspects of the software, 2) phonetics (verbal communication technique), and 3) digital presentation technique, supplemented with practical training (Combination of 1, 2, and 3).

The present training of web-educators at DTU is primarily offered to persons with acknowledged teaching experience. They have to have demonstrated teaching potential in the form of good student evaluations as well as a commitment to teaching. A new group of partners from the hi-tech industry has already agreed on participating in the training of web-educators, realizing the unique possibility of employing this technology in the technical training of staff in far-away destinations.

### **3.1 Training the technical aspects of the software**

The training program is initiated by an introduction to the use of the software. A small group of participants is placed in the same room so that both the person who is acting as teacher and those acting as students is able to view both screens simultaneously.

Many computers these days have a graphics card which enables the connection of two monitors at the same time – by attaching a long cable to one of the monitors it is possible to have a bit of distance in order to give the teachers computer some distance and privacy from the students.

This is done so that the teacher can view the consequences of his/her actions and thereby learn the basic operating procedures of the software and its application in an actual dynamic educational environment. It is expected that the participants during the course of this module is acquainted with use of the chat-system, web-camera, audio recording facilities, the digital whiteboard, shared internet surfing and application sharing in general. The future web-educators are strongly advised to “play” with the software at home, in order to maximize their familiarity with it. Obviously the participants taking part in the training program take turns in acting as the teacher.

### **3.2 Training phonetics**

After the training in the technical aspects the participants takes part in a brief, but intensive training in phonetics (proper speech), didactic and the problems associated with teaching online. The goal of this part is to allow the web-educator to keep his/her style of teaching, but to adapt it to this new medium. The web-educator has to be trained to be self-assured in the educational situation both mentally and psychologically.

The verbal communication part of the course is based in learning how to control the basic functions in voice, speech and breath in order to avoid that the teachers own verbal communication skills is a hindrance for the communication in the virtual classroom. The basic functions, which we focus on, are:



- Placement of the voice
- Tempo of the speech
- Breathing
- Diction/language
- Communication skills (modulation, phrasing).

### **3.3 Training in digital presentation technique**

The third part of the course contains directions on how to prepare the optimal digital presentation on the internet and in the virtual classroom. A particular focal point is the design of overheads or slides. In the near future even video transmission over the platform will be possible. It is important to have a solid knowledge, since presentation material is often unsuitably designed.

The method we use here is simply a demonstration of what to do and what not to do in order to make the teacher aware of some of the possible pitfalls. Many trained educators already have a firm grasp of this and only need little help, but some of the animations and effects commonly used are currently not suited for use online. Limitations in bandwidth and other technicalities make it impractical to employ all the features of the modern presentational software. It is important that the web-educator is aware of the limitations of the software used in the educational situation.

### **3.4 Practical training**

The training is finalized with practical training, where the future web-educators have to combine all the disciplines of the previous lessons. Each of the participants has to prepare a series of lectures in his/her field. The aim is to focus on the didactic part while practicing the technology, the phonetics, and the digital presentation technique.

The lectures primarily take place on the university campus, but could easily take place from other geographical locations. During the lectures several PC's are connected. The web-educator is physically separated from the other participants. More participants can follow the lecture on a projector. The participants are required to follow lectures both as a teacher and as a student since it is important that the web-educators gain insight in both roles of the educational experience. This also develops the technical skills of the web-educators and enables them to improve their online teaching skills. At this moment in time synchronous online education is still in its infancy and in the foreseeable future we are considered pioneers in the field. The teaching sessions are evaluated on a scientific, didactic, and phonetic level.

### **3.5 Test and certificate**

When the web-educator is deemed to have reached an appropriate level of expertise, the KnowledgeComm ApS at DTU offers a one-hour test judged by a group of experts in speaking, education and IT –specialists.

The test is an online synchronous elearning lecture on a subject chosen by the candidate himself/herself. The web-educator may choose to demonstrate his/her abilities acting also as a moderator for someone else, by inviting another web-educator. The educational experience has to be arranged so that the academic judge is actively drawn into the session to demonstrate a certain degree of improvisation during the lecture for instance by co-operating on a task on the digital white-board.

The test should reflect that suitable skills in operating the software have been obtained that the phonetic and digital presentation has a quality that ensures an optimal communication of the subject and that the web-educator is able to activate the students. If the evaluating judges decide that the test is successfully completed, KnowledgeCom ApS will issue a certificate that enables the web-educator the right to offer academic courses on the software platform made available by the KnowledgeCom ApS at DTU.

#### **4. Concluding remarks**

Experiences so far can be summed up like this;

- The industry and the industrial organizations in Denmark, among which is the Danish Engineering Association (IDA), wholly support the idea. The following citations illustrate this;
  - “Lecturers are trained as TV stars. The University has developed its own concept for a second generation elearning, which can be compared to a direct TV transmittance” [5]
  - “A concept, which may facilitate Danish industry’s future competitiveness - to collaborate effectively on development and delivery of the products the customers request” [6]
  - “The companies requests flexible, effective and modular based in-service training, which makes it possible to learn according to needs and at times when it does not interfere with the daily work. Here real time elearning may be the decisive factor.” [7]
- Off course there have been technical problems in the establishment of the platform. Such problems have been solved in cooperation with the software developer. In the foreseeable future new problems will emerge, while the technology is new. This is a law of nature when one is a pioneer in a field. – It is important that the problems are tackled professionally in order to distinguish between software development and actual application problems so that they can be solved in dialogue between the developer and the user. As of now the software is sufficiently advanced for the newly trained web-educators to enable them to offer quality education in complex theoretical academic courses on the Internet.
- The educators are very committed and several have already established web-courses.
- Interested students and colleagues surrounding the core of the elearning group have also contributed to the unique knowledge gathered about synchronous elearning. It has only been by the constant experiments in the academic environment and with the educators as principle actors and constructive critics, that it has been possible to create useable results. Quality elearning probably cannot be created outside of environments where education is a central activity.

- The learning efficiency obtained through synchronous elearning is very high, and the students find the medium most inspiring and challenging. One can spend a few hours in front of the computer at home or at work without having to travel or be absent from normal work, supporting the future objectives of learning: On location, on demand, on-line, just in time.

## Aknowledgements

The section on training phonetics is based on work by Dan Sclosser given in [4].

## References

1. "Report Of The Web-Based Education Commission" Moving From Promise To Practice. (Published By The American Senate In The Year 2000)
2. Newsweek, May 16 2005, pages 34, 64, and 65
3. E-learning ordbog developed for E-learning-consortium.org (Danish – English elearning dictionary), downloaded 13 May 2005 from <http://www.knowledgecomm.org/>
4. Per Møller, Niels Gjerløff, Jørgen Jørgensen and Dan Schlosser: Regarding the development of a new standard for the education of teachers in delivering scientific training on synchronous E-learning platforms. <http://www.knowledgecomm.org/>
5. Niels Christian Nielsen, Interview of Jørgen Jørgensen Knowledge.com ApS, Ingeniøren, 27<sup>th</sup> August 2004
6. Torben Bo Jansen, President, Design Centre for Social Innovation (Institut for Anvendt Fremtidsforskning), September 2004
7. Hanne Schou, Chief Consultant, Danish Industry, October 2004



## **Graduate Education in a Global Market**

M.R. de Rooij  
Delft University of Technology, The Netherlands

### **Abstract**

In a short presentation it is sketched that graduate students have lots of options to tailor make their educational part of their program (at Delft University of Technology), but that reality is that hardly any tailor made technical courses are provided at graduate level. Still it is known that certain blocks of information are very useful for many graduate students in the cement and concrete research, as each graduate student needs a general basis preferably on a higher level than the Master of Science level.

It is suggested to set up a graduate course system around the world (or starting in Europe / USA if the world is too ambitious) that take graduate students for a short but intensive amount of time and educate them at the highest level (Summer School type). Various universities could contribute and should preferably coordinate their topics and agendas, thus providing a general school system for graduate students.

This would stimulate cooperation at university level (coordinating education) as well as at graduate level (easier transfer of knowledge) as well as future contacts (people already know each other in an early stage).

### **1. Introduction**

Work in the field of concrete construction is suffering from the perception that it is a very simple profession industry. Construction workers are typically ridiculed as drop outs from school, whose education stopped after they learnt how to make money. Trying to teach something as simple as making concrete to hardly educated, non motivated students cannot be seen by the general public as a high level university study, because when even a construction worker can handle and make concrete, how hard can it be?

As is known within the concrete industry, it is not that simple anymore. The time of making 1-2-3 concrete has long since passed. There is now a whole variety of concrete mixtures possible and used more and more. In fact in the new Eurocode standard regulations have surfaced on the family concept, meaning groups of concrete mixtures are being given regulations and

specifications instead of every single concrete mixture possibility by itself. The concrete mixture design had become too complicated for regulations at such an individual level and the family concept tries to simplify things again.

Another example of showing the progress in concrete construction is the influence of the environment which is realized more and more. Again, taken from the Eurocode standards there have now been defined eighteen exposure classes. The same thing has happened with the workability classes: seven different classes divided over three different tests make up a total of fifteen workability classes. In other words, concrete construction has grown, has matured and (to keep things interesting) has not reached the end of its possibilities.

Knowing this from our own inner circle is thrilling, but as professors we should get the message across to the outside world starting with our civil engineering (graduate) students. Furthermore, we should do this in such a way, that we not only teach what we know, but go onwards with our Ph.D. students to the areas that we do not know (yet). In this article I have put down my thoughts on a possible way to achieve the aforementioned goals.

## **2. Undergraduate level education**

Starting at the university where I am teaching is giving me a reference point. In the discussion it should be considered as such and not in any way be mistaken for a model how things should or should not be.

Delft University of Technology used to have a five year education program for Civil Engineering students providing them upon graduation with a Masters of Science in Civil Engineering. Within the unifying process in the European Union at Delft University we have changed a few years ago to the Bachelor Masters structure: the original study program has been cut in a three year Bachelor and a two year Master of Science program. The European message is to create more transfer of students between universities: follow a BSc education at one university and a MSc education at another.

Since the introduction of a European BSc – MSc system is still relatively new the effects are not showing clearly yet. Delft is participating actively in the stimulation of European education e.g. through the so-called IDEA league. This group of universities, Imperial College London, Delft University of Technology, ETH Zurich and RWTH Aachen, try to learn from each other's experiences and work towards a coherent educational program.

Inside or outside the IDEA league it is fair to say that the undergraduate educational program provides a general and sound basic training in Civil Engineering Science. This fact will be the starting point for the next step, the main topic of this article: the graduate education.

## **3. Graduate level education**

Again starting from the Delft situation, graduate students are offered general courses like setting up research, presenting research and structured writing of a thesis. Besides these general courses, graduate students have the opportunity to follow courses in their specific field of interest related to their Ph.D. topic. However, graduate students ordinarily have to find these courses themselves. The university on a regular basis offers the general courses, but no regular program exists for the specific field related courses.

In this perspective Delft is different from the general American education of graduate students. In the States graduate students do have a regular scheduled school program, usually the first two years of their Ph.D. program. The level is higher than the MSc level, but since the program is given yearly to groups of graduate students, the content keeps to a general focus.

I am sure within Europe there is a variety for the graduate level education between these two examples going from completely free and use what you need (and can find) like in Delft, to the more structured school program as used in the example from the States.

Time for some numbers. Within our group we would be very happy with two-three new graduate students each year. With a general Ph.D. period of five year, this would mean a group with 10 – 15 graduate students, which would be considered already quite a large group. Let's suppose that Ph.D. students from another groups are also interested in courses on our specific field. For argument sake this is estimated to be 1 – 2 graduate students per year. This would mean we have about 3 – 5 graduate students each year to set up a specific class program on concrete technology related topics.

From an economic point of view this might seem a little overdone: setting up a complete class program for such a small number of students. The effort does not seem to be in relation with number of students. Furthermore, the expected level of education should be of the highest grade for the graduate students. However, as has been shown in the beginning of this article, the world of concrete technology becomes more and more complex, and as a professor one can only know so much; some parts are better left to others to teach.

#### **4. Specialized course weeks**

Moving in the direction of a possible solution, the key issues from the previous sections are first formulated:

- a) Specific education for graduate students within one university has a very limited number of participants.
- b) The level of education necessary rapidly rises above the professor's knowledge for courses outside his own field of interest.

To solve these issues we need to:

- Ad a) Increase the number of participants (hence look outside the own universities).
- Ad b) Ask other specialists to teach their field of interest (person often from another university).

Learning from the European ideas for undergraduate education and the experiences from the IDEA-league a possibility is to have students travel around more for their education. Since in many European universities the graduate students are working on their Ph.D. project when they are not in classes, the educational programs cannot be too long. Therefore, as a first suggestion I am thinking of short intensive learning sessions of one week, or two weeks at the most for one topic.

Such small programs with a variety of participants from various places has many benefits:

- The new generation scientists learn to know each other and their specialties.
- They are being trained by the best in the field.

- It is anticipated that the graduate students will receive new insight on their own topic from fellow graduate students with a different view.
- The graduate students will see new cultures and new approaches.
- The professors will be able to teach their knowledge to a larger group of students.
- The professors can limit themselves to what they know best and enjoy most.
- Professors will only have to prepare their specialized courses instead of a complete course program.
- Professors will have the ability to set up a research program coherent with colleagues from the course week circuit. Hence, they can focus their own research and benefit more from results of other research groups.

## **5. If this where to work?**

What should be done to make it happen? First of all, it should be realized that a leaning program is pursued. It should not become workshop weeks in which various professors give a speech about their work. First and foremost there should be an educational line in the course weeks preferably with learning goals and objectives. Hence, it would mean a tuning of the content of the talks. It does not necessarily mean that a whole variety of professors have to come by and teach. This is only necessary if the topic demands this. It is very well possible that a topic can be taught by one or two professors only.

There should be made a discussion on the topics. Naturally at first everybody is specialist in all topics. However, there are many topics and specialists are always more specialist in one area than in another. To give some examples for possible topics one could think of: characterization, workability, hydration, early age properties, modeling, transportation, and degradation.

A topic that should be discussed amongst the group starting with this concept is calendar coordination. When are which courses taught keeping in mind the various programs and courses of the individual home universities. Also the exchange and costs should be discussed. What do graduate students have to pay? What do they get? What is decided for the traveling and exchange of professors? Are there possibilities for funding the program through the European Union?

## **6. Summary**

In this article a sketch is given of an idea to set up graduate level education on the highest level by specialized course weeks. Specialized course weeks are not new. They already exist, like the modeling week at NIST, the Knud Højgaard Summer School at DTU and recently the Concrete Microscopy Course in Delft. However, these types of specialized course weeks are not connected to each other in a large educational program. It is described in this article how a larger research community could benefit from a coordinated graduate education in a global market.



## **From slump test to Gibbs' free energy: The Science of Construction Materials**

Ole Mejlhede Jensen<sup>(1)</sup> and Sidney Diamond<sup>(2)</sup>

<sup>(1)</sup>Technical University of Denmark, Denmark

<sup>(2)</sup>School of Civil Engineering, Purdue University, U.S.A

### **Abstract**

“In its classical form, the science of construction materials is a descriptive, empirical discipline related to certain types of materials, e.g. the study of the properties of wood, steel, concrete and plastics. This traditional division of the science into the separate study of the different material types is appropriate as long as the purpose is to collect, disseminate and use knowledge about the simple physical and chemical properties of specific materials. Through generations, research, teaching and engineering practice have all functioned within this framework without problems.

However, during the last few decades the nature of the research being pursued within construction materials has changed. Increasingly, construction materials research is carried out by specialists within theoretical disciplines such as physics, chemistry and physical chemistry. The methods used for investigations have become more sophisticated, and it is often necessary to "interpret" the results before they become meaningful for the practical civil engineer.

This development has given rise to an unfortunate gap between research and engineering practice in the field of building materials. Fundamental research has gradually been fragmented into a number of narrow specialist disciplines, making it difficult for the researchers to communicate fundamental new knowledge in a form that can be utilized by the construction materials engineer. And the schism becomes more and more noticeable as research has resulted in development of a number of new construction materials.” [1].

The present talk describes a new concept of teaching construction materials at the university level. The concept which is developed by the late professor Per Freiesleben Hansen aims at overcoming the abovementioned problems. As opposite to classical construction materials teaching, the new concept contains a scientifically coherent treatment where phenomena within construction materials are treated as examples. In this way, the construction materials knowledge of the students is generated through inductive catalysis rather than by deductive teaching.

Per Freiesleben Hansen Danish text book [1] is presently being translated into English: *The Science of Construction Materials*. The translation is expected to be finished during 2005. The text book forms the basis for teaching construction materials on this new teaching concept.

## References

1. P. Freiesleben Hansen, Materialefysik for bygningsingeniører – Beregningsgrundlag, SBI-anvisning 183, Statens Byggeforskningsinstitut, Hørsholm, Denmark (1995) 267 pp.

## **Teaching Building Materials at the Technion – Israel Institute of Technology**

Konstantin Kovler

Faculty of Civil and Environmental Engineering, Technion – Israel Institute of Technology,  
Haifa, Israel

### **Abstract**

This paper describes the place of Building Materials courses in the overall program for undergraduate and graduate studies given in the Faculty of Civil and Environmental Engineering at the Technion - Israel Institute of Technology. The goal in teaching Building Materials is not only to acquaint a student with the main properties of building materials, their production technologies and practical applications, but also to by-pass the limitation of laboratory capacity, labor, time and budget constrains. This target was achieved by building a comprehensive program which includes new laboratory architectural design, library and new multimedia tools to improve the current teaching techniques and to approach a virtual laboratory.

The flow chart of the Building Materials courses is presented. The considerations standing behind the redesign of the Building Materials laboratory are explained. It is shown how the following instruments are used in the teaching process: (a) Internet-based laboratory textbook; (b) Remote access to examples and exercises; (c) Remote experiments; (d) Using the library for construction methods, equipment and materials.



## **The Challenge of teaching cement chemistry to civil engineering**

Karen Scrivener  
EPFL, Lausanne, Switzerland

### **Abstract**

Concrete is a complex solid formed by chemical reaction. In my view it is not possible to properly understand the properties of concrete without an appreciation of chemistry. This is even more true when concrete durability is considered. Despite this Chemistry is not an area with which most civil engineering students are at ease. One can often here a collective wince the moment a chemical symbol is written on the blackboard. This is not helped by the so called cement chemists notation or shorthand, whereby C stands for calcium oxide (or lime!) not carbon. This presentation discusses these experiences and reflects on ways in which civil engineering students can be taught to appreciate cement chemistry.



## **Experiences with Interactive Classroom Technologies for the Implementation of Problem-Based, Peer-Interaction Learning Environment**

Jason Weiss, Sebastian Fait, Tom Schmit and Farshad Rajabipour  
School of Civil Engineering, Purdue University, West Lafayette IN, USA

### **Abstract**

Are you a faculty member who is curious if the class is following what you are presenting? Ever curious to know what the student in the third row is thinking while you are talking about the hydration of cement? Do you spend many sleepless nights wondering how you will increase class participation? Then this presentation is for you. This talk will describe the implementation of an interactive classroom technology that was designed to address each of these questions and to improve your students experience in the classroom.

This presentation will describe the experience of incorporating an interactive classroom response system in a required sophomore/junior level course on Civil Engineering Materials. The course deals with cement, concrete, asphalt, and wood. Since the course is a required class with typically 70 to 100 students, it is often difficult to develop the type of personal interaction that can be achieved in a smaller classroom setting. To prevent the lack of participation that is typical in a large classroom, this course made use of remote response (i.e., remote control) technology that enabled every student to participate and interact throughout the course of the lecture. In addition to encouraging nearly 100% participation and enabling instant grading and attendance, the developed methodology enabled problem-based, peer-interactive learning during the large lecture format. This format enabled students to work on practical problems by teaching one another, thereby reinforcing important class concepts.

This presentation will describe: 1) the interactive system, 2) the methodology for incorporating it in class, 3) the theory and thought process behind the problem-based, peer-interactive learning, 4) examples of the problem-based, peer-interactive activities, 5) outcomes assessment of the approach, and 6) suggestions for future development and use.





## Concrete as an Introduction to Civil Engineering

Eric N. Landis

Department of Civil and Environmental Engineering, University of Maine, Orono, Maine, USA

### Abstract

In order to introduce engineering topics early in the undergraduate curriculum, University of Maine civil engineering students get a taste of engineering analysis and design their first semester freshman year through a course on properties of construction materials. The course serves a variety of functions in the curriculum. As the course title suggests, students get an introduction to the properties of a variety of construction materials, certain microstructure-property relationships, and fabrication issues. However, a second function is to introduce the students to a wide range of issues common to all disciplines of engineering, including experimental analysis, the engineering design process, construction issues, and basic mechanics. We start with basic concepts of material variability and reliability. We then move to basic ways to describe material properties (strength, stiffness, toughness...) and fundamental materials science concepts (bonding, surface energy, defects...). We then focus on specific properties of different common construction materials, of which concrete receives the most attention. While the curriculum is typical of a course in construction material, presenting this subject to first year students is not. While we do sacrifice some rigor by offering the course to first year students, we have found the subject of materials, concrete in particular, to be an excellent means of introducing general topics of engineering analysis and design. This course offers the students a fairly comprehensive and rigorous introduction, far beyond what a typical "survey of engineering" is capable of doing. We have found it contributes to increased retention among first and second year students.



## Author Index

- |                                     |                            |                                  |
|-------------------------------------|----------------------------|----------------------------------|
| Dale P. Bentz 135                   | Eric N. Landis 323, 395    | Hans-Wolf Reinhardt 363          |
| Jens Borrmann 351, 363              | David A. Lange 77          | M.R. de Rooij 383                |
| Klaas van Breugel 205, 311          | Peter Laugesen 335         | Erik Schlangen 311               |
| Sidney Diamond 155,<br>349,387      | Victor Li 233              | Tom Schmit 393                   |
| Lars Dick-Nielsen 265, 277          | Zhi Hua Li 247             | G. De Schutter 205               |
| Raissa P. Douglas 19                | Yi-Shi Liu 77              | Joachim Schwarte 351, 363        |
| Oskar Esping 103                    | Pietro Lura 119            | Karen Scrivener 169, 391         |
| Sebastian Fait 393                  | Ingemar Löfgren 103        | Surendra P. Shah 19              |
| W.R. Franklin 323                   | Per Møller 375             | H. Stander 89                    |
| Mette Geiker 31, 215, 375,<br>IX    | E.N. Nagy 323              | Henrik Stang 31, 265, 277,<br>IX |
| Zachary C. Grasley 77               | G. Nagy 323                | Zhihui Sun 19                    |
| Amedeo Gregori 19                   | Toyoharu Nawa 147, 347     | L. Taerwe 205                    |
| Nynke ter Heide 311                 | Erik Pram Nielsen 215      | Niels Thaulow 155                |
| R.D. Hooton 171                     | Lars-Olof Nilsson 187      | Lars N. Thrane 31                |
| Ole Mejlhede Jensen 119,<br>387, IX | John Forbes Olesen 265     | Jason Weiss 293, 393             |
| Peter Kofoed 1                      | Brad Pease 293             | G. Ye 205                        |
| Konstantin Kovler 59, 389           | Bertil Persson 43          | T. Zhang 323                     |
| Peter Kroes 3                       | Peter Noe Poulsen 265, 277 | Jun Zhang 247                    |
| Kiyofumi Kurumisawa 147,<br>347     | Aleksandra Radlinska 293   | GPAGvan Zijl 89                  |
|                                     | Farshad Rajabipour 393     |                                  |
|                                     | Paul Ramsden 17            |                                  |

